Geology and Genesis of Volcanic-hosted Massive Sulphide Deposits in the Tasik Chini District, Central Peninsular Malaysia

by

Mohd Basril Iswadi Basori
B.Sc. (Hons.), MSc. (Geology)

UNIVERSITY OF TASMANIA

A thesis submitted in fulfillment of the requirements for the degree of Doctor of Philosophy

CODES ARC Centre of Excellence in Ore Deposits
University of Tasmania

November 2014

Declaration

I declare that this thesis does not contain any information or material that has been accepted for the award of any other degree or diploma at any other institution. To the best of the authors' knowledge, this thesis contains no material previously published or written by any other person, except where due acknowledgement is made in the text. All referenced material is listed at the back of the thesis.

Mohd Basril Iswadi Basori

November 2014

Geology and genesis of volcanic-hosted massive sulphide deposits in the Tasik Chini district, Central Peninsular Malaysia

Mohd Basril Iswadi Basori

ABSTRACT

The Tasik Chini volcanic-hosted massive sulphide district is located about 250 km southeast of Kuala Lumpur in Pahang State, Central Peninsular Malaysia. The district comprises two significant ore deposits, the Bukit Botol and Bukit Ketaya of precious metal-rich, polymetallic massive sulphides with barite and silica-iron-manganese oxide within the Permo-Triassic volcano-sedimentary sequence of rhyodacitic-rhyolite flows and related volcaniclastic units. LA-ICPMS U-Pb zircon dating of footwall and hangingwall sequences from the Bukit Botol deposit yielded an Early Permian (273 ± 8, 286 ± 4 and 292 ± 3 Ma) age. Similarly, the zircon U-Pb age results at Bukit Ketaya reveal a well-constrained age of Early Permian (286 ± 2 to 288 ± 4 Ma). These zircon U-Pb results demonstrate that the felsic volcanic units and associated mineralisation at both deposits are consistent with the broader Early Permian volcanism within the East Malaya Block. Triassic volcanic and plutonic rocks are also widespread in the Tasik Chini deposit and surrounding area. Their LA-ICPMS U-Pb zircon ages are constrained at 233 ± 4 to 242 ± 2 Ma.

The XRF whole rock trace element compositions of the Early Permian host rhyodacite-rhyolite at the both Bukit Botol and Bukit Ketaya deposits show high to moderate HFSE (e.g., Nb, Y, Zr) contents and are characterised by transitional-calc-alkaline affinity of a subduction-related volcanic island arc type setting. Trace element patterns for these units normalised to primitive mantle show strong negative Nb and Ti anomalies relative to Th and La. The chondrite-normalised REE patterns of these rocks are also enriched in the LREE showing near-flat trends for the HREE with negative Eu anomalies. All trace element and REE data are consistent with a tectonic environment of a volcanic arc setting. In comparison, the trace element data of the later Triassic volcanics and intrusions from the Tasik Chini area demonstrate a moderate to low HFSE composition, transitional to tholeiitic affinities, but has a similar magmatic arc signature. The differences in geochemical data between the Early Permian host rhyodacite-rhyolite and the later Triassic volcanics and intrusions are likely due to the Permo-Triassic tectonic progression from a volcanic arc environment to collisional setting within the East Malaya Block.

The Sm-Nd isotopic studies also support the tectonic progression of arc-related magmatic events. Early Permian host rhyodacite-rhyolite is characterised by high $\varepsilon_{Nd}(T)$ values (-0.8 to +0.4) with calculated Nd model ages (T_{DM2}) of 0.97 to 1.05 Ga, whereas Triassic volcanic and related intrusions ($\leq$ 250 Ma), show lower $\varepsilon_{Nd}(T)$ values (-3.6 to -1.0) for volcanic rocks and $\varepsilon_{Nd}(T)$ (-5.2 to -4.5) for intrusive rocks with the older T_{DM2} age (1.02 to 1.38 Ga). These differences show that the Early Permian host rhyodacite-rhyolite from Bukit Botol and Bukit Ketaya deposits are slightly evolved having less crustal influence, whereas the Triassic volcanic and plutonic rocks are significantly more evolved and relatively contaminated.

The Bukit Botol and Bukit Ketaya deposits delineate a similar style of mineralisation and sulphide assemblages, but their alteration styles are different. In general, the stringer zone with minor massive sulphides/layers form directly below the mineralised zone at the footwall, whereas the barite, Fe-Mn and Fe-Si layers occur at the top of the mineralised zone or the upper part of the stratigraphic levels. The main sulphide phases include pyrite, chalcopyrite, sphalerite, rare galena and trace Sn-bearing minerals. Gold- and Ag-bearing minerals are present in the massive sulphide and barite layers at the Bukit Botol deposit but absent at the Bukit Ketaya deposit. At both the deposits, there are pure chemical sediments deposited during formation of the massive sulphide lenses, as a result of changing oxidation-reduction conditions and fluid compositions with increasing distance from the hydrothermal vent site in a local submarine environment. The Fe-Mn layer is discontinuously formed at Bukit Botol, whereas the Fe-Si layer has developed as a stratigraphic marker at Bukit Ketaya, both forming distinctive exhalite assemblages.

The geometry of alteration assemblages at the Bukit Botol and Bukit Ketaya deposits show that they occur as semi-conformable or stratabound zones around the ore lenses. The Bukit Botol deposit is characterised by proximal quartz-sericite-pyrite and distal quartz-sericite alteration zones, whereas distal quartz-chlorite-sericite-pyrite-pyrophyllite±kaolinite and proximal quartz-chlorite-pyrite±carbonate±pyrophyllite form the alteration assemblages of the Bukit Ketaya deposit. In addition, the molar elemental ratios of Na_2O/Al_2O_3 versus K_2O/Al_2O_3 and MgO/Al_2O_3 versus K_2O/Al_2O_3 support that the abundance of muscovite (sericite) and chlorite controlled the intensity of alteration at the both deposits. Therefore, the difference in quartz-chlorite-sericite alteration assemblages between the Bukit Botol and Bukit Ketaya deposits, in combination with the presence of pyrophyllite and kaolinite as shown by SWIR and XRD results in Bukit Ketaya

deposit suggest variable mixing of hydrothermal fluids with seawater and a possible minor magmatic contribution.

Electron microprobe analysis of sphalerite from the Bukit Botol deposit reveals a range of 0 to 24.0 mole% FeS, whereas sphalerite from the Bukit Ketaya deposit shows a range of 0 to 3 mole% FeS. Although the sphalerite has a wide variation in composition, a discernible decreasing Fe trend is exhibited from the stringer zone towards massive sulphide. This compositional variation in sphalerites reflects variable temperature and activity of sulphur during ore formation. LA-ICPMS analytical data, coupled with textural characteristics, provide evidence for significant variations of trace elements in different pyrite types at Bukit Botol, having pyrite 1, pyrite 2 and pyrite 3 in paragenetic sequence. The suite of As, Se, Te, Cu, Zn and Pb trace elements show decreasing trends from pyrite 1 to pyrite 3, and a high Co but lower Ni contents in pyrite 1 and pyrite 3 compared to moderate Ni and low Co values in pyrite 2. Review of all data and trace element patterns from Bukit Botol suggests that the precipitations of Au, As and trace element in pyrites are likely to be related to reduction of sulphur from seawater under specific pressure and temperature conditions. However, a minor magmatic fluid contribution may also be inferred from the high Se (7−650 ppm) and Co (0−1192 ppm) concentrations in pyrites.

Measured $\delta^{34}S$ values of sulphides from the Bukit Botol deposit range between -0.8 and +4.1‰, and one sample displays a higher $\delta^{34}S$ value of +8.3‰. Meanwhile, the $\delta^{34}S$ values for sulphides from the Bukit Ketaya deposit are characterised by a range of $\delta^{34}S$ between -2.9 to +3.6‰. These data suggest that ore-forming fluids for these deposits are likely to have originated from a mixed sulphur source of reduced seawater sulphate with the possible addition of magmatic sulphur. The sulphur isotope values for barite from the Bukit Botol and Bukit Ketaya deposits are similar and range from 11‰ to 22‰, with a mode of 13 to 19‰. These ranges are close to the published composition of seawater sulphate during Permian time, and provide supporting evidence that these deposits formed during a submarine Permian volcanic event.

Lead isotope values of sulphides from the Bukit Botol and Bukit Ketaya deposits are 18.04 to 18.20 for $^{206}Pb/^{204}Pb$, 15.43 and 15.56 for $^{207}Pb/^{204}Pb$ and 37.96 to 38.35 for $^{208}Pb/^{204}Pb$ ratios, less radiogenic and similar to those of the host volcanic rocks (18.10 to 18.20 for $^{206}Pb/^{204}Pb$, 15.53 and 15.59 for $^{207}Pb/^{204}Pb$ and 37.96 to 38.26 for $^{208}Pb/^{204}Pb$). The Pb isotopes exhibit a primitive arc (i.e., island-arc setting) with a significance ocean island volcanic arc input and

suggesting a mixed source from crust/juvenile arc and mantle. These similarities of lead isotopic composition of the sulphides and host volcanic rocks may indicate that lead for the both deposits were sourced mainly from the host sequence with some lead being derived from a basement lead reservoir during the Permian.

Microthermometric analysis of fluid inclusions in quartz and barite from the Bukit Botol and Bukit Ketaya deposits yields homogenisation temperatures of 180-310^{o}C with no fluid inclusion evidence of boiling. Salinities, densities, pressure and depth of ore forming fluids range from 1.0 to 14.3 wt% NaCl equivalent, 0.711 to 0.970 g/cm^3, 12 to 93 bars, and ~ 1500 m depth of seawater. Laser Raman spectroscopic analysis show the presence of CO_2 (100 mol%). Seawater is suggested as the main ore fluid in the formation of these deposits, but contribution from a magmatic source is indicated by higher salinities relative to seawater (3.2 wt % NaCl) and the presence of CO_2.

All present geological, geochemical, isotopic and fluid inclusions data indicate that the Bukit Botol and Bukit Ketaya deposits are seafloor volcanic-hosted massive sulphide deposit type, and correspond to many criteria of the bimodal felsic-hosted type. With respect to broad geological setting, this Early Permian volcanic-hosted massive sulphide deposits in the Tasik Chini district has similar features to the setting of the Miocene Kuroko deposits in Japan, which formed in an arc-related environment. The deposits are suggested to have formed during the Early Permian subduction-related arc/back arc volcanism, which is considered to be a part of the Palaeo Tethys Ocean evolution at the eastern Gondwana margin of the East Malaya Terrane. The deposits are considered to have formed during an early period of active volcanism and sedimentation, and the area was probably associated with a small rhyolite dome within a submarine felsic dominated volcanic centre. The exhalation of mineralising hydrothermal fluids was coeval with the effusive rhyolitic volcanism and then terminated by the deposition of sedimentary units that directly overlie the volcanic sequences and mineralised zones at the both deposits. Evolved seawater significantly played a major role in the ore forming process with a minor magmatic fluid contribution as supported by the mineralisation characteristics, alteration assemblages, S-isotopes and fluid inclusion data.

ACKNOWLEDGEMENTS

This PhD thesis has benefited from the expertise, assistance and support of numerous people over the past four years. First and foremost, I would like to thank Government of Malaysia and National University of Malaysia (UKM) for providing me the initial support and scholarship, and funding from Ore Deposit of SE Asia Projects led by Prof. Khin Zaw for supporting to the completion of this PhD project.

I especially would like to acknowledge and thank Prof. Khin Zaw, my main doctoral supervisor for his excellent research discussion, technical and field guidance, support, encouragement, his time to read and re-read my endless versions of thesis chapters and editing, and all of the patience he has shown to me over the life of my research. I am also grateful to my co-supervisor Prof. Ross Large for his mentorship, interesting ideas and critical reading of thesis chapters.

I would like to express my gratitude of acknowledgement to Professor Ross Large, Professor Bruce Gemmell and Professor Jocelyn McPhie who have coordinated the progress of my PhD program. Thanks to Dr. Garry Davidson, Dr. Sebastien Meffre, Dr. Andrew McNeil and Dr. Kenzo Sanematsu for their encouragement, helpful comments and input for thesis chapters. Prof. V. Maslennikov from the Russian Academy of Science is thanked for his time and patience during a fruitful discussion about 'exhalite'.

Thank you to Dr. Sandrin Feig, Dr. Karsten Goemann and Ms. Christine Cook of the Central Science Laboratory (CSL), UTAS for the electron microprobe with SEM analyses, and the sulphur isotopes analyses. I also wish to thank Prof. Leonid Danyushevsky for teaching me on how to do pyrite mapping, and same goes to Dr. Sebastien Meffre for his knowledge and

expertise in zircon age dating and Pb isotopes analyses. Thanks also to Dr. Nic Jansen and Dr Lejun Zhang for helping me to get started and interpreted the SWIR data.

Dr. Ralph Bottrill and Mr. Woolley of the Mineral Resources Tasmania (MRT) are thanked for their assistances in the XRD analyses. I am grateful to Dr. Terry Mernagh of the Geoscience Australia (GA), Canberra for his patience in analysing the fluid inclusions by Laser Raman spectroscopy. Many thanks also to Dr. Roland Mass of the University of Melbourne (UniMelb) for his patient instruction and assistance in analysing the whole rock samples for Sm-Nd isotopes. I wish also to thank Dr. Matthew Steele-MacInnis (Matt) from the Virginia Tech, USA for his kindness in providing me the $H_{OKIE}F_{LINCS}$_H2O-N_AC_L spreadsheet.

While at CODES/SES, UTAS I have benefited from formal and informal discussions and help with many of the postgraduates, staff and visiting staffs. In particular, Takayuki Manaka, Abhisit Salam, Charles Makoundi, Jeff Steadman, Yungu Lim, Lee Xuan Truong, Joe Knight, Dr. Somboon Khositanont, Dr. Jacqueline Halpin, Dr. Zaoshan Chang, Dr. Mike Crow, Dr. Andri Subandrio and Dr. Mega Rosana were all happy to help with lab tasks and constructive discussions. In the labs, I appreciated the assistance of the following people: Peter Cornish, Al Cuison, Phil Robinson, Katie McGoldrick, Jay Thompson, Isabella (Izzy), Ian Little, Keith Dobson, Christian McKenzie, Christine Higgins and Sarah Gilbert. In the administrative issues many thanks to Nilar Hlaing, Karen Mollross, Helen Scott, Rose Pongratz and Deborah Macklin.

My gratitude also goes to Prof. Wan Fuad Wan Hassan (UM), Prof. Hamzah Mohamad (UKM), Prof. Basir Jasin (UKM), Prof. Mohd Shafeea Leman (UKM), Prof. Teh Guan Hoe (UM), Dr. Kamal Roslan (UKM), Dr. Azimah Hussin (UKM), all academics and staffs from Geology Department in National University of Malaysia, the staffs from Tasik Chini Research Centre,

UKM and Study Leave Unit, UKM for their help and supports throughout these past years. Prof. Ir. Datuk Hassan Basri (UKM), Prof. Ir. Marzuki (UKM), Mr. Zaidi Harun of Monument Mining Limited and Mr. Noor Hazin and their families for a meaningful visit and support for me. Not forgetting to Imam Sabri Samson and wife, Mariatun for their care during my stay here in Hobart.

I owe my both parents and parents in law a debt that I will never be able to repay. I only hope that the final production of this PhD thesis will go some way of expressing my love to them. Finally, I would like to thank my beloved wife Mazlinfalina Mohd Zin for providing me the love, the friendship and the understanding when it matters the most. Although I cannot thank her enough, without her help this PhD thesis would not have come into existence.

TABLE OF CONTENTS

Declaration…….. ii

Abstract…… iii

Acknowledgements…….. vii

Table of Contents……. x

List of Figures……... xvii

List of Tables…… xxi

Chapter 1 Introduction……..

1.1 Introduction……... 1

1.2 Location, Access and Physiography…….. 1

1.3 Mining History and Previous Studies…… 5

1.4 An Overview of VHMS Deposits…….. 5

1.4.1 Introduction/definition…….…….. 5

1.4.2 Distribution…….……... 6

1.4.3 Tectonic setting…… 7

1.4.4 Classification…….……... 8

1.4.5 Genetic model…….……... 11

1.5 Objectives…… 12

1.6 Methodology…… 13

1.6.1 Field studies…….…….. 13

1.6.2 Petrographic investigation …….……... 13

1.6.3 LA-ICPMS U-Pb zircon geochronology……..…… 13

1.6.4 Lithogeochemistry…….…….. 14

1.6.5 Isotopic studies …….……... 14

1.6.6 Fluid inclusions studies…….. 14

1.7 Thesis organisation…… 14

Chapter 2 Tectonic and Geological Setting……..

2.1 Introduction……... 17

2.2 Tectonic Setting of Southeast Asia…….. 17

2.2.1 Main continental terranes…….……... 17

2.2.2 Main suture zones…….. 20
2.3 Tectonic Setting of Peninsular Malaysia …… 22
2.4 Palaeotectonic Reconstruction of Southeast Asia and Peninsular Malaysia …… 25
2.5 Geology of Peninsular Malaysia……... 30
2.5.1 Palaeozoic sedimentary rocks ……..… 30
2.5.2 Mesozoic sedimentary rocks …… 33
2.5.3 Cenozoic sedimentary rocks…… 34
2.5.4 Volcanism…….. 34
2.5.5 Plutonism…….. 36
2.6 Regional Structure and Deformation …… 38
2.7 Mineralisation in Peninsular Malaysia……. 39
2.8 Summary……. 41

Chapter 3 District- and Deposit-Scale Geology……..
3.1 Introduction……... 43
3.2 District-scale Geology of the Tasik Chini Area……. 43
3.2.1 Carboniferous Sequence…… 45
3.2.2 Permian-Triassic Sequence…… 46
3.2.3 Jurassic-Cretaceous Sequence…… 49
3.2.4 Igneous rocks …… 50
3.3 Structure and Metamorphism……... 54
3.4 Deposit-scale Geology of the Bukit Botol Deposit…… 54
3.5 Deposit-scale Geology of the Bukit Ketaya Deposit…….. 59
3.6 Summary…… 62

Chapter 4 Geochemistry and Geochronology ……..
4.1 Introduction…….. 64
4.2 Methods……..…….. 64
4.2.1 Geochemistry analyses……..… 64
4.2.1.1 Major, trace and rare earth (REE) elements analyses… 65
4.2.1.2 Sm-Nd and Rb-Sr isotope analyses……. 65
4.2.2 Geochronology analyses …… 67

4.3 Geochemistry Results……..……... 67
4.3.1 Major element chemistry……... 71
4.3.1.1 District-scale…….. 71
4.3.1.2 Deposit-scale……. 71
4.3.2 Trace and rare earth element (REE) chemistry …… 73
4.3.2.1 District-scale……. 73
4.3.2.2 Deposit-scale…… 73
4.3.3 Immobile element chemistry …… 76
4.3.4 Geochemical classification…… 78
4.3.4.1 District-scale…… 79
4.3.4.2 Deposit-scale……. 79
4.3.5 Sm-Nd and Rb-Sr results……. 81
4.4 Geochronology Results……..……... 84
4.4.1 Rock formations……... 84
4.4.2 Igneous rocks……... 90
4.4.2.1 Tasik Chini district…….. 90
4.4.2.2 Bukit Botol deposit…… 93
4.4.2.3 Bukit Ketaya deposit…… 94
4.5 Discussion……..……... 95
4.5.1 Petrogenesis of felsic rocks in the Tasik Chini area……... 95
4.5.2 Felsic volcanic rocks geochemistry and related VHMS environments… 96
4.5.3 Sm-Nd isotopic characteristics of felsic rocks…….. 99
4.5.4 Significance of zircon age determination of the rock……. 101
4.6 Summary ……..……... 103

Chapter 5 Mineralisation and Alteration……..
5.1 Introduction……... 105
5.2 Sampling and Methods ……... 105
5.3 Main Ore Types……... 106
5.3.1 Bukit Botol deposit……... 106
5.3.1.1 Massive sulphide…….. 106
5.3.1.2 Stringer and disseminated sulphides……. 109

5.3.1.3 Barite layer……. 110
5.3.2 Bukit Ketaya deposit……... 111
5.3.2.1 Massive sulphide…… 112
5.3.2.2 Stringer and disseminated sulphides …… 112
5.3.2.3 Barite layer …… 113
5.3.3 Fe-Mn and Fe-Si layers at the Bukit Botol and Bukit Ketaya deposits… 114
5.3.3.1 Occurrence and distribution…….. 114
5.3.3.2 Petrographic characteristics of the Fe-Mn and Fe-Si layers …... 115
5.3.3.3 Chemistry …….. 116
5.4 Mineralogy and Paragenesis…….. 122
5.4.1 Bukit Botol deposit……... 122
5.4.2 Bukit Ketaya deposit……... 130
5.5 Alteration…….. 135
5.5.1 Methods……... 136
5.5.1.1 Petrography, Short-Wave Infrared (SWIR) ……. 136
5.5.1.2 Lithogeochemical analyses……. 137
5.5.2 Petrography, Short-Wave Infrared (SWIR) …….. 139
5.5.2.1 Alteration assemblages of the Bukit Botol deposit…… 139
5.5.2.2 Alteration assemblages of the Bukit Ketaya deposit…… 142
5.5.3 Lithogeochemistry results……... 144
5.5.3.1 Bukit Botol deposit……. 144
5.5.3.2 Bukit Ketaya deposit…….. 146
5.6 Discussion……..…….... 148
5.6.1 Mineralisation characteristics……... 148
5.6.2 Significance of Fe+Mn±Si layers ……... 150
5.6.3 Alteration characteristics……... 152
5.7 Summary……..……..... 154

Chapter 6 Mineral Chemistry……..……..

6.1 Introduction……... 156
6.2 Sphalerite Chemistry ……... 156
6.2.1 Introduction…….……... 156
6.2.2 Methods …… 157

6.2.3 Chemical compositions of sphalerite……..……... 158
6.2.3.1 FeS content…….. 158
6.2.3.2 Minor element contents…… 160
6.3 Pyrite Geochemistry……... 164
6.3.1 Introduction…….……... 164
6.3.2 Methods …… 165
6.3.3 Chemical compositions of pyrite…….……. 167
6.3.3.1 Spot analysis…… 167
6.3.3.2 Image analysis…… 171
6.4 Discussion……..…….. 175
6.4.1 Sphalerite trace element chemistry…….……... 175
6.4.2 Pyrite trace element chemistry…….……... 179
6.5 Summary……... 184

Chapter 7 Sulphur Isotope Characteristics……..

7.1 Introduction……... 186
7.2 Methods……..…….. 187
7.3 Sulphur Isotope Results…….. 187
7.3.1 Bukit Botol deposit…….……... 187
7.3.2 Bukit Ketaya deposit…….……... 189
7.4 Discussion……... 191
7.4.1 Significance of sulphur isotopes…….. 191
7.4.2 Source of sulphur…….. 192
7.5 Summary……... 195

Chapter 8 Lead Isotope Studies……..

8.1 Introduction……... 196
8.2 Methods……..…….. 197
8.3 Lead Isotope Results…….. 198
8.3.1 Bukit Botol deposit…….……... 198
8.3.2 Bukit Ketaya deposit…….……... 199
8.4 Discussion……... 202

8.4.1 Constraints on possible lead ore-forming sources …… 202
8.4.2 Comparison with other deposits in Peninsular Malaysia……... 204
8.4.3 Comparison with several other deposits in East Malaya-Indochina …. 206
8.5 Summary……... 208

Chapter 9 Fluid Inclusions……..
9.1 Introduction……... 210
9.2 Samples and Methods ……... 211
9.2.1 Microthermometric measurements……. 211
9.2.2 Laser Raman microprobe…… 212
9.3 Fluid Inclusion Petrography…….. 213
9.4 Results……... 216
9.4.1 Microthermometry…….……... 216
9.4.1.1 Bukit Botol deposit…… 216
9.4.1.2 Bukit Ketaya deposit…….. 219
9.4.2 Laser Raman spectroscopy …….……... 222
9.5 Discussion ……... 224
9.5.1 Comparison of Bukit Botol and Bukit Ketaya fluid inclusion data…. 224
9.5.2 Origin of the high salinity and CO_2-bearing fluids……. 226
9.5.3 Possible density, pressure, behavior and depth of ore formation……... 229
9.6 Summary……... 231

Chapter 10 Summary and Conclusions……..
10.1 Introduction……... 233
10.2 Summary and Conclusions…….. 233
10.2.1 Regional geology and tectonic setting…….. 233
10.2.2 Local geological setting……. 235
10.2.3 Mineralisation features…….. 237
10.2.4 Chemistry of ore-forming fluids…… 238
10.2.5 Source of sulphur…….. 239
10.2.6 Fluid chemistry…….. 240
10.3 Comparison with Other VHMS Deposits ……... 241
10.4 Tectonic Model……..…… 246

10.5 Exploration Implications …….. 250
10.6 Future Research ……... 251

References…….. 254

Appendices

Appendix I: Rock Catalogue……..
Appendix II: Sample localities/Sampling details……...
Appendix III: LA-ICPMS zircon U-Pb age results…….....
Appendix IV: XRF whole-rock geochemical results…….....
Appendix V: SWIR results…….....
Appendix VI: XRD results…….....
Appendix VII: Microprobe results of sphalerite geochemistry……..
Appendix VIII: LA-ICPMS pyrite trace element geochemical results…….
Appendix IX: Fluid inclusion microthermometric results……
Appendix X: Laser Raman Spectroscopic results……..
Appendix XI: Calculated density and pressure of fluids.....

LIST OF FIGURES

Chapter 1

Fig. 1.1. Location of the Tasik Chini area in Pahang State of Peninsular Malaysia ……. 2

Fig. 1.2. Location of the Bukit Botol and Bukit Ketaya deposits in the Tasik Chini area……. 4

Fig. 1.3. Idealised model of a typical VHMS deposit (modified after Lydon, 1984)…… 6

Fig. 1.4. Possible setting of VHMS deposits in convergent and divergent setting …… 8

Fig. 1.5. An example of geochemical classifications for VHMS deposits …… 9

Fig. 1.6. Graphic representation showing the lithological classification for VHMS deposits... 10

Chapter 2

Fig. 2.1. Distribution of principal continental fragments of Southeast Asia including……. 18

Fig. 2.2. Tectonic belts of Peninsular Malaysia…….. 23

Fig. 2.3. Reconstruction maps of Southeast Asia showing the relative position…… 28

Fig. 2.4. Geological map of the Peninsular Malaysia …… 31

Fig. 2.5. Distribution of igneous rocks in Peninsular Malaysia……... 35

Fig. 2.6. Map of Peninsular Malaysia showing mineral belts…… 39

Chapter 3

Fig. 3.1. District-scale geology of the Tasik Chini area…… 44

Fig. 3.2. Schematic stratigraphic column and contact relationship of rock units…….. 45

Fig. 3.3. Field photographs of the Carboniferous Sequence…… 46

Fig. 3.4. Photographs of various rock successions of the Permo-Triassic Sequence…….. 48

Fig. 3.5. Outcrop photos of the Jurassic-Cretaceous Sequence…… 49

.

Fig. 3.6. Outcrops of the granite bodies…… 52

Fig. 3.7. A. Hand specimens of dacite/andesite subvolcanic unit in the vicinity……..... 53

Fig. 3.8. Surface geological map and schematic cross-section of the Bukit Botol deposit… 55

Fig. 3.9. Host rocks at the Bukit Botol deposit…… 57

Fig. 3.10. A. Outcrop of the volcaniclastic rocks at the Bukit Botol deposit…….. 58

Fig. 3.11. Surface geological map and schematic cross-section of the Bukit Ketaya deposit….. 60

Fig. 3.12. Host rocks at the Bukit Ketaya deposit…….. 61

Chapter 4

Fig. 4.1. Harker variation diagrams; silica (SiO_2wt %) plotted…… 72

Fig. 4.2. Harker variation diagrams; silica (SiO_2wt %) plotted..…… 74

Fig. 4.3. A. Chondrite-normalised rare earth element plots……...… 76

Fig. 4.4. Harker variation diagrams; zircon (Zr ppm) plotted..……. 77

Fig. 4.5. Various immobile element discrimination diagrams……. 81

Fig. 4.6. Initial $^{87}Sr/^{86}Sr$ versus $^{143}Nd/^{144}Nd$ isotope correlation diagram..... 84

Fig. 4.7. Cathodoluminescence (CL) images of representative detrital zircons…… 86

Fig. 4.8. Cathodoluminescence (CL) images of representative detrital zircons...……... 87

Fig. 4.9. Cathodoluminescence (CL) images of representative detrital zircons...…… 88

Fig. 4.10. Cathodoluminescence (CL) images of representative detrital zircons…….. 90

Fig. 4.11. Cathodoluminescence (CL) images of representative zircons…….……. 92

Fig. 4.12. Cathodoluminescence (CL) images of representative zircons…….…….. 93

Fig. 4.13. Cathodoluminescence (CL) images of representative zircons…… 95

Fig. 4.14. Binary classification diagrams of Zr versus Zr/Y ratios…….. 98

Fig. 4.15. Initial $^{87}Sr/^{86}Sr$ versus $^{143}Nd/^{144}Nd$ for the igneous rocks……. 100

Chapter 5

Fig. 5.1. Surface map and schematic cross-section of the of the Bukit Botol deposit…… 107

Fig. 5.2. A. Photograph showing outcrop of massive sulphide mineralisation at Bukit Botol.. 108

Fig. 5.3. Photographs of different sulphide ores from the Bukit Botol deposit…….……. 109

Fig. 5.4. Photographs showing nature of stringer zone at the Bukit Botol deposit……..……. 110

Fig. 5.5. Examples of barite layer at the Bukit Botol…….……. 110

Fig. 5.6. Surface map and schematic long cross-section of the Bukit Ketaya deposit……. 111

Fig. 5.7. A. Outcrop of massive sulphide mineralisation at Bukit Ketaya deposit……...… 112

Fig. 5.8. Photographs showing nature of the stringer zone at the Bukit Ketaya deposit…..… 113

Fig. 5.9. Examples of barite layer at the Bukit Ketaya deposit…….…… 113

Fig. 5.10. Fe-Mn layer at Bukit Botol…...…….. 114

Fig. 5.11. Fe-Si layer at Bukit Ketaya…..…… 115

Fig. 5.12. Textures of the Fe-Mn and Fe-Si layers…….. 116

Fig. 5.13. Al-Fe-Mn (wt%) ternary diagram showing the composition of Fe-Mn...…… 120

Fig. 5.14. Discrimination diagrams of Fe-Mn and Fe-Si samples.…… 121

Fig. 5.15. Paragenetic sequence for the mineralisation at the Bukit Botol deposit…….. 123
Fig. 5.16. Textural characteristics of pyrite with other sulphides from the Bukit Botol deposit. 125
Fig. 5.17. Photomicrographs showing the characteristics and textural relationships...…….. 127
Fig. 5.18. SEM Back-scattered electron (BSE) images showing Sn- and silver-bearing…..…. 128
Fig. 5.19. Photomicrographs showing the textural relationships of iron oxide minerals…… 129
Fig. 5.20. Paragenetic sequences for the mineralisation formations at the Bukit Ketaya….. 131
Fig. 5.21. Photomicrographs showing the characteristic and textural relationships…… 132
Fig. 5.22. Photomicrographs showing the characteristic and textural relationships……... 133
Fig. 5.23. Photomicrograph showing occurrence of barite in barite layers……..... 134
Fig. 5.24. Characteristic features of the quartz-sericite alteration at Bukit Botol……... 140
Fig. 5.25. Characteristics of quartz-sericite-pyrite±chlorite alteration at Bukit Botol deposit…142
Fig. 5.26. Photomicrographs showing the characteristics of quartz-chlorite-sericite-pyrite… 143
Fig. 5.27. Characteristics of quartz-chlorite-pyrite±carbonate±pyrophyllite alteration.…… 144
Fig. 5.28. Alteration box plots (modified after Large et al., 2001a)…....…….. 145
Fig. 5.29. Molar element ratio plot of Bukit Botol altered samples…….…… 146
Fig. 5.30. Alteration box plots (modified after Large et al., 2001a)…….…… 147
Fig. 5.31. Molar element ratio plot of Bukit Ketaya altered samples……...…. 148

Chapter 6

Fig. 6.1. Frequency distributions diagram for the mole% FeS in sphalerite...……. 160
Fig. 6.2. Plot showing mole% FeS, MnS and CdS variations in sphalerite…….. 162
Fig. 6.3. A ternary diagram of mole% FeS–mole% MnS x10–mole% CdS x10 compositions. 163
Fig. 6.4. Details of LA-ICPMS spot analysis of py1 from the Bukit Botol deposit……. 169
Fig. 6.5. Details of LA-ICPMS spot analysis of py2 from the Bukit Botol deposit……. 170
Fig. 6.6. Details of LA-ICPMS spot analysis of py3 from the Bukit Botol deposit…… 170
Fig. 6.7. Trace element LA-ICPMS map of pyrite crystal in massive sulphide ore……... 172
Fig. 6.8. LA-ICPMS trace element images of composite pyrite …….. 173
Fig. 6.9. Binary plots of selected trace elements in different varieties of pyrite…..…….. 175
Fig. 6.10. Comparison of compositional ranges in sphalerites……...….. 177

Fig. 6.11. Scatter plots of selected trace elements to discriminate pyrite ……. 182

Chapter 7

Fig. 7.1. Histogram of $\delta^{34}S$ values for sulphides and sulphates from the Bukit Botol deposit.. 189

Fig. 7.2. Frequency distribution of $\delta^{34}S$ values of sulphides and sulphates for Bukit Ketaya… 190

Fig. 7.3. Comparison of $\delta^{34}S$ values for Bukit Botol and Bukit Ketaya deposits…….. 194

Chapter 8

Fig. 8.1. Lead isotope ratio plot for volcanic rocks, massive pyrite and galena samples…. 200

Fig. 8.2. Lead isotope ratio plot for volcanic rocks, massive pyrite and galena samples.... 201

Fig. 8.3. Published $^{208}Pb/^{204}Pb$ data of several VHMS deposits……... 203

Fig. 8.4. $^{206}Pb/^{204}Pb$ versus $^{207}Pb/^{204}Pb$ diagram showing the lead isotope ratios plot…. 204

Fig. 8.5. $^{206}Pb/^{204}Pb$ versus $^{207}Pb/^{204}Pb$ diagram showing the lead isotope ratio…….. 206

Chapter 9

Fig. 9.1. Photomicrographs showing characteristics of fluid inclusions in quartz…….. 213

Fig. 9.2. Photomicrographs of fluid inclusions in barite…… 214

Fig. 9.3. Photomicrographs showing different inclusion types in quartz and barite.…… 215

Fig. 9.4 Histograms of homogenisation temperatures of Type I fluid inclusions.....…… 217

Fig. 9.5. Histograms of salinity data measured for fluid inclusions……..…….. 218

Fig. 9.6. Frequency histograms of Type I fluid inclusions from the Bukit Ketaya deposit…… 220

Fig. 9.7. Frequency plots of the salinities of fluid inclusions from the Bukit Ketaya deposit… 221

Fig. 9.8. Examples of Laser Raman spectra for the vapour phase within fluid inclusions….. 223

Fig. 9.9. Summary of salinity versus homogenisation temperature (Th) plot...…….. 225

Fig. 9.10. Salinity and temperature data for fluid inclusions…….…… 225

Fig. 9.11. Salinity versus homogenisation temperature (Th) plot for fluid inclusion data… 227

Fig. 9.12. Homogenisation temperature (Th) versus salinity plot for fluid inclusions data…. 230

Chapter 10

Fig. 10.1. Schematic diagrams that illustrate the proposed tectonic environment……. 247

Fig. 10.2. Schematic diagrams that illustrate the formation of the Tasik Chini deposits…… 249

LIST OF TABLES

Chapter 2

Table 2.1. Summary of the gold and base metal deposits in Peninsular Malaysia…… 41

Chapter 4

Table 4.1. Geochemical characteristic of felsic rocks from the Tasik Chini district…… 68

Table 4.2. Lithogeochemical values for volcanic rocks of the Bukit Botol deposit……. 69

Table 4.3. Lithogeochemical values for volcanic rocks of the Bukit Ketaya deposit…….. 70

Table 4.4. Chemical and isotopic compositions of Sm, Nd, Rb and Sr…….…… 82

Table 4.5. Descriptions of the samples analysed for the LA-ICPMS U-Pb dating…… 85

Chapter 5

Table 5.1. Major and trace elements of Fe-Mn layer from the Bukit Botol deposit.…… 117

Table 5.2. Major and trace elements Fe-Si layers from the Bukit Ketaya deposit..…… 118

Chapter 6

Table 6.1. Average chemical compositions of the representative sphalerite..…… 158

Table 6.2. Average chemical compositions of the representative sphalerite…… 159

Table 6.3. Average chemical compositions of the representative sphalerite…...…… 159

Table 6.4. Average chemical compositions of the representative sphalerite……..…… 160

Table 6.5. Average Zn/Mn, Zn/Cd, and Zn/Fe ratios of sphalerites…… 164

Table 6.6. LA-ICPMS analyses of selected pyrite types from the Bukit Botol deposit…… 167

Chapter 7

Table 7.1. Sulphur isotope data for sulphides and sulphates at the Bukit Botol deposit…….. 188

Table 7.2. Sulphur isotope data for the Bukit Ketaya deposit…….…… 190

Chapter 8

Table 8.1. Lead isotope data for the Bukit Botol and Bukit Ketaya deposits…….198

Chapter 9

Table 9.1. Summary of microthermometric data for primary fluid inclusions..... 216

Table 9.2. Laser Raman Spectroscopic analysis of fluid inclusion vapour compositions……. 222

Chapter 10

Table 10.1. Summary of geological characteristics of the Bukit Botol and Bukit Ketaya……...241

Table 10.2. Comparison between the Tasik Chini deposits, the Mount Chalmers deposits..…...242

CHAPTER 1 INTRODUCTION

1.1 Introduction

The Tasik Chini deposit is located in Central Peninsular Malaysia. Historically, the Central Peninsular Malaysia area has several occurrences of orogenic/sediment-hosted Au-Ag deposits/prospects in the province (Scrivenor, 1928; Yeap, 1993). In addition, recognition that the Tasik Chini deposit in Central Peninsular Malaysia as being Kuroko style volcanic-hosted massive sulphide (VHMS) deposit (Hutchison, 1986) has highlighted the potential for base metal mineralisation in the area.

Massive sulphide, barite and Fe-Mn-Si layers, and zones of intense hydrothermal alteration are exposed at numerous localities throughout the Tasik Chini area. As a result, many prospecting, mining and exploration activities have been undertaken at different localities/prospects in the area, from geochemical grab sampling to diamond drilling, extensive mapping and several small local operations. The Bukit Botol and Bukit Ketaya deposits are the two most extensively explored prospects in the Tasik Chini area. Due to their recognition as VHMS occurrences, there are many significant aspects of the formation that have needed to be defined in detail. However, only a few studies have been undertaken to understand origin of the deposit at Tasik Chini prior to this study.

1.2 Location, Access and Physiography

The Tasik Chini area is situated in the southern (south-central) part of Pahang State, Central Peninsular Malaysia, about 250 km southeast of Kuala Lumpur (Fig. 1.1).

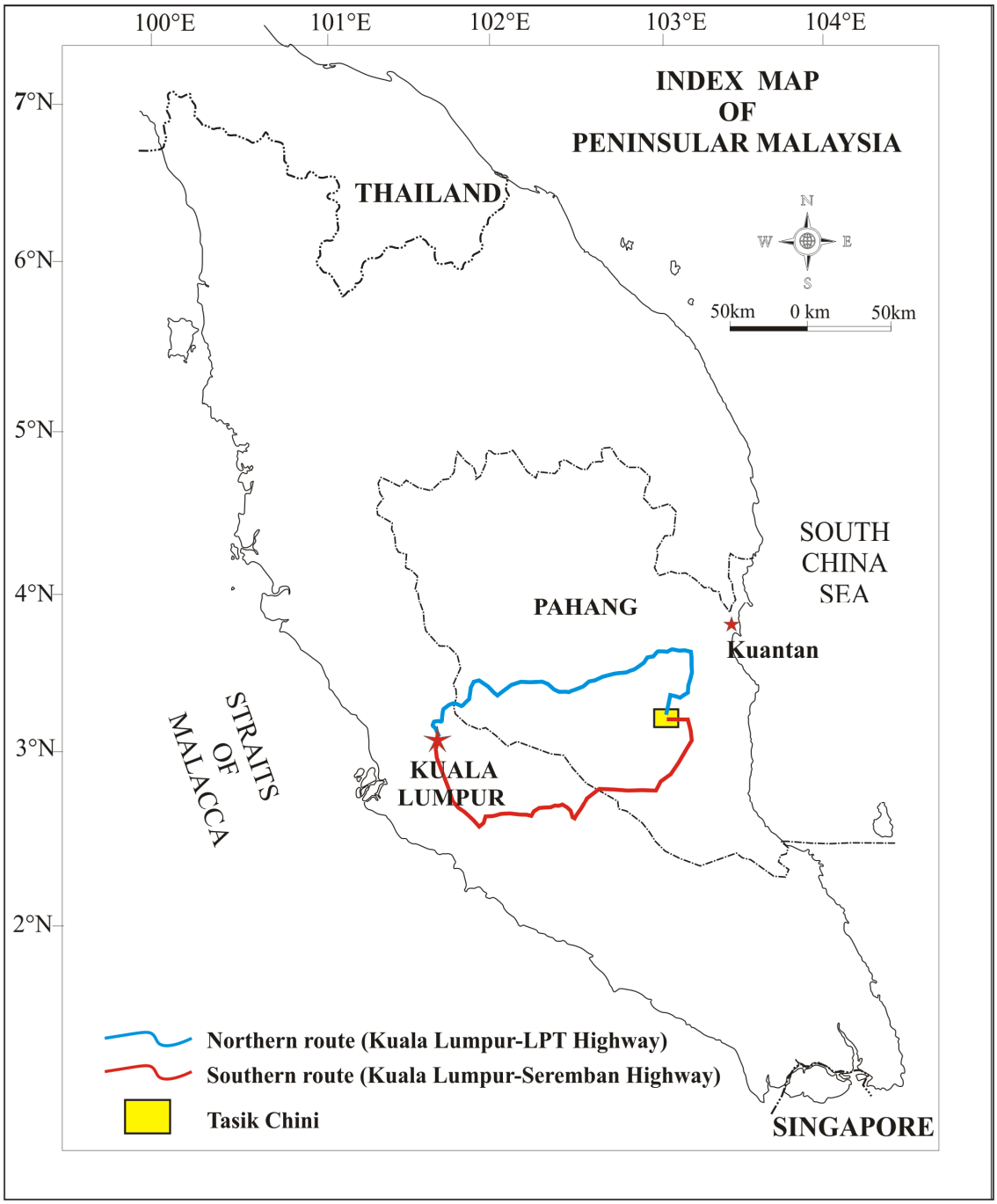

Fig. 1.1. Location of the Tasik Chini area in Pahang State of Peninsular Malaysia.

The area can be reached by vehicles from Kuala Lumpur via a northern route (Kuala Lumpur - LPT Highway) or a southern route (Kuala Lumpur - Seremban Highway) in about four to five hours.

Tasik Chini (Lake Chini), the second largest natural freshwater lake in Malaysia is part of a major catchment system in the study area. It functions as the water retention area for flood control and also as the main drainage system in the surrounding Tasik Chini area. In 2009, the lake and the surrounding area have been declared as a Biosphere Reserve (BR) by the UNESCO.

The climate of the Tasik Chini area is characterised by moderate average annual rainfall, temperature and humidity. The area has two monsoon seasons, the SW and NE monsoons which bring variable annual rainfall. Most of the land surrounding the Tasik Chini area is used for permanent settlements, agriculture, mining and tourism. However, some of the land has natural forests and is preserved as protected area. People in the area consist of majority of Malays with minor Chinese and Indians who settle down in the town centre. In addition, a few communities of Aboriginal people or Orang Asli of Jakun live in the small villages or kampongs around the lake.

The Bukit Botol and Bukit Ketaya deposits are located towards the southern part of the Tasik Chini (Chini Lake). These deposits are separated by a distance at about 6 km (Fig. 1.2), and four wheel-drive vehicles are the most convenient way of accessing the deposits. At the first field work in this research in 2009, mining was already abandoned at the both deposits.

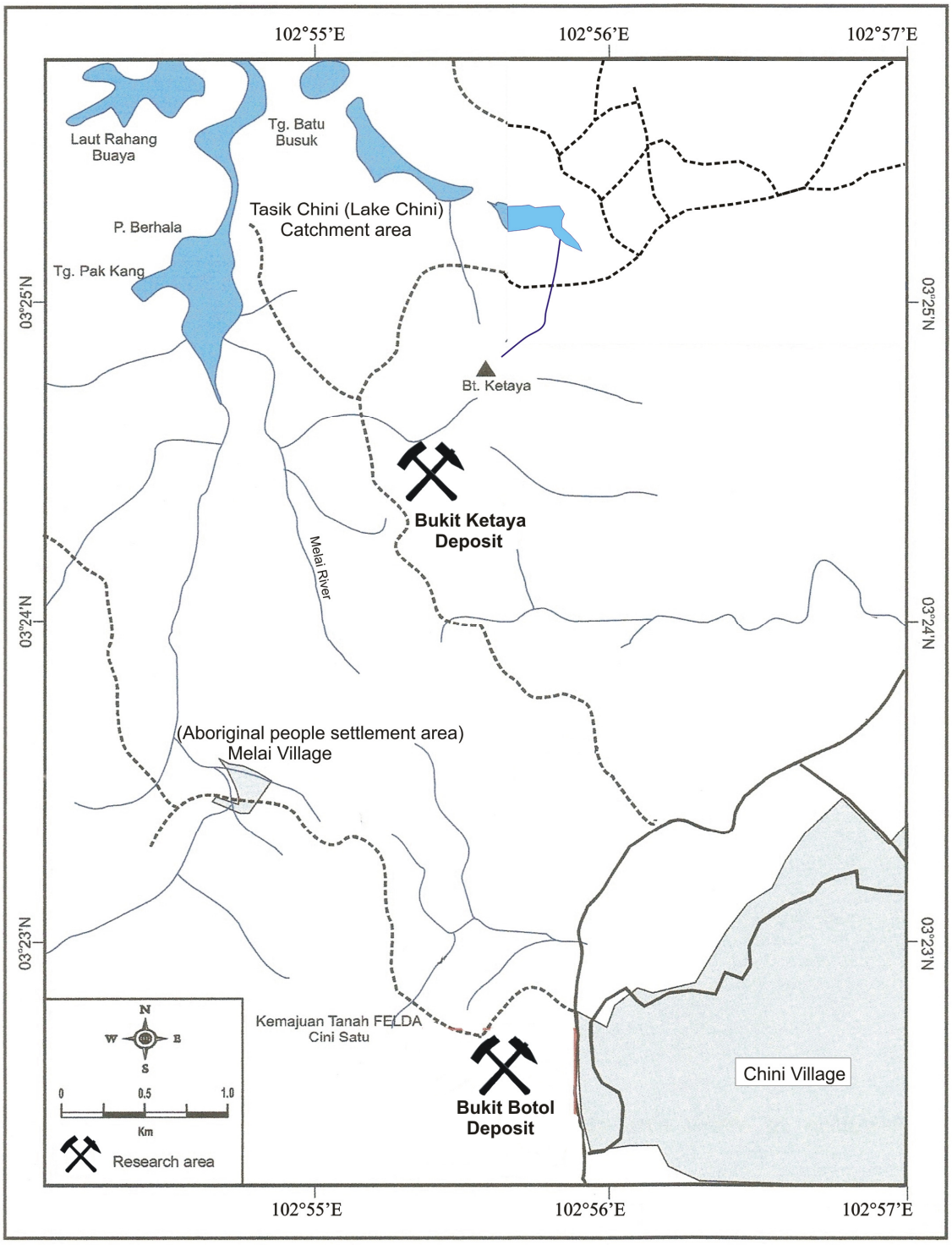

Fig. 1.2. Location of the Bukit Botol and Bukit Ketaya deposits in the Tasik Chini area, Central Peninsular Malaysia.

1.3 Mining History and Previous Studies

Early mining at the Bukit Botol deposit focused on the barite ores which contained an average reserve from 28,000 to 500,000 tonnes, and 92 to 97 percent $BaSO_4$ (Murthy, undated; Cook, undated; Aw, 1978). Although the mineralisation occurrence at the Bukit Botol deposit was first classified as being Kuroko-sytle by Hutchison (1986), the overall geologic setting of the deposit are not known in detail. Prior to the recent study, the best documented studies on a deposit scale and mineralisation at Bukit Botol are published by Teh et al. (1991, 2004, 2006, 2008). During the four years of this PhD research, active communal development activities on the Bukit Botol and its surrounding area were already started. In the late 2012, this old mine-site has totally changed into large government public school area.

Mining activities began in the Bukit Ketaya deposit after the discovery of mixed manganese-iron ore formation in 1965, and the production is reported at about 93,000 tonnes (MacDonald, 1970). The mine was temporarily reopened for barite mining between 1975 and 1976, and produced approximately 9,000 tonnes of ore (Cook, undated; Aw, 1978). Although massive sulphide orebody is present, mining of base metals from the orebody has not been conducted, probably due to lack of geological understanding of the Bukit Ketaya deposit.

1.4 An Overview of VHMS Deposits

1.4.1 Introduction/ definition

The volcanic-hosted massive sulphide (VHMS) deposits (Large, 1992) or commonly termed as volcanogenic massive sulphide deposits (Franklin et al., 1981; Lydon, 1984, 1988; Ohmoto, 1996; Barrie and Hannigton, 1999), are stratabound accumulations of sulphide minerals that precipitated at or near the seafloor in spatial, temporal and genetic association with contemporaneous volcanism (Franklin et al., 2005). The geometry of VHMS deposits is varied and broad. However, the idealised VHMS deposits are characterised by a stratiform mound-shaped to tabular sulphide bodies, underlain by a stringer zone of discordant veins and

disseminated mineralisation and hydrothermal alteration. In addition, the massive sulphide zone may grade laterally into bedded chemical precipitates termed tuffite or exhalite (Lydon, 1984) (Fig. 1.3).

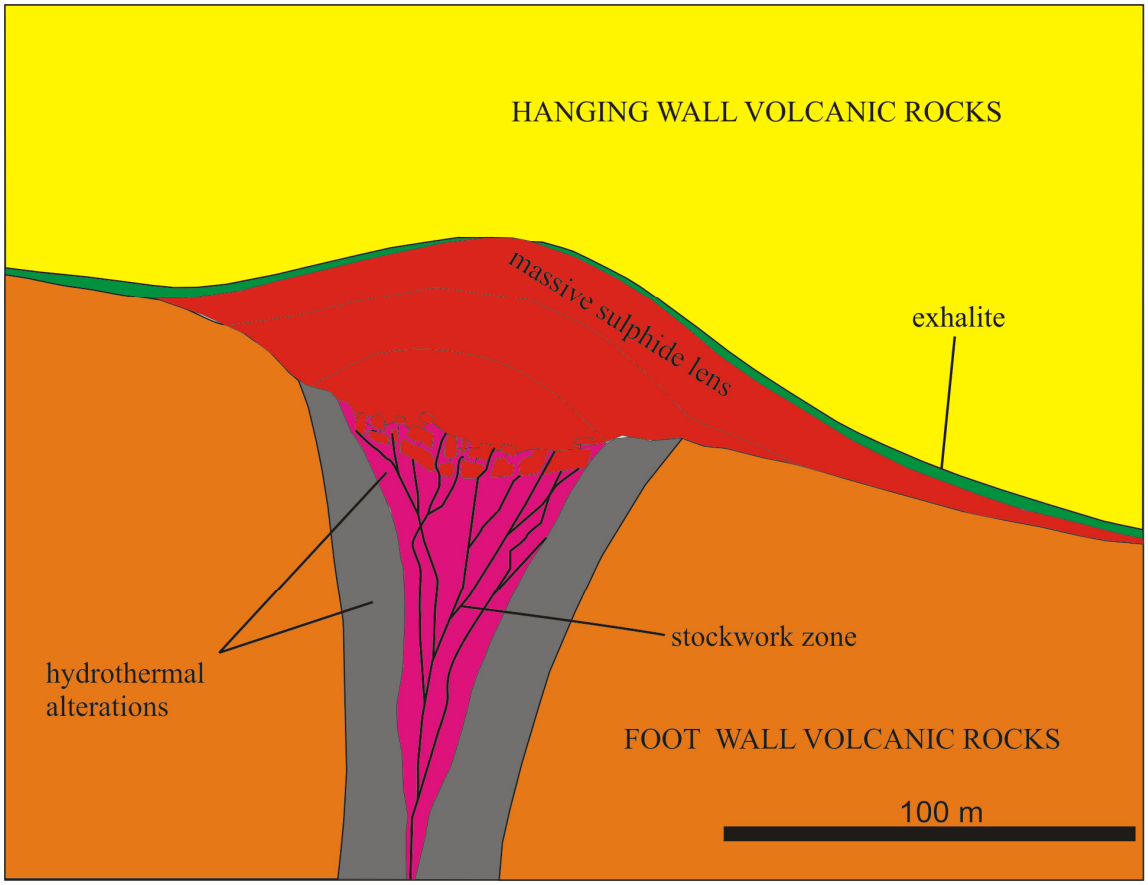

Fig. 1.3. Idealised model of a typical VHMS deposit (modified after Lydon, 1984).

1.4.2 Distribution

The VHMS deposits are known to occur in age from Archean to present-day submarine environment but not uniformly distributed through time. Franklin et al. (2005), Groves et al. (2005) and Huston et al. (2010) noted that VHMS deposits are particularly concentrated in six major time intervals in earth history from Late Archean (2.85-2.60 Ga), Paleoproterozoic (2.0-1.7 Ga), Neoproterozoic (900-700 Ma), Cambrian-Ordovician (550-450 Ma), Devonian-Carboniferous(Mississippian) (400-320 Ma), and Early Jurassic to Recent (200-0 Ma).

Although uncommon, Permian VHMS deposits are known in the East Shasta district in California (Eastoe and Nelson, 1988; Gustin and Eastoe, 2000), and the Mt Chalmers deposit, central Queensland, Australia (Khin Zaw et al., 2003). Franklin et al. (2005) and Huston et al. (2010) interpreted that this variation in abundance with specific geologic times is strongly influenced by the changes in crustal and tectonic cycles through time.

1.4.3 Tectonic setting

Regardless of any major divisions of tectonic systems proposed by numerous workers (e.g., Hutchinson, 1973; Hannington et al., 2005; Franklin et al., 2005), tectonic setting in which VHMS deposits occur can be grouped into two specific geodynamic environments: divergent and convergent (Huston et al., 2010). Most modern VHMS deposits (i.e., "black smokers") have been discovered in divergent setting along mid-oceanic ridges and intra-continental rifts (Hannington et al., 2005). In the convergent setting, formation of both the modern and ancient VHMS deposits is related closely with extensional environment during subduction (e.g., back-arc) (Huston et al., 2010) (Fig. 1.4). In addition, formation of VHMS deposits can be also associated with post-collisional extension environments (e.g., Crawford and Berry, 1992; Tornos, 2006).

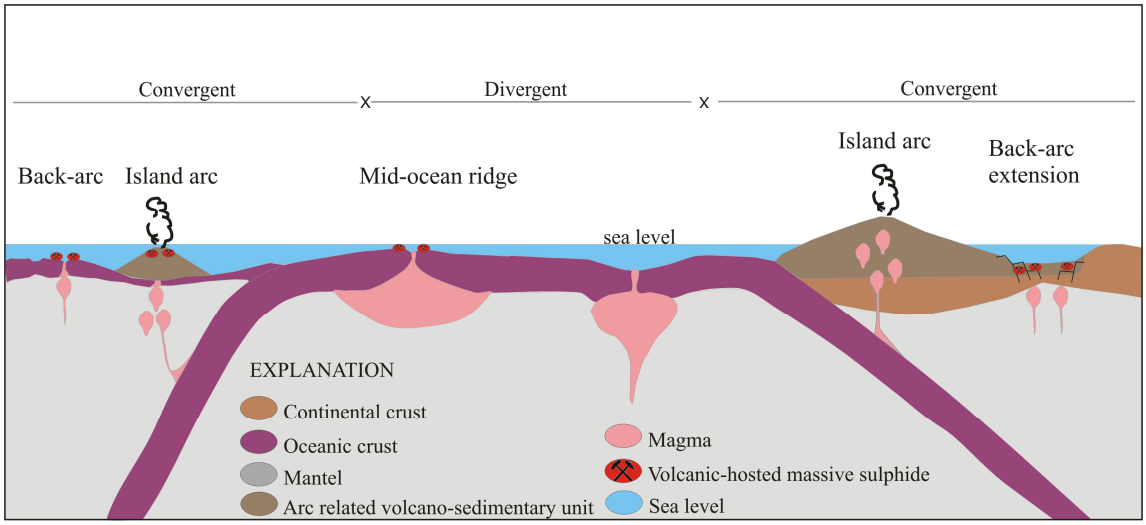

Fig. 1.4. Possible setting of VHMS deposits in convergent and divergent setting (modified after Schmincke, 2004; Huston et al., 2010).

1.4.4 Classification

Many classification schemes have been proposed for VHMS deposits. Early attempts on the classification are based mainly on geological and tectonic setting and a three fold classification scheme was firstly proposed by Sawkins (1976), which defines Kuroko-, Besshi- and Cyprus- type deposits.

The Kuroko-type deposits are characterised by the presence of polymetallic sulphide lenses hosted by felsic volcanic rocks of bimodal suite that formed in island arc and arc rift setting (e.g., Hokuroko district; Ohmoto and Skinner, 1983). The Besshi-type deposits are predominantly Cu-rich sulphide lenses that are hosted by mafic volcanic rocks with abundant sedimentary rocks. This type of deposit is interpreted to have formed within fore-arc and back-arc setting (e.g., Middle Valley; Goodfellow et al., 1999). The Cyprus-type deposits are massive Cu-Zn-rich sulphide deposits named after classic deposits in the ophiolite terranes in Cyprus (Galley and Koski, 1999). This deposit type is found in fore-arc and back-arc ophiolites, mid-ocean ridges. These deposits are hosted mainly in mafic volcanic rock sequences.

Geochemical classification for VHMS deposits has been proposed by Solomon (1976), Franklin et al. (1981), Large (1992), and Franklin (1993, 1995) and VHMS deposits were grouped into Cu-Zn, Zn-Cu and Zn-Pb-Cu based on ratios of base metals (Cu, Zn, Pb) in the sulphide bodies (Fig. 1.5). In this classification, Cu-Zn dominated group is distinguishable from a Zn-Pb-Cu group; and many of the Besshi and Cyprus style deposits would be classified within the Cu-Zn group, while the Kuroko style deposit would accumulate within the Zn-Pb-Cu group.

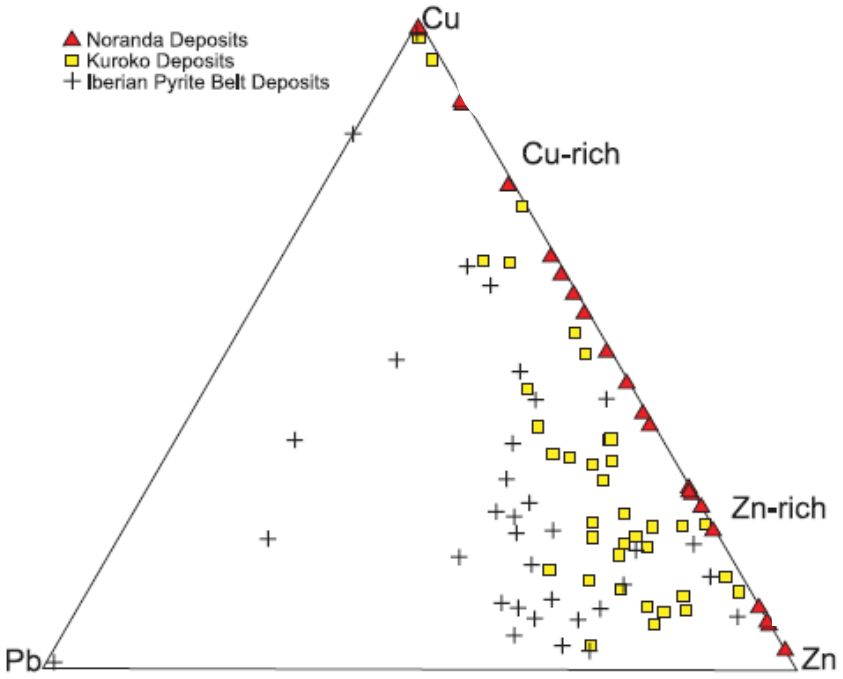

Fig. 1.5. An example of geochemical classifications for VHMS deposits based on the Cu-Pb-Zn ratios showing the distributions of the Archean deposits from Noranda Camp and the Phanerozoic deposits from Kuroko and Iberian Pyrite Belts. Note that the Noranda deposits are fall in the Zn-Cu field and most the Kuroko and Iberian Pyrite Belts deposits are plot in the Zn-Pb-Cu field. Data from Shimazaki (1974), Gibson and Watkinson (1990), Marcoux et al. (1996) and Goutier et al. (2009).

The most recent classification of VHMS deposits are provided by Barrie and Hannington (1999), Franklin et al. (2005) and Galley et al. (2007), in which deposits are grouped by litostratigraphy of the host volcanic assemblages (Fig. 1.6). Their classification is based on the compositional variations of host rocks (e.g., volcanic and sedimentary host rocks).

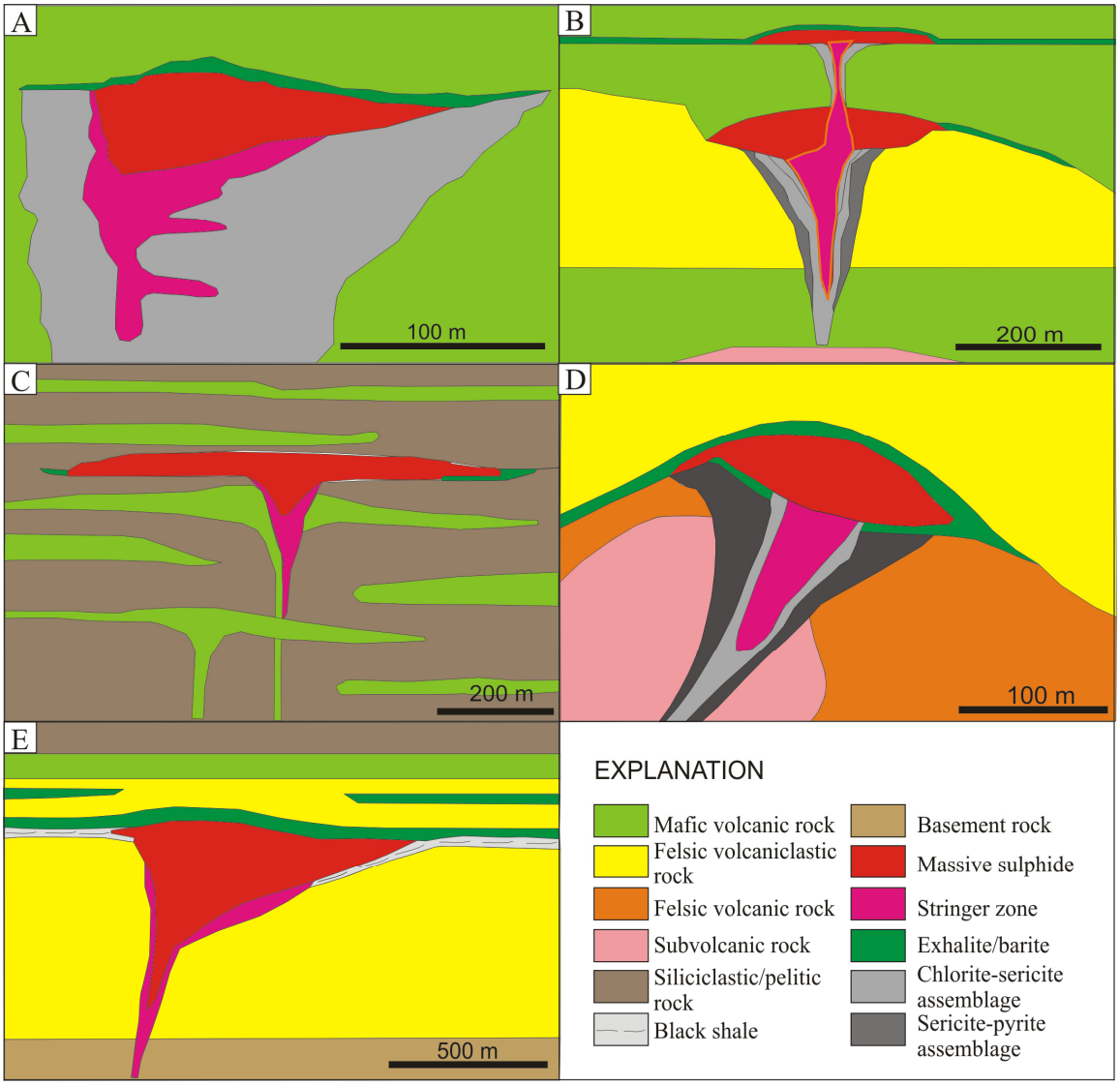

Fig. 1.6. Graphic representation showing the lithological classification for VHMS deposits with modification after Barrie and Hannington (1999). **A**. Mafic. **B**. Bimodal-mafic. **C**. Pelitic-mafic. **D**. Bimodal-felsic and **E**. Felsic-siliciclastic.

The five lithostratigraphic types are:

1. Mafic: Characterised by ophiolite sequences with <10% sedimentary rocks.

2. Bimodal-mafic: Typified by flows consisting largely of basalt and <25% of felsic volcanic rocks.

3. Pelitic-mafic: Dominated by mafic volcanic sequences with a significant pelitic component.

4. Bimodal-felsic: Dominantly bimodal felsic volcanic rocks.

5. Felsic-siliciclastic: Characterised by siliciclastic successions with an abundant felsic volcanic constituent.

Franklin et al. (2005) also noted that the mafic, bimodal-mafic and pelitic-mafic types are related to the subduction or spreading processes of oceanic crust, whereas the bimodal-felsic and felsic-siliciclactic types are associated with subduction along continental margins. Piercey (2010, 2011) further refined the classification and grouped the first three types into one that is characterised by mafic volcanic rocks with minor variations in associated felsic volcanic units or siliciclastic components. These deposits are enriched in Cu-Zn with lesser Pb, and are related with juvenile environments. The last two deposit types are dominated by felsic volcanic and sedimentary rocks. These types are commonly Zn-Pb-Cu rich and are associated with mature tectonic environments. The advantage of this classification method is that it provides a relationship between lithostratigraphic assemblages on deposit- and/or district-scale and tectonic setting regardless of geologic age.

1.4.5 Genetic model

The VHMS deposits are considered to have formed at and near the seafloor by the discharge of a high temperature, evolved, seawater-dominated hydrothermal fluid (Franklin et al., 1981; Lydon, 1984; Franklin et al., 2005).

Although VHMS deposits are intimately associated with submarine volcanic activities, various sources of the metals are considered such as, underlying rocks, contemporaneous magmas and coeval seawater. As discussed by Galley (1993) and Franklin et al. (2005), the source of metals in the VHMS systems are interpreted to have been leached from hydrothermal reactions zones by heated, compositionally modified seawater convection under

a steep geothermal gradient through the volcanic pile with or without a magmatic contribution of metals.

According to Franklin et al. (1981), sulphide precipitation is caused by cooling and oxidation of ore-forming fluids due to mixing with ambient seawater, or by boiling of the ore solution as it approaches toward the seafloor. In addition, Huston et al. (2010) noted that the hydrothermal fluid-seawater mixing in VHMS systems can also precipitate and preserve sulphate-bearing minerals such as barite, anhydrite and gypsum. The presence of sulphate mineral is an indicator of the presence of sulphate in seawater and the redox (reduced) state of the seafloor. Moreover, the advance argillic alteration assemblages, uniformly high salinities (>3 times modern seawater values), very ^{18}O-enriched and extremely Sn-rich characteristics are diagnostic of a significant magmatic hydrothermal inputs (Huston et al., 2011)

1.5 Objectives

This thesis focuses on the establishment of a genetic model of the Tasik Chini deposit through a combination of studies of geology, geochemistry and isotopic analysis of host volcanic rocks and sulphide assemblages. The specific aims are as follows:

- To characterise geological setting and tectonic environment of the Tasik Chini deposit in Central Belt, Peninsular Malaysia.
- To establish geochemical and geochronological relationships between ore and host volcano-sedimentary sequence and the style of mineralisation.
- To determine mineralogic, paragenetic and isotopic signatures, in particular sulphur and lead isotopes of the Tasik Chini deposit systems.

- To constrain the nature and source of ore fluids and metals (magmatic vs. sea water leaching processes) for constructing the genetic model of the deposits.

1.6 Methodology

The following field and laboratory works have been undertaken in the study area:

1.6.1 Field studies

Field studies were carried out within the Tasik Chini area to provide a geological framework of detailed geochronology, lithogeochemical, isotopic and fluid inclusions characteristics. Systematic sampling of surface rocks from selected geologic traverses of the main study area provided background information for preparation of analysis and interpretation of analytical results. Three seasons of field studies were initiated during the period of this research; in July-September 2010, March-May 2011 and July-September 2011.

1.6.2 Petrographic investigation

Representative samples were prepared for petrographic investigation by using thin sections, polished thin sections and mounts. Petrography study was used: i) to identify mineralogy and textures of various rock types, ores, fluid inclusions and degree of alteration within the rock types; and ii) to select least altered samples for whole-rock geochemical analysis.

1.6.3 LA-ICPMS U-Pb zircon geochronology

LA-ICPMS U-Pb zircon age determinations of volcanic rocks from the study area provide the first radiometric age of the host volcano-sedimentary succession in the study area. Analytical procedures are outlined in Chapter 4.

1.6.4 Lithogeochemistry

Lithogeochemical studies (major, trace and REE elements) of major rock units were employed to interpret the palaeotectonic setting of rock sequences (sedimentary, volcanic and plutonic rocks) in the study area. Further details are presented in Chapter 4.

1.6.5 Isotopic studies

The stable sulphur and radiogenic lead isotope studies were undertaken to evaluate isotopic zonation within the deposit and to trace the source of the studied minerals. Sm-Nd-Sr-isotope geochemistry was also studied as tracers to support and constrain the degree of metallogenic evolution between the host rocks and mineralisation. Detailed procedures of S- and Pb-isotope analyses are presented in Chapters 7 and 8, whereas Sm-Nd-Sr-isotopes method is outlined in Chapter 4.

1.6.6 Fluid inclusions studies

Detailed fluid inclusion study was carried out to understand the nature, source, variation and thermal aspects of ore-fluids. Details of methodology, precision and accuracy are presented in Chapter 9.

1.7 Thesis organisation

The thesis is presented into ten chapters and the subject of each chapter is outlined below.

Chapter 1 introduces an overview of the Bukit Botol and Bukit Ketaya deposits in Tasik Chini area including a review of previous work, general review of VHMS deposits, purposes and objectives of the research, methods used to achieve those objectives and structure of the thesis.

Chapter 2 provides the regional tectonic setting of Southeast Asia, geology and mining history in Peninsular Malaysia. It discusses reviews, current ideas and makes a significant

contribution to the overall understanding of the tectonomagmatic framework and evolution of Peninsular Malaysia, and its context within the Tasik Chini area in the Central Belt.

Chapter 3 describes the district-scale geology of the Tasik Chini area based on available published literature and data obtained during this study. The geological setting within the Tasik Chini area at the Bukit Botol and Bukit Ketaya deposits is also characterised in detail. This chapter is structured to provide give the reader with information from field mapping, detailed hand specimen and petrographic descriptions, contact relationships between units, and the deposit-scale distribution of the main rock types.

Chapter 4 provides data about whole rock geochemistry, LA-ICPMS zircon U-Pb geochronology and Sm-Nd isotopes. This chapter uses lithogeochemical data to refine the stratigraphic units, and provides an interpretation regarding geochemical trends with respect to district- and deposit-scale tectonics. The U-Pb age dating and Sm-Nd results obtained in this study are the first reported radiometric ages and isotopic data for the rocks of this area. They constrain the stratigraphic framework and the overall geological evolution of this region, such as the timing of volcanism and the duration of the volcanic arc sequence and the timing of mineralisation of the Tasik Chini deposit.

Chapter 5 discusses the mineralisation and alteration characteristics of the Bukit Botol and Bukit Ketaya deposits. This Chapter documents detailed mineralisation observations of each ore zone and addresses the paragenetic history of the both deposits. This Chapter also examines alteration assemblages identified in the Bukit Botol and Bukit Ketaya deposits using petrography, lithogeochemistry, Short-Wave Infrared (SWIR) spectroscopy and X-Ray diffractometry (XRD). Similar mineralisation sequence and alteration assemblages may be useful as a vector to similar mineralised systems.

Chapter 6 provides results of the trace element geochemistry of ore-bearing sulphides (i.e., sphalerite and pyrite) using electron microprobe and LA-ICPMS techniques. Variations in trace element distributions in sphalerite reflect the temperature and chemistry of the mineralising fluids. Similarly, trace element signatures of pyrite also show a chemical evolution of ore fluids. Thus, the source and chemistry of ore-fluids is constrained based on the data.

Chapters 7 and 8 focus on the isotopic characteristics of the Bukit Botol and Bukit Ketaya deposits. The sulphur isotope data from sulphide and sulphates and the Pb isotope signatures of both deposits are compared and interpreted together with published S- and Pb-isotopic data from similar types of mineralisation worldwide. The implications for both the nature of basement and ore-forming fluids are accessed.

Chapter 9 investigates the fluid inclusion petrographic features and microthermometric properties at the Bukit Botol and Bukit Ketaya deposits. The data were used to establish the ore-forming temperatures and thermal history of the deposits, and the range and variations in the salinity of the mineralising fluids in relation to the source of ore-fluids and the depositional mechanism.

Chapter 10 presents the overall conclusions of the thesis. A genetic model implication for exploration of this type of deposit and future research program are also discussed and given in this chapter.

CHAPTER 2 TECTONIC AND GEOLOGICAL SETTING

2.1 Introduction

This Chapter reviews the tectonic and geological setting of the Southeast Asia and Peninsular Malaysia using previous and current published information and data obtained from this study. It aims to provide background information for readers to understand the tectonic and metallogenic framework of Peninsular Malaysia.

2.2 Tectonic Setting of Southeast Asia

2.2.1 Main continental terranes

Many attempts have been made by previous workers to reconstruct the tectonic setting of Southeast Asia (e.g., Bunopas, 1982; Sengor, 1984; Hutchison, 1989, 2007; Metcalfe, 1988, 2011, 2013; Sone and Metcalfe, 2008; Barber and Crow, 2009; Hall, 2011, 2012; Morley, 2012; Khin Zaw et al., 2014). Generally, Southeast Asia is recognised to be made up of a collage of continental blocks or terranes including the South China Terrane, the Simao Terrane and the Indochina-East Malaya Terrane to the east and the Sibumasu Terrane, the West Myanmar (Burma) Terrane, the West Sumatra and the Woyla Terranes to the west (Fig. 2.1). The origin of all the Southeast Asia Terranes on the margin of Gondwana is also well discussed and detailed evidence can be found in a series of papers by Metcalfe (1988, 1996, 2006), Burrett and Stait (1985) and Burrett et al. (1990). As Peninsular Malaysia is located on the mainland Southeast Asia, an overview of the two major terranes; the Sibumasu Terrane and the Indochina-East Malaya Terrane (Metcalfe 1996, 2006) are discussed in detail in this thesis. The South China Terrane and the West Myanmar (Burma) Terrane are also discussed as they play significant roles in the formation of mainland Southeast Asia.

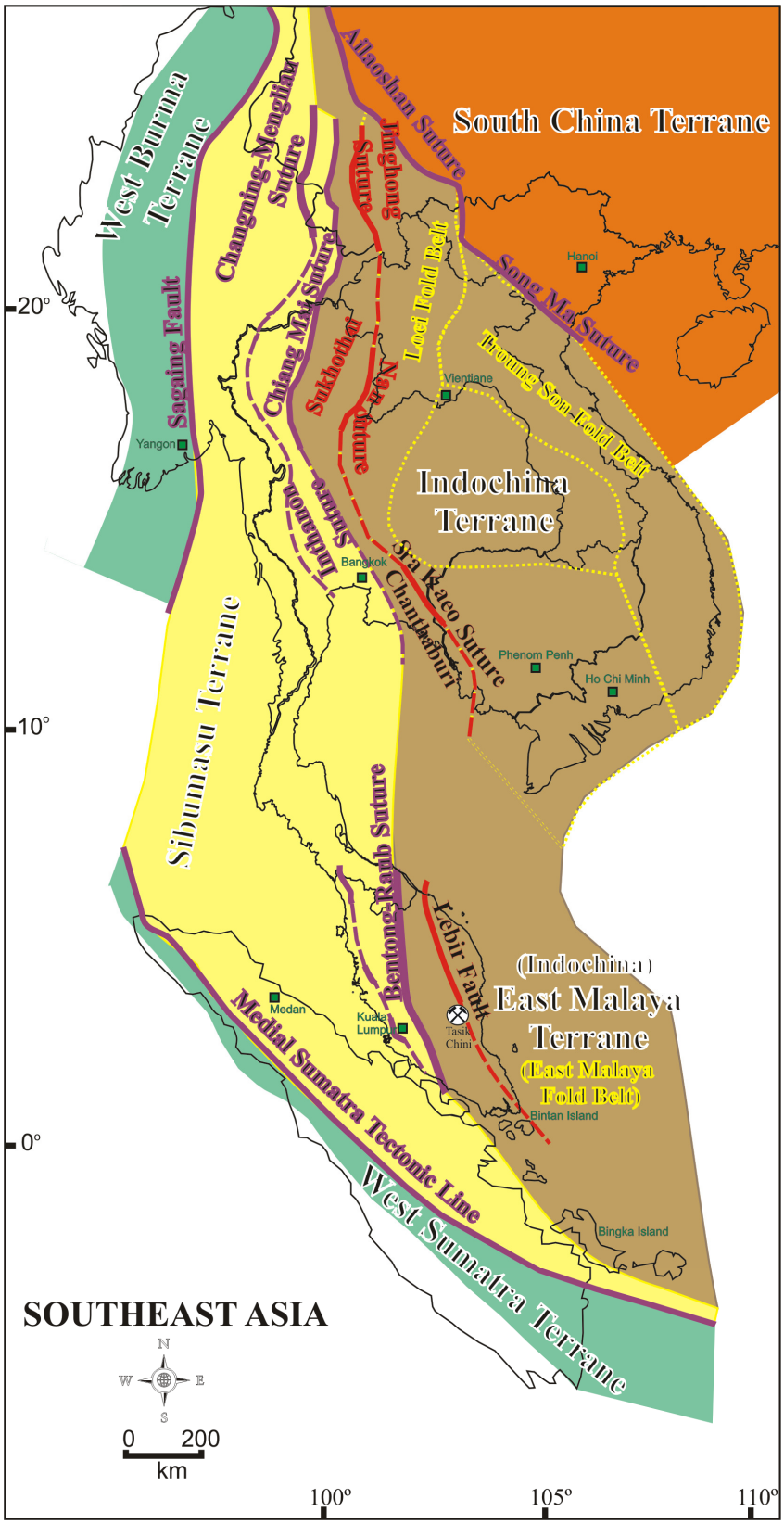

Fig. 2.1. Distribution of principal continental fragments of Southeast Asia including the main suture zones, back-arc and volcanic arcs, and major fold belts in Southeast Asia (redrawn and modified after Sone and Metcalfe, 2008; Barber and Crow, 2009; Metcalfe, 2009, 2011, 2013; Hall, 2011; Ridd, 2013; Khin Zaw et al., 2014).

a) Sibumasu Terrane

The Sibumasu Terrane forms the western region of Southeast Asia. Following Metcalfe (1988, 2013), the Sibumasu Terrane includes parts of western Yunnan (China), eastern Myanmar (Burma), western Thailand, western Peninsular Malaysia and the eastern part of Sumatra. It is bounded to the west by the Sagaing Fault, Andaman Sea and further southwest by the Medial Sumatra Tectonic Line (Fig 2.1). This terrane is characterised by the presence of glacial-marine diamictite (or pebbly mudstones: e.g., Barber and Crow, 2009) and Gondwana Palaeozoic flora and fauna (Metcalfe, 2011).

b) Indochina-East Malaya Terrane

The Indochina-East Malaya Terrane to the east covers a broad area of Vietnam, Cambodia, Laos, northeastern Thailand and continues to the eastern part of Peninsular Malaysia. In the northeast, the Indochina-East Malaya Terrane is bounded by the Ailaoshan-Song Ma Suture but its eastern and southern boundaries are poorly constrained (Fig. 2.1). This terrane is characterised by a Cathasyian Permian flora and fauna (Barber and Crow, 2009), and has experienced complex tectono-magmatic history that has been important for formation of different types of mineralised systems (e.g., Goldfarb et al., 2013; Khin Zaw et al., 2013; this study).

c) South China Terrane

The South China Terrane is a composite region and consists of two tectono-stratigraphic terranes: Yangtze and Cathaysia. The Yangtze and Cathaysia Terranes are separated by Jiangshao fault zone/tectonic suture zone (Zhou et al., 2002). Charvet et al. (1999) proposed that the amalgamation of the two terranes occurred around 900–950 Ma. Similar to the Indochina-East Malaya Terrane, this terrane has Early to Late Permian flora and fauna of Cathasyian type (Metcalfe, 1996).

d) West Myanmar (Burma) Terrane

The West Myanmar (Burma) Terrane (Hutchison, 1989, 2007; Metcalfe, 1996) including the Mount Victoria Land of Mitchell (1989) lies to west of the Mogok Belt. Following Hutchison (1989), Barber and Crow (2009) argued that the West Myanmar (Burma) Terrane forms the whole of western Myanmar, and is defined at its eastern and western boundaries by the Sagaing strike-slip fault and the Indo-Burman Ranges. The presence of Middle Permian fauna of Cathaysian type (Oo et al., 2002) at the West Myanmar (Burma) Terrane suggests that this terrane belongs to the same group of crustal blocks as the Cathaysialand provinces (i.e., Indochina-East Malaya and South China Terranes).

2.2.2 Main suture zones

Most known boundaries of the terranes that made up Southeast Asia are marked by major geological discontinuities, either by the suture zones of the main Palaeo-Tethys Ocean or the back-arc basins. In addition, a volcanic arc system is also identified (e.g., Sone and Metcalfe, 2008; Metcalfe, 2011) and has been established as part of the terranes. Furthermore, mineralised fold belts were also developed (e.g., Goldfarb et al., 2013; Khin Zaw et al., 2014). The main suture zones, back-arc basins, volcanic arc terranes and fold belts are shown in Figure 2.1, and are briefly discussed below:

The Changning-Menglian, Inthanon (Chiang Mai) and Bentong-Raub Sutures are regarded as the main Palaeo-Tethys Suture Zones (Fig. 2.1). In addition, according to Metcalfe (2011), the Ailaoshan and Song Ma Sutures are also included in other branches of the Palaeo-Tethys Ocean. Other postulated Palaeo-Tethys sutures include the Sagaing Fault in Myanmar and its southward extension the Medial Sumatra Tectonic Zone in Sumatra (Fig. 2.1) (e.g., Barber and Crow, 2003; Wakita and Metcalfe, 2005), both of which are currently present as a strike-slip shear zone (Barber and Crow, 2009).

The Jinghong-Nan-Sra Kaeo Suture is indicated by Sone and Metcalfe (2008) as the back-arc basin for the Sukhothai Arc System. This indication is based on the short age range of the chert found in these sutures from Early to Late Permian (Metcalfe, 2011) and they are considered to link the Sukhothai Island Arc System (Fig. 2.1) to the Permian volcanic arc terrane that was developed on the western margin of the Indochina-East Malaya Terrane during the Permian (e.g., Sone and Metcalfe, 2008).

The southern continuation of the arc system in Peninsular Malaysia is still controversial. Sone and Metcalfe (2008) and Metcalfe (2011, 2013) extended this Permian arc system to the entire East Malaya Terrane of the Peninsular Malaysia based on the widespread distribution of Permo-Triassic I-type subduction-related granitoids within the Central and Eastern Belts. However, Khin Zaw et al. (2014) prefer to call the eastern part of Peninsular Malaysia including the Central and Eastern Belts of East Malaya Terrane, the East Malaya Fold Belt (Fig. 2.1), which contains orogenic Au mineralisation, as detailed lithostratigraphic and magmatic-volcanic correlations are lacking for the correlation. In this study, the Central Belt and Eastern Belt are considered similar in origin at the earliest stage of East Malaya Terrane, but later separated by back-arc spreading and re-assembled by back-arc collapse (Chapter 4). Thus, it is suggested that the Central Belt of Peninsular Malaysia (Fig. 2.1) represents the volcanic arc system, and the Lebir Fault zone to the east as a possible of the back-arc suture. The extent of these island arc and back-arc systems in Peninsular Malaysia, are interpreted here extending towards the SE through the Bintan and Bangka islands of Indonesia following Hutchison (1989) and Barber et al. (2005) (Fig. 2.1).

The Truong and Loei Fold Belts are regarded as major fold belts within the Indochina Terrane (Fig. 2.1) (Khin Zaw et al., 2014). The NW-trending Truong Son Fold Belt is characterised by volcanic, plutonic and metamorphic rocks from Late Carboniferous to Late Triassic (310–230 Ma) ages, which formed as a result of a long–lived subduction–collision–extension with two

magmatic events between the Indochina and South China Terranes (e.g., Khin Zaw et al., 2010; Meffre, et al., 2011; Manaka et al., 2014). This fold belt contains skarn, epithermal and orogenic/sediment hosted deposit systems (Goldfarb et al., 2013; Khin Zaw et al., 2014; Manaka et al., 2014). The Permian Loei Fold Belt or Loei–Phetchabun Volcanic Belt hosts abundant of skarn and epithermal mineralisation systems (e.g., Goldfarb et al., 2013; Khin Zaw et al., 2014). It is dominated by volcaniclastics and marine sedimentary rocks that range in age from Devonian through Early Permian to Triassic (e.g., Goldfarb et al., 2013), and which experienced multiple magmatic tectonic events (e.g., Khin Zaw et al., 2014).

2.3 Tectonic Setting of Peninsular Malaysia

The Peninsular Malaysia consists of three main belts from the west to the east: Western Belt, Central Belt and Eastern Belt; and two suture zones: the Bentong Raub Suture Zone (Hutchison, 1975) and the Lebir Fault Zone (Tan, 1984) (Fig. 2.2).

a) The Western Belt

The Western Belt in the Peninsular Malaysia is part of the Sibumasu Terrane and is characterised by a Palaeozoic passive margin sequences. The sequences include Late Carboniferous–Early Permian glacial marine diamictites (Stauffer and Lee, 1986; Metcalfe, 1988) and cold–water brachiopods (Archbold et al., 1982; Shi and Waterhouse, 1991; Mohd Shafeea, 2003) found in the Singa Formation on the Langkawi Islands.

b) The Central and Eastern Belts

The Central and Eastern Belts of Peninsular Malaysia occur on the East Malaya Terrane (East Malaya Fold Belt). Carboniferous plant fossils at Kuantan, Pahang (Asama, 1973) and at Tanjung Mat Amin, Terengganu (Ohana et al., 1991) in the Eastern Belt and the Permian Cathasyian floras from the Jengka Pass, Pahang (Kon'no and Asama, 1970) and the Gunung Blumut area (Linggiu Formation), Johor (Kon'no et al., 1971) in the Central Belt are typical of warm climate flora and fauna indicators (Asama, 1984).

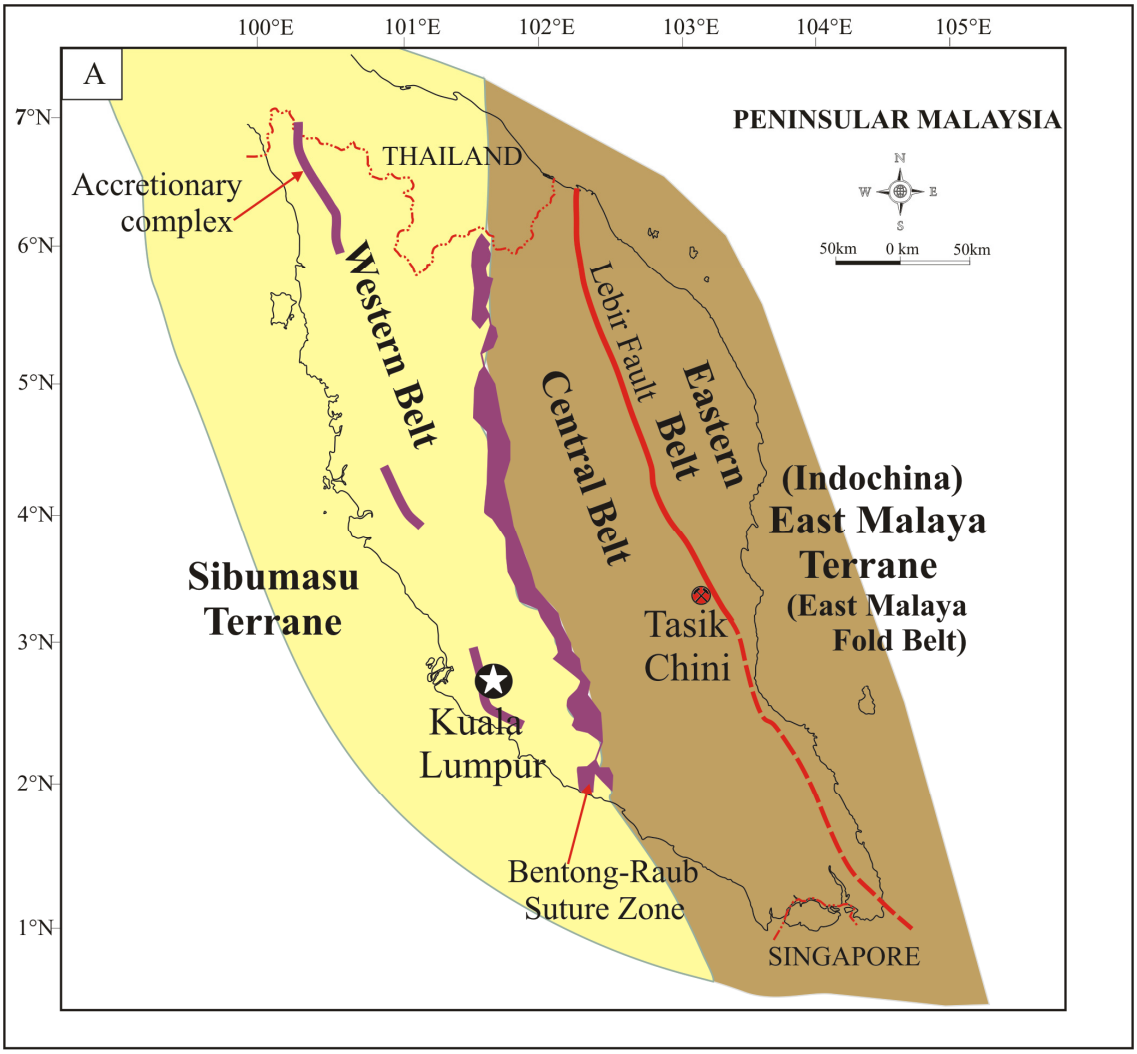

Fig. 2.2. Tectonic belts of Peninsular Malaysia. **A**. Map showing the Western, Central and Eastern Belts of Peninsular Malaysia with the Bentong–Raub Suture Zone and Lebir Fault.

Both Central and Eastern Belts have a broad similar stratigraphy. In addition, evidence obtained in this study, including the U–Pb detrital zircon and radiogenic isotopic data, also supports that the both Central and Eastern Belts have a similar origin of the East Malaya Terrane (Chapter 4).

The Central Belt reveals continuity in stratigraphic sequences but with a different tectonic environment from the Permian to Cretaceous ages. The Permo–Triassic sequence in the Central Belt is dominated by submarine volcano–sedimentary rocks and is unconformably

overlain by the Jurassic–Cretaceous continental sedimentary rocks. The confirmed oldest rocks in the Eastern Belt are predominantly of submarine Carboniferous siliciclastic and carbonate rocks (Metcalfe, 2013) with the absence of Triassic sedimentary rocks (Hutchison, 2007). The stratigraphic successions of the Central Belt represent the Permian volcanic arc that formed on the margin of the East Malaya Terrane (Eastern Belt).

c) The Bentong–Raub Suture Zone

The Bentong–Raub Suture Zone is regarded as a collisional zone between the Sibumasu Terrane and the East Malaya Terrane (East Malaya Fold Belt) during the Triassic (Fig. 2.2; Hutchison, 1975; Tjia, 1989; Metcalfe, 2000). It comprises mélange, ribbon bedded chert and schist with small bodies of serpentinised mafic–ultramafic rocks that are ophiolitic in nature (Hutchison, 1989; Tjia, 1989) and the accretionary complex of widespread chert sequences at the west of the Bentong–Raub Suture Zone (Ridd, 2013; Metcalfe, 2013). The radiolarians found in the bedded chert along the ophiolitic suture zone yielded ages from Late Devonian to Late Permian (e.g., Spiller and Metcalfe, 1995; Spiller, 1996; Basir Jasin and Che Aziz Ali, 1997a, 1997b). Meanwhile, the chert sequences of the accretionary prism revealed radiolarian ages from Early Carboniferous to Late Triassic (Basir Jasin and Zaiton Harun, 2011; Metcalfe, 2013; Ridd, 2013) and were deposited in deep marine environments (Basir Jasin and Zaiton Harun, 2011; Ridd, 2013). From these constrained ages, Metcalfe (2000, 2013) interpreted that Palaeo–Tethys started opening in the Late Devonian. The collision event of the Sibumasu Terrane with East Malaya Terrane (East Malaya Fold Belt) is considered to have occurred in the Late Triassic following Hutchison (1989; 2007), which is later than the Early–Middle Triassic as proposed by Metcalfe (2013).

d) The Lebir Fault Zone

The Lebir Fault Zone represents a tectonic boundary between the Central and Eastern Belts of Peninsular Malaysia. This fault zone has a well–defined boundary between the Central and Eastern Belt granites in the northeastern part of Peninsular Malaysia (Tjia, 1972) but its southern continuation is poorly defined. Although the significance of the Lebir Fault Zone is not well pronounced as a suture zone such as the Bentong–Raub Suture, the occurrence of sheared diamictite (olistostrome) (Metcalfe and Chakraborty, 1988) and serpertinite bodies (Tan and Khoo, 1981) within the Lebir Fault Zone are possibly ophiolitic components suggesting the fault is a suture zone. Additionally, a consistent and extensive distribution of the confirmed oldest rocks (predominantly Carboniferous) in the Eastern Belt, from the eastern part of Kelantan through Terengganu, and at the eastern part of Pahang into east Johor to the south (e.g., Lee, 2004, 2009; Surjono, 2007) is considered here to mark the southern continuation of the Lebir Fault zone between the Central and Eastern Belts (Fig. 2.2). Thus, this author follows the suggestion of Sevastjanova et al. (2011) that the Lebir Fault represents a suture zone, as the remnant of postulated closed back–arc basin developed on the margin of the Permian East Malaya volcanic arc (Sone and Metcalfe, 2008) between the Central and Eastern Belts.

2.4 Palaeotectonic Reconstruction of Southeast Asia and Peninsular Malaysia

Although there are still many uncertainties regarding the detailed geometry of terrane attachments and timing of rifting, amalgamation and accretion events to form the present–day Southeast Asia, the current development and present–day configuration of palaeogeographic reconstructions of Tethys Oceans and continental drift model by several authors (e.g., Wakita and Metcalfe, 2005; Barber and Crow, 2009; Metcalfe, 2011; Khin Zaw et al., 2014) have provided important clues and constraints to understand the tectonic evolution of the Southeast Asia.

On the modified palaeogeographic maps of Metcalfe (2011) (Fig. 2.3), including data obtained in this study, the tectonic features of Peninsular Malaysia resulted from the collision of the Sibumasu Terrane and the Sukhothai Arc–East Malaya Terrane (East Malaya Fold Belt).

The East Malaya Terrane (East Malaya Fold Belt) had rifted together with several collages of terranes comprising North China, South China, Tarim, Indochina, West Myanmar (Burma) and West Sumatra from Gondwana by the Late Devonian or Early Carboniferous. This rifting formed a Palaeo–Tethys Ocean (Metcalfe, 1996). During this time, the Indochina–East Malaya Terranes amalgamated with the South China Terrane along the Song Ma Suture. The Truong Song Fold Belt formed during the subduction–collision related process of these two terranes (e.g., Goldfarb et al., 2013; Khin Zaw et al., 2014) (Fig. 2.3A).

During the Permian and Early Triassic, the Palaeo–Tethys closed due to extensive subduction–collision processes beneath the North China, South China, Tarim and Indochina–East Malaya Terranes (Figs. 2.3B, C and D). As a result, Gondwana rotated clockwise with the Cimmerian Continent of Sengör (1984) containing Western Cimmerian, Qiangtang and Sibumasu drifting from Gondwana far north across the opening of Palaeo–Tethys Ocean (Figs. 2.3B), followed by opening of the newly formed Meso–Tethys behind the Cimmerian Continent (Wakita and Metcalfe, 2005) (Fig. 2.3C).

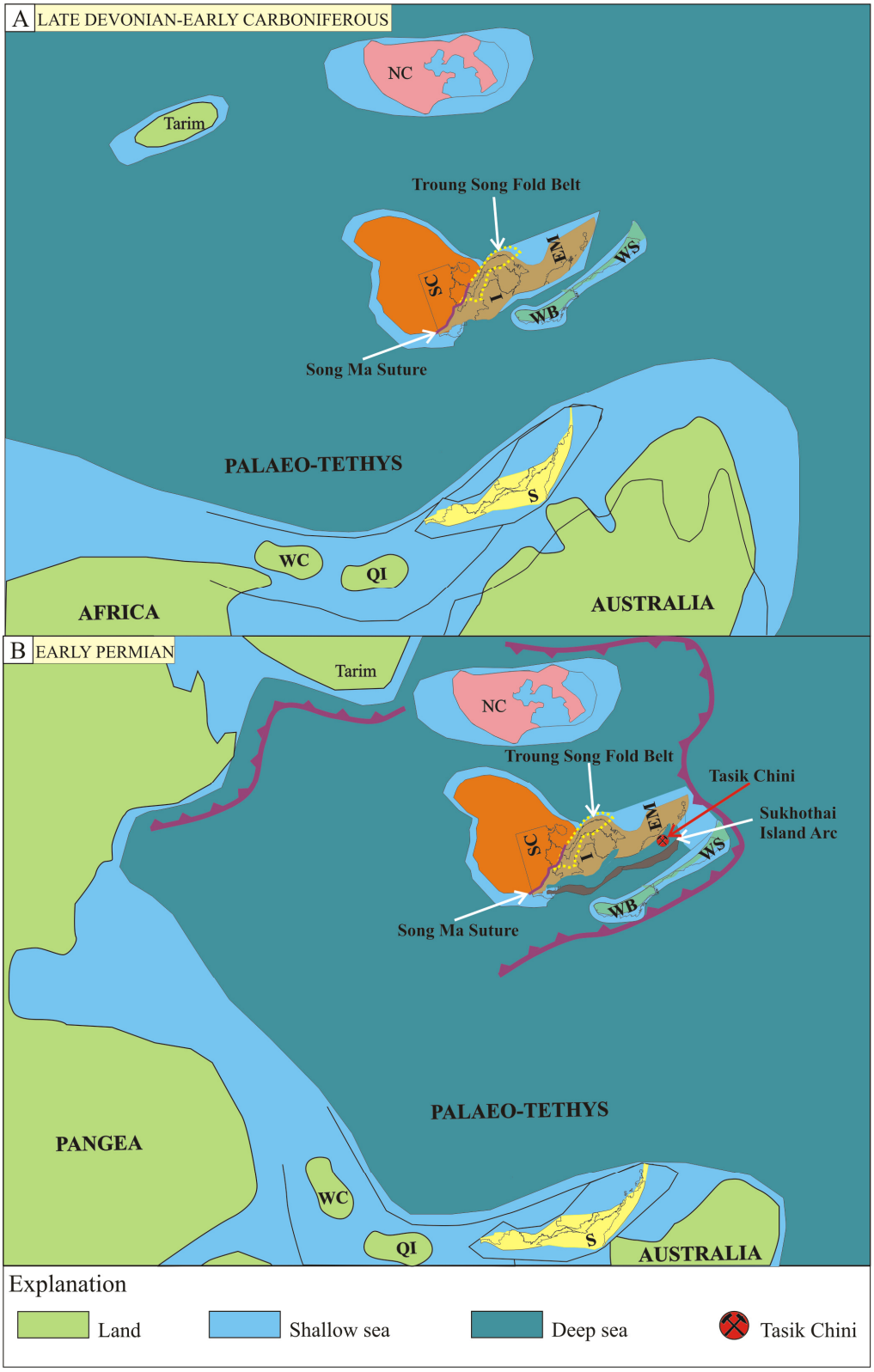
A LATE DEVONIAN-EARLY CARBONIFEROUS
NC
Tarim
Troung Song Fold Belt
SC
I
EM
WS
WB
Song Ma Suture
PALAEO-TETHYS
S
WC
QI
AFRICA
AUSTRALIA
B EARLY PERMIAN
Tarim
NC
Troung Song Fold Belt
Tasik Chini
Sukhothai
Island Arc
SC
I
EM
WS
WB
Song Ma Suture
PALAEO-TETHYS
PANGEA
WC
QI
S
AUSTRALIA
Explanation
Land
Shallow sea
Deep sea
Tasik Chini

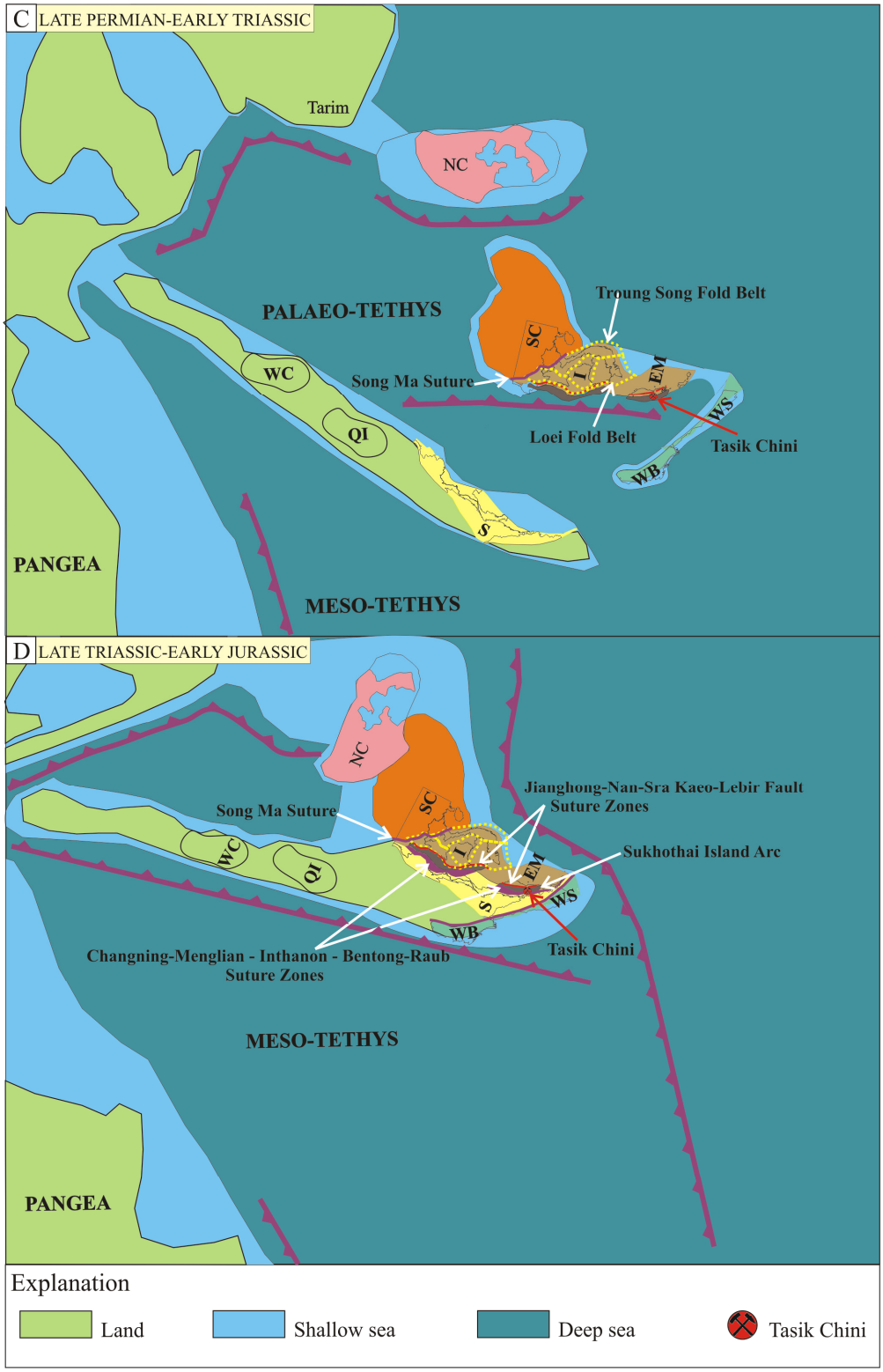

Fig. 2.3. Reconstruction maps of Southeast Asia showing the relative position of the Tasik Chini location on the East Malaya (EM). A. Late Devonian–Early Carboniferous. B. Early Permian. C. Late Permian–Early Triassic. D. Late Triassic–Early Jurassic. Annotation: S=Sibumasu, EM=East Malaya, SC=South China, NC=North China, I=Indochina, WS=West Sumatra, WB=West Burma, QI=Qiangtang and WC=Western Cimmerian. Diagram modified from Wakita and Metcalfe (2005); Barber and Crow (2009); Metcalfe (2011).

The closing of the Palaeo–Tethys generated a Permo–Triassic volcanic rock and I–type granitoids of the Sukhothai Arc on the margin of Indochina–East Malaya which were separated by a back–arc basin, and also formed the main oceanic suture and remnant of back–arc basin suture zones that now bind the mainland Southeast Asia terranes to each other as a result of several collisions (e.g., Sone and Metcalfe, 2008; Metcalfe, 2013). The Sukhothai island arc is represented by the Lincang–Sukhothai–Chanthaburi fragments on the Indochina Terrane (Sone and Metcalfe, 2008), and by the Central Belt, Peninsular Malaysia on the East Malaya Terrane (part of East Malaya Fold Belt). Furthermore, the main oceanic suture zones include the Changning–Menglian Suture and Inthanon Suture (Sone and Metcalfe, 2008), and the Bentong–Raub Suture (Hutchison, 1975; 2009), whereas the Sukhothai back–arc basin is defined by the Jinghong–Nan–Sra Kaeo suture zones (Sone and Metcalfe, 2008; Metcalfe, 2013), and the Lebir Fault Zone (Sevastjanova et al., 2011; this study). The Loei Fold Belt may have been created during this time (e.g., Goldfarb et al., 2013; Khin Zaw et al., 2014) (Figs. 2.3B and C).

By the Late Triassic, the Meso–Tethys Ocean continued to move northwards and the assembly of Sundaland had formed. During this time, the subduction of the Meso–Tethys occurred outside of the Sundaland. This subduction progressed continuously through to the present day in west Sumatra and through to south Java (Fig. 2.3D). At the same time, the final suturing of Peninsular Malaysia created crustal thickening of both sides of the collision terranes through to the end of Triassic, resulting in the extensive emplacements of S–type tin–bearing granites. In addition, Sone and Metcalfe (2008) and Metcalfe (2011) speculated that the Loei–Phetchabun Volcanic Belt in Thailand developed during this time.

2.5 Geology of Peninsular Malaysia

A brief introduction to the geology of Peninsular Malaysia is herein presented based on two publications: "Geology of the Malay Peninsula" by Gobbett and Hutchison (1973) and "Geology of Peninsular Malaysia" by Hutchison and Tan (2009) and other local published information (e.g., Hutchison, 1989; Lee et al., 2004).

In general, all geological and stratigraphic sequences ranging from the Palaeozoic to Cenozoic ages are present in Peninsular Malaysia. Based on the stratigraphic data, two sedimentary basins are recognised, the western basin and the eastern basin. The western basin is characterised by the Late Cambrian to Late Triassic rock sequence and the eastern basin consists of an Early Carboniferous to Permian sequence. The pre-Triassic rocks are principally of marine origin, whereas the post-Triassic rocks are essentially non-marine sediments. However, the Triassic rocks have both marine and non-marine origins; with the continental sedimentary rocks being Jurassic-Cretaceous in age. Two deep marine basins were formed: Semanggol fore-deep basin devoid of volcanism and Semantan fore-arc basin associated with volcanism (Metcalfe, 2000).

2.5.1 Palaeozoic sedimentary rocks

The Palaeozoic rocks of Peninsular Malaysia are distributed in the Western, Central and Eastern belts. The Early Palaeozoic rocks are confined to the northwestern and western parts of Western Belt, and the Late Palaeozoic rocks are found in all three belts.

a) Cambrian

The Cambrian rocks in Peninsular Malaysia comprise sandstone/metasandstone with subordinate siltstone, shale and conglomerate. On Langkawi Island, the Late Cambrian to Ordovician Machinchang Formation is a 3250m thick sequence composed of quartzitic sandstone with subordinate conglomerate, siltstone and mudstone (Fig. 2.4; Jones, 1961).

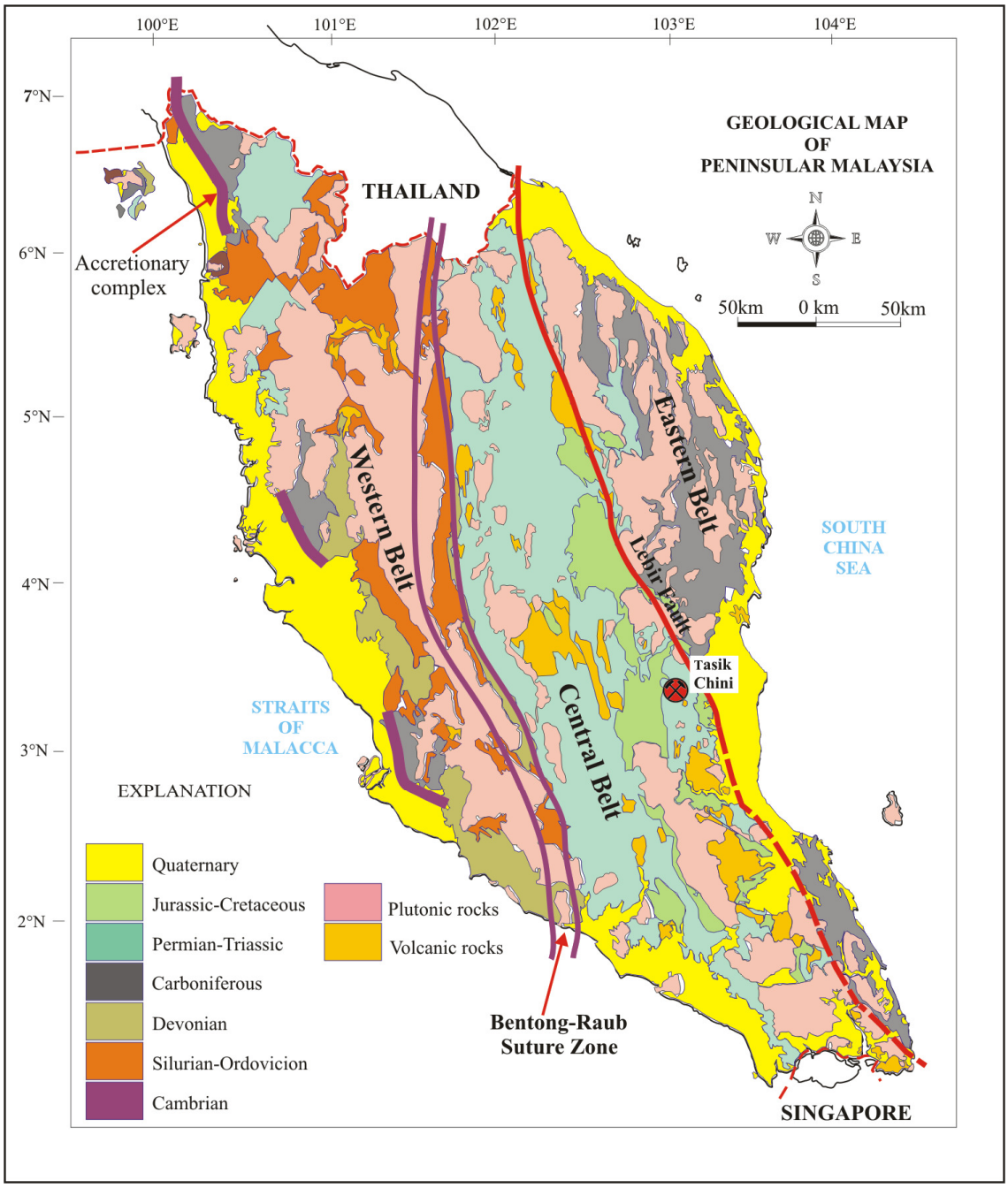

Fig. 2.4. Geological map of the Peninsular Malaysia (modified after Minerals and Geoscience Department of Malaysia, 2004).

In central Kedah, possible Cambrian equivalent rocks are reported to occur and are known as the Jerai Formation (Bradford, 1972). In the western part of the Western Belt, the Papulut quartzite in north Kedah constitutes a well-defined unit of quarzite, lithic greywacke and conglomerate with chert and quartzite pebbles (Jones, 1973) that are probably comparable

with the Machinchang and Jerai Formations. Towards the south, the similar Cambrian–Ordovician rocks are called the Dinding Schist in Kuala Lumpur area (Gobbett, 1965).

b) Ordovician–Silurian

The Ordovian–Silurian rocks in Peninsular Malaysia are composed of schist, phyllite, slate and limestone with minor intercalation of sandstone and volcanic rocks. The rocks conformably overlie the Cambrian formations in the northwestern and western parts (Fig. 2.4; Hutchison, 1989). The Setul Group, the Mahang and Kroh Formations and Kinta Limestone occupy the Western Belt. The most southerly occurrence of Silurian limestone is the 1830m thick Kuala Lumpur Limestone (Gobbett, 1965).

c) Devonian

The Devonian stratigraphy in Peninsular Malaysia is dominated by the deposition of shale/black shale, abundant limestone and sandstone, some conglomerate, chert and rare volcanic rocks. The Devonian limestone is intercalated with carbonaceous shale sequences up to 3000m thick and is exposed in the Kinta Valley, Perak (Ingham and Bradford, 1960).

d) Carboniferous–Permian

Carboniferous sequences in Peninsular Malaysia are composed of carbonaceous argillaceous rocks and significant limestone sequence with a local presence of volcanic rocks. In the Western Belt, the Carboniferous–Late Permian Singa Formation on the Langkawi Island is about 1625m thick and includes pebbly mudstones and diamictites (Fig. 2.4; Ahmad Jantan, 1973). In Kedah and Perlis, the Carboniferous–Permian sequence consists of the Kubang Pasu and the Chuping/Kodiang Limestone. However, the Carboniferous rocks outside the diamictite zone comprise limestone, red beds and black shale successions. In the Eastern Belt, Late Palaeozoic sedimentary rocks of predominantly Carboniferous to Permian age are

distributed from the eastern part of Kelantan through Terengganu, and eastern part of Pahang into east Johor to the south (Lee, 2004, 2009; Surjono, 2007).

2.5.2 Mesozoic sedimentary rocks

Mesozoic rock formations are widespread in the northwestern part of the Western and Central belts of Peninsular Malaysia. Some of the Mesozoic rock formations are parts of the Permian units (Mohd Shafeea Leman, 2004). However, the Triassic sedimentary rocks were not found in the Eastern Belt, including the non-marine red bed and grey sandstone facies (Hutchison, 2007).

a) Permo–Triassic

The Permo-Triassic rock formations comprise flysch sequences consisting of mudstone, shale, siltstone and sandstone and, in places, limestone. The Permo-Triassic rocks comprise the Chuping/Kodiang Formation, Semanggol Formation in the Western Belt and the Semantan and Gua Musang formations in the Central Belt (Fig. 2.4; Mohd Shafeea Leman, 2004). In addition, all the Permo–Triassic formations in the Central Belt are interbedded with a volcanic rock of rhyolitic to andesite composition (Mohd Shafeea Leman, 2004).

b) Jurassic–Cretaceous

In general, the sedimentary succession of the Jurassic–Cretaceous comprises conglomerate, mudstone and sandstone of continental deposits, and they unconformably overlie the Triassic sedimentary rocks. In the Western and Eastern belts, the Jurassic–Cretaceous rocks occur in several isolated basins (Fig. 2.4; Mohd Shafeea Leman, 2004). The Tembeling Group in southeast Pahang and the Koh Formation in southern Kelantan are the two main Jurassic–Cretaceous formations occur in the Central Belt.

2.5.3 Cenozoic sedimentary rocks

The Cenozoic sedimentary rocks that occur onshore in Peninsular Malaysia are Quarternary sediments comprising unconsolidated to semi-consolidated boulders, gravel, sand, silt and clay in the coastal and inland regions. The onshore Tertiary sequences are sparsely distributed (Kamaludin, 1990, 2004) and coal–bearing sediments are deposited in swampy, alluvial flood–plain to lacustrine environments in pull–apart basins (Raj et al., 1998) that may be up to 50 km wide (Raj, 2009).

2.5.4 Volcanism

Three phases of volcanism are recognised in Peninsular Malaysia: (a) Early Palaeozoic, (b) Early to Late Permian and Triassic, and (c) Cenozoic (Hutchison, 1973; Ghani, 2009b). The Early Palaeozoic volcanic sequences are the Jerai Formation in Kedah, the Lawin Tuff in Perak and the Genting Sempah Complex in Pahang (Fig. 2.5; Hutchison, 1973; Ghani, 2009b). The volcanic rocks consist of foliated rhyolite and tuffs. The Early to Late Permian and Triassic volcanic rocks occur in the Kelantan and Pahang States, and southern part of Johor State (Fig. 2.5). They consist of rhyolite, rhyodacite and andesite, and they are interpreted to have been emplaced by subduction–related volcanism (e.g., Metcalfe, 2000).

The volcanic rocks in the Kelantan and Pahang States are formerly referred as the Pahang Volcanic Series (Willbourn, 1917). In the southern part of Peninsular Malaysia, the volcanic province extends from the Tasik Chini area of this research project (Fig. 2.5) in the north to the Pengerang area in the south (Grubb, 1968). Around Bukit Ibam and Tasik Chini areas, the volcanic rock sequences are comparable to the Sedili Volcanic Formation which unconformably overlies the Dohol Formation (Taylor, 1971; Taylor and Toh, 1981).

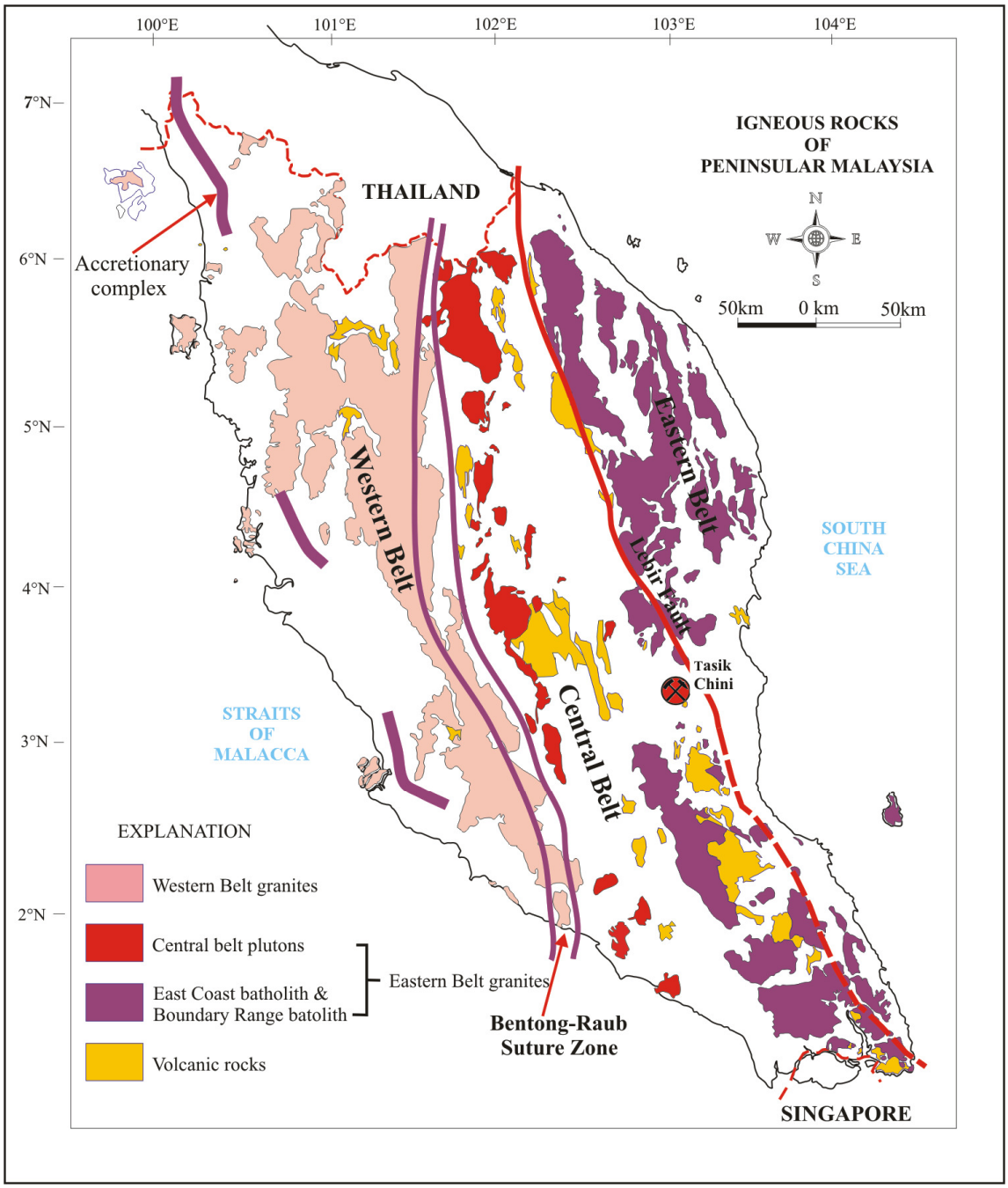

Fig. 2.5. Distribution of igneous rocks in Peninsular Malaysia (modified after Hutchison, 1973; Schwartz et al., 1995).

The Cenozoic explosive volcanism of basalt flows are known at two locations in the Peninsular Malaysia: (1) in the Jabor area north of Kuantan, Pahang and (2) at Segamat, Johor (Hutchison, 1973; Ghani, 2009b).

2.5.5 Plutonism

The granites in Peninsular Malaysia have been grouped into two main granite provinces namely Western and Eastern granite belts (Cobbing et al., 1992). These granitic provinces mainly record the closure of the Paleo−Tethys and the suturing of the Sibumasu Terrane and Indochina-East Malaya Terrane (East Malaya Fold Belt) (e.g., Hutchison, 1975; Cobbing et al., 1986; Metcalfe, 1988, 2000), with a small number of Cretaceous aged plutons associated with post-orogenic magmatism (e.g. Cobbing et al., 1986; Metcalfe, 2000). The two granite belts are separated by the Bentong-Raub Suture Zone and most of the intrusions of this plutonic process are aligned parallel to the N−S structural trend, but some are found to cut-across the N−S structural trend.

The Western Belt granitoids are characterised by the Main Range batholith to the east and the Bintang batholith immediately to the west and they form as major topographic features of the Peninsular Malaysia (Fig. 2.5). The Western belt corresponds to the Central Granitoid Province of Southeast Asia of Cobbing et al. (1992). Further to the west, small intrusive bodies form as individual plutons in the Bukit Mertajam-Kulim, Penang and Langkawi Island (Ghani, 2000). The main granitoid rock type is biotite granite of S−type affinities (Hutchison, 1977), which has ilmenite-series characteristics (Ishihara et al., 1979). In addition, recent studies by Mohd Rozi Umor et al. (2011) found that the Western Belt granites are peraluminous, high−K calc−alkaline series, suggesting their emplacement was syn−collisional in a within-plate setting. Previous studies on the Rb−Sr whole rock isochron and U−Pb zircon ages of the granites in the Western Belt shown age ranges from 207±14 Ma to 230±9 Ma (e.g., Liew and Page, 1985b; Cobbing et al., 1986; Darbyshire, 1988; Hutchison, 1989; Cobbing et al., 1992; Schwartz et al., 1995). The most recent study by Searle et al. (2012) also provided a similar group of ages from Late Triassic to the earliest Jurassic .

In comparison, the Eastern Belt granitoids correspond to the Eastern Granitoid Province of Southeast Asia of Cobbing et al. (1992), and they form as small and composite batholiths and plutons. Two main batholiths and one narrow belt consisting of isolated plutonic bodies are found along this belt. They are the East Coast batholith at the eastern most part, the Boundary Range batholith at the west and the Central Belt plutons further to the west (Fig. 2.5; Schwartz et al., 1995). The intrusions of the East Coast and Boundary Range batholiths consist of granite, granodiorite and quartz diorite, whereas the representative major plutons in the Central Belt are mafic to intermediate and felsic in compositions (Mohd Rozi Umor et al., 2011). In general, the Eastern Belt granites contain both I and S type granitoids (Hutchison, 1977), and show a mixed signature of magnetite– and ilmenite–series (Ishihara et al., 1979). However, recent studies by Mohd Rozi Umor et al. (2011) recognised that the two batholiths of the Eastern Belt granites are mainly metaluminous with minor peraluminous, calc–alkaline to high–K calc–alkaline series with only I–type granite affinity and classified as volcanic arc granite (VAG) with minor within plate granite (WPG) environment. Meanwhile, the Central Belt plutons are metaluminous to minor peraluminous, high–K calc–alkali to shonshonite series, and contain both I– and S–type granites and plot in syn-collision (Syn–COLG) to within-plate granite (WPG) setting.

Available Rb–Sr whole rock isochrones and U–Pb zircon data show that the East Coast and the Boundary Range batholiths have ages between 220 Ma (Triassic) and 263 Ma (Permian) (Liew and Page, 1985; Cobbing et al., 1986; Darbyshire, 1988; Hutchison, 1989; Cobbing et al., 1992; Schwartz et al., 1995), whereas the Central Belt plutons yield ages from 79 Ma to 219 Ma (Liew and Page, 1985; Cobbing et al., 1986; Darbyshire, 1988; Hutchison, 1989; Cobbing et al., 1992; Schwartz et al., 1995; Mohd Rozi Umor and Syed Sheikh Almashoor, 2000). Combining previous age data with their new U–Pb zircon ages, Searle et al. (2012) and

Oliver et al. (2014) indicated the Eastern Belt granite ages for the two batholiths and Central Belt plutons as ranging from Middle Permian to Late Triassic.

2.6 Regional Structure and Deformation

Three major phases of folding and uplift have been recorded in Peninsular Malaysia from the stratigraphic and structural records. The Late Permian to Early Triassic folding episode in Peninsular Malaysia is a major orogenic mountain-building phase as suggested by Harbury et al. (1990). This folding is indicated by different structural deformation styles within the Palaeozoic and Mesozoic strata in Peninsular Malaysia, and it is interpreted to represent collision events between the Sibumasu Terrane and Indochina–East Malaya Terrane (East Malaya Fold Belt) (Metcalfe, 2013), related to the formation of the Bentong–Raub Suture and Lebir Fault Zone. The Late Triassic–Early Jurassic folding and uplift event in Peninsular Malaysia was caused by the Indosinian Orogeny (Hutchison and Sivam, 1992; Oliver et al., 2014). However, Metcalfe (2000) argued that the Indosinian deformation was weakly developed in Peninsular Malaysia and is not related to the formation of the Bentong–Raub Suture. Middle–Late Cretaceous to Cenozoic structural evolution in Peninsular Malaysia is related to the strike–slip movements along major fault zones between the old Sibumasu Terrane and East Malaya Terrane (East Malaya Fold Belt) (Hutchison, 1989; Tjia, 1989). In addition, Metcalfe (2000) noted that the Middle–Late Cretaceous deformation involved SW–NE shortening in Peninsular Malaysia. Throughout Southeast Asia, this deformation is regarded as the result of the Himalayan Orogeny due to collision of the Indian plate against Eurasia (e.g., Tapponnier et al., 1986).

2.7 Mineralisation in Peninsular Malaysia

Scrivenor (1928) firstly divided the Peninsular Malaysia into three mineralisation belts: the Western Tin Belt, the Eastern Tin Belt and the Central Gold Belt based on the different distribution of mineralisation style found in these belts (Fig. 2.6).

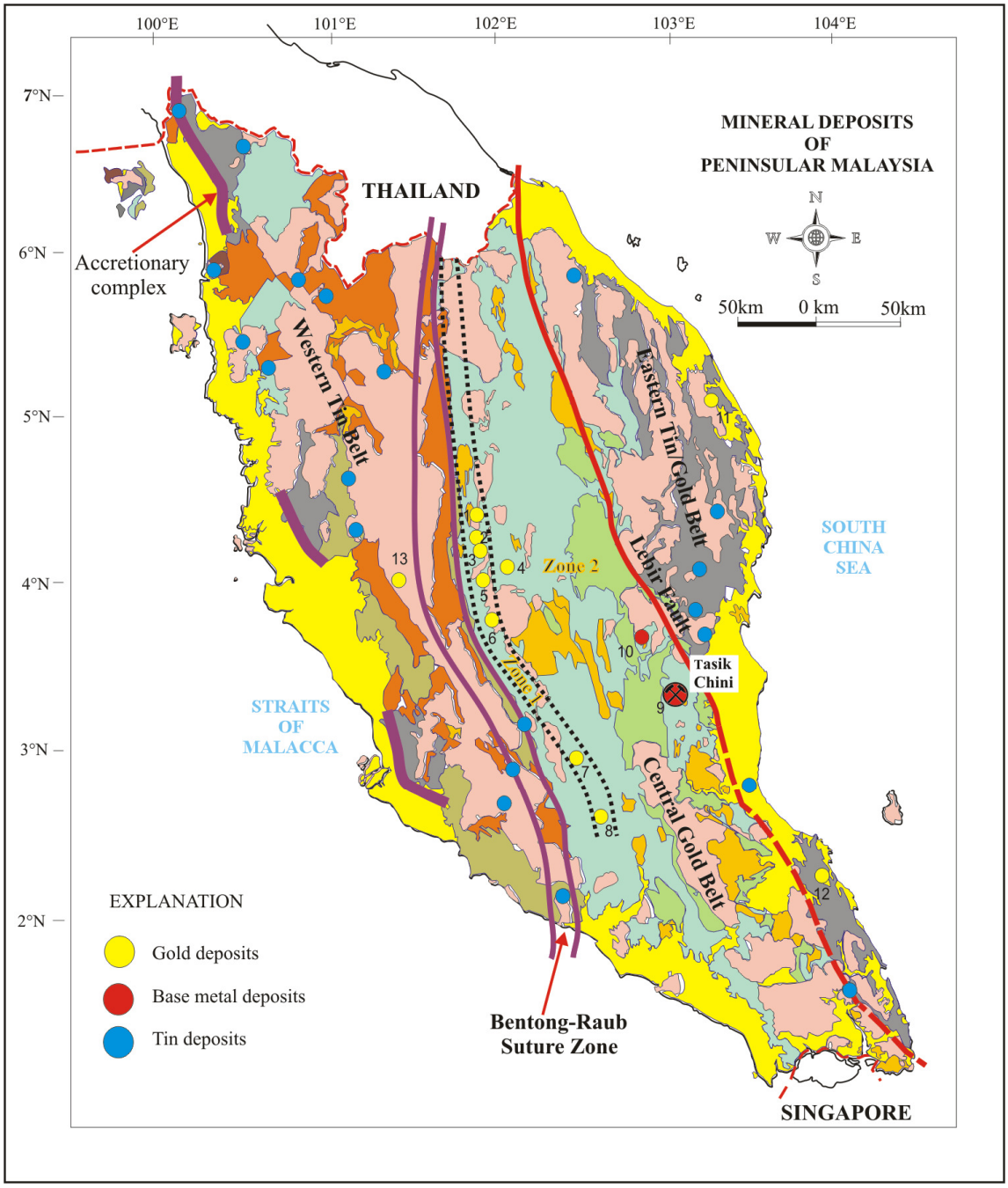

Fig. 2.6. Map of Peninsular Malaysia showing mineral belts and location of tin, gold and base metal deposits (modified after Chu et al., 1988; Yeap, 1993).

a) The Western Tin and the Eastern Tin/Gold Belts

During the active tin mining time of the 1970s, the Western and the Eastern Tin belts were regarded as one of the world's richest metallogenic tin provinces. The tin mineralisation in both belts has been studied in detail (e.g., Hosking, 1979; Schwartz et al., 1995). However, the decline and demise of the tin mining activity in 1985 caused the closure of all the tin mines in Peninsular Malaysia. Although the Western and the Eastern Belts have been known for the tin deposits, available reports (e.g., Yeap, 1993; Dube, 2006) suggested that gold mineralisation does occur in various places in both belts. The known gold mineralisation has been recorded at Bidor of Perak in the Western Belt, and is being mined at Lubuk Mandi of Terengganu and Mersing of Johor in the Eastern Belt (Fig. 2.6 and Table 2.1).

b) The Central Gold Belt

The gold mineralisation in the Central Gold Belt occurs along a major N–S zone. The following characteristics of the gold mineralisation in Central Gold Belt are described by Yeap (1993):

(1) The Central Gold Belt is dominated by orogenic/sediment–hosted gold and base metals deposits (Table 2.1);

(2) The first mineralisation zone (Zone 1) is located immediately to the east of the Main Range granite and the Bentong-Raub Suture Zone; with a significant orogenic/sediment-hosted style of gold mineralisation. This narrow zone extends from the north near the Thailand border, to the central parts of major gold fields which include the Rubber Hill, Buffalo Reef, Selinsing, Tersang and Penjom deposits, and continues further south at the Gunung Ledang deposit; and

(3) The second mineralisation zone (Zone 2), which is situated at the eastern most part of the Central Gold Belt, exhibits a broader variety of gold mineralisation (Fig. 2.6). For instance, according to Wan Fuad Wan Hassan and Purwanto (2002), the Mengapur deposit is typified by gold mineralisation in skarn and the Tasik Chini (subject of this research) is characterised by gold mineralisation in massive sulphides.

Table 2.1. Summary of the gold and base metal deposits in Peninsular Malaysia.

No.	Locality	Location	Mineralisation style
1	Rubber Hill	Central Gold Belt	Orogenic/sediment hosted
2	Buffalo Reef	Central Gold Belt	Orogenic/sediment hosted
3	Selinsing	Central Gold Belt	Orogenic/sediment hosted
4	Penjom	Central Gold Belt	Orogenic/sediment hosted
5	Tersang	Central Gold Belt	Orogenic/sediment hosted
6	Raub	Central Gold Belt	Orogenic/sediment hosted
7	Batu Bersawah	Central Gold Belt	Orogenic/sediment hosted
8	Gunung Ledang	Central Gold Belt	Orogenic/sediment hosted
9	Tasik Chini	Central Gold Belt	Base metal/VHMS
10	Mengapur	Central Gold Belt	Base metal/Skarn
11	Lubuk Mandi	Eastern Tin/Gold Belt	Orogenic/sediment hosted
12	Mersing	Eastern Tin/Gold Belt	Orogenic/sediment hosted
13	Bidor	Western Tin/Gold Belt	Orogenic/sediment hosted

In addition, other types of deposits are also found in a number of districts within these three belts, such as iron, manganese, barite and bauxite mineralisation. However, all of these deposits are currently either considered as having less economic importance or have been already exploited/ mined in the past.

2.8 Summary

1) The Peninsular Malaysia forms part of mainland Southeast Asia and comprises two tectonic terranes, the Sibumasu Terrane to the west and the East Malaya Terrane (East Malaya Fold Belt) to the east. A former Permian volcanic arc system which forms part of the East Malaya Terrane lies between the Sibumasu Terrane and East Malaya Terrane (East Malaya Fold Belt).

2) The Peninsular Malaysia is characterised by three parallel north-south geological belts, the Western, Central and Eastern Belts. The Western Belt is part of the Sibumasu Terrane and is characterised by a Palaeozoic passive margin sequence from Cambrian to Late Permian. In this study, the Central and Eastern Belts are considered to have a similar origin of the East Malaya Terrane based on similar Carboniferous to Permian ancient flora and fauna affinities, including the U–Pb detrital zircons and radiogenic isotopic data signatures (Chapter 4). However, the Central Belt is considered here to represent the Permian volcanic arc on the margin of the East Malaya Terrane (Eastern Belt).

3) The Tasik Chini occurs in the Central Belt of Peninsular Malaysia which is part of the Permian volcanic arc of the East Malaya Terrane (East Malaya Fold Belt). This island-arc and back-arc magmatic belt also hosts a wide variety of other mineral deposits including skarn, volcanic-hosted massive sulphide and orogenic/sediment hosted gold mineralisation related to long-lived Permo–Triassic magmatism.

CHAPTER 3 DISTRICT- AND DEPOSIT-SCALE GEOLOGY

3.1 Introduction

This chapter documents the district- and deposit-scale geology of the Tasik Chini area that encompasses the Bukit Botol and Bukit Ketaya deposits. The district-scale geology of Tasik Chini is described based on the author's field investigation and previous published work such as MacDonald (1970). The detailed deposit-scale geology of the Bukit Botol and Bukit Ketaya is established based on the author's three seasons of field mapping in July-September 2010, March-May 2011 and July-September 2011.

3.2 District-scale Geology of the Tasik Chini Area

The district-scale geological map of the Tasik Chini area is shown in Figure 3.1 and the interpreted stratigraphic column is presented in Figure 3.2. The Tasik Chini area is located at the southern portion of the Central Belt of Peninsular Malaysia. Its location in the Central Belt is west of the Lebir Fault Zone, the marker zone that limits the eastern boundary of the Central Belt and the Eastern Belt. The district geology of this area was also briefly described by MacDonald (1970). The area comprises of four stratigraphic groups: the oldest to the youngest are the Carboniferous metasedimentary rocks, the mixed Permo-Triassic sedimentary and volcanic rocks, the Jurassic-Cretaceous sedimentary rocks and the Quaternary sediments. Plutonic and volcanic rocks are also widespread and exposed as small separate bodies.

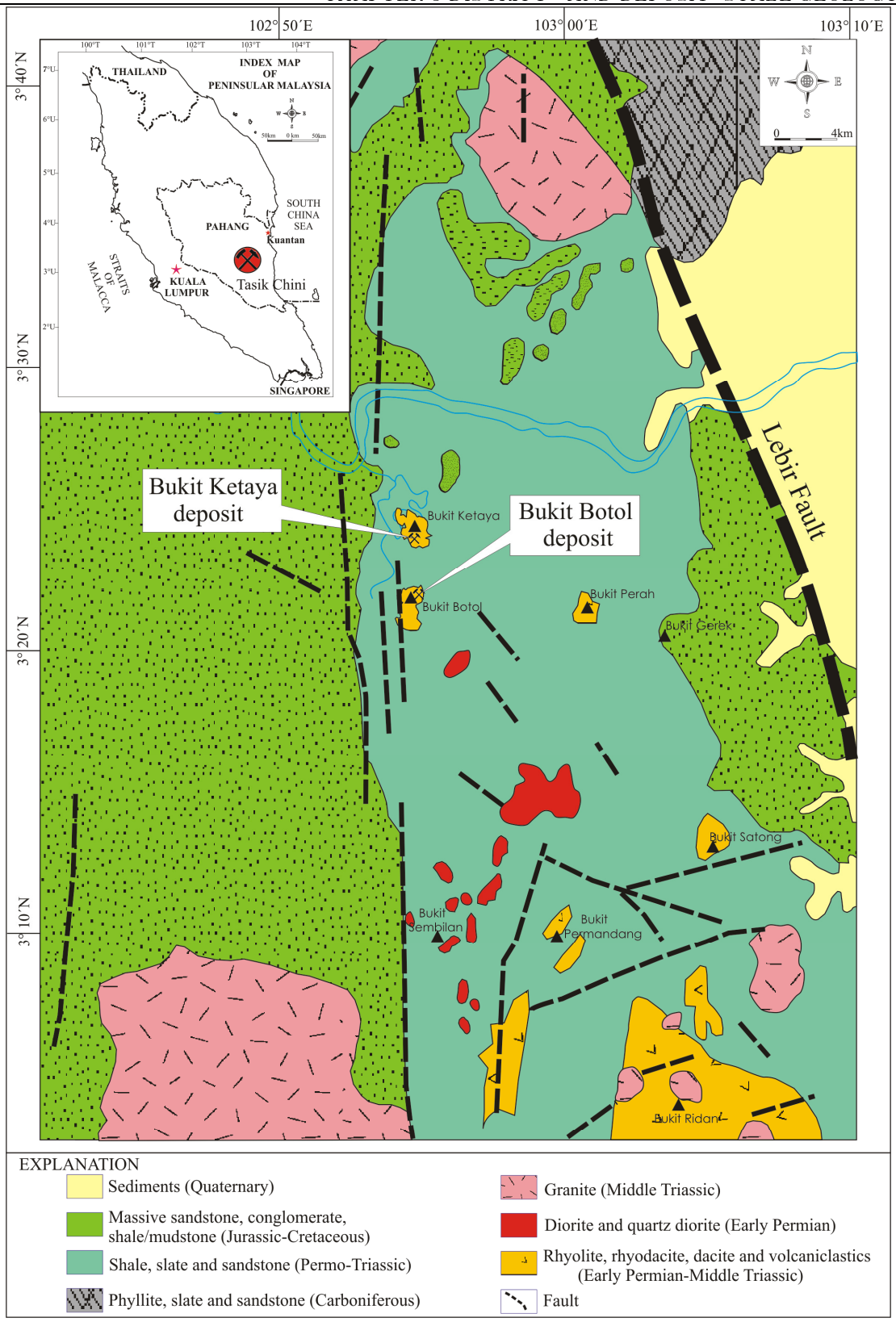

Fig. 3.1. District-scale geology of the Tasik Chini area including Bukit Botol and Bukit Ketaya deposits, Pahang, Central Belt of Peninsular Malaysia (modified after Minerals and Geoscience Department of Malaysia, 2004).

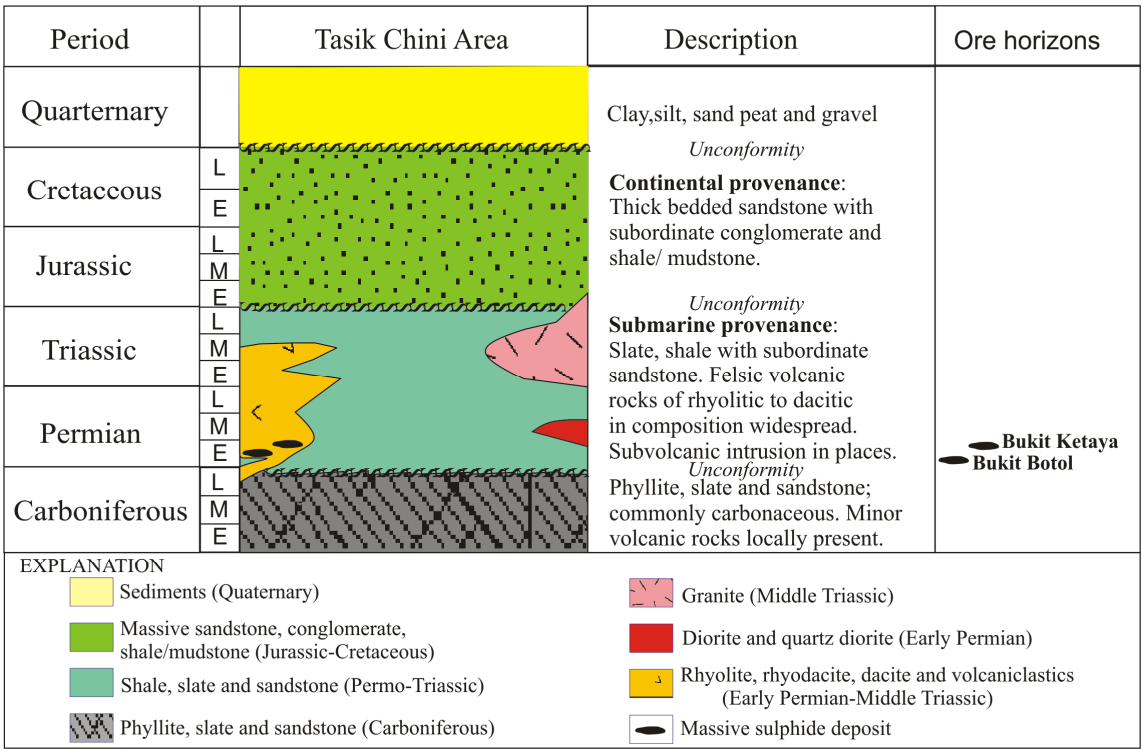

Fig. 3.2. Schematic stratigraphic column and contact relationship of the rock units in the Tasik Chini area.

3.2.1 Carboniferous Sequence

The rock units of the Carboniferous Sequence are exposed at the northeastern part of the Tasik Chini area (Fig. 3.1), which is correlated to the Eastern Belt of rock distributions. The sequence is a part of the Kuantan Group of Foo (1983) which is locally developed in the Kuantan area. The lithology is dominantly characterised by metamorphic rocks of interbedded slate, phyllite, schist and quartzite (metasandstone) (Minerals and Geoscience Department of Malaysia, 2004). Based on fossils, the age of the Kuantan Group is constrained as the Early to Late Carboniferous (Metcalfe et al., 1980; Jenning and Lee, 1985), and its depositional condition is interpreted as a shallow marine environment (Foo, 1983). On the road cutting east of Kuantan (at approximate easting/northing of 103.0619, 3.6937), the exposure shows interbedded slate-phyllite and metasandstone units with a moderate (30^{o}–50^{o}) southward dipping trend (Figs. 3.1 and 3.3).

3.2.2 Permian-Triassic Sequence

Rocks overlying the Carboniferous rocks are a succession of mixed volcano-sedimentary units of Permian-Triassic ages (Fig. 3.1; Minerals and Geoscience Department of Malaysia, 2004).

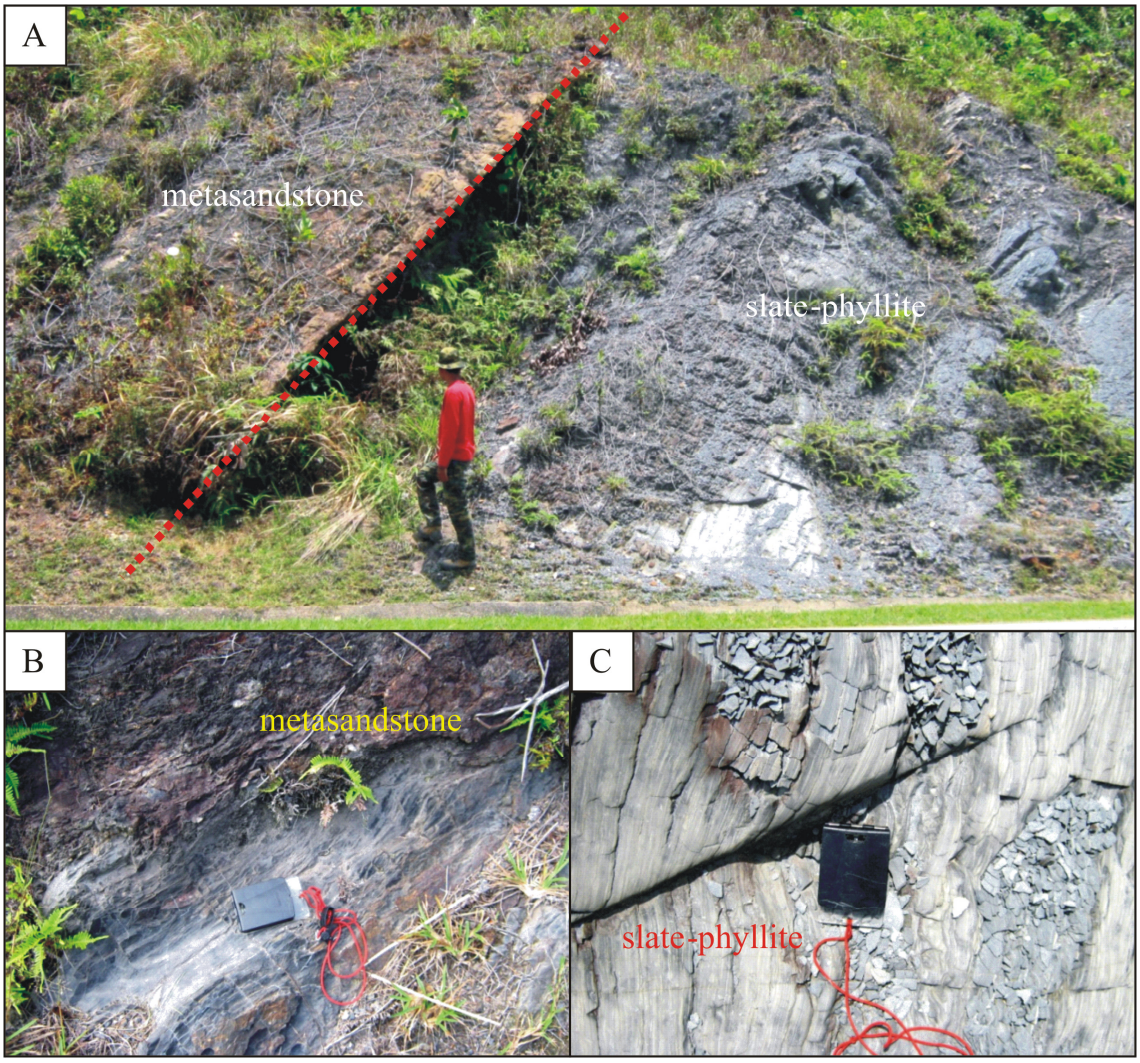

Fig. 3.3. Field photographs of the Carboniferous Sequence. **A**. Outcrop of interbedded slate-phyllite and metasandstone at road cutting east of Kuantan. **B**. Close up of the metasandstone unit in Figure A. **C**. Close up of the slate-phyllite unit in Figure A.

The rocks comprise a sedimentary succession of flysch units consisting of mudstone, shale, siltstone, sandstone, and in places limestone. No limestone unit outcrops in the Tasik Chini area, however they are exposed in a few localities at the Jengka Pass area further to the north.

Volcanic rocks of Permo-Triassic ages are widespread in the Tasik Chini area. These are composed of andesitic-rhyolitic lava flows and volcaniclastic rocks (Minerals and Geoscience Department of Malaysia, 2004).

Until now, the stratigraphic relationships, age and constraints on depositional environment for the Permo-Triassic Sequence in the Tasik Chini area are not well established due to lack of detailed studies. The volcano-sedimentary rocks do not yield any fossils in the Tasik Chini area. Therefore, they have been loosely interpreted to be a continuation of the Early to Late Permian Dohol and Sedili Formations of Rajah (1968) which are well exposed and distributed in the eastern Johor State to the south.

Detailed field investigation and mapping of the sequence (Minerals and Geoscience Department of Malaysia, 2004), and recently by the author in the Tasik Chini area, indicate that the volcano-sedimentary rock units include a thick to massive mudstone and sandstone, some thin bedded shale, siltstone and sandstone (Figs. 3.4A and 3.4B). The volcanic unit of the area is found to be dominated by lava flow and associated volcaniclastic rocks ranging mainly from rhyolite to rhyodacite with minor dacite/andesite composition (Figs. 3.4C, D, E and F). This study reveals a flow texture typical of coherent felsic volcanic rocks (rhyolite-rhyodacite) and associated volcaniclastic rocks that form an individual body such as at both the Bukit Botol and Bukit Ketaya deposits (Section 3.4). The volcaniclastic units are directly associated with the sedimentary sequence.

On the basis of precise U-Pb age determination of the sedimentary and volcanic rocks with its related intrusions presented in this study (described in Chapter 4), it is clearly evident that the Permo-Triassic ages of these lithologic units in the Tasik Chini area are largely confirmed.

Thus, these Permo-Triassic sequences are interpreted here as probably parts of the thick accumulations of Permo-Triassic volcaniclastic turbidite, volcanic rocks and reef limestone packages deposited in relatively deep basins in the Central Belt of Peninsular Malaysia (Metcalfe et al., 1982; Metcalfe, 2013).

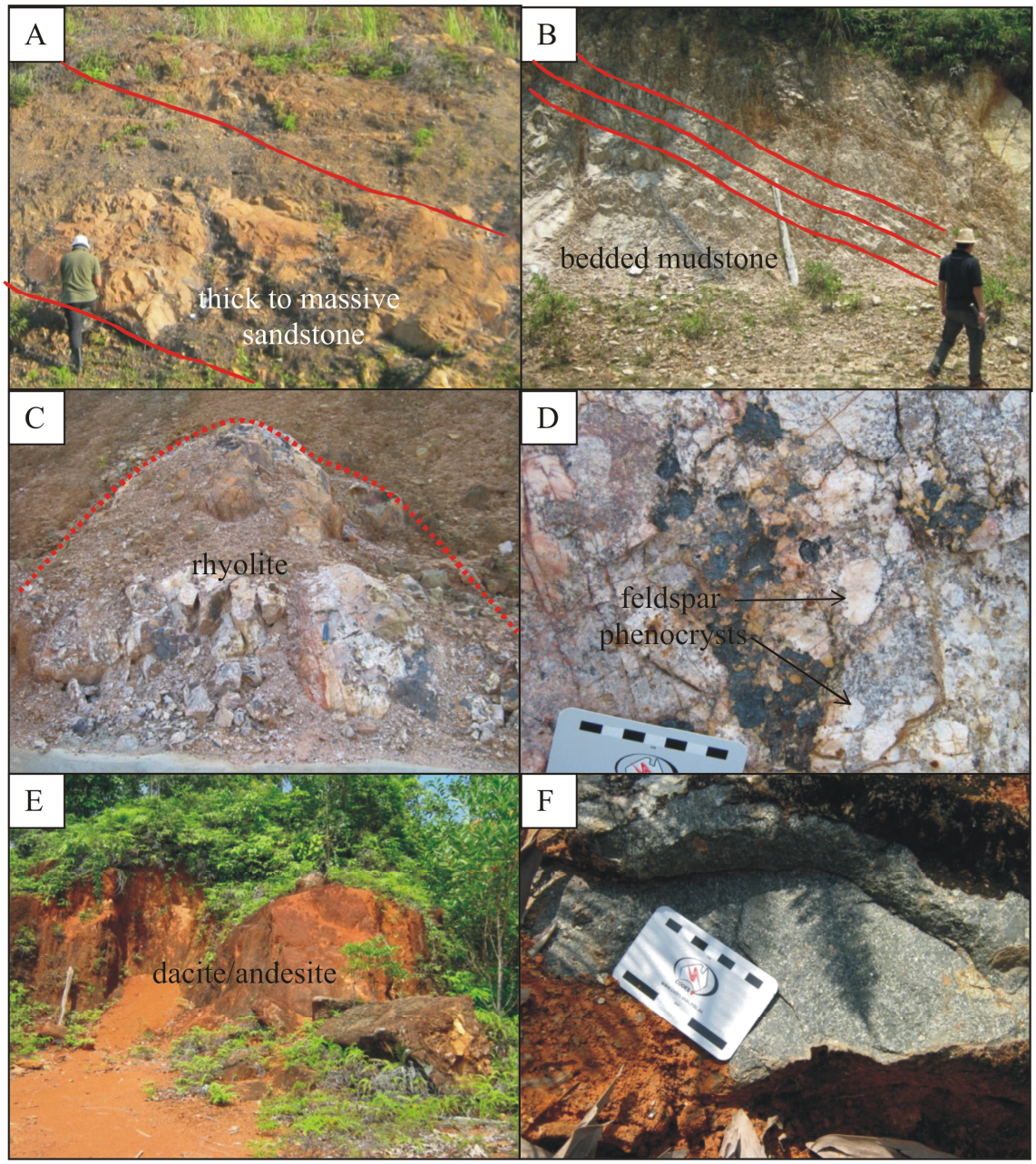

Fig. 3.4. Photographs of various rock successions of the Permo-Triassic Sequence. **A**. Thick to massive sandstone. **B**. Bedded mudstone. **C**. Rhyolite body outcrop. **D**. Rhyolite showing well preserved porphyritic texture. **E**. Exposure of the dacite/andesite body. **F**. The dacite/andesite rock showing fine-grained feldspar-phyric texture.

3.2.3 Jurassic-Cretaceous Sequence

The Mesozoic sedimentary rocks unconformably overlie the Permian-Triassic succession, and are distributed along the eastern margin of the Central Belt (Burton, 1973; Khoo, 1983; Tjia, 1996). In the Tasik Chini area, this Jurassic-Cretaceous unit, together with the possible Bertangga Sandstone and Gerek Sandstone Formations of Khoo (1983) are exposed to the west and east of the Permo-Triassic rock units, and the boundaries are described by Tjia (1996) to be fault bounded (Fig. 3.1). It comprises sedimentary facies of continent-derived sediments dominated by thick bedded sandstone with subordinate shale/mudstone and conglomerate (Minerals and Geoscience Department of Malaysia, 2004).

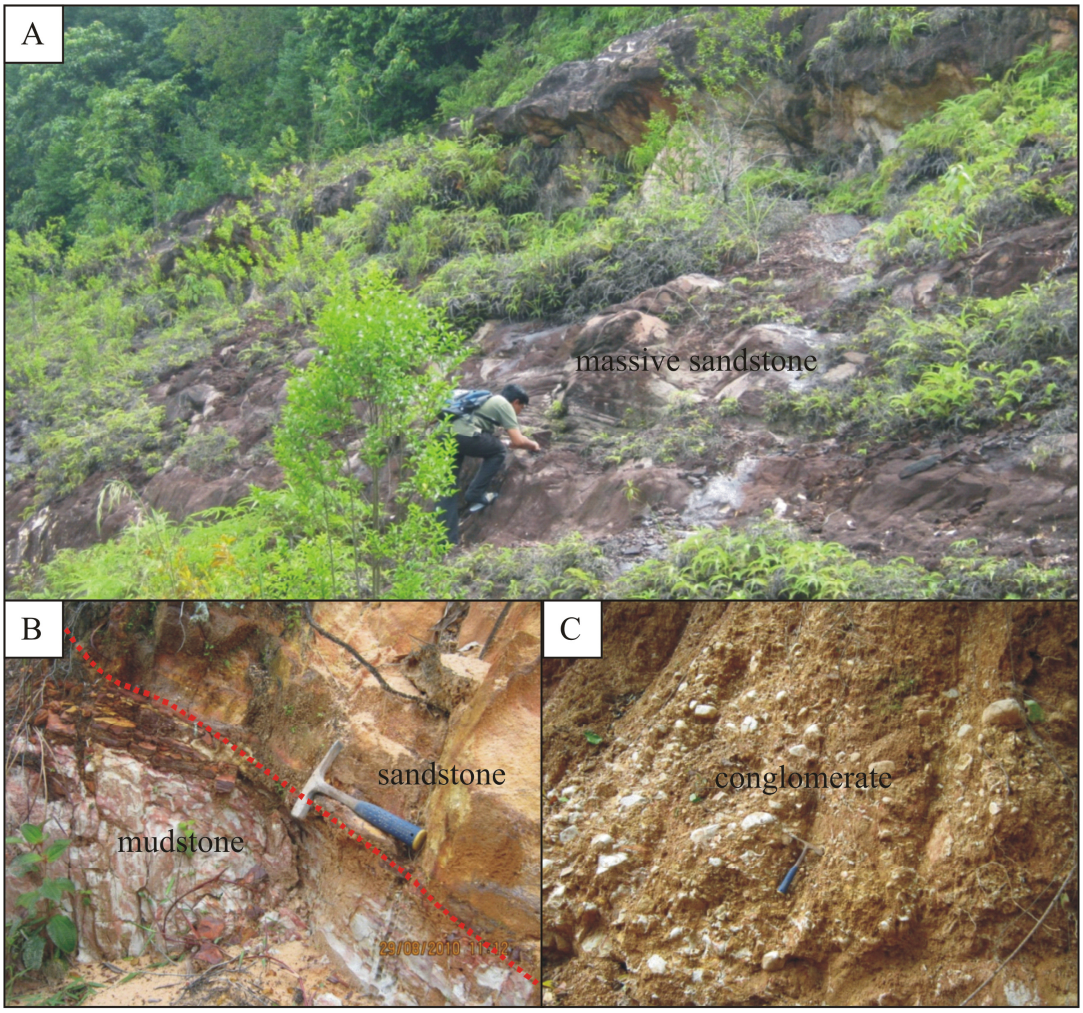

Fig. 3.5. Outcrop photos of the Jurassic-Cretaceous Sequence. **A.** Massive sandstone succession. **B.** Interbedded sandstone and mudstone. **C.** Conglomerate unit.

The depositional environment of this sedimentary succession is thought to have formed in a fluvial/channel setting. In the Tasik Chini area, the relatively well-exposed outcrops of mudstone and sandstone layers of the Gerek Sandstone can be found along the Kuantan-Segamat Highway. Westward, the rocks of the Bertangga Sandstone are rarely exposed and conglomerate units are dominant in some localities (Fig. 3.5).

3.2.4 Igneous rocks

The geology of the Tasik Chini area is dominated by various phases of volcanic-plutonic rocks. The plutonic bodies are scattered in the northern and southern parts of the area, and several small intermediate intrusive bodies emplaced the Permo-Triassic succession to the south. Moreover, there are widespread occurrences of volcanic rocks of Permo-Triassic ages (Fig. 3.1; Minerals and Geoscience Department of Malaysia, 2004).

The granitoids in the northern and southern parts range from gabbro to monzogranite in composition and are dominated by the biotite granite (MacDonald, 1970; Schwartz et al., 1995). A few occurrences of granodiorite and minor diorite are present southwest of the Tasik Chini area (MacDonald, 1970). As also defined by MacDonald (1970), the volcanic rocks in the area mainly comprises rhyolite with only minor rhyodacite, dacite and trachyte. Petrology and geochemistry of these plutonic and volcanic rocks are not well documented in previous studies, and age of emplacement of the units was also unavailable or unknown prior to this study.

During this study only three granitoid bodies were found and sampled in the southern part of the mapped area. Due to the weathering and the lack of exposures, it is not possible to classify these granitoids into different rock types in the field. Thus, throughout this chapter the term granite is used to define the plutonic body, with the major characteristics of individual samples described as follows.

The microgranite body exposed in the vicinity of Bukit Ridan is medium-grained and shows a porphyritic texture (Sampel BR317). The original igneous texture of this rock is well preserved, containing phenocryts of quartz and feldspars with a reddish clay dominanted groundmass. The feldspars have been mostly altered into clay minerals and are consequently difficult to identify (Figs. 3.6A and B).

The coarser granite body is exposed northeast of Bukit Ridan and is also mostly weathered, and yellowish in colour (Sampel BR326). This fine- to medium-grained rock is rarely porphyritic with phenocrysts of quartz and feldspars. Both the phenocryts and groundmass are intensely altered to clay and sericite (Figs. 3.6C and D).

The other igneous rock outcrop is located in the vicinity of Bukit Sembilan and is part of the small intermediate granitoid body exposed in the map area (Sampel BR318). The rock is intensely weathered, and is difficult to distinguish from the sedimentary rocks it intruded. Its texture is fairly homogeneous and all the plagioclase is a major mineral that has been altered to clay minerals. In addition, rare quartz and probably pyroxene phenocrysts are present and observed throughout this rock (Figs. 3.6E and F).

Four regional volcanic rock units were collected from the Tasik Chini area. Sample BR3 is a massive dacite/andesite subvolcanic unit from the vicinity of the Bukit Perah, west of the Bukit Botol deposit. The sample is greenish grey to dark green in colour and exhibits a porphyritic texture (Fig. 3.7A). It contains phenocrysts of plagioclase, hornblende (replaced by clay mineral and chlorite), quartz and opaque mineral. The groundmass is very fine-grained and consists of a feldspar, quartz and Fe-Ti oxide assemblage (Fig. 3.7B).

Fig. 3.6. Outcrops of the granite bodies. **A.** Exposure of granite body in the vicinity of Bukit Ridan. **B.** The granite texture containing phenocryts of quartz and feldspars in a reddish clay dominant groundmass, Sample No. BR317. **C.** Highly weathered granite rocks exposed to the northeast from the Bukit Ridan. **D.** Hand specimen sample of the granite is yellowish in colour, fine to medium-grained, rarely porphyritic with phenocrysts of quartz and feldspars, Sample No. BR326. **E.** Intermediate igneous rock (diorite?) body outcrop near Bukit Sembilan. **F.** Texture of the diorite is fairly homogeneous, with all the plagioclase as major mineral and altered to clay minerals-only rare quartz and probably pyroxene phenocrysts are present and observed throughout this rock, Sample No. BR318.

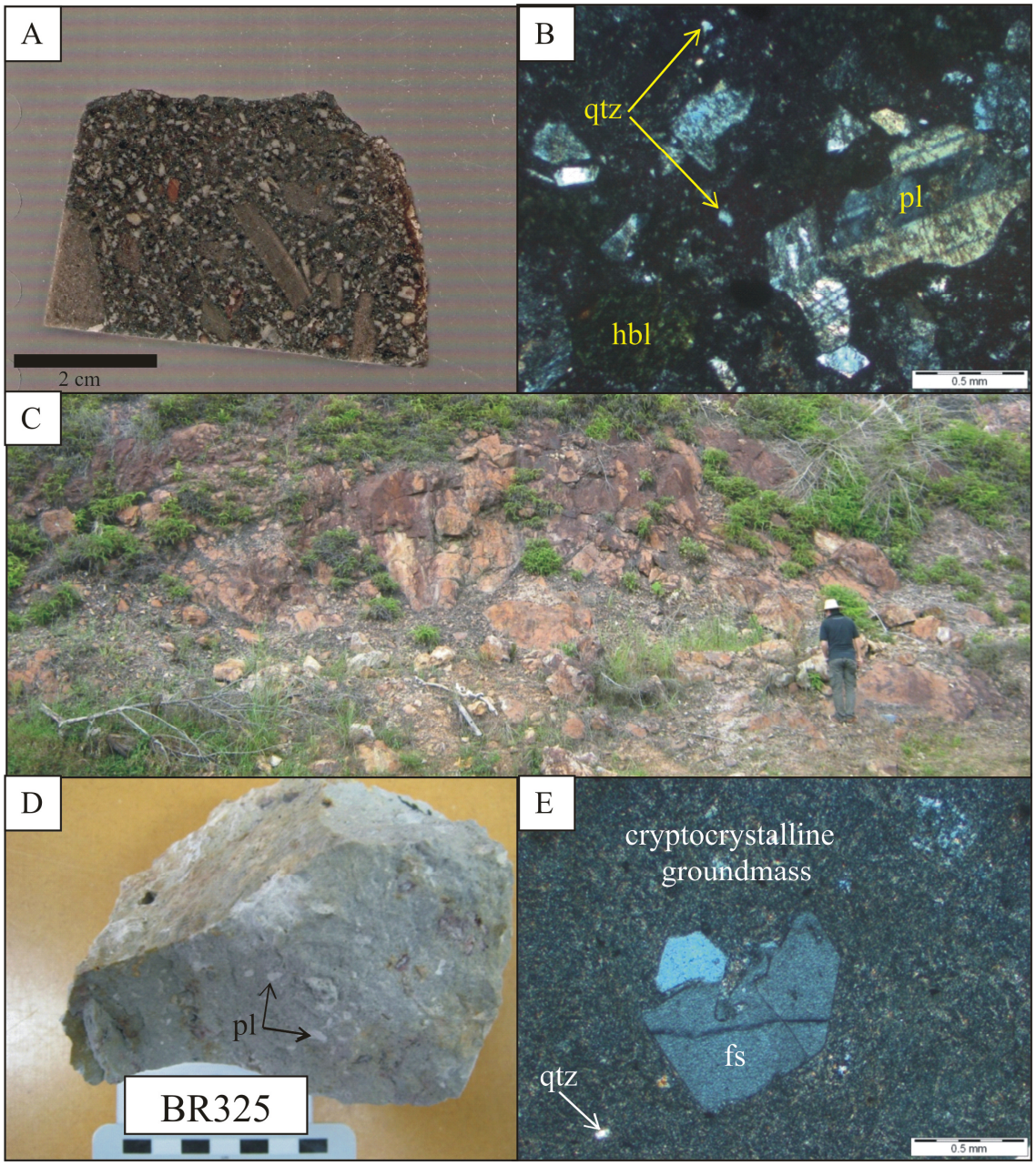

Fig. 3.7. **A.** Hand specimen of dacite/andesite subvolcanic unit in the vicinity of the Bukit Perah, west of the Bukit Botol deposit. **B.** Photomicrograph of the dacite/andesite comprising phenocrysts of plagioclase, hornblende (replaced by clay mineral and chlorite), quartz and opaque mineral. The groundmass is very fine-grained and consists of feldspars, quartz and Fe-Ti oxides, Sample No. BR3. **C.** Outcrop of the mixed felsic volcaniclastic and siliciclastic rocks. **D.** Hand specimen sample of felsic volcaniclastic rock, Sample No. BR325 **E**. Photomicrograph of the felsic volcaniclastic rock showing feldspar and quartz phenocrysts in a cryptocrytalline groundmass of feldspar and quartz assemblage, Sample No. BR325. Annotation: qtz=quartz, pl=plagioclase, hbl=hornblende and fs=feldspar.

Sample BR325 is from a mixed sequence of felsic volcaniclastic and siliciclastic rocks, which occurs approximately 20 km southeast of the Tasik Chini deposit area. The felsic volcaniclastic rock is composed of feldspar and quartz phenocrysts in a cryptocrytalline groundmass of feldspar and quartz (Figs. 3.7C, D and E).

The third and fourth volcanic body outcrops are located in the vicinity of the Bukit Botol and Bukit Ketaya areas, which host the Bukit Botol and Bukit Ketaya deposits in the Tasik Chini area (Fig. 3.1). Both the volcanic bodies consist of rhyolite to rhyodacite flows and volcaniclastic rocks, and their characteristics are presented in Section 3.4.

3.3 Structure and Metamorphism

The district-scale structures identified based on the correlation of field mapping observations and air photo interpretations in the Tasik Chini area by MacDonald (1970) include: a folding (anticline and syncline) with a northwest-southeast axis; an east-west striking fold to the southern portion of the area; and a major north-south trending fault system (Fig. 3.1). There are no previous studies which constrain degree of the metamorphism that affected all the rock formations in the Tasik Chini area. However, according to Macdonald (1970) all the rock assemblages of the Tasik Chini area have been regionally metamorphosed to very low-grade metamorphism, including the vicinity near the granite contact.

3.4 Deposit-Scale Geology of the Bukit Botol Deposit

The deposit geology of the Bukit Botol deposit as mapped by the author is shown in Figure 3.8. At Bukit Botol deposit, the mine succession is dominated by coherent felsic volcanic and associated volcaniclastic units. Exposures of the rocks are white to light grey and extremely silicified. Based on difference in size and abundance of phenocrysts, two types of rhyolite can be distinguished.

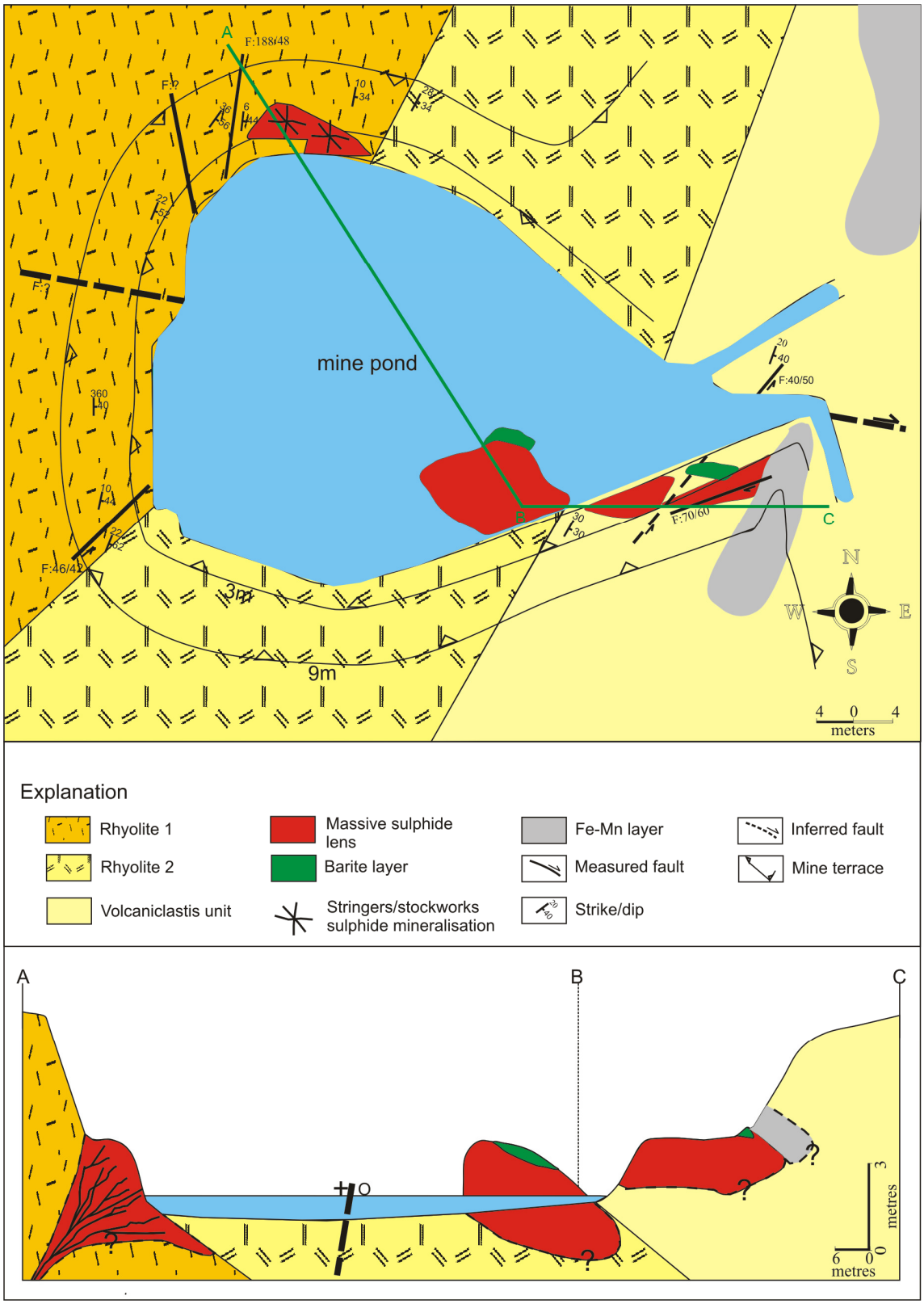

Fig. 3.8. Surface geological map and schematic cross-section of the Bukit Botol deposit looking northwest showing the stratigraphic sequence and mineralisation styles.

Rhyolite type 1 occurs in the footwall of the mine sequence and is overlain by rhyolite type 2. Rhyolite type 1 hosts stringer sulphide veins and is moderately to strongly altered, and poorly to moderately porphyritic. It is composed of quartz and feldspar phenocrysts in a fine-grained quartz-feldspar groundmass (Figs. 3.9A, B, and C). It's typical groundmass texture is dominated by perlitic cracks.

The rhyolite type 2 appears to be porphyritic in texture, and forms the immediate footwall or ore horizon to massive sulphide mineralisation. The unit is characterised by the presence of coarse quartz crystals with rare feldspars in a fine-grained matrix consisting of quartz, feldspar and/or sericite (Figs. 3.9D, E and F). It is less altered than the footwall felsic volcanic rocks, and forms a massive and gradational unit with associated volcaniclastic rocks, and it underlies the massive sulphide ores.

The volcaniclastic unit comprises volcanic breccia with minor sedimentary rocks. The clasts of the breccia are mainly made up of the fragments of the coherent rhyolite type 2. Meanwhile, the sedimentary rocks are mainly mudstone and occur as interbedded layers with the volcanic breccia unit (Fig. 3.10). At the top of the sequence, the hangingwall sedimentary units are composed of mudstone, shale, siltstone and sandstone that directly overlie the volcanic facies.

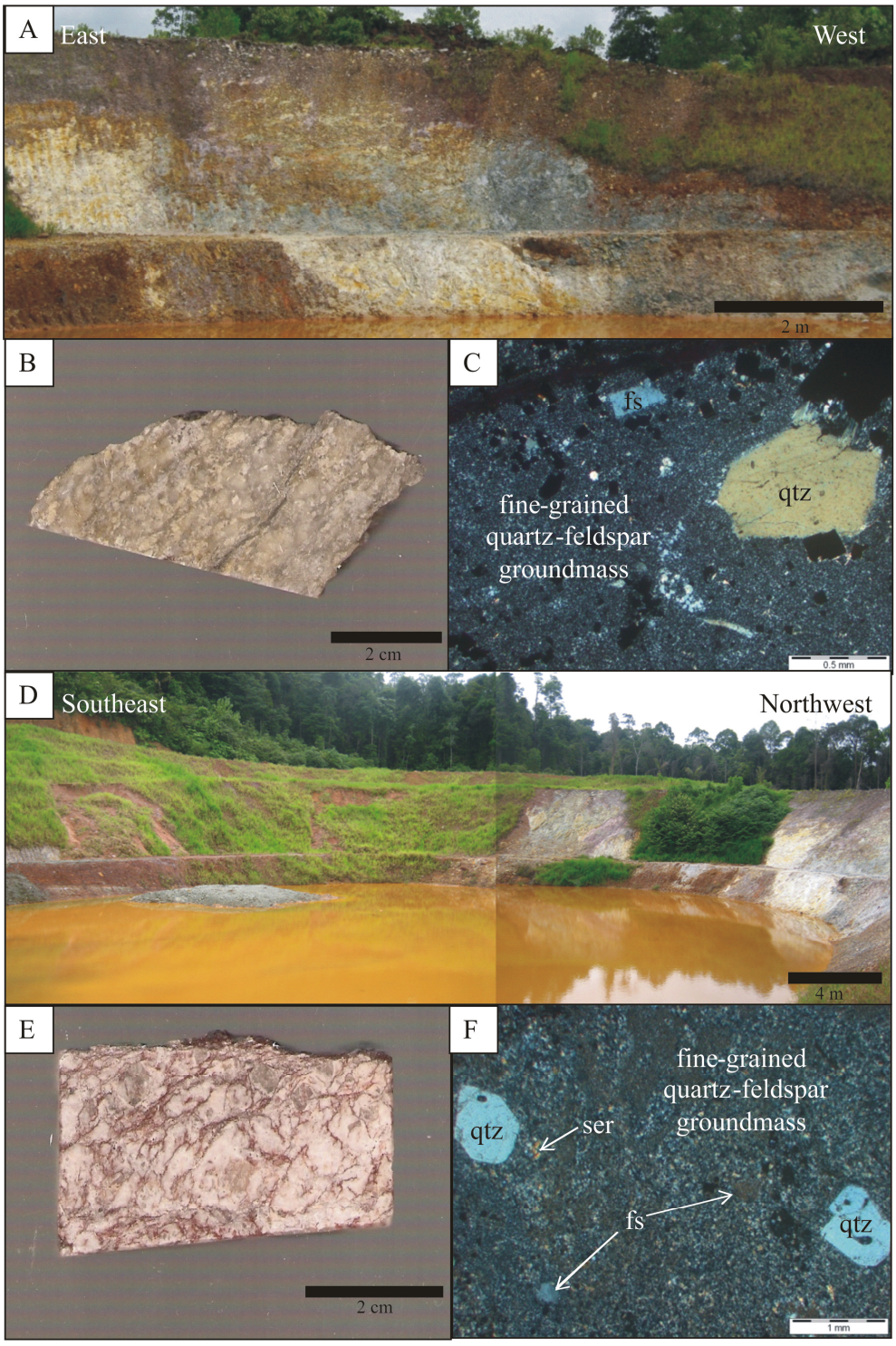

Fig. 3.9. Host rocks at the Bukit Botol deposit. **A.** Outcrop of the rhyolite type 1 in the footwall. **B.** Hand specimen sample of the silicified rhyolite type 1, Sample No. BB10. **C.** Rhyolite type 1 composed of quartz and feldspar phenocrysts in a fine-grained quartz-feldspar groundmass, Sample No. BB10. Cross-polarised light. **D.** Exposure of rhyolite type 2 at the ore horizon. **E.** Hand specimen sample showing poorly sorted blocky clasts, Sample No. BB6. **F.** The rhyolite type 2 showing the presence of coarse quartz crystals and rare feldspars in a fine-grained matrix consisting of quartz, feldspar and/or sericite assemblage, Sample No. BB6. Cross-polarised light. Annotation: qtz=quartz, fs=feldspar and ser=sericite.

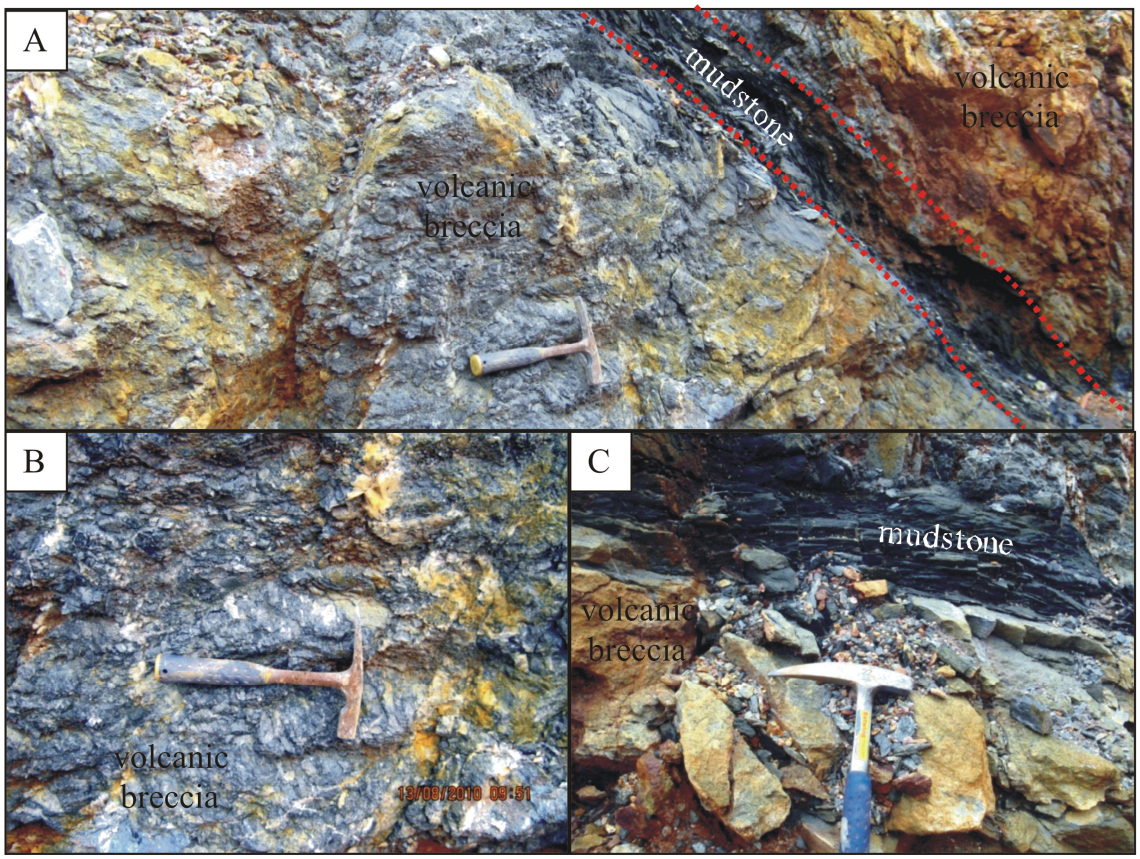

Fig. 3.10. **A.** Outcrop of the volcaniclastic rocks at the Bukit Botol deposit. **B.** Outcrop of volcanic breccia. **C.** Interbedded volcanic breccia and mudstone.

The mine stratigraphy strikes from 20° to 36° and dips moderately to the east. In addition, there are several faults in the mine area, including N-S and NE-SW trends. Most of these faults transect and offset both mine stratigraphic units and sulphide lenses. An E-W trending major fault is also present at the centre of the deposit area. Movement of this main fault is dextral which separates the upper part of massive sulphide mineralisation from the lower part of the stringer sulphide mineralisation. Although the rock units at the Bukit Botol deposit have been affected by various degrees of structural deformation, the metamorphic grade of the units do not exceed lower greenschist facies.

The Bukit Botol deposit shows four types of mineralisation which are vertically zoned from the bottom to the top, including (1) sulphide rich stockwork veins with disseminated sulphides,

(2) massive sulphide lenses, (3) a thin barite layer and (4) a Fe-Mn layer. The massive sulphide zones are present as several small lenses, and are separated and offset by faulting each other. A well mineralised zone of the sulphide stringer veins commonly is surrounded by silicification to chloritisation. In addition, a Fe-Mn layer is well developed at the top of the massive sulphides (Fig. 3.8). The detailed description of the mineralisation types is presented in Chapter 5.

3.5 Deposit-Scale Geology of the Bukit Ketaya Deposit

The deposit geology of the Bukit Ketaya deposit as mapped by the author is shown in Figure 3.11. The stratigraphy of the Bukit Ketaya deposit is characterised mainly by felsic volcanic units. Based on their relationship to the massive sulphide mineralisation and the associated alteration phases, the succession can be subdivided into footwall and ore horizon units (Fig. 3. 11).

The footwall sequence is dominated by coherent facies of siliceous quartz-feldspar phyric rhyolite that are white-grey in colour (Figs. 3.12A and B). Under the microscope, rocks of the unit contain distinct plagioclase and embayed quartz phenocrysts, with well-preserved spherulites in a fine-grained groundmass (Fig. 3.12C).

In contrast to the footwall sequence, the ore horizon comprises purple to purplish-black, graded massive to brecciated rhyolite. Regardless of either coherent or incoherent (volcaniclastic) texture, all of the rocks of the unit share a similar petrographic feature; quartz and feldspar phenocrysts in a microcrystalline quartz-feldspar groundmass (Figs. 3.12D, E, and F). Poorly-sorted blocky clasts occur only in the brecciated part of the rhyolite. Moreover, these units typically show abundant perlitic cracks with rare spherulites in the groundmass.

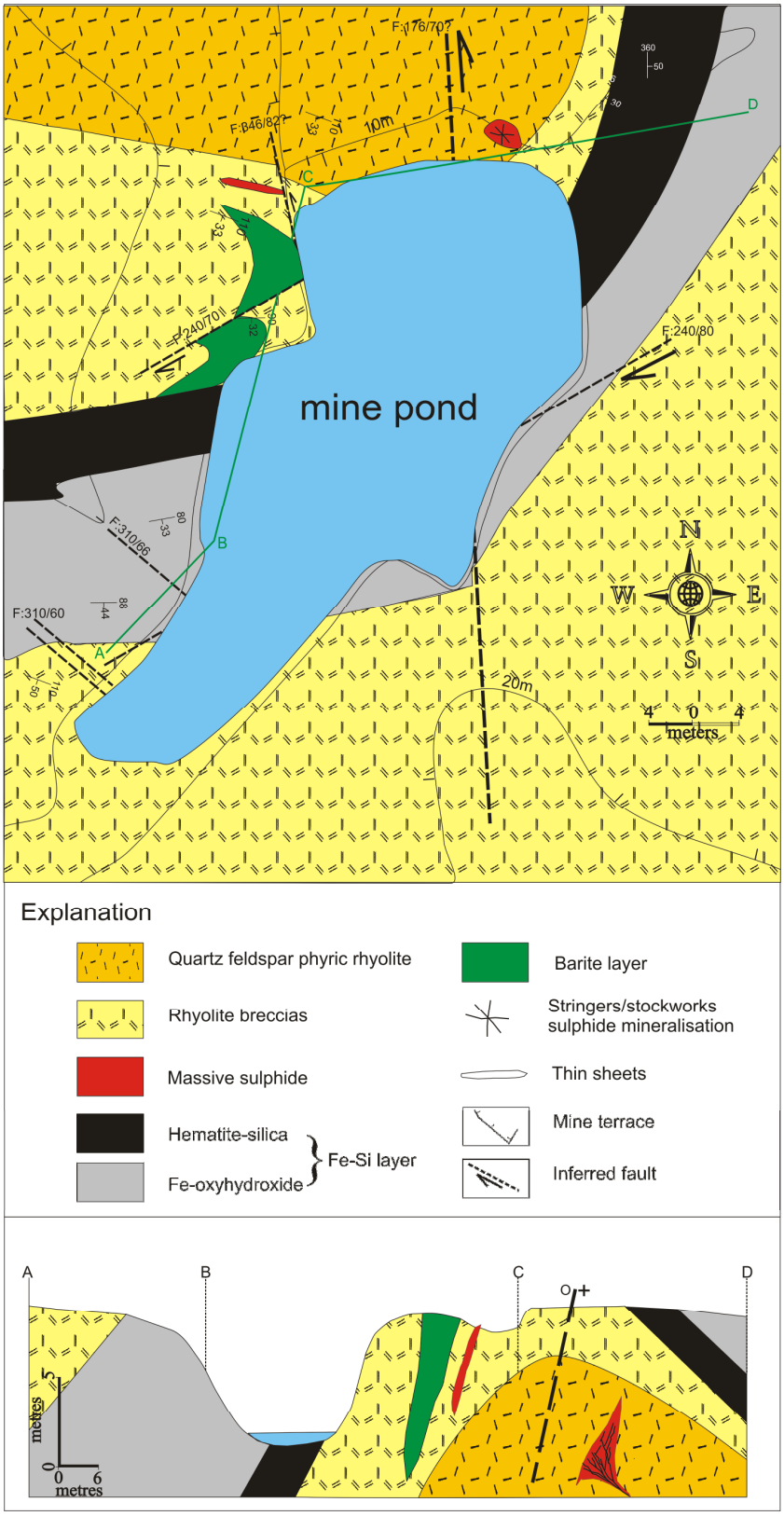

Fig. 3.11. Surface geological map and schematic cross-section of the Bukit Ketaya deposit looking southwest showing the stratigraphic sequence and mineralisation styles.

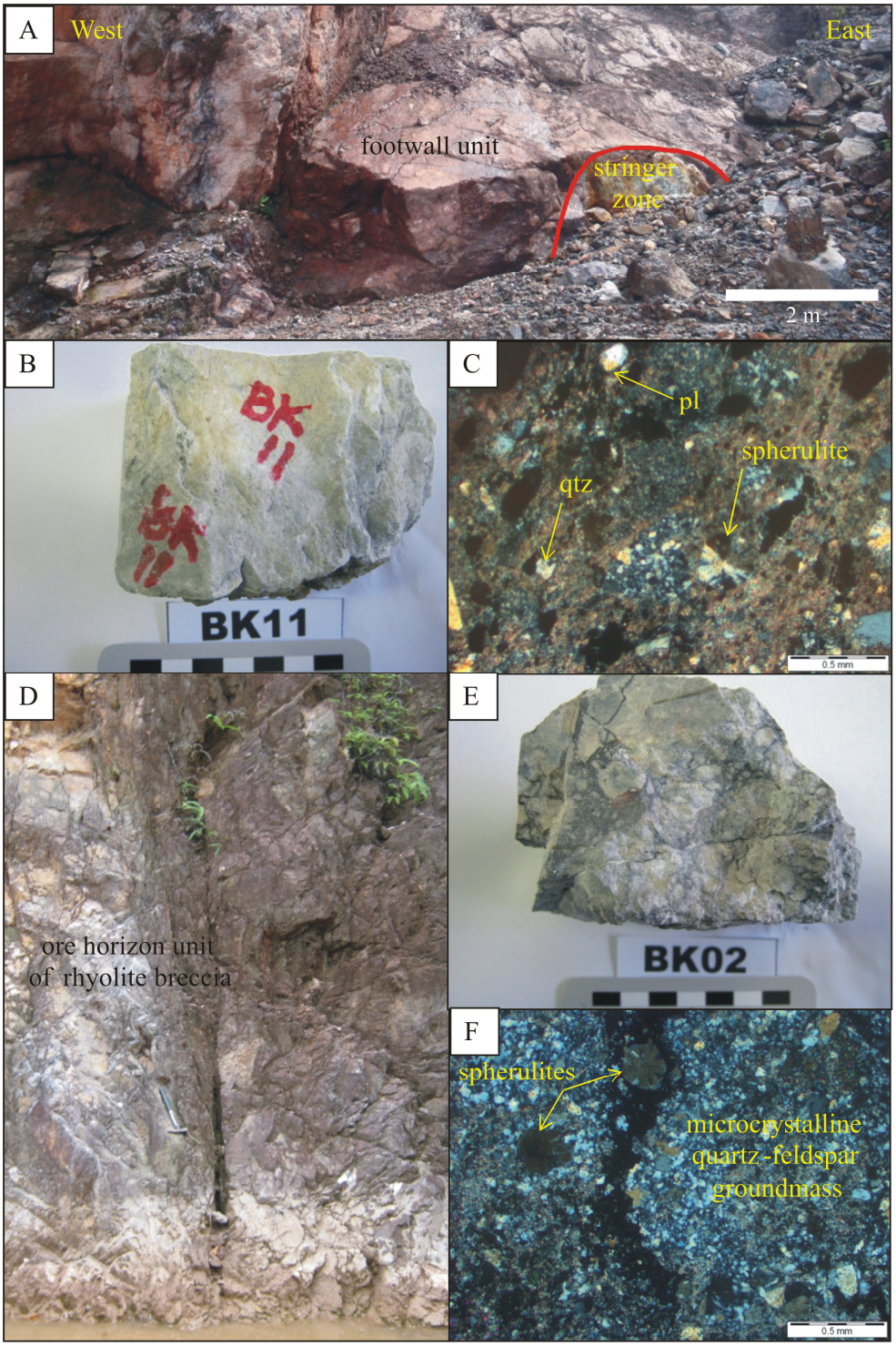

Fig. 3.12. Host rocks at the Bukit Ketaya deposit. **A.** Outcrop of the footwall volcanic unit of quartz-feldspar phyric rhyolite. **B.** Hand specimen sample of the siliceous quartz-feldspar phyric rhyolite, Sample No. BK11. **C.** Quartz-feldspar phyric rhyolite showing a distinct plagioclase and embayed quartz phenocrysts, and well-preserved spherulites in the fine-grained groundmass, Sampel No. BK11. Cross-polarised light. **D.** Exposure of rhyolite breccia. **E.** Hand specimen showing poorly sorted blocky clasts, Sample No. BK02. **F.** The rhyolite breccia consists of quartz and feldspar phenocrysts in a microcrystalline quartz-feldspar groundmass, Sampel No. BK01. Cross-polarised light. Annotation: qtz=quartz and pl=plagioclase.

The hangingwall unit consisting of sedimentary rocks is similar to the upper unit at the Bukit Botol deposit, exposed to the east of the mine area. However, the weathered exposure limits further detailed study of the nature of the sequence.

On the map scale from the west to the east, the strike of the bedding in the mine area shifts inconsistently from south facing to nearly N-S trending. These features suggest that the mine sequences were formed as a large faulted syncline structure. Thus, it is postulated that a syncline with SE axial plane was present in the Bukit Ketaya deposit and was later cut by a N-S trending strike-slip fault. Moreover, several faults of minor displacement are identified by offsets in the bedding of mine sequences. Even though the rocks in the vicinity of the Bukit Ketaya deposit area are highly faulted and deformed, regional metamorphism is weak, at lower greenschist facies.

Mineralisation at the Bukit Ketaya deposit is dominated by barite and Fe-Si layers of orebodies with minor/small stockwork-like zone and thin massive sulphide mineralisation. In general, the Fe-Si layer extends along strike and downdip, closely associated with the barite lens, and caps the zone of thin sheet and stringer of massive sulphides (Fig. 3.11). Details of the mineralisation characteristics are presented in Chapter 5.

3.6 Summary

1) Geology of the Tasik Chini and surrounding area is composed of four main stratigraphic groups: the Carboniferous metasedimentary rocks, the Permo-Triassic volcano-sedimentary rocks, the Jurassic-Cretaceous sedimentary rocks and the Quaternary sediments. The Permo-Triassic volcano-plutonic bodies are widespread in the area.

2) The Bukit Botol and Bukit Ketaya deposits are hosted by the earliest rhyolite to rhyodacite

and volcaniclastic rocks of the Permo-Triassic volcanic episode and are located relatively west of the Lebir Fault Zone, the eastern boundary of the Central Belt with the Eastern Belt.

3) Structural data at both the Bukit Botol and Bukit Ketaya deposits demonstrate that the ore mineralisations and their host rocks have been displaced and deformed by faults.

CHAPTER 4 GEOCHEMISTRY AND GEOCHRONOLOGY

4.1 Introduction

This Chapter deals with the geochemistry and geochronology of the stratigraphic sequences present within the Tasik Chini area (district-scale), as well as those from the Bukit Botol and Bukit Ketaya deposits (deposit-scale). This fourth Chapter emphasises how geochemical data can be used to help identify or classify rock units and geotectonic settings. The geochemistry of the intrusive and volcanic rocks is also examined to better define the geochemical criteria in diagnostic diagrams that may help in recognising the different rock types and their tectonic settings. This study also reports on detrital zircon U-Pb geochronology of rocks from the Tasik Chini area providing maximum depositional ages for the Central Belt Palaeozoic and Mesozoic sequences. New U-Pb LA-ICPMS zircon ages of magmatic emplacement ages are reported for intrusive and volcanic rocks from the area.

4.2 Methods

4.2.1 Geochemistry Analyses

The samples described in Chapter 3 were analysed for major and trace elements at the CODES, University of Tasmania (see Appendix II for details). Whole rock Sm-Nd and Rb-Sr isotope were measured from felsic volcanic rocks from the both Bukit Botol and Bukit Ketaya deposits and subvolcanic and volcanic rocks in the district to further constrain their magma sources and tectonic environments.

4.2.1.1 Major, trace and rare earth (REE) elements analyses

All analyses for major (Si, Ti, Al, Fe, Mn, Mg, Ca, Na, K and P) and trace (Rb, Sr, Ba, Sc, V, Cr, Ni, Zn, Y, Zr, Nb and Pb) elements using the X-ray Fluorescence (XRF) at CODES, the University of Tasmania were done with the help of Phil Robinson, Katie McGoldrick and Jay Thompson. The detailed method is outlined by Norrish and Chappell (1977), Bennett and Oliver (1992), Watson (1996) and Norman et al., (2003). Rare earth elements (REE: La, Ce, Pr, Nd, Sm, Eu, Gd, Tb, Dy, Ho, Er, Tm, Yb and Lu) of 12 of these samples were also analysed using the solution ICP-MS technique at the University of Tasmania. The detailed analytical method for the solution ICP-MS technique is described by Yu et al. (2000).

The samples analysed were carefully selected from the least-altered hand specimen samples. However, most samples have experienced the effects of hydrothermal alteration. They were initially crushed using a jaw crusher to make rock fragments several centimetres in size and were subsequently ground using a tungsten carbide ring mill to produce rock powder. The XRF analyses were on fused glass and pressed pellets. The solution ICPMS were performed on 100 mg of sample which was digested with 1 ml of HF and 0.5 ml of HNO_3 in screw top PTFE-lined stainless steel bombs at 190°C for 12 hours. After this initial digest, an insoluble residue was dissolved using 8 ml of 40% HNO_3 heated to 110°C for 3 hours. Analytical calibration was accomplished using aqueous standard solutions. The precisions of ICP-MS analysis were better than ±5% and the analytical precisions of the XRF were 1–2%.

4.2.1.2 Sm-Nd and Rb-Sr isotope analyses

The Sm-Nd and Rb-Sr isotope analyses were conducted on rhyolitic volcanic rocks from the both Bukit Botol and Bukit Ketaya deposits and regional microgranite/subvolcanic and volcanic rocks.

Rb-Sr and Sm-Nd isotope dilution analyses were carried out at the University of Melbourne, following procedures described in Maas et al. (2005). Rock powders (22-197 mg) were weighed into Krogh-type high-pressure dissolution vessels and spiked with ^{85}Rb-^{84}Sr and ^{149}Sm-^{150}Nd tracers. The wide range in sample weights reflects the need to accommodate the diverse Sr (1.3-330 ppm) and Nd (2.4-94 ppm) concentrations. Samples were dissolved in an oven (160^{o}C) over 3 days using HF/HNO_3 and 6M HCl. All samples yielded clear solutions in HCl. Rb, Sr, Sm and Nd were extracted using a combination of Eichrom resins and conventional cation exchange. Total analytical blanks were <0.1 ng, resulting in sample/blank ratios $\geq 10^3$ in all cases; blank corrections were therefore unnecessary.

Isotopic analyses were carried out in static mode on a NU Plasma multi-collector ICP-MS coupled to a CETAC Aridus desolvating system operated at low uptake. Typical signal sizes used were ~8V total Sr and 12-20V total Nd. Instrumental mass bias was corrected by normalising to $^{88}Sr/^{86}Sr$=8.37521 and $^{146}Nd/^{145}Nd$=2.0719425 (equivalent to $^{146}Nd/^{144}Nd$ = 0.7219, Vance and Thirlwall, 2002), using the exponential law as part of an on-line iterative spike-stripping/internal normalisation procedure. Data are reported relative to La Jolla Nd = 0.511860 and SRM987 = 0.710230. Mass bias corrections for Rb isotope dilution runs were done using Zr doping. Typical in-run precisions (2sd) are better than ±0.000014 (Nd) and ±0.000020 (Sr), while external precision (reproducibility, 2sd) is ±0.000020 (Nd) and ±0.000040 (Sr). External precision for $^{87}Rb/^{86}Sr$ and $^{147}Sm/^{144}Nd$ obtained by isotope dilution is ±0.5% and ±0.2%, respectively. Results for international rock and solution standards agree with TIMS reference values. For example, BCR-2 yields $^{147}Sm/^{144}Nd$ = 0.1382±2, $^{143}Nd/^{144}Nd$ = 0.512640±20, $^{87}Rb/^{86}Sr$ = 0.400±5, $^{87}Sr/^{86}Sr$ = 0.705020±40 (all errors ±2sd). Σ_{Nd} values are calculated relative to a model bulk earth (CHUR) composition with $^{147}Sm/^{144}Nd$ = 0.1967 and $^{143}Nd/^{144}Nd$ = 0.512638. Nd model ages (T_{DM1}) are calculated relative to a modern depleted mantle with $^{147}Sm/^{144}Nd$ = 0.2136, $^{143}Nd/^{144}Nd$ = 0.513151.

Two-stage Nd model ages (T_{DM2}) use a default upper-crustal $^{147}Sm/^{144}Nd = 0.1100$ for the first stage. Age-corrected initial Σ_{Nd} values have an uncertainty (2sd) of ±0.5 units. Uncertainty in initial $^{87}Sr/^{86}Sr$ strongly depends on Rb/Sr and ranges from ±0.0001 to ±0.0108 for the data presented here. Decay constants are: ^{87}Rb 1.42 10^{-11}/yr; ^{147}Sm 6.54 10^{-12}/yr.

4.2.2 Geochronology analyses

Zircons were separated from the samples using standard separation techniques at CODES, University Tasmania. Approximately 200 gram of crushed sample was pulverised in a Cr-steel ring mill to a grain size of <400 micron. Heavy minerals were then separated using a gold pan and followed by a hand magnet. Representative zircon grains (e.g., clear crystals, crack free and lacking visible inclusions) were handpicked under a binocular microscope, placed on double sided sticky tape, cast in epoxy-filled mounts/Terranes and then polished to expose the crystals. Cathodoluminescence (CL) images of internal structures for representative zircons were taken with a FEI Quanta 600 MLA/ESEM at the CSL, University of Tasmania.

Zircons grain from all samples were analysed with reference to their CL images. The analyses were performed using LA-ICPMS also at the CODES, University of Tasmania, using procedures and detailed operating conditions described by Meffre et al. (2008). Over the duration of this study, the precision and accuracy of the method used were monitored through the repeated analyses of international standards zircons.

4.3 Geochemistry Results

Thirty-one samples of igneous rock from the Tasik Chini area were analysed, including nine samples from the district-scale, thirteen from the Bukit Botol deposit and nine samples from the Bukit Ketaya deposit (Tables 4.1, 4.2 and 4.3).

Table 4.1. Geochemical characteristic of felsic rocks from the Tasik Chini district. Rocks are group by rock types.

	Tasik Chini area								
	Dacite			Rhyolite			Microgranite		
Element	BR3	BR3(a)	BR315	BR321	BR323	BR325	BR317	BR326	BR318
XRF									
Wt%									
SiO_2	63.67	63.81	61.53	72.85	79.53	82.5	80.56	76.06	85.74
TiO_2	0.64	0.65	0.75	0.193	0.071	0.16	0.27	0.107	0.18
Al_2O_3	16.03	16.06	16.59	13.90	12.90	11.12	12.72	16.88	8.62
Fe_2O_3	5.06	5.04	5.59	2.47	1.03	0.82	0.50	0.42	0.21
MnO	0.09	0.09	0.12	0.07	0.01	0.01	0.01	0.00	0.01
MgO	1.66	1.67	1.59	0.16	0.45	0.08	0.14	0.08	0.53
CaO	3.42	3.45	3.72	0.64	0.01	0.01	0.01	0.00	0.00
Na_2O	4.21	4.23	5.27	3.91	0.16	0.04	0.04	0.03	0.11
K_2O	1.86	1.87	1.48	4.59	3.52	2.79	1.87	0.64	2.34
P_2O_5	0.14	0.14	0.17	0.01	0.01	0.02	0.02	0.02	0.01
BaO	0.07	0.07							
CuO									
ZnO	0.01	0.01							
PbO	0.00	0.00							
Loss inc.S-	2.62	2.61	2.85	1.18	2.45	2.04	1.33	5.92	2.13
Total	99.48	99.70	99.73	100.07	100.22	99.67	99.95	100.16	99.87
S	<0.01	<0.01	<0.01	<0.01	<0.01	<0.01	<0.01	<0.01	0.06
Ppm									
Sc	17.0	17.0	19	9	5	5	4	2.7	8.8
Ba	639	641	545	1538	919	973	238	28.7	498
V	83	81	92	<3	<3	8	4	3.7	<3
Cr	10.5	10.5	10	2	1	2	4	2.1	3.1
Ni	9	10	9	4	2	1	3	3.2	5.7
Cu	10	10	8	6	4	26	2	12.9	15.2
Zn	81	82	86	113	16	7	6	5.5	7.8
As	4	4	6	4	8	31	3	26	4.7
Rb	63	63	42	193	141	175	199	63.1	88.1
Sr	333	332	365	135	25	5	3	1.9	5.3
Y	175.1	175.0	246	34	42	58	27	47.5	31.5
Zr	180	182	182	202	104	242	267	159	180
Nb	6.1	6.2	5.3	11.5	10.6	13.1	9.7	11.6	10.2
Sn	<2	2	<2	6	<2	300	22	2.9	2.6
Pb	14	14	9	45	27	65	10	46.6	6.7
Bi	<2	<2	<2	<2	<2	<2	192	<2	<2
U	2.6	2.4	3	8	5	7	6	5.8	3.8
Th	9.0	8.3	7	27	12	23	25	38.2	10.4
La	84	86	118	48	56	54	48	37.4	17.2
Ce	53	51	60	96	102	114	109	96.0	42.8
Nd	110	113	151	38	43	49	41	32.7	14.3

Table 4.2. Lithogeochemical values for volcanic rocks of the Bukit Botol deposit. Rocks are separated into ore horizon and footwall units.

	Bukit Botol												
				Ore horizon*					Footwall				
Element	BB6*	BB11*	BB25*	BB25(a)*	BB30*	BB30a*	BB40*	MBTCS2	MBTCS4(1)	BB3	BB3b	BB10a	TasikChini-2
XRF													
Wt%													
SiO_2	82.95	83.81	86.70	86.66	84.24	84.72	85.10	73.08	74.74	75.44	75.84	86.21	83.51
TiO_2	0.20	0.21	0.39	0.37	0.32	0.32	0.24	0.45	0.35	0.35	0.35	0.14	0.20
Al_2O_3	9.43	9.72	8.30	8.24	9.79	9.80	9.31	12.79	11.27	11.23	11.49	6.97	4.95
Fe_2O_3	2.43	1.58	0.16	0.17	0.73	0.74	0.71	3.74	4.3	3.57	3.45	1.50	5.50
MnO	<0.01	<0.01	<0.01	<0.01	0.01	0.01	<0.01	0.01	0.02	0.02	0.01	0.01	0.00
MgO	0.20	0.16	0.12	0.15	0.26	0.26	0.15	0.59	0.55	0.50	0.61	0.25	0.11
CaO	0.01	0.01	0.01	0.01	0.01	0.01	0.01	0.01	0.01	0.01	0.01	0.01	0.00
Na_2O	0.14	0.17	0.15	0.16	0.38	0.36	0.13	0.06	0.05	0.05	0.05	0.05	0.05
K_2O	2.45	2.44	1.97	1.94	1.98	1.98	2.17	3.86	3.42	3.21	3.45	2.02	1.14
P_2O_5	0.03	0.02	0.02	0.02	0.02	0.02	0.02	0.05	0.04	0.06	0.06	0.01	0.01
BaO	0.08	0.06	0.26	0.25	0.11	0.11	0.47	0.41	0.37	0.34	0.35	0.14	0.70
CuO								0.01	0.01				
ZnO	0.00	0.00	0.01	0.01	0.04	0.04	0.00	0.38	0.28	0.82	0.02	0.06	
PbO	0.01	0.01	0.15	0.16	0.05	0.05	0.00	0.52	0.48	0.26	0.55	0.40	
Loss inc.S-	1.62	1.59	1.47	1.46	1.83	1.80	1.59	4.16	4.13	4.16	3.81	2.28	3.71
Total	99.54	99.76	99.69	99.59	99.76	100.21	99.90	100.12	100.01	100.00	100.04	100.04	99.88
S	0.01	0.01	0.05	0.05	0.04	0.04	0.01	3.16	3.46	3.12	2.80	1.30	4.41
Ppm													
Sc	7.6	14.4	5.0	6.0	6.5	6.2	7.0	16	14	13.1	13.0	4.6	4
Ba	718	572	2300	2250	997	991	4230	3700	3290	3040	3140	1256	6300
V	11	12	28	28	12	12	7	3	4	6	5	7	<3
Cr	1.2	1.3	1.8	1.6	2.4	1.7	1.1	1	<1	1.5	1.7	1.9	3
Ni	3	2	<1	2	2	2	2	2	4	6	3	5	6
Cu	4	5	92	93	94	94	15	72	129	51	64	5	33
Zn	4	7	142	138	340	331	17	3010	2265	6560	130	488	31
As	4	7	3	<3	3	<3	13	17	20	16	25	17	111
Rb	71	65	69	69	75	74	75	133	118	109	124	62	39
Sr	24	19	22	22	52	52	20	9	7	9	10	7	10
Y	40.1	28.6	22.4	25.6	33.4	33.6	29.1	28	24	13.0	23.5	11.2	26
Zr	143	160	127	126	158	158	142	105	96	93	112	95	135
Nb	5.6	5.9	5.9	6.1	7.0	6.9	5.2	5	4	3.5	4.2	3.5	5.6
Sn	4	3	<2	3	3	<2	4	2	3	<2	<2	<2	14
Pb	48	48	1350	1470	446	440	39	4850	4410	2370	5060	3750	44
Bi	3	3	<2	<2	<2	<2	<2	<2	<2	<2	<2	<2	94
U	2.4	2.7	3.4	3.4	3.3	3.1	2.7	3	4	2.6	3.5	3.5	3
Th	5.3	5.9	4.8	4.8	6.7	6.4	6.6	3	4	<2	3.7	3.1	4
La	22	19	23	25	22	18	29	13	7	20	14	8	12
Ce	49	48	65	66	54	50	62	44	28	41	50	40	31
Nd	22	23	25	23	24	21	29	11	9	10	12	6	12
REEs ICPMS													
7 Li	1.20				7.12			1.29	1.30		1.54		
9 Be	0.69				1.06			1.19	1.00		1.21		
45 Sc	7.44				6.58			14.64	13.34		12.27		
47 Ti	1179.83				1873.49			2651.57	2022.41		1927.69		
51 V	11.94				13.81			6.73	6.52		7.00		
52 Cr	1.14				0.52			0.75	0.86		1.40		
53 Cr	1.23				0.57			0.80	0.89		1.38		
55 Mn	11.43				101.95			93.40	115.09		48.05		
59 Co	70.33				54.38			32.93	65.91		38.16		
60 Ni	1.730				1.430			0.986	2.246		1.338		
63 Cu	3.450				108.423			83.759	130.565		73.584		
65 Cu	3.560				107.799			84.020	139.324		73.520		
66 Zn	5.405				335.417			2507.472	1852.792		116.452		
71 Ga	11.205				10.488			11.589	11.441		11.982		
75 As	3.689				<2			7.616	5.026		9.973		
85 Rb	69.845				71.275			125.084	110.179		116.010		
88 Sr	23.093				49.936			7.154	5.883		8.557		
89 Y	39.545				33.990			27.087	22.481		23.519		
90 Zr	113.228				134.389			97.532	91.326		102.631		
93 Nb	3.673				4.457			3.454	2.688		3.340		
95 Mo	1.289				0.690			0.533	0.653		1.224		
107 Ag	0.147				0.965			1.340	1.384		1.085		
111 Cd	<0.00				2.372			43.628	32.593		8.229		
118 Sn	4.091				1.378			1.177	1.172		1.307		
121 Sb	0.538				1.255			2.309	3.000		1.695		
125 Te	0.402				<0.1			<0.1	<0.1		<0.1		
133 Cs	0.727				1.598			0.837	0.805		0.837		
137 Ba	747.491				877.076			1442.484	1902.304		1437.084		
139 La	24.775				20.418			12.655	6.947		12.259		
140 Ce	50.357				44.513			26.240	16.607		25.428		
141 Pr	5.948				5.085			3.267	1.976		3.216		
146 Nd	23.175				19.829			13.542	8.270		13.269		
147 Sm	5.05				5.11			3.48	2.25		3.22		
153 Eu	1.59				1.53			0.99	0.57		0.75		
157 Gd	5.30				5.76			4.25	2.93		3.50		
159 Tb	0.96				0.99			0.78	0.60		0.65		
163 Dy	6.28				5.95			4.96	3.99		4.22		
165 Ho	1.43				1.24			1.07	0.90		0.94		
166 Er	4.37				3.58			3.10	2.70		2.86		
169 Tm	0.65				0.52			0.45	0.41		0.43		
172 Yb	4.26				3.37			2.87	2.70		2.79		
175 Lu	0.67				0.52			0.45	0.42		0.44		
178 Hf	3.39				3.61			2.78	2.55		2.91		
181 Ta	0.89				0.83			0.44	0.71		0.53		
182 W	599.70				495.91			319.96	544.40		361.01		
205 Tl	0.98				0.86			2.87	2.74		2.78		
208 Pb	48.77				439.71			3848.94	3410.67		4161.20		
209 Bi	3.21				1.81			<0.1	<0.1		<0.1		
232 Th	6.45				6.73			3.78	3.66		4.31		
238 U	1.90				2.00			1.30	1.16		1.35		

Table 4.3. Lithogeochemical values for volcanic rocks of the Bukit Ketaya deposit. Rocks are separated into ore horizon and footwall units.

	Bukit Ketaya									
	Ore horizon*					Footwall				
Element	BK01*	BK01(a)*	BKHOST-2*	KIRI2/3*	KIRI3*	KNN2	BK11	BK11a	HR1	MBTCBK
XRF										
Wt%										
SiO_2	73.08	74.74	75.44	75.84	86.21	83.51	82.95	83.81	86.70	88.69
TiO_2	0.45	0.35	0.35	0.35	0.14	0.20	0.20	0.21	0.39	0.26
Al_2O_3	12.79	11.27	11.23	11.49	6.97	4.95	9.43	9.72	8.30	0.18
Fe_2O_3	3.74	4.3	3.57	3.45	1.50	5.50	2.43	1.58	0.16	6.65
MnO	0.01	0.02	0.02	0.01	0.01	0.00	<0.01	<0.01	<0.01	<0.01
MgO	0.59	0.55	0.50	0.61	0.25	0.11	0.20	0.16	0.12	0.03
CaO	0.01	0.01	0.01	0.01	0.01	0.00	0.01	0.01	0.01	<0.01
Na_2O	0.06	0.05	0.05	0.05	0.05	0.05	0.14	0.17	0.15	<0.03
K_2O	3.86	3.42	3.21	3.45	2.02	1.14	2.45	2.44	1.97	0.04
P_2O_5	0.05	0.04	0.06	0.06	0.01	0.01	0.03	0.02	0.02	0.01
BaO	0.413	0.367	0.339	0.351	0.140	0.70	0.080	0.064	0.257	0.07
CuO	0.009	0.016								0.115
ZnO	0.375	0.282	0.817	0.016	0.061		0.001	0.001	0.018	0.001
PbO	0.522	0.475	0.255	0.545	0.404		0.005	0.005	0.145	0.005
Loss inc.S-	4.16	4.13	4.16	3.81	2.28	3.71	1.62	1.59	1.47	3.74
Total	100.12	100.01	100.00	100.04	100.04	99.88	99.54	99.76	99.69	99.79
S	3.16	3.46	3.12	2.80	1.30	4.41	0.01	0.01	0.05	5.33
Ppm										
Sc	16	14	13.1	13.0	4.6	4	7.6	14.4	5.0	2
Ba	3700	3290	3040	3140	1256	6300	718	572	2300	612
V	3	4	6	5	7	<3	11	12	28	<3
Cr	1	<1	1.5	1.7	1.9	3	1.2	1.3	1.8	1
Ni	2	4	6	3	5	6	3	2	<1	14
Cu	72	129	51	64	5	33	4	5	92	920
Zn	3010	2265	6560	130	488	31	4	7	142	9
As	17	20	16	25	17	111	4	7	3	55
Rb	133	118	109	124	62	39	71	65	69	2
Sr	9	7	9	10	7	10	24	19	22	6
Y	28	24	13.0	23.5	11.2	26	40.1	28.6	22.4	23
Zr	105	96	93	112	95	135	143	160	127	161
Nb	5	4	3.5	4.2	3.5	5.6	5.6	5.9	5.9	6
Sn	2	3	<2	<2	<2	14	4	3	<2	13
Pb	4850	4410	2370	5060	3750	44	48	48	1350	42
Bi	<2	<2	<2	<2	<2	94	3	3	<2	7
U	3	4	2.6	3.5	3.5	3	2.4	2.7	3.4	3
Th	3	4	<2	3.7	3.1	4	5.3	5.9	4.8	7
La	13	7	20	14	8	12	22	19	23	8
Ce	44	28	41	50	40	31	49	48	65	20
Nd	11	9	10	12	6	12	22	23	25	9
REEs ICPMS										
7 Li					2.06	4.44			1.79	1.57
9 Be					0.15	0.25			0.96	0.27
45 Sc					1.78	2.30			13.90	2.11
47 Ti					1396.03	1876.29			1706.21	1392.60
51 V					8.02	12.95			4.05	0.43
52 Cr					0.930	1.087			1.718	1.114
53 Cr					< 0.5	2.61			1.11	0.72
55 Mn					1.591	1.208			66.118	14.050
59 Co					29.152	42.230			44.879	152.407
60 Ni					0.611	0.995			1.149	5.378
63 Cu					5.058	4.535			22.604	962.871
65 Cu					5.206	4.776			22.718	985.594
66 Zn					1.886	2.042			7.530	10.709
71 Ga					3.452	2.877			11.167	0.192
75 As					0.0 < x < 2.0	2.107			45.852	24.327
85 Rb					17.779	36.197			70.316	1.252
88 Sr					44.512	22.238			43.974	6.252
89 Y					6.493	8.003			21.431	22.387
90 Zr					219.218	281.714			134.966	133.038
93 Nb					3.868	4.795			4.341	1.977
95 Mo					0.821	2.167			2.758	1.909
107 Ag					0.454	0.619			16.306	12.217
111 Cd					0.0 < x < 0.1	0.0 < x < 0.1			0.0 < x < 0.1	0.060
118 Sn					4.829	18.600			1.307	4.503
121 Sb					1.130	3.530			0.949	4.729
125 Te					0.134	0.727			0.0 < x < 0.1	0.950
133 Cs					0.551	1.166			0.495	0.047
137 Ba					407.450	399.517			1364.205	742.978
139 La					5.688	8.572			15.683	10.185
140 Ce					11.795	19.222			31.374	19.305
141 Pr					1.382	2.226			4.026	2.216
146 Nd					4.931	8.638			16.593	8.376
147 Sm					0.872	1.764			3.960	1.778
153 Eu					0.219	0.289			0.957	0.551
157 Gd					0.707	1.156			3.405	2.251
159 Tb					0.145	0.202			0.569	0.478
163 Dy					1.074	1.431			3.664	3.483
165 Ho					0.260	0.351			0.822	0.848
166 Er					0.912	1.231			2.738	2.775
169 Tm					0.158	0.214			0.440	0.451
172 Yb					1.132	1.564			2.962	3.055
175 Lu					0.19	0.26			0.48	0.50
178 Hf					6.88	8.50			4.04	3.80
181 Ta					0.32	0.41			0.95	0.65
182 W					310.90	440.55			468.73	669.12
205 Tl					0.27	0.43			0.79	0.37
208 Pb					19.60	8.50			113.95	46.60
209 Bi					1.61	5.76			0.10	6.46
232 Th					3.71	4.87			5.69	6.64
238 U					2.85	3.14			1.53	2.74

4.3.1 Major element chemistry

4.3.1.1 District-scale

Element mobility was assessed by plotting the selected major elements against silica contents on Harker variation diagrams, and it is clear that some of the major elements were mobile during hydrothermal alteration. In general, volcanic rocks and intrusions define overlapping trends. The SiO_2 contents of the six volcanic and three microgranite/subvolcanic rock samples are; volcanic: 62 to 83 wt% SiO_2 and microgranite: 76 to 86 wt% SiO_2. Both volcanic and intrusion rocks show a decrease in Al_2O_3, TiO_2, P_2O_5, Fe_2O_3 and MgO values with increasing SiO_2 except for K_2O and Na_2O (Fig. 4.1).

The good correlations in some of the elements above are most likely due to the fractionation by combination of hornblende, sphene, plagioclase, apatite and Fe-Ti oxide minerals, whereas the poor correlations of K_2O and Na_2O with increasing in SiO_2 may reflect the influence of hydrothermal alteration and possibility of constant sums effect.

4.3.1.2 Deposit-scale

Volcanic rocks from both the Bukit Botol and the Bukit Ketaya deposits are dominantly felsic with SiO_2 contents > 73 wt%. Similar to the district-scale igneous rocks, the Harker variation diagrams show negative correlations of SiO_2 with Al_2O_3, TiO_2, P_2O_5, Fe_2O_3 and MgO (Fig. 4.1). Although for the chemistry of the volcanic rocks significantly overlap, there are obvious differences between the footwall and ore horizon units from the both deposits.

The ore horizon unit from the Bukit Botol and Bukit Ketaya deposits tend to have rocks with high SiO_2 contents (70 to 87 wt %), whereas the silica contents in the footwall unit has both low and high SiO_2 rocks (62 to 88 wt % SiO_2) reflecting the abundance of quartz.

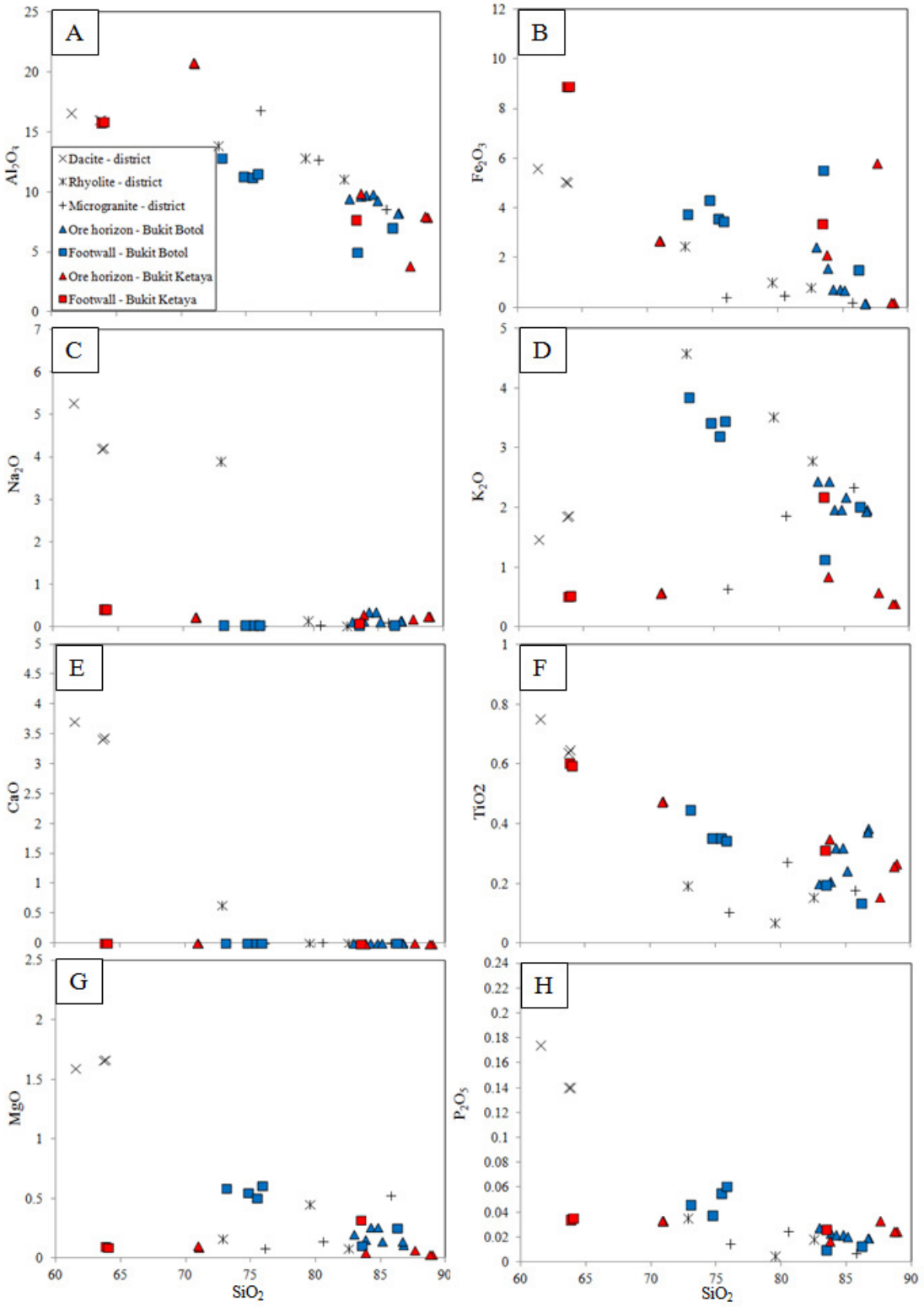

Fig. 4.1. Harker variation diagrams; silica (SiO_2wt %) plotted against a range of major elements (in wt %) from the igneous rocks of Tasik Chini area and the ore horizon and footwall felsic volcanic rocks units of the Bukit Botol and Bukit Ketaya deposits. **A.** SiO_2 versus Al_2O_3. **B.** SiO_2 versus total Fe_2O_3. **C.** SiO_2 versus Na_2O. **D.** SiO_2 versus K_2O. **E.** SiO_2 versus CaO. **F.** SiO_2 versus TiO_2. **G.** SiO_2 versus MgO. **H.** SiO_2 versus P_2O_5.

The lower Al_2O_3 in the footwalls relative to the ore horizons at the both deposits are consistent with the petrographic observations which show that the plagioclase is more abundant in the footwall than the ore horizon/hangingwall rocks (see Chapter 3). However, fractionation of plagioclase is not illustrated in the Na_2O and CaO geochemical data because most of the samples are altered.

K_2O contents are mostly high (>0.5 wt %) which reflects the presence of sericite in all samples. However, a decrease trend is observed from footwall to ore horizon at Bukit Botol deposit, whereas K_2O compositions for both footwall and ore horizon at Bukit Ketaya deposit display a flat trend.

4.3.2 Trace and rare earth element (REE) chemistry

4.3.2.1 District-scale

Most trace element concentrations in the igneous rocks of the Tasik Chini area demonstrate a systematic variation with SiO_2 (Fig. 4.2). Almost all element show a decrease with increasing SiO_2 content >77 wt% silica suggesting depletion of the elements as a result of silica alteration. The volcanic rocks have higher Sr content compared to intrusions. However, the decrease of both Sr and Al_2O_3 with increasing SiO_2 in the volcanic suite and intrusions suggests the importance of plagioclase fractionation, and could also be due to alteration.

4.3.2.2 Deposit-scale

Most of the selected trace element concentrations for the ore horizon and footwall felsic volcanic rocks from both the Bukit Botol and the Bukit Ketaya deposits show a wide range but display negative correlations with SiO_2 (Fig. 4.2).

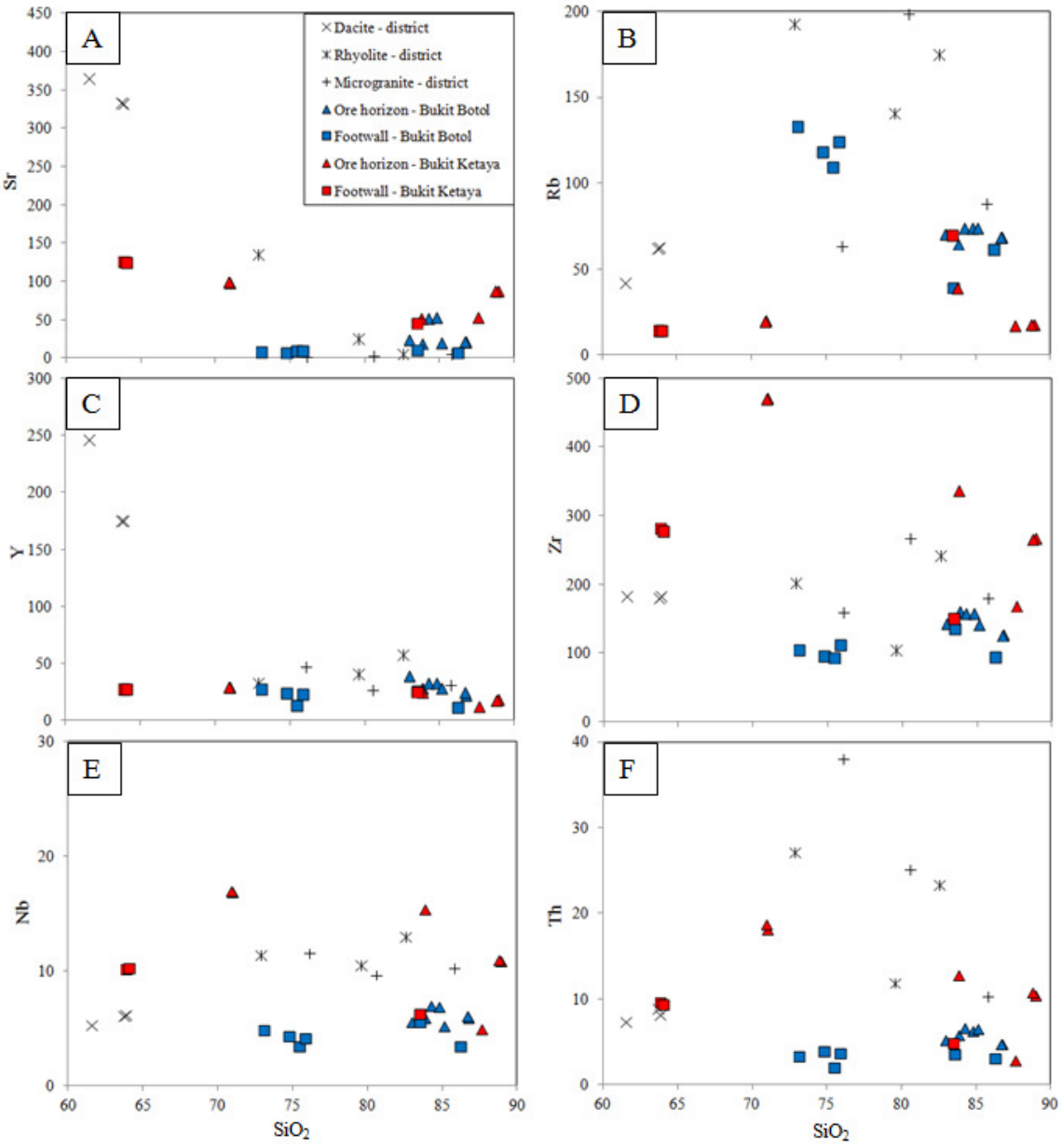

Fig. 4.2. Harker variation diagrams; silica (SiO_2wt %) plotted against a range of trace elements (in ppm) from the igneous rocks of Tasik Chini area and the ore horizon and footwall felsic volcanic rocks units of the Bukit Botol and Bukit Ketaya deposits. **A.** SiO_2 versus Sr. **B.** SiO_2 versus Rb. **C.** SiO_2 versus Y. **D.** SiO_2 versus Zr. **E.** SiO_2 versus Nb. **F.** SiO_2 versus Th.

Normalised REE plots of each felsic volcanic rocks unit from both Bukit Botol and Bukit Ketaya were made to examine their internal consistencies and compare their overall geochemical signatures. Chondrite and primitive mantle-mantle normalising values from Sun and McDonough (1989) were used for normalisation. The chondrite-normalised REE pattern

for footwall and ore horizon/hangingwall rhyolites at Bukit Botol deposit are shown in Fig. 4.3A. The footwall rhyolite exhibits a slight enrichment in the LREE but a near-flat trend for the HREE and a negative Eu anomaly. A similar REE pattern is also shown by ore horizon/hangingwall unit. The incompatible element normalised to primitive mantle patterns also show the similarities between the ore horizon and footwall felsic volcanic rocks (Fig. 4.3B). Samples of each unit show a negative Nb anomaly relative to Th and La as well as a negative Ti anomaly. The negative Nb and Ti anomalies are typical of volcanic rocks erupted in subduction-related setting (e.g., Pearce and Cann, 1973; Pearce and Peate, 1995).

The chondrite-normalised plots of the quartz-feldspar phyric rhyolite of the footwall unit and the rhyolite breccias of the ore horizon unit from Bukit Ketaya deposits show similar trends. They are characterised by moderately LREE enrichment, slightly higher HREE in the coherent units compared to the flow breccias and weakly negative Eu anomaly (Fig. 4.3C). The incompatible element patterns for these two rock units normalised to primitive mantle are also comparable and relatively consistent, and have a pattern that is similar to felsic volcanic rocks from the Bukit Botol deposit with moderate to strong negative Nb and Ti anomalies relative to Th and La (Fig. 4.10D). These features all indicate an origin from a volcanic source in a subduction-related tectonic setting, similar to rocks from the Bukit Botol units and they were derived from relatively fractionated magma sources.

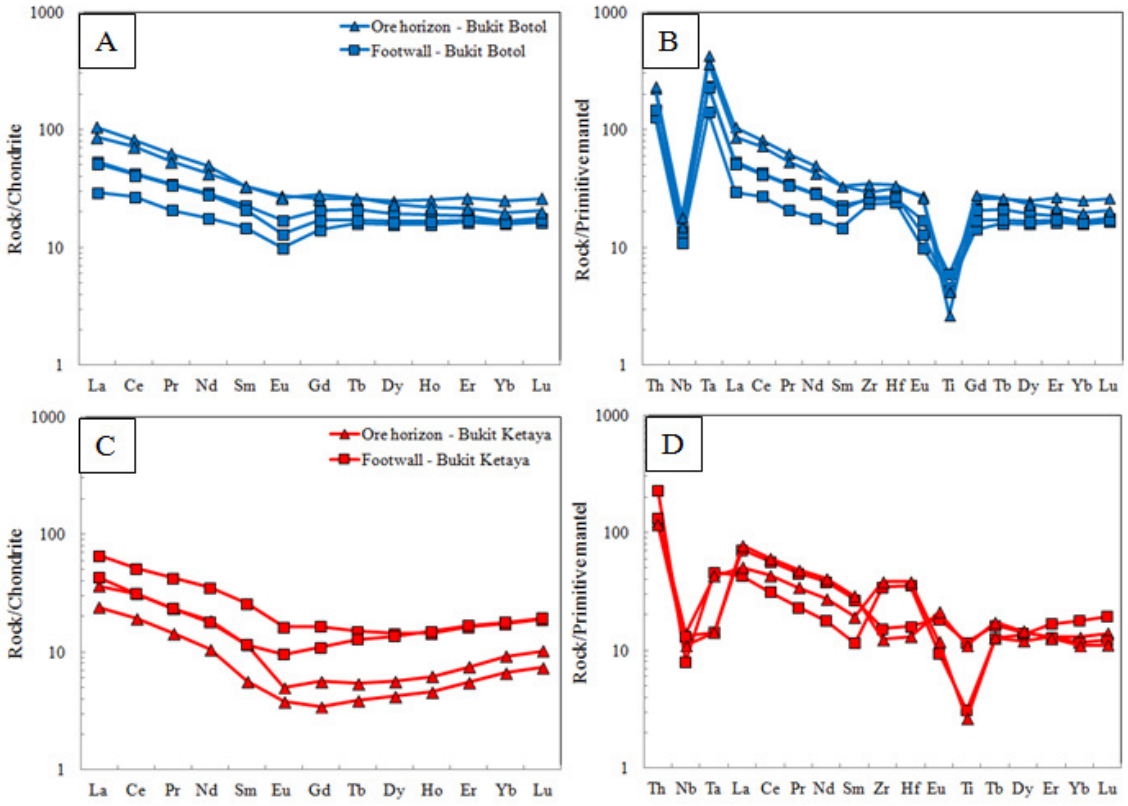

Fig. 4.3. **A.** Chondrite-normalised rare earth element plots for the ore horizon and footwall felsic volcanic rocks of the Bukit Botol deposit. **B.** Primitive mantle-normalised trace element diagrams for ore horizon and footwall felsic volcanic rocks of the Bukit Botol deposit. **C.** Chondrite-normalised rare earth element plots for the ore horizon and footwall felsic volcanic rocks of the Bukit ketaya deposit. **D.** Primitive mantle-normalised trace element diagrams for ore horizon and footwall felsic volcanic rocks of the Bukit Ketaya deposit. Element order and normalising values follow Sun and McDonough (1989).

4.3.3 Immobile element chemistry

Due to alteration related to mobility of some major- and trace elements, the present chemical composition of the rocks differs from the original composition. Therefore, the mobility of elements in volcanic and intrusions from the district and deposit areas were further assessed using several Harker Zr plots in monitoring alteration and fractionation trends (Fig. 4.4.). Zr is considered immobile under most metamorphism conditions (e.g., Pearce and Cann, 1973; Winchester and Floyd, 1977), and Ti, Zr, Nb and Y are relatively immobile during hydrothermal alteration (MacLean and Kranidiotis, 1987; MacLean and Barrett, 1993; Skirrow and Franklin, 1994). Mass changes caused by alteration will occur along separate

alteration lines for each chemically distinct rock compositions (e.g., MacLean and Barrett, 1993; Barrett et al., 1994). Furthermore, Murphy and Hynes (1986) showed that elements which are immobile during alteration within the samples will plot on a straight line through the origin of a binary element plot, if the population of altered rocks is derived from the same least-altered composition.

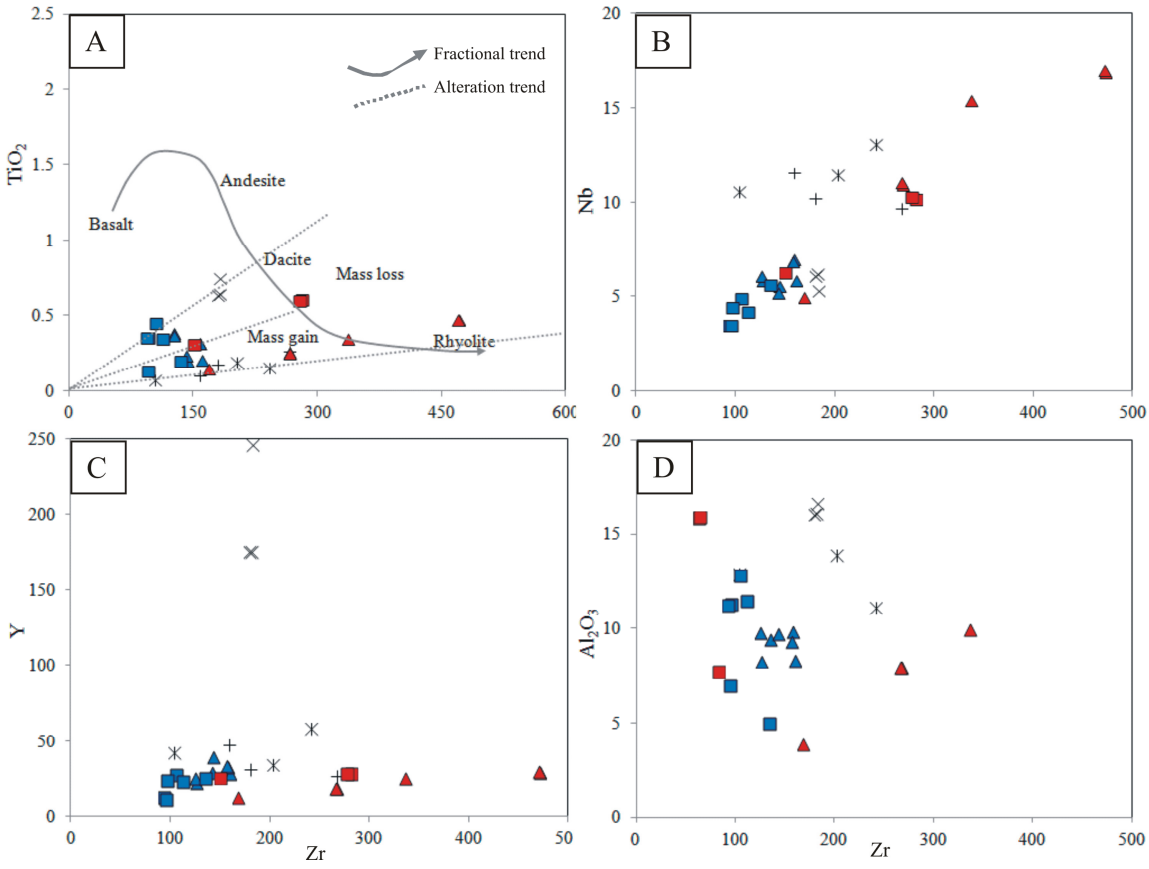

Fig. 4.4. Harker variation diagrams; zircon (Zr ppm) plotted against a range of trace elements (in ppm) from the igneous rocks of Tasik Chini area and the ore horizon and footwall felsic volcanic rocks units of the Bukit Botol and Bukit Ketaya deposits. **A.** Zr versus TiO_2. **B.** Zr versus Nb. **C.** Zr versus Y. **D.** Al_3O_2 versus Zr.

A plot of the samples on the Zr versus TiO_2 diagram after Barrett et al. (1994) displays two possible populations. The majority of the volcanic rocks from district and deposit areas are rhyolites, which is consistent with the chemical composition of the least-altered samples of rhyolitic to rhyodacitic, whereas the dacite plot mainly as dacite. In comparison, the three

intrusion samples with low TiO_2 plot as rhyolite. Most samples experienced mass gain and form an alteration lines that plot through the origin toward a least-altered composition (Fig. 4.4A).

Binary diagrams of Zr versus Nb and Y also show good to moderate straight line correlations, implying that the condition of immobility is satisfied (Figs. 4.4B and C). However, Zr does not correlate with Al_2O_3. This could be due to the mobility of Al_2O_3 during alteration (Fig. 4.4D).

Thus, it is concluded that TiO_2, Nb, Y and Zr are immobile, and the altered rocks used in this study are derived from the same rock type of least-altered compositions.

4.3.4 Geochemical classification

The major and trace elements data show that all the rocks have experienced variable degree of hydrothermal alteration. However, most studies of altered volcanic rocks in near VHMS systems indicate that the high-field strength elements (HFSE), Ti, Zr, Nb and Y, are relatively immobile during hydrothermal alteration (MacLean and Kranidiotis, 1987; MacLean and Barrett, 1993; Skirrow and Franklin, 1994; this study). Additionally, other elements including Al, heavy REE (Lu, Yb), Hf and Ta are essentially immobile during alteration (MacLean and Kranidiotis, 1987; MacLean and Barrett, 1993; Gifkins et al., 2005). Although Zr, Y, and Nb are immobile, they are generally incompatible and their ratios vary according to magmatic affinity (MacLean and Barrett, 1993; Gifkins et al., 2005). In this section, the immobile element features of the district-scale igneous rocks together with Bukit Botol and Bukit Ketaya volcanic rocks are plotted in a series of discrimination diagrams.

4.3.4.1 District-scale

The district-scale igneous rocks include felsic compositions only (dacite, rhyolite and microgranite). Dacite and andesitic have a relatively low Zr/TiO_2 values contents and low Nb/Y (~0.04), indicating a strongly sub-alkaline affinity. Meanwhile, the geochemical characteristics of the rhyolite are very similar to the microgranite intrusions. Both of these volcanic and intrusion rocks have high Zr/TiO_2 and Nb/Y values and sub-alkaline affinities. On a Winchester and Floyd (1977) discrimination diagram, these compositional differences are well identified, where both rhyolite and microgranite plot mainly in field of rhyolite whereas dacitic/andesitic rocks fall in the andesite area (Fig. 4.5A).

On Zr versus Y plot, all the rhyolite and microgranite samples mostly plot in transitional field with some samples overlap the tholeiitic field whereas dacitic/andesitic rocks plot within the tholeiitic field (Fig. 4.5B). The HFSE contents (e.g., Nb, Y, Zr) within the rhyolite and microgranite rocks are moderate to low with the lowest concentrations in dacitic/andesitic rocks. Using the tectonic discrimination diagrams of Pearce et al. (1984), the rhyolite and microgranite display mainly volcanic arc of I-type characteristics. However, the low HFSE contents for dacite/andesite rocks are reflected in these diagrams. The samples plot more towards ocean floor field and are not within the volcanic arc field in the Nb versus Y diagram but fall mainly into the within plate category in the Y+Nb versus Rb diagram (Figs. 4.5C and D).

4.3.4.2 Deposit-scale

Both the ore horizon and footwall felsic volcanic rocks from Bukit Botol deposit have similar geochemical features with distinctly low to moderate Zr/TiO_2 values and subalkaline Nb/Y ratios. These samples clearly displayed a single modal grouping and mostly plot well within the rhyodacite/dacite field of Winchester and Floyd (1977) discrimination diagram, although a few of them fall on the edge of the andesite field (Fig. 4.5A).

In a plot of Zr versus Y after Barrett and MacLean (1994), the felsic volcanic rocks demonstrate a transitional to mildly tholeiitic magmatic affinity (Fig. 4. 5B). These rocks are moderately HFSE enriched and in Nb versus Y and Y+Nb versus Rb plots of Pearce et al. (1984) fall within the field of I-type volcanic arc (Figs. 4.5C and D).

In the plot using immobile elements Nb/Y versus Zr/TiO_2 of Winchester and Floyd (1977), all the Bukit Ketaya felsic volcanic rocks have a sub-alkaline character. However, ore horizon unit has slightly higher Zr/TiO_2 values and Nb/Y ratios compared to the moderate Zr/TiO_2 and Nb/Y ratios in footwall unit, and it falls in the rhyolite field, whereas most of the footwall samples plot in the rhyodacite/dacite field similar to those of the Bukit Botol unit (Fig. 4.4A).

On the Y versus Zr diagram of Barrett and MacLean (1994), most of the felsic volcanic rocks plot in the calc-alkaline field (Fig. 4.5B). The HFSE contents of these rocks are relatively high to moderate. Thus, as for the rhyolite-rhyodacite unit at the Bukit Botol deposit, these rhyolite-rhyodacite units also plot entirely within the volcanic arc field with mostly I-type of the Y versus Nb and Y+Nb versus Rb plots of Pearce et al. (1984) (Figs. 4.5C and D).

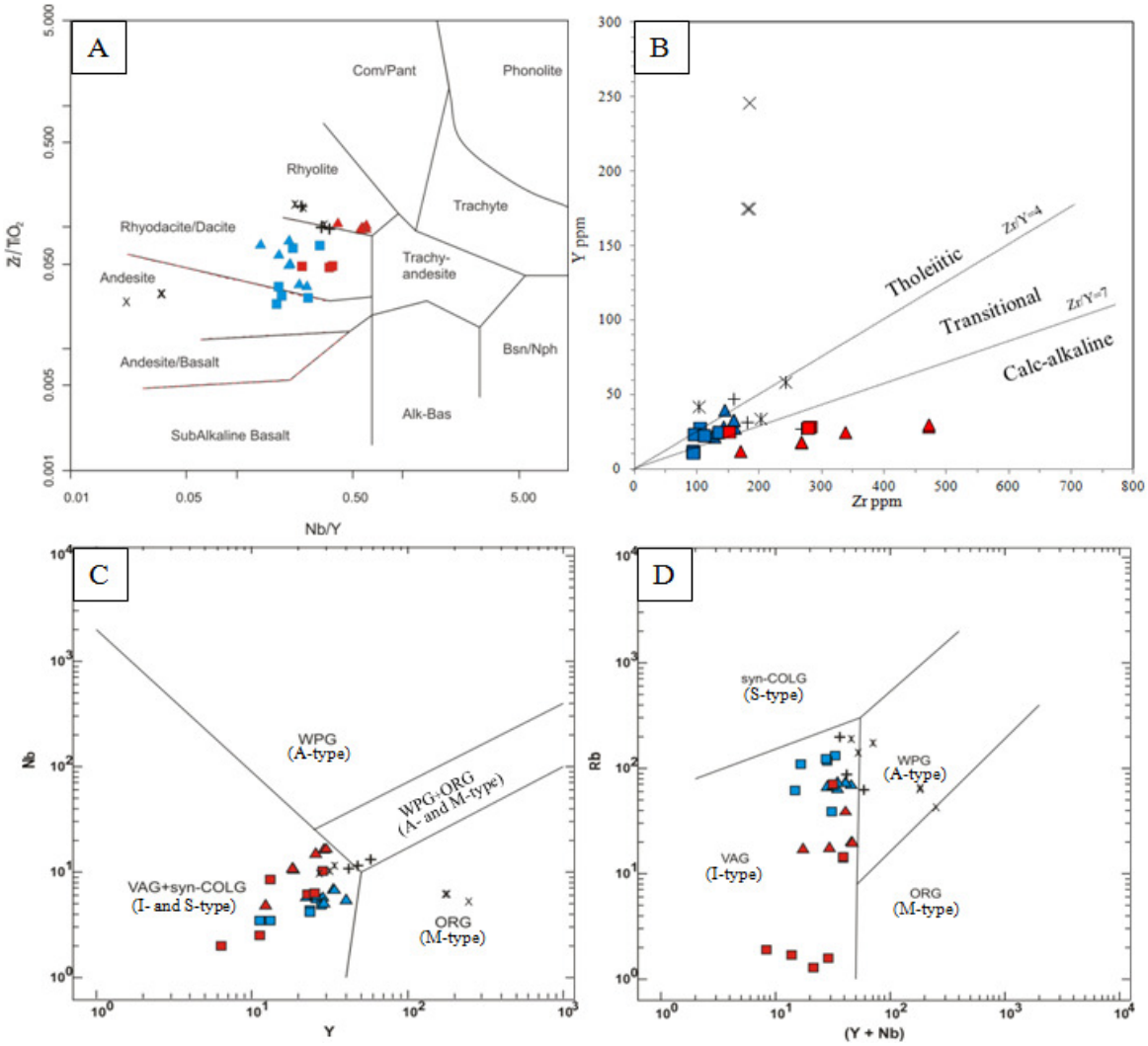

Fig. 4.5. Various immobile element discrimination diagrams showing the classifications, magmatic affinities and tectonic settings for igneous rocks of Tasik Chini area and the ore horizon and footwall felsic volcanic rocks units of the Bukit Botol and Bukit Ketaya deposits. **A.** Nb/Y versus Zr/TiO2 plot of Winchester and Floyd (1977). **B.** Zr versus Y plot of tholeiitic versus calc-alkaline affinity of the felsic volcanic rocks from Barrett and MacLean (1994). Primitive mantle-normalised trace element diagrams for ore horizon and footwall felsic volcanic rocks of the Bukit Botol deposit. **C.** Modified Nb-Y discrimination diagram of Pearce et al. (1984). **D.** Y+Nb versus Rb tectonic discrimination diagram after Pearce (1984) with modification. Annotation: WPG=within plate field, VAG=volcanic arc field, syn-COLG=syncollisional field and ORG=ocean ridge field.

4.3.5 Sm-Nd and Rb-Sr results

The results of whole rock Sm-Nd and Rb-Sr isotopic analyses of selected district- and deposit-scales volcanic-plutonic rocks from the Tasik Chini area are presented in Table 4.4. These data are not used here for geochronology because U-Pb zircon ages of samples are already determined by the U-Pb LA-ICPMS method (see Sections 4.4).

Table 4.4. Chemical and isotopic compositions of Sm, Nd, Rb and Sr from dacite, rhyolite and microgranite of the Bukit Botol, Bukit Ketaya and Tasik Chini area.

	BB6	BB11	BB25	HR1	BK01	BK11	BR3*	BR321**	BR323**	BR318***	BR326***
	Rhyodacite - Bukit Botol			Rhyodacite-rhyolite - Bukit Ketaya			Dacite*, rhyolite** and microgranite*** - district				
Rb (ppm)	71.09	64.35	69.05	70.33	19.36	13.93	62.20	193.30	140.72	87.37	61.47
Sr (ppm)	23.46	19.11	21.82	47.17	97.53	110.75	329.99	133.79	24.60	4.80	1.26
$^{87}Rb/^{86}Sr$	8.793	9.774	9.184	4.321	0.574	0.364	0.545	4.185	16.64	53.68	146.15
$^{87}Sr/^{86}Sr$	0.74081	0.74586	0.74347	0.72644	0.70895	0.70976	0.70929	0.72153	0.76502	0.90083	1.10612
Sm (ppm)	4.77	4.59	4.52	4.04	6.02	0.81	27.50	7.77	6.96	3.51	6.46
Nd (ppm)	22.07	21.44	23.02	17.69	37.11	2.35	94.52	39.96	40.71	16.65	32.35
$^{147}Sm/^{144}Nd$	0.1304	0.1293	0.1186	0.1380	0.0980	0.2081	0.1757	0.1174	0.1032	0.1274	0.1206
$^{143}Nd/^{144}Nd$	0.512492	0.512488	0.512481	0.512487	0.512427	0.512680	0.512462	0.512331	0.512445	0.512242	0.512288
eNd now	-2.85	-2.93	-3.06	-2.95	-4.12	0.82	-3.43	-5.99	-3.76	-7.72	-6.83
age, Ma	288	288	288	288	288	288	235	235	235	288	235
Initial $^{87}Sr/^{86}Sr$; I_{sr}	0.7048	0.7058	0.7058	0.7087	0.7066	0.7083	0.7075	0.7075	0.7094	0.6808	0.6176
error (2sd)	0.0007	0.0007	0.0007	0.0003	0.0001	0.0001	0.0001	0.0003	0.0012	0.0038	0.0108
Initial $^{143}Nd/^{144}Nd$	0.512246	0.512244	0.512257	0.512227	0.512242	0.512288	0.512192	0.512150	0.512286	0.512002	0.512102
Initial Nd; $\varepsilon_{Nd}(T)$	-0.4	-0.4	-0.2	-0.8	-0.5	0.4	-2.8	-3.6	-1.0	-5.2	-4.5
TDM1	1.21	1.20	1.07	1.34	0.95	12.58	2.75	1.30	0.97	1.60	1.41
TDM2	1.03	1.03	1.01	1.05	1.03	0.97	1.16	1.22	1.02	1.38	1.29

The two microgranite and three volcanic samples from the district-scale display a variable range of calculated $^{87}Rb/^{86}Sr$ from 0.545 to 146.15 and measured $^{87}Sr/^{86}Sr$ ratios between 0.70929 and 1.10612. Both the $^{147}Sm/^{144}Nd$ and $^{143}Nd/^{144}Nd$ ratios are low ranging from 0.1032 to 0.1757 and from 0.512242 to 0.5122462. An average of well constrained U-Pb LA-ICPMS age at 235 Ma was used to recalculate the initial $^{87}Sr/^{86}Sr$ compositions (I_{sr}) and the initial Nd isotopic composition $\varepsilon_{Nd}(T)$.

The two microgranite samples are extremely high in Rb/Sr ratios and showed a wide range of age corrected I_{sr} from 0.6176 to 0.6808 (lower). Nevertheless, both granites have very similar Nd isotopic compositions with the $\varepsilon_{Nd}(T)$ values of -5.2 to -4.5 and the model age of granitoid protoliths (T_{DM2}) of 1.29 to 1.38 Ga. Meanwhile, the initial Nd isotopic composition of the volcanic rocks yield a variation of $\varepsilon_{Nd}(T)$ values from -3.6 to -1.0 with the model age of protoliths (T_{DM2}) between 1.02 and 1.22. In addition, all the volcanic rocks have homogeneous calculated initial $^{87}Sr/^{86}Sr$ compositions (I_{sr}) ranging from 0.7075 to 0.7094.

In both Bukit Botol and Bukit Ketaya deposits, the average constrained U-Pb LA-ICPMS age data from the both deposits at 288 Ma were used and assumed as the emplacement time of the volcanic rocks. All these volcanic rocks have homogeneous isotopic ratios with the calculated initial $^{87}Sr/^{86}Sr$ compositions (I_{sr}) range from 0.7048 to 0.7087 whereas $\varepsilon_{Nd}(T)$ parameter vary from −0.8 to +0.4 and mantle-depleted Nd model ages (T_{DM2}) range of 0.97 to 1.05 Ga.

The radiogenic isotopic data suggest that different sources contributed to the source materials of the volcanic-plutonic emplacements in the Tasik Chini area. A part from the unrealistic calculated initial $^{87}Sr/^{86}Sr$ compositions (I_{sr}) (<0.7000), the microgranite that postdates the mineralisation have large negative $\varepsilon_{Nd}(T)$ values (-5.2 to -4.5) and much older Sm-Nd model ages (T_{DM2} = 1.29 to 1.38 Ga), implying an important of old crustal material in their source. Similarly, the volcanic rocks have lower $\varepsilon_{Nd}(T)$ values (-3.6 to -1.0) and Nd modal age (T_{DM2}) range of 1.02 and 1.22 Ga, suggesting a significant crustal input in their source. Futhermore, consistent with their relative age of emplacements, the rhyolite to rhyodacite rock samples hosting the VHMS deposit in Tasik Chini show slightly higher $\varepsilon_{Nd}(T)$ parameter (-0.8 to +0.4) and lower Nd model ages (T_{DM2}) range of 0.97 to 1.05 Ga, favouring a derivation from younger crustal source but less contaminated.

Zindler and Hart (1986) proposed five main isotopic reservoirs in the mantle characterised by distinct isotopic compositions: DMM=depleted mantle component; high $^{143}Nd/^{144}Nd$ and low $^{87}Sr/^{86}Sr$, MORB=mid-ocean ridge basalt, isotopic compositions same as depleted mantle compositions, OIB=oceanic island basalt, intermediate $^{143}Nd/^{144}Nd$ and low $^{87}Sr/^{86}Sr$ EMI=enriched mantle I of lower crust affinity; low $^{87}Sr/^{86}Sr$, and EMII=enriched mantle II with the upper crust signatures; high $^{87}Sr/^{86}Sr$. $^{87}Sr/^{86}Sr$ versus $^{143}Nd/^{144}Nd$ from Bukit Botol and Bukit Ketaya deposits as well as other volcanic rocks in Tasik Chini district have been

plotted on Zindler and Hart (1986) diagram (see Fig. 4.6). The result shows that both the district and deposit volcanic rocks have relatively large variation but with low initial $^{87}Sr/^{86}Sr$ ratios from 0.7048 to 0.7094 whereas $^{143}Nd/^{144}Nd$ ratios are relatively uniform with intermediate initial ratios between 0.5122 and 0.5123. In addition, all samples seem to be plotted between the OIB- and EMI-reservoirs. Therefore, both the district and deposit volcanic rocks could be interpreted as a mixture between oceanic island basalt and enriched mantle I related to subduction magmatism.

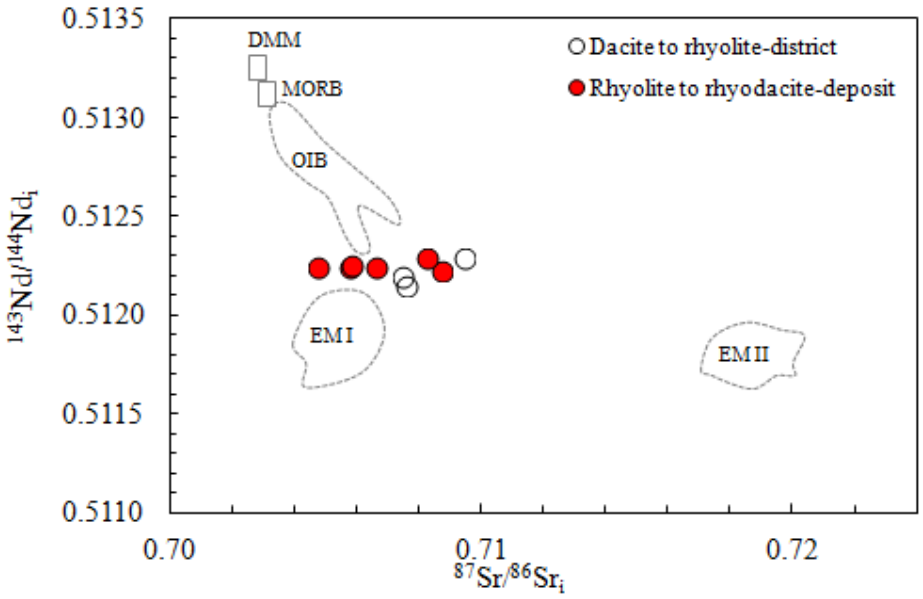

Fig. 4.6. Initial $^{87}Sr/^{86}Sr$ versus $^{143}Nd/^{144}Nd$ isotope correlation diagram for volcanic rocks from the district and deposit-scales of Tasik Chini area (after Zindler and Hart, 1986). Annotation: DMM=depleted mantle, MORB=mid-ocean ridge basalt, OIB=oceanic island basalt, EMI=enriched mantle I and EMII=enriched mantle II.

4.4 Geochronology Results

All the processed data from the LA-ICPMS zircon U-Pb analyses undertaken as part of this study are listed in Appendix III. Detailed sample locations are shown in Appendix II.

4.4.1 Rock formations

Carboniferous sequence

Age constrains for the Carboniferous succession were previously provided through fossils (e.g., Jenning and Lee, 1985; Metcalfe et al., 1980). In this study, age of detrital zircons from one Carboniferous slate (402) and one phyllite (402(2)) were determined to investigate the maximum deposition age and the source of the rocks (Table 4.5). Both samples contained many zircons with subrounded to euhedral shapes. Most of the zircons show simple oscillatory zoning (Figs. 4.7A and C).

Table 4.5. Descriptions of the samples analysed for the LA-ICPMS U-Pb dating.

Locality	Sample	Description	Age (Ma)	Easting (mE)	Northing (mN)
District-scale Tasik Chini					
1 Carbonifeus metasedimentary rocks at road cutting east of Kuantan (Kuantan Group)	402	Interbedded slate-phyllite	336 ± 6.6	103.0619	3.6937
	402(2)	Interbedded slate-phyllite-sandstone	330 ± 3.0	103.0619	3.6937
2 Permo-Triassic sedimentary sequences	BR4	Massive sandstone	≤ 310 ± 3	102.9804	3.3596
3 Jurassic-Cretaceous sedimentary sequence at the eastern part (Bertangga Sandstone)	BR 305	Massive sandstone	≤ 148 ± 2	102.8937	3.4573
	BR 307	Massive sandstone	≤ 139 ± 6	102.8249	3.4777
4 Jurassic-Cretaceous sedimentary sequence at the western part (Gerek Sandstone)	BR 1A	Massive sandstone	≤ 207 ± 8	103.1016	3.4527
	BR 2	Massive sandstone	≤ 150 ± 3	103.1098	3.3971
5 ~20 km southeast of Bukit Botol deposit	BR 325	Mixed sequence of rhyolite and sedimentary rocks	237 ± 1.7	103.0374	3.1041
6 At vicinity of Bukit Perah west of Bukit Botol deposit	BR 3	Massive dacite	233 ± 3.8	103.0349	3.3525
7 South of Tasik Chini area - At vicinity of Bukit Ridan	BR 317	Medium-grained microgranite porphyry	235 ±1.5	103.0511	3.0983
8 South of Tasik Chini area - Northeast of Bukit Ridan	BR 326	Fine- to medium-grained microgranite	234 ± 2.2	103.1045	3.1409
Deposit-scale					
9 Within Bukit Botol mine area	BB 6	Ore horizon unit - rhyolite type 2 comprises of coarse-grained quartz and rare feldspar phenocrysts, strongly porphyritic	292 ± 3.1	102.9410	3.3664
	BB 11	Footwall unit - rhyolite type 1 consists of quartz and feldspar phenocrysts, poorly to moderately porphyritic	286 ± 3.6	102.9281	3.3771
10 Within Bukit Ketaya mine area	S/6a3	Ore horizon unit - rhyolite breccias	286 ± 2.0	102.9215	3.4091
	BK10	Footwall unit - quartz-feldspar phyric rhyolite	288 ± 4.0	102.9215	3.4091

Fifteen zircons were analysed from sample 402. The zircons in the sample are largely Carboniferous with a minor but significant Meso- to Neoarchean (2536 Ma) population. The maximum depositional ages reported here are based on the age of the youngest coherent

population with a mean square weighted deviation (MSWD) less than 2. The ages are reported at the 95% confidence level (2 σ). The five youngest zircons in the sample yield ages between 330 and 343 Ma, and the maximum depositional age is 336.4 ± 6.6 Ma (MSWD=0.87) (Figs. 4.7A and B).

The phyllite sample (402(2)) yielded twenty-four zircon grains with a similar in age range in (329 to 1910 Ma) and maximum deposition age to sample 402, Carboniferous grains are dominant with a distinct population of Meso- to Palaeoproterozoic zircons. Two Devonian grains (393 to 399 Ma) are also found in this sample. The maximum depositional age of this sample is 330.4 ± 3.0 Ma (MSWD=0.87) based on the three zircon grains (Figs.4.7C and D).

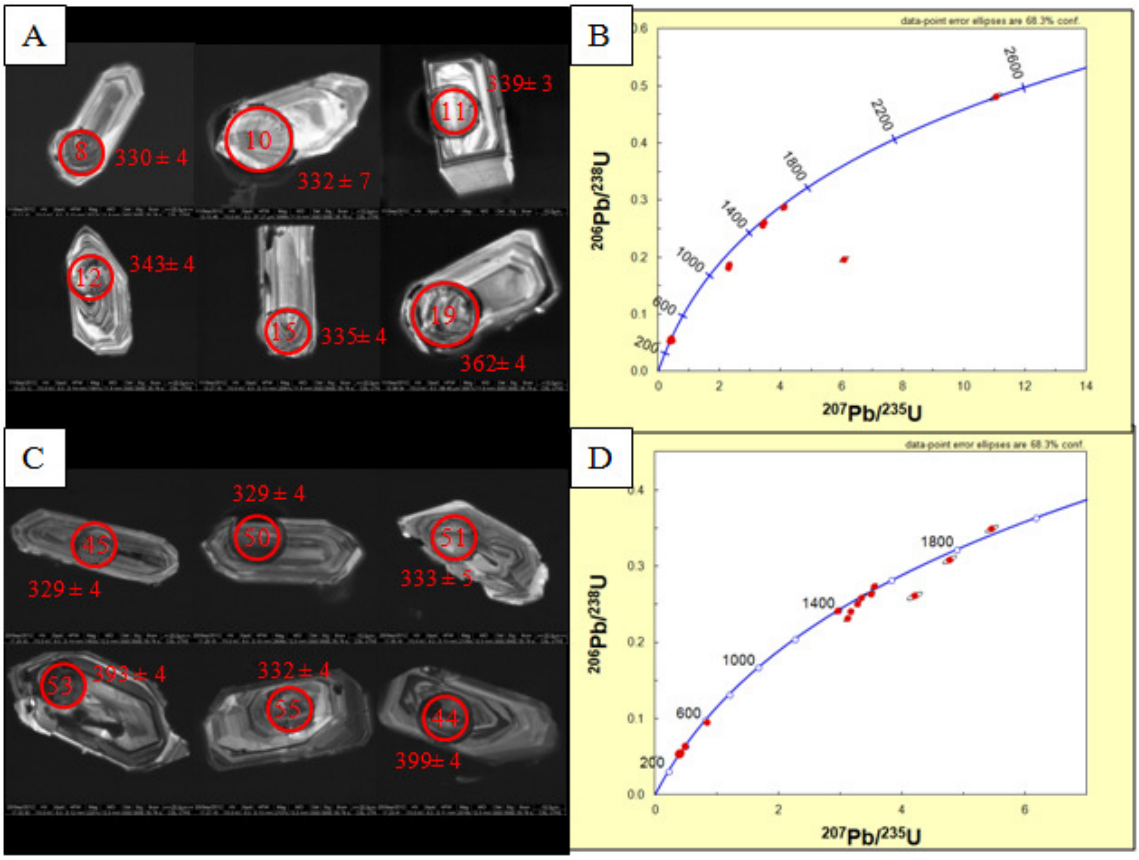

Fig. 4.7. Cathodoluminescence (CL) images of representative detrital zircons and concordia diagram showing LA-ICPMS U–Pb analytical points for the detrital zircons of Carboniferous metasedimentary rocks from Tasik Chini area. **A** and **B.** Sample, 402. **C** and **D.** Sample, 402 (2).

Permian-Triassic sequence

The zircons from one sandstone sample from the Permian-Triassic sequence were analysed to investigate the relationship between magmatism and sedimentation of the Permian-Triassic sequences in the Tasik Chini area (Table 4.5). Sixteen detrital zircons from sample BR4 range in age from 310 ± 3 to 2485 ± 27 Ma. Only one of the grain yields Late Carboniferous age, whereas the remaining grains show an almost continuous Neoproterozoic to Palaeoproterozoic ages from 565 to 2485 Ma (Figs. 4.8A and B). Thus, the interpreted maximum deposition age for this sequence is inferred to be younger than Late Carboniferous.

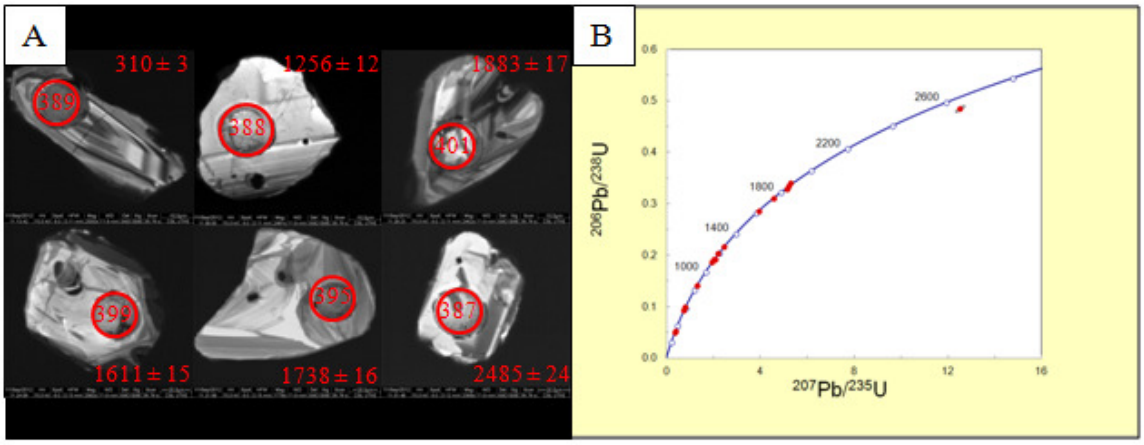

Fig. 4.8. Cathodoluminescence (CL) images of representative detrital zircons and concordia diagram showing LA-ICPMS U–Pb analytical points for the detrital zircons of Permo-Triassic sedimentary rocks from Tasik Chini area. **A** and **B**. Sample, BR4. Note that the circles indicate the spots of LA-ICPMS U–Pb dating and trace element analyses marked with ages.

The single youngest detrital zircon grain of 310 ± 3 Ma is consistent with the Permo-Triassic age for the formation of this sequence and the constraints from the ages of intrusive units such as (the latest Early-Permian-Late Permian Boundary Range batholith) (Liew and Page, 1985b; Cobbing et al., 1986; Darbyshire, 1988; Hutchison, 1989; Cobbing et al., 1992; Schawtz et al., 1995, this study).

Jurassic-Cretaceous sequence

Four sandstone samples, two each from the Jurassic-Cretaceous sequences to the west and to the east of Permo-Triassic sequences were analysed in this study. Sample BR305 and BR307 were collected from two localities in the western part of the Jurassic-Cretaceous succession (Table 4.5). These sandstones are generally very coarse grained, with subangular to subrounded grains that are well sorted. Zircon grains recovered are variable in morphology from euhedral long prismatic to rounded, and from colourless to pink in colour. They exhibit complex internal structures, but well preserved oscillatory zonations were commonly present (Figs. 4.9A and C).

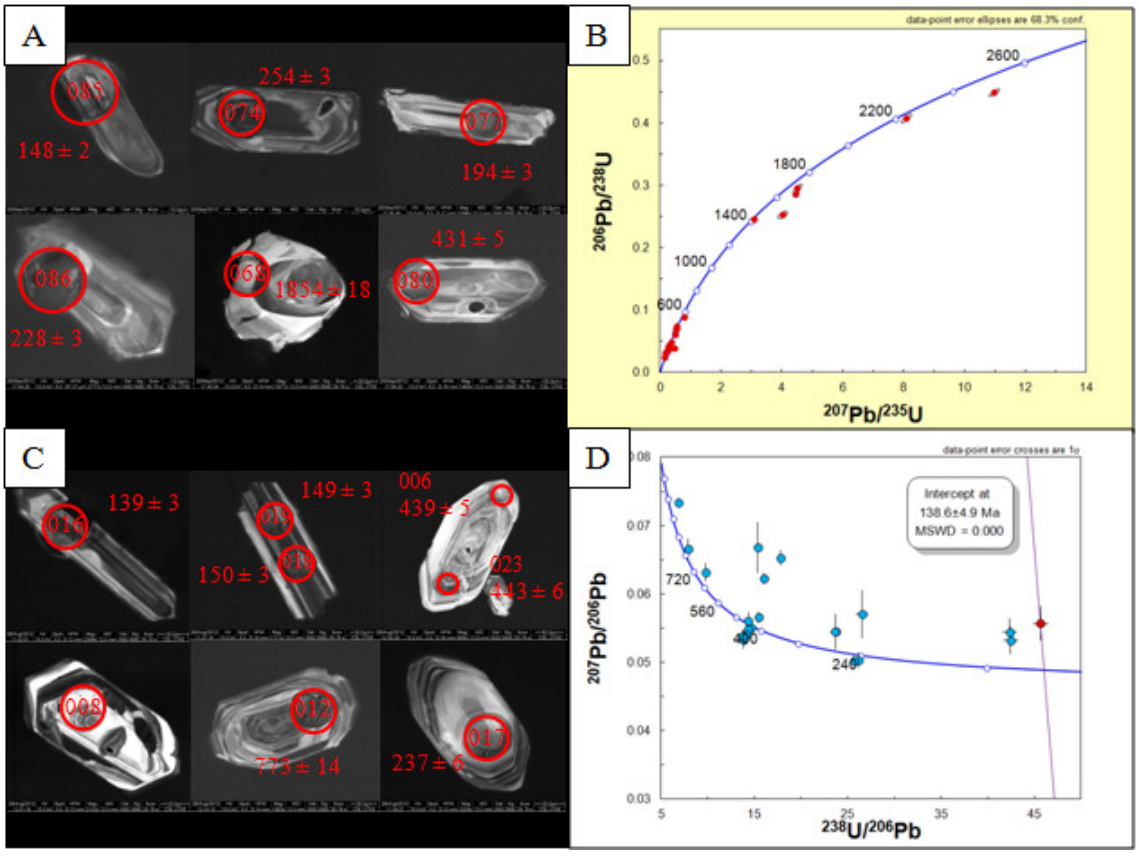

Fig. 4.9. Cathodoluminescence (CL) images of representative detrital zircons and concordia diagram showing LA-ICPMS U–Pb analytical points for the detrital zircons of Jurassic-Cretaceous sedimentary rocks at the western part from Tasik Chini area. **A** and **B**. Sample, BR305. **C** and **D**. Sample, BR307. Note that the circles indicate the spots of LA-ICPMS U–Pb dating and trace element analyses marked with ages.

Sample BR305 has detrital zircon ages ranging from 148 to 2629 Ma. The youngest single zircon yields an age of 148 ± 2 Ma which indicates a maximum age of deposition to be Late Jurassic or younger for this unit (Fig. 4.9B). The second sandstone sample (BR307) yielded twenty-one zircons that range in age between 139 and 876 Ma. Based on the youngest single detrital zircon age, the sample is latest Jurassic=139 ± 6 Ma or younger (Fig. 4.9D). Overall, there are five age populations exhibited by these two sandstone samples: Jurassic (139 to 194 Ma), Permo-Triassic (226 to 274 Ma), Ordovician-Devonian (372 to 459 Ma), Neoproterozoic (631 to 876 Ma) and Meso- to Palaeoproterozoic (1448 to 2629 Ma).

The eastern Jurassic-Cretaceous sandstones are coarse- to medium grained, moderately sorted, mostly subangular to subrounded grains framework with little matrix. A total of fourteen single zircon grains were analysed from sample BR1A, and twenty-five from sample BR2 for the two sandstone samples of the eastern Jurassic-Cretaceous succession. In general, zircons from the two sandstone samples are fine- to coarse-grained in size, pink to colourless, and largely euhedral in shape. The cathodoluminescene images of the analysed zircon crystals show clear oscillatory internal structures (Figs. 4.10A and C).

The fourteen well-constrained ages in the sandstone sample BR1A yield an almost continuous range of ages from Early Carboniferous through to the Late Triassic with the youngest single zircon dated at 207 ± 8 Ma, with the remaining detrital zircon grains yielding Devonian (n=1) and Neoproterozoic (727 Ma) (n=5) ages (Fig. 4.10B). The twenty-five detrital zircons ages in the sandstone sample BR2 are similar to sample BR1A. Most of the zircons have Palaeozoic (Early Carboniferous) to Mesozoic (Late Jurassic) ages, with the youngest of zircon ages (n=4) suggests a maximum depositional age is 150.5 ± 3.0 Ma. However, this sample contains

distinct group of Neo- to Palaeoproterozoic (1873 Ma) zircon grains. Additional age of 447 Ma (Ordovician) is also present in this sample (Fig. 4.10D).

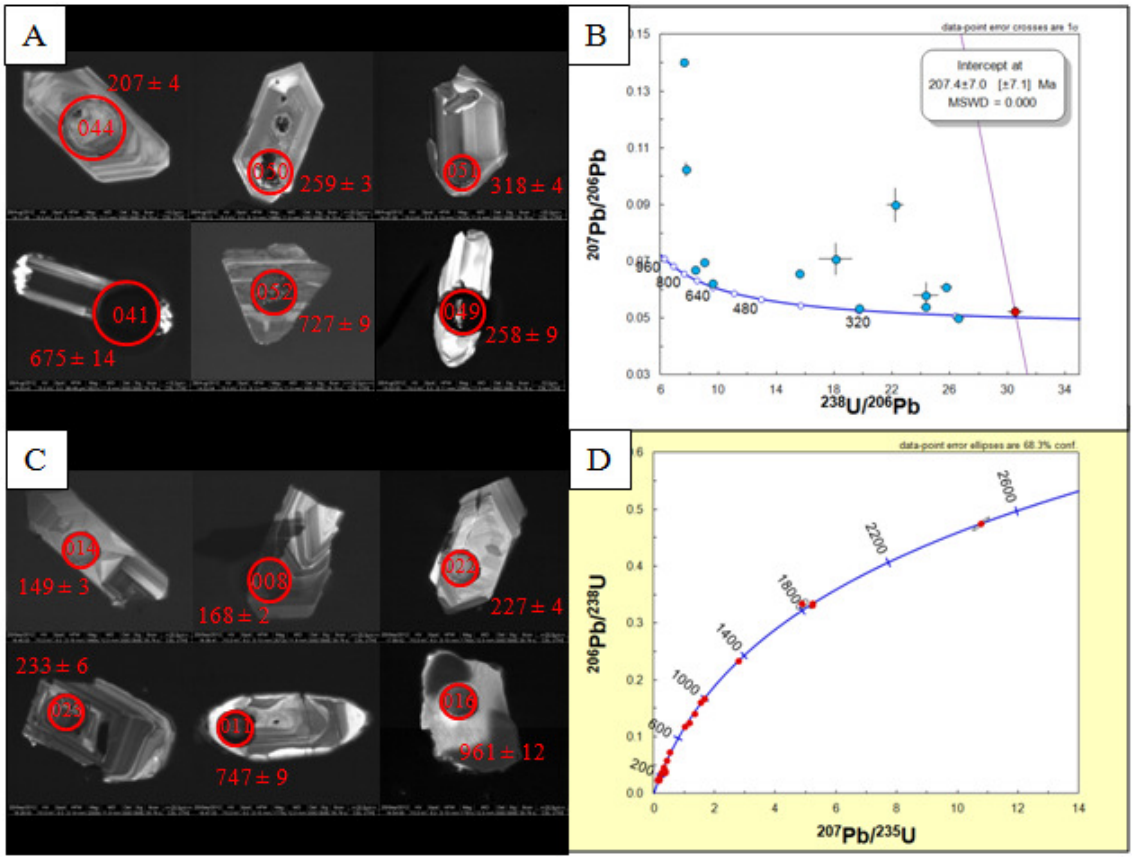

Fig. 4.10. Cathodoluminescence (CL) images of representative detrital zircons and concordia diagram showing LA-ICPMS U–Pb analytical points for the detrital zircons of Jurassic-Cretaceous sedimentary rocks at the eastern part from Tasik Chini area. **A** and **B**. Sample, BR1A. **C** and **D**. Sample, BR2. Note that the circles indicate the spots of LA-ICPMS U–Pb dating and trace element analyses marked with ages.

4.4.2 Igneous rocks

4.4.2.1 Tasik Chini district

In this study, the three microgranite and two volcanic rocks samples (Table 4.5) described in Chapter 3 were dated in an attempt to provide the new and better constraints on the age of emplacement and also to examine the possibility of a coeval relationship between all of the different rock types.

Sample BR325 is from a mixed sequence of felsic flows and siliciclastic rocks, which is located approximately 20 km southeast of the Tasik Chini VHMS deposits. The twelve concordant U-Pb ages have a weighted mean age of 237.4±1.7 Ma (MSWD=0.47). All the zircons analysed show zonation typical of magmatic zircons (Figs. 4.11A and B).

Sample BR3 was collected from a massive dacite/andesite subvolcanic intrusion in the vicinity of Bukit Perah west of the Bukit Botol deposit. Morphologies of zircons in this sample are euhedral to subhedral-prismatic grains with well-preserved magmatic oscillatory zoning. A total of eleven concordant U-Pb ages were obtained with a weighted mean of 232.7 ± 3.8 Ma (MSWD=2.1) (Figs. 4.11C and D).

Sample BR317 and BR326 are taken from a two small igneous bodies exposed to the south of the Tasik Chini area. Zircons from these two samples are mostly euhedral to subhedral with prismatic to stubby shapes. A typical magmatic oscillatory zonation is common in the most crystals (Figs. 4.11E and G). Sample BR317 yielded thirteen concordant zircon grains with an age of 234.9±1.5 Ma (MSWD=0.66) (Fig. 4.11F). Fifteen crystals were analysed in sample BR326, six of them have weighted mean age of 234.4 ± 2.2 Ma (MSWD=0.58) but seven of the crystals are slightly older (242.0 ± 2.2 Ma) (MSWD=0.76) (Fig. 4.11H).

Sample BR318 was an intermediate igneous rock sample (diorite?) collected from Bukit Sembilan. All 12 of the zircons analysed were concordant with a weighted average age of 294.0±4.0 Ma (MSWD=4.1) (Appendix III).

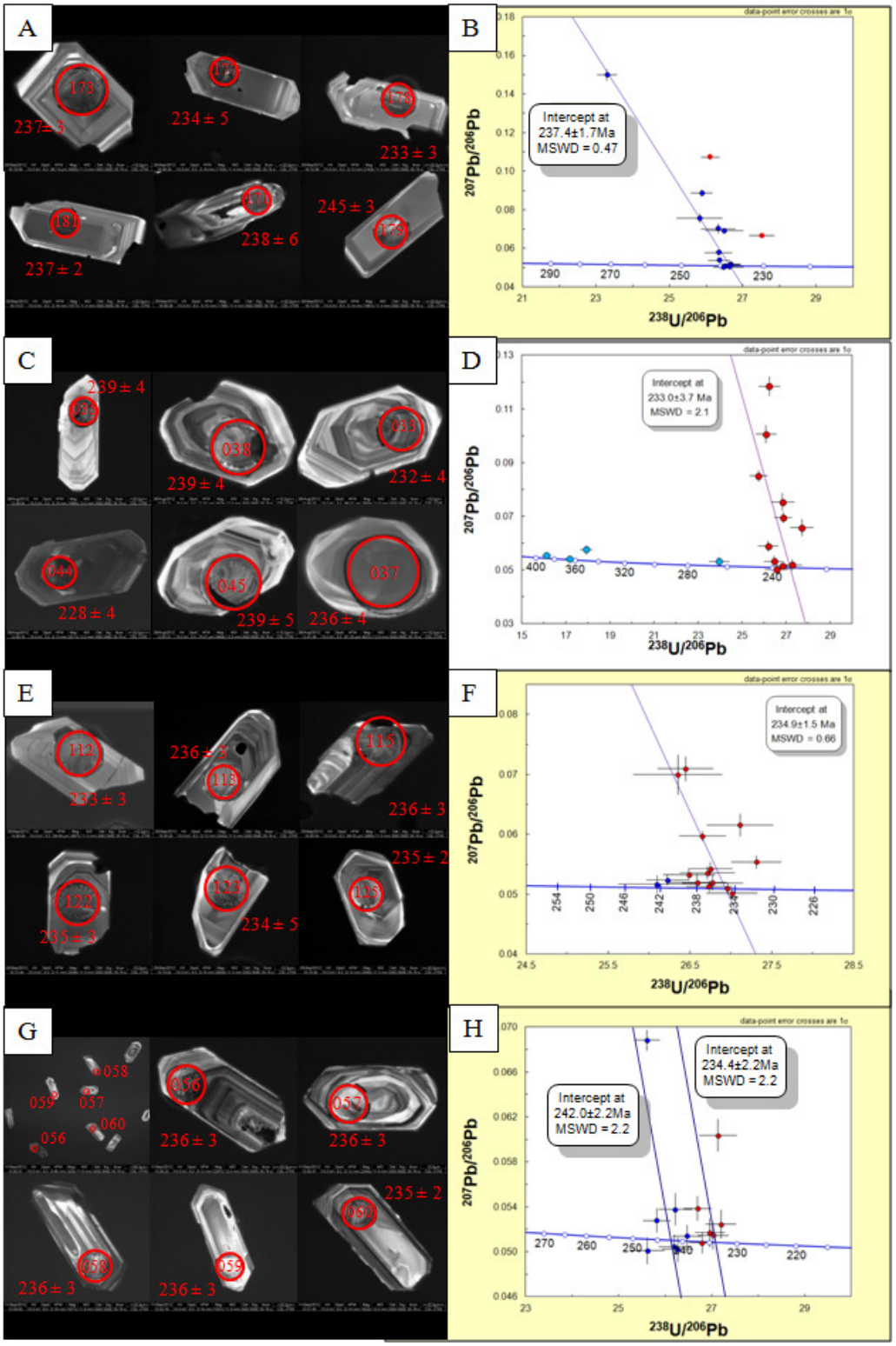

Fig. 4.11. Cathodoluminescence (CL) images of representative zircons and concordia diagram showing LA-ICPMS U–Pb analytical points for the zircons of igneous rocks from Tasik Chini area. **A** and **B**. Sample, BR325. **C** and **D**. Sample, BR3. **E** and **F**. Sample, BR317. **G** and **H**. Sample, BR326. Note that the circles indicate the spots of LA-ICPMS U–Pb dating and trace element analyses marked with ages.

4.4.2.2 Bukit Botol deposit

U-Pb ages of zircons from two felsic volcanic rocks in the Bukit Botol mine area were analysed by the LA-ICPMS method. Both samples contained only a small amount of zircons Sample BB11 is from a rhyolite (type 1) in the footwall of the Bukit Botol deposit. Zircons from this sample form clear to pale pink euhedral to subhedral prismatic grain, and commonly displaying oscillatory zonations with rare inherited cores (Fig. 4.12A). Of seventeen single zircons crystal analysed, eleven zircons gave overlapping results with an average age of 286.1±3.6 Ma (MSWD=1.8) (Fig. 4.12B).

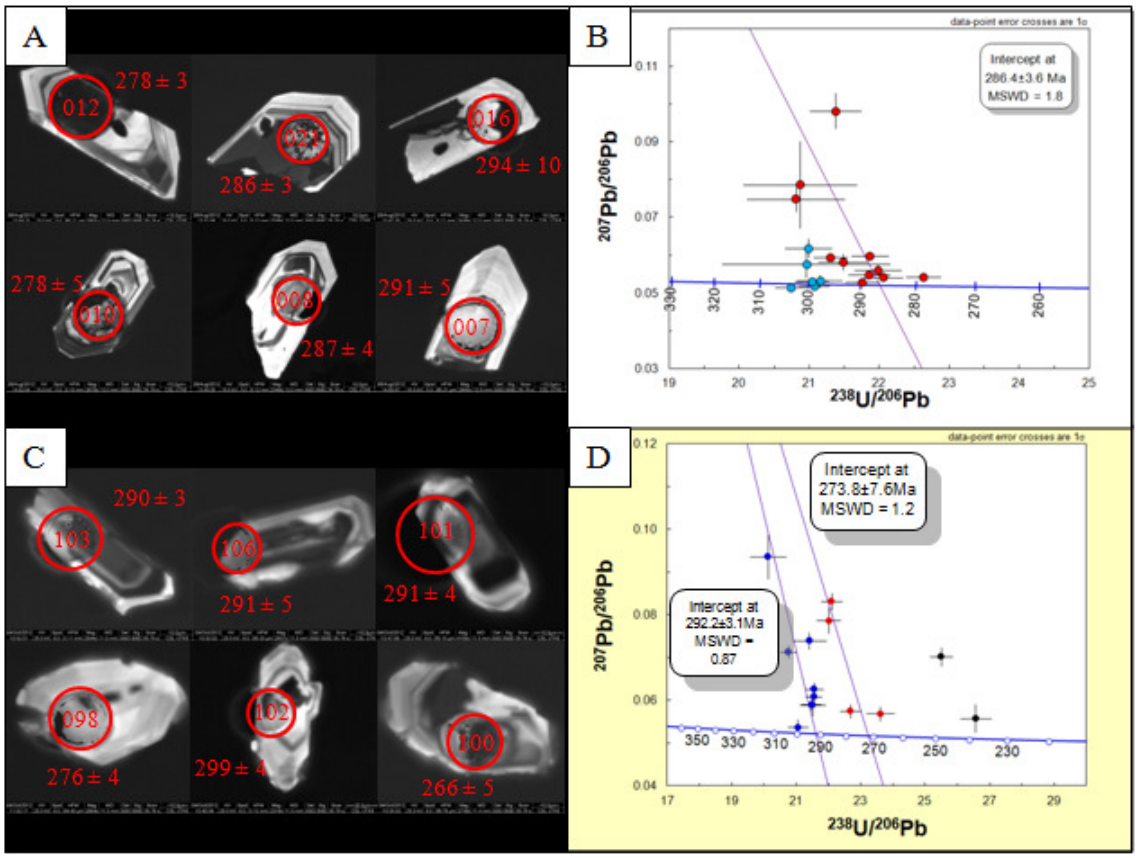

Fig. 4.12. Cathodoluminescence (CL) images of representative zircons and concordia diagram showing LA-ICPMS U–Pb analytical points for the zircons of felsic volcanic rocks from Bukit Botol deposit. **A** and **B**. Sample, BB11. **C** and **D**. Sample, BB6. Note that the circles indicate the spots of LA-ICPMS U–Pb dating and trace element analyses marked with ages.

Zircons from sample BB6 from the ore horizon/immediate footwall to the massive sulphide mineralization were morphologically similar to those described on sample BB11 (Fig. 4.12C), but eight analyses of zircon crystals gave results with a weighted average age of 292.2 ± 3.1 Ma (MSWD=0.87), and four of the zircon were slightly younger at 272.8 ± 7.6 Ma (MSWD=1.2) (Fig. 4.12D).

4.4.2.3 Bukit Ketaya deposit

Two rhyolite samples from the Bukit Ketaya deposit were also analysed. Sample S/6a3 was collected from an ore horizon outcrop of purplish-black rhyolite breccias in the western portion of the mine area. Zircons from this sample are euhedral and prismatic, and showing a core-rim structure with a well-developed oscillatory zoning (Fig. 4.13A). Ten zircon grains give ages between 283 and 294 Ma, with a weighted mean of 286.0 ± 2.0 Ma (MSWD=1.5) (Fig. 4.13B).

Sample BK10 is a representative sample of quartz-feldspar phyric rhyolite in the footwall sequence at the Bukit Ketaya deposit. Zircon grains obtained are also euhedral and prismatic in shape. In CL images, most of the zircons exhibit oscillatory zones with rare inheritance (Fig. 4.13C). A group of eight zircon grains provides a weighted mean $^{206}Pb/^{238}U$ age of 288.3 ± 4.0 Ma (MSWD=1.6) (Fig. 4.13D).

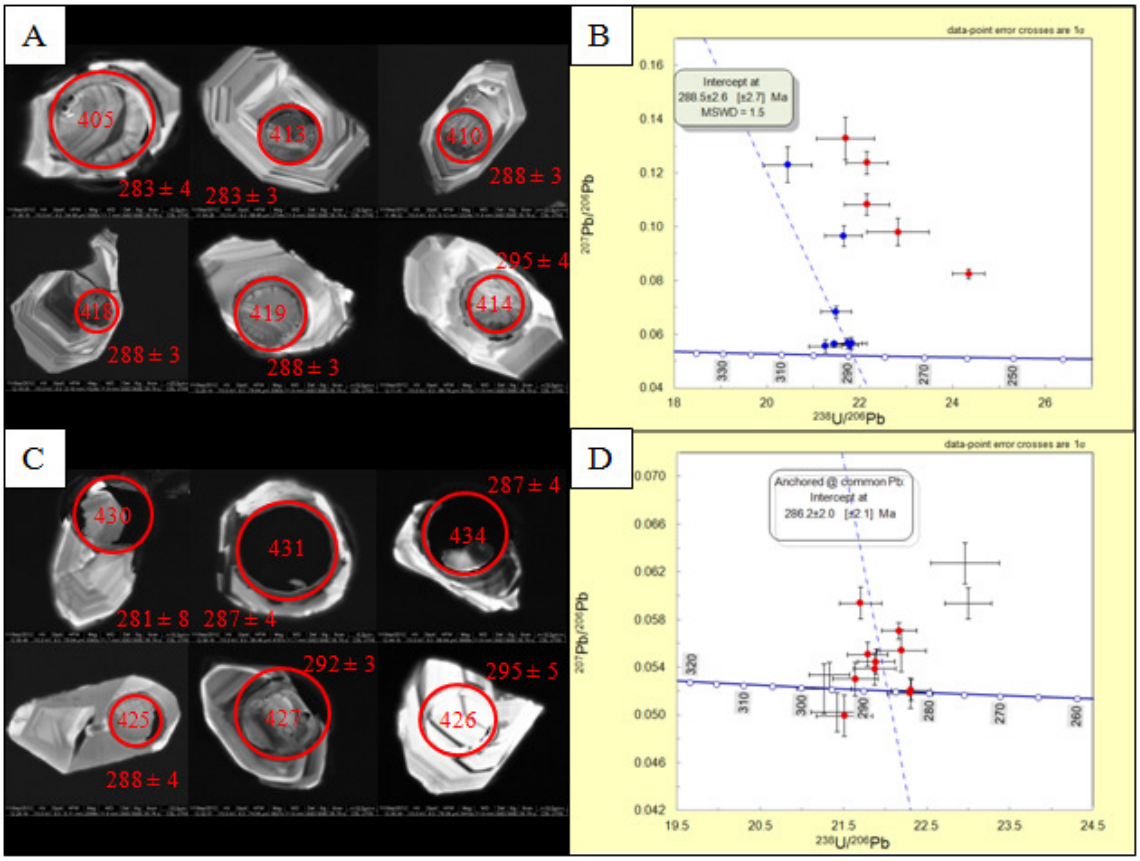

Fig. 4.13. Cathodoluminescence (CL) images of representative zircons and concordia diagram showing LA-ICPMS U–Pb analytical points for the zircons of felsic volcanic rocks from Bukit Ketaya deposit. **A** and **B**. Sample, S/6a3. **C** and **D**. Sample, BK10. Note that the circles indicate the spots of LA-ICPMS U–Pb dating and trace element analyses marked with ages.

4.5 Discussion

4.5.1 Petrogenesis of felsic rocks in the Tasik Chini area

Overall, the geochemical data from the district-scale felsic volcanic rocks and its related intrusions within the Tasik Chini area display a systematic increase and decrease of the least mobile major and trace elements. The moderate to low Zr/Y ratios indicate a transitional to tholeiitic magmatic affinities (Fig. 4.4). Moreover, the moderate to low HFSE contents (e.g., Nb, Y, Zr) displayed by all the felsic rocks (dacite, rhyolite and microgranite) are consistent with typical of felsic rocks from arc affinity (e.g., Pearce and Cann, 1973; Pearce and Peate, 1995). These geochemical affinities are supported by the Nb versus Y and Y+Nb versus Rb diagrams of Pearce et al. (1984).

The felsic volcanic rocks hosting the Bukit Botol and Bukit Ketaya deposits show broadly similar patterns on normalised trace element plots to the regional rocks. Moderate LREE enrichment relative to HREE and pronounced negative Nb and Ti anomalies displayed by these rocks suggest compositional similarities with rocks erupted in typical arc setting (e.g., Pearce and Cann, 1973; Pearce and Peate, 1995).

Volcanic arc rocks are commonly associated with VHMS deposits in the geologic record (e.g., Franklin et al., 1981, 2005). VHMS deposits tend to form in extensional structural and tectonic regimes (Franklin et al., 1981; Silitoe, 1982). Although the structural setting of the deposits in the Tasik Chini area has not yet been comprehensively established, Sone and Metcalfe (2008) suggested that the Central Belt of Peninsular Malaysia assemblage of rocks formed in a back-arc environment, and the presence of mélange (the Lebir Fault Zone) along its eastern margin (Metcalfe and Chakraborty, 1988) represents strongly deformed back-arc rifting sequences. The Tasik Chini area is located near the Lebir Fault Zone (see Chapter 3), suggesting that these were also formed in a back-arc environment. Examples of VHMS deposits in similar setting include Kuroko deposits, Japan (Ohmoto, 1996), Mount Windsor districts, Queensland (Duhig et al., 1992) and Kutcho Creek deposit, Canada (Barrett et al., 1996). This type of deposits is also found in mainland Southeast Asia such as the Dapingzhang VHMS deposit in the Lancangjiang zone or Lincang Terrane of Sone and Metcalfe (2008) in Yunnan. The Dapingzhang deposit is identified to be related with an early evolution of rifting and back-arc event at the northeastern Gondwana of the Simao Terrane part of Indochina Terrane (Lehmann et al., 2013).

4.5.2 Felsic volcanic rocks geochemistry and related VHMS environments

The geochemistry of felsic volcanic rocks associated with VHMS deposits have been used by many workers in order to understand the relationships between the petrogenesis of felsic

volcanic and the environment of formations (e.g., Lesher et al., 1986; Barrie et al., 1993, Lentz, 1998; Hart et al., 2004; Piercey, 2010) because there are variations on the type and age of crust where the VHMS deposit formed.

The felsic volcanic rocks at Tasik Chini both from district- and deposit-scales are compared to the fields for these different Archean and post-Archean binary classification diagrams (Lesher et al., 1986; Barrie at al., 1993, Lentz, 1998; Hart et al., 2004) based on immobile HFSE of Y versus Zr/Y ratios. Compared to the types of rhyolites of Lesher et al., (1996) and Hart et al., (2004), district felsic volcanic samples are more scattered and partly overlap the FIII to FIV types for rhyolite with the exception of three dacite rocks. The Zr/Y ratios for both ore horizon and footwall units of the Bukit Botol deposit and the footwall unit to the Bukit Ketaya deposit are less scattered and most of the samples lie within the FII and FIII types, with a few samples partly plotting in the FIV type. However, the ore horizon unit of the Bukit Ketaya deposit is significantly scattered and partly overlap the FI group (Fig. 4.14A).

Comparison with the Archean Superior Province VHMS rhyolites (e.g., Barrie et al., 1993), show that most of the district felsic rocks plot between Misema and Noranda districts. The felsic volcanic rocks from the Bukit Botol deposit and footwall unit of the Bukit Ketaya deposit plot predominantly within the Selbaie districts. However the ore horizon unit of the Bukit Ketaya deposit is partly overlapped the Upper Skead and Timiskaming districts (Fig. 4.14B).

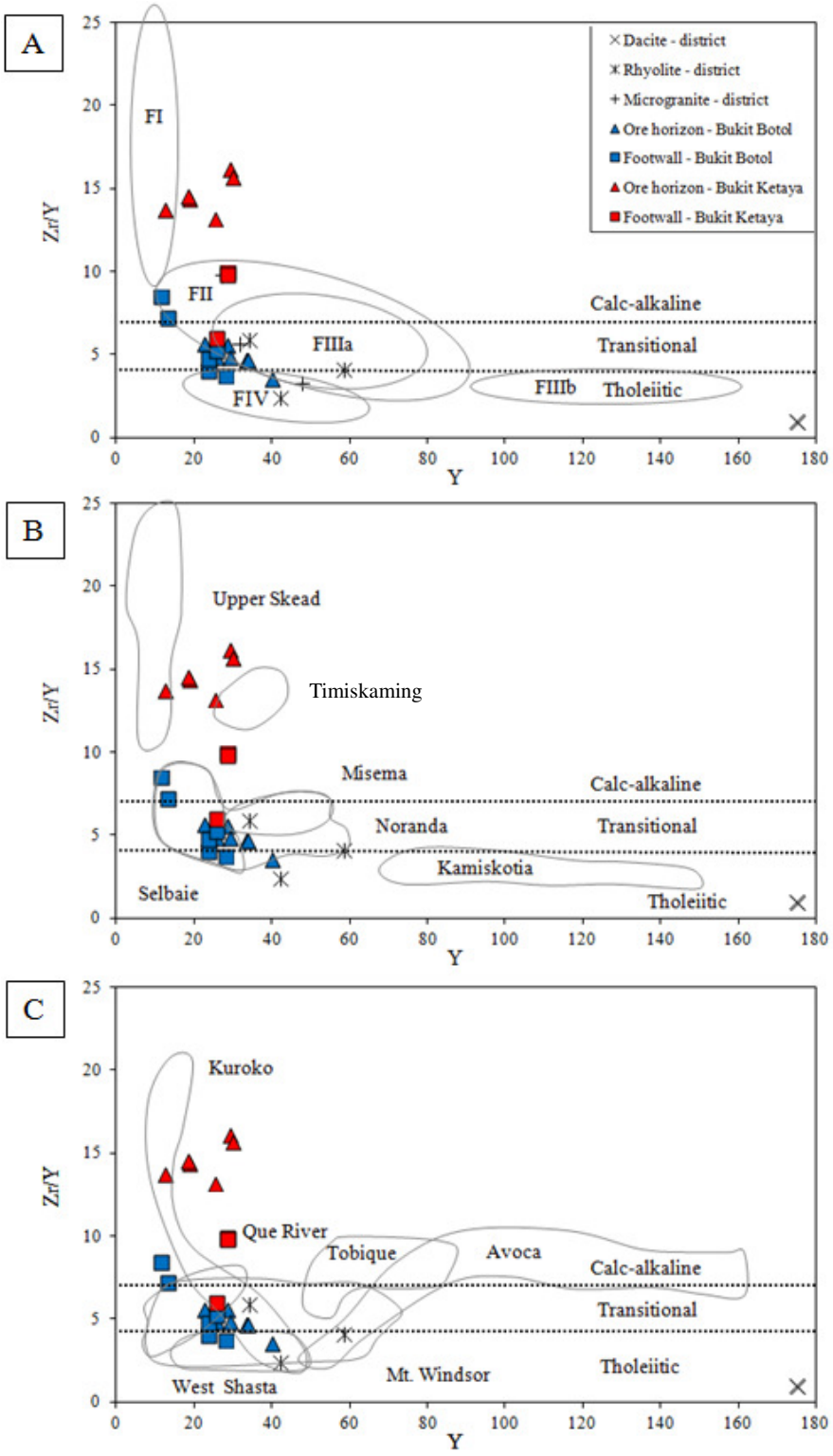

Fig. 4.14. Binary classification diagrams of Zr versus Zr/Y ratios showing the distributions of felsic volcanic rocks from the district Tasik Chini area and the both Bukit Botol and Bukit Ketaya deposits. **A.** Rhyolite types diagram with field subdivisions after Lesher et al. (1986). **B.** Archean VHMS associated rhyolites districts of Barrie et al. (1993). **C.** Post-Archean VHMS associated rhyolites groups after Lentz (1998).

In the Y versus Zr/Y binary classification of post-Archean VHMS associated rhyolite groups after Lentz, (1998), most of the felsic volcanic rocks from district-scale and both the Bukit Botol and Bukit Ketaya deposits plot within the Kuroko, Que River and Mount Windsor groups, examples for a group of VHMS formed in back-arc or intra arc rift environments (4.14C).

The difference in the geochemical signatures of the felsic volcanic rocks between Tasik Chini district area and both the Bukit Botol and Bukit Ketaya deposits suggest a change in petrogenetic process related to their emplacement environments. The Bukit Botol and Bukit Ketaya deposits samples plot on the FII and FIII groups with exception on FI group for the ore horizon unit of Bukit Ketaya show strong characteristics of VHMS deposits formed evolved environments (e.g., back-arc and island arc settings). In post-Archean evolved terrains, most VHMS rhyolites are calc-alkaline plotting in the FII, FIII and FI fields, whereas in Archean juvenile terrains VHMS deposits are associated with tholeiitic, low La/Yb, Zr/Y ratios and strongly HFSE depleted rhyolites that mostly overlap FII and FIV (Piercey, 2011).

4.5.3 Sm-Nd isotopic characteristics of felsic rocks

On the basis of Sm-Nd isotopic studies of felsic rocks, the presence of low εNd(T) and old (T_{DM2}) values indicate that crustal material was involved in their genesis. However, there are variations in the amount of crustal contamination as revealed by variability of the Nd data.

The wide range of Nd isotopic data of felsic rocks, $\varepsilon_{Nd}(T)$ (-5.2 to -4.5) for intrusive rocks and $\varepsilon_{Nd}(T)$ values (-3.6 to -1.0) for volcanic rocks in the district of Tasik Chini area, and the old (T_{DM2}) age (1.02 to 1.38 Ga) signatures strongly suggest influence of a Proterozoic? sedimentary source. In contrast, the overlap and narrow range with slightly high of Nd isotopic signatures (-0.8 to +0.4) of the felsic volcanic rocks from Bukit Botol and Bukit

Ketaya deposits indicate less crustal influence and a composite crustal of oceanic and continental source.

The $^{87}Sr/^{86}Sr$ versus $^{143}Nd/^{144}Nd$ isotopic compositions of volcanic rocks obtained and discussed in this study are plotted with the published Nd–Sr isotope data of Permian–Triassic, I-S type granitoids in the Peninsular Malaysia from Liew and McCulloch (1985a) together with the main reservoirs of Zindler and Hart (1986) (Fig. 4.15). The Western Belt S-type granites are higher in high ^{87}Sr /^{86}Sr and plot towards the EMII reservoir (upper crustal signature), whereas the Eastern Belt I- and S-type granitoids exhibit low ^{87}Sr /^{86}Sr values and plot towards the EMI reservoir (lower crust affinity).

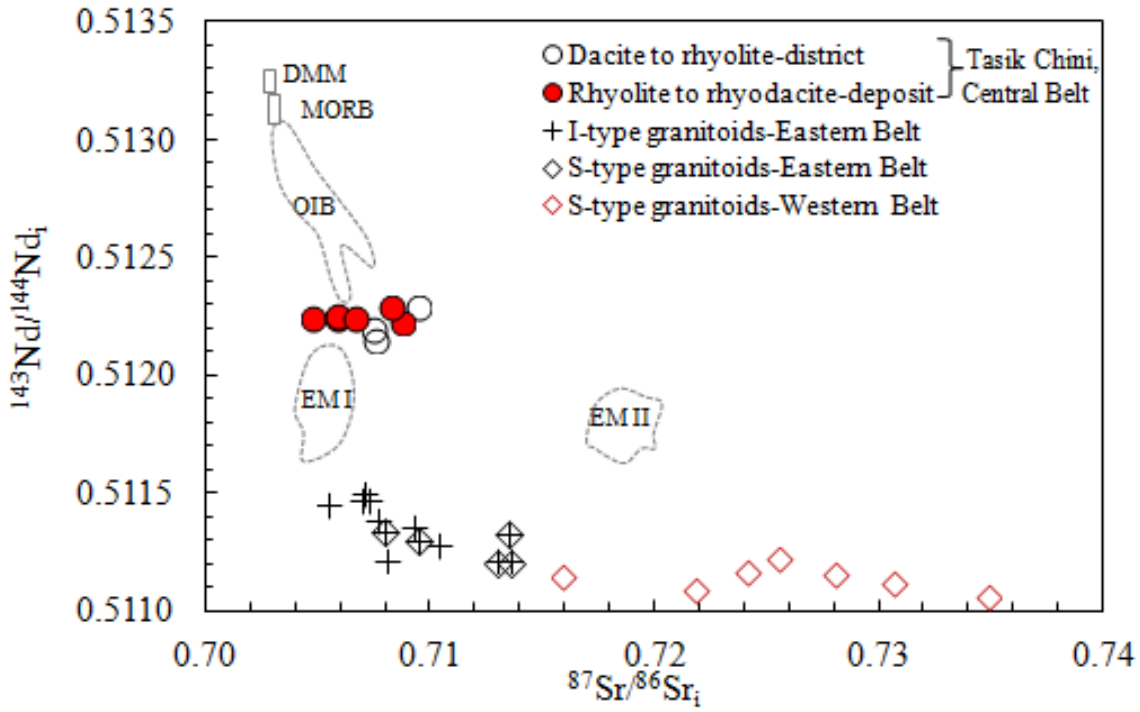

Fig. 4.15. Initial ^{87}Sr /^{86}Sr versus $^{143}Nd/^{144}Nd$ for the igneous rocks of the Peninsular Malaysia in a diagram after Zindler and Hart (1986). District- and deposit-scales volcanic rocks data of the Central Belt (Tasik Chini area)-this study, and S- and I-type granitoids data of the Western Belt and Eastern Belt – Liew and McCulloch (1985a). Annotation: DMM=depleted mantle, MORB=mid-ocean ridge basalt, OIB=oceanic island basalt, EMI=enriched mantle I and EMII=enriched mantle II.

The contrasting isotopic signatures of the new data for the volcanic rocks from the Tasik Chini compared to the surrounding magmatic rocks are consistent with the postulated back-arc rift in the Early-Middle Permian (Metcalfe, 2013), containing composite crust of oceanic and continental input.

The results obtained in this study are also consistent with the suggested Proterozoic basement age of 1100–1400 Ma for East Malaya Terrane indicated by Nd–Sr isotope and U–Pb zircon dating of Permian–Triassic granitoids in the Peninsular Malaysia (Liew and McCulloch, 1985a), and recent detrital zircon U–Pb and Hf isotope data for East Malaya Terrane (Sevastjanova et al., 2011; Hall and Sevastjanova, 2012). The presence of this basement is however controversial as it is very difficult to differentiate between true Precambrian continental basement from Palaeozoic basement containing abundant Precambrian detrital material.

4.5.4 Significance of zircon age determination of the rock formations and igneous rocks in Tasik Chini area and its implication for the tectonic setting

Analysis of detrital zircon from previously geochronologically unconstrained rock formations in the Tasik Chini area using U– Pb LA-ICPMS provides a maximum depositional age for these formations. The zircons analysed in this study were collected directly from outcrop of Late Palaeozoic to Mesozoic sedimentary rocks in the Central Belt and from the Late Palaeozoic metasedimentary rocks in the Eastern Belt.

In this study, the detrital zircons obtained from the Late Palaezoic to Early Mesozoic sedimentary rocks sequence in the Central Belt is younger than the Late Carboniferous, whereas the Jurassic-Cretaceous sedimentary rocks succession show latest Late Jurassic age

or younger for this unit. These data are consistent with widespread and continuously Permian-Triassic marine sedimentation in the Central Belt, unconformably overlain by Jurassic-Cretaceous sedimentary rocks of non-marine source (Mohd Shafeea, 2004). These sequences are comparable to the characteristics of Sukhotai Arc in the Chanthaburi and Sukhothai terranes in Thailand (Sone et al., 2012). Therefore, the Central Belt of Peninsular Malaysia probably formed a continuation of this Sukhothai Arc.

The age data of the detrital zircons from Carboniferous metasedimentary rocks from the Eastern Belt, Peninsular Malaysia reveals that the older populations of zircon in these rocks were sourced from Neoproterozoic–Paleoproterozoic rocks (581–2535 Ma) and the maximum depositional age varies between 330.4 ± 3.0 Ma to 336.4 ± 6.6 Ma. These data are consistent with the extensive distribution of Carboniferous rocks in the Eastern Belt, from the eastern Kelantan through Terengganu, and in the eastern part of Pahang into east Johor to the south (Lee, 2004, 2009; Surjono, 2007). Additionally, the absence of Triassic sedimentary rocks formations in the Eastern Belt (Hutchison, 1989) are consistent with the suggested Indosinian I unconformity that characterised the western Indochina Terrane in Thailand (Sone et al., 2012). Thus, it is suggested here that the Central Belt is part of the Sukhothai Arc and the Eastern Belt represents the East Malaya Terrane part of the western Indochina Terrane in Peninsular Malaysia.

The Central Belt and Eastern Belt were considered to be similar in origin at the earliest stage of East Malaya Terrane, but later separated by back-arc spreading and assembled back by back-arc collapse (e.g., Sone and Metcalfe, 2008; Sevastjanova et al., 2011). The similarity in origin of these two belts is evident by the presence of the same oldest detrital zircons populations of Proterozoic age (Sevastjanova et al., 2011; Hall and Sevastjanova, 2012; this

study) and the initial Hf isotopic compositions of the detrital zircons from both the Terranes that suggest a mixed of crustal and mantle source basements (Sevastjanova et al., 2011). These detrital zircons are similar in age to those of Indochina Terrane (Usuki et al., 2013) and Tethyan Himalaya Terrane (e.g., Zhu et al., 2011), suggesting a similar source provenance or origin.

The presence of a well-constrained age of Permian volcanic rocks hosting VHMS mineralisation at Bukit Botol and Bukit Ketaya deposits, Tasik Chini (this study) and similar bodies (e.g., andesite at Kampung Awah, Jengka = 266±0.69 to 269 Ma−Wan Fuad and Purwanto, 2004; Ghani et al., 2013) and intrusive rocks (e.g., diorite? of Early Permian age, this study) in Central Belt, and a maximum Middle Triassic age yielded by the felsic volcanic rocks and related intrusions in Tasik Chini area confirmed the products of the Sukhothai Arc (Early-Mid Permian) and the subduction-related I-type granitoids and volcanic rock (mainly Middle Triassic) occurrences in the Central Belt, as interpreted by Metcalfe (2013).

4.6 Summary

1) The petrogenesis of felsic rocks of the Tasik Chini area is associated with two volcanic events of transitional-calc-alkaline rhyolite-rhyodacite suite and transitional-tholeiitic dacite-rhyolite suite with volcanic arc magmatic affinities.

2) The Bukit Botol and Bukit Ketaya deposits samples plot on the FI, FII and FIII groups of the VHMS classification of Lesher et al. (1986); Barrie at al. (1993), Lentz (1998) and Hart et al. (2004), and show strong characteristics of evolved VHMS emplaced in a back-arc environment.

3) In this study, the U-Pb LA-ICPMS zircon dates of 272.8 ± 7.6 Ma, 286.1±3.6 Ma and 292.2 ± 3.1 Ma were obtained from felsic volcanic rocks of rhyolite-ryhodacite from the

Bukit Botol deposit mine sequences. These date indicate an Early Permian age for mineralisation at Bukit Botol. Similarly, the dates determined by U-Pb LA-ICPMS of zircons for felsic volcanic rocks in the Bukit Ketaya deposit mine successions are also an Early Permian age of 286.0 ± 2.0 Ma to 288.3 ± 4.0 Ma. The similarity suggests that these two deposits are comparable in age and tectonic setting.

4) The Nd-Sr radiogenic isotopic data suggest that different sources contributed to the volcanic and plutonic magmatic rocks of the Tasik Chini area. The rhyolite to rhyodacite rock samples hosting the Bukit Botol and Bukit Ketaya deposit in Tasik Chini show slightly higher $\varepsilon_{Nd}(T)$ (-0.8 to +0.4) and lower Nd model ages (T_{DM2}) range of 0.97 to 1.05 Ga than the regional magmatic rocks which may be attributed to a mixing of a MORB mantle with crustal sources in a back-arc rift environment. The felsic volcanic rocks and related intrusions that postdates the mineralisation have large negative $\varepsilon_{Nd}(T)$ values (-5.2 to -1.0) and much older Sm-Nd model ages (T_{DM2} = 1.02 to 1.38 Ga) implying an importance of old crustal component in their source.

5) The Central Belt of the Peninsular Malaysia represents the volcanic arc and continental basement of the Sukhothai Arc that was developed on the margin of the East Malaya Terrane part of western Indochina Terrane (derived from Gondwana in the Devonian), separated from East Malaya in the Permian by back-arc spreading, and re-attached with East Malaya in the Triassic.

6) Nd–Sr isotope and U–Pb zircon dating of Permian–Triassic igneous rocks in the Central Belt of Peninsular Malaysia demonstrate a mixture between oceanic island basalt and enriched mantle I of subduction-related magmatism reservoirs of 0.97 to 1.38 Ga old. Moreover, the U-Pb detrital zircon ages reveal that the basement of the East Malaya Terrane is ~0.58 to 2.5 Ga old which is similar to those of Indochina and Tethyan Himalaya Terranes.

CHAPTER 5 MINERALISATION AND ALTERATION

5.1 Introduction

This Chapter describes the style, stratigraphic position, distribution, mineralogy and textures of the mineralisation at the Bukit Botol and Bukit Ketaya deposits. In addition, chemical compositions of Fe-Mn and Fe-Si layers at both the deposits are provided to understand their possible origin. Fe-Mn ores are referred to as Tetsusekiei in the Kuroko deposit, Japan (Kalogeropoulus and Scott, 1983), tuffaceous exhalites in the Noranda district, Canada (Kalogeropoulus and Scott, 1989), silica iron exhalite overlying some of the Australia VHMS deposits (Duhig et al., 1992; Davidson et al., 2001) and ferruginous or manganiferous rocks related to VHMS deposits of the Urals (Maslennikov et al., 2012) or collectively known as 'exhalite' of Ridler (1971). They are commonly associated with VHMS deposits (Large, 1977; Peter and Goodfellow, 1996; Spry et al., 2000; Peter et al., 2003; Grenne and Slack, 2005).

Furthermore, this Chapter also includes a description of the nature of alteration assemblages in the Bukit Botol and Bukit Ketaya deposits as indicated by mineralogical and lithologeochemical data of the rock samples collected during mapping (see Section 5.5). The significance of these data also are discussed. There have been no previous studies undertaken on these deposits.

5.2 Sampling and Methods

The mineralisation of Bukit Botol and Bukit Ketaya was documented by field mapping and detailed petrographic examination of ore characteristics, using polished mounts and polished

thin sections of ore samples. For the minerals that show very similar optical properties or are fine-grained or have complex mineral textures, further examination was made using scanning electron microscopy (SEM) equipped with an energy dispersive x-ray spectrometer (EDS). Chemical compositions including major and trace elements of the Fe-Mn and Fe-Si layers at both the deposits were analysed by the XRF technique. The methods were described in the section 4.2 of Chapter 4.

In addition, electron microprobe (EMPA) and LA-ICPMS analyses of sulphides (see Chapter 6) were used to identify ore mineralogy, distribution and trace element variations throughout the mineralised zone. All the analyses were obtained at the in-house facilities both at CODES and the Central science Laboratory (CSL), University of Tasmania.

5.3 Main Ore Types

5.3.1 Bukit Botol deposit

Four main ore types are present in the Bukit Botol deposit: massive sulphide, stringer and disseminated sulphides, a barite layer and a Fe-Mn horizon. The spatial distribution of the mineralisation is shown in Figure 5.1.

5.3.1.1 Massive sulphide

Two small massive sulphide lenses have been recorded at the Bukit Botol deposit. They strike north to north-east, are moderately east-dipping and are separated from each other by the mine stratigraphy. The first lens is the upper massive sulphide lens. It has a thickness of 1.5 m and a width of 4 m, whereas the second lens represents the main massive sulphide orebody of the Bukit Botol deposit and is located slightly below the upper lens. This larger lens is about 4 m thick and 10 m wide and is moderately east-dipping (Figs. 5.1 and 5.2).

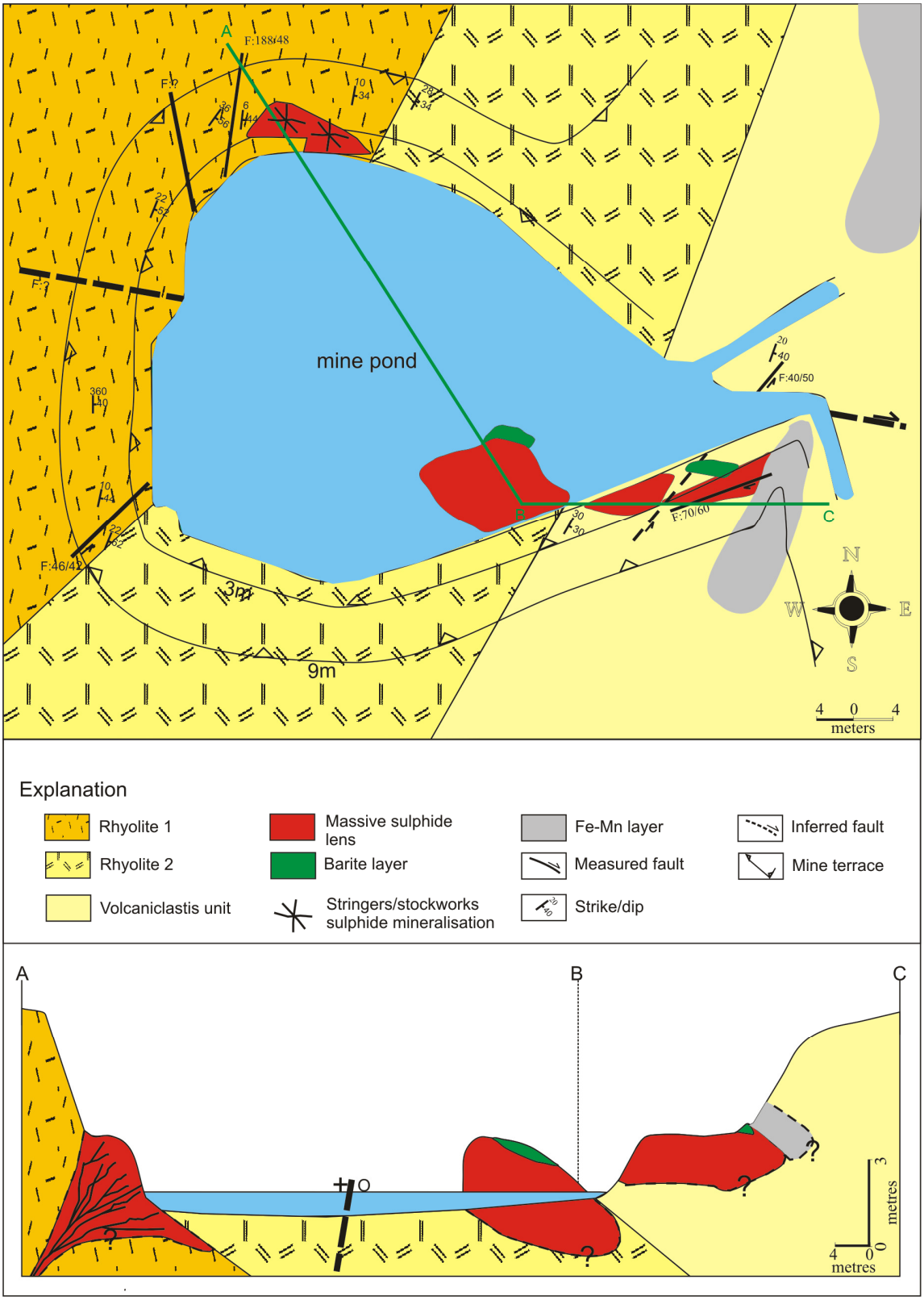

Fig. 5.1. Surface map and schematic cross-section of the Bukit Botol deposit looking northeast showing the stratigraphic sequence and mineralisation styles.

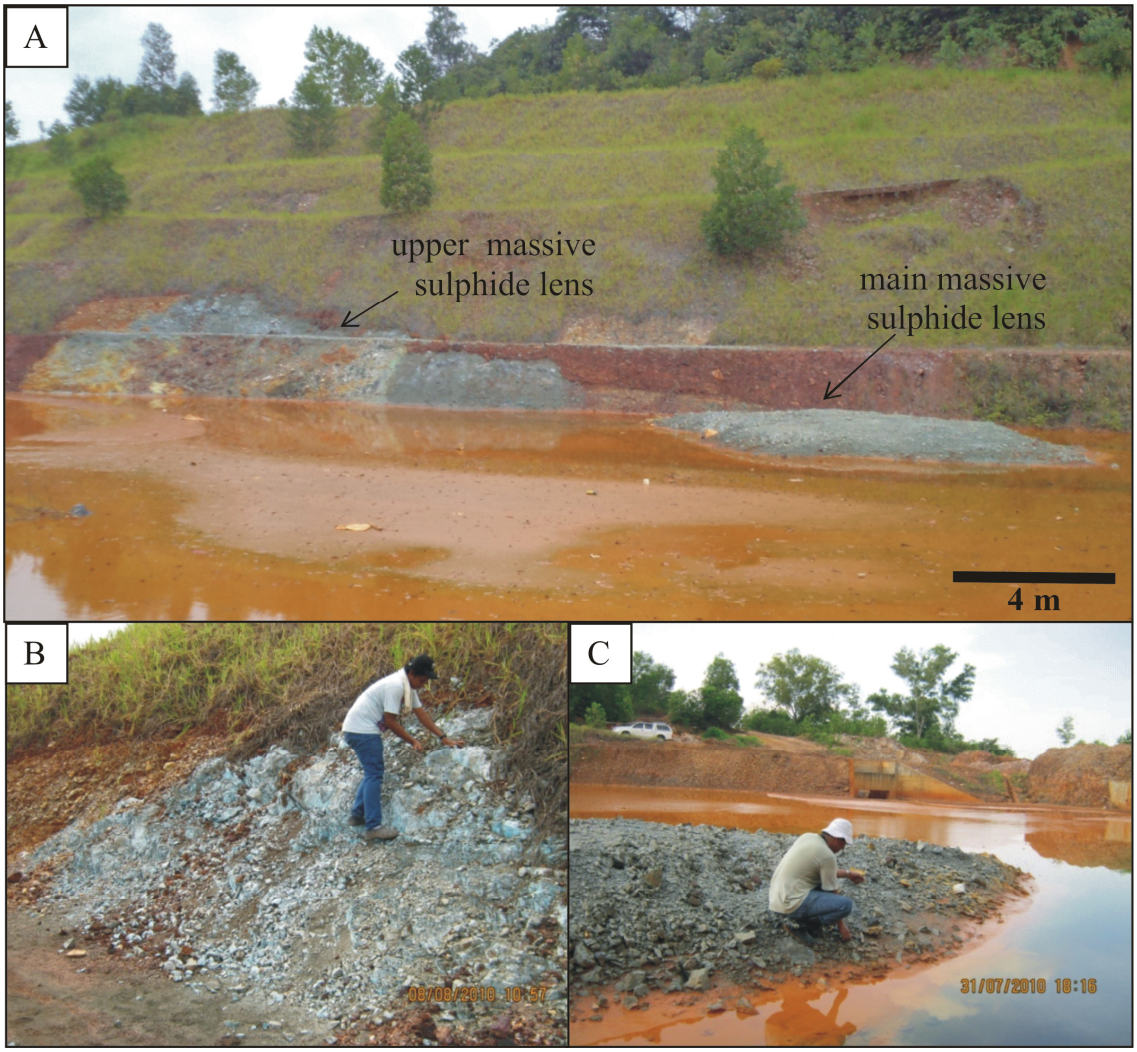

Fig. 5.2. **A.** Photograph showing outcrop of massive sulphide mineralisation at the Bukit Botol deposit looking south. **B.** Close up view of the upper lens massive sulphide. **C.** Close up view of the main massive sulphide lens.

The massive sulphide lenses are generally fine-grained and homogeneous, but millimetre to centimetre-scale layering is locally present. Pyrite, chalcopyrite with minor amounts of sphalerite and rarely galena are common sulphide minerals in the massive sulphide lenses and show no direct evidence of clastic origin. Supergene copper minerals include malachite and subordinate azurite (Fig. 5.3). In addition, minor ore minerals present include a tin-bearing mineral (detail unknown), native silver and electrum, recognised by SEM examination. The different textures they exhibit are discussed in Section 5.4.

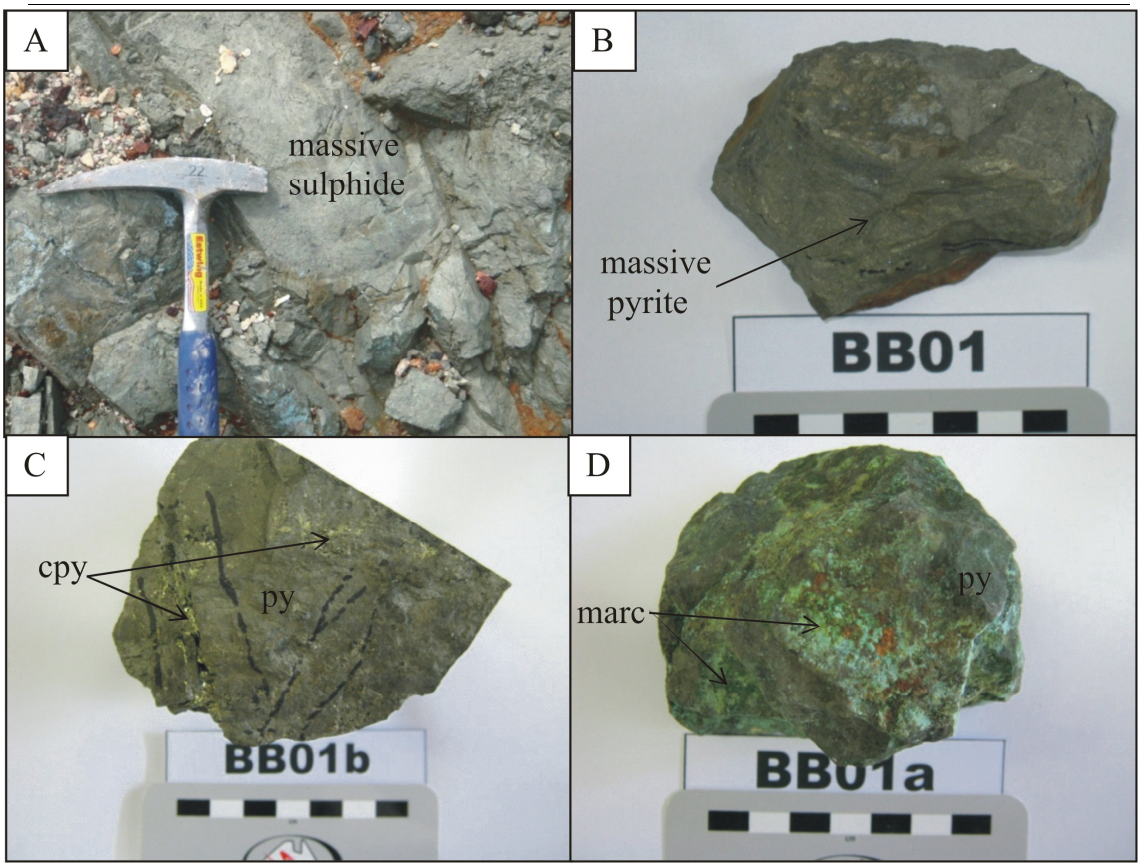

Fig. 5.3. Photographs of different sulphide ores from the Bukit Botol deposit. **A.** Outcrop of massive sulphide lens showing a millimetre to centimetre-scale layering. **B.** Fine-grained and homogeneous massive sulphide ore consisting mainly of pyrite. **C.** Massive sulphide ore comprises pyrite (py) and chalcopyrite (cpy) association. **D.** Replacement of massive sulphide ore by malachite (marc) mineral, from the upper part of the massive sulphide lens.

5.3.1.2 Stringer and disseminated sulphides

The stringer sulphide mineralisation in Bukit Botol occurs within the footwall rhyolite. It consists of irregular veinlets of fine-grained quartz ± barite + sulphides up to 20 mm wide within strongly silicified to weakly sericitised and brecciated host rocks (Figs. 5.4). The stringer mineralisation consists of dominantly pyrite with lesser sphalerite, chalcopyrite and galena within and between quartz ± barite assemblage. The same mineral associations are also abundant in host rocks away from the stringer zone, up to a few centimeters.

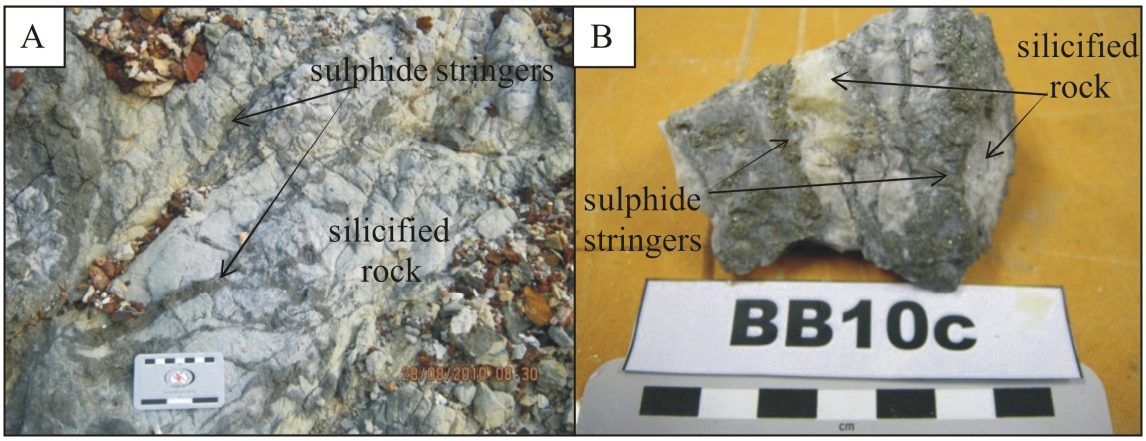

Fig. 5.4. Photographs showing nature of stringer zone at the Bukit Botol deposit. **A.** View north at the Bukit Botol deposit stringer sulphide mineralisation. **B.** Close-up view of the irregular veinlets of sulphides within strong silicified-sericitised and brecciated host rock from the stringer zone, Sample No BB10c.

5.3.1.3 Barite layer

The barite layer with a minimum 2 m thickness at Bukit Botol is a small lens covering the massive sulphide bodies. Its contact with the massive sulphide is gradational and comprises a white, grey or pale brown massive to banded barite with a foliated texture. In hand specimen, the barite crystals typically show euhedral, rhombohedral and tabular shapes (Figs. 5.5A and B).

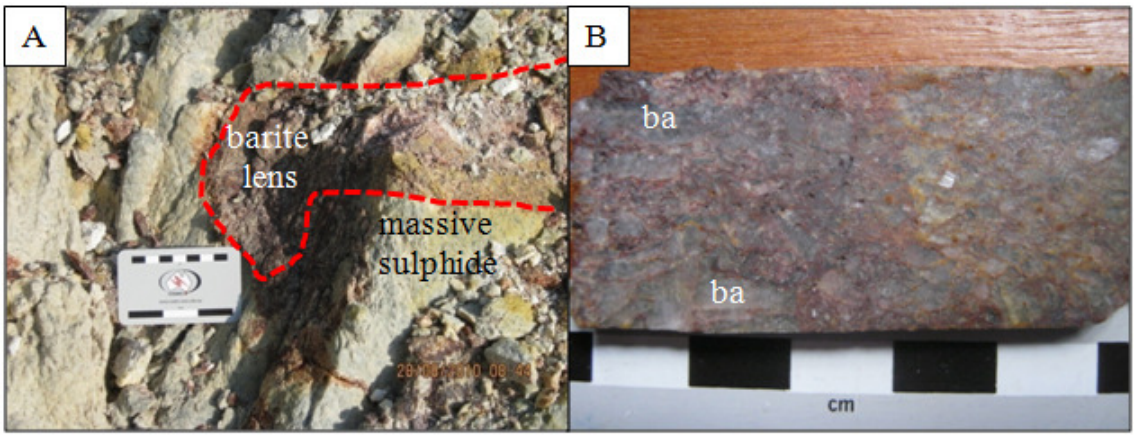

Fig. 5.5. Examples of barite layer at the Bukit Botol. **A.** View of gradational contact between barite layer and massive sulphide at the upper massive sulphide lens in the Bukit Botol deposit. **B.** A grey or pale brown massive to banded barite ore hand specimen from Bukit Botol. Barite crystals show euhedral, rhombohedral and tabular forms, Sample No. BBarite. Annotation: ba = barite.

5.3.2 Bukit Ketaya deposit

At Bukit Ketaya deposit, the mineralisation also can be divided into four ore types: massive sulphide layer, stringer sulphide, barite and Fe-Si layers. However, no evidence for the occurrence of sulphide lens (pre-mining or present study) was found at the Bukit Ketaya deposit (Fig. 5.6).

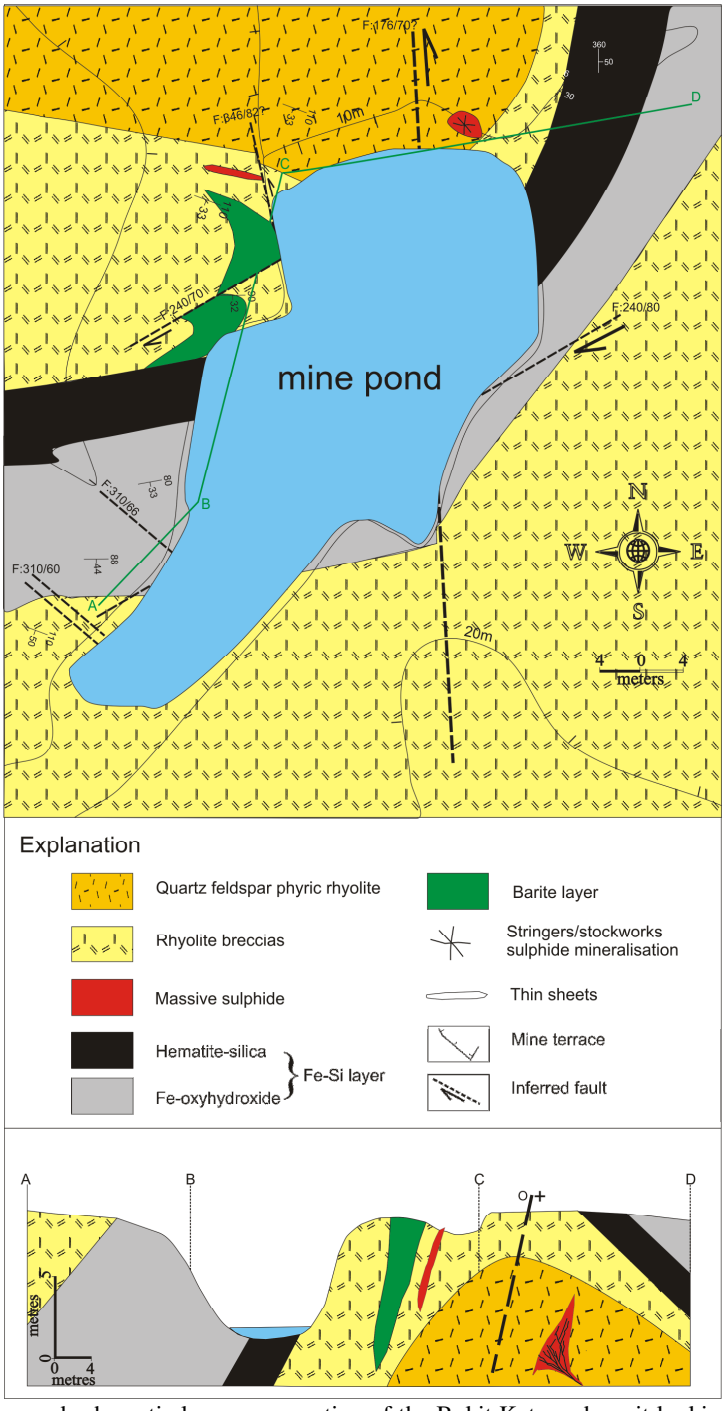

Fig. 5.6. Surface map and schematic long cross-section of the Bukit Ketaya deposit looking southwest showing the stratigraphic sequence and mineralisation styles.

5.3.2.1 Massive sulphide

Massive sulphide at the Bukit Ketaya deposit occurs in thin stratiform layers. This ore comprises several smaller, bedding-parallel, sulphide layers with an overall thickness of as much as 1.0 m. The thin-layered massive sulphide ore consists predominantly of pyrite, minor amounts of chalcopyrite and sphalerite and rarely, galena. Malachite is the most abundant secondary sulphide replacing primary sulphides on the surface of massive sulphide ore (Fig. 5.7).

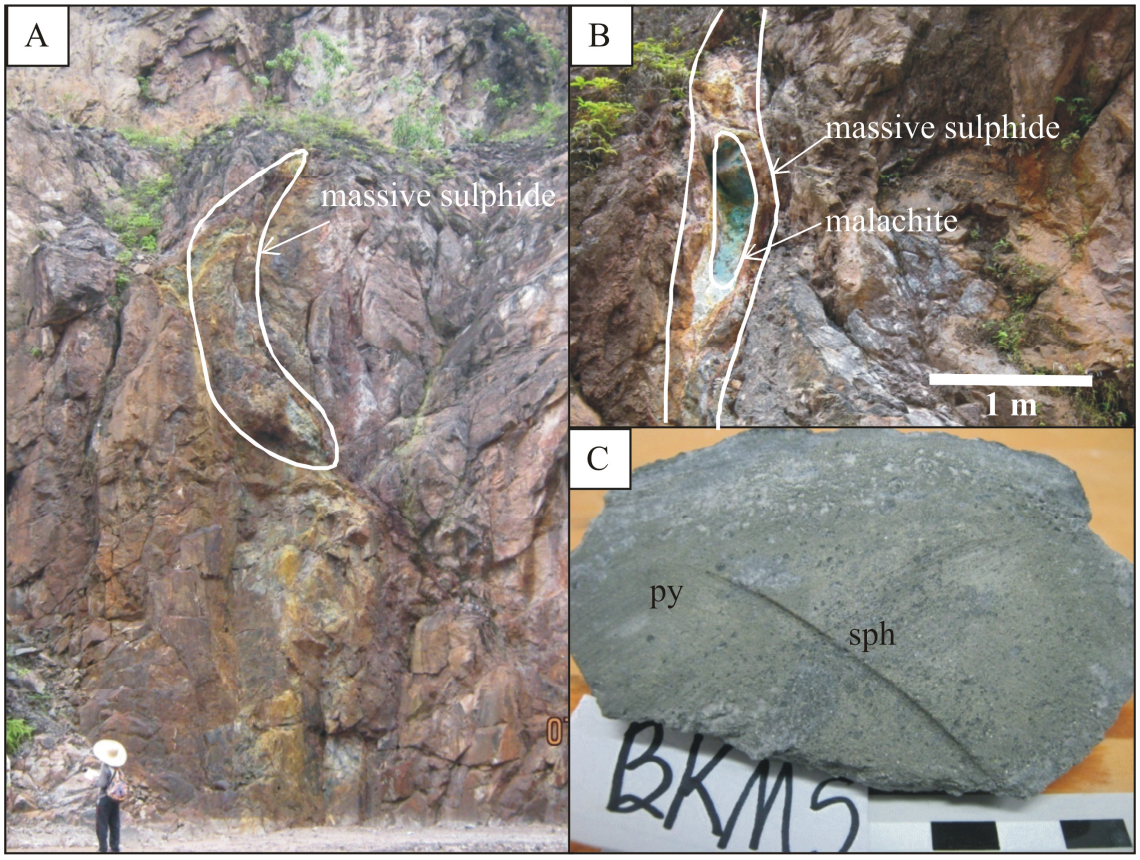

Fig. 5.7. **A.** Outcrop of massive sulphide mineralisation at Bukit Ketaya deposit looking east. **B.** Close up view of the thin sulphide ore layer that is approximately 0.5 m thick. Note the occurrence of malachite as a replacement product of the primary sulphides. **C.** Hand specimen of the thin sulphide ore layer consisting dominantly of pyrite (py) with lesser sphalerite (sph).

5.3.2.2 Stringer and disseminated sulphides

At Bukit Ketaya, a weak stringer and disseminated sulphide mineralisation, probably representing part of a feeder zone to the massive sulphides, are present discordantly in the

lower most part of the footwall sequence, and lacks a significant alteration envelope (Figs. 5.8A and B).

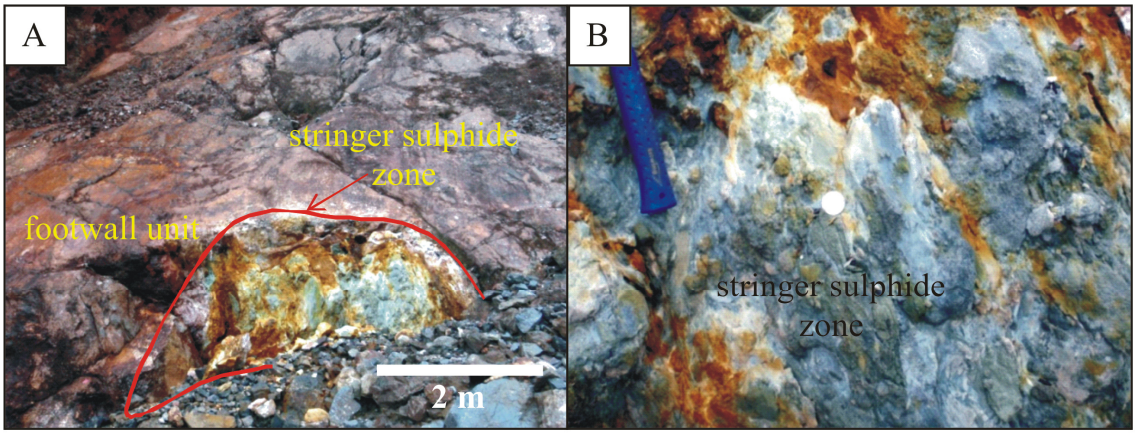

Fig. 5.8. Photographs showing nature of the stringer zone at the Bukit Ketaya deposit. **A.** View towards the south at the Bukit Ketaya deposit showing the stringer sulphide zone. **B.** Close-up photograph of the stringer zone shown in A.

5.3.2.3 Barite layer

A barite layer is well preserved at the Bukit Ketaya deposit. Barite lenses at Bukit Ketaya crop out and can be traced along strike to the west, although they are covered by overburden to the east. The layer shows a massive to banded structure and a cleavage texture. The layer is coarsely crystalline, with barite consisting of masses of euhedral to subhedral crystals and typically ranges in size up to 1 cm in length (Figs. 5.9A and B).

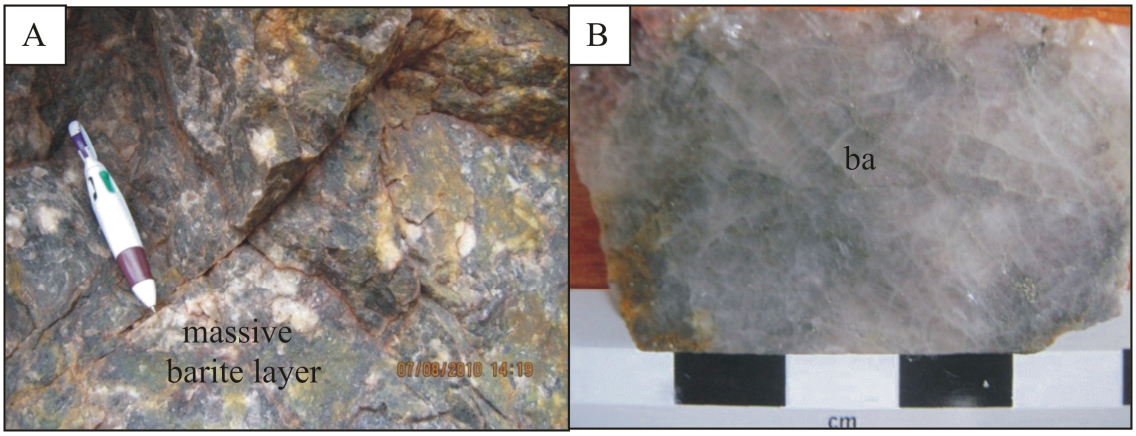

Fig. 5.9. Examples of barite layer at the Bukit Ketaya deposit. **A**. Massive barite outcrop at Bukit Ketaya. **B.** Well crystallized barite layer from Bukit Ketaya showing consolidated mass of euhedral to subhedral crystals growth up to 1 cm in length transected by fine-grained sulphide and thin reticulate networks of second generation fine barite. Annotation: ba = barite.

5.3.3 Fe-Mn and Fe-Si layers at the Bukit Botol and Bukit Ketaya deposits

5.3.3.1 Occurrence and distribution

The Fe-Mn layer was removed and mined during the past mining activities at the Bukit Botol deposit and only minor outcrops are found above the massive sulphide orebody. However, a discontinuous and well-developed area of the Fe-Mn cap horizon varying in colour from reddish brown to darkish brown is seen in the north and in the south hangingwall to the mineralisation. The unit rarely outcrops but does produce Fe-Mn boulders. Layers vary in thickness from 1 cm to 2 m. In addition, the contact with the overlying massive sulphide body is irregular (Figs. 5.10A, B, C and D).

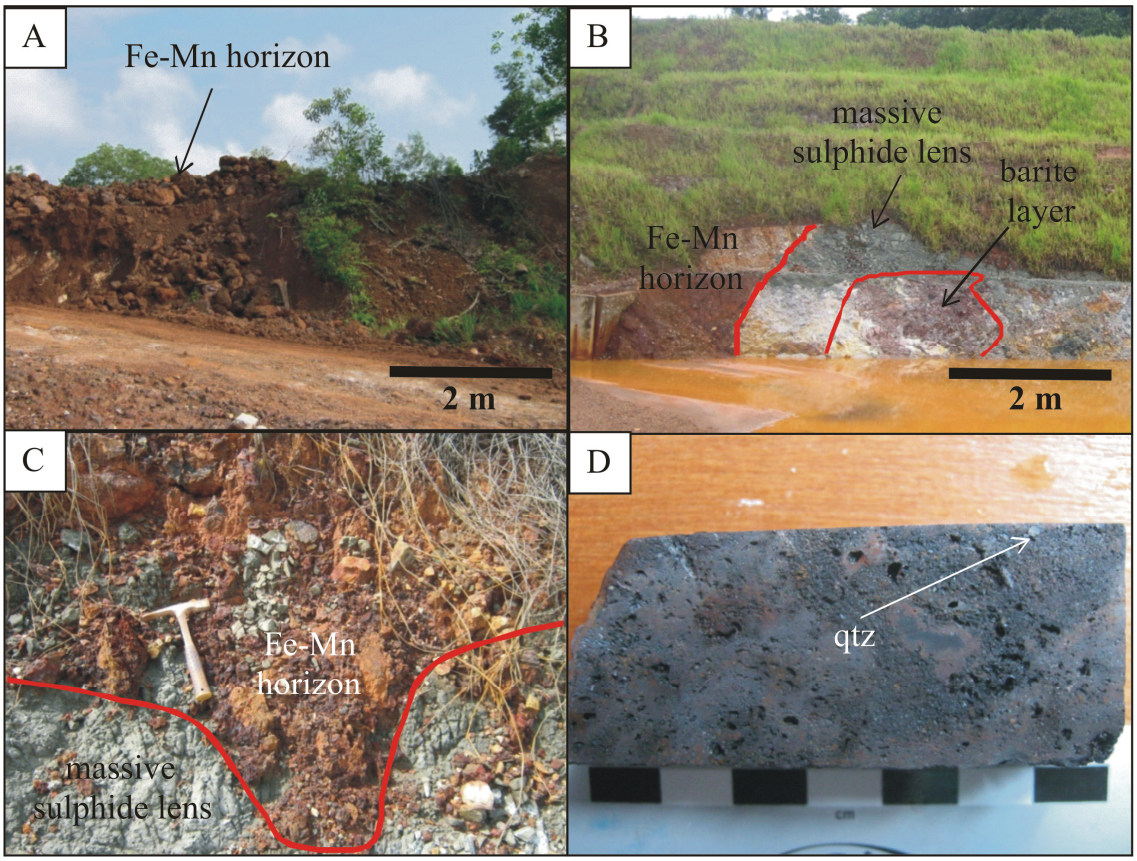

Fig. 5.10. Fe-Mn layer at Bukit Botol. **A.** Fe-Mn formation towards the north at the hangingwall unit in Bukit Botol. **B.** Fe-Mn layer outcrops towards the southern part of the mine area. Note that the Fe-Mn layer overlies both the massive sulphide lens and barite layer. **C.** Close up of the irregular contact between Fe-Mn horizon and massive sulphide lens **D.** Fe-Mn rock slab surface. Note the presence of quartz clasts in the Fe-Mn matrix, Sample No. 301. Annotation: qtz = quartz.

At Bukit Ketaya, the Fe-Si layer is best developed at the top of the volcanic sequence, and attains a thickness of about 10 m, and has a strike length of over 50 m. Where present, such layers are recognised by their purplish to red colour. They commonly show layered internal morphology and occur as lenses or stratiform bodies which are conformable with the mine stratigraphy. Two variants occur, separated on Figure 5.6. The hematite-silica layers are generally massive or finely banded, and are resistant to weathering, whereas the Fe-oxyhydroxide layers are relatively friable, with microbreccia-like textures or have been completely decomposed to very fine-grained Fe and/or Mn oxyhydroxide (Figs. 5.11A and B).

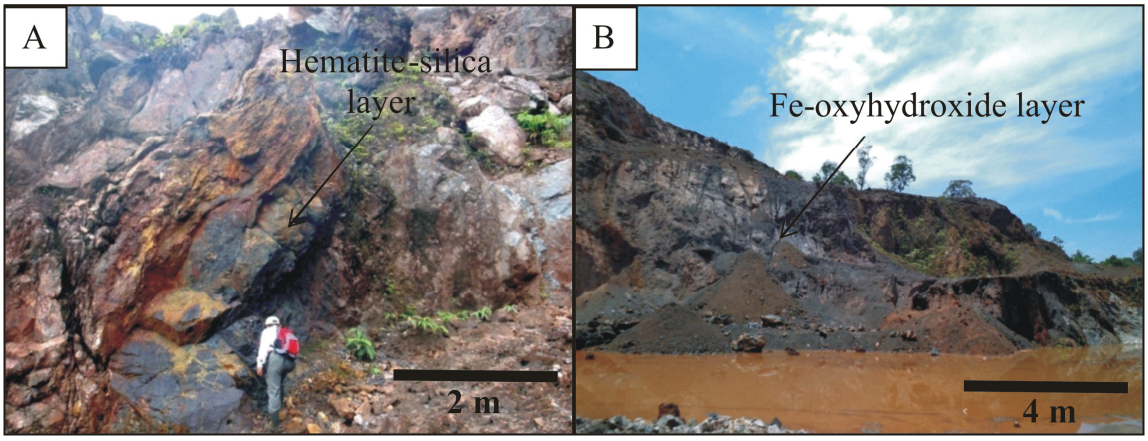

Fig. 5.11. Fe-Si layer at Bukit Ketaya. **A.** Massive and banded hematite-silica layer outcrops at top of the mine sequence. **B.** Fe-oxyhydroxide layer at upper stratigraphic level at Bukit Ketaya mine has been decomposed to very fine-grained Fe or Mn oxyhydroxide.

5.3.3.2 Petrographic characteristics of the Fe-Mn and Fe-Si layers

At both the Bukit Botol and Bukit Ketaya, the Fe-Mn and Fe-Si layers commonly exhibit massive iron-silica banding to microbreccia-like textures. The massive bands mainly consist of fine-grained hematite with cryptocrystalline quartz disseminated throughout. The microbreccia-like textures are composed entirely of quartz, barite and a clastic constituent (rhyolite-rhyodacite of ore horizon unit) with trace amounts of magnetite and pyrite pseudo-clasts in a fine-grained hematite matrix. The mineral pseudo-clasts in microbreccia-like textures can be mixed in any proportion and their grain sizes are variable from

cryptocrystalline size up to about 1 cm (Fig. 5.12). Sulphide minerals are absent or rarely present in the Fe-Mn and Fe-Si layers.

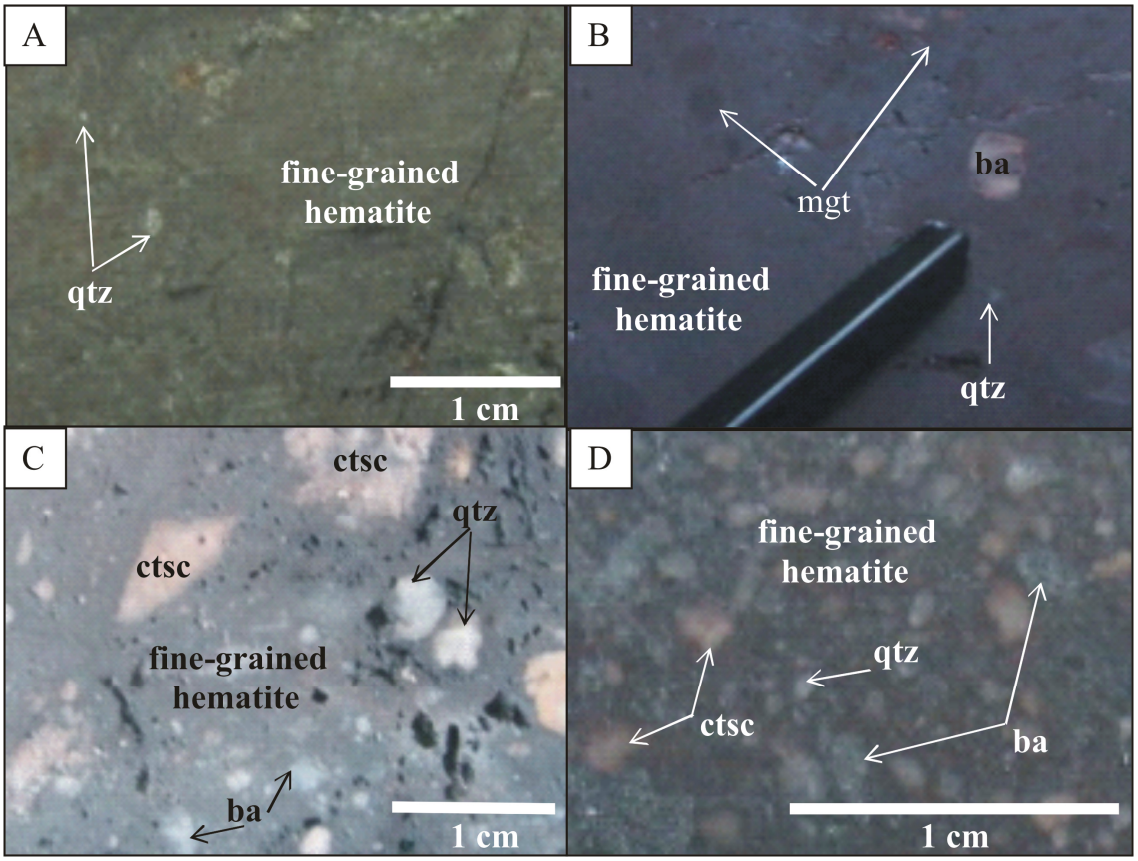

Fig. 5.12. Textures of the Fe-Mn and Fe-Si layers. **A.** Massive banded Fe-Mn ore made up of fine-grained hematite with cryptocrystalline silica disseminated throughout (Bukit Botol deposit). **B.** Microbreccia textures of Fe-Si ore showing the presence of magnetite, barite and quartz in a fine-grained hematite groundmass (Bukit Ketaya deposit). **C.** Microbreccia textures of Fe-Si ore consists of coarse-grained mixed proportions of quartz, barite and clastic constituent (rhyolite-rhyodacite of ore horizon unit) clasts (Bukit Ketaya deposit). **D.** Microbreccia textures of Fe-Mn ore consists of variable grain size of quartz, barite and clastic constituent (rhyolite-rhyodacite of ore horizon unit) clasts (Bukit Ketaya deposit). Annotation: qtz = quartz, ba = barite, ctsc = clastic constituent and mgt = magnetite.

5.3.3.3 Chemistry

Chemical compositions of the Fe-Mn±Si–rich rocks from Bukit Botol and Bukit Ketaya deposits were determined to assess their origin (Tables 5.1 and 5.2), because diagnostic elemental assemblages of major, minor and trace elements can be used to distinguish Fe-Mn deposits that are formed under different geological environments. The analysed samples were from outcrops that include five samples from the Bukit Botol deposit and twelve samples

from the Bukit Ketaya deposit. Methods are described in section 5.2, and sampling details are listed and shown in Appendix II.

Table 5.1. Major and trace elements of Fe-Mn layer from the Bukit Botol deposit, Central Peninsular Malaysia.

			Bukit Botol			
Element	405	301[a]	301[b]	302[a]	302[b]	
wt%						
SiO_2	2.96	4.95	4.91	3.68	4.66	
TiO_2	0.099	0.054	0.064	1.13	1.14	
Al_2O_3	5.58	3.76	3.84	2.56	2.62	
Fe_2O_3[1]	46.41	35.72	35.82	72.96	73.2	
MnO	25.36	32.67	32.87	5.52	5.56	
MgO	0.06	0	0	0.1	0.12	
CaO	0	0.02	0.04	0.02	0.02	
Na_2O	0.03	0.1	0.12	0.02	0.04	
K_2O	0.21	0.29	0.31	0.02	0.02	
P_2O_5	0.193	0.112	0.112	0.204	0.204	
BaO	3.53	2.30	2.30	0.560	0.562	
CuO		0.204	0.206			
ZnO	0.809	0.258	0.256			
PbO		5.60	5.61	1.47	1.50	
Loss inc.S-	14.30	12.32	12.70	9.33	9.19	
Total	99.54	98.35	99.16	97.58	98.84	
S	0.10	0.16	0.15	0.25	0.25	
ppm						DL[2]
Sc	8.8	5.3	6.1	8.5	7.6	1.5
Ba	31617	20600	20600	5016	5034	4
V	18.1	47.5	43.9	194.9	197.7	3
Cr	7.1	4.6	5.2	44.5	44.3	1
Ni	7.8	9.6	8.3	<1	<1	1
Cu	290	1630	1645	1293	1283	1
Zn	6500	2073	1655	782	783	1
As	135	386	391	3696	3787	3
Rb	5.2	4.5	3.9	1	1.2	0.5
Sr	52.9	22.9	22.1	5.7	5.4	1
Y	13.9	32.2	33.9	106	105	1
Zr	42.6	13.3	13.6	287	293	1
Nb	0.8	<0.5	<0.5	16.0	18.4	0.5
Sn	6.7	16.3	13.6	11.7	12.6	1
Pb	668	51987	52079	13646	13925	1
Bi	<2	8.4	10	42.7	42.4	2
U	2.0	9.8	12.2	4.4	8.3	2
Th	2.0	2.0	2.0	2.0	2.0	2
La	30.1	72.2	72.0	28.8	28.6	4
Ce	BDL[3]	BDL	BDL	BDL	BDL	6
Nd	BDL	BDL	BDL	BDL	BDL	4

Notes: Major elements: XRF, trace elements: ICP-MS methods
[1]Total Fe as Fe_2O_3
[2] DL = Detection limits (ppm)
[3] BDL = Below detection limits (ppm)

At Bukit Botol, the Fe-Mn variety contains high concentrations of iron (Fe_2O_3 = 35–73 wt %), manganese (MnO = 6–33 wt %) and alumina (Al_2O_3 = 2.6-5.6 wt %) but are silica poor, with low contents of all other elements (i.e., rarely exceed 1 wt % with the exception of wt. percent of BaO and PbO in some Ba- and Pb-rich samples). However, some elements still have higher ranges in concentration relative to crustal abundances, notably Cu (290 to 1645 ppm), Pb

(between 600−52000 ppm), Zn (782−6500 ppm) and Ba (5016−20600 ppm). In addition, all samples have also relatively high As (135−3787 ppm) and U (2−12.2 ppm) contents.

Table 5.2. Major and trace elements Fe-Si layers from the Bukit Ketaya deposit, Central Peninsular Malaysia.

	Bukit Ketaya												
Element	BK02	BK03	BK04	FeMn1-KNN	FeMn2	BK05	BK05a	BK13	BK13a	BK13b	FeMn3	Mn1	
wt%													
SiO_2	90.12	90.18	96.10	64.49	65.05	5.11	2.58	19.53	6.61	13.07	7.98	16.48	
TiO_2	0.30	0.23	0.42	0.277	0.601	0.25	0.28	0.12	0.10	0.11	0.351	0.405	
Al_2O_3	3.67	6.78	1.43	0.44	1.68	0.13	0.12	0.25	0.50	0.19	0.12	1.77	
Fe_2O_3[1]	4.22	0.43	0.93	33.98	31.29	68.45	73.33	79.71	92.87	85.53	91.23	78.42	
MnO	0.00	0.00	0.01	0.001	0.001	0.01	0.02	0.01	0.01	0.01	0.005	0.01	
MgO	0.03	0.04	0.01	0.03	0.04	0.01	0.02	0.01	0.01	0.01	0.03	0.06	
CaO	<0.01	0.01	<0.01	0.01	0.02	0.09	0.10	0.07	0.05	0.08	0.08	0.07	
Na_2O	0.15	0.26	0.08	0.03	0.12	0.13	0.13	0.03	0.03	0.03	0	0.01	
K_2O	0.52	0.59	0.16	0.02	0.22	<0.01	<0.01	0.01	0.02	<0.01	0.01	0.02	
P_2O_5	0.02	0.02	0.03	0.014	0.034	0.03	0.03	0.05	0.02	0.01	0.015	0.127	
BaO	0.041	0.062	0.013			16.51	15.32	0.043	0.094	0.574	0.141		
CuO													
ZnO	0.000	0.000	0.000			0.002	0.002	0.002	0.004	0.002			
PbO	0.002	0.001	0.002			0.064	0.053	0.011	0.021	0.016			
Loss inc.S-	1.00	1.52	0.51	0.27	0.40	0.99	0.68	0.18	0.35	0.49	0.27	1.68	
Total	100.07	100.12	99.68	99.57	99.45	91.79	92.64	99.98	100.62	100.07	100.23	99.05	
S	0.01	0.01	0.02	0.03	0.04	3.61	3.37	0.06	0.06	0.21	0.10	0.20	
ppm													DL[2]
Sc	7.8	6.2	6.3	3	11.6	4	4	4	4	4	11.2	7.2	1.5
Ba	364	553	121	37.8	324	148000	137000	388	841	5140	321	504	4
V	3	4	8	16.7	29.2	32	38	8	16	20	29.5	14.1	3
Cr	1.5	1.7	3.3	1.5	10.5	2.0	2.0	3.4	7.8	5.9	9.1	1	1
Ni	2	4	3	2.1	4.7	13	8	<4	<4	<4	4.5	2.3	1
Cu	15	15	35	148	217	72	67	272	214	232	217	4.2	1
Zn	2	1	1	6.4	8.6	16	17	16	29	19	7	1.4	1
As	4	3	4	70.7	57.4	228	243	70	162	177	56.2	<3	3
Rb	25	25	6.9	1.5	8.2	2.8	2.7	1.6	2.3	1.3	8	39.8	0.5
Sr	67	52	58	14.3	58.9	1576	1472	23	25	55	58.3	51.6	1
Y	14.1	13.7	12.8	15.0	30.6	3.6	6.2	6.5	2.0	6.0	29.8	25.5	1
Zr	280	234	278	222	649	63	112	72	20	62	651	337	1
Nb	10.5	9.5	9.6	10.8	13.8	0.9	2.0	3.6	2.0	3.8	13.9	15.4	0.5
Sn	7	2	19	11.8	135	98	89	15	44	126	136	19.7	1
Pb	21	11	18	30.4	85.8	595	492	106	195	149	86.6	9.3	1
Bi	4	<2	3	<2	15.1	84	119	75	101	18	15.2	5.8	2
U	4.0	2.9	5.6	2.5	7.8	4.0	4.0	4.0	4.0	4.0	7.7	3.4	2
Th	11.3	7.7	9.8	11.1	14.4	2.0	2.0	2.0	2.0	2.0	13.3	12.9	2
La	18	22	29	12.0	29.0	BDL	BDL	10	<4	5	29.9	30.1	4
Ce	34	46	63	10.0	61.5	BDL	BDL	4	<6	BDL	59.4	72.5	6
Nd	12	16	28	10.7	33.3	BDL	BDL	10	<6	<6	33.4	28.7	4

Notes: Major elements: XRF, trace elements: ICP-MS methods
[1]Total Fe as Fe_2O_3
[2] DL = Detection limits (ppm)
[3] BDL = Below detection limits (ppm)

The Fe-Si layers of Bukit Ketaya are geochemically distinct from the Fe-Mn layer of Bukit Botol. Two varieties are distinguished based on their chemical compositions, and these correspond with the field divisions (Fig. 5.6). The massive hematite-silica layer (Table 5.2) has high Fe_2O_3 contents (68 to93 wt %) and has a lower silica composition (SiO_2 = 3-20 wt %). Meanwhile, the Fe-oxyhydroxide layer with microbreccia-like textures consists mainly of

silica (SiO_2 = 65-96 wt %), iron (Fe_2O_3 = 1-34 wt %) and alumina (Al_2O_3 = 0.5-6.8 wt %). MnO contents are uniformly low (<0.1 wt %) with all other constituent elements less than 1 wt % in both types. In contrast to the Bukit Botol, all Fe-Si layers constitute uniformly low to moderate Cu, Pb and Zn content, whereas concentrations of Ba, As, U are relatively high. However, the massive hematite-silica layer has slightly lower concentrations of these elements than the microbreccia Fe-oxyhydroxide textures.

A ternary diagram in terms of Al, Fe, and Mn shows the relative contributions of hydrothermal (Fe, Mn) and detrital (Al) material to the Fe-Mn and Fe-Si samples at both the Bukit Botol and Bukit Ketaya deposits, together with well-defined fields of hydrothermal, non-hydrothermal sediments after Böstrom and Peterson (1969) and modern chemical precipitates or metalliferous sediments from Böstrom (1973) and Hein et al. (2005) (Fig. 5.13). As shown in the diagram, the Fe-Si samples are considerably more enriched in hydrothermal material, except for a few samples from the Bukit Ketaya deposit that plot towards the Al join due to their high detrital content. In comparison, the Fe-Mn samples at Bukit Botol deposit exhibit a similar compositional range to modern hydrothermal chemical sediments of the East Pacific Rise.

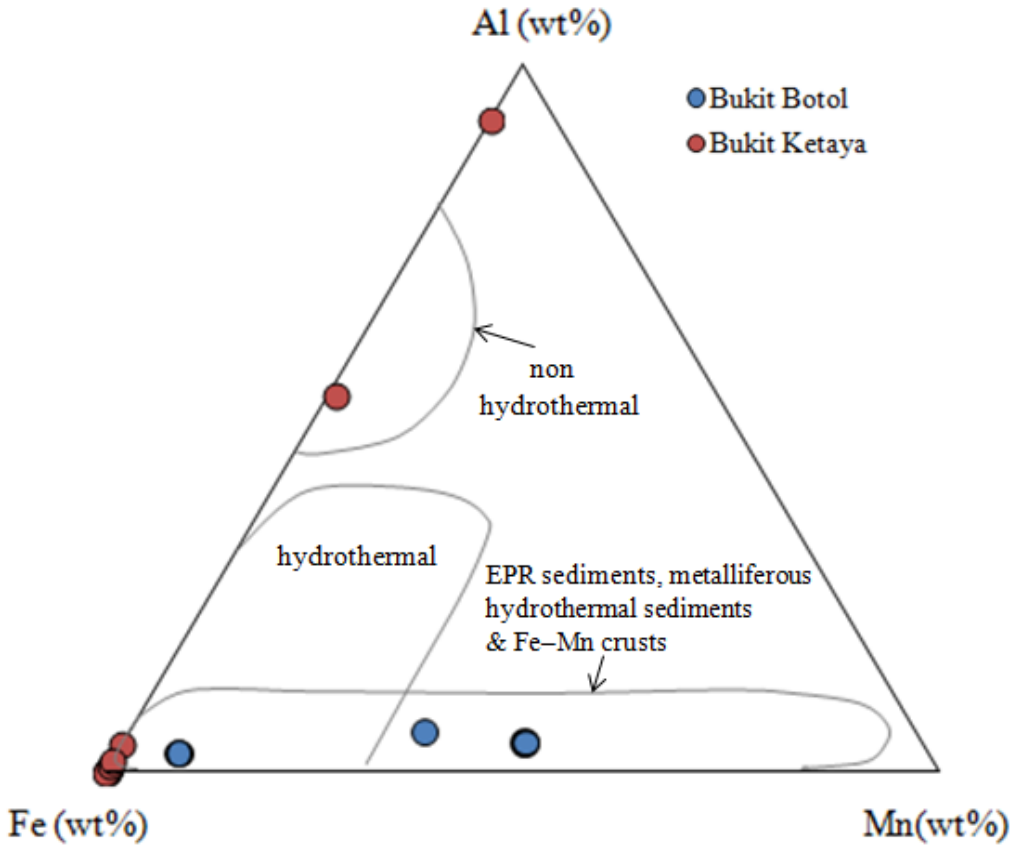

Fig. 5.13. Al-Fe-Mn (wt%) ternary diagram showing the composition of Fe-Mn and Fe-Si samples from both the Bukit Botol and Bukit Ketaya deposits relative to the compositional fields of hydrothermal and non-hydrothermal sediments. Fields of hydrothermal and non-hydrothermal sediments are from Böstrom and Peterson (1969), EPR sediments, metalliferous hydrothermal sediments and Fe-Mn crusts from Böstrom (1973) and Hein et al. (2005). Annotation: EPR = East Pacific Rise.

The SiO_2 - Al_2O_3 diagram (Fig. 5.14A) is useful to distinguish hydrothermal deposits from hydrogenous deposits (Bonatti, 1975; Wonder et al., 1988). In the SiO_2 - Al_2O_3 discrimination diagram of Wonder et al. (1988), the data from the Bukit Botol, Fe-Mn samples fall in the area for hydrogenous field and deep sea sediments, whereas the Bukit Ketaya, Fe-Si samples are clearly plotted in the hydrothermal field (Fig. 5.14A)

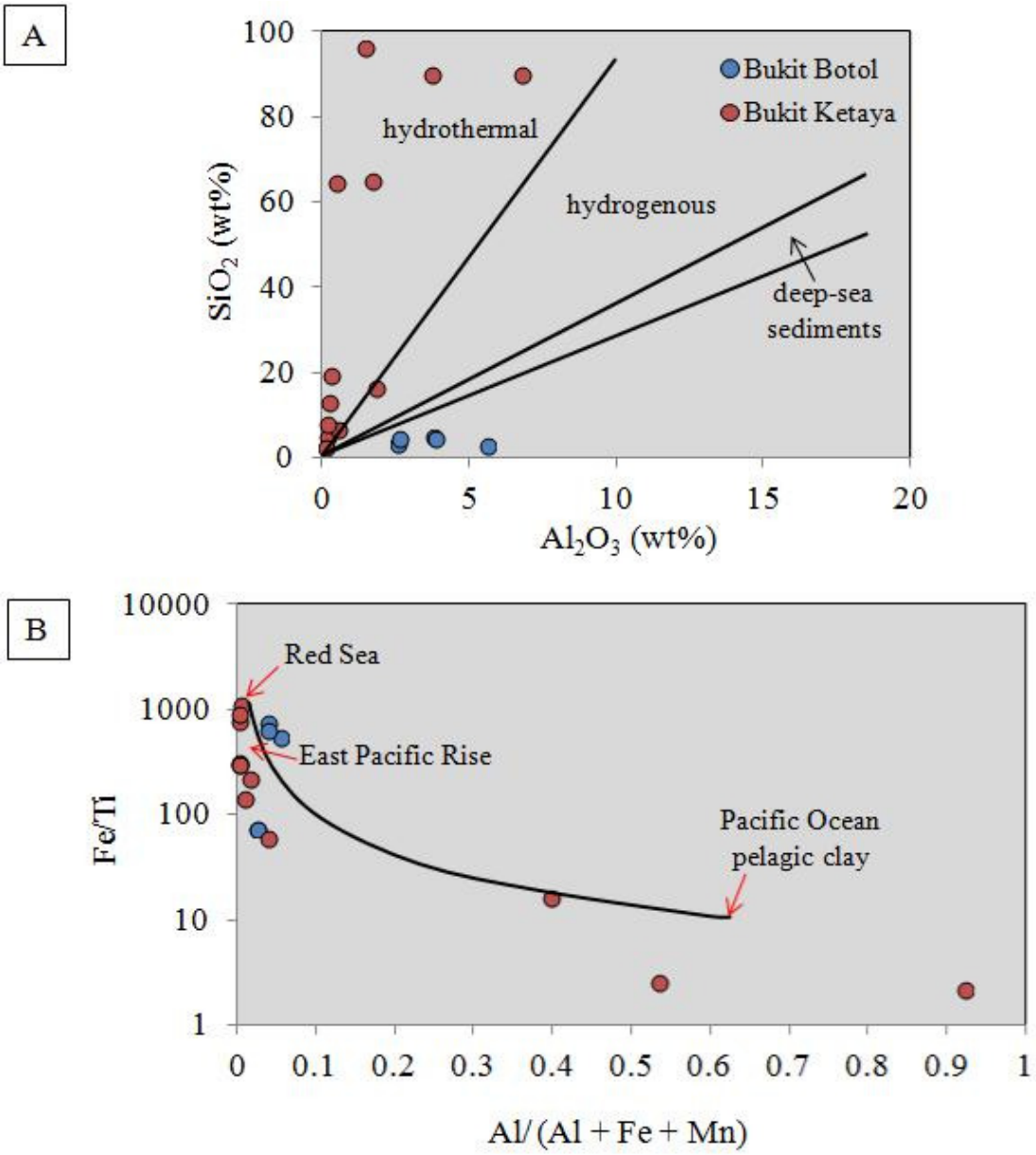

Fig. 5.14. Discrimination diagrams of Fe-Mn and Fe-Si samples from both the Bukit Botol and Bukit Ketaya deposits. **A.** SiO_2-Al_2O_3 diagram showing the Bukit Botol Fe-Mn samples fall in the hydrogenous area, whereas the Bukit Ketaya Fe-Si samples are plotted on the hydrothermal field. **B.** Composition of Fe-Mn and Fe-Si samples in term of Fe/Ti vs. Al/(Al+Fe+Mn). Curve represents the ideal mixing line between hydrothermal sediments with terrigenous or pelagic sediment (modified from Barrett, 1981; Wonder et al., 1988).

Although the Bukit Botol samples are hydrogeneous, a hydrothermal origin cannot be ruled out as the SiO_2-Al_2O_3 diagrams do not consider the possibility of in-situ subsurface replacement and infill, an origin which has been demonstrated for the Tetsusekei of Japan (e.g., Kalogeropoulus and Scott, 1983). Regarding the presence of clastic constituents that are

incorporated in some samples, the Al is primarily considered to be a measure of detrital or clastic grain abundance (Crerar et al., 1982).

The Fe/Ti vs. Al/ (Al + Fe + Mn) diagram (Fig. 5.14B) is efficient in testing the presence of hydrothermal chemical sediment compositions (Barrett, 1981). Pure hydrothermal chemical sediments contain high Fe/Ti ratio and less Al whereas contamination of these sediments by addition of detrital or volcanic material dilutes the Fe/Ti and enriches the proportion of Al with respect to the hydrothermal elements, Fe and Mn (e.g., Barrett, 1981; Wonder et al., 1988). In this diagram, the Fe-Mn and Fe-Si samples from Bukit Botol and Bukit Ketaya deposits plot on an ideal mixing line between modern metalliferous seafloor hydrothermal sediments (e.g., Red Sea and East Pacific Rise) and pelagic or terrigenous sediments (e.g., Pacific Ocean). In fact this data suggests that Pacific Ocean clay is not extreme enough in terms of Al/ (Al + Fe + Mn) to comprise an end member in the Bukit Ketaya deposit. Thus, this pattern reveals a major input of hydrothermal source for the formation of the Fe-Mn±Si layers in both the Bukit Botol and Bukit Ketaya deposits. Additionally, the trends towards the pelagic or terrigenous sediment implies that both the Bukit Botol and Bukit Ketaya Fe-Mn and Fe-Si layers had significant clastic input although they do not allow differentiation between host rock replacement and mixing with detrital material.

5.4 Mineralogy and Paragenesis

5.4.1 Bukit Botol deposit

The mineral paragenesis at the Bukit Botol deposit is established based on the cross-cutting textural relationships, as summarised in Figure 5.15. Characteristics and textural relationships of the minerals are described below.

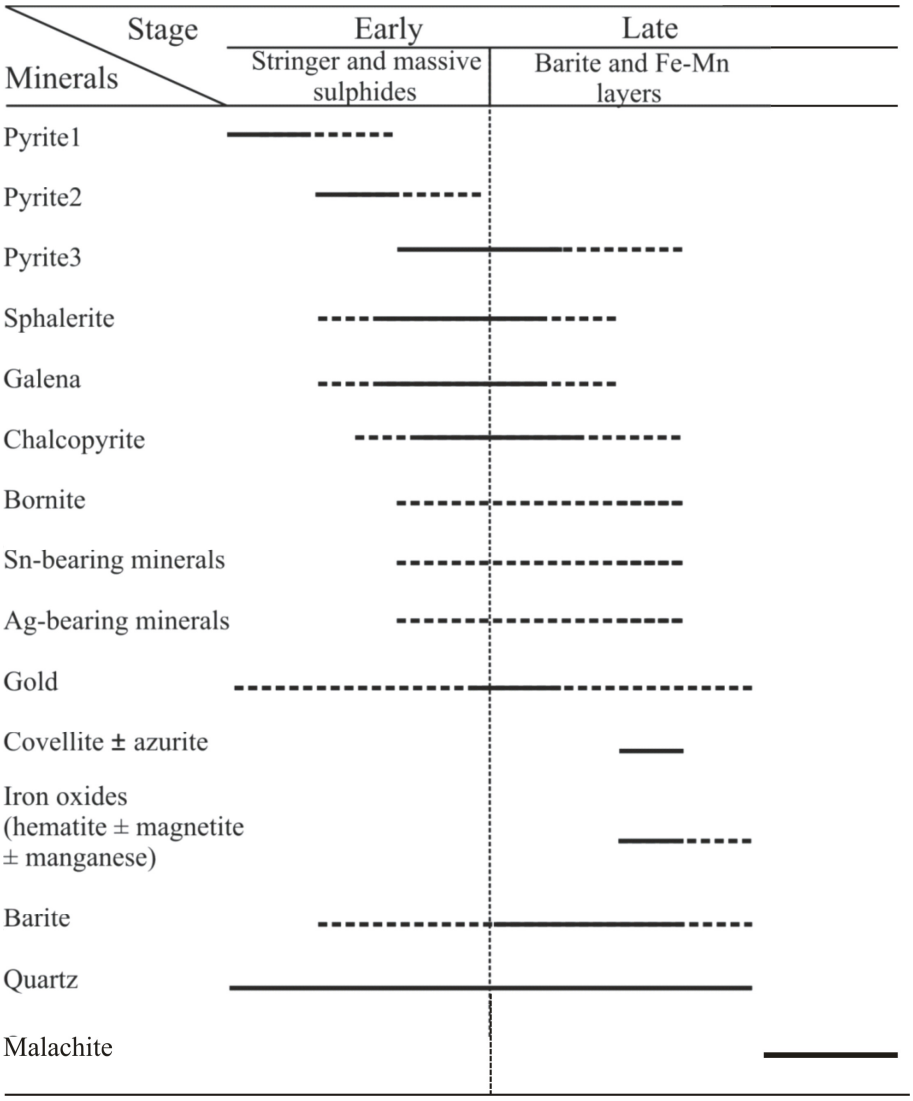

Fig. 5.15. Paragenetic sequence for the mineralisation at the Bukit Botol deposit. The earliest phase sulphide is spongy to elongate py1 forming aggregates in the stringer and massive sulphides, followed by a later anhedral-subhedral py2. Probable contemporaneous sphalerite 1 and galena occur as isolated crystals, coprecipitate and filling micro-cavities within the py2 with few or no chalcopyrite inclusions. During this stage, barite was also precipitated in both the stringer and massive sulphide zones as fine anhedral-subhedral grains. As the hydrothermal system evolved, later subhedral-euhedral py3 formed. Associated with this late py3 are various proportions of chalcopyrite, sphalerite 2, galena, Sn- and Ag-bearing minerals and gold. Additionally, coarse-grained barite crystal developed and deposited as a cap on the massive sulphide, and as a minor component in both the stringer and massive sulphide zones. With respect to the Fe-Mn layer formation at the upper stratigraphic levels, the iron oxide minerals were probably deposited in the late stage. This is supported by the presence of significant barite and clastic component in the Fe-Mn samples. Annotation: solid lines = major and dashed-lines = minor or trace.

Pyrite

Pyrite is the most abundant sulphide intergrown with other sulphides in the massive sulphide lens and stringer sulphide zones with the exception of the barite and Fe-Mn layers. It

commonly occurs in three textural varieties: 1) fine-grained anhedral spongy to elongate grains; 2) medium coarse-grained anhedral-subhedral grains; and 3) coarse-grained aggregates of subhedral to euhedral pyrite.

Fine-grained anhedral spongy to elongate grains

Fine-grained anhedral spongy to elongate pyrite (py1) ranges from 10 μm to 300 μm in diameter. This pyrite occurs as isolated or aggregate grains and is commonly overgrown by medium coarse-grained anhedral-subhedral pyrite and rarely by coarse-grained aggregates of subhedral to euhedral pyrite (Figs. 5.16A and B).

Medium coarse-grained anhedral-subhedral grains

Medium-grained anhedral-subhedral pyrite (py2) ranges in size from 40 μm to 300 μm. Polyphase sulphides intergrown with this pyrite include sphalerite and galena grains with rare barite inclusions (Figs. 5.16C and 5.16D).

Coarse-grained aggregates of subhedral to euhedral

Coarse-grained subhedral to euhedral pyrite (py3) grains are up to 1.5 mm in size. These pyrites commonly have square and pyritohedral outlines. Aggregates of this pyrite are typically intergrown with chalcopyrite, sphalerite, galena and late phase sulphide minerals, and cross-cut the early phase sulphides (Figs. 5.16E and F).

Additionally, inclusions of gold most commonly occur in the coarse-grained subhedral to euhedral pyrite grains, several in medium coarse-grained subhedral-euhedral pyrite and less commonly in fine-grained anhedral spongy to elongate pyrite. Details of trace elements geochemistry of the pyrite types are described in Chapter 6.

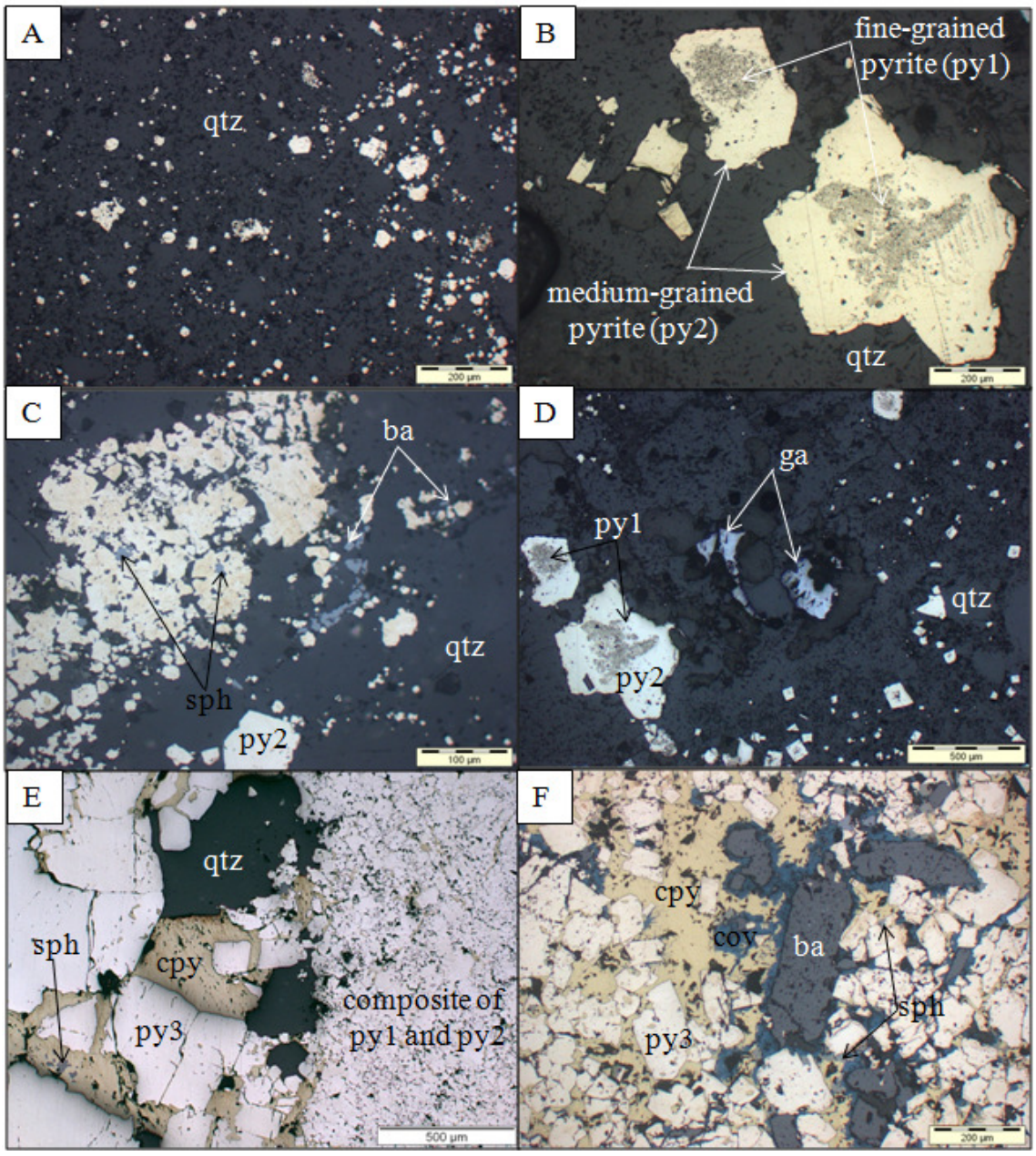

Fig. 5.16. Textural characteristics of pyrite with other sulphides from the Bukit Botol deposit. **A.** Isolated, fine-grained aggregates of anhedral spongy pyrite 1 in cross polarised-light, Sample No. BB02. **B.** Fine-grained pyrite 1 is overgrown by medium-grained anhedral-subhedral pyrite 2, Sample No. BB10. **C.** Composite of py1 overgrown by py2. Note that rare occurrences of sphalerite and galena are enclosed within the py2. In addition barite is present as an inclusion within these mineral associations, Sample No. BB02. **D.** Irregular galena grain occurs as an isolated crystal intergrown with pyrite, Sample No. BB10. **E.** Aggregate of coarse-grained euhedral py3 intergrown with anhedral chalcopyrite minerals, and crosscutting the early phase sulphide precipitations consist of pyrite 1 and pyrite 2, Sample No. BB-DUMP. **F.** Aggregate of coarse-grained py3 intergrowth within and between chalcopyrite, sphalerite and other late sulphide phase. Note the coarse-grained euhedral barite crystal developed as a minor component in the mineral associations. Meanwhile, covellite replaces chalcopyrite along the grain boundaries, Sample No. MBTCS1. Annotation: py1 = fine-grained anhedral spongy to elongate pyrite, py2 = medium coarse-grained anhedral-subhedral pyrite, p3 = coarse-grained subhedral to euhedral pyrite, sph = sphalerite, ga = galena, cov = covellite, ba = barite and qtz =quartz.

Chalcopyrite

The chalcopyrite is a major mineral constituent associated with the late sulphide mineral precipitations (Figs. 5.16E and F). It presents as anhedral grain intergrowths within and between pyrite, sphalerite crystals and other late sulphide phases, cross-cutting the early phase sulphides, as veinlets and interstitial to other sulphides.

Sphalerite

Sphalerite forms as a fine-grained to irregular grain type and occurs in all mineralisation styles. The fine-grained sphalerite intergrowths with galena are associated with the overgrowth pyrite and are most commonly abundant in the stringer zone (Fig. 5.16C). Meanwhile, the irregular-grained sphalerite is up to 500 μm in size intergrown with galena, chalcopyrite and pyrite. Several inclusions of fine-grained, subhedral to rounded Sn-bearing minerals are present in both massive and stringer mineralisation (Figs. 5.17A and B).

Galena

Galena is observed in both the stringer zones and massive sulphide lenses. It occurs as irregular shapes in contact with sphalerite or as isolated grains (Figs. 5.16D and 5.17B), and as small rounded to subangular grains enclosed with pyrite and silver-bearing minerals. Galena dominantly occurs intergrown with pyrite, sphalerite and as inclusions.

Bornite and covellite

Bornite and covellite are present in minor amounts in the ore samples. The bornite occurs as anhedral grains and inclusions associated with pyrite (Fig. 5.17C). Meanwhile, covellite forms mainly as the replacement product of chalcopyrite, yielding complex intergrowths along crystal planes (Fig. 5.17D).

Sn-bearing minerals

Sn-bearing minerals are widely disseminated in the massive sulphide and barite ores. They form as small (~50 µm), rounded to subhedral crystal, inclusions or associated with pyrite, sphalerite, chalcopyrite and barite (Figs. 5.17B and D). A BSE image shows the Sn ore minerals exhibit a composition ranging from tin oxide (cassiterite-SnO_2) to tin sulphide (stannite-Cu_2FeSnS_4 or mohite-Cu_2SnS_3) (Figs. 5.18A and B).

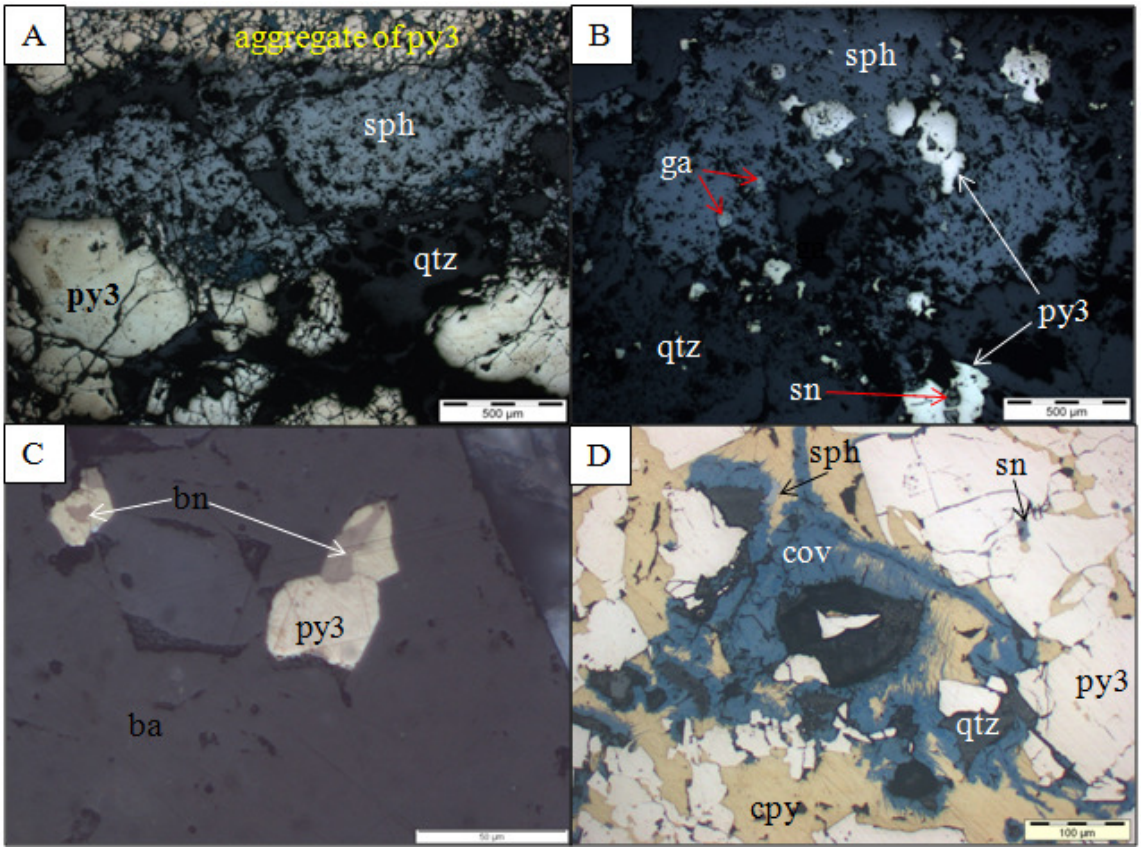

Fig. 5.17. Photomicrographs showing the characteristics and textural relationships of sulphide minerals. **A.** Irregular-grained sphalerite up to 1.5 mm in size intergrowths with pyrite in massive sulphide. Cross-polarised light, Sample No. BB1A. **B.** Irregular-grained sphalerite intergrowths with galena and pyrite. Note the rare Sn mineral inclusions within pyrite grains, Sample No. BK11. **C.** Bornite occurs as anhedral grains and as inclusions associated with pyrite in barite ore, Sample No. BB-DUMP. **D.** Associations of pyrite, chalcopyrite and covellite. Note that the covellite replaces chalcopyrite along crystal planes and yields complex intergrowths. Sn-bearing mineral forms as an inclusion in the pyrite grain, Sample No. MBTCS1. Annotation: py3 = coarse-grained subhedral to euhedral pyrite, sph = sphalerite, cpy = chalcopyrite, ga = galena, bn = bornite, cov = covellite, sn = Sn-bearing mineral, qtz=quartz and ba = barite.

Silver minerals and electrum

Silver minerals identified using BSE imaging techniques include Ag-Cu sulphide probably (mckinstryite; AgCuS) and native silver (Fig. 5.18C). Gold or electrum is uncommon but was observed by both BSE imaging and ore microscopic studies. Gold is hosted in the core of py3 (Fig. 5.18D). Most of the mineral analysed by BSE imaging occurs in the barite samples, associated with typical late sulphide mineral associations of chalcopyrite, sphalerite, galena and pyrite.

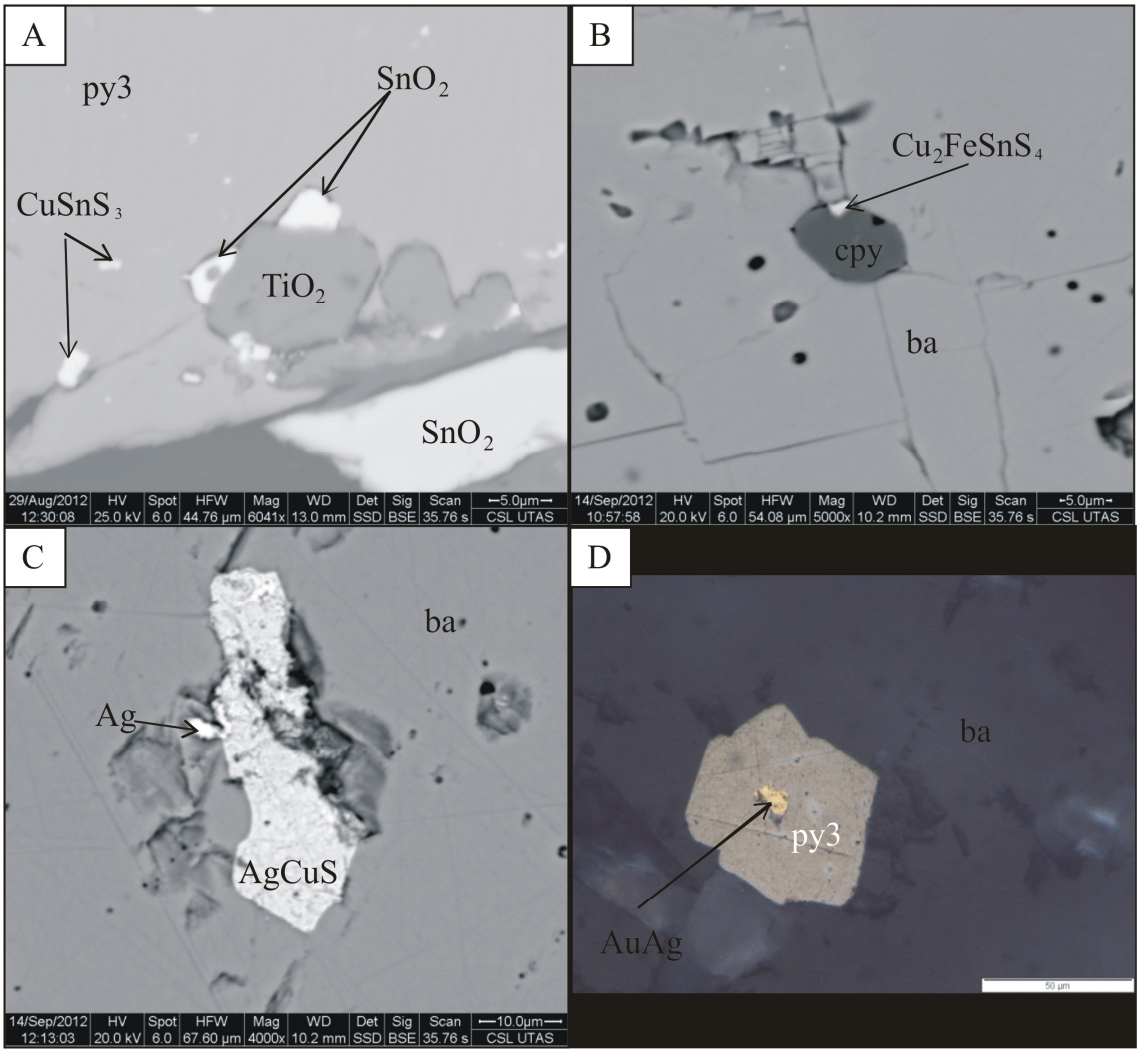

Fig. 5.18. SEM Back-scattered electron (BSE) images showing Sn- and silver-bearing minerals at the Tasik Chini VHMS deposits. **A.** The association of cassiterite (SnO_2) and mohite ($CuSnS_3$) with and between pyrite (py3) and rutile (TiO_2) mineral, Sample No. BB10. **B.** Stannite ($CuSnS_3$) intergrowths with chalcopyrite in barite, Sample No. BBotol. **C.** Barite fractures filled by native silver (Ag) and mckinstryite (AgCuS), Sample No. B1. **D.** Photomicrograph showing electrum as inclusions in pyrite within barite crystal, Sample No. B1.

Barite

Barite is a common sulphate mineral throughout the stringer sulphide, main massive sulphide, Fe-Mn layer and as a major component in the barite lenses. It forms as anhedral to subhedral inclusions in all the mineralisation stages and occurs as a groundmass of foliated laths enclosing other sulphide, oxide, silver minerals and gold in the barite lenses (see Fig. 5.23A).

Iron oxide minerals

Hematite is the major iron oxide mineral of the Fe-Mn layers. It forms as fine-grained micro-crystalline mesh in the Fe-Mn layers. Magnetite is an accessory and is present as mixed assemblages with quartz, barite and clastic constituents forming clast aggregates of variable proportions in the hematite groundmass (Figs. 5.19).

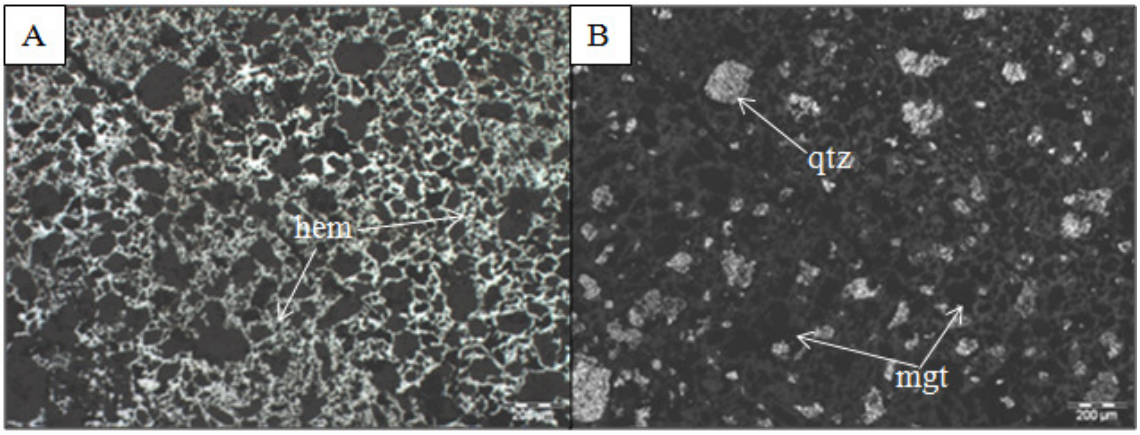

Fig. 5.19. Photomicrographs showing the textural relationships of iron oxide minerals. **A.** Hematite occurs as a matrix of fine-grained micro-crystalline of the Fe-Mn ore in cross polarised-light. **B.** Same view as A showing disseminated euhedral-subhedral magnetite and quartz clasts in the fine-grained hematite matrix in plane polarised-light. Annotation: hem = hematite, mgt = magnetite and qtz = quartz.

Quartz

Quartz is a common gangue mineral in massive and stringer sulphides, but only a minor component in the barite and Fe-Mn layers. It occurs as a matrix in the massive and stringer sulphides which form equigranular, rounded grains up to 0.2 mm, and also as infill or interstitial to sulphide minerals. In barite layer, where present, quartz occurs as scattered

grains within and between the barite crystals. Meanwhile, in Fe-Mn layers, quartz forms subangular to subrounded clasts-like aggregates which vary in size from 2 mm to 5 mm and are disseminated in the hematite groundmass.

5.4.2 Bukit Ketaya deposit

The mineralogy of the sulphides at the Bukit Ketaya deposit in thin massive sulphide and weakly developed stringer sulphide mineralisation, in general is very simple. The sulphide minerals identified in the microscopic studies of both ore types are pyrite, sphalerite, minor galena and chalcopyrite with lesser tin-bearing minerals compared to Bukit Botol. Minor amounts of these sulphides are also found in the Fe-Si and barite layers. The minerals in the Fe-Si layer consist mainly of hematite with variable proportions of disseminated quartz, barite, lithic clasts of rhyolite-rhyodacite and minor magnetite. The major constituent of the barite lenses is barite. A summary of mineral paragenesis in relation to textural characteristics is presented in Figure 5.20. The mineralogical assemblages and textural relationships are addressed below.

Pyrite

Two types of pyrite were distinguished in the thin massive sulphide and weakly developed stringer sulphide zone: 1) fine-grained anhedral to spongy (py1); and 2) medium coarse-grained anhedral-subhedral grains (py2). The fine-grained anhedral to spongy pyrite occurs as disseminated grains or aggregates within quartz polycrystalline groundmass, whereas the medium coarse-grained anhedral-subhedral pyrite typically forms overgrowths around fine-grained anhedral or spongy pyrite. This is shown by the presence of fine-grained anhedral or spongy pyrite in their cores. In addition, sphalerite and galena crystals with rare chalcopyrite and Sn-bearing mineral inclusions formed during the crystallisation of this pyrite (Fig. 5.21).

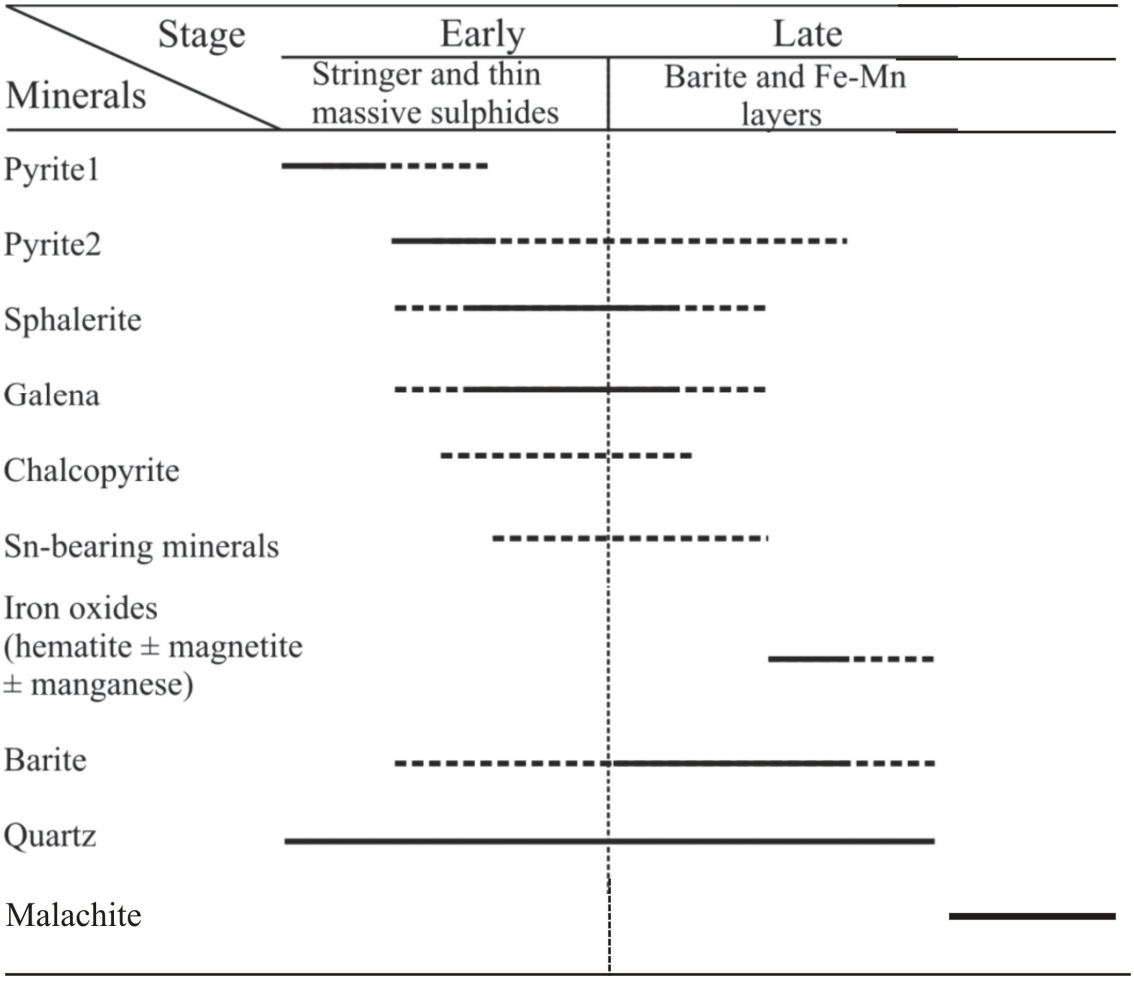

Fig. 5.20. Paragenetic sequences for the mineralisation formations at the Bukit Ketaya deposit. Early hydrothermal activity has deposited the earliest sulphide and sulphate minerals in both the weakly-developed stringer sulphide and massive sulphide. The earliest phase sulphide is fine-grained anhedral to spongy pyrite, characterised by the absence of any sulphide associations and free of inclusions. As the hydrothermal system evolved with time, medium coarse-grained anhedral-subhedral pyrite (py2) grains formed as overgrowths on the py1 and make up most of the pyrite in the thin massive and stringer sulphide. Associated with them are isolated grains of sphalerite and galena, and fine-grained inclusions of Sn-bearing minerals and barite. During this stage, sphalerite without chalcopyrite disease replaces the chalcopyrite and both stages of pyrite. The late events are characterised by distinctive precipitations of sulphate and iron oxide minerals that occur throughout of the deposit. Iron oxide minerals were probably deposited at a later stage at the upper stratigraphic levels forming the Fe-Si layer. Evidence of late stage precipitation of the iron oxide minerals are shown by the presence of significant barite and clastic component clasts in the Fe-Si samples. Annotation: solid lines = major and dashed-lines = minor or trace.

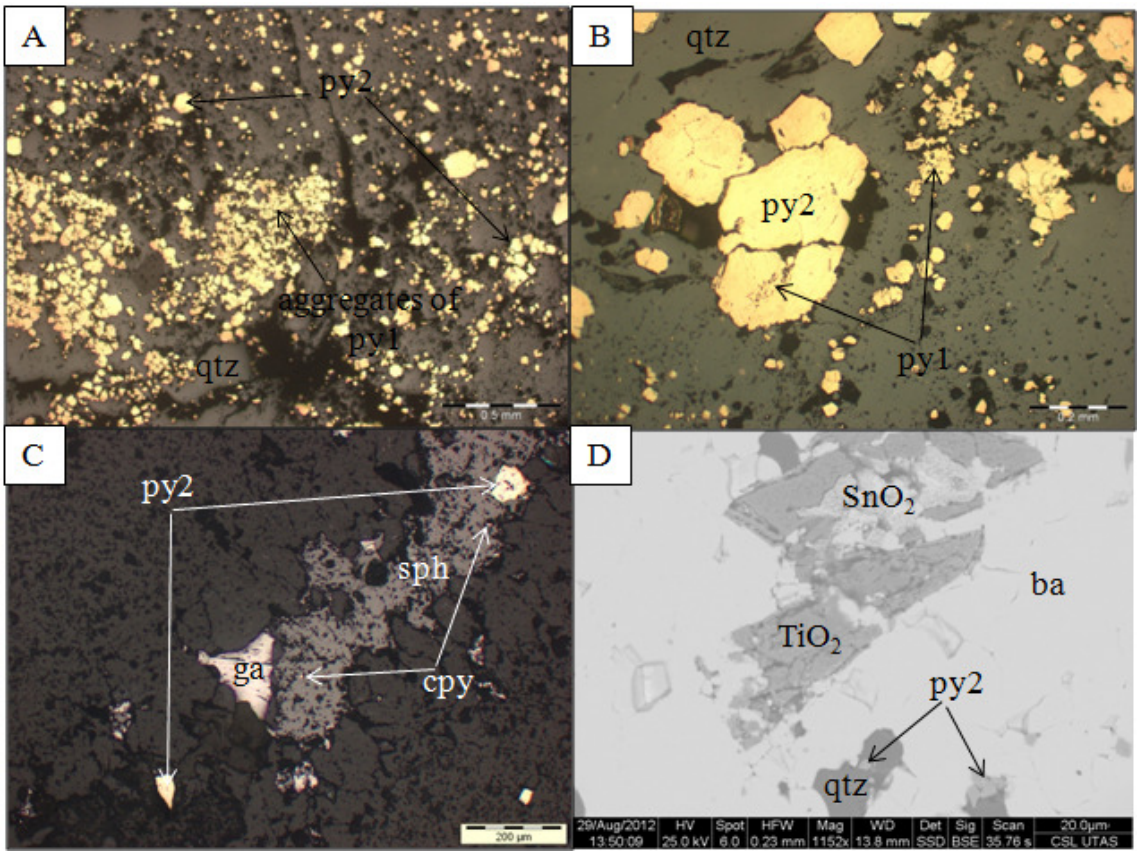

Fig. 5.21. Photomicrographs showing the characteristic and textural relationships of sulphide minerals at Bukit Ketaya deposit. **A.** Fine-grained anhedral to spongy pyrite occurring as disseminated grains or aggregates within quartz polycrystalline groundmass. Note occurrence of py2 in places, Sample No. BK12. **B.** Medium coarse-grained anhedral-subhedral pyrite forming overgrowths around fine-grained anhedral or spongy pyrite. Note the presence of fine-grained anhedral or spongy pyrite (py1) in py2 core and occurs as disseminated grains, Sample No. BK12. **C.** Py2 intergrown with sphalerite and galena minerals. Note the presence of rare chalcopyrite inclusions within the sphalerite grain and the mutual grain boundaries between galena and sphalerite, Sample No. BK12A. **D.** SEM Back-scattered electron (BSE) image showing association of cassiterite (SnO_2), pyrite (py2) and rutile (TiO_2) within a fracture in barite, Sample No. BB10. Annotation: py1 = fine-grained anhedral spongy pyrite, py2 = medium coarse-grained anhedral-subhedral pyrite, sph = sphalerite, ga = galena, cpy=chalcopyrite, ba = barite and qtz =quartz.

Sphalerite

Sphalerite is found as isolated crystals together with other sulphides. Some crystals display evidence of having filled micro-cavities or micro-fissures. The isolated sphalerite crystals accompanied by pyrite and galena normally contain cha1copyrite inc1usions, examples of chalcopyrite “disease” texture (Barton and Bethke, 1987). These inc1usions are irregularly distributed, or commonly arranged in a wavy pattern roughly parallel to the crystallographic planes (Figs. 5.21C and 5.22A). The disease texture is weakly developed both in the thin massive sulphide lens and in stockwork zones.

Galena

Galena is present in both the stringer zones and thin massive sulphide. It occurs as single crystals or associated with other sulphide minerals. Galena dominantly forms intergrown with pyrite and sphalerite, but some galena also forms as inclusions and fills cavities within pyrite and sphalerite (Figs. 5.21C and 5.22A).

Chalcopyrite

The chalcopyrite is less abundant in the massive and stringer sulphide at the Bukit Ketaya deposit. Chalcopyrite occurs as fine crystals found as inclusions within sulphide minerals (Fig. 5.21C) and is commonly found dispersed and as blebs in sphalerite showing chalcopyrite disease texture (Fig. 5.22B).

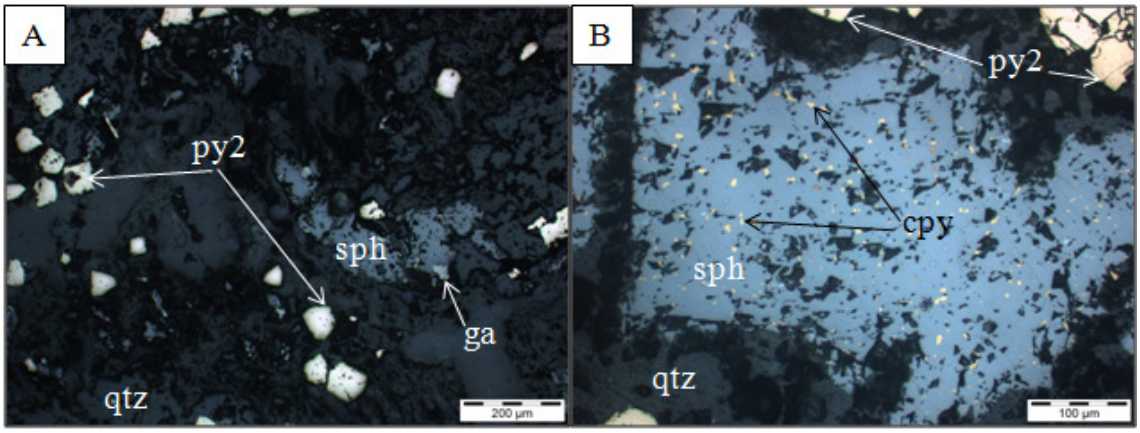

Fig. 5.22. Photomicrographs showing the characteristic and textural relationships of sulphide minerals. A. Isolated sphalerite crystals forming together with pyrite and galena, Sample No. BK11. B. Chalcopyrite presents as inc1usions which cause disease texture in sphalerite grain. The inc1usions are irregularly distributed, or sometimes arranged in a wavy pattern roughly parallel to the crystallographic planes, Sample No. BKCL. Annotations: py2 = medium coarse-grained anhedral-subhedral pyrite, sph = sphalerite, ga = galena, cpy=chalcopyrite and qtz =quartz.

Sn-bearing minerals

Sn-bearing minerals are rare in the Bukit Ketaya ores. They do form in barite lenses as small crystals of rounded inc1usions. BSE imaging combined with EDS of a representative Sn mineral gives a composition of mainly tin oxide (cassiterite-SnO_2) (Fig. 5.21D).

Barite

At the Bukit Ketaya deposit, barite is a common non-metallic mineral present in all the mineralisation types. In thin massive sulphide, stringer zone and Fe-Si and Fe-oxyhydroxide layers, barite is scattered as fine-grained crystals and aggregates associated with quartz and sulphide minerals. In the barite lenses, the barite crystals typically show euhedral to subhedral form with variable degree of cementation and colour (Fig. 5.23B).

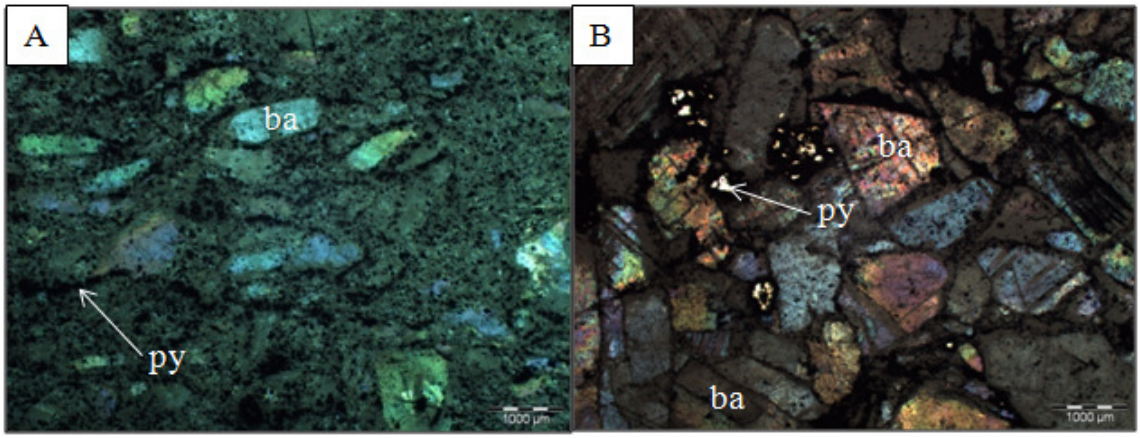

Fig. 5.23. Photomicrograph showing occurrence of barite in barite layers. **A.** Foliated barite laths with pyrite disseminated in the groundmass of the barite layer from Bukit Botol deposit in cross-polarised light, Sample No. BBarite. **B.** Aggregates of euhedral to subhedral, rhombohedral barite crystals of the barite from Bukit Ketaya deposit in cross-polarised light. Note the fracture in barite is filled by pyrite, Sample No. S5/6a12. Annotation: ba = barite and py = pyrite.

Iron oxide minerals

Hematite and minor magnetite are two common oxide minerals present as the main component of the Fe-Si layers. The hematite commonly occurs as a matrix of fine-grained micro-crystalline textures of the Fe-Si samples. Magnetite forms as euhedral to subhedral crystals up to 40 µm either disseminated or forming aggregates associated with quartz, barite and clastic constituent in the hematite groundmass (Fig. 5.19).

Quartz

Quartz is the most abundant gangue mineral present in all the mineralisation types at Bukit Ketaya. It commonly occurs within cavities in the sulphides. Uncommonly, quartz occurs as large to fine-grained disseminated, isolated and aggregates in barite and Fe-Si layers.

5.5 Alteration

Alteration is defined as a change in the chemical or mineralogical composition and texture of a rock affected by hydrothermal solution or weathering. Element mobility records the chemical changes which take place in a rock after its formation (Lapidus and Winstenly, 1990). According to Reed (1997), hydrothermal alteration is a chemical replacement of the original minerals in a rock by new minerals where a hydrothermal fluid delivers the chemical reactants and removes the aqueous reaction products.

Hydrothermal alteration related to the host rocks of VHMS deposits has been widely studied and extensively documented. In many cases of VHMS deposits, areas of hydrothermally altered rock occur proximal to VHMS deposits and act as a guide to mineral exploration because they are much larger than the deposit itself (Gifkins et al., 2005). The most common investigations of hydrothermal alteration associated with VHMS deposits concentrate on the footwall alteration pipes and semi-conformable alteration in the lower parts of the footwall below the deposits (Franklin et al., 1981; Morton and Franklin, 1987; Large, 1992; Franklin, 1993; Galley, 1995) because hangingwall alteration is not commonly well-developed (Lentz and Goodfellow, 1994a, 1994b; Large et al., 2001a; Franklin et. al., 2005). However, where present, hangingwall alteration may extend for tens to hundreds m into the hangingwall, for instance in the Hellyer deposit, Tasmania (Gemmell and Large, 1992).

Previous works on hydrothermal alteration assemblages of volcanic-hosted massive sulphide (VHMS) deposits were focused and assigned from mineralogical, textural, and stable isotope perspectives (e.g., Franklin et al., 1981; Urabe et al., 1983; Lydon and Galley, 1986; Eastoe et al., 1987; Gemmell and Large, 1992; Large, 1992; Huston, 1993; Solomon and Groves, 1994; Khin Zaw et al., 1996a; McArthur, 1996). However, studies post-dating this work used quantitative tools for measuring and discriminating alteration intensity (e.g., Leitch and Lentz, 1994; Large et al., 2001a; Davies and Whitehead, 2006) which allowed quantification of elemental gains and losses and characterisation of specific types of alteration. Numerous workers have applied these techniques to alteration studies in VHMS systems (Galley et al., 1993; Goodfellow and Peter, 1994; Barrett and MacLean, 1999; Gemmell and Fulton, 2001; Large et al., 2001a; Piercey, 2009). Moreover, recent studies based on SWIR analyses in VHMS districts also show that spectral parameters related to the composition of these minerals vary systematically with proximity to ore (e.g., Pontual et al., 1997; Huston et al., 1999; Thompson et al., 1999; Herrmann et al., 2001).

5.5.1 Methods

As a result of limited outcrop, the alteration study was based on systematic sampling and description using surface samples. Samples were then selected to be representative of the alteration types. In this study, petrography, Short-Wave Infrared (SWIR) and lithogeochemistry have been used to characterise the hydrothermal alteration. In addition, a few altered samples were selected from the Bukit Ketaya deposit for X-Ray diffractometer (XRD) analysis to define qualitatively the alteration mineral assemblages.

5.5.1.1 Petrography, Short-Wave Infrared (SWIR) and X-Ray diffractometer (XRD) analyses

Petrographic examinations of thin section samples were made using a standard petrographic

microscope to document mineralogy of alteration assemblages. Photomicrographs were taken by a microscope-attached Nixon digital camera installed with image analySIS software.

Short-Wave Infrared (SWIR) analysis of altered samples was applied on flat, sawed surfaces of dry rock with multiple analyses on individual samples. Spectra were measured with ASD Terraspec Spectrometers at CODES, University of Tasmania, Australia. In order to estimate relative mineral proportions for every spectra, graphical comparison of the spectral weightings was done automatically by using the TSA v.7 software where it compares the sample spectra to a standard reference library.

The selected altered samples from the Bukit Ketaya deposit for X-Ray diffractometer (XRD analysis were prepared, examined and analysed in the MRT laboratories, Rosny Park, Tasmania. They were run on an automated Philips X-Ray diffractometer (XRD) system: PW 1729 generator, PW 1050 goniometer and PW 1710 microprocessor with nickel-filtered copper radiation at 40kV/30mA, a graphite monochromator (PW1752), sample spinner and a proportional detector (sealed gas filled PW1711). The PW1710 system is presently driven by the CSIRO XRD software: "PW1710 for Windows" and "XPLOT for Windows". Interpretation and quantification is largely manual, using a series of prepared standards of the more common minerals to enable some semi-quantitative analysis.

5.5.1.2 Lithogeochemical analyses

Lithogeochemical data of variably altered footwall and ore horizon rhyolite-rhyodacite from surface samples were obtained from both the Bukit Botol and Bukit Ketaya deposits. The same geochemical data as discussed in Chapter 4 (see Tables 4.2 and 4.3) along with additional samples from both the deposits (Appendix IV) are applied to characterise the alteration by means of alteration indices. Details of the analytical methods are also presented

in Chapter 4. Measurements and discriminations of the alteration intensity were made on an alteration box plot of Large et al. (2001a), which includes the Ishikawa (AI) and the chlorite-carbonate-pyrite (CCPI) indexes for better understanding the relationships between alteration mineralogy and lithogeochemistry. Combination of these indices on a box plot (Large et al., 2001a) yields a clear identity of alteration processes that affect whole-rock composition. Moreover, this approach allows individual reactions to be identified and offers potential for discriminating between the effect of diagenetic and hydrothermal processes.

The Ishikawa alteration index (AI) plotted in the horizontal axis is used to measure the breakdown of sodic plagioclase, volcanic glass and their replacement by sericite and chlorite (Ishikawa et al., 1976). The AI is calculated using the following equation:

$$AI = 100\ (K_2O + MgO)/\ (K_2O + MgO + Na_2O + CaO)$$

Meanwhile, the chlorite-carbonate-pyrite index (CCPI) plotted on the vertical axis is used to measure the increase in MgO and FeO associated with Mg-Fe chlorite which commonly replaces albite, K-feldspar or sericite in volcanic rocks that lead to the loss of Na_2O and K_2O (Large et al., 2001a). The CCPI is calculated using the equation as below:

$$CCPI = 100\ (MgO + FeO)/\ (MgO + FeO + Na_2O + K_2O)$$

Furthermore, K_2O/Al_2O_3, Na_2O/Al_2O_3 and MgO/Al_2O_3 molar ratios plots after Davies and Whitehead (2006) were constructed to demonstrate the relationship between major elements and lithogeochemical variations and the alteration mineral assemblages. In these diagrams, the different types of alteration can be measured directly because both the chemical and mineralogical trends corresponding to the difference K_2O/Al_2O_3, Na_2O/Al_2O_3 and MgO/Al_2O_3 values are included.

5.5.2 Petrography, Short-Wave Infrared (SWIR) and X-Ray Diffractometer results

Based on field observations, petrographic study and Short-Wave Infrared (SWIR) analysis, four major alteration assemblages have been defined at the Tasik Chini deposit. The main alteration minerals are quartz, sericite, pyrite and chlorite with lesser amounts of pyrophyllite, carbonate and paragonite.

The distribution of alteration mineralogy observed in outcrop, in hand sample and thin section coupled with the SWIR spectral analysis interpretations of the Tasik Chini deposit (this study) at both the Bukit Botol and Bukit Ketaya deposits are described below. In addition, X-Ray diffractometer (XRD) results were used to further constrain the alteration assemblages at Bukit Ketaya deposit. Both the SWIR and XRD data are shown in Appendices V and VI.

5.5.2.1 Alteration assemblages of the Bukit Botol deposit

Quartz-sericite±paragonite alteration

This zone forms in the ore horizon or immediate rock proximal to the massive sulphide lenses at the Bukit Botol deposit and extends east towards the volcaniclastic unit. It is a purplish colour in outcrop but has a white and hard appearance in hand specimens. It is characterised by pervasive disseminated and weak foliation of sericite throughout the groundmass. Moreover, sericite has also replaced the feldspar phenocrysts and groundmass grains (Fig. 5.24). Most of the SWIR spectra show an absorption feature of normal muscovite. However, few spectra have a relatively weak paragonite absorption feature (Appendix V).

Quartz-sericite-pyrite±chlorite alteration

The quartz-sericite-pyrite±chlorite alteration occurs in the stratigraphic footwall in the stringer zones at the Bukit Botol deposit. This alteration zone exhibits a bleached, sugary texture with abundant disseminated grains of pyrite in hand specimen.

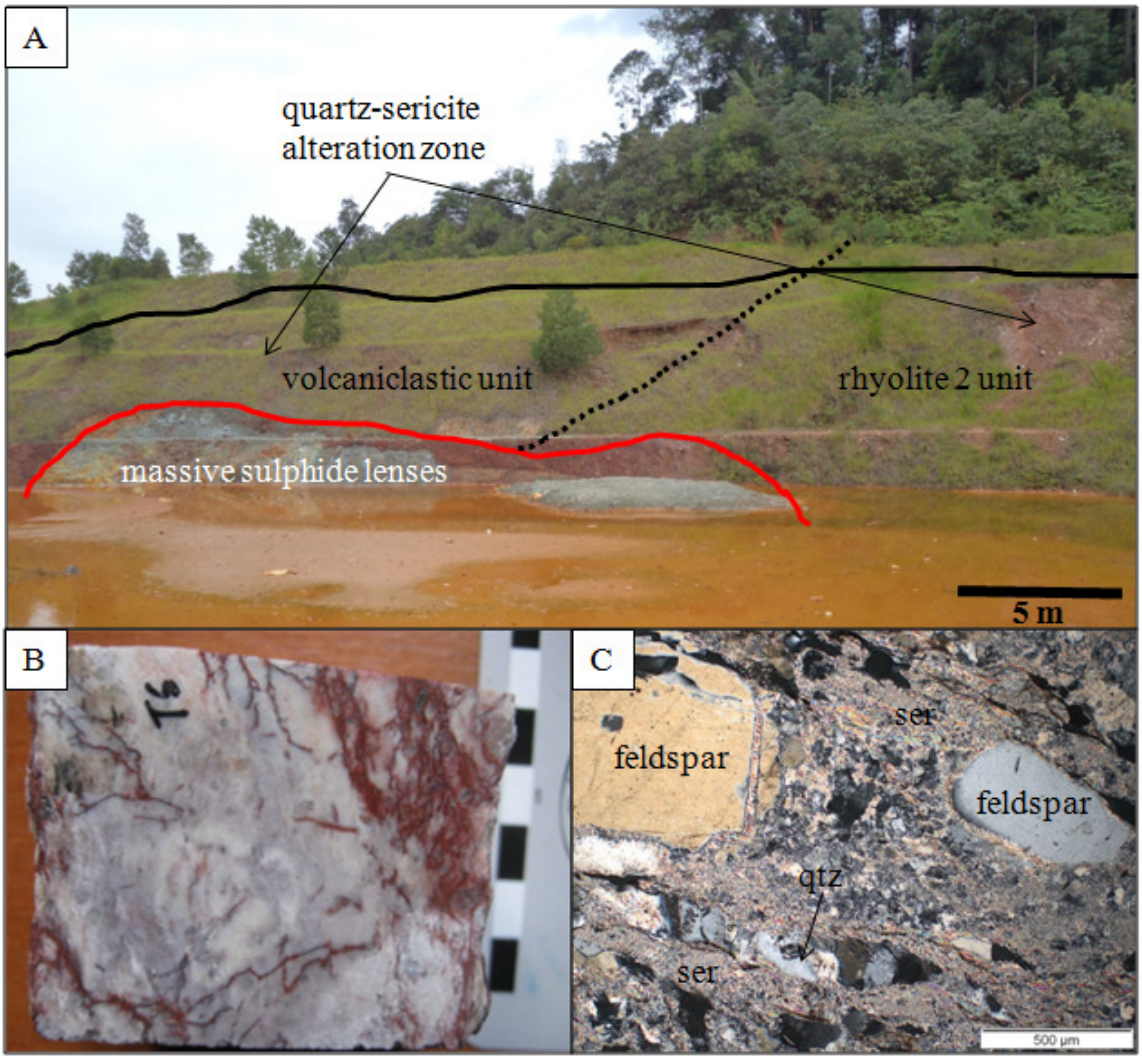

Fig. 5.24. Characteristic features of the quartz-sericite alteration at Bukit Botol, Tasik Chini VHMS deposit. **A.** An outcrop of the quartz-sericite alteration zone looking south of the Bukit Botol mine. **B.** Representative sample of the quartz-sericite altered rock with white colour and hard appearance, Sample No. BB11. **C.** Photomicrograph showing the quartz-sericite alteration characterised by pervasive disseminated and weak foliation of sericite throughout the groundmass. In addition, sericite has also replaced the feldspar phenocrysts and groundmass grains. Annotation: ser = sericite, qtz = quartz.

In thin section, the quartz-sericite-pyrite±chlorite alteration comprises a partly recrystallised quartz and feldspar phenocrysts and the groundmass is completely replaced by fine-grained quartz-sericite (Fig. 5.25). Apart from this most extensive zone, minor chlorite-pyrite-quartz alteration is also present. The chlorite-pyrite-quartz alteration zone is dark greenish/grayish in colour and contains pervasive disseminated and veinlets of pyrite. It commonly shows replacement of sericite by chlorite and depletion of quartz.

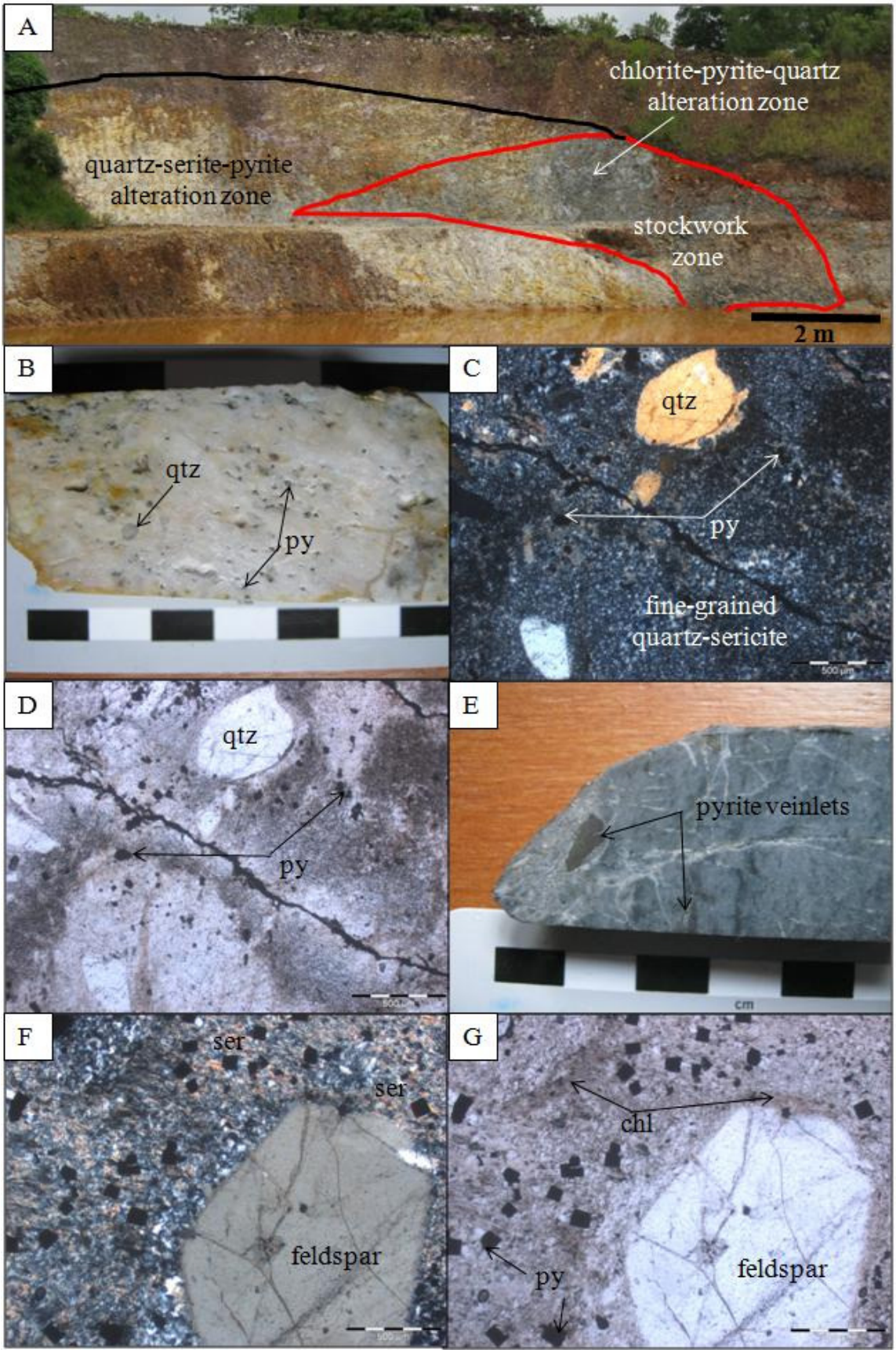
A
chlorite-pyrite-quartz alteration zone
quartz-serite-pyrite alteration zone
stockwork zone
2 m
B
qtz
py
C
qtz
py
fine-grained quartz-sericite
D
qtz
py
E
pyrite veinlets
F
ser
ser
feldspar
G
chl
py
feldspar

Fig. 5.25. Characteristics of quartz-sericite-pyrite±chlorite alteration at Bukit Botol deposit. **A.** An outcrop of quartz-sericite alteration zone looking north of the Bukit Botol mine. **B.** Representative samples of the quartz-sericite-pyrite altered rock exhibit a bleached, sugary texture with abundant pyrite in disseminated grains, Sample No. 2. **C.** Photomicrograph showing the quartz-sericite-pyrite alteration comprising partly recrystallised quartz and feldspar phenocrysts and the groundmass is completely replaced by fine-grained quartz-sericite, Sample No. Sqs1. Cross-polarised light. **D.** Same view as C showing some of the sericite replaced by fine-grained chlorite. Plane-polarised light. **E.** Representative sample of the dark greenish/grayish chlorite-pyrite-quartz altered rock, Sample No. CL3. **F.** Photomicrograph of the chlorite-pyrite-quartz alteration showing replacement of sericite by chlorite and depletion of quartz in its compositions, Sample No. Sqs4. Cross-polarised light. **G.** Same view as F showing extensive replacement of sericite by chlorite. Plane-polarised light. Note the presence of coarse-grained pyrite in the rock groundmass. Annotation: ser = sericite, qtz = quartz, py = pyrite and chl = chlorite.

Pyrite is coarser-grained than that found in the quartz-sericite-pyrite±chlorite assemblages (Fig. 5.25). In contrast to the distal alteration zones, the measurable absorption features in SWIR spectra show that the white micas in the quartz-sericite-pyrite±chlorite alteration are normal muscovite to phengite in compositions (Appendix V).

5.5.2.2 Alteration assemblages of the Bukit Ketaya deposit

Quartz-chlorite-sericite-pyrite-pyrophyllite±kaolinite alteration

The quartz-chlorite-sericite-pyrite-pyrophyllite±kaolinite alteration occurs in the rocks at the upper part of ore horizon above the feeder zone at the Bukit Ketaya deposit, but is not laterally extensive. This alteration is distinguished from the quartz-chlorite-carbonate zone by the presence of pervasively disseminated sericite and chlorite in the groundmass and the absence or lack of pyrite and carbonate minerals. Moreover, most of the primary volcanic textures are completely destroyed except the mineral phenocrysts (Fig. 5.26).

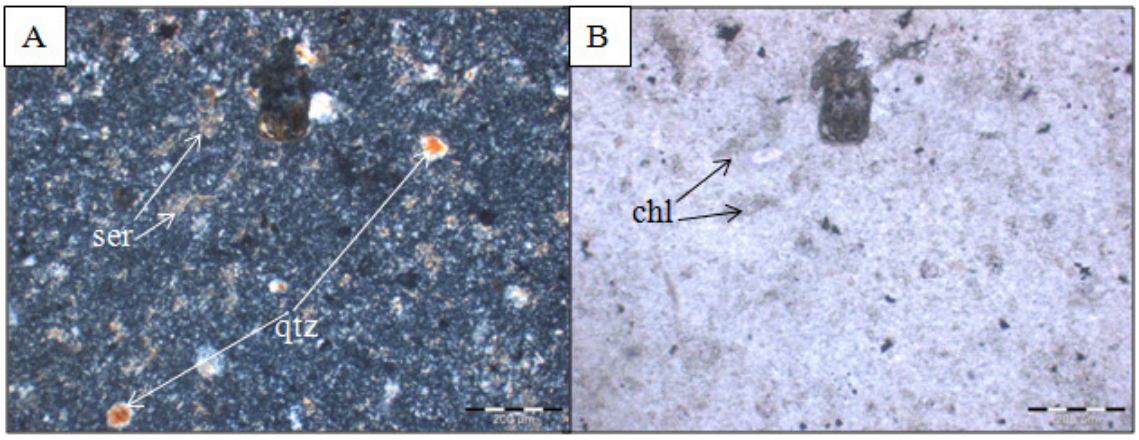

Fig. 5.26. Photomicrographs showing the characteristics of quartz-chlorite-sericite-pyrite-pyrophyllite±kaolinite alteration at the Bukit Ketaya deposit. **A.** Quartz-chlorite-carbonate assemblage pervasively altered by sericite and chlorite in groundmass. Note primary volcanic textures are completely destroyed but mineral phenocrysts, Sample No. SQT1-BK. Cross-polarised light. **B.** Same view as A showing some of the sericite replaced by fine-grained chlorite. Plane-polarised light. Annotation: ser = sericite, qtz = quartz and chl = chlorite.

SWIR spectral analysis shows that the spectra are dominated by absorption features of pyrophyllite and muscovite with lesser paragonite (Appendix V). The whole rock XRD analysis has detected quartz as a major constituent of this alteration assemblage. Similar to SWIR data, the presence of pyrophyllite is confirmed by XRD analysis. Additionally, the results also detect a significant amount of kaolinite mineral. However, no chlorite mineral was detected except the unidentified 'mica' (Appendix VI).

Quartz-chlorite-pyrite±carbonate±pyrophyllite alteration

The quartz-chlorite-pyrite±carbonate±pyrophyllite alteration is restricted to the footwall rhyodacite of the weakly developed feeder zone at the Bukit Ketaya deposit. It is dark-green in colour and entirely siliceous with abundant pyrite in the form of disseminated grains and veinlets. This zone is characterised by the presence of significant chlorite minerals throughout the recystallised rock groundmass besides the presence of carbonate and sericite minerals (Fig. 5.27). The diagnostic absorption features in the SWIR spectra show the presence of muscovite and lesser pyrophyllite in this alteration assemblage (Appendix V). Similar to the ore horizon alteration assemblage, the XRD analysis of two altered samples show that they are also quartz-rich, absent of chlorite and present of unidentified 'mica'. In contrast, this alteration is characterised by the presence of moderate amount of pyrite and pyrophyllite with minor paragonite (Appendix VI).

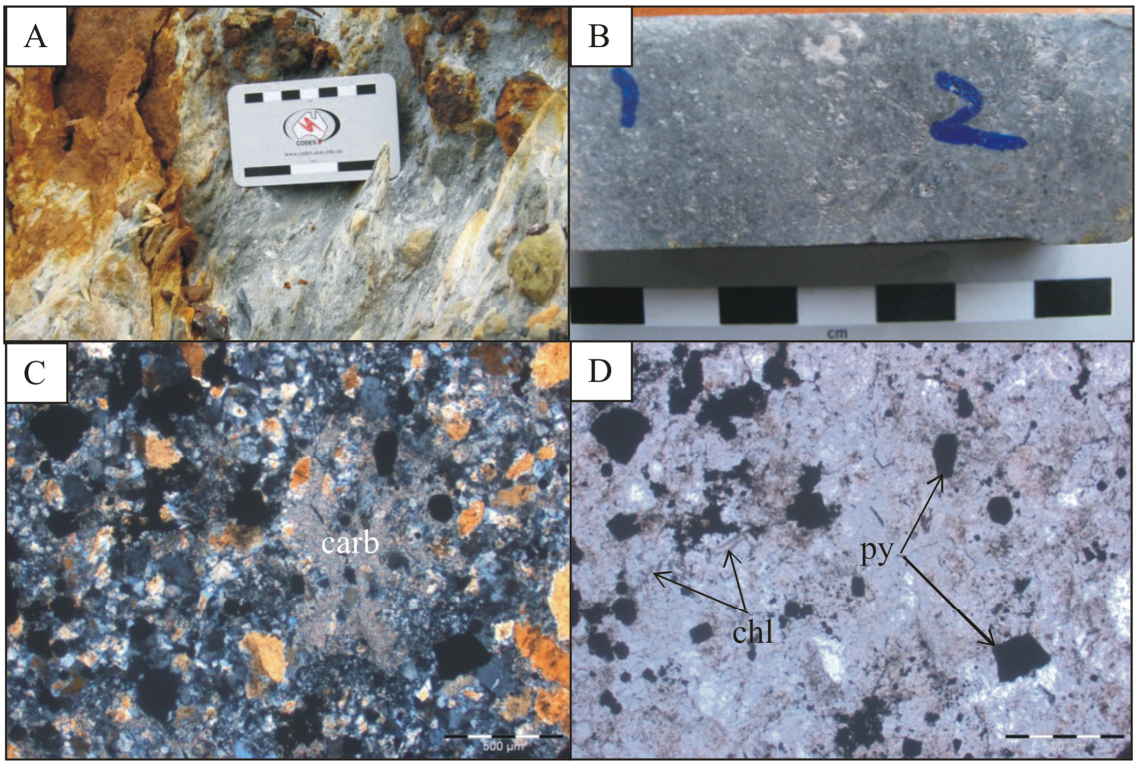

Fig. 5.27. Characteristics of quartz-chlorite-pyrite±carbonate±pyrophyllite alteration at Bukit Ketaya deposit. **A.** Outcrops of the quartz-chlorite-carbonate alteration at the rhyolite footwall of the weakly developed feeder zone at the Bukit Ketaya deposit. **B.** Representative sample of the quartz-chlorite-carbonate altered rock with abundant pyrite in disseminated grains and veinlets, Sample No. BKCL-3. **C.** Photomicrograph showing the quartz-chlorite-carbonate alteration characterised by the presence of significant carbonate and chlorite minerals throughout the recystallised rock groundmass, Sample No. SQT2-BK. Cross-polarised light. **D.** Same view as C showing some of the sericite replaced by fine-grained chlorite. Plane-polarised light. In addition, disseminated pyrite is also abundant. Annotation: carb = carbonate, qtz = quartz and chl = chlorite.

5.5.3 Lithogeochemistry results

5.5.3.1 Bukit Botol deposit

An alteration box plot based on the CCPI and the Ishikawa alteration index (AI) of Large et al. (2001a) of the altered rock samples from the Bukit Botol deposit are shown in Figure 5.28. The results indicate two main alteration trends with an increasing intensity towards the ore centre and are relatively consistent with the mineralogical and textural observation previously outlined in Section 5.5.2.1. In the box plots, both the ore horizon and footwall altered samples tend to plot along the right side of hydrothermal field and overlap in places.

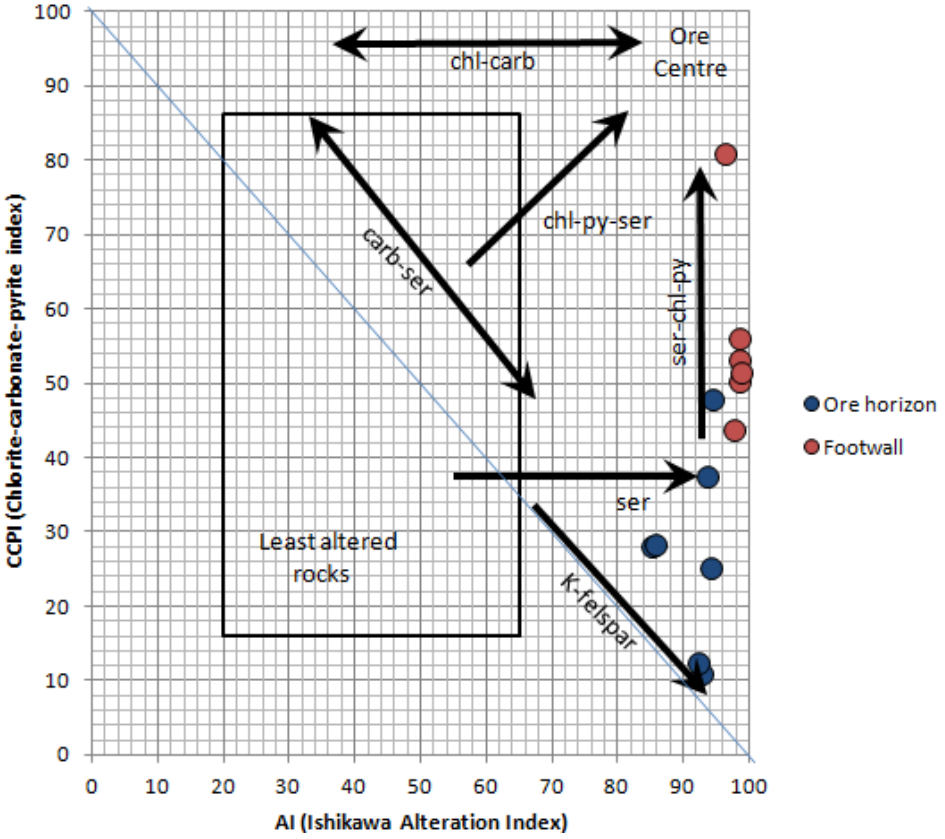

Fig. 5.28. Alteration box plots (modified after Large et al., 2001a) for lithogeochemical data from the ore horizon and footwall host rocks from the Bukit Botol deposit. Annotation: chl=chlorite, carb=carbonate, py=pyrite and ser=sericite.

The quartz-sericite±paragonite alteration assemblages in ore horizon rhyolite rocks has 85< AI <95 and 10< CCPI <50, forming a sericite-rich trend whereas the footwall samples from the quartz-sericite-pyrite±chlorite alteration tend to plot in a tight cluster toward the right corner and upper margins of the box within a restricted range of AI >95 and of CCPI >50, corresponding to the sericite-chlorite-pyrite trend.

The Na_2O/Al_2O_3 versus K_2O/Al_2O_3 molar ratio plot for the altered samples from Bukit Botol shows relatively overlapping trends among the ore horizon and footwall units with the variations of Na_2O and K_2O controlled mainly by muscovite and chlorite. Although, only a small range of Na_2O and K_2O with low values are displayed, the altered ore horizon samples mostly plot at and near the muscovite control point compared to the elevated Na_2O and K_2O of footwall samples toward the chlorite control point (Fig. 5.29A).

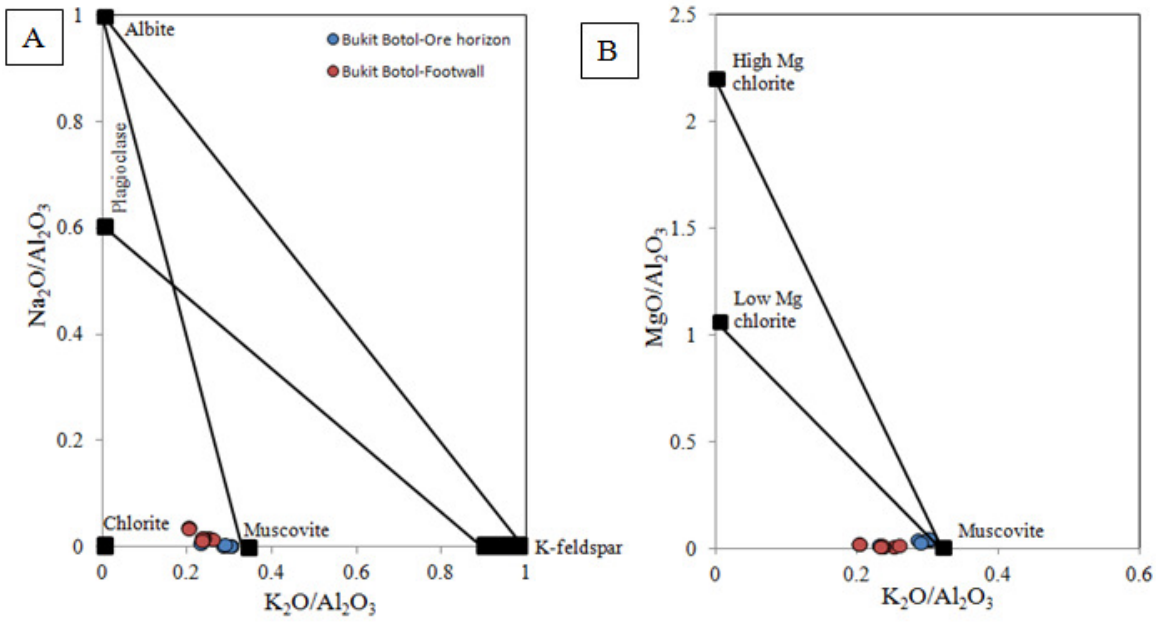

Fig. 5.29. Molar element ratio plot of Bukit Botol altered samples from the ore horizon and footwall units. **A.** K_2O/Al_2O_3 versus Na_2O/Al_2O_3. **B.** MgO/Al_2O_3 versus K_2O/Al_2O_3. The trend subdivisions after Davies and Whitehead (2006).

In the MgO/Al_2O_3 versus K_2O/Al_2O_3 molar ratio plot (Fig. 5.29B), most of the samples lie below the low Mg chlorite line and are MgO poor. However, they exhibit similar trends displayed by the Na_2O and K_2O ratios as discussed above, suggesting that the alterations are mostly controlled by muscovite, with lack of chlorite in footwall altered rocks.

5.5.3.2 Bukit Ketaya deposit

Lithogeochemical data from eight ore horizon rhyolite breccias and nine footwall rhyolite-rhyodacite successions from the Bukit Ketaya deposit are plotted in the alteration box plot in Figure 5.30. Comparable with the alteration mineral assemblages recognised in Section 5.5.2.2, the samples plotted were distinctly distinguished. On the box plot, both ore horizon quartz-chlorite-sericite-pyrite-pyrophyllite±kaolinite and footwall quartz-chlorite-pyrite±carbonate±pyrophyllite samples plot toward the upper margin of the diagram, except for two samples from the ore horizon rocks that fall in the field of least altered rhyolite. Both the alteration zones are characterised by higher CCPI values with variable AI values relative

to the least altered rhyolite. These trends resemble alteration assemblages of a chlorite-sericite-pyrite trend for the ore horizon and a chlorite-carbonate trend for the footwall rocks.

At the Bukit Ketaya deposit the Na_2O/Al_2O_3 versus K_2O/Al_2O_3 molar ratio plot clearly demonstrates that the ratios of Na_2O and K_2O of alteration assemblages are controlled by chlorite and muscovite, but the samples from each of the altered zones form distinctive groups. Ore horizon samples have relatively lower Na_2O and K_2O molar ratios than the footwall samples, and display a slight positive trend. Meanwhile, the footwall samples clearly show the negative correlation (Fig. 5.31A). The MgO/Al_2O_3 versus K_2O/Al_2O_3 molar ratio plot of both samples reveals that the chlorite is the lowest low Mg chlorite, but has a slightly higher value in the footwall than that of the ore horizon altered samples (Fig. 5.31B).

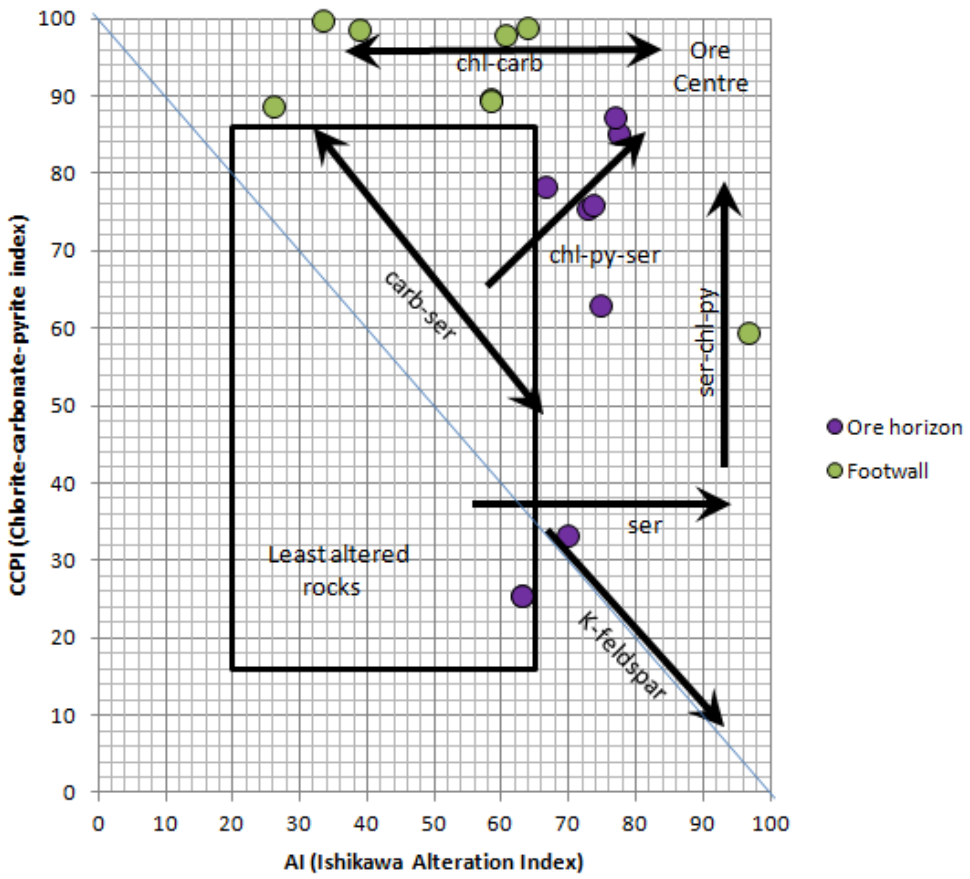

Fig. 5.30. Alteration box plots (modified after Large et al., 2001a) for lithogeochemical data from the ore horizon and footwall volcanic host rocks from the Bukit Ketaya deposit. Annotation: chl=chlorite, carb=carbonate, py=pyrite and ser=sericite.

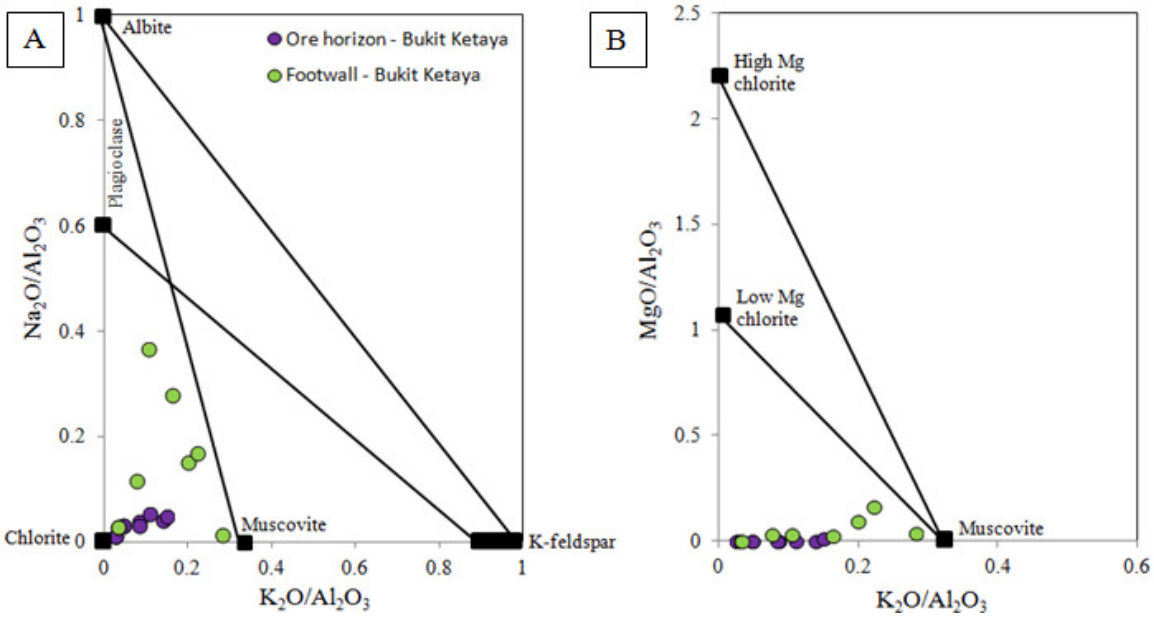

Fig. 5.31. Molar element ratio plot of Bukit Ketaya altered samples from the ore horizon and footwall units. **A.** K_2O/Al_2O_3 versus Na_2O/Al_2O_3. **B.** MgO/Al_2O_3 versus K_2O/Al_2O_3. The trend subdivisions after Davies and Whitehead (2006).

Additionally, the trends for both the Na_2O/Al_2O_3 versus K_2O/Al_2O_3 and MgO/Al_2O_3 versus K_2O/Al_2O_3 diagrams which plot toward the origin may be due to the presence of significant pyrophyllite or kaolinite in the alteration assemblages.

5.6 Discussion

5.6.1 Mineralisation characteristics

The Bukit Botol and Bukit Ketaya deposits have many similarities in their styles of mineralisation. At each deposit, the mineralisation shows distinct ore zonation forming stringer to massive sulphides at the footwall followed by barite and Fe+Mn±Si layers at the stratigraphic top, and exhibits conformable bedding or banding within felsic volcanic host rocks. These forms are consistent with a VHMS deposit formed at the seafloor because the presence of Fe+Mn±Si layers "exhalites" are diagnostic criteria of seafloor VHMS formation (e.g., Doyle and Allen, 2003), although this definition is intended to include subseafloor replacement immediately below the seafloor (e.g., Kalogeropoulus and Scott, 1983).

The sulphide mineral assemblages are largely pyrite as the major mineral, with subordinate chalcopyrite, sphalerite and rare galena. Additionally, traces of Sn- and Ag-bearing minerals, with gold, are also present in the massive sulphide and barite layers. Chalcopyrite, Ag-bearing minerals and gold are locally abundant at the Bukit Botol deposit, but were not observed at Bukit Ketaya deposit. In general, the sulphide assemblages of both Bukit Botol and Bukit Ketaya are comparable with descriptions of the VHMS class of deposits, as summarised by many workers including Franklin et al. (2005) and Galley et al. (2007). The association of Sn-bearing minerals with sphalerite indicates cogenetic formation similar to other VHMS deposits (e.g., Kidd Creek, Neves-Corvo; Hannington et al., 1999a; 1999b). With the exception of later stage barite and iron oxide precipitation during barite and Fe+Mn±Si layer formations, the local distribution of barite in the stockwork and massive sulphides in both the Bukit Botol and Bukit Ketaya deposits suggest that this barite developed as a result of hydrothermal and seawater fluid mixing similar to formation of barite recognised from the JADE active hydrothermal field in the Central Okinawa Trough by Luders et al. (2001).

Additionally, the Bukit Botol and Bukit Ketaya deposits most closely resemble the polymetallic lens and sheet-like deposits (e.g., Roseberry, Hellyer, Que River, Thalanga) when compared to the VHMS deposits of the Mount Read belt. According to Large (1992) and Large et al., (2001b), the Mount Read VHMS deposits range from Cu, Zn-Cu, and Zn-Pb-Cu types with varying amounts of Ag and Au and have varying morphologies from lens-shaped to sheet like (Zn-Pb-Cu and Zn-Cu type; e.g., Roseberry, Hellyer, Que River, Thalanga), to pipe and stringer deposits (Cu-Au type; e.g., Mount Lyell and Highway Reward).

5.6.2 Significance of Fe+Mn±Si layers

At both the Bukit Botol and Bukit Ketaya deposits, Fe+Mn±Si layers are closely associated with the massive sulphide mineralisation. They form as lenses or extensive layers of a few metres in thickness that can be traced along strike for over 50 metres, stratigraphically above and in the mine sequences. The stratigraphic continuity of these Fe+Mn±Si layers are identical to many ancient VHMS related jasper beds or siliceous iron formations deposits, including those at the Mount Windsor volcanic belt, Queensland (Duhig et al., 1992; Davidson et al., 2001); the Løkken ophiolite, Norway (Grenne and Vokes, 1990); the Mount Morgan deposit, Queensland (Taube, 1986); the Iberian Pyrite Belt, Spain and Portugal (Leistel et al., 1998), the Bathurst VHMS district, New Brunswick (Peter and Goodfellow, 1996); the Windy Craggy deposit in British Columbia (Peter and Scott, 1999) and several Kuroko and Noranda deposits (Kalogeropoulos and Scott, 1983; 1989).

The texture, mineralogy and chemical features of the Bukit Botol and Bukit Ketaya Fe+Mn±Si layers are also similar to other typical deposits of VHMS-associated exhalites as listed above. In both Bukit Botol and Bukit Ketaya deposits, Fe+Mn±Si layers display massive iron-silica banding that is transitional to microbreccia-like textures. Fine-grained hematite matrix and widespread cryptocrystalline quartz are the major compositions of the Fe-Mn and Fe-Si layers, and they comprise varying proportions of quartz, barite and clastic constituents (rhyolite-rhyodacite of ore horizon unit) with trace amounts of magnetite and pyrite, with an overall microbreccia-like texture. These textural and mineralogical features are mostly similar to mixed clastic and hydrothermal chemical deposits from the Kuroko and Noranda deposits particularly the Tetsusekiei of Fukazawa deposit, Japan (Kalogeropoulos and Scott, 1983); the tuffaceous exhalite of Millenbach deposit, Noranda (Kalogeropoulos and Scott, 1989) and the iron formations of Bathurst VHMS district, New Brunswick (Peter and Goodfellow, 1996).

In term of chemical signatures, the major and trace element compositions of Fe+Mn±Si layers demonstrate a contribution from both hydrothermal and possibly hydrogenous origins. The relatively high concentrations of Fe and Mn exhibited by the Fe-Mn layers, show characteristics of formation by hydrothermal and hydrogenous sediments on the seafloor (Slack et al., 2007), because the oxides and oxyhydroxides of these elements are essentially insoluble in oxic seawater and precipitate rapidly (e.g., Brezonik, 1994). In addition, significant enrichment of Cu, Pb, Zn, Ba, As and U shown in Fe-Mn layers, is typical for Mn and Fe oxides associated with felsic volcanism (hydrothermal sources) having high concentrations of As, Ba, Cu, Mo, Pb, Sr, V and Zn (Cruzat Ossa, 1970; Moore, 1971; Sillitoe, 1975; Zantop, 1981).

As mentioned by Panagos and Varnavas (1984), Fe compounds are less stable than Mn compounds, which means Fe tends to precipitate first close to its hydrothermal source, compared to Mn. Thus, the high Fe-enriched in the Bukit Ketaya deposit with moderate to low contents of trace elements (e.g., Mn, Cu, Pb, Zn, Ba, As, U) relative to the high Mn nature of the Bukit Botol Fe-Mn ores and other trace element (e.g., Fe, Cu, Pb, Zn, Ba, As, U) concentrations, may reflect differences in Fe/Mn or Mn/Fe ratios of the hydrothermal fluids, probably because of differences in location and spreading rate (e.g., German and Von Damm, 2003) due to Fe-Mn fractionation in fluid compositions of the local submarine environments. The Fe-Mn layers from the Bukit Ketaya deposit were interpreted to have first precipitated during the active hydrothermal cycle because high Fe/Mn ratios could be due to very high temperatures and near the critical point of the related vent fluids (e.g.,Von Damm et al., 2003). This cycle was followed by the precipitation of Fe-Mn layers with high Mn content at the Bukit Botol deposit because accumulation of oxidised Mn in rocks occurred due to the remoteness from hydrothermal sources (Brusnitsyn and Zhukov, 2012).

The associations of hematite and jasper (exhalites) with barite indicate an oxidising environment (e.g., Ohmoto and Skinner, 1983) where formation of barite was a result of the injection of acidic but reduced barium-bearing hydrothermal fluid into an oxidised sulphate bearing water trap (Large, 1977). As for both the Bukit Botol and Bukit Ketaya deposits, the close associations of Fe+Mn±Si and barite layers may indicate that the submarine environment was suboxic, which is also a common feature for VHMS deposits that occur in modern volcanic arc and back-arc settings (e.g., Hannington et al., 2005).

5.6.3 Alteration characteristics

Alteration assemblages developed at both the Bukit Botol and Bukit Ketaya sequences are significantly different between the two deposits. At the Bukit Botol deposit, the host felsic volcanic rocks are overprinted by two distinct hydrothermal alteration zones. An intense quartz-sericite-pyrite of the footwall represents a proximal zone and has Ishikawa (AI) indices higher than 95 and chlorite-carbonate-pyrite (CCPI) indices less than 60. A weak quartz-sericite assemblage occurs in the ore horizon rocks and represents a distal alteration zone. This zone has much lower AI (85-95) and CCPI less than 50. The hydrothermal zonations associated with the Bukit Botol deposit probably resemble the stratabound or semi-conformable quartz-sericite±chlorite-pyrite altered zone (e.g., Large, 1992) such as the Mount Chalmers deposit (Large and Both, 1980; Hunns, 2001) and the Brunswick No. 12 deposit, Canada (Yang et al., 2003).

Within the Bukit Botol deposit alteration zones, normal muscovite, phengite and paragonite were also identified on the SWIR profiles, and their assemblages can be clearly distinguished. In proximal alteration zones, the composition of muscovite shows a normal to phengitic muscovite, whereas the distal alteration zone is characterised by normal muscovite and paragonite. Molar element ratios of Na_2O/Al_2O_3 versus K_2O/Al_2O_3 and MgO/Al_2O_3 versus K_2O/Al_2O_3 demonstrate and support the formation of muscovite and chlorite as alteration

minerals controlled the intensity of alteration at the Bukit Botol deposit. The occurrence of phengite in the proximity of ore bodies has been described in several VHMS deposits such as Prince Lyell, Tasmania (Hendry, 1981) and Draa Sfar, Morocco (Belkabir et al., 2008). In addition, a distal paragonite zone surrounding the main sericite zone has also been described in the VHMS deposits of Aljustrel and Neves Corvo (Relvas et al., 1997).

Two types of alteration assemblages occur in the Bukit Ketaya deposit. The ore horizon rocks or distal alteration are characterised by quartz-chlorite-sericite-pyrite-pyrophyllite±kaolinite assemblages, whereas the weakly enveloped proximal alteration to the footwall is an intense quartz-chlorite-pyrite±carbonate±pyrophyllite assemblage. Both alteration zones are characterised by higher CCPI values more than 60 and variable AI values but slightly higher in the ore horizon than the footwall altered rocks. The Bukit Ketaya deposit also has a semi-conformable alteration type similar to that of the Bukit Botol deposit but probably demonstrates the chlorite altered zones described by Large (1992). Examples of the chlorite altered zones associated with VHMS deposits include the Woodlawn deposit, in Lachlan Fold Belt, NSW Australia and the Scuddle deposit, Western Australia (Large, 1992).

The SWIR spectra from both alterations show distinctive muscovite with minor pyrophyllite and paragonite but no chlorite spectral profile was identified. In addition, the XRD results also detect the presence of significance pyrophyllite, kaolinite and unidentified‘mica’. Chlorite was not identified in both alterations. However, molar element ratios of Na_2O/Al_2O_3 versus K_2O/Al_2O_3 and MgO/Al_2O_3 versus K_2O/Al_2O_3 show that chlorite and muscovite are the main alteration minerals reflecting the intensity of alteration at the Bukit Ketaya deposit, and the chlorite is mainly Mg-rich chlorite. Thus, it is evident that chlorite is present at both the alteration zone characteristics in the Bukit Ketaya deposit. However, the minor chlorite presence does not reflect on the XRD data identification; the mixed assemblages of muscovite

and carbonate have absorption features at the same wavelength as the MgOH feature of chlorite, so the degree of Fe and Mg exchange cannot be easily determined by SWIR (Herrman et al., 2001, Jones et al., 2005). These distributions probably indicate a chlorite alteration pattern with a proximal Mg-chlorite and an intermediate to Fe-chlorite distal zone (McLeod and Stanton, 1984). This pattern has been observed in several VHMS deposits such as Thalanga (Paulick et al., 2001), Noranda (Riverin and Hodgson, 1980), Myra Falls (Jones et al., 2005) and at the Kuroko deposits, Japan (Urabe et al., 1983). In addition, the presence of pyrophyllite and kaolinite has also been reported from a few VHMS deposits such as the Western Tharsis deposit, Mount Lyell, Tasmania (Huston and Kamprad, 2001), the LaRonde Penna deposit, Abitibi, Quebec (Dube et al., 2007) and from several VHMS deposits in the Iberian Pyrite Belts (Relvas et al., 1997). According to Huston et al. (2011), the presence of advanced argillic alteration assemblages, clearly suggesting a significant magmatic-hydrothermal contribution.

5.7 Summary

1) The Bukit Botol and Bukit Ketaya deposits are characterised by distinctive mineralisation features forming stringer to massive sulphides at the footwall followed by barite and Fe+Mn±Si layers at the top that are comparable with those seen in many ancient felsic-hosted VHMS deposits. Preservation of these distinct ore zonations on the seafloor are capped by the formation of Fe+Mn±Si layers or 'exhalites'.

2) The main sulphide phases common at both of the deposits are pyrite, chalcopyrite, sphalerite, rare galena and trace of Sn-bearing minerals. Ag-bearing and gold minerals are also present in the massive sulphide or barite ores and have been found locally at the Bukit Botol deposit, but are absent at the Bukit Ketaya deposit. Late hydrothermal activity resulted in the formation of barite and Fe+Mn±Si layers.

3) The field relationships, texture, mineralogy and chemical features of the Fe+Mn±Si layers

at both the deposits suggest that they were pure chemical sediments developed during formation of the massive sulphide deposit. The Fe+Mn±Si layers demonstrate a mixing of hydrothermal and hydrogenous origins. They were formed as a result of changing oxidation-reduction condition of fluid compositions with increasing distance from hydrothermal sources of the local submarine environments.

4) Different alteration assemblages were identified within the host volcanic rocks of the Bukit Botol and Bukit Ketaya deposits. These alteration zones form semi-conformable or stratabound-like alteration around both the deposits. The Bukit Botol deposit is characterised by proximal quartz-sericite-pyrite and distal quartz-sericite alteration zones, whereas distal quartz-chlorite-sericite-pyrite-pyrophyllite±kaolinite and proximal quartz-chlorite-pyrite±carbonate±pyrophyllite form the alteration assemblages of the Bukit Ketaya deposit. These data suggest that the different alteration assemblages may represent the deposits in one large hydrothermal system.

CHAPTER 6 MINERAL CHEMISTRY

6.1 Introduction

This Chapter describes the chemical compositions of sphalerite and pyrite from the Tasik Chini deposit. The primary objectives of this study are to evaluate:

- variations in trace element compositions of these minerals within the mineralised system
- variations in trace element contents among different textural varieties and paragenetic stages of the system
- chemical constraints on the ore−forming fluids

6.2 Sphalerite Chemistry

6.2.1 Introduction

Geochemical compositions of sphalerite can provide important information on the changes in temperature and chemistry of mineralising fluids (e.g., Barton and Bethke, 1987). Sphalerite is enriched by a wide variety of elements, such as Fe, Mn, Cd, Cu, Sn, Ag, Ga and In (Cook et al., 2009b), and is the most important source of indium in many tin polymetallic deposits (Murakami and Ishihara, 2013). The potential of the FeS contents as an indicator of sulphide deposition was first recognised by Kullerud (1953). The Fe composition of sphalerite in assemblages with pyrite and pyrrhotite is widely known as a sphalerite geobarometer (Scott, 1973), and it has been applied to measure the pressure and depth of many metamorphosed massive sulphide deposits with variable success (e.g., Hutchison and Scott, 1981; Moles, 1983; Sundblad et al., 1984; Brill, 1989; Khin Zaw, 1991; Khin Zaw and Large, 1996).

Sphalerite with low FeS contents (pale coloured sphalerite) forms at relatively low temperatures from oxidising solutions (Urabe, 1974; Hannington and Scott, 1989; Ames et al., 1993). Hannington et al. (1999a) used the FeS content of sphalerite in some Archean Canadian VHMS deposits to differentiate between high temperature Zn−Cu−rich (high FeS) and low temperature Zn−rich (low FeS) sulphide mineralisation. In actively forming seafloor hydrothermal deposits, the FeS contents of sphalerite show a wide variation from as low as 0 to 20 mole% FeS, ranging up to 44 mole% FeS (Hekinian et al., 1980; Scott, 1983; Peter and Scott, 1988; Moss and Scott, 2004). In other cases, Hill (1996) also interpreted the uniformly high FeS contents of sphalerite at Thalanga (8 to 12 mole% FeS) as relating to sphalerite−pyrite recrystallisation and re−equilibration during peak metamorphism.

6.2.2 Methods

The sphalerite compositions from the Bukit Botol and Bukit Ketaya deposits presented in this study were obtained in different mineralisation styles from the massive sulphide lenses and stockwork zones. The analysed sampels are from the same polished thin sections and mounted epoxy blocks used for transmitted and reflected microscopic observations. A total of seventy eight analyses were carried out on sphalerite: fifty four from the Bukit Botol deposit and twenty four from the Bukit Ketaya deposit. The sphalerite chosen for analysis was free of exsolved pyrite and chalcopyite.

Chemical analyses were made at the Central Science Laboratory (CSL), University of Tasmania using a Cameca SX50 electron microprobe with the following analytical conditions: acceleration voltage, 20 kV, beam current at 20 nA and 5−10 μm probe diameter. Raw count data were corrected using a ZAF correction program. Concentrations of 12 elements including S, Pb, Ag, Cu, Zn, Sn, Sb, As, Mn, Fe and Cd were determined at each point. However, compositions of Pb, Ag, Sn, Sb and As were very low or below detection limits. The standards

for correction were natural sphalerite (ZnS_2) for Zn and S, galena for Pb, marcasite for Fe, cassiterite for Sn, stibnite for Sb, cuprite for Cu, synthetic gallium–arsenide for As and synthetic pure metals Au, Ag and Cd.

6.2.3 Chemical compositions of sphalerite

6.2.3.1 FeS content

The chemical results of sphalerite from different types of mineralisations of the Bukit Botol and Bukit Ketaya deposits are shown in Appendix VII and the average chemical compositions of representative sphalerite are summarised in Tables 6.1, 6.2, 6.3 and 6.4. The FeS composition of sphalerite for the Bukit Botol deposit exhibits a consistent value from 0 to 24.0 mole% FeS. A uniform level of FeS in massive sulphide ranging from 0.3 to 1.8 mole% FeS (n=54) is distinguished from the wide range of values in FeS content from 4.5 to 23.5 mole% FeS (n=24) in the stringer zone (Fig. 6.1).

Table 6.1. Average chemical compositions of the representative sphalerite in a massive sulphide lens from the Bukit Botol deposit, Central Peninsular Malaysia.

Deposit	**Bukit Botol**						
Ore type/Sample	MS: BB1d	MS: BB1d–A	MS: BB1d–B	MS: BB1d–C	MS: BB1d–D	MS: BB1d–E	MS: BB1d–F
No. spot	10	6	10	5	8	5	10
wt% S	32.98	33.08	33.14	33.23	33.08	32.91	32.90
Pb	<0.10	<0.10	<0.10	0.10	<0.10	<0.10	0.13
Ag	0.07	0.10	0.07	<0.07	<0.07	0.11	0.08
Cu	0.21	0.34	0.13	0.26	0.17	0.11	0.11
Zn	66.01	65.72	66.11	65.91	65.81	66.13	66.09
Sn	<0.03	<0.03	<0.03	<0.03	<0.03	<0.03	<0.03
Sb	<0.03	<0.03	0.04	<0.03	0.05	<0.03	0.04
As	0.03	<0.02	<0.02	<0.02	<0.02	<0.02	<0.02
Mn	0.00	0.00	0.09	0.01	0.00	0.00	0.01
Fe	0.38	0.51	0.43	0.50	0.40	0.23	0.22
Cd	0.53	0.53	0.53	0.56	0.57	0.54	0.51
Total	100.14	100.22	100.43	100.50	100.04	99.96	99.88
Mole%							
FeS	0.64	0.86	0.71	0.84	0.67	0.39	0.37
CdS	0.54	0.54	0.53	0.57	0.58	0.55	0.52
MnS	0.00	0.00	0.16	0.02	0.00	0.00	0.01
ZnS	40.00	50.00	50.00	50.00	50.00	50.00	50.00

Annotations: MS=massive sulphide lens.

Table 6.2. Average chemical compositions of the representative sphalerite in a stringer zone from the Bukit Botol deposit, Central Peninsular Malaysia.

Deposit	**Bukit Botol**						
Ore type/Sample	SZ: BB2b	SZ: BB2b–A	SZ: BB2b–B	SZ: BB2b–C	SZ: BB2b–2A	SZ: BB2b–2B	SZ: BBotolDump–1
No. spot	3	1	3	3	2	7	5
wt% S	34.21	36.07	32.89	32.71	32.70	33.03	32.81
Pb	0.16	<0.10	<0.10	0.12	0.18	0.20	<0.10
Ag	0.09	0.09	0.08	0.07	0.20	0.11	0.07
Cu	4.09	1.26	3.85	1.89	2.81	6.39	4.37
Zn	53.79	54.94	58.65	62.35	60.44	53.48	57.25
Sn	<0.03	<0.03	<0.03	<0.03	<0.03	0.03	<0.03
Sb	<0.03	0.04	<0.03	<0.03	<0.03	<0.03	0.04
As	<0.02	<0.02	<0.02	<0.02	<0.02	<0.02	0.03
Mn	0.00	0.01	0.00	0.00	0.00	0.00	0.00
Fe	7.23	8.01	4.05	2.67	3.47	6.50	4.73
Cd	0.22	0.24	0.24	0.26	0.28	0.23	0.22
Total	99.63	100.66	99.73	99.93	99.98	99.71	99.41
Mole%							
FeS	13.36	13.92	7.27	4.53	6.02	12.30	8.67
CdS	0.28	0.29	0.27	0.28	0.31	0.29	0.25
MnS	0.00	0.03	0.00	0.00	0.00	0.00	0.00
ZnS	50.00	50.00	50.00	50.00	50.00	42.86	50.00

Annotations: SZ=stringer zone.

Table 6.3. Average chemical compositions of the representative sphalerite in a massive sulphide layer from the Bukit Ketaya deposit, Central Peninsular Malaysia.

Deposit	**Bukit Ketaya**								
Ore type/Sample	MS:BMSE1	MS:BMSE1–A	MS: BK11A	MS: BK11B	MS: BK11	MS: BK11–A	MS: BK11–B	MS: BK11–C	MS:BK11–D
No. spot	3	3	3	3	4	8	6	10	5
wt% S	32.93	32.76	33.07	33.08	32.26	32.46	32.35	32.37	32.57
Pb	<0.10	<0.10	<0.10	<0.10	0.14	<0.10	<0.10	<0.10	0.13
Ag	<0.06	0.06	0.09	<0.06	0.09	0.07	<0.06	0.07	0.08
Cu	0.09	0.19	0.08	0.05	0.05	0.06	0.05	0.04	0.06
Zn	66.63	66.45	66.59	66.64	64.70	66.04	65.89	66.21	64.91
Sn	<0.03	<0.03	<0.03	<0.03	<0.03	<0.03	<0.03	<0.03	<0.03
Sb	<0.03	<0.03	0.05	<0.03	0.07	<0.03	<0.03	<0.03	<0.03
As	<0.02	<0.02	<0.02	<0.02	0.03	<0.02	<0.02	<0.02	<0.02
Mn	0.00	0.00	0.01	0.00	0.00	0.00	0.00	0.01	0.00
Fe	0.39	0.50	0.35	0.19	0.20	0.19	0.19	0.29	0.18
Cd	0.23	0.25	0.18	0.20	0.21	0.21	0.20	0.20	0.20
Total	100.28	100.18	100.37	100.16	97.52	98.99	98.68	99.11	97.95
Mole%									
FeS	0.65	0.84	0.59	0.32	0.33	0.32	0.32	0.49	0.30
CdS	0.24	0.25	0.18	0.20	0.22	0.21	0.21	0.20	0.20
MnS	0.00	0.00	0.02	0.01	0.00	0.00	0.00	0.01	0.01
ZnS	50.00	50.00	50.00	50.00	50.00	50.00	50.00	50.00	50.00

Annotations: MS=massive sulphide lens.

In comparison, there are no significant variations in FeS content among the sphalerites of different types of mineralisation from the Bukit Ketaya deposit. The FeS content in sphalerite is more homogeneous, and displays low values with a narrow compositional range of 0.3–1.2 mole% FeS (average= 0.4 mole% FeS; n=45) from massive sulphide to a slight increase in the stringer zone at a range of 0.7–2.5 mole% FeS (average= 1.0 mole% FeS; n=48) (Fig. 6.1).

Table 6.4. Average chemical compositions of the representative sphalerite in the stringer zone from the Bukit Ketaya deposit, Central Peninsular Malaysia.

Deposit	**Bukit Ketaya**							
Ore type/Sample	SZ: BKCL1	SZ: BKCL1−A	SZ: BKCL1−B	SZ: BKCL1−C	SZ: BKCL1−D	SZ: BKCL1−E	SZ: BKCL1−F	SZ:BK12a
No. spot	6	5	6	7	7	10	4	3
wt% S	33.07	33.13	32.98	33.06	33.02	33.09	33.30	33.07
Pb	<0.10	<0.10	<0.10	<0.10	0.15	0.12	<0.10	<0.10
Ag	<0.06	<0.06	<0.06	0.07	0.08	0.09	0.06	<0.06
Cu	0.20	0.17	0.53	0.07	0.08	0.10	0.37	0.75
Zn	65.85	65.98	65.16	66.08	65.99	65.86	64.57	64.97
Sn	<0.03	<0.03	<0.03	<0.03	0.03	<0.03	<0.03	<0.03
Sb	<0.03	<0.03	<0.03	<0.03	0.04	<0.03	<0.03	<0.03
As	<0.02	<0.02	<0.02	<0.02	0.03	<0.02	<0.02	<0.02
Mn	0.05	0.05	0.01	0.13	0.06	0.03	0.00	0.02
Fe	0.64	0.55	0.83	0.53	0.58	0.52	0.71	0.87
Cd	0.30	0.29	0.30	0.27	0.27	0.30	0.29	0.52
Total	100.12	100.17	99.82	100.15	100.06	99.94	99.26	100.21
Mole%								
FeS	1.07	0.92	1.40	0.88	0.96	0.87	1.20	1.46
CdS	0.31	0.29	0.31	0.28	0.28	0.30	0.30	0.54
MnS	0.08	0.08	0.02	0.22	0.10	0.05	0.01	0.04
ZnS	50.00	50.00	50.00	50.00	50.00	50.00	50.00	50.00

Annotations: SZ=stringer zone.

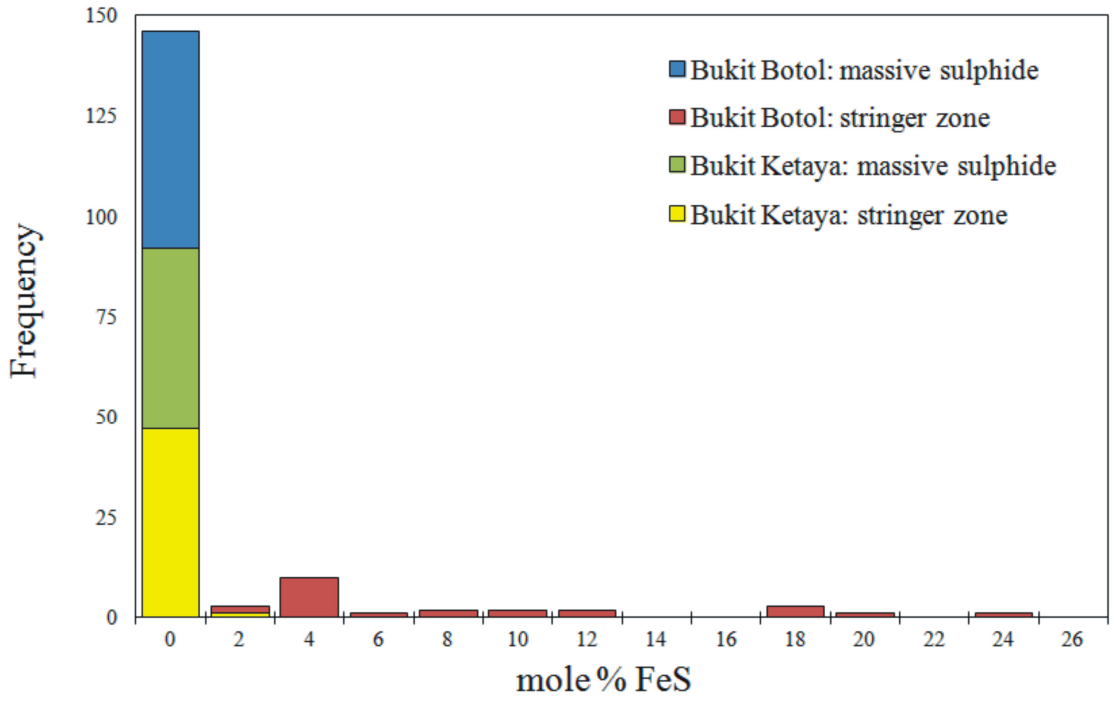

Fig. 6.1. Frequency distributions diagram for the mole% FeS in sphalerite from the Bukit Botol and Bukit Ketaya deposits, Central Peninsular Malaysia.

6.2.3.2 Minor element contents

Minor elements in sphalerite of the Bukit Botol and Bukit Ketaya deposits are Cu, Mn and Cd. The Cu contents range from 700 to 35,000 ppm. The Cd values are within 2100 to 5400 ppm and the Mn contents are slightly lower, having a range of 0 to 1700 ppm. Excluding the Cd

contents, the compositions of Cu and Mn show a more uniform enrichment in the stringer zone than those in the massive sulphide lenses at the both deposits. The concentration of Ag is very low but where present the value is up to 0.20 wt% (2000 ppm), whereas the Pb, Sn, As and Sb contents are below detection limits.

On the mole% FeS versus mole% MnS diagram (Fig. 6.2A), the MnS concentrations of sphalerite show an extremely low and nearly constant value for the two mineralisation types at both deposits. Sphalerite from Bukit Botol deposit contains <0.1 mole% MnS, whereas sphalerite from the Bukit Ketaya deposit has a slightly higher content, up to 0.2 mole% MnS.

The correlation between the FeS and CdS compositions of the sphalerite from both the Bukit Botol and Bukit Ketaya deposits are shown in Figure 6.2B. The CdS concentrations of all the studied samples are mainly in the range of 0.2 to 0.6 mole% CdS. The mole% CdS in the sphalerite from massive sulphide at Bukit Botol is significantly higher than that from the stringer sulphide. The Cd value is generally more than 0.5 mole% CdS for the sphalerite in the massive sulphide, whereas nearly constant (about 0.3 mole% CdS) recorded in the sphalerite from the stringer sulphide. In comparison, sphalerites from both the massive and stringer sulphides of the Bukit Ketaya display a narrow range from 0.2 to 0.3 mole% CdS.

In a FeS−MnS−CdS ternary diagram (Fig. 6.3), the sphalerite compositions from the Bukit Botol and Bukit Ketaya deposits show a variable field. Sphalerite from the Bukit Botol deposit shows two populations. The sphalerite from the massive sulphide has higher MnS with variable CdS contents, whereas the sphalerite in the stringer zone contains low MnS but high FeS with very low CdS composition. In contrast, sphalerites from Bukit Ketaya have uniform characteristics of high MnS concentrations with variable CdS contents in both those from the massive and stringer sulphide zones.

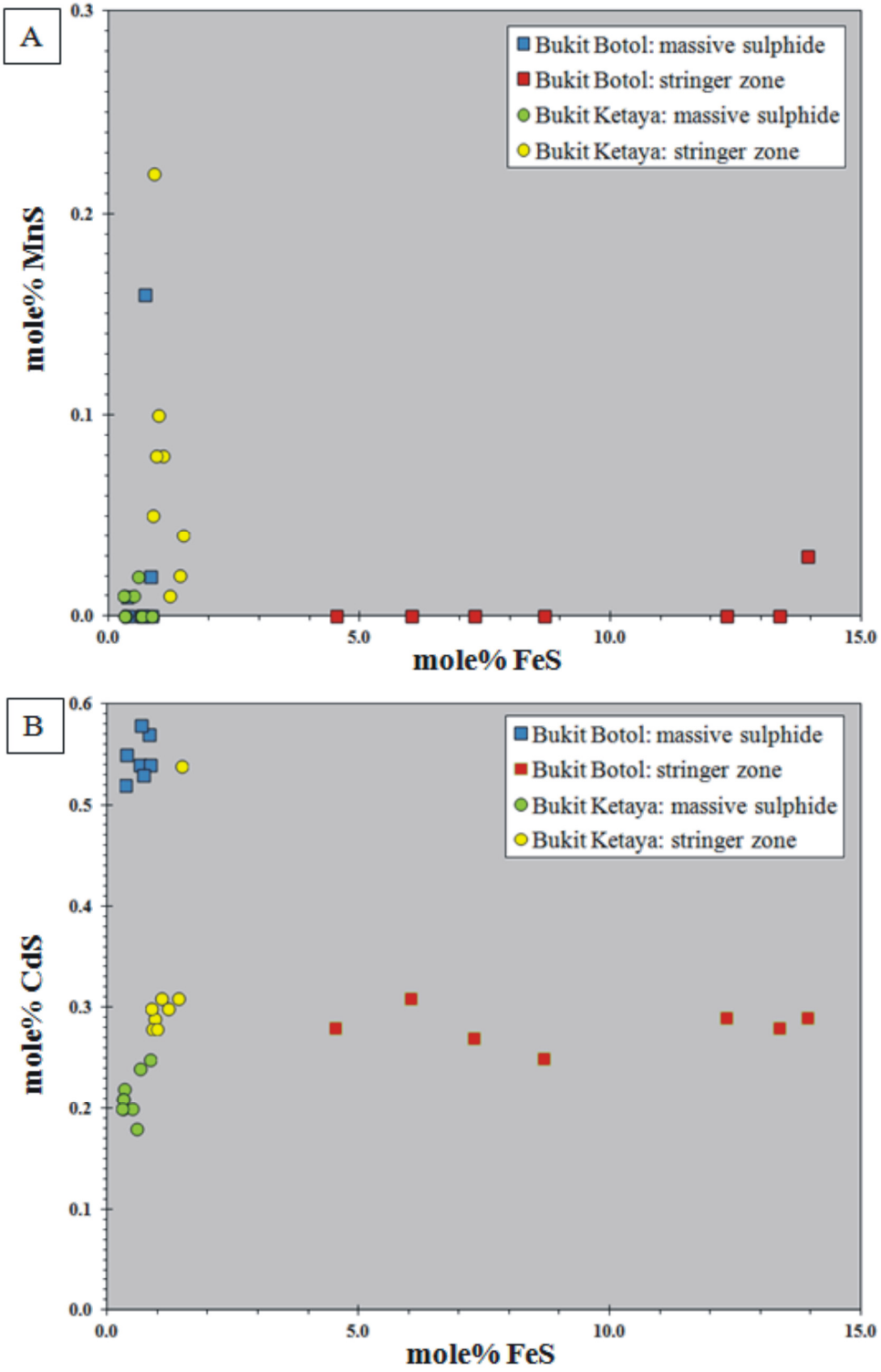

Fig. 6.2. Plot showing mole% FeS, MnS and CdS variations in sphalerite from the Bukit Botol and Bukit Ketaya deposits, Central Peninsular Malaysia. **A.** The relations between mole% MnS and mole% FeS. **B.** The relationships between mole% CdS and mole% FeS.

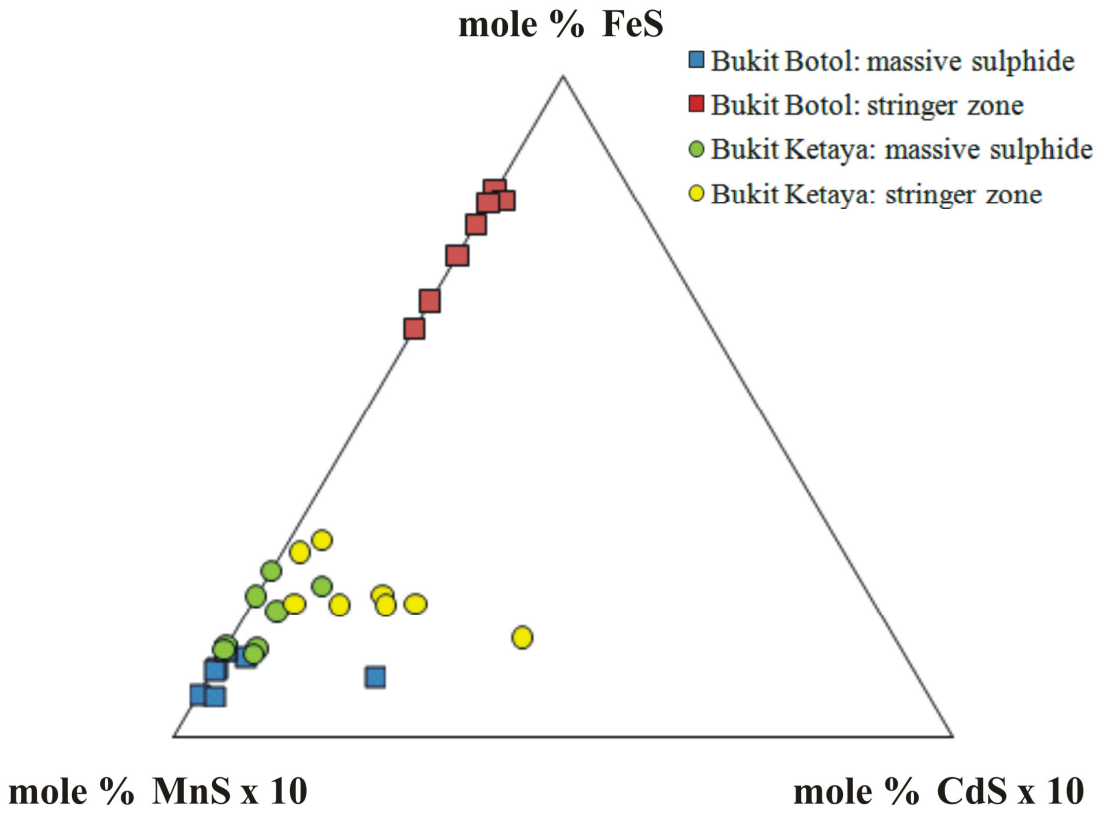

Fig. 6.3. A ternary diagram of mole% FeS – mole% MnS x 10 – mole% CdS x 10 compositions in sphalerite from the Bukit Botol and Bukit Ketaya deposits, Central Peninsular Malaysia.

Table 6.5 displays the average values of Zn/Mn, Zn/Cd and Zn/Fe of sphalerite from different mineralisation styles at the Bukit Botol and Bukit Ketaya deposits. It is also noted that the higher Zn/Mn (1149), lower Zn/Cd (123), and higher Zn/Fe (200) values of sphalerite in massive sulphide compared with the sphalerite in stringer sulphide Zn/Mn (256), Zn/Cd (240) and Zn/Fe (16) are clearly shown from the Bukit Botol deposit. However, only small variations of Zn/Mn, Zn/Cd, and Zn/Fe ratios are displayed by sphalerite associated with the massive and stringer sulphides from the Bukit Ketaya deposit. The massive sulphide shows average Zn/Mn (854), Zn/Cd (320) and Zn/Fe (278), whereas the stringer sulphides exhibits Zn/Mn (1161), Zn/Cd (218) and Zn/Fe (111).

Table 6.5. Average Zn/Mn, Zn/Cd, and Zn/Fe ratios of sphalerites from the Bukit Botol and Bukit Ketaya deposits.

Deposit & ore types	Zn/Mn ratio	Zn/Cd ratio	Zn/Fe ratio
Bukit Botol			
massive sulphide (n=7)	1149	123	200
stringer sulphide (n=7)	256	240	16
Bukit Ketaya			
massive sulphide (n=9)	854	320	278
stringer sulphide (n=8)	1161	218	111

6.3 Pyrite Geochemistry

6.3.1 Introduction

Pyrite is the most abundant sulphide constituent in many types of ore deposits, sustained during metamorphism (low to high grade) (Craig et al., 1998), which makes it a potential indicator of fluid compositions and ore genesis (Cook and Chryssoulis, 1990; Large et al., 2009). Pyrite can contain minor elements such as Au, Ag, Cu, Pb, Zn, Co, Ni, As, Sb, Se, Te, Hg, Tl, and Bi (Cook and Chryssoulis, 1990; Fleet et al., 1993; Huston et al., 1995b; Hannington et al., 1999a; Large et al., 1999, 2009; Palenik et al., 2004; Vaughan and Kyin, 2004; Reich et al., 2005, 2006; Yamaguchi and Ohmoto, 2006; Barker et al., 2009; Cook et al., 2009a; Deditius et al., 2009a, b, 2011; Sung et al., 2009; Koglin et al., 2010; Ulrich et al., 2011) that commonly persist through metamorphism (Craig et al., 1998).

However, the minor and trace element chemistry studies of pyrite from VHMS deposits are very limited. One of the more comprehensive studies is that of Huston et al. (1995), who investigated the concentrations of Cu, Zn, Pb, Ba, Bi, Ag, Sb, As, Tl, Au, Mo Co, Ni, Se and Te in pyrite and other sulphides from six VHMS deposits in Australia. Analyses were obtained using a proton microprobe. The authors divided the elements into three groups, namely:– (1) elements that are considered to be present in pyrite mainly in the form of inclusions of other phases (Cu, Zn, Pb, Ba, Bi, Ag and Sb), (2) elements that enter the pyrite lattice via non

stoichiometric substitution during mineral formation (As, Tl, Au and possibly Mo), (3) elements that enter the pyrite lattice via stoichiometric substitution (Co, Ni, Se and Te).

6.3.2 Methods

Analysis of pyrite was carried out on polished mounted epoxy blocks from Bukit Botol deposit samples. The chemical composition of pyrite was determined by multi element LA−ICPMS spot analysis and element imaging using Agilent HP 7700 and HP 4500 Quadrupole instrument at the CODES LA−ICPMS analytical facility, University of Tasmania.

Spot analysis

Spot analysis was performed by ablating spots ranging in size from 40 to 60 μm, depending on the size of ablated pyrite. Laser repetition rate was typically 5 Hz and laser beam energy at the sample was maintained between 4 and 5 J/cm2. Data for each sample were collected during 100 s, comprising a 30−s measurement of background (laser off) and a 70−s analysis with laser on. Acquisition time for all masses was set to 0.02 s. Data reduction was undertaken according to standard methods (Longerich et al., 1996). Fe was used as the internal standard for quantification of pyrite and chalcopyrite and Zn was used as an internal standard for quantification of sphalerite. Concentrations of the internal standard were calculated assuming stoichiometry. In cases when a significant degree of fine−grained mineral intergrowth occurred within the ablated volume, values for the internal standard concentration were adjusted such that the total of major elements (Fe, Cu, Zn, and S, the latter calculated assuming stoichiomentry) is 100 percent.

An in−house Li borate fused glass of a pyrite and/or sphalerite mixture (Danyushevsky et al., 2003, Danyushevsk et al., 2011) was used as the primary calibration standard. The standard was analyzed twice every one and a half hours to account for the instrument drift, with a 100−μm beam and at 10 Hz. The elements analysed were Al, Si, Ti, V, Cr, Mn, Fe, Co, Ni, Cu, Zn, As, Se, Mo, Ag, Sb, Te, W, Pt, Au, Hg, Tl, Pb, Bi and U.

Image analysis

The pyrite imaging was performed by ablating an equally spaced set of parallel lines across pyrite grains. A beam size of 15 μm or 25 μm was ablated for the lines set with energy of 3.5 J/cm2 at a frequency of 10 Hz traveling at a speed of 15 or 25 μm/s. This results in an unprocessed effective resolution that matches the beam size. Each individual sweep forms a single pixel in the image, around 5 microns in size, assuming a sweep time of ~0.2 second and speed of 25μms^{-1}. Samples were ablated to a depth of approximately 5 microns, estimated from the depth of ablation in a single shot (0.5 μm) and the number of shots in a single point of the sample (repetition rate = 10).

A set of 20 elements was chosen for analysis, with acquisition time for the majority of elements set to 0.002 second; exceptions were Se (0.004 s), and Ag, Te and Au (0.04 s). Total sweep time was ~0.2 second. A 13 second delay was left after each line to allow for cell washout. Background levels and drift were measured on the primary standard before and after every image (Danyushevsky et al., 2011). Maps were generally generated over a period of one to two hours where drift in sensitivity is minimal. Occasionally larger maps were generated and a drift correction was undertaken, with instrument drift considered to be linear between the standards. Image processing involved drift correction (if necessary), application of a median filter to remove artefacts generated during processing, subtraction of background from filtered counts, replacement of filtered counts less than background with the standard deviation value for that element; finally, images were produced for each element using a logarithmic colour scale. Re−deposition of the sample was kept to a minimum by pre−ablating each line immediately prior to analysis.

For each image, the elements analysed were Na, Mg, Al, S, K, Ca, Ti, V, Cr, Mn, Fe, Co, Ni, Cu, Zn, As, Se, Mo, Ag, Sb, Te, W, Pt, Au, Hg, Tl, Pb, Bi and U with a total ICP−MS detector

sweep time of ~0.2 s. Line data was compiled, converted to spatial coordinates and imaged using an in−house software package (Large et al., 2009).

6.3.3 Chemical compositions of pyrite

6.3.3.1 Spot analysis

The thirty three LA−ICPMS spot analyses measured for this study are derived from the representative of the three pyrite types distinguished at Bukit Botol deposit (see Section 5.4.1 in Chapter 5). Table 6.6 presents the results of the pyrite analyses that include fifteen measurements of pyrite 1 (py1), ten of pyrite 2 (py2) and seven of pyrite 3 (py3).

Table 6.6. LA−ICPMS analyses of selected pyrite types from the Bukit Botol deposit, Central Peninsular Malaysia.

Sample no.	Analysis no.	Mineral	Au (ppm)	As (ppm)	Ag (ppm)	Al (ppm)	Ti (ppm)	V (ppm)	Cr (ppm)	Mn (ppm)	Fe IS	Co (ppm)	Ni (ppm)
Bukit Botol													
BB02/bluepy1	JL13A03	py1	0.28	885.1	432.6	141.7	<4.24	0.5	3.8	503.5	465000.0	4.1	21.4
BB02/bluepy2	JL13A04	py1	0.20	1163.7	287.9	312.6	21.5	0.8	<3.76	356.5	465000.0	6.4	26.9
BB02/bluepy3	JL13A05	py1	0.17	1059.1	102.6	144.8	<7.71	0.3	<7.75	93.7	465000.0	7.9	22.5
BB02/bluepy4	JL13A06	py1	0.24	1302.4	344.7	150.9	<3.90	0.7	4.4	184.7	465000.0	8.7	27.8
BB02/bluepy8	JL13A010	py1	0.47	689.9	56.3	1442.1	31.7	1.9	2.5	296.7	465000.0	0.2	14.1
MBTCS1/TOP	JL13A027	py1	2.65	8511.4	595.6	12.1	4.4	3.4	6.5	2383.9	465000.0	145.2	34.3
MBTCS1/TOP	JL13A029	py1	1.29	1241.7	224.5	181.8	19.1	0.9	<3.02	10.4	465000.0	304.2	14.9
MBTCS1/TOP	JL13A039	py1	3.44	3555.8	242.7	250.6	7448.7	31.4	24.1	582.3	465000.0	559.0	22.1
MBTCS1/TOP	JL13A040	py1	3.24	2910.3	613.4	925.4	35.4	15.5	25.9	285.3	465000.0	280.4	46.0
BB01/top	JL13A018	py1	1.45	2593.0	787.3	88.3	35.3	2.4	<4.78	126.5	465000.0	98.3	11.8
BB01/top	JL13A019	py1	1.69	1735.8	1213.9	73.1	71.7	1.4	<3.55	162.0	465000.0	143.9	22.2
BB01/top	JL13A020	py1	1.38	2012.6	1362.6	1958.0	112.6	10.4	5.1	53.8	465000.0	55.9	19.5
BB01/top	JL13A023	py1	1.81	2001.4	1400.7	36.7	282.2	2.3	4.8	136.2	465000.0	164.0	35.4
MBTCS1/TOP	JL13A030	py1	1.00	882.4	76.1	109.2	10.2	0.5	3.7	16.9	465000.0	279.6	8.2
MBTCS1/Others	JL13A035	py1	3.09	2695.0	107.5	149.2	4.7	0.2	<3.29	5.6	465000.0	1078.2	35.2
	mean		1.49	2216.0	523.2	398.4	538.5	4.8	5.4	346.5	465000.0	209.1	24.2
BB02/bluepy5	JL13A07	py2	<0.06	1214.4	44.0	69.4	<3.47	0.2	<4.53	140.9	465000.0	2.9	29.6
BB02/bluepy6	JL13A08	py2	0.08	932.7	18.5	64.3	73.1	0.2	<4.37	137.5	465000.0	6.5	139.2
BB02/bluepy7	JL13A09	py2	0.14	1408.6	185.8	177.6	4.2	0.4	5.1	121.4	465000.0	5.3	30.9
BB02/bluepy9	JL13A011	py2	0.06	998.9	29.2	1092.2	6.3	1.6	7.4	315.0	465000.0	6.8	68.0
BB02/bluepy10	JL13A012	py2	0.24	1934.7	95.5	288.1	3.8	0.6	11.4	148.2	465000.0	12.1	97.9
BB02/bluepy11	JL13A013	py2	0.29	1241.8	91.3	387.7	20.6	1.5	12.5	250.5	465000.0	4.3	45.3
BB01/top	JL13A022	py2	3.06	3746.5	1841.9	214.6	445.3	4.9	13.1	348.0	465000.0	188.5	40.6
BB01/top	JL13A024	py2	0.72	1469.5	322.3	433.7	97.1	0.4	<3.27	120.4	465000.0	59.7	87.1
MBTCS1/TOP	JL13A031	py2	2.64	4768.9	194.3	216.4	20.7	5.9	9.6	876.9	465000.0	63.7	46.9
MBTCS1/Others	JL13A036	py2	2.45	2231.8	221.0	8.7	<3.41	0.2	3.0	20.2	465000.0	1192.2	28.1
	mean		0.97	1994.8	304.4	295.3	67.1	1.6	6.2	247.9	465000.0	154.2	61.4
BB01/top	JL13A021	py3	0.14	630.5	88.4	62.0	16.7	0.2	<3.74	26.6	465000.0	33.8	1.8
MBTCS1/TOP	JL13A028	py3	0.18	203.1	3.4	1.7	<4.26	<0.1	<2.63	<0.8	465000.0	83.1	4.3
MBTCS1/TOP	JL13A032	py3	0.12	5001.7	12.0	318.1	<4.00	1.3	3.7	56.9	465000.0	59.4	10.3
MBTCS1/Others	JL13A033	py3	<0.04	1730.7	1.7	1.9	<3.57	0.8	<2.82	2.4	465000.0	483.8	61.5
MBTCS1/Others	JL13A034	py3	<0.04	4384.6	0.1	1.4	<3.96	<0.1	<2.73	0.9	465000.0	400.5	88.3
MBTCS1/Others	JL13A037	py3	0.31	89.9	39.0	27.0	10.0	0.2	<2.40	23.2	465000.0	26.0	4.2
MBTCS1/Others	JL13A038	py3	0.20	195.6	15.2	13.0	4.5	0.7	<3.01	0.9	465000.0	711.1	24.0
	mean		0.14	1748.0	22.8	60.7	4.5	0.4	0.5	15.8	465000.0	256.8	27.8

Annotations: py1 = fine−grained anhedral spongy to elongate pyrite, py2 = medium coarse−grained anhedral−subhedral pyrite, p3 = coarse−grained subhedral to euhedral pyrite and IS = internal standard.

Py1 is enriched in trace elements of V, Mn, Cu, Zn, Mo, Ag, W, Pb and Bi, whereas the contents of Ni (mean = 24 ppm), Sb (10–385 ppm; mean = 71 ppm) and Tl (mean = 30 ppm) are relatively low in py1. Gold in py1 is also detectable and has concentration varying from 0.17 to 3.44 ppm. A representative spot analysis within the py1 texture is shown in Fig. 6.4. The relatively uniform counts for the Fe, Bi, Pb, Ag, As, Mn, Sb, Mo, Te, Ni and Au elements, suggest that these elements are bounded in the py1.

Table 6.6. LA–ICPMS analyses of selected pyrite types from the Bukit Botol deposit, Central Peninsular Malaysia (Cont.).

Sample no.	Analysis no.	Mineral	Cu (ppm)	Zn (ppm)	Se (ppm)	Mo (ppm)	Sb (ppm)	Te (ppm)	W (ppm)	Tl (ppm)	Pb (ppm)	Bi (ppm)	U (ppm)
Bukit Botol													
BB2/bluepy1	JL13A03	py1	1179.8	47.4	88.5	1.7	18.7	1.1	0.5	4.6	518.0	50.1	0.5
BB2/bluepy2	JL13A04	py1	1152.0	34.3	61.4	5.8	24.4	0.9	1.0	8.9	490.3	38.1	10.0
BB2/bluepy3	JL13A05	py1	717.9	17.2	42.4	2.9	19.6	1.3	1.6	7.1	284.8	55.7	1.5
BB2/bluepy4	JL13A06	py1	1218.4	22.7	56.7	5.7	24.2	1.2	0.9	9.2	415.8	46.2	0.3
BB2/bluepy8	JL13A010	py1	46234.0	20.1	21.0	0.3	30.2	0.9	1.2	201.2	1094.9	63.5	0.1
MBTCS1/TOP	JL13A027	py1	1526.8	184.6	130.8	135.5	310.3	49.4	1.0	94.9	2536.9	1002.4	<0.013
MBTCS1/TOP	JL13A029	py1	2554.3	31.7	318.5	231.0	23.4	25.2	14.9	1.1	1852.0	433.1	0.9
MBTCS1/TOP	JL13A039	py1	7755.6	27.6	262.8	649.9	21.4	36.5	102.6	10.2	2177.4	684.8	12.7
MBTCS1/TOP	JL13A040	py1	7234.0	280.1	778.7	98.2	37.0	91.3	10.9	70.2	9477.4	1877.0	0.9
BB1/top	JL13A018	py1	2875.0	131.7	647.9	62.3	44.3	50.8	12.7	0.9	366.3	735.1	2.0
BB1/top	JL13A019	py1	3616.8	84.1	353.7	191.0	39.0	61.4	8.8	2.4	528.2	836.8	14.6
BB1/top	JL13A020	py1	1017.1	22.5	407.5	31.2	59.4	72.2	2.4	1.2	1517.0	1379.1	2.2
BB1/top	JL13A023	py1	5979.0	301.4	362.3	383.9	24.0	77.6	18.5	3.2	482.0	747.5	27.9
MBTCS1/TOP	JL13A030	py1	1238.5	99.2	102.7	12.1	10.1	16.5	50.0	9.8	2884.1	346.2	0.3
MBTCS1/Others	JL13A035	py1	1727.8	140.5	56.7	10.1	384.8	28.5	12.8	23.6	1724.5	201.2	0.0
	mean		5735.1	96.3	246.1	121.4	71.4	34.3	16.0	29.9	1756.6	566.4	4.9
BB2/bluepy5	JL13A07	py2	644.6	8.0	91.2	1.3	25.0	0.4	0.8	20.4	1266.1	42.3	0.4
BB2/bluepy6	JL13A08	py2	372.2	5.4	81.5	2.4	9.8	0.6	2.0	30.2	323.5	8.8	0.5
BB2/bluepy7	JL13A09	py2	1108.1	13.2	91.1	3.3	25.1	0.8	1.2	21.2	721.3	36.5	0.3
BB2/bluepy9	JL13A011	py2	291.0	17.8	90.1	29.0	16.8	0.5	2.6	51.5	672.0	33.8	0.0
BB2/bluepy10	JL13A012	py2	2639.5	23.8	65.5	4.2	65.8	1.1	0.8	23.4	1566.2	97.0	0.0
BB2/bluepy11	JL13A013	py2	781.5	17.2	89.7	2.8	32.2	0.8	1.4	13.7	596.9	50.9	5.2
BB1/top	JL13A022	py2	3440.2	267.8	567.5	449.0	78.1	91.3	18.9	9.4	1089.5	1108.1	36.0
BB1/top	JL13A024	py2	765.7	172.8	58.6	74.3	363.4	28.4	1.8	2.9	3002.6	553.9	0.0
MBTCS1/TOP	JL13A031	py2	1765.4	162.6	72.8	14.3	30.7	46.0	0.2	530.2	1410.9	391.9	0.1
MBTCS1/Others	JL13A036	py2	2818.2	176.8	131.2	42.1	493.2	33.3	5.4	15.7	5168.3	717.0	0.0
	mean		1462.6	86.5	133.9	62.3	114.0	20.3	3.5	71.9	1581.7	304.0	4.3
BB1/top	JL13A021	py3	76.7	10.7	36.5	18.5	5.6	13.9	0.6	0.1	265.9	243.1	0.6
MBTCS1/TOP	JL13A028	py3	384.0	1.6	121.0	0.2	0.3	12.4	<0.026	0.0	8.9	34.7	<0.005
MBTCS1/TOP	JL13A032	py3	292.1	12.7	6.6	3.3	9.3	2.4	<0.054	320.6	172.9	26.2	<0.014
MBTCS1/Others	JL13A033	py3	1466.0	1.9	146.7	5.2	0.3	0.8	14.2	0.0	9.4	6.5	0.0
MBTCS1/Others	JL13A034	py3	1.6	1.1	203.4	0.1	<0.2	0.4	<0.070	0.0	0.1	0.0	<0.005
MBTCS1/Others	JL13A037	py3	1614.2	53.4	37.6	3.6	5.2	57.6	0.3	0.5	13.3	99.9	0.0
MBTCS1/Others	JL13A038	py3	2066.6	76.9	125.3	0.9	1.0	47.5	0.1	0.0	2.5	29.3	0.0
	mean		843.0	22.6	96.7	4.5	3.1	19.3	2.2	45.9	67.6	62.8	0.1

Annotations: py1 = fine–grained anhedral spongy to elongate pyrite, py2 = medium coarse–grained anhedral–subhedral pyrite, p3 = coarse–grained subhedral to euhedral pyrite and IS = internal standard.

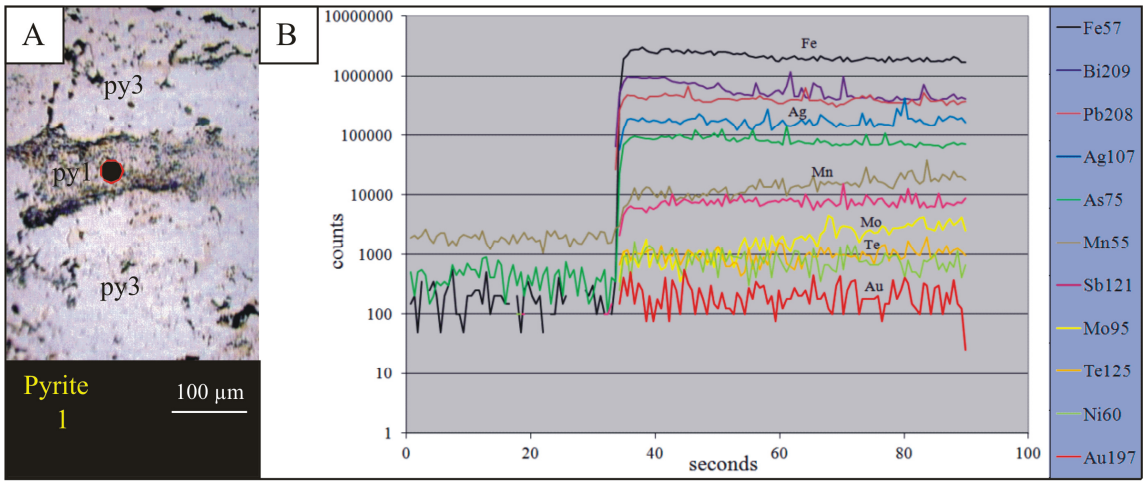

Fig. 6.4. Details of LA–ICPMS spot analysis of py1 from the Bukit Botol deposit. A. Photomicrograph of elongate–spongy py1 overgrown by py3 and the LA–ICPMS spot position in py1. B. ICPMS count output obtained from py1, Analysis no. JL13A020.

Among all the analysed elements, Ni (28–139 ppm), Sb (10–493 ppm; mean = 114 ppm) and Tl (mean = 72 ppm) are the most abundant in py2. Except these three elements and Au, the V, Mn, Cu, Zn, Mo, Ag, W, Pb and Bi elements are commonly present with significantly higher concentrations in py2 relative to py1. The Au content of py2 is lower than py1, varying from <0.06 to 2.64 ppm, with one single spot analysis reaching 3.06 ppm. An LA–ICPMS output for spot analysis in a representative sample of py2 is shown in Figure 6.5. Similar to py1, there is a significant association with Fe, Bi, Pb, Ag, As, Mn, Sb, Mo, Te, Ni and Au elements indicating that they are concentrated in the py2 structure.

The concentrations of trace elements are variable in py3 but significantly lower in V (<0.1 to 1.3 ppm), Mn varies between <0.8 and 26.6 ppm, Ni (mean = 28 ppm), Mo (4.5 ppm) and Sb from <0.2 to 5.6 ppm than those in py1 and py2. A decrease in Au content was also observed (<0.31 ppm), which was most likely related to the presence of invisible Au within the structure of pyrite.

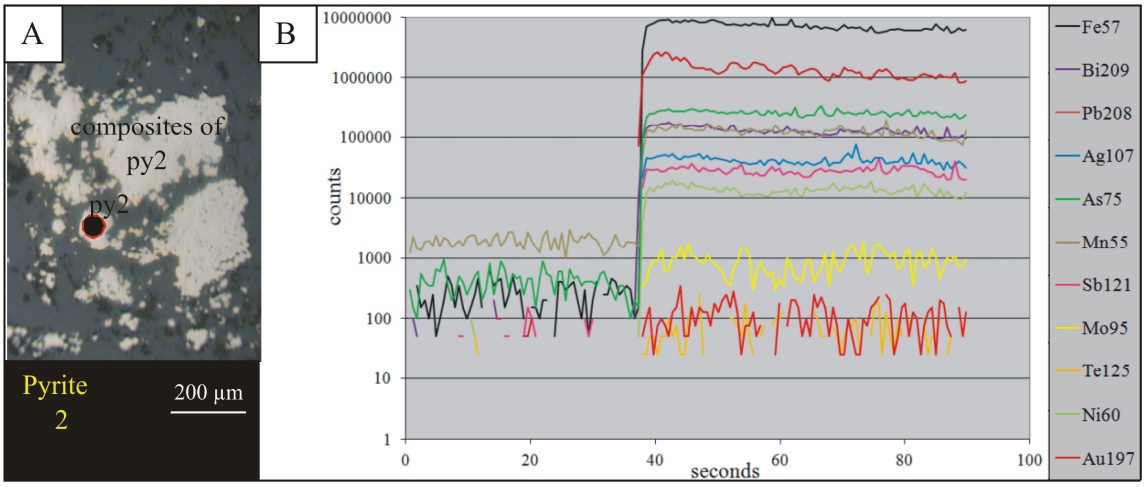

Fig. 6.5. Details of LA–ICPMS spot analysis of py2 from the Bukit Botol deposit. A. Photomicrograph of the typical textural arrangement of coarser disseminated and composite py2. B. ICPMS count output obtained from py2, Analysis no. JL13A012.

Figure 6.6 shows the LA–ICPMS spot analysis signals obtained during the ablation of a representative sample of py3. It is evident that the py3 sample is significantly less abundant in the same suite of elements (e.g., Fe, Pb, As, Mn, Sb, Mo, and Ni) enriched in py1 and py2. However, counts for Au, Ag, Te and Bi show several correlated spikes. These features suggest that there are some fine particles or mineral inclusions of solid Au–Ag, Au–Te–Ag and Au–Bi in py3 (Fig. 6.6).

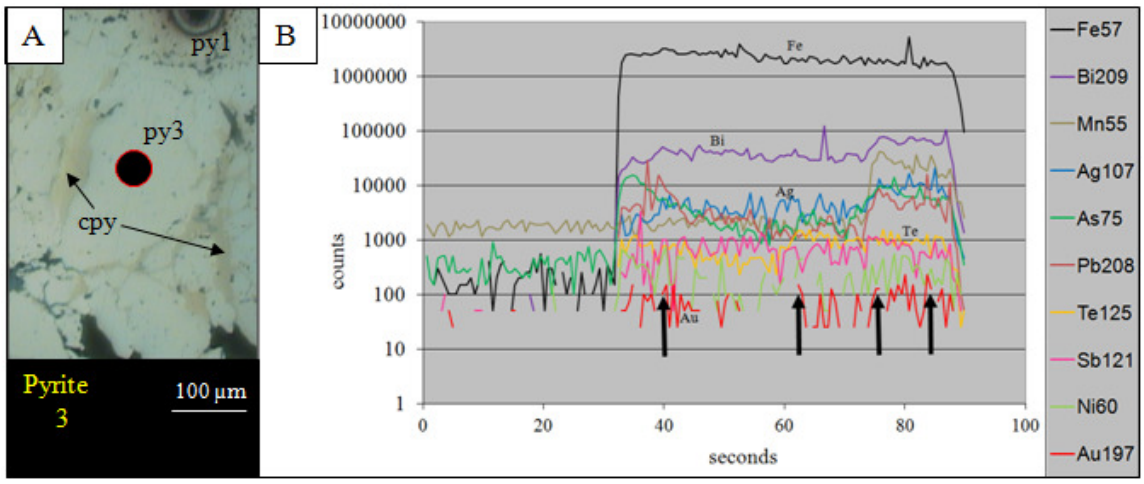

Fig. 6.6. Details of LA–ICPMS spot analysis of py3 from the Bukit Botol deposit. **A**. Photomicrograph of late euhedral–subhedral py3 intergrowth within and between chalcopyrite. **B**. ICPMS count output obtained from py3; note the decrease of most trace elements. However, the spikes in Au, Ag and Te are due to inclusion of electrum or gold telluride in the matrix (black arrows), Analysis no. JL13A037.

The suite of As, Se, Te, Cu, Zn and Pb shows a decreasing trend from py1 to py3, suggesting that these elements are homogeneously distributed in the pyrite types. Moreover, Co and Ni contents also show a distinct trend in the different pyrite types. Py1 is relatively high in Co (mean = 209 ppm) but less in Ni (8–35 ppm; mean = 24 ppm). Similar to py1, py3 also has less Ni (mean = 28) but higher Co (mean = 257 ppm) concentrations and are slightly enriched compared with py1. In contrast, Co (mean = 154 ppm) is depleted in py2 but Ni has moderate values (28–139 ppm; mean = 61 ppm).

6.3.3.2 Image analysis

In addition to the spot analyses, two pyrite samples from the Bukit Botol deposit were imaged in detail by LA–ICPMS. The first sample mapped in Figure 6.7 comprises an elongate–spongy py1 in a composite of subhedral py3. The elongate–spongy py1 is relatively enriched in V, As, Se (Te), Ag, Tl and Mn compared to py3. Gold content is also the highest in py1 compared to py3. However, inclusions of gold are observed within the structure of py3.

Three distinct varieties of pyrite were present in the second sample from the Bukit Botol deposit mapped by LA–ICPMS. The pyrite texture contains a core of spongy py1 which is overgrown by subhedral py2 and overgrown again by py3 (Fig. 6.8). The imaging shows that the spongy py1 core is enriched in V, As, Se (Te), Ag, Tl and Mn compared to the subhedral py2. Meanwhile, the overgrowth py3 shows enrichment of Ni and Co. In addition, gold is higher in the py1 with elevated micro inclusions of gold within the py3 matrix.

In both the pyrite samples, the LA–ICPMS maps demonstrate a zonation of trace elements from the core towards the rim of the pyrite. The py1 in the core is enriched in invisible Au, whereas the py3 contains intermediate invisible Au contents but has inclusions of gold in the pyrite structure. However, the py2 where present, has very low gold values between those of py1 and py3.

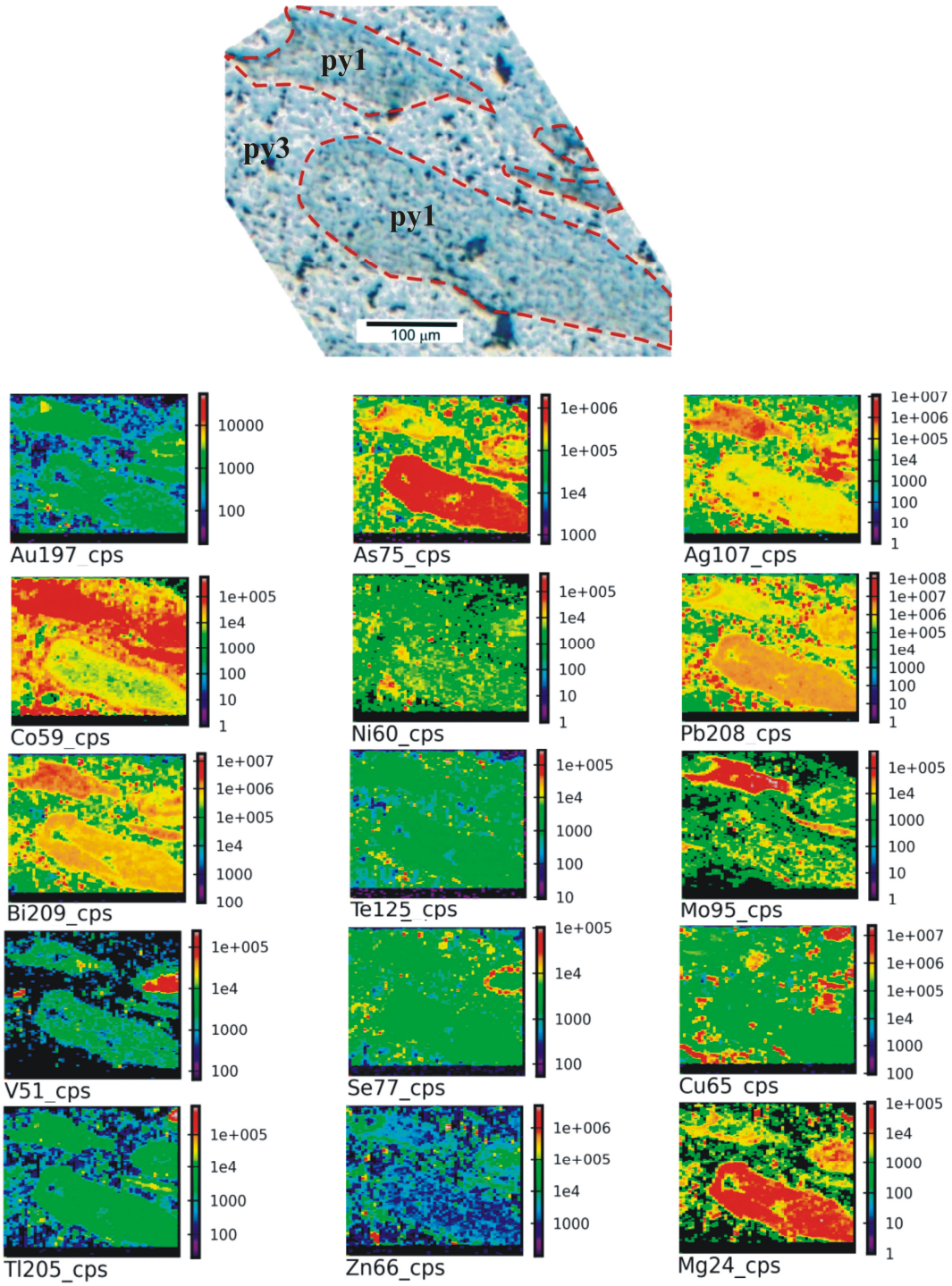

Fig. 6.7. Trace element LA–ICPMS map of pyrite crystal in massive sulphide ore from the Bukit Botol deposit. The mapping highlights two pyrite types in the sample; py1 and py3. Note that the py1 is relatively enriched in V, As, Se (Te), Ag, Tl and Mn compared to the py3. Gold content is also highest in py1 compared to py3. However, inclusions of gold are observed within the structure of py3. Annotation: py1=pyrite 1, py2=pyrite2 and py3=pyrite 3.

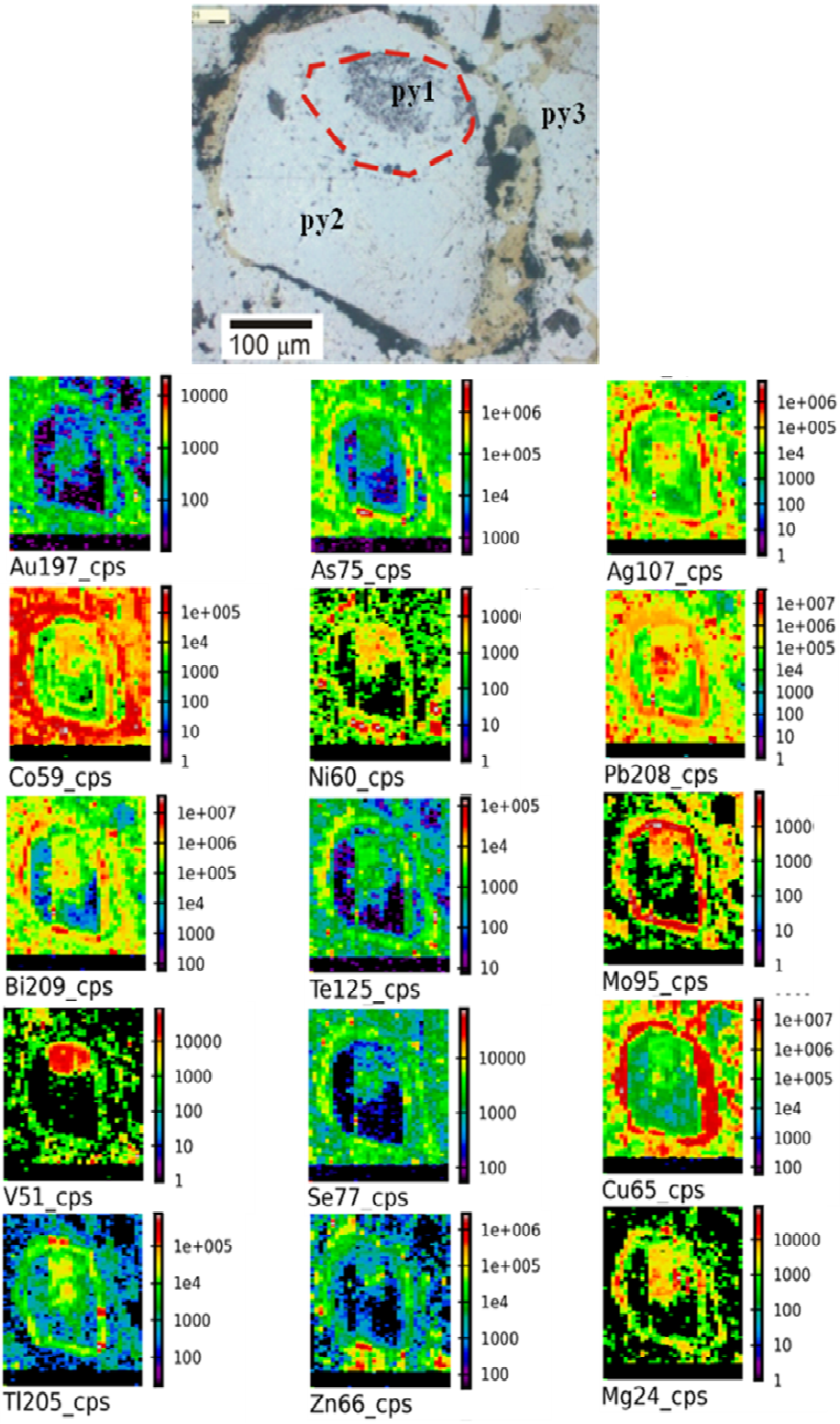

Fig. 6.8. LA–ICPMS trace element images of composite pyrite from massive sulphide mineralisation in the Bukit Botol deposit. This sample consists of py1 core surrounded by coarse–grained py2 and have been overgrown or embedded by late py3. Note that the spongy py1 core is enriched in V, As, Se (Te), Ag, Tl and Mn compared to the subhedral py2. Meanwhile, the overgrowth py3 shows enrichment of Ni and Co. In addition, gold is higher in the py1 with elevated micro inclusions of gold within the py3 matrix. Annotation: py1=pyrite 1, py2=pyrite2 and py3=pyrite 3.

In order to compare the trace element signatures for each of the pyrite types observed, further analysis of the LA–ICPMS spot data (Table 6.6) plotting these values in a series of bi–variant diagrams against Au. This approach was used to determine the relationship between Au and the other trace element compositions in different pyrite types.

In the plot of Au versus As, py2 shows an almost similar or a slightly increased trend in As with py1, whereas a relatively less abundant py3 (Fig. 6.9A). The strong correlation between As and Au implies that the As was already enriched in py1 and py2 structures before py3 formation. The substitution of As may provide favorable sites for the precipitation of gold. The variable trends exhibited by py3 are most likely due to the very low invisible gold content and the presence of inclusions within the py3 structure that were ablated during analysis.

The depletion trends are clearly shown by Au versus Ag and Au versus Cu from py1 to py2, but are variable in py3 (Figs. 6.9B and C). The correlations shown by py1 through to py3, in general indicate that the Ag and Cu are within the pyrite structure, and these elements gradually decrease from p1 to py3. Meanwhile, the several variations of Ag and Cu in py3 may reflect a presence of abundant inclusions of chalcopyrite and electrum in the pyrite grains.

Strong to moderate Au–Sb and Au–Bi trends are displayed by pyrite types (Figs. 6.9D and E), whereas the bi–variant diagram of Au–Te shows three distinct positive trends between the different pyrite types (Fig. 6.9F). These elemental trends reveal that they are sitting together in the structure of pyrites. However, several large ranges of values for Bi and Te, as well as Au in py3 compared to the nearly uniform and overlapping compositions in py1 and py2 suggest that gold inclusions are present within py3, probably as Au–Te and Au–Bi alloys.

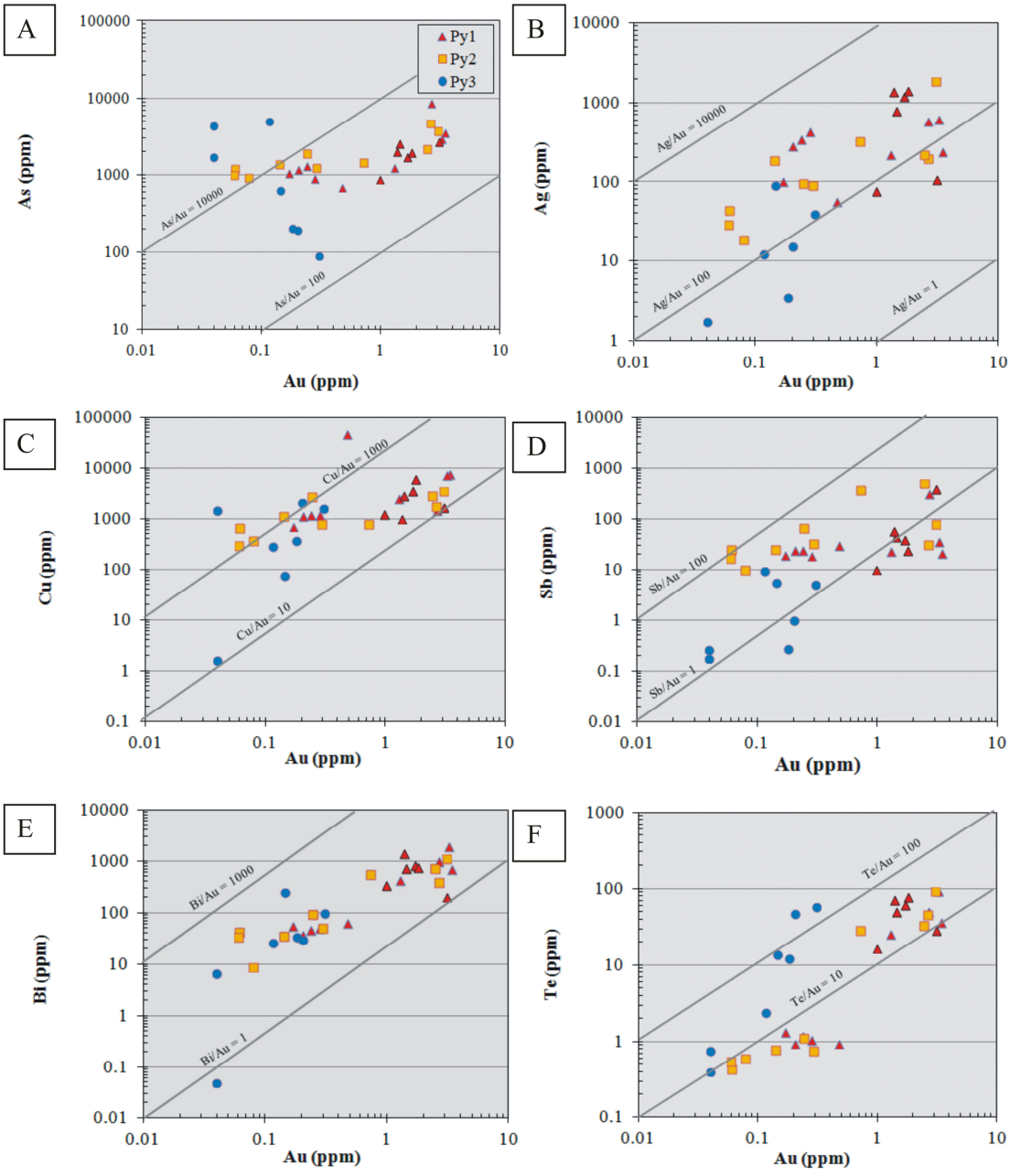

Fig. 6.9. Binary plots of selected trace elements in different varieties of pyrite from the Bukit Botol deposit against Au. **A.** Au–As. **B.** Au–Ag. **C.** Au–Cu. **D.** Au–Sb. **E.** Au–Bi and **F.** Au versus Te trends.

6.4 Discussion

6.4.1 Sphalerite trace element chemistry

Significance of sphalerite chemistry

The chemical composition of sphalerite varies significantly with the location and type of ore

deposits. However, the amount of FeS in sphalerite is mainly controlled by the temperature, pH, pressure and a_{FeS} (average FeS content) in any of these ore deposition environments (e.g., Khin Zaw, 1991; Khin Zaw and Large, 1996). Urabe (1974) reported that the FeS content in sphalerite from several Kuroko deposits in Japan decreases with decreasing temperatures, and Scott and Barnes (1971), Barton and Skinner (1979), Hannington and Scott, (1989), Craig and Vaughan (1994) considered that the FeS content of sphalerite can be used to constrain sulphur activity in ore−forming fluids, but is dependent in total sulphur concentration during mixing of the ore fluids with seawater (Khin Zaw, 1991; Khin Zaw and Large, 1996).

In the Bukit Botol deposit, variations of FeS content are clearly shown by the sphalerite from different mineralisation styles indicating high FeS content in the stringer zone and low in the massive sulphide. Although the FeS content in sphalerite at the Bukit Ketaya deposit is more homogeneous with a narrow range in compositions (0.3−2.5 mole% FeS), the trend also shows a slight increase from massive sulphide towards the stringer zone. Thus, a declining trend is suggested in FeS from the lower to the upper stratigraphic levels at both deposits, as suggested by Urabe (1974) for the Kuroko deposits.

The relatively lower FeS contents of sphalerite in massive sulphide at both deposits indicate high sulphidation conditions and lower temperatures of formation, whereas higher FeS contents of sphalerite in the stringer sulphide may be related to the higher temperature conditions at Tasik Chini deposit. This suggestion is also supported by an increase of $\delta^{34}S$ value from the stringer zone to the massive sulphide through to barite mineralisations (see Chapter 7). Additionally, the relatively high copper contents ranging from 1.3 and up to 6.4 wt% Cu in sphalerite from the Bukit Botol stringer zone may indicate the abundant presence of chalcopyrite mineral in this zone. Lower copper compositions in sphalerite from the Bukit Botol and Bukit Ketaya massive sulphides and also in the stringer sulphide zones may be

related to lower amounts or the absence of chalcopyrite minerals in these zones. The chemical compositions of sphalerite exhibited in both the Bukit Botol and Bukit Ketaya deposits are consistent with the results of a few VHMS deposits such as the Kuroko deposits, Japan (Urabe, 1974) and the Rosebery–Hercules deposits, Tasmania (Green et al., 1981; Khin Zaw, 1991; Khin Zaw and Large, 1996) (Fig. 6.10).

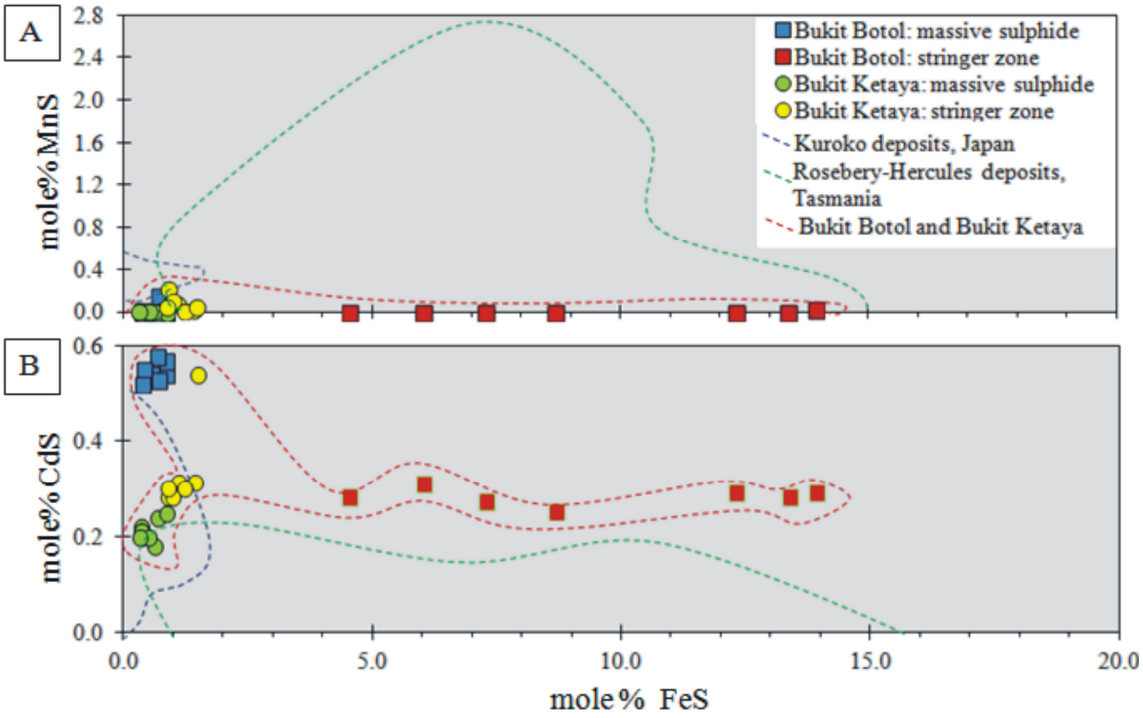

Fig. 6.10. Comparison of compositional ranges in sphalerites between the Bukit Botol and Bukit Ketaya deposits with the Kuroko deposits, Japan and the Rosebery–Hercules deposits, Tasmania. **A**. Plot of mole% FeS versus mole% MnS. **B**. Plot of mole% FeS versus mole% CdS. The field of sphalerite data from the Kuroko deposits, Japan is from Urabe (1974) and Mizuta (1988), whereas the boundary of sphalerite compositions from the Rosebery–Hercules deposits, Tasmania is from Khin Zaw and Large (1996).

Implications of major and trace elements in sphalerite

The Cd content and the Zn/Cd ratios of sphalerite have been used as a distinguishing parameter for ore deposit types. According to a classification based on a compilation of literature data by Schwartz (2000), the Cd concentrations in sphalerite from VHMS deposits (mean=2360 ppm) and SEDEX deposits (mean=2560 ppm) are the lowest. MVT and veins in carbonate rock deposits have the highest Cd content (mean between 4850 and 7260 ppm),

whereas the moderate Cd values are characterised by skarn and veins in low carbonate rock deposits (mean from 3540 to 4100 ppm).

Xuexin (1984) calculated Zn/Cd ratios and average values in sphalerite from various genetic types of deposit. He also reported that the volcano−sedimentary and Alpine (MVT) type deposits have the highest Zn/Cd ratios of 417 to 531. The hydrothermal deposits, including volcano−hydrothermal and skarn deposits, exhibit the lowest Zn/Cd ratios between 104 and 214, with the metamorphosed sedimentary carbonate hosted stratiform deposits showing moderate Zd/Cd ratios (252−330). Moreover, the relatively higher Zn/Cd values ranging between 250 and 400 were considered to be related to volcanic source rocks, as for example those of the Valu Fa Ridge, Pacific Ocean (Fouquet et al., 1993) and Roseberry−Hercules Cambrian VHMS deposits (Khin Zaw, 1991; Khin Zaw and Large, 1996). Meanwhile, Zn/Cd ratios lower than 250 are thought to be associated with granitic magmatism as for instances the Devonian Pb−Zn vein deposits in western Tasmania (Khin Zaw and Large, 1996).

The sphalerite from both the Bukit Botol and Bukit Ketaya deposits show Cd values ranging within 2100 to 5400 ppm (average=3273 ppm). However, the Zn/Cd ratios in sphalerite for the Bukit Botol deposit vary with an average of 123 for the massive sulphide and 240 for the stringer zone, whereas the ratios of Zn/Cd at the Bukit Ketaya deposit exhibit an average of 320 in the massive sulphide and 218 in the stringer zone. In comparison, these data demonstrate that the low Cd concentration in sphalerite at both the Bukit Botol and Bukit Ketaya deposits is comparable with the lowest Cd content in many VHMS and SEDEX deposits. Additionally, the variability of the Zn/Cd ratio in sphalerite from both these deposits is also similar to those of the volcano−sedimentary deposits with a volcanic origin. However, the slight difference in the Cd concentrations and the Zn/Cd ratios between the Bukit Botol deposit and the Bukit Ketaya deposit may suggest a change in the chemical composition of

the volcanic host rocks. This suggestion is based on the occurrence of mainly rhyodacite in the Bukit Botol deposit but higher proportions of rhyodacite–rhyolite in the Bukit Ketaya deposit (see Chapter 4), and the average Zn/Cd ratios in felsic igneous rocks ranging from 154 to 200 and in mafic igneous rock between 477 and 500 (Turekian and Wedepohl, 1961; Taylor, 1964). In addition, mixing of different fluids (seawater dominant and minor magmatic fluids; see Chapters 7 and 8) is also considered responsible in controlling the chemistry of the sphalerite at both deposits, similar to the Eskay Creek VHMS deposit, Canada as was suggested by Sherlock et al. (1999). Furthermore, the complex relationship of Zn/Cd ratios in sphalerite between the Bukit Botol and Bukit Ketaya deposits is also probably due to the differences in temperature, pH, pressure and a_{FeS} (average FeS content) contributions during their deposition (e.g., Khin Zaw, 1991; Khin Zaw and Large, 1996; this study).

6.4.2 Pyrite trace element chemistry

Significance of trace element distribution in pyrite

The trace element abundance in pyrite grains examined by LA–ICPMS technique and both the spot and image analyses, clearly reveals three pyrite types from the Bukit Botol deposit which are consistent with the mineral assemblages and paragenesis interpretations (see Chapter 5). The py1 (pyrite 1) is enriched in trace elements of V, Mn, Cu, Zn, Mo, Ag, W, Pb and Bi. However, the contents of Ni, Sb and Tl are relatively low in the py1. The same elements enriched in py1 are also enriched in py2 (pyrite 2) excluding the Ni, Sb and Tl which are the most abundant in py2. The later py3 (pyrite 3) becomes poor in all trace elements. In general, the overall compositional change in pyrite types from the Bukit Botol deposit are similar to those of the pyrite characteristics from several VHMS deposits (e.g., the Kidd Creek deposit, Canada–Cabri et al., 1985; the eastern Australia VHMS deposits–Huston et al., 1995b; the Mobron VHMS deposit, Quebec–Larocque et al., 1995; the Boliden deposit, Sweden–Wagner et al., 2007; the Yaman–Kasy deposit, Urals– Maslennikov et al., 2009; the

Brunswick No. 12 deposit, Canada–McClenaghan et al., 2009). For examples, the enrichment of Mn is a typical feature of colloform pyrite which precipitates on the seafloor during massive sulphide growth (Eremin, 1983). The Mn enrichment in colloform or fine–grained pyrite suggests a relatively oxygenated subalkaline condition of seawater, whereas low Mn content in the later pyrite forms as a result of high–temperature reduced fluids (Maslennikov et al., 2009).

The suite of As, Se, Te, Cu, Zn and Pb patterns with a decreasing trend from py1 to py3, and a high Co but lower Ni in the py1 and py3 contents compared with moderate Ni and low Co values in py2 are also similar to that of the pyrite characteristics for several VHMS deposits. The highest As contents are typically associated with colloform or fine–grained pyrite which is a result of rapid precipitation (Cook and Chryssoulis, 1990; Huston et al., 1995b), during mixing of sulphides with seawater near the seafloor interface (McClenaghan et al., 2009). Moreover, the high concentrations of Co and Se in pyrite also suggest a typical feature of high–temperature Cu–rich ores in several VHMS deposits (e.g., Walshe and Solomon, 1981; Huston et al., 1995; Raymond, 1996; Hannington et al., 1999a, b). Although the Ni contents show two contrasting patterns, the overall concentrations are relatively low (8–139 ppm). This low Ni content signature is in agreement with literature data from a few VHMS deposits that show the Ni value of pyrite decreasing in felsic volcanic–hosted deposits relative to those in mafic volcanic–hosted deposits (Bajwah et al., 1987). Thus, it is suggested that the Ni concentration in pyrite at the Bukit Botol deposit is controlled by its primary ore–forming fluids and is also influenced by the felsic volcanic hosting rocks.

The Co/Ni ratio of pyrite in sulphide deposits varies according to their mode of formation (Loftus–Hills and Solomon, 1967; Seccombe, 1977; Campbell and Ethier, 1984; Bajwah et al., 1987) but can vary depending on temperature and f_{S2} of ore–fluids (Maslennikov et al., 2009).

As summarised by Brill (1989), the volcanogenic pyrite commonly has Co>500 ppm and Co/Ni ratios between 5 and 50 (average=8.7), pyrite of sedimentary origin has Co<100 ppm and Co/Ni<1 (average=0.63), and pyrite from hydrothermal veins usually shows Co>400 ppm with Co/Ni ratios in the range 1–5 (average=1.7). At the Bukit Botol deposit, the Co/Ni ratios of py1 (0.2–34; mean = 10), py2 (0.0–43; mean = 5) and py3 (5–30; mean = 13). Therefore, the high Co/Ni ratios indicate that the pyrites from this deposit were precipitated from volcanogenic–hydrothermal fluids. The variability in the Co/Ni ratios of pyrites and greater than one are also characteristic of several VHMS deposits such as the Ruttan deposit, Canada (Co/Ni ratio = 2: Barrie et al., 2005) and Roseberry deposit, Tasmania (Co/Ni ratio = 1.5: Huston et al., 1995b).

The ore style of the Bukit Botol deposit based on pyrite compositions was tested on a series of Co–Ni, Au–Ag and Bi–Pb scatter plots as developed by Large et al. (2013) to discriminate pyrite of VHMS association from pyrite of orogenic gold (Fig. 6.11). The results demonstrate that the trend of Co/Ni, Au/Ag and Bi/Pb ratios in pyrites from the Bukit Botol deposit are mostly plotted towards the VHMS sections. Thus, it is suggested that the Bukit Botol deposit is a VHMS deposit, and the pyrite compositions/ratios are relatively similar to a few other VHMS deposits such as the Degussa, Jaguar and Gossan Hill VHMS deposits in Western Australia (e.g., Large et al., 2013).

Distribution of Au in the pyrite and its possible source

Pyrite in the Bukit Botol deposit displays two distinctive Au enrichments: 1) a positive Au and As correlation in both py1 and py2 of spot and image analyses, and 2) a significant negative relationship between Au and As in py3.

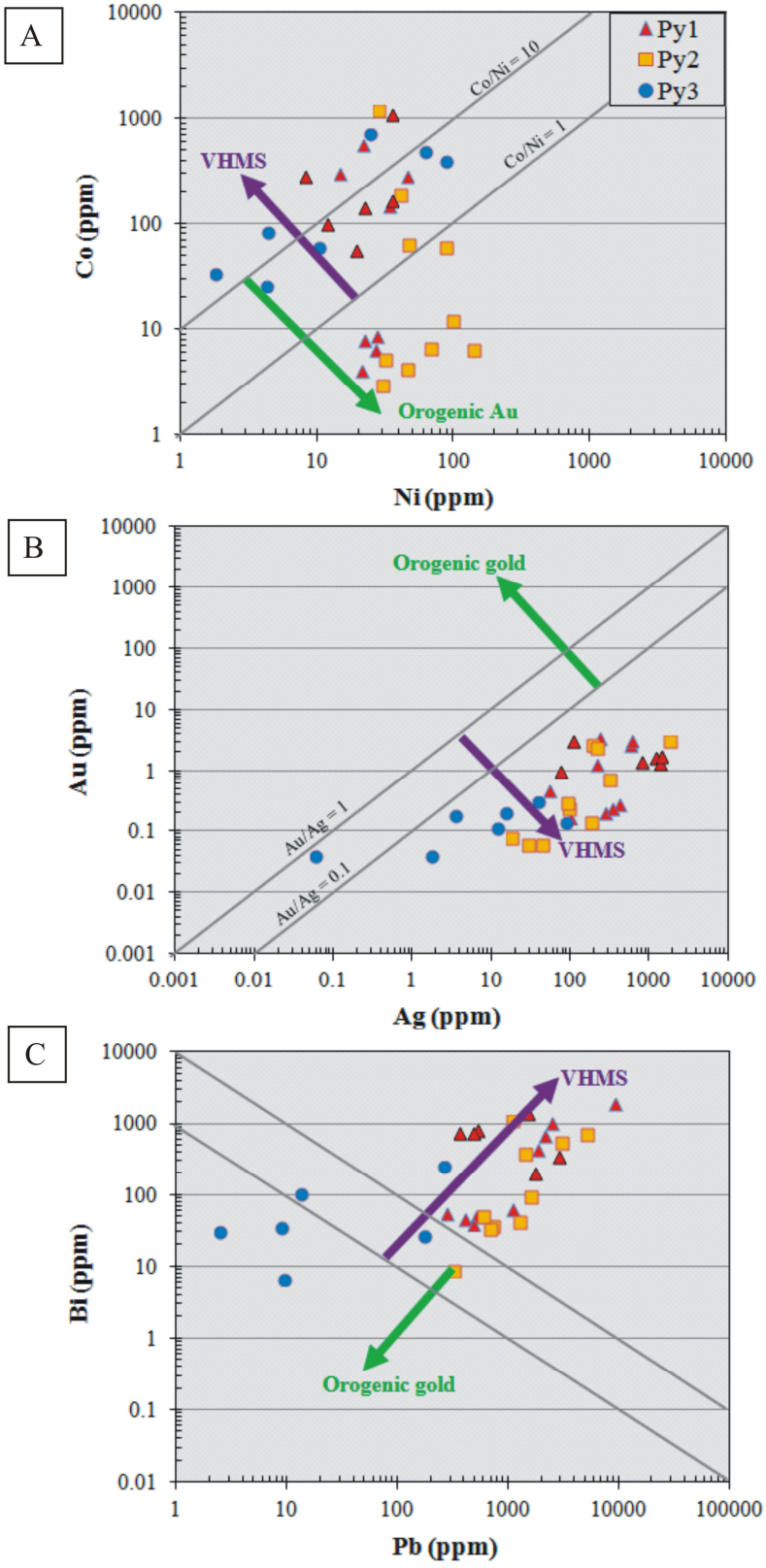

Fig. 6.11. Scatter plots of selected trace elements to discriminate pyrite of VHMS association from pyrite of orogenic gold (modified after Large et al., 2013)**. A.** Co–Ni. **B.** Au–Ag. and **C.** Bi–Pb. The field divisions and boundaries of pyrite for VHMS and orogenic gold deposits are from Large et al. (2013).

However, there are several correlated spikes in spot analysis and the maximum concentration of Ag, Te and Bi elements in image analysis accompanying the Au enrichment in py3. For comparison, the first pattern of Au enrichment is referred to as 'invisible gold' (Cook and Chryssolis, 1990), and it is similar to published data of common features for arsenian pyrite in many epithermal, orogenic and Carlin−type gold deposits that usually carry the highest contents of invisible gold (Reich et al., 2005; Large et al., 2009).

For the second style, it was considered that the Au enrichment in py3 consists of inclusions of native Au, Au−Ag, Au−Te and Au−Bi−Te minerals within its matrix. These minerals were formed when gold−bearing arsenian pyrite changed to gold−poor arsenian pyrite and native gold (Simon et al. 1999a), or when relatively acidic or oxidised fluids were involved with gold−bearing arsenian pyrite and remained saturated with gold (Su et al. 2008). The presence of Au−Te and Au−Bi−Te minerals in felsic−hosted VHMS deposits such as in the Urals districts, Russia demonstrated that the minerals may have been precipitated on a seafloor environment by oxidation of hydrothermal fluids due to their interaction with oxygenated seawater (Maslennikov et al., 2013).

On the basis of a LA−ICPMS study and the other evidence discussed above, it is considered that there was a seawater source for the ore−forming fluid at the Bukit Botol deposit. The precipitations of Au, As and trace elements in pyrites related to the reduction of sulphur from seawater at specific pressure and temperature conditions. However, a minor magmatic source was also significant as shown by the two Au trends and related trace element enrichments in pyrites. In addition, the high Se (7−650 ppm) and Co (0−1192 ppm) concentrations in pyrite may also suggest a magmatic contribution. These considerations are further supported by the sulphur, lead and fluid inclusion data obtained in this study (see Chapters 7 and 8). Moreover, the presence of bornite and pyrite assemblage in sulphide ores also indicate a high a_{S2} and

hydrothermal conditions which may have been favorable for the transportation and subsequent deposition of a large amount of gold from $Au(HS)^{-2}$ (Hannington and Scott, 1989).

6.5 Summary

1) The sphalerite chemistry studied by electron microprobe reveals that the Bukit Botol and Bukit Ketaya deposits display similarities in FeS concentrations in both massive sulphides and stringer zones. Trends in sphalerite content are similar to those exhibited in the Kuroko VHMS deposits, Japan and the Rosebery–Hercules deposits, Tasmania.

2) Although the application of sphalerite alone as geobarometer cannot be used because of the absence of sphalerite–pyrite–hexagonal pyrrhotite assemblage, the other primary sphalerite composition data such as Cu, Cd contents and Zn/Cd ratios coupled with the S and Pb isotopes and fluid inclusions data suggest that mixing of dominantly seawater and minor magmatic fluids are considered responsible in controlling the chemistry of sphalerite at both deposits.

3) The LA–ICPMS analysis of trace element concentrations in pyrite from the Bukit Botol deposit demonstrates that significant variation of trace elements in different pyrite types indicates different mechanisms of pyrite formation. Py1 is enriched in trace elements of V, Mn, Cu, Zn, Mo, Ag, W, Pb and Bi, whereas the contents of Ni, Sb and Tl are relatively low in py1. The same elements enriched in py1 are also enriched in py2. However, the Ni, Sb and Tl contents are significantly abundant in py2. The later py3 has lower amounts of all trace elements. Gold is present in pyrite in two forms: invisible gold in early pyrite and as an inclusion of native Au, Au–Ag and Au–Bi–Te minerals in the pyrite structure. The trace element content of the pyrite is controlled by the evolution of ore–forming fluids through time, comprising largely seawater source fluids with minor inputs from magmatic fluids.

5) The trend of Co/Ni, Au/Ag and Bi/Pb ratios in pyrites from the Bukit Botol deposit are mostly comparable with those of VHMS systems.

CHAPTER 7 SULPHUR ISOTOPE CHARACTERISTICS

7.1 Introduction

This Chapter provides the first comprehensive study of sulphur isotope data for the VHMS deposits in the Tasik Chini area. Research was carried out to (1) determine the sulphur isotope characteristics for the massive sulphide mineralisation and (2) establish the sources of mineralising fluids at Tasik Chini.

The sulphur isotope studies of hydrothermal ore deposits define information regarding the origin of the sulphur present in the orebody in the form of sulphides and sulphates (Ohmoto, 1972). Hence, the source of sulphur can be traced on the basis of the total sulphur isotope compositions in an ore deposit (Hoefs, 1997, 2004). Comprehensive studies of sulphur isotope characteristics in ancient VHMS deposits have been produced by Ohmoto (1986); Huston (1999); Huston et al., (2010) and in modern VHMS deposits by Shanks (2001); Rouxel et al. (2004).

Sangster (1968) was the first researcher to recognise that the trend of $\delta^{34}S$ variation in Proterozoic and Phanerozoic VHMS deposits closely parallels the ancient seawater curve but is offset to lighter $\delta^{34}S$ values by about 18‰, or ~16‰ (Huston, 1999; Huston et al., 2010). Subsequent studies have confirmed the general trend that seawater sulphate provides a source of reduced sulphur for many VHMS deposits (e.g., Large, 1992; Downes and Seccombe, 2004; Scotney et al., 2005; Inverno et al., 2008). More recent works on modern seafloor

hydrothermal sulphide systems also indicate a consistent role of reduced sulphur in addition to seawater $\delta^{34}S$ source (e.g., Shanks, 2001; Rouxel et al., 2004).

7.2 Methods

Samples for sulphur isotope analyses were determined in sulphide minerals within the different styles of mineralisations (massive sulphide ore, disseminated sulphide and stringer zone) and in barite samples from barite exposure at both the Bukit Botol and Bukit Ketaya deposits. The sulphur isotope analyses were carried out via two methods at CODES and the CSL, UTAS: (1) conventional and (2) laser ablation technique.

The conventional technique involves sulphides and sulphates extracted by hand-drilling of hand samples. Measurements of sulphur isotopes were performed using conventional procedures of Robinson and Kusakabe (1975) on a VG Sira Series II mass spectrometer. By contrast, the laser ablation analyses of sulphur isotopes were determined on fine-grained intergrowth and coarse-grained crystals sulphides on ~200 μm thick polished sections using laser ablation methods of Huston et al. (1995a). Determinations were made on an 18W Quantronix 117 Nd:YAG model laser in an oxidising atmosphere (at 25 torr oxygen pressure) and a ~35mA current for 2 seconds on single or multiple sites (up to 5) to yield sufficient SO_2 for analysis. All results are reported as permil (‰) variations from the Canon Diablo Troilite (CDT). The analytical precision (1δ) of sulphur based on repeated analyses of internal standard for both sulphides and sulphates is 0.2 ‰ from both techniques.

7.3 Sulphur Isotope Results

7.3.1 Bukit Botol deposit

The $\delta^{34}S$ composition of twenty-two sulphides and twelve sulphates from the Bukit Botol deposit are presented in Table 7.1 and summarised in Fig 7.1. With the exception of one sample having a 8.3 permil sulphur value, the sulphide $\delta^{34}S$ values range from –0.8 to 4.1

permil. These values are also indistinguishable based on types of mineral and the style of mineralisation, suggesting a homogenous source. The sulphur isotope values for pyrites from the massive sulphide ore range from 0.5 to 8.3‰, and analyses of mixed pyrite-chalcopyrite yielded $\delta^{34}S$ content range between 1.4 and 4.1 permil. Mixed pyrite-chalcopyrite from a stringer zone mineralisation has low $\delta^{34}S$ values of -0.8 to 1.4‰. A single analysis of chalcopyrite yielded a $\delta^{34}S$ content of 0.5 permil. Three analyses of disseminated pyrite in altered host felsic volcanic host rocks gave a value of 2.1 to 4.1 ‰.

The $\delta^{34}S$ values for twelve barite samples from the Bukit Botol deposit yielded a range varying from 11 to 18‰.

Table 7.1. Sulphur isotope data for sulphides and sulphates at the Bukit Botol deposit. Annotation: py=pyrite, cpy =chalcopyrite and ba=barite.

Deposit	*Sample*	*Mineral*	*Type of mineralisation*	*$\delta^{34}S$ (‰)*	*Method*
Bukit Botol					
1	BB1	py-cpy	massive ore	1.88	conventional
2	BB1a	py-cpy	massive ore	4.12	conventional
3	BB1b	py-cpy	massive ore	1.54	conventional
4	BB2	py	massive ore	8.30	conventional
5	BB2a	py-cpy	massive ore	1.57	conventional
6	BB2b	py-cpy	massive ore	1.38	conventional
7	BB2c	py-cpy	massive ore	2.25	conventional
8	BB2d	py	massive ore	1.37	conventional
9	BB2f	cpy	stringer zone	0.48	conventional
10	T5-1	py	massive ore	2.58	laser
11	T5-2	py	massive ore	1.57	laser
12	T6-1	py	massive ore	3.15	laser
13	T6-2	py	massive ore	1.57	laser
14	T7-1	py	disseminated	2.08	laser
15	T7-2	py	disseminated	2.47	laser
16	T8-1	py	massive ore	3.99	laser
17	T8-2	py	massive ore	2.30	laser
18	T10-1	py	massive ore	2.57	laser
19	T10-2	py	massive ore	0.58	laser
20	BB10	py	disseminated	4.13	conventional
21	BB10c-1	py-cpy	stringer zone	1.36	conventional
22	BB10c-2	py-cpy	stringer zone	-0.80	conventional
23	Tasik 1	ba	barite ore	16.15	conventional
24	Tasik 2	ba	barite ore	11.60	conventional
25	Tasik 3	ba	barite ore	17.66	conventional
26	Barite	ba	barite ore	17.42	conventional
27	MBTC-S3	ba	barite ore	18.15	conventional
28	BB1 (barite)	ba	barite ore	15.95	conventional
29	BB2 (barite)	ba	barite ore	16.24	conventional
30	B1	ba	barite ore	13.65	conventional
31	B2	ba	barite ore	14.85	conventional
32	BB2-X	ba	barite ore	11.82	conventional

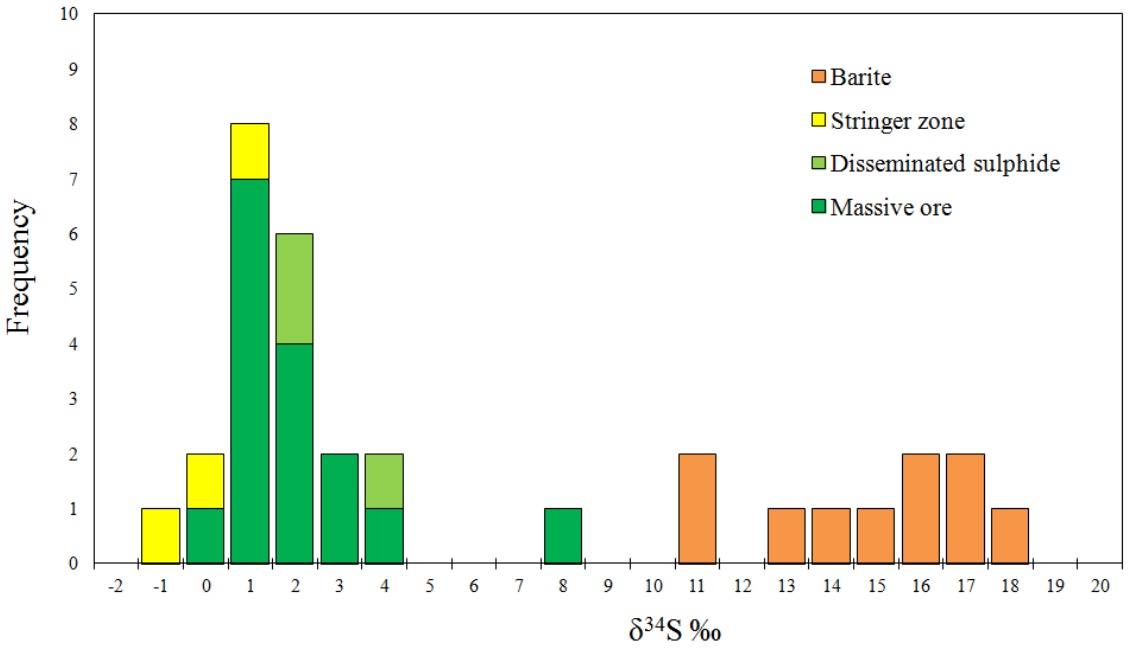

Fig. 7.1. Histogram of $\delta^{34}S$ values for sulphides and sulphates from the Bukit Botol deposit, Central Peninsular Malaysia.

7.3.2 Bukit Ketaya deposit

The sulphur isotope values of eleven sulphides and eleven sulphates samples from the Bukit Ketaya deposit are shown in Table 7.2 and presented in Figure 7.2. The Bukit Ketaya sulphides have a narrow range of $\delta^{34}S$ values, from -2.9 to 3.6 permil relative to those of the Bukit Botol deposit, also indicating a homogeneous source. Based on the classified mineral and ore types, the sulphur isotope values for pyrite from the thin sheet massive sulphides have higher sulphur isotope values, ranging from 2.2 to 3.6‰. The disseminated and feeder zone mineralisations have a lower range of $\delta^{34}S$ values, with a pyrite value of between -2.9 and 0.2‰. Based on the $\delta^{34}S$ data obtained, the values for the thin sheet massive sulphide and feeder zone mineralisation at the Bukit Ketaya deposit are almost identical, suggesting that they have a common sulphur source.

Barite from the barite-bearing layer and lens yield $\delta^{34}S$ values of 15 to 19 permil with two exceptional heavier (+22‰) and lighter (+11‰) values (Fig. 7.2).

Table 7.2. Sulphur isotope data for the Bukit Ketaya deposit. Annotation: py=pyrite, cpy=chalcopyrite and ba= barite.

Deposit	*Sample*	*Mineral*	*Types of mineralisation*	*$\delta^{34}S$ (‰)*	*Method*
Bukit Botol					
1	BK12a	py	stringer zone	-2.87	conventional
2	BK12a-lower	py	stringer zone	-2.56	conventional
3	BK12a-upper	py	stringer zone	-2.35	conventional
4	KZMA-1	py	stringer zone	-0.77	conventional
5	KZMA-2	py	stringer zone	-0.36	conventional
6	KZMA-3	py	stringer zone	-0.66	conventional
7	BKCL-1	py	disseminated	0.15	conventional
8	BKCL-2	py	disseminated	-1.66	conventional
9	BMSE1	py	massive ore	2.19	conventional
10	BMSE1-1	py	massive ore	3.28	conventional
11	BMSE1-2	py	massive ore	3.51	conventional
12	BK06	ba	barite ore	22.61	conventional
13	BK08	ba	barite ore	18.54	conventional
14	BK08a	ba	barite ore	16.86	conventional
15	BK09	ba	barite ore	18.46	conventional
16	14AR	ba	barite ore	11.58	conventional
17	S 6/7a12	ba	barite ore	20.66	conventional
18	S 6/7a13	ba	barite ore	20.39	conventional
19	BK01 (ba)	ba	barite ore	16.02	conventional
20	BK02 (ba)	ba	barite ore	15.68	conventional
21	BKX	ba	barite ore	17.00	conventional
22	S 5/6 a4	ba	barite ore	18.87	conventional

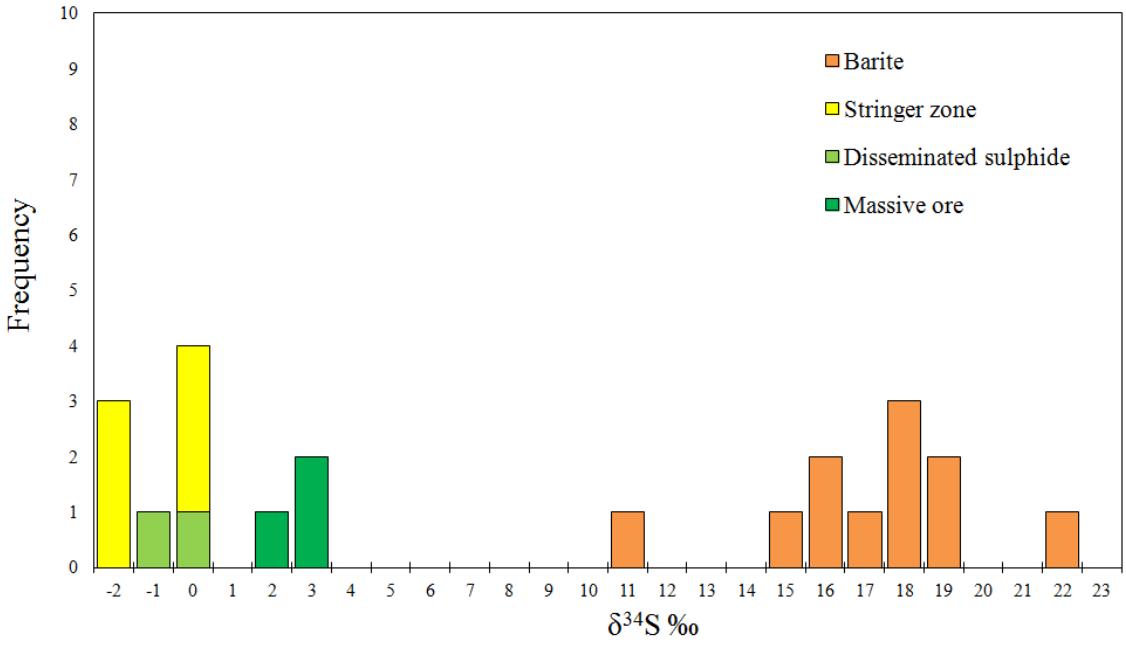

Fig. 7.2. Frequency distribution of $\delta^{34}S$ values of sulphides and sulphates for Bukit Ketaya deposit, Central Peninsular Malaysia

7.4 Discussion

7.4.1 Significance of sulphur isotopes

The sulphur isotope data of sulphides from the Bukit Botol deposit exhibit a uniform range of $\delta^{34}S$ values between -0.8 and +4.1‰, and one sample displays a higher $\delta^{34}S$ value of +8.3‰. Meanwhile, the $\delta^{34}S$ values for sulphides from the Bukit Ketaya deposit are characterised by a narrow and restricted range of $\delta^{34}S$ between -2.9 and +3.6‰. In general, the range of sulphur values obtained from both the deposits are comparable and within the typical $\delta^{34}S$ values range from -20 to 27‰ in sulphides and 10 to 40‰ in sulphates variability of global VHMS deposits (Ohmoto and Rye, 1979; Huston, 1999).

In comparison, the significantly narrow ranges of sulphides with a cluster toward positive $\delta^{34}S$ value, in both the deposits are similar to several ancient VHMS deposits including the Osborne Lake deposit in the Snow Lake area, Canada (-1.1 to +6.0‰; Sangameshwar, 1972), the El Cobre deposit, Cuba (-1.4 to +7.3‰; Cazañas et al., 2003), the Mount Morgan deposit, Australia (-1.6 to +5.3‰; Ulrich et al., 2002), the Lewis Ponds, Mount Bulga, Belara and Accost deposits in the Lachlan Fold Belt, New South Wales (range of -1.7 to +5.9‰; Downes and Seccombe, 2004). However, the abundance of significant low $\delta^{34}S$ values in sulphides at the Bukit Ketaya deposit is also probably comparable with a $\delta^{34}S$ signature exhibited by the Mount Lyell deposits, Tasmania (-10 to +10‰; Huston et al., 2011). Moreover, most sulphates (barites) from both deposits have $\delta^{34}S$ values (11 to 18‰, Bukit Botol; 11‰ to 22‰; Bukit Ketaya). As the host volcanic rocks of both deposits are of Early Permian ages (see Chapter 4), this sulphur isotope value ranges are similar to or slightly higher than Permian seawater sulphate (+10% to +12%; Claypool et al., 1980; Kampschulte and Strauss, 2004), indicating a large component of marine sulphate in this mineral.

7.4.2 Source of sulphur

Sulphur in VHMS deposits usually comes from: (1) a magmatic source (Ohmoto, 1996) through a direct contribution from a vapour-rich magmatic fluid (Ohmoto, 1986; Stanton, 1990; Gemmell and Large, 1992; Sillitoe et al., 1996; Herzig et al., 1998, Galley et al., 2000b; Solomon et al., 2004a) or leaching from subsurface magmatic rocks (Ohmoto and Goldhaber, 1997); (2) an inorganic reduction of seawater sulphate during a deep circulation process (Ohmoto et al., 1983; Solomon et al., 1988); and (3) a bacterial reduction of seawater sulphate (Sangster, 1976; Çagatay and Eastoe, 1995).

The ranges of sulphur isotope values of the Bukit Botol and Bukit Ketaya deposits are plotted with a sulphur value range from various rocks and shown in Figure 7.3. The uniform and almost identical $\delta^{34}S$ values of sulphides from both deposits suggest a homogeneous hydrothermal system, and the closeness to 0‰ is consistent with a magmatic source (e.g., 0 ± 2‰; Ohmoto and Rye, 1979). Thus, the data suggest a probable source of sulphur in the sulphides were leached from the igneous rocks most likely the volcanic host rocks at the both deposits. Nevertheless, a direct magmatic source seem unlikely because a direct magmatic contribution would be more effective in supplying metals in particular the Cu, Au, Bi and Te to VHMS deposits (Large, 1992), and is significant in the formation of giant VHMS deposits (Ulrich et al., 2002). The presence of pyrophyllite as an alteration mineral also has significant genetic implications (see Chapter 5).

Furthermore, the relatively narrow range and nearly positive $\delta^{34}S$ values of sulphides from both deposits also rules out a bacterial sulphate source for the sulphur, such as in many VHMS deposits of the Iberian Pyrite Belt, Portugal (e.g., Velasco et al., 1998). However, these characteristic are an indicator of an inorganic reduction process of seawater sulphate in many other VHMS deposits of high temperature formation (Sasaki and Kajiwara, 1971) with

the presence of ferrous iron as a reduction agent (Ripley and Ohmoto, 1977; Mottl et al., 1979; Shanks et al., 1981; Shanks and Seyfried, 1987; Kerridge et al., 1983). This similar interpretation is suggested for the $\delta^{34}S$ of sulphide characteristics at both the Bukit Botol and Bukit Ketaya deposits because there are occurrences of the Fe-Mn±Si layers at the top of the mineralised systems. In addition, reduction of seawater sulphate can also occur within the fluid discharge zone (Woodruff and Shanks, 1988), the recharge zone (Janecky and Shanks, 1988) or the deep high temperature reaction zone (Bluth and Ohmoto, 1988).

As discussed above, the similarity of $\delta^{34}S$ values in sulphates also suggests a contribution from seawater sulphate during Permian time might be possible because the close association of $\delta^{34}S$ for sulphate in Permian seawater is clearly shown in Figure 7.3 by several VHMS deposits from the Permian time interval including the Tasik Chini deposit systems (both the Bukit Botol and Bukit Ketaya). However, the higher $\delta^{34}S$ values present in the Tasik Chini deposit and other VHMS deposits could be due to the contribution of hydrothermal sulphate (Ohmoto, 1996; Solomon et al., 2004a; Scotney et al., 2005). This interpretation is consistent with the diagenetic or hydrothermal barite deposits than the marine (pelagic) barites to infer seawater sulphur isotope records (Eagle et al., 2003; Griffith and Paytan, 2012). Therefore, the sulphur isotope ratio of these barite deposits is either equal to, or may be higher or lower than contemporaneous seawater (Paytan et al., 2002), depending on the relative fraction of sulphur of hydrothermal origin (H_2S oxidation) in the mixture sources (Hannington and Scott, 1988). Additionally, the highly variable $\delta^{34}S$ for sulphide within the Permian deposits in Figure 7.3, including the Tasik Chini deposit, are consistent with the relationship between the deposits and seawater (Sangster, 1968). The values on average are ~16 per mil more depleted than that of the co-existing seawater (Huston, 1999; Huston et al., 2010).

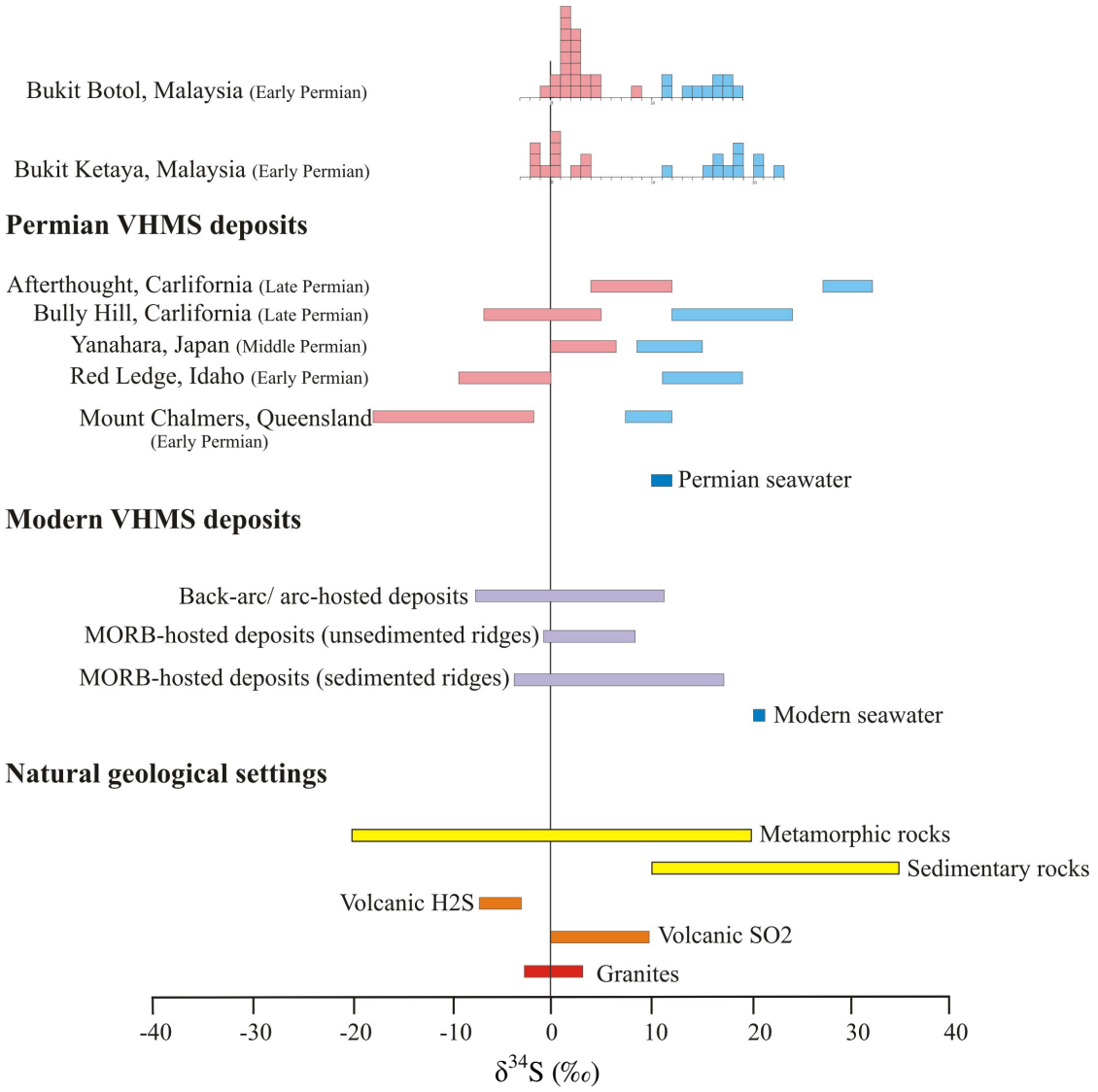

Fig. 7.3. Comparison of $\delta^{34}S$ values for Bukit Botol and Bukit Ketaya deposits with selected Permian VHMS deposits, modern seafloor VHMS deposits from various tectonic settings and natural geological settings. Source of data: Permian VHMS deposits; Afterthought and Bully Hill, California—Gustin (1990), and Eastoe and Gustin (1996); Yanahara, Japan—Yamamoto et al. (1968), and Kajiwara and Date (1971); Red Ledge, Idaho—Fifarek et al. (1984), and Fifarek (1985); Mount Chalmers, Queensland—Huston (1999), and Hunns (2001); Permian seawater—Claypool et al. (1980), and Kampschulte and Strauss (2004). Modern VHMS deposits; back-arc/ arc-hosted deposits; Okinawa Trough, Japan—Halbach et al. (1989); Manus Basin—Lein et al. (1993); Mariana Trough—Kusakabe et al. (1990); Brothers Volcano, Kermadec Tonga—de Ronde et al. (2005); MORB-hosted deposits (unsedimented ridges); Southern Juan de Fuca Ridge (SJFR)—Shanks and Seyfried (1987); Galapagos Rift—Skirrow and Coleman (1982), and Knott et al. (1995); Axial Seamount—Hannington and Scott (1988); Broken Spur—Duckworth et al. (1995); Snakepit—Kase et al. (1990); TAG—Herzig et al. (1998), Chiba et al. (1998), and Gemmell and Sharpe (1998); East Pacific Rise (EPR)—McConachy (1988), Bluth and Ohmoto (1988), Stuart et al. (1994), Hekinian et al. (1980), Arnold and Sheppard (1981), Styrt et al. (1981), Kerridge et al. (1983), Zierenberg et al. (1984), Woodruff and Shanks (1988), and Marchig et al. (1990); MORB-hosted deposits (sedimented ridges); Escanaba Trough—Koski et al. (1988), Zierenberg et al. (1993), and Böhlke and Shanks (1994); Guayamas Basin—Peter and Shanks (1992), and Shanks et al. (1995); Middle Valley—Goodfellow and Blaise (1988), Duckworth et al. (1994), Zierenberg (1994), and Stuart et al. (1994); modern seawater—Rees et al. (1978). Natural geological settings: metamorphic rocks, sedimentary rocks, volcanic H_2S, volcanic SO_2 and granites—Hoefs (2004).

7.5 Summary

1) The sulphur isotope ratios of the sulphides at both the Bukit Botol and Bukit Ketaya deposits are distributed in a narrow range, close to the average ratio in the magmatic sulphur, whereas the $\delta^{34}S$ composition of sulphates is similar to or slightly higher than that of Permian seawater sulphate.

2) These features demonstrate that the derivation of hydrothermal sulphide sulphur from the seawater involved an inorganic or chemical reduction of seawater sulphate. The source of sulphur in the Tasik Chini hydrothermal fluids, prior to mixing with seawater is mainly from the seawater sulphate and is similar to that of Permian seawater sulphate at about 10 to 12 permil.

3) A magmatic source contribution is also significant when considering the presence of a narrow range of $\delta^{34}S$ values and nearly to 0‰ for sulphides. This sulphur was most likely derived from the volcanic rocks that hosted the mineralisation at the both deposits.

CHAPTER 8 LEAD ISOTOPE STUDIES

8.1 Introduction

Lead isotope signatures can be used to define the source of Pb (Doe and Zartman, 1979), and to fingerprint mineral systems with model age information for an individual deposit (Downes and Seccombe, 2004). Therefore, the application of lead isotope analysis can provide important data to be used in constraining the process of ore formation (Harkins et al., 2008; Zartman and Smith, 2009; Bozkaya, 2011; Huston et al., 2010; 2011).

Sources of ore metals and associated igneous rocks in porphyry copper systems have long been studied using lead isotope geochemistry such as in the North and Central Andes (e.g., McNutt et al., 1979; Tilton et al., 1981; Sillitoe and Hart, 1984; Kontak et al., 1990; Mukasa et al., 1990; Tosdal and Munizaga, 2003), as well as in the North American Cordillera (e.g., Bouse et al., 1999). Moreover, most Mississippi Valley-type (MVT) Pb-Zn deposits in particular show extreme ranges of Pb isotope composition and mixing between multiple reservoirs near the site of ore deposition (Kesler et al., 1994a and 1994b). Compared to MVT deposits, there is only limited previous work dealing with VHMS Pb isotopic characteristics and only for the well-known and sizeable (giant) deposits (e.g., the Thalanga, Dry River and Mount Chalmers deposits, Australia; Gulson and Vaasjoki, 1987; the VHMS deposits in Iberian Pyrite Belt and Mt. Read Volcanics, Marcoux, 1998; Huston et al., 2011; the Middle Valley VHMS deposit, Juan de Fuca Ridge ; Stuart et al., 1999; Sangster et al., 2000; the Macuchi VHMS districts, Western Cordillera; Chiaradia and Fontbote, 2001; the Neves Corvo VHMS deposit, Portugal; Relvas et al., 2001; the VHMS deposits on Prince of Wales

Island, Southern Alaska, Ayuso et al., 2005; and the VHMS deposits in Guerrero Terrane, Central Mexico; Mortensen et al., 2008).

Lead isotope studies were undertaken in this study to (1) characterise the lead isotope signatures (2) identify the sources of lead for Bukit Botol and Bukit Ketaya mineralisations and (3) determine the lead reservoirs of Tasik Chini.

8.2 Methods

Isotopic measurements of Pb were made on sulphide minerals including galena separated from the ore samples and whole massive pyrite ore from the Bukit Botol and Bukit Ketaya deposits and whole rock samples of the host rhyolite at both the deposits, by solution and laser methods.

The Pb isotope analyses on whole rock sulphide and volcanic rocks samples were performed using the procedure and method of Townsend et al. (1998), whereas the Pb isotopes of the galena crystals were determined using a laser method developed at CODES, University of Tasmania. The laser method is similar to that used to determine the in-situ Pb isotopic composition of pyrite (e.g., Meffre et al., 2008) with some modifications to enable the analysis of galena. Determination of the Pb isotopic composition of the galena used a small spot size (8 μm) and a low repetition rate (4 Hz) due to the high concentration of Pb in galena. The machine sensitivity was also reduced to keep all of the Pb isotopic count rates within the "pulse" range of the detector (electron multiplier). Mass bias was determined using a sample of Broken Hill galena (UTAS sample 154202) and checked with four different secondary standards previously analysed by solution ICP-MS using the method of Townsend et al. (1998). After analysis of the background gas composition, long lines and raster patterns (240 s at 1 μ/s) were ablated on the galena crystal while measuring the Pb isotopes, Hg, U and Th. One primary standard and one secondary standard were analysed for every four unknowns.

Although, very slightly less precise than solution ICP-MS, the results on the secondary standard show that this method is significantly accurate. The Pb isotopes ratios for all samples were measured using the Agilent quadrupole instrument at CODES, University of Tasmania.

8.3 Lead Isotope Results

8.3.1 Bukit Botol deposit

The lead isotope values for three massive pyrites and two galena minerals from the Bukit Botol deposit fall within narrow ranges. The $^{206}Pb/^{204}Pb$ ratios are from 18.14 to 18.20 and $^{207}Pb/^{204}Pb$ between 15.52 and 15.56. The $^{208}Pb/^{204}Pb$ ratios for all sulphide samples are also within the range of 37.96 to 38.35. The Pb isotope ratios from the three host felsic volcanic rocks (rhyolite) at Bukit Botol are very similar to the sulphide minerals lead isotope compositions. The $^{206}Pb/^{204}Pb$ shows a range of composition from 18.18 to 18.20, $^{207}Pb/^{204}Pb$ between 15.53 and 15.59 and $^{208}Pb/^{204}Pb$ from 37.96 to 38.26 (Table 8.1).

Table 8.1. Lead isotope data for the Bukit Botol and Bukit Ketaya deposits.

No	Sample	Mineral/rock unit	Lead isotope compositions						Method
			$^{206}Pb/^{204}Pb$	+/-1s	$^{207}Pb/^{204}Pb$	+/-1s	$^{208}Pb/^{204}Pb$	+/-1s	
Bukit Botol									
1	MBTCS4(1)	volcanic rock	18.20	0.336	15.55	0.323	38.10	0.311	Soln-Q-ICPMS
2	MBTCS2	volcanic rock	18.18	0.337	15.53	0.360	37.96	0.341	Soln-Q-ICPMS
3	BB10a	volcanic rock	18.20	0.046	15.59	0.043	38.26	0.108	Soln-Q-ICPMS
4	BB 1b	pyrite	18.14	0.067	15.52	0.050	37.96	0.065	Soln-Q-ICPMS
5	BB 2d	pyrite	18.15	0.062	15.52	0.038	37.98	0.069	Soln-Q-ICPMS
6	BB 10c	pyrite	18.13	0.072	15.55	0.051	38.06	0.070	Soln-Q-ICPMS
7	BB9-1	galena	18.20	0.086	15.53	0.071	38.26	0.218	La-Q-ICPMS
8	BB9-2	galena	18.17	0.042	15.55	0.041	38.35	0.124	La-Q-ICPMS
Bukit Ketaya									
1	BK11a	volcanic rock	18.10	0.035	15.56	0.032	38.08	0.046	Soln-Q-ICPMS
2	BK11	volcanic rock	18.11	0.038	15.57	0.026	38.26	0.081	Soln-Q-ICPMS
3	BK12a	pyrite	18.11	0.051	15.56	0.042	38.12	0.063	Soln-Q-ICPMS
4	BMSE1	pyrite	18.06	0.071	15.54	0.048	38.04	0.081	Soln-Q-ICPMS
5	KZMA-3	pyrite	18.04	0.053	15.55	0.055	37.99	0.076	Soln-Q-ICPMS
6	BK11-1	galena	18.05	0.058	15.43	0.050	37.96	0.143	La-Q-ICPMS
7	BK11-2	galena	18.20	0.048	15.57	0.043	38.30	0.130	La-Q-ICPMS
8	BK11-3	galena	18.18	0.067	15.56	0.052	38.21	0.147	La-Q-ICPMS
9	BK12a	galena	18.14	0.083	15.48	0.057	38.11	0.152	La-Q-ICPMS

Annotation: Soln-Q-ICPMS = solution ICPMS, La-Q-ICPMS = laser ICPMS

In the $^{206}Pb/^{204}Pb$ versus $^{207}Pb/^{204}Pb$ plot with the bulk crust/juvenile arc of Stacey and Kramers (1975) and the upper crust and mantle evolution curves of Doe and Zartman (1979), the results from sulphides and volcanic rocks lie below or close to the field of the bulk crust/juvenile arc, but are slightly scattered (Fig. 8.1A). Moreover, the narrow and partial overlapping of the sulphides with volcanic rocks of Bukit Botol suggest a single source. Thus, it is indicated that the Pb reservoirs for both are derived from mixed sources of bulk crust and mantle. In the $^{206}Pb/^{204}Pb$ versus $^{207}Pb/^{204}Pb$ plot of the tectonic model (after Zartman and Doe, 1981), which show the modern fields for broad geologic environments, all the data plots in the field of a primitive arc and are most consistent with derivation mainly from a mantle source (Fig. 8.1B).

8.3.2 Bukit Ketaya deposit

The sulphides consisting of four galena and three massive pyrite samples from the Bukit Ketaya deposit present values of $^{206}Pb/^{204}Pb$ from 18.04 to 18.20, $^{207}Pb/^{204}Pb$ between 15.43 and 15.56 and $^{208}Pb/^{204}Pb$ from 37.96 to 38.30. However, there is a small difference in lead isotope ratios between the galena and massive pyrite samples, where the $^{206}Pb/^{204}Pb$ ratios of galena minerals are uniformly higher than those of the massive pyrites, but both are slightly less radiogenic. The lead isotope signature of two whole-rock felsic volcanic samples hosting the Bukit Ketaya deposit shows a $^{206}Pb/^{204}Pb$ from 18.10 to 18.11, $^{207}Pb/^{204}Pb$ between 15.56 and 15.57 and $^{208}Pb/^{204}Pb$ of 38.08 to 38.26. These Pb isotopic compositions are similar to those of the sulphide samples (Table 8.1).

The results from sulphides and volcanic rocks were plotted on $^{206}Pb/^{204}Pb$ versus $^{207}Pb/^{204}Pb$ diagram with the Stacey and Kramers (1975) bulk crust/ juvenile arc growth curve and the Doe and Zartman (1979) upper crust and mantle growth curves. In the lead evolution curves, the Pb isotope ratios of galena, massive pyrite and hosted volcanic rocks are distinctive in

having low $^{207}Pb/^{204}Pb$ ratios and plot between the mantle and the bulk crustal growth curves, with two galena samples clearly shifted and plotted on and near the mantle curve.

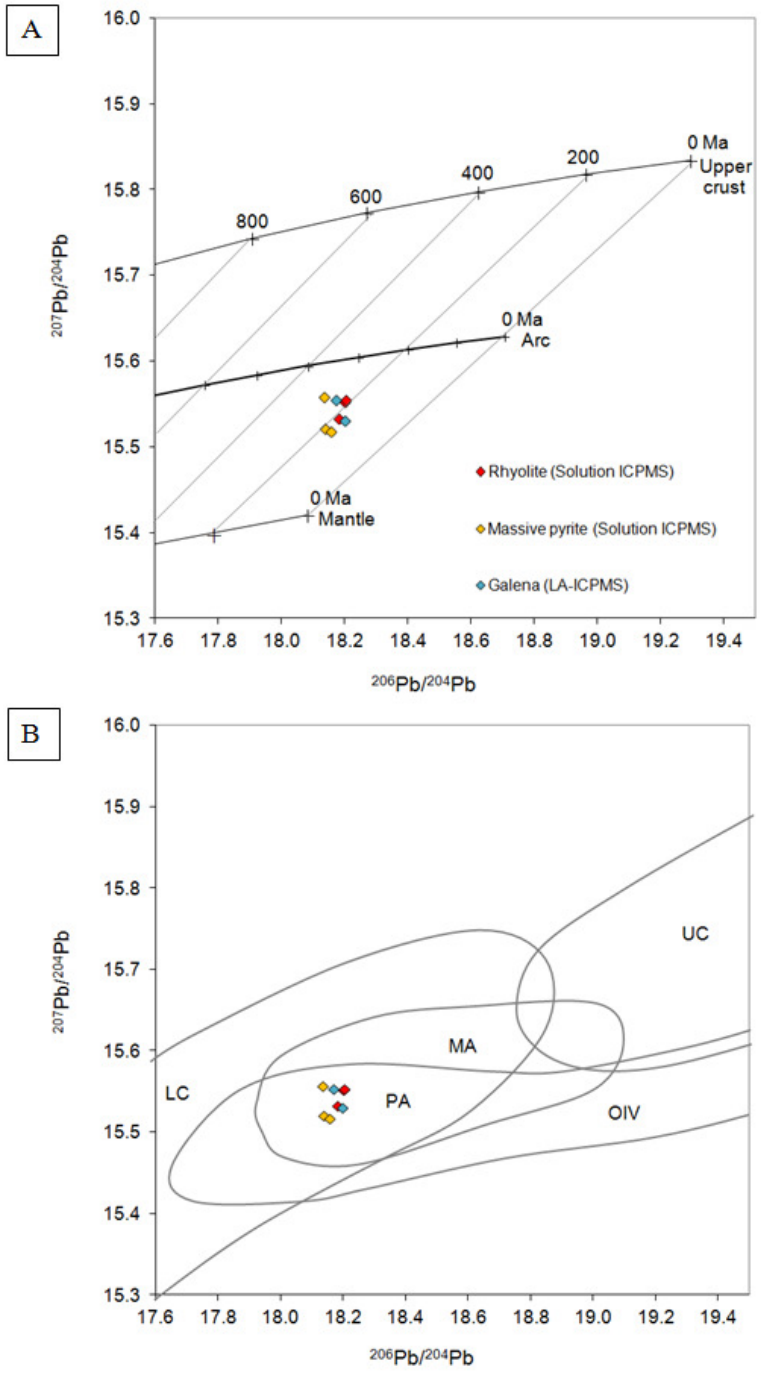

Fig. 8.1. Lead isotope ratio plot for volcanic rocks, massive pyrite and galena samples from Bukit Botol deposit. **A**. Data plotting along the lead growth curves of upper crust and mantle from Doe and Zartman (1979) and juvenile arc from Stacey and Kramers (1975). **B**. Data are plotted on the tectonic model diagram with the subdivision of fields after (Zartman and Doe, 1981). Annotation: UC = upper crust, LC = lower crust, MA = mature arc, PA = primitive arc and OIV = ocean island volcanic rocks.

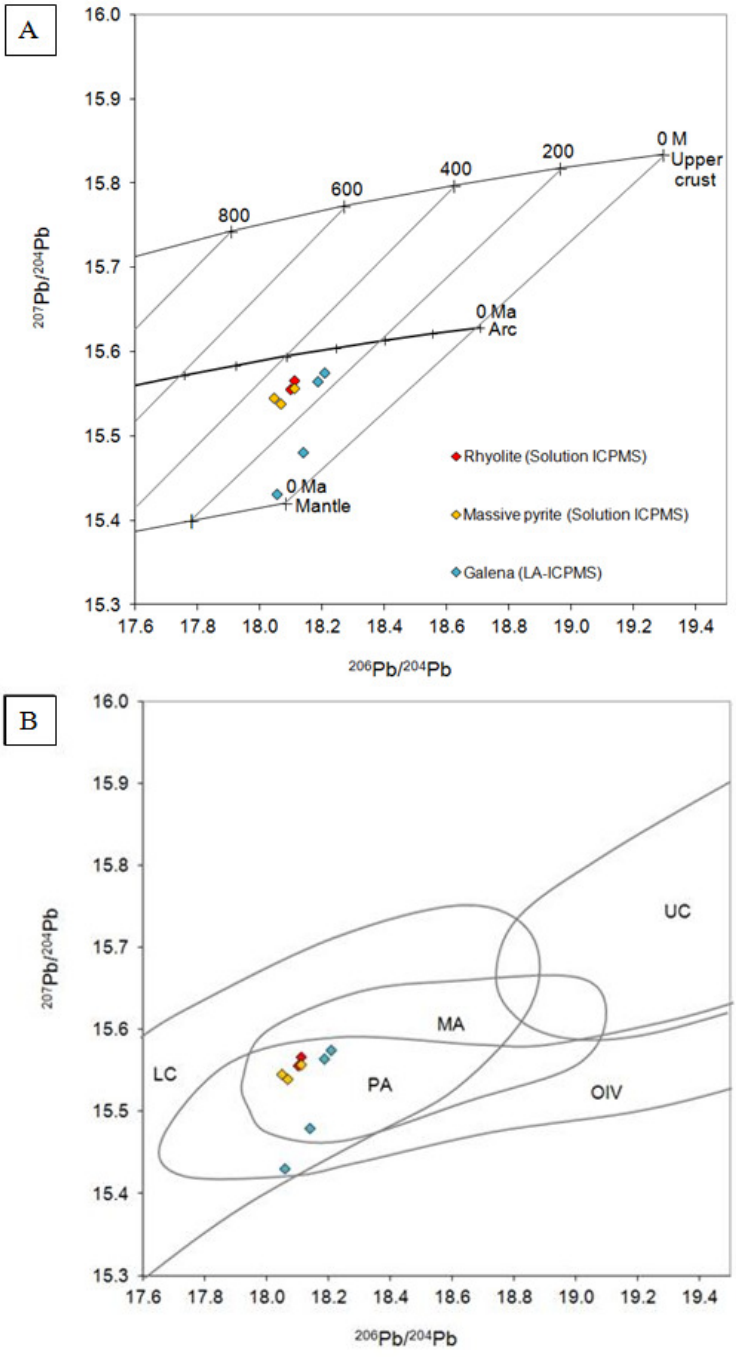

Fig. 8.2. Lead isotope ratio plot for volcanic rocks, massive pyrite and galena samples from Bukit Ketaya deposit. **A**. Data plotting along the lead growth curves of upper crust and mantle from Doe and Zartman (1979) and juvenile arc from Stacey and Kramers (1975). **B**. Data are plotted on the tectonic model diagram with the subdivision of fields after (Zartman and Doe, 1981). Annotation: UC = upper crust, LC = lower crust, MA = mature arc, PA = primitive arc and OIV = ocean island volcanic rocks.

The slight linear trend detected in galena samples has no isochron significances or radiogenic enrichment trends, and this may represent the source with different value characteristics (Fig. 8.2). Thus, the similarity of all data that plot above the bulk crustal growth line may indicate that they shared a common Pb isotope source, which is consistent with mixing of bulk crust/juvenile arc and mantle sources. The concentration of the Pb isotope data mainly in the field of primitive arc, with some within oceanic island volcanic rocks on the $^{206}Pb/^{204}Pb$ versus $^{207}Pb/^{204}Pb$ plot of Zartman and Doe (1981), also suggests a mixed source from crust/juvenile arc and mantle.

8.4 Discussion

8.4.1 Constraints on possible lead ore-forming sources

The lead isotope signature for the Bukit Botol deposit is very similar to that of the Bukit Ketaya deposit, with a homogeneous lead composition within each deposit. These features are a typical of many VHMS deposits (Gulson, 1986). At both deposits, the lead isotopic composition data of all sulphides plot below the lead growth curve of a juvenile arc with a few samples scattered toward the lead growth curve of the mantle. Similarly, results of the volcanic hosting rocks from the both deposits also fall below this juvenile arc curve and plot within the field of Pb isotopic compositions of sulphides. These data are in agreement with host rocks controlling the metal content in VHMS deposits (e.g., Franklin et al., 1981). Therefore, it is suggested that the lead in the Bukit Botol and Bukit Ketaya deposits may be derived from volcanic rocks.

In term of Pb tectonic model, the sulphides and ore-hosting volcanic rocks from both deposits were derived from a source with some mantle constituent, and plotted within the primitive arc (i.e., island-arc setting) with a significant ocean island volcanic arc input. Thus, the volcanic hosting rocks lead isotopic signature and some of the sulphide lead may be derived directly from a magmatic and minor mantle sources. According to these features the Bukit Botol and

Bukit Ketaya deposits in the Central Belt were probably emplaced in an area of uniformly thin crust underneath. This is in agreement with an interpretation of Bouguer gravity anomalies for Peninsular Malaysia after Ryall (1982) who proposed that the thinning of sialic layer is the basement of the Central Belt. More recently, following the interpretation of Ryall (1982), a thinned lithosphere is assumed under the Central Belt by Oliver et al. (2014). An alternative interpretation is that the basement of the Central Belt area is of uniformly thin crust underneath probably a back-arc setting.

Comparison of both the Bukit Botol and Bukit Ketaya deposits' lead isotopic compositions is made to those of several modern VHMS deposits hosted in back-arc/arc setting, sediment-free MORB and MORB sedimented ridges in Figure 8.3. Both deposits display a range of lead compositions which are typical of back-arc hosted VHMS deposits. Possible modern tectonic and associated deposits include the VHMS deposits at Manus Basin and Lau Basin.

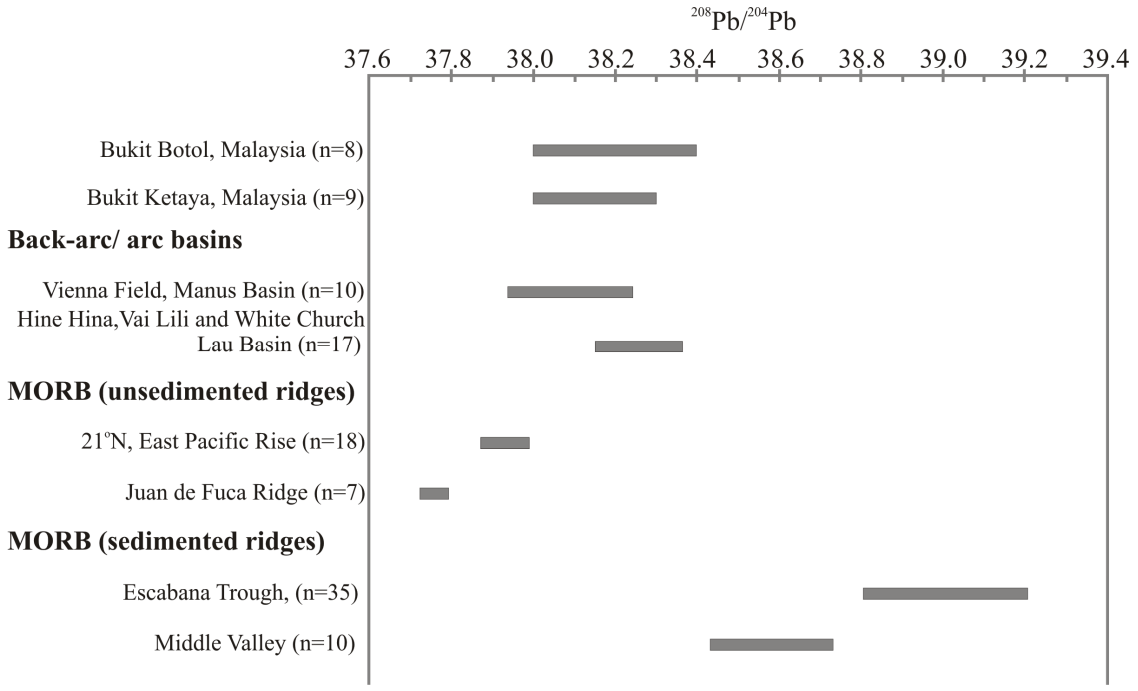

Fig. 8.3. Published $^{208}Pb/^{204}Pb$ data of several VHMS deposits from a modern tectonic setting and the comparison with the lead isotopic compositions in both the Bukit Botol and Bukit Ketaya deposits, Malaysia. Source of data: Vienna Field, Manus Basin—Agapova et al. (1994); Lau Basin—Agapova et al. (1994); 21°N, East Pacific Rise—Vidal and Clauer (1981); Juan de Fuca Ridge—Hegner and Tatsumoto (1987); Escabana Trough—Zierenberg et al. (1993); and Middle Valley—Goodfellow and Franklin (1988).

8.4.2 Comparison with other deposits in Peninsular Malaysia

The Pb isotopic compositions of the Botol and Bukit Ketaya deposits with other deposits in Peninsular Malaysia are plotted in $^{206}Pb/^{204}Pb$ versus $^{207}Pb/^{204}Pb$ diagram with the Stacey and Kramers (1975) bulk crust growth curve and the Doe and Zartman (1979) upper crust and mantle growth curves (Fig. 8.4). The Bukit Botol and Bukit Ketaya data have a distinct signature when compared with available Pb isotope results for a few tin deposits including two granitic samples from the Western Belt, the tin mineralisations in the Eastern Belt and the orogenic-gold together with base metal deposits from the Central Belt in Peninsular Malaysia. The lead isotope signatures of both the Bukit Botol and Bukit Ketaya deposits are less radiogenic and suggest a magmatic and minor mantle origin. However, almost all the data of the tin deposits, granitic samples, orogenic-gold deposits and base-metal deposits are more radiogenic, concentrated and formed of a mixed of upper crust and juvenile arc reservoir, suggesting a subduction origin with a variable contribution of upper crust component. The different lead isotope signatures of these deposits can be related to their different formation environments.

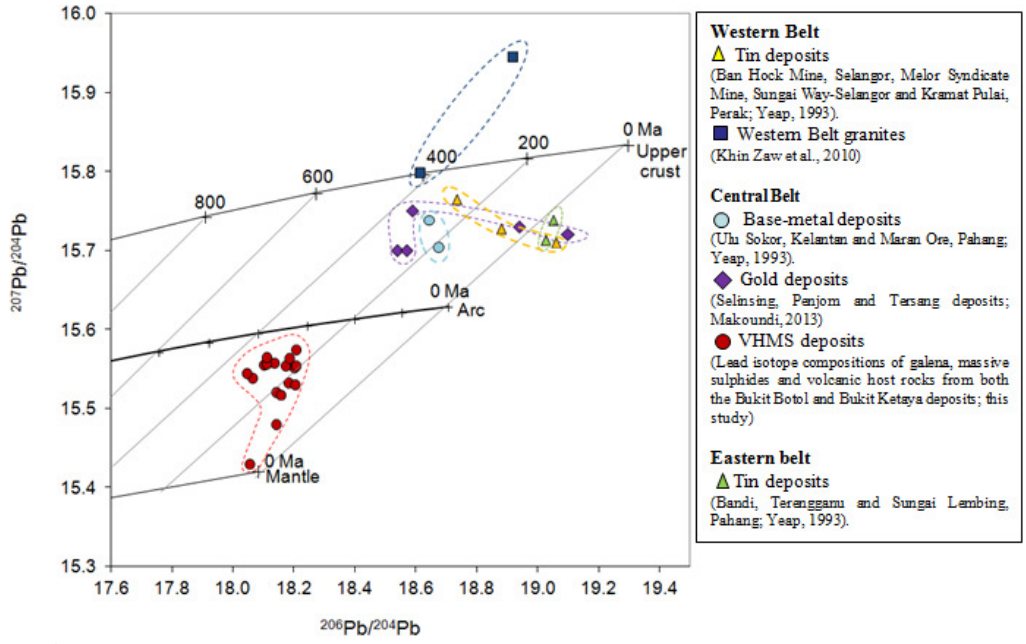

Fig. 8.4. $^{206}Pb/^{204}Pb$ versus $^{207}Pb/^{204}Pb$ diagram showing the lead isotope ratios plot of a few deposits and granitic rocks from the Western, Central and Eastern Belts of Peninsular Malaysia.

Although Yeap (1993) has presented lead isotope data for galena from a few tin, gold and base metal deposits in different mineralisation belts in Peninsular Malaysia, he only mentioned that the Pb isotope sources of the tin deposits in both the Western and Eastern Belts were derived from the upper crust, whereas the Pb source of base metal and gold deposits in the Central Belt was loosely interpreted to be located within the field of lower crust to mature arc and close to field of pelagic sediments. Thus, based on the results obtained in this study and the Pb isotopic data from Yeap (1993), Khin Zaw et al. (2010) and Makoundi (2012) (see Fig. 8.3) it is re-interpreted and suggested that the tin deposits (five data; Yeap, 1993) and associated granitic rocks (two data; Khin Zaw et al., 2010) for both the Western and Eastern Belts have been derived from a subduction magmatic origin with a significant contribution of upper crust component, consistent with the interpretation of Yeap (1993). Similarly, the Pb sources of orogenic gold deposits (five data; Makoundi, 2012) and base metal deposits (two data; Yeap, 1993) with a mix of juvenile arc and upper crust reservoirs also suggest a subduction-related magmatic origin but with a slight contribution of upper crust components. In addition, the characteristics indicating a lower crust to mature arc location, close to a field of pelagic sediments (Yeap, 1993) are interpreted here as most likely to represent a continental margin arc for the formation of gold and base metal deposits in the Central Belt. In contrast, the lead isotope signatures of both the Bukit Botol and Bukit Ketaya deposits in the Central Belt as discussed above suggest a magmatic and minor mantle origin and are probably emplaced in an area of uniformly thin crust underneath a back-arc setting. Alternatively, the Pb isotope signatures of a primitive arc with a significant ocean island volcanic arc input of volcanic rocks, including the sulphide deposits at both deposits, are consistent with the characteristics of intra-oceanic arc rocks or environments (e.g., Sun, 1980).

8.4.3 Comparison with several other deposits in East Malaya-Indochina Terranes, SE Asia

Recent comprehensive studies in SE Asia have developed Pb isotope signatures of ore deposits for evaluating both the crustal Pb and the genesis of related ore deposits evolution (e.g., Khin Zaw et al., 2010). In this model, they compiled all Pb isotope data obtained (unpublished) and were supported by the zircon and Re-Os dating (unpublished) from various ore deposits and host rocks throughout SE Asia. In this section, the Pb isotopic compositions of the Bukit Botol and Bukit Ketaya deposits and other mineralisation styles in Peninsular Malaysia are compared with those of several other deposits in the East Malaya-Indochina Terrane, SE Asia (Fig. 8.5).

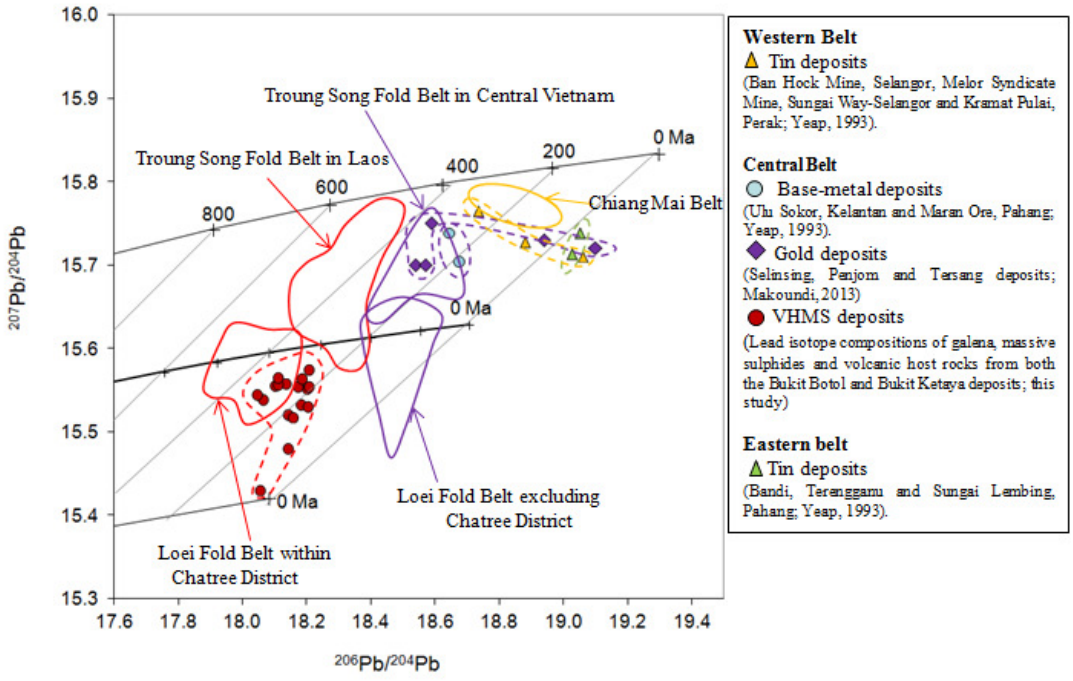

Fig. 8.5. $^{206}Pb/^{204}Pb$ versus $^{207}Pb/^{204}Pb$ diagram showing the lead isotope ratio of the ore deposits in Western, Central and eastern belts of Peninsular Malaysia compared with those of several deposits in East Malaya-Indochina Terrane, SE Asia. The field of deposits from Troung Song Fold Belt in Laos, Troung Song Fold Belt in Central Vietnam, Loei Fold Belt in Chatree District and Loei Fold Belt excluding Chatree District are modified from Manaka (2013) based on the lead isotope composition of sulphides data from Khin Zaw et al. (2010), Salam (2013) and Manaka (2014) .

The tin deposits from the Western Belt overlap with a deposit in the Chiang Mai Belt in Thailand, whereas the Eastern Belt tin deposits did not share this common lead source. This

contrast is consistent with a different characteristic of the granitic rocks for these two belts. The Western Belt tin granites are recognised as being of the S-type (Hutchison, 1977; Cobbing et al., 1992), whereas the Eastern Belt has both I and S-types granites (Rajah et al., 1977; Cobbing et al., 1992), and the tin deposit is only associated with the S-type granites (i.e., the Bukit Besi Tin Mine; Yeap, 1993).

Data for economic gold and base metal deposits in the Central Belt overlap the deposits in the Loei Fold Belt excluding the Chatree District. In addition, they also show a trend with a deposit in Truong Son Fold Belt in Central Vietnam. In contrast, the Bukit Botol and Bukit Ketaya deposits, which are also in the Central Belt, overlap the deposits within the Chatree District in the Loei Fold Belt, and also define a trend to those of the deposits within the Truong Son Fold Belt in Laos.

Although these two distinct Pb isotope compositional fields probably avoid genetic links between them, the uniformly comparable lead isotope signatures within those mineralised belts suggest that they share a nearly similar magmatic-hydrothermal system. The first stage magmatic event is responsible for the mineralisation within the Truong Son Fold Belt in Laos (Khin Zaw et al., 2010; Manaka, 2014) and within the Chatree District in the Loei Fold Belt (Khin Zaw et al., 2010; Salam, 2013), whereas the later stage magmatic event relates to the mineralisation in the Truong Son Fold Belt of Central Vietnam (Khin Zaw et al., 2010; Manaka, 2014) and in the Loei Fold Belt excluding the Chatree District (Khin Zaw et al., 2010; Salam, 2013).

These data agree with Metcalfe et al. (1982), Metcalfe and Chakraborty (1996), Metcalfe (2013), who mentioned that the Permian volcanic rocks of Sukhothai Arc and the Middle Triassic volcanic rocks of subduction-related I-type granitoids are common in the Central Belt

of the Peninsular Malaysia and show a younging trend towards the Bentong-Raub Suture Zone (Hutchison, 2009a). Some evidence obtained from this study, such as the well constrained age of ore hosting rocks of Early Permian ages from both the Bukit Botol and Bukit Ketaya deposits (see Chapter 4), the location of the Tasik Chini area within the Central Belt and relatively located west of the Lebir Fault Zone (see Chapters 3 and 4) and the lead isotope signatures of probable magmatic and minor mantle origin formed in an island arc and back-arc environment (this chapter), support the interpretation that the Central Belt of Peninsular Malaysia represents the Sukhothai Arc (e.g., Sone and Metcalfe, 2008; Metcalfe, 2013; Sevastjanova et al., 2011), and the remnant of the back-arc basin is represented by the Lebir Fault Zone. Moreover, the Pb data of the orogenic-gold deposits and base-metal deposits in the Central Belt, which show a mixture of juvenile arc and upper crust reservoir, but have lower crust to mature arc and are close to field of pelagic sediments characteristics (Yeap, 1993), is interpreted here to indicate a subduction-related magmatic origin within a continental margin arc environments. This interpretation is also significantly consistent with the Central Belt as the only Sukhothai Arc in Peninsular Malaysia.

8.5 Summary

1) The Pb isotope compositions of galena, pyrite and felsic volcanic rocks for the Bukit Botol and Bukit Ketaya deposits are uniform, and plot below and between the juvenile arc and mantle lead growth curves.

2) The Pb isotopic ratio of sulphides are partly derived from their host volcanic rocks, and both the volcanic hosting rocks lead isotopic signature and partly the sulphide lead may also be derived directly from a magmatic and minor mantle sources.

3) The variability of Pb isotope signatures of different mineralisation styles in Western, Central and Eastern Belts of Peninsular Malaysia indicate different isotopic sources and

genesis. This distinction can be correlated to the different mixing of Pb reservoir sources and the age of the mineralisation within these three different belts.

4) The Pb isotopic data from this East Malaya Terrane is also consistent with the distribution of many ore deposit styles in the Indochina Terrane as a result of the long-lived subduction-collision related magmatic events. Thus, a similar and common metallogenic event was involved in the formation and distribution of all these deposits.

CHAPTER 9 FLUID INCLUSIONS

9.1 Introduction

Studies of fluid inclusions provide a constraint on the physical and chemical conditions of ore deposition, and fluid inclusion data are useful to understand metal transports in hydrothermal systems (e.g., Roeddar, 1984; Wilkinson, 2001). For VHMS deposits, much of the complex physical and chemical evolution of hydrothermal systems comes from the study of fluid inclusions of both modern (e.g., Lecuyer et al., 1999; Lüder et al., 2001; Yang and Scott, 2002; Vanko et al., 2004) and ancient VHMS systems (e.g., Khin Zaw et al., 1996, 2003; Hou et al., 2001, 2008; Pisutha et al., 1983; Solomon et al, 2004a; 2004b; Scotney et al., 2005; Inverno et al., 2008; Moura, 2008b)

To date, no detailed fluid inclusion studies have been undertaken on the samples from the Bukit Botol and Bukit Ketaya deposits. As a result, primary fluid inclusions hosted in quartz from the stockwork zones and in barite from the barite-bearing lenses are studied and discussed in this Chapter. Measurement of these fluid inclusions was performed to understand the thermal history and salinity between the deeper stockwork zone and the shallower part of the ore system. In addition, the primary inclusions in quartz are trapped as quartz precipitates from hydrothermal fluids (Roeddar 1984), and its properties can provide information on the physical and chemical conditions of quartz precipitation in the deeper zone (Steele-MacInnis et al., 2012a); the same characteristics can be also found at the shallow zone (Steele-MacInnis et al., 2012a). Accordingly, fluid inclusion investigation is made in this study from the

primary inclusions from both barite occurrences on the top and quartz from the stockwork zone of the mineralisation sequence. Hence, the fluid inclusion study data will provide significant information on hydrothermal systems to understand the origin of the Tasik Chini massive sulphide system.

9.2 Samples and Methods

The samples used in this study are representative of the different types of mineralisation at the Bukit Botol and Bukit Ketaya deposits taken from the lower levels (stockwork zone) to upper parts (barite-bearing lenses) of the mineralised systems. The fluid inclusion samples were first examined using standard petrography, and were analysed by microthermometric and Laser Raman spectroscopic techniques.

In total twenty-four sections were prepared for fluid inclusion analysis. However, a detailed investigation of fluid inclusions were only conducted based on twelve doubly polished thick sections that were suitable for microthermometric measurements; seven from the Bukit Botol deposit and five from the Bukit Ketaya deposit. The doubly polished 150 μm thick fluid inclusion wafers were prepared at CODES/SES University of Tasmania. The sections were viewed under conventional microscopy to map out target areas, photomicrographs were captured to be used for reference before fluid inclusion analysis. In addition, cathodoluminescence (CL) petrography was also undertaken to record mineral growth zones in a few sections using the FEI Quanta 600 MLA/ESEM instrument at the CSL, University of Tasmania.

9.2.1 Microthermometric measurements

Standard microthermometric techniques were applied using a LINKAM MDS600 heating and freezing stage at CODES, University of Tasmania. Calibration was made using synthetic fluid

inclusions provided by Synflinc Inc. The accuracy of the experiment was ±1.0 for the heating temperature and ±0.3 for the freezing temperature. Salinities were measured as wt% NaCl equivalent and was calculated using the equation of Bodnar (1993) from the temperatures of ice melting. For fluid inclusions with CO_2 clathration, salinities were calculated using the equation of Bozzo et al. (1973) based on the melting point of clathrate (Tmclathrate).

9.2.2 Laser Raman microprobe

Laser Raman spectroscopic analysis was carried out on representative fluid inclusions with a Dilor Super-Labram spectrometer at Geoscience Australia. The presence and absence of CO_2, O_2, N_2, H_2S and CH_4 in a gas phase were investigated. The machine was equipped with a holographic notch filter with 600 and 1800 g/mm gratings. It also had a 2000 x 450 pixel CCD detector that was liquid N_2 cooled.

The individual mineral pieces within the wafer were examined under microscope to select the areas with abundant fluid inclusions. The fluid inclusions were illuminated with a 633 nm laser excitation, using 5 mW of power at the samples. An Olympus BX40 microscope with a 100X objective was used to focus the laser beam and collect the scattered light. The focused laser spot on the samples was approximately 1 μm in diameter and wave numbers are accurate to ± 1 cm-1 as determined by plasma and neon emission lines. For the analysis of CO_2, O_2, N_2, H_2S and CH_4 in the vapour phase, spectra were recorded from 1000 to 3800 cm-1 using a single 30 second integration time per spectrum (Mernagh and Wygralak, 2007). The detection limits (~1 mole %) are stated as being dependent on the partial pressure of each gas, instrumental sensitivity, and the optical quality of each fluid inclusion (Wopenka and Pasteris, 1987). The Laser Raman analyses were performed by Dr. Terry Mernagh of Geoscience Australia.

9.3 Fluid Inclusion Petrography

Abundant fluid inclusions are found in quartz and barite from the two different mineralisation units at both the Bukit Botol and Bukit Ketaya deposits. The fluid inclusions occur as isolated inclusions along crystal growth zones and in trails (Figs. 9.1 and 9.2).

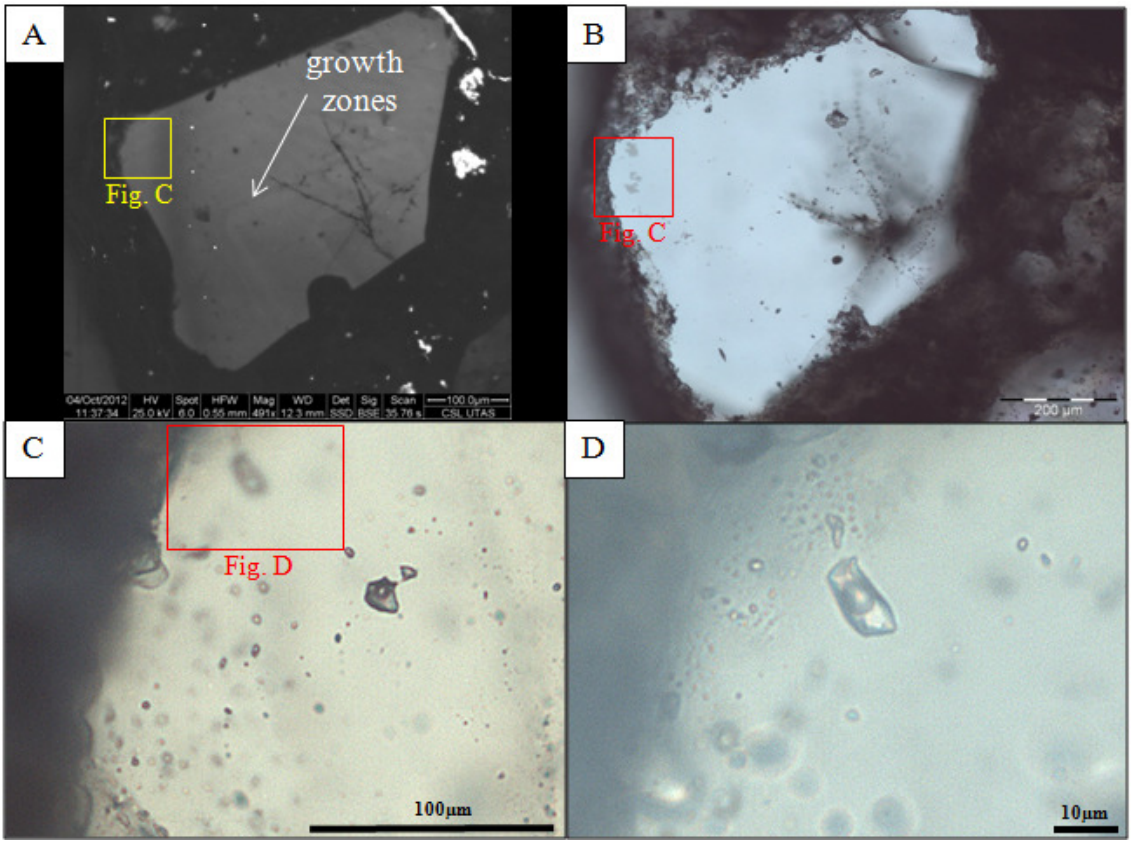

Fig. 9.1. Photomicrographs showing characteristics of fluid inclusions in quartz from Bukit Ketaya deposit. **A**. CL image showing growth zones in quartz, Sample No. BK11A - AB. **B**. Same view as A. Growth zones in quartz containing primary inclusions. Cross-polarised light. **C** and **D**. Primary fluid inclusions located parallel to growth zones.

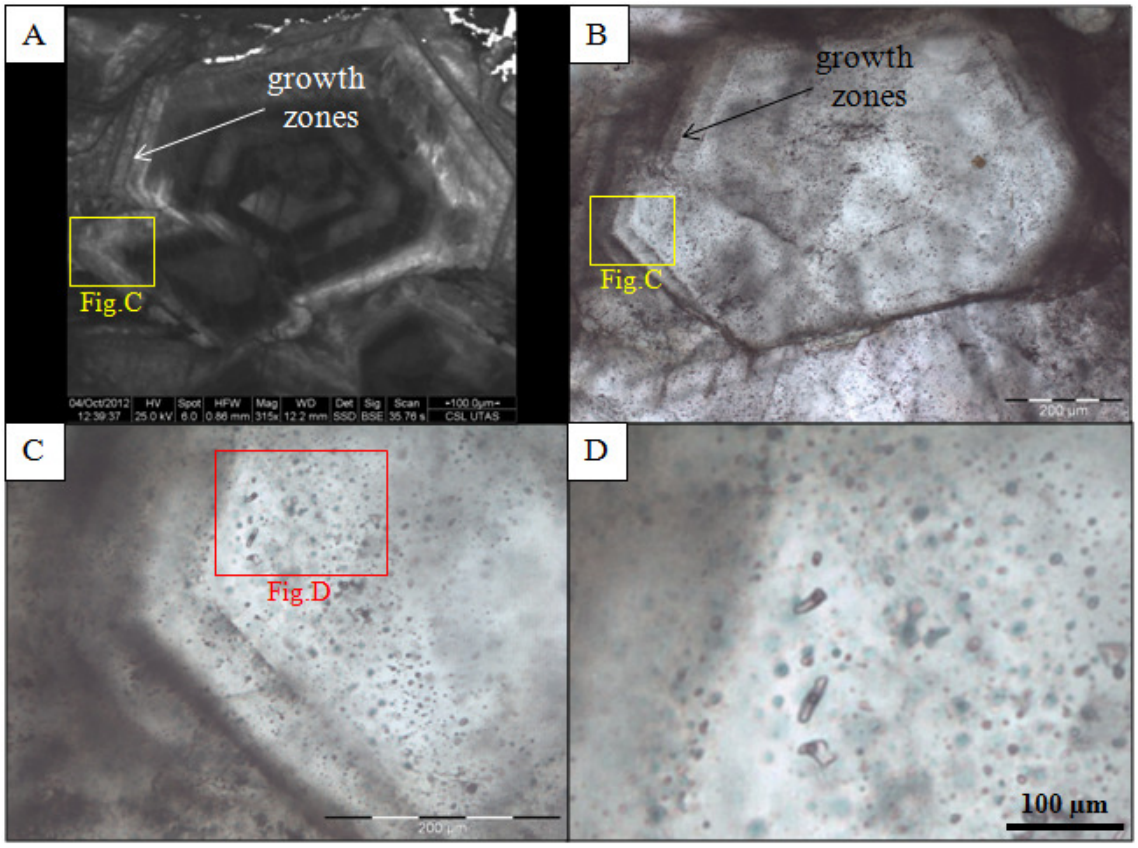

Fig. 9.2. Photomicrographs of fluid inclusions in barite from Bukit Ketaya deposit. **A.** CL photomicrograph of barite showing growth zones, Sample No.TC10-AB. **B.** Same view as A. Many inclusions precipitated in growth zones in barite in plane-polarised light. **C** and **D.** Primary fluid inclusions along trails of the growth zones.

In the present study, only the fluid inclusions which can be classified as primary according to the criteria of Roedder (1984), Shepherds et al. (1985) and Goldstein and Reynolds (1994) have been measured. Fluid inclusion types are identified based on their phases (L-V-S) at room temperature (21^{o}C), phase transitions observed during heating and cooling (-190 to 400^{o}C), and Laser Raman spectroscopy. Two types of primary fluid inclusions are recognised in the quartz and barite minerals (Fig. 9.3):

Type I: Two phase, liquid-vapour inclusions without daughter minerals according to the nomenclature of Shepherd et al. (1985). The type I inclusions are the most common type of inclusions found in the quartz and barite grains. They are mostly liquid-rich, rounded to

elongated, polygonal and negative crystal in shapes, occur along growth zones and are isolated. They are small and vary in size from 2 to 5 µm, with some up to 10 µm (Figs. 9.3A, B, D and E), and are homogenised by the disappearance of vapor upon heating. The type-I inclusions were present in most samples from the Bukit Botol and Bukit Ketaya deposits.

Type II: Three phase, liquid CO_2-bearing carbonic inclusions. These three phase inclusions include liquid H_2O, liquid CO_2 and vapour CO_2, with variable CO_2 content. Inclusions of this type are rare in the quartz and barite minerals at both deposits. They are small, a few µm in size, and occur along growth zones or as isolated inclusions, and are easy to decrepitate before complete homogenisation. Only a few analyses were able to be undertaken on the Bukit Botol deposit samples.

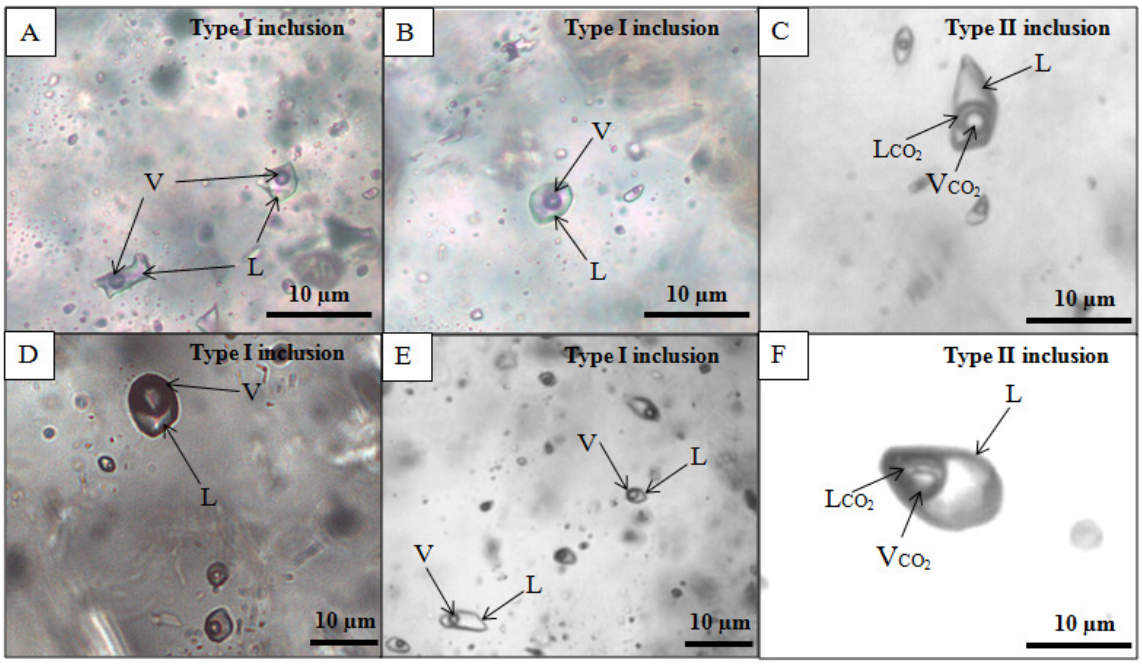

Fig. 9.3. Photomicrographs showing different inclusion types in quartz and barite from Bukit Botol and Bukit Ketaya deposits. **A** and **B.** Primary Type I, liquid-vapour inclusions in quartz, Sample No. BBDump-1. **C.** Type-II, three phase inclusions in quartz, Sample No. BBDump-1. **D** and **E.** Primary Type I, two phase inclusions in quartz, Sample, S67_a12. **F**. Type II, liquid CO_2-bearing carbonic inclusions in quartz, Sample, S67_a12. Annotations: L = liquid H_2O, V = vapour H_2O, LCO_2 = liquid CO_2 and VCO_2 = vapour CO_2.

9.4 Results

9.4.1 Microthermometry

9.4.1.1 Bukit Botol deposit

Table 9.1 summarises the microthermometric results of the fluid inclusions in samples of quartz and barite from the different mineralisation of the Bukit Botol and Bukit Ketaya deposits, and full results are listed in Appendix IX. Microthermometric data of primary fluid inclusions in quartz from the stockwork zone shows higher homogenisation temperatures and a spread in salinity than those in barite from the barite-bearing lenses.

Table 9.1. Summary of microthermometric data for primary fluid inclusions at the Bukit Botol and Bukit Ketaya deposits, Central Peninsular Malaysia.

Deposit	Mineral	Inclusion type	Number of analyses	Te, ice (°C) min/max	Tm, ice (°C) min/max	Tm, clath (°C) min/max	Tm, CO_2 (°C) min/max	Th,CO_2 (°C) min/max	Th, (°C) min/max	Salinity (wt% NaCl equiv.) min/max
Bukit Botol	quartz	Type I	62	-25.0/-17.0	-6.5/-0.8				183.0/306.0	1.2/9.9
	barite	Type I	48	-39.7/-19.4	-6.4/-0.5				187.0/299.0	0.9/9.7
	quartz	Type II	2			7.4/8.0	-57.5/-57.1	30.1/30.3		4.0/5.1
Bukit Ketaya	quartz	Type I	46	-27.4/-19.0	-10.3/-0.8				201.0/311.0	1.4/14.3
	barite	Type I	61	-23.4/-17.0	-9.4/-1.0				192.0/307.0	1.7/13.3

The microthermometric results of primary fluid inclusions of Type I for the Bukit Botol deposit came from six quartz and three barite individual mineral grains. Sixty-two homogenisation temperatures (Th) observed in quartz show a range from 180.0°C to 300.0°C, whereas the homogenisation temperatures obtained in barite lie between 180.0°C and 290.0°C (n=48) (Figs. 9.4A, B and C). Both in the quartz and barite, these Type I fluid inclusions showed final ice melting temperatures (Tm_{ice}) between -6.5°C to -0.5°C, indicating salinities from 0.9 to 9.9 wt% NaCl equivalent (Figs. 9.5A, B and C). Meanwhile, euthectic temperature (Te) values range between -25.0°C and -17.0°C for quartz and from -39.7°C to -19.0°C for barite. This range in euthectic temperature suggests that some amounts of $CaCl_2$, KCl, $MgCl_2$ and other hydrohalite crystals may be present (Crawford, 1981).

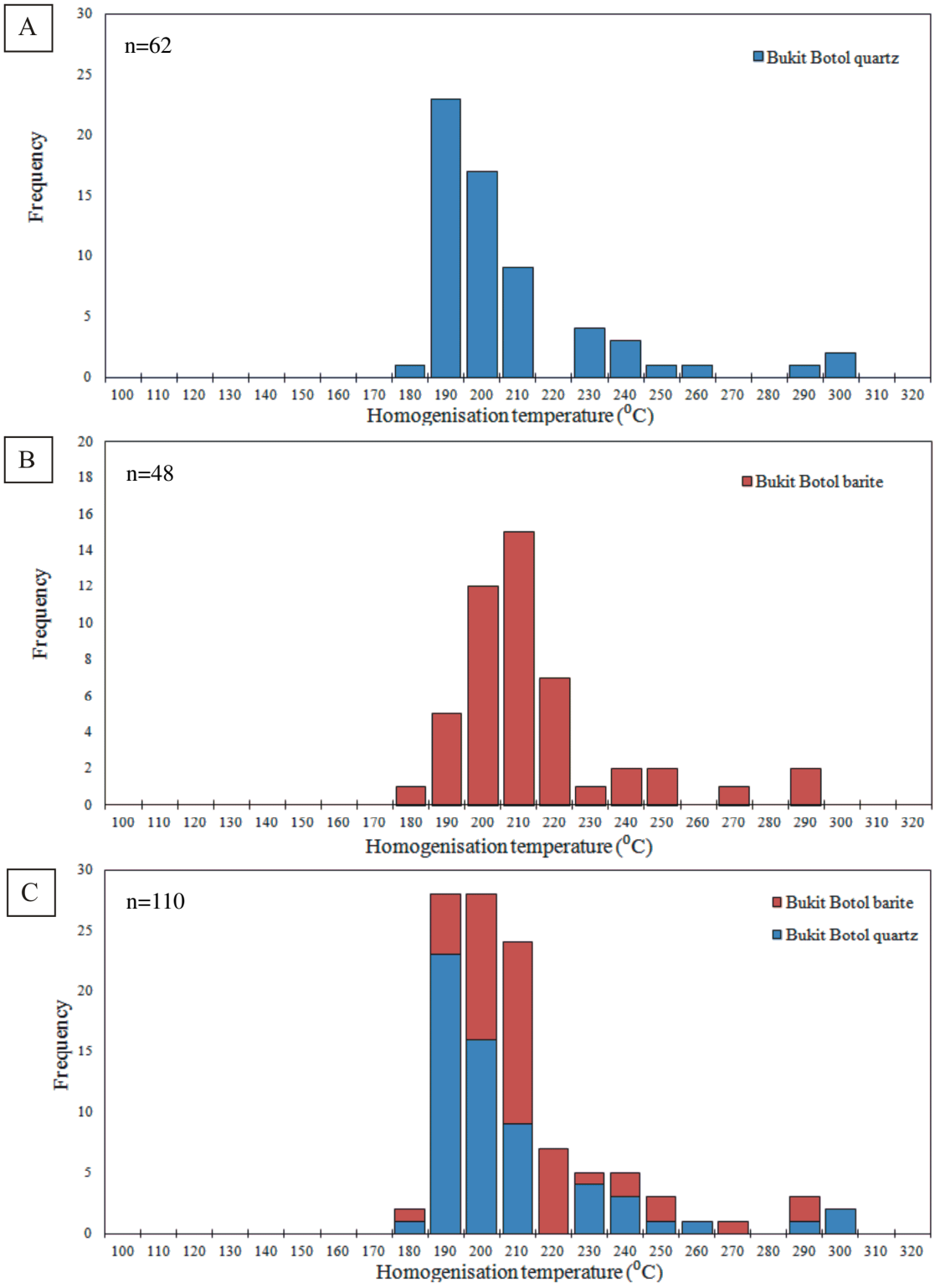

Fig. 9.4. Histograms of homogenisation temperatures of Type I fluid inclusions from the Bukit Botol deposit. **A.** Total homogenisation temperatures in quartz. **B.** Total homogenisation temperatures in barite. **C.** Combination of homogenisation temperature results of quartz and barite.

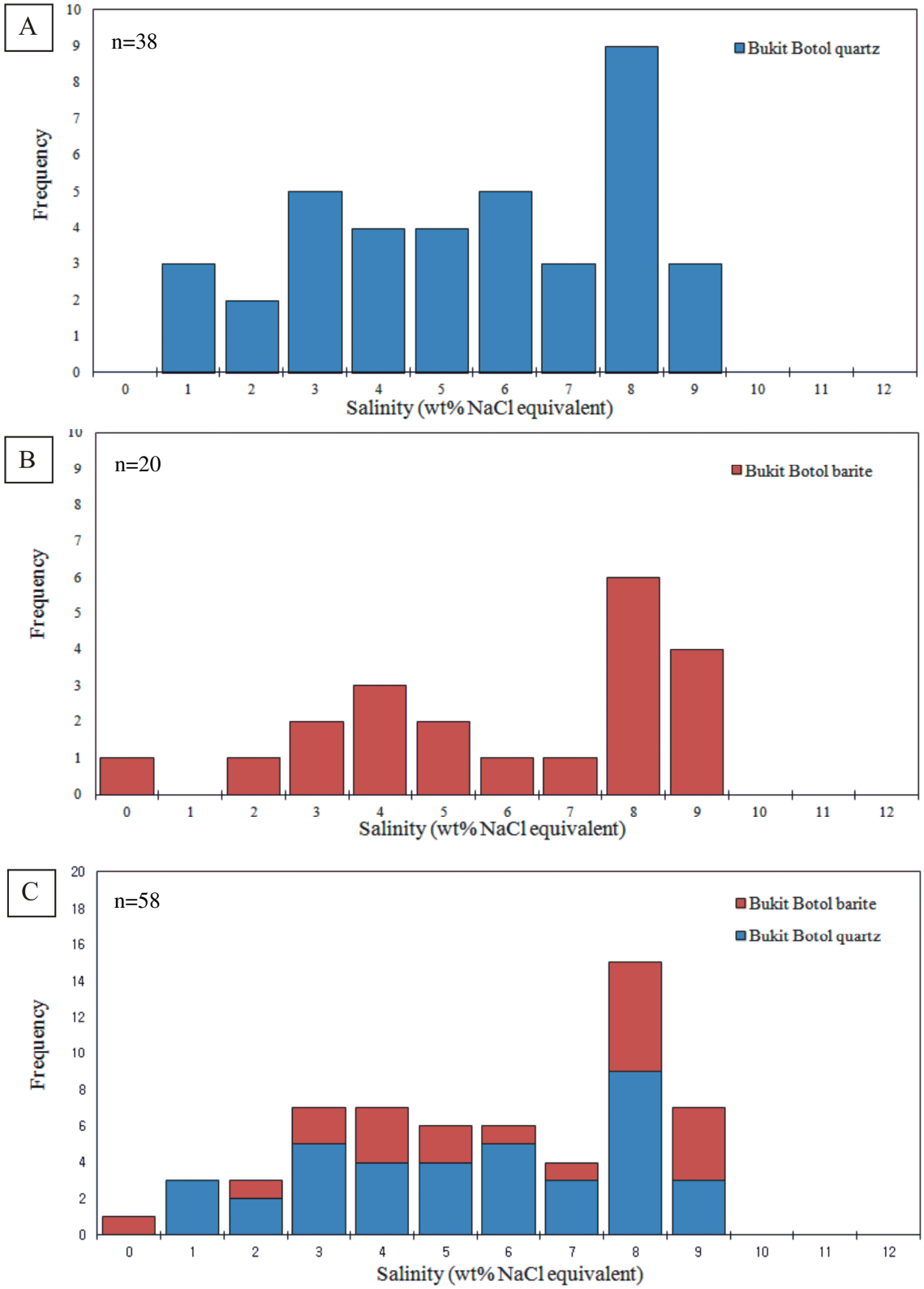

Fig. 9.5. Histograms of salinity data measured for fluid inclusions from the Bukit Botol deposit. **A.** Salinity data in quartz. **B.** Salinities data in barite. **C.** Combination of salinities data of quartz and barite.

Microthermometric data for Type II, CO_2 bearing fluid inclusions are difficult to measure due to the small size and decrepitation before complete homogenisation (Th). However, limited data obtained (n=2) from the Bukit Botol deposit yielded a melting temperature range of -57.1°C to -57.5°C, clathrate melting temperature ($Tm_{clathrate}$) of 7.4°C to 8.0°C and CO_2 homogenisation temperature (Th_{CO_2}) between 30.1°C and 30.3°C (Table 9.1), below the critical temperature of pure CO_2 at 31.1°C. Salinity determined for this Type II inclusions ranges from 4.0 to 5.1 wt% NaCl equivalent.

9.4.1.2 Bukit Ketaya deposit

A total of fifteen individual minerals from five samples were examined in microthermometric analyses from the Bukit Ketaya deposit. Six of the mineral samples are from quartz and nine from barite. Primary fluid inclusions of Type I in quartz reveal homogenisation temperatures (Th) ranging from 200.0oC to 310.0oC (n=46), and the salinities estimated from Tmice values of -10.3oC to -0.8oC are between 1.4 to 14.3 wt% NaCl equivalent (Figs. 9.6A, C and 9.7A, C). There appear to be two modes in the Bukit Ketaya salinity data, one at ~6% and a second smaller mode at ~10%. This is different to Bukit Botol, where the data are more uniform over a range from 3-7%, with an additional spike at 8-9%, and the barite and quartz measurements produce overall similar results.

The results of sixty-one two phase fluid inclusions in barite are homogenised into liquid phase at 190.0°C to 300.0°C with final ice melting temperatures (Tm_{ice}) of -9.4°C to -1.0°C, indicating salinities from 1.7 to 13.3 wt% NaCl equivalent (Figs. 9.6B, C and 9.7B, C). Moreover, first ice melting (Te) recorded is from -27.4°C to -19.0°C in the quartz, whereas in the barite the values are between -23.4°C and -17.0°C. Comparable to the Bukit Botol deposit, the measured Te results in all the quartz and barite inclusions are close to -21°C and up to approximately -35°C, suggesting the presence of $CaCl_2$, KCl, $MgCl_2$ and other salts in the fluid composition (Crawford, 1981).

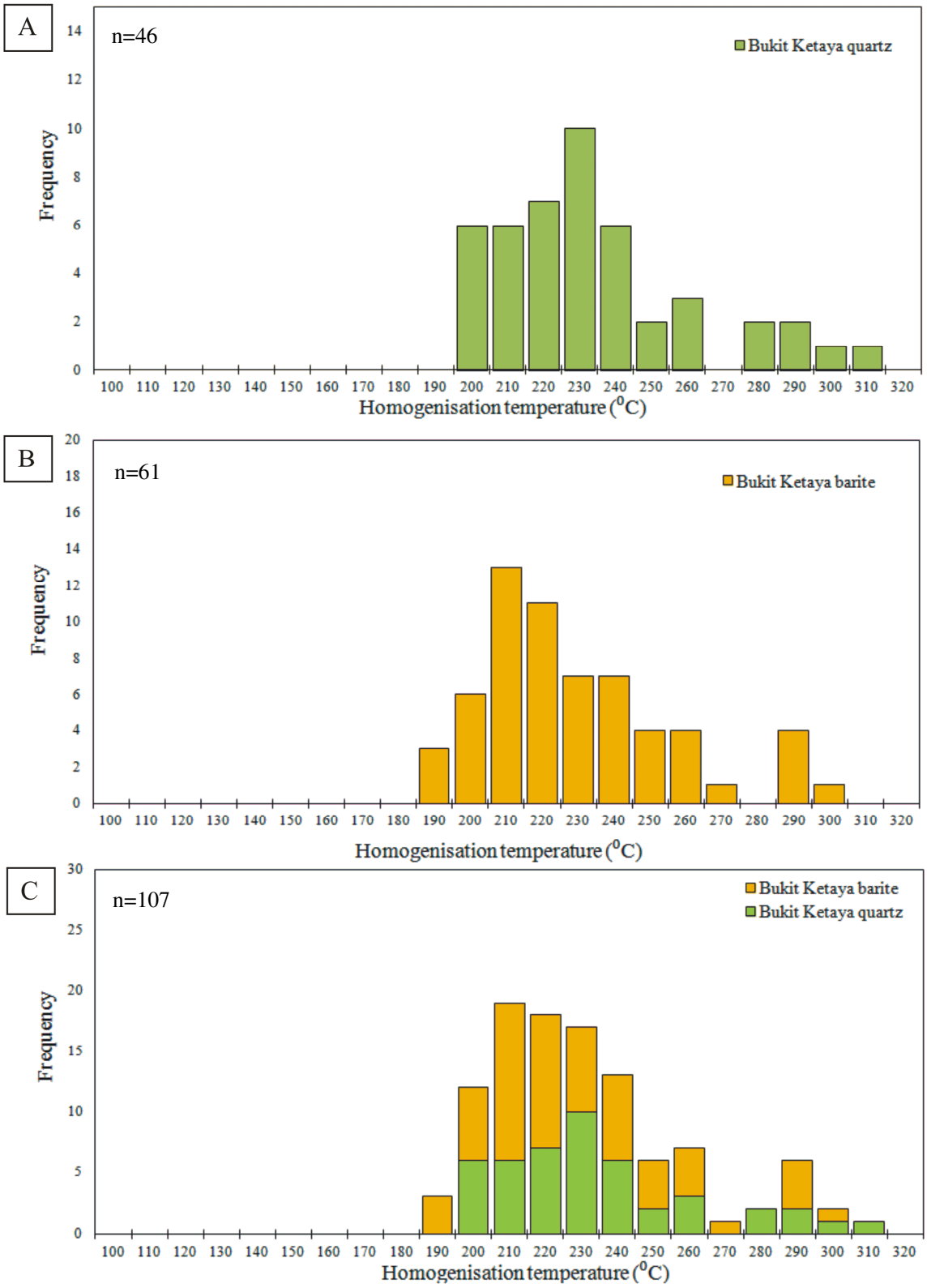

Fig. 9.6. Frequency histograms of Type I fluid inclusions from the Bukit Ketaya deposit. **A.** Homogenisation temperatures in quartz. **B.** Homogenisation temperatures in barite. **C.** Combination of homogenisation temperature results of quartz and barite.

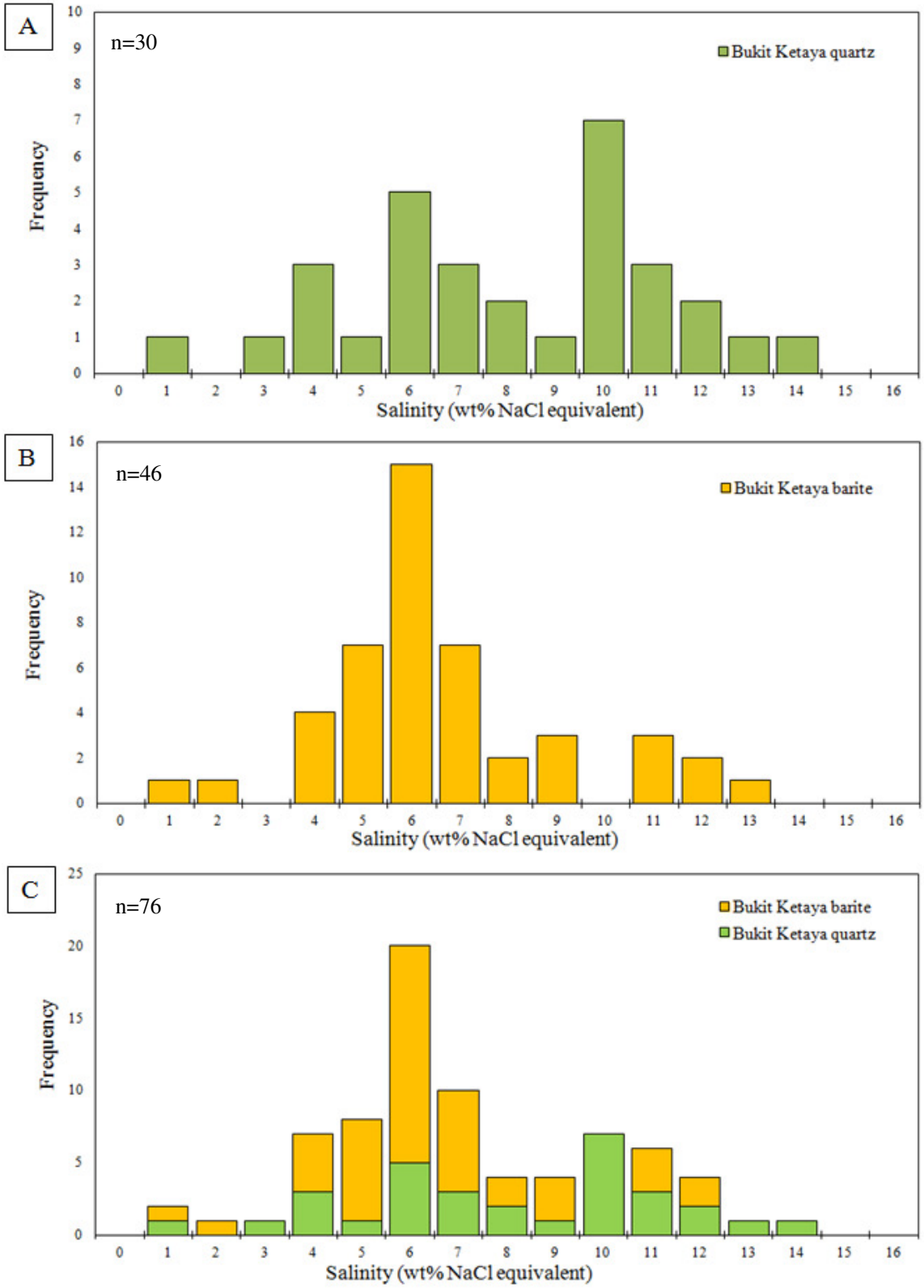

Fig. 9.7. Frequency plots of the salinities of fluid inclusions from the Bukit Ketaya deposit. **A.** Distribution of salinity data in quartz. **B.** Salinity of fluid inclusions in barite. **C.** Combination of salinity data of quartz and barite.

9.4.2 Laser Raman spectroscopy

Representative samples of fluid inclusions from both the Bukit Botol and Bukit Ketaya in quartz and barite were analysed using Laser Raman spectroscopy to characterise the gas component. No significant differences were observed in the Raman spectra. The results show that the majority of the fluid inclusions contain mainly CO_2 gas composition (Table 9.2). The CO_2 gas phase composition of fluid inclusions in quartz consists of relatively pure CO_2 (100 mol%) at two peak values ranging from 1272 to 1283 cm^{-1} and between 1380 to 1387 cm^{-1} (n=8); whereas a representative Raman spectra of almost pure CO_2 (100 mol%) in barite shows two frequencies at 1282 cm^{-1} and 1382-1386 cm^{-1} (n=4). The examples of Raman spectra of fluid inclusions in quartz and barite showing no trace of gases other than CO_2 are shown in Figs. 9.8A and B, and detailed results of gas composition identification are listed in Appendix X.

Table 9.2. Laser Raman Spectroscopic analysis of fluid inclusion vapour compositions in quartz and barite from representative samples of Bukit Botol and Bukit Ketaya deposits.

Sample No	Mineral	Gas ratio (mol %)								
		SO_2	CO_2	N_2	H_2S	C_3H_8	CH_4	C_2H_6	NH_3	H_2
Bukit Botol										
Barite	ba	0	100	0	0	0	0	0	0	0
BBotolDump1_1_1	qtz	0	100	0	0	0	0	0	0	0
BBotolDump1_1_2	qtz	0	100	0	0	0	0	0	0	0
BBotolDump1_1_3	qtz	0	100	0	0	0	0	0	0	0
BBotolDump1_1_4	qtz	0	100	0	0	0	0	0	0	0
BBotolDump2_2_1	qtz	0	100	0	0	0	0	0	0	0
BBotolDump2_2_2	qtz	0	100	0	0	0	0	0	0	0
BBotolDump2_2_3	qtz	0	100	0	0	0	0	0	0	0
BBotolDump2_2_4	qtz	0	100	0	0	0	0	0	0	0
Bukit Ketaya										
S6/7a12_1	ba	0	100	0	0	0	0	0	0	0
S6/7a12_2	ba	0	100	0	0	0	0	0	0	0
S6/7a12_3	ba	0	100	0	0	0	0	0	0	0

Annotation: ba=barite and qtz=quartz.

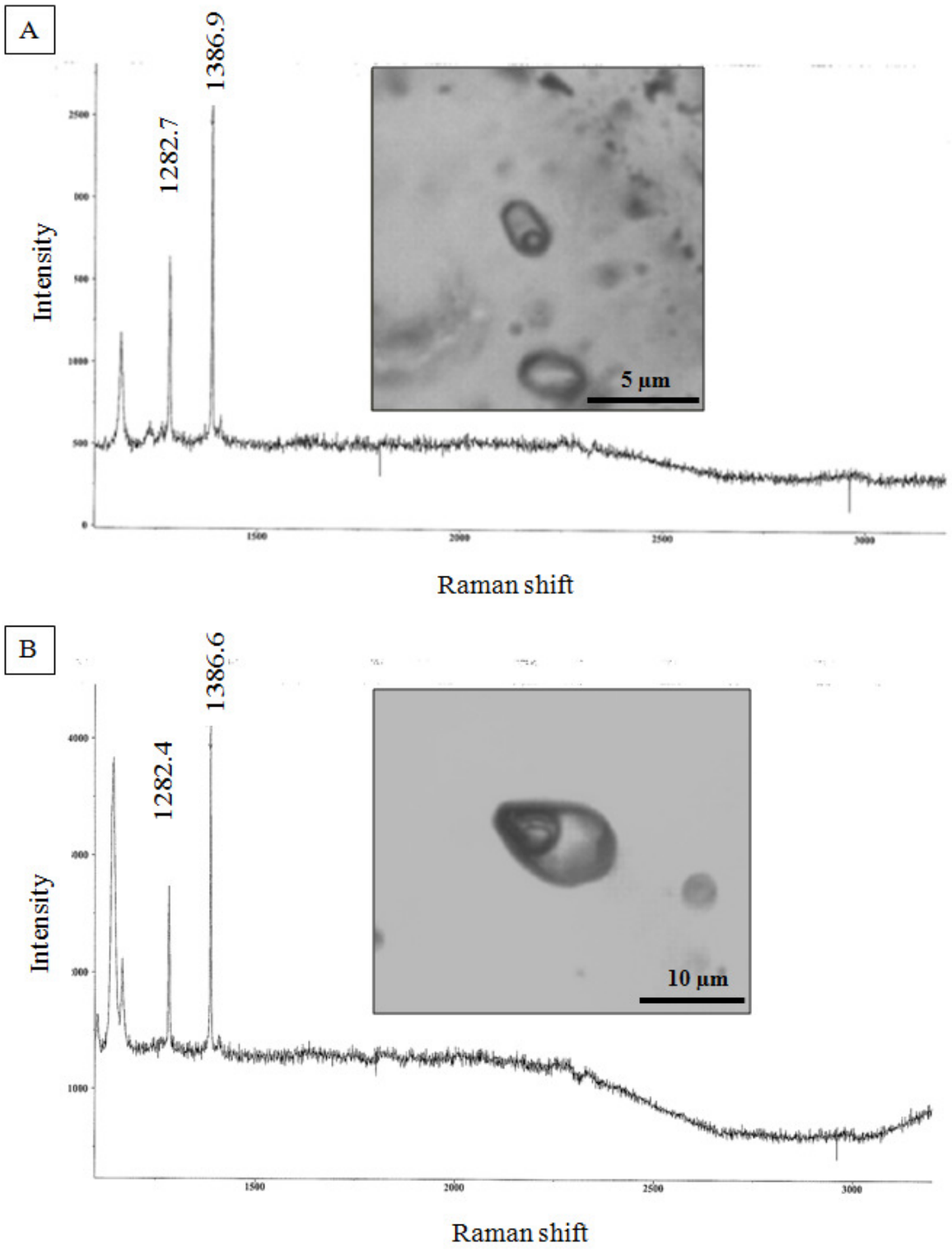

Fig. 9.8. Examples of Laser Raman spectra for the vapour phase within fluid inclusions. **A.** Fluid inclusion from quartz of stockwork zone showing spectra for CO_2 gas, Sampel, BBotolDump1_1_1. **B.** Fluid inclusion in barite from the massive barite ore with two peak values of CO_2 gas, Sampel, S6/7a12_2.

9.5 Discussion

9.5.1 Comparison of Bukit Botol and Bukit Ketaya fluid inclusion data

The fluid inclusion data of the Bukit Botol and Bukit Ketaya deposits reveal that the salinities and homogenisation temperatures in quartz from the stockwork mineralisations are similar to those in barite from the barite-bearing lenses. In general, this similar trend probably suggests a same fluid was responsible for the quartz and barite precipitations. The possible minor magmatic input is supported by the salinities of primary two-phase, liquid-vapour fluid inclusions in the quartz (1.0 to 14.3 wt% NaCl equivalent) and in the barite (1.0 to 13.3 wt% NaCl equivalent) that are similar but slightly higher than normal seawater (3.2 wt% NaCl equivalent: Bischoff and Rosenbauer, 1985; Turner and Campbell, 1987). However, a large source of modified seawater input is evident as the main hydrothermal fluid responsible for the Tasik Chini submarine hydrothermal systems because it is possible that Permian seawater was significantly more saline than modern seawater (e.g., Knauth, 2005).

The presence of $CaCl_2$, KCl, $MgCl_2$ and other salts in the fluid composition (Crawford, 1981) based on the first melting temperature data (Te) of the fluid inclusions may also demonstrate that the ore forming fluids were mainly seawater. These results are comparable to the widely accepted seawater origin for the formation of the many VHMS deposits (e.g., Peter and Scott, 1988; Ulrich et al., 2002). Moreover, the temperature range of 180^{o}C to 310^{o}C of fluid inclusions at the Bukit Botol and Bukit Ketaya deposits are also comparable to typical VHMS hydrothermal fluids (250°C-350°C; de Ronde, 1995). As illustrated in Figure 9.9 of total salinities (wt% NaCl equivalent) versus homogenisation temperatures (Th) diagram (after Roedder, 1984; Wilkinson, 2001), the fluid inclusions of both deposits plot in the field of Kuroko style deposits. In addition, these fluids are also comparable to several others ancient and modern VHMS deposits as shown in Figure 9.10.

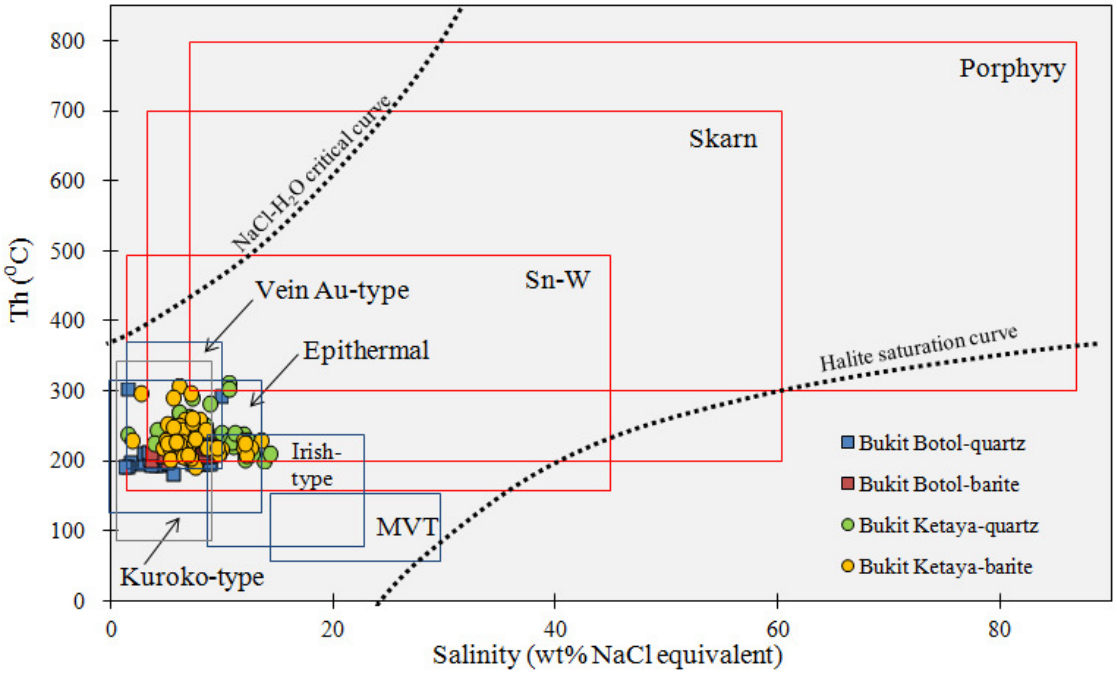

Fig. 9.9. Summary of salinity versus homogenisation temperature (T_h) plot for fluid inclusion data from the Bukit Botol and Bukit Ketaya deposits together with fields of typical ranges for fluid inclusions from other different deposit types (modified after Roedder (1984) and Wilkinson (2001). The plot shows the similarity of the fluid inclusion data from both the deposits which fall within the Kuroko-style deposits.

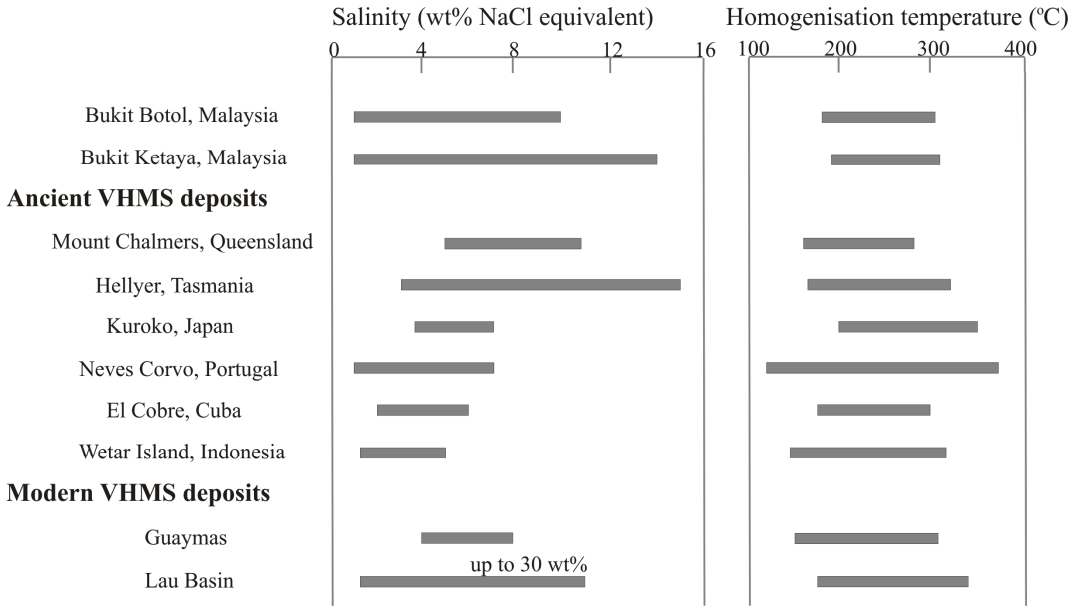

Fig. 9.10. Salinity and temperature data for fluid inclusions found in a few ancient and modern VHMS deposits, and a comparison with the fluids inclusion characteristics in both the Bukit Botol and Bukit Ketaya deposits, Malaysia. Source of data: Mount Chalmers, Queensland—Khin Zaw et al. (2003); Hellyer, Tasmania—Khin Zaw and Large (1996); Kuroko, Japan—Pisutha-Arnond and Ohmoto (1983); Neves Corvo, Portugal—Moura (2008a, b); El Cobre, Cuba—Cazanas et al. (2008); Wetar Island, Indonesia—Scotney et al. (2008); Guaymas—Peter and Scott (1988); and Lau Basin—Lécuyer et al., 1999.

The presence of high salinity fluids greater than normal seawater at both the deposits is also found in other VHMS deposits (e.g., the Atlantis II Deep, Red Sea, Ramboz et al., 1988; the Windy Craggy deposit, Canada; Peter and Scott, 1993; the Hellyer deposit, Tasmania; Khin Zaw et al., 1996). Additionally, the presence of carbonic fluids in both the Bukit Botol and Bukit Ketaya deposits are also recognised in several other VHMS deposits such as the VHMS deposits in Skellefte district, Sweden (Broman, 1987), the Hellyer deposit, Tasmania (Khin Zaw et al., 1996) and the Baiyinchang deposit, China (Hou et al., 2008).

9.5.2 Origin of the high salinity and CO_2-bearing fluids

Several processes have been suggested to explain the sources of high salinity fluids in some ancient and modern VHMS and SEDEX deposits: 1) phase separation or boiling (e.g., the Mid Atlantic Ridge, Delaney et al., 1987; the Atlantis II Deep, Red Sea, Ramboz et al., 1988), 2) leaching of evaporite (e.g., the Atlantis II Deep, Red Sea, Miller et al., 1966), and 3) magmatic input in ore-forming fluids (e.g., the East Pacific Rise venting systems, Urabe et al., 1995; the Manus back-arc basin, Yang and Scott, 1996, 2002; the Gacun deposit, China, the JADE field, Japan and the Baiyinchang deposits, China, Hou et al., 2001, 2005, 2008; Neves Corvo, Portugal, Relvas et al., 2001; the northern Iberian Pyrite Belt deposits, SW Spain, Sánchez España et al., 2003).

No direct evidence of fluid boiling was observed at the Bukit Botol and Bukit Ketaya deposits by the co-existence of both liquid- and vapour-rich fluid inclusions in the quartz and barite. In contrast, the Tasik Chini VHMS fluids showed a mixing trend. The variation of total salinities (wt% NaCl equivalent) versus homogenisation temperatures (Th) plot of the liquid-rich fluid inclusions from both the Bukit Botol and Bukit Ketaya deposits is shown in Figure 9.11. As shown in the diagram, the patterns suggest an isothermal mixing trend similar to the typical trends of various fluid evolution processes outlined by Wilkinson (2001).

Hence, the possibility of these inclusions being trapped under boiling conditions (Roedder, 1984) cannot account for the high salinity fluid. The extensive boiling at temperatures below 350°C is relatively unlikely to produce a high salinity fluid (Tornos, 2006). Additionally, the derivation of high salinity fluids from leaching of evaporite is also not favored here because there is no evidence of evaporite deposits/beds identified or reported in the Tasik Chini area or in the vicinity of the deposits. The fluid mixing is the most favored process controlling salinity variation of fluid inclusions when the leaching of evaporite is absent (Wilkinson, 2001). Therefore, the presence of possible magmatic input into the Tasik Chini submarine hydrothermal systems, which is characterised by uniformly high salinities, three times higher than the modern seawater values (e.g., Huston et al., 2011), is considered to have produced the high salinity fluids.

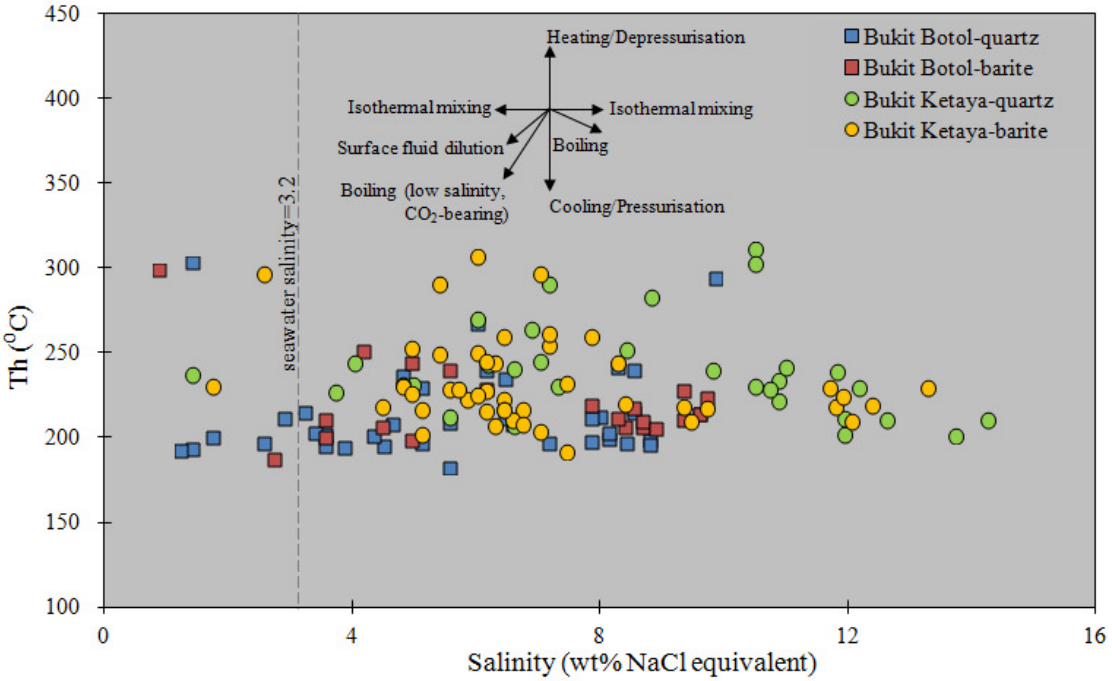

Fig. 9.11. Salinity versus homogenisation temperature (T_h) plot for fluid inclusion data from the Bukit Botol and Bukit Ketaya deposits, with typical trends of fluid evolution patterns of Wilkinson (2001). The plot demonstrates an isothermal mixing trend at both the deposits. Normal seawater salinity boundary at 3.2 wt NaCl equivalent is from Bischoff and Rosenbauer (1985); Turner and Campbell (1987).

This possibility is also evident by the uniform and almost identical $\delta^{34}S$ values from both deposits and the closeness to 0‰ is consistent with an indirect magmatic source (Chapter 7). This suggestion is also supported by the Pb isotopic data where the sources of sulphides are shown to be derived from their host volcanic rocks and directly from a magmatic and minor mantle source (Chapter 8).

The significant association of CO_2-rich fluid inclusions and the high salinity fluids (up to 14 wt% NaCl equivalent) might also relate to a minor contribution of magmatic fluid source at Tasik Chini. Most of the CO_2 inclusions in both quartz and barite are pure CO_2 with 100 mol% CO_2 as measured by Laser Raman spectroscopic analysis. These fluid features are relatively different than those of the low salinity fluids thought to be of metamorphic origin (e.g., ≤5 wt% NaCl equivalent, 3–14 mol% CO_2: Moura et al., 1997; Moura, 2005, 2008a; Sánchez-España et al., 2000, 2003), where the CO_2 (plus CH_4) was derived from interaction with the organic constituent in the host rocks (Moura, 2005; 2008a). In comparison, the evidence for CO_2-rich fluids in a variety of intrusion-related deposits (e.g., Goldfarb et al., 1998; Thompson et al., 1999) may correlate directly with a magma or mantle source (Lowenstern, 2001). Thus, the presence of CO_2 in fluid inclusions at both the Bukit Botol and Bukit Ketaya deposits are indicative of degassing from a sub-seafloor magma-hydrothermal system below the Tasik Chini deposits. This is comparable with the enrichment of CO_2 in the H_2O-CO_2-NaCl fluid system in a few VHMS deposits that are characteristic of fluids derived from the last-stage felsic magmatic differentiation (Sakai et al., 1990; Yang and Scott, 1996, 2002; Hou and Zhang, 1998; Hou et al., 2005, 2008).

9.5.3 Possible density, pressure, behavior and depth of ore formation

The density and pressure of ore-fluids from Bukit Botol and Bukit Ketaya deposits are estimated using a Microsoft Excel spreadsheet $H_{OKIE}F_{LINCS}$_H2O-N_AC_L to interpret H_2O-NaCl microthermometric data following the procedure developed by Steele-MacInnis et al. (2012b) and shown in Appendix XI.

The density of fluid inclusions from quartz and barite from both deposits ranges from 0.711 to 0.970 g/cm^3, indicating a low density fluid. This is consistent with a typical density-driven flow mechanism, where low density hydrothermal behavior is inferred as being responsible for the localisation of mineralisation (Wilkinson, 2001). The pressure data calculated from quartz and barite of both the Bukit Botol and Bukit Ketaya deposits by vapour disappearance demonstrate a wider range of values from 12 to 93 bars, suggesting slightly low fluid pressure characteristics. These variations in pressure are a common signature promoting mineral precipitation (e.g., Moura, 2008b).

The fluid behavior and depth of fluid entrapment/water depth were estimated by plotting the homogenisation temperature (Th) versus total salinities (wt% NaCl equivalent) in a diagram (Fig. 9.12) modified from Sangster (2002). As shown in the diagram, the fluids at both the Bukit Botol and Bukit Ketaya deposits precipitate as a direct result of a buoyant plume when first discharged on the seafloor. This is suggested by the uniform fluid concentration plot below the line A-C in the diagram.

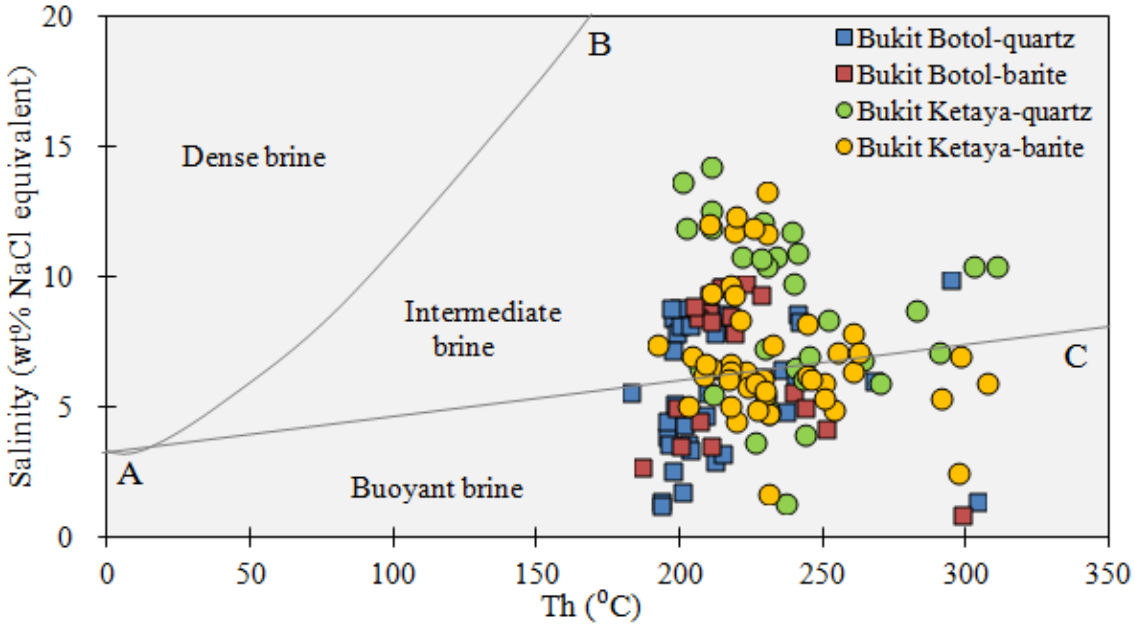

Fig. 9.12. Homogenisation temperature (T_h) versus salinity plot for fluid inclusion data from the Bukit Botol and Bukit Ketaya deposits in a diagram modified after Sangster (2002). Point A represents seawater at 2°C. Line A-B is the seawater isodensity line with ρ=1.028 g/cm^3. Fluids plotting below this line are less dense than seawater, whereas fluids plotting above the line have higher density than seawater. Line A-C corresponds to a lower limit of the field of buoyancy reversal. The intermediate brine field located between A-B and A-C defines fluids which are denser than seawater which formed from a buoyant plume. The fluids in this field become dense after mixing with seawater and can sink on the seafloor as dense brine.

The fluid inclusions at both the Bukit Botol and Bukit Ketaya deposits have similar salinities slightly higher than normal seawater. As the fluids from a buoyant plume flow through to a vent and mix with cold seawater, some fluids became denser, and are then trapped and drop onto the seafloor. These fluid inclusions are characterised by a significantly higher salinity and are located in the intermediate brine field of Figure 9.12. Available data suggest that ore-forming fluids at both the Bukit Botol and Bukit Ketaya deposits are saline and reduced and they would behave as black smokers by basin filling, similar to the Kuroko model (e.g., Solomon, 1981). The other criteria of the inferred Tasik Chini deposits are dominantly black smoker in this study include: (1) significant of vertical variation in sphalerite chemical compositions (Chapter 6), and (2) no evidence of a bacterial sulphate source for the sulphur (Chapter 7). However, some criteria such as no evidence of chimneys might also suggest that part of the both deposits have been formed as a reversal of buoyant plume as suggested for

some other VHMS deposits including the Rosebery, Tasmania and Brunswick no. 12, New Brunswick, Canada (e.g., Solomon et al., 2004b).

According to the interpretation by Sangster (2002), the fluids falling below the line A-C were discharged at water depths of 1500 m (e.g., Rona, 1988; Sangster, 1990) during the formation of modern seafloor mineral deposits in a spreading center setting, under deep marine environment. In contrast, the fluids plotting above the line A-B are interpreted to have formed at a minimum water depth, shallower than 5 m (Haas, 1971). Therefore, based on the signatures and characteristics of the fluid-behavior revealed at both the Bukit Botol and Bukit Ketaya deposits, it is likely that the water depth of the submarine environment at the Tasik Chini area during the formation of these deposits (both the Bukit Botol and Bukit Ketaya) was a deep marine setting (c.a. 1500m). This suggestion is consistent with the location of the Tasik Chini area in the Central Belt of the Peninsular Malaysia that contains thick packages of Permo-Triassic volcaniclastic turbidite deposited in deep marine environments (Metcalfe et al., 1982; Metcalfe, 2000; Metcalfe, 2013). A deep water environment for the Central Belt is also supported by the presence of radiolarians in bedded chert with siliceous shale from the Genting Serampang area, Jengka District, Pahang (Basir et al., 1995).

9.6 Summary

1) The fluid inclusion studies in quartz from the stockwork zone and in barite from a barite-bearing lens for both the Bukit Botol and Bukit Ketaya deposits indicate that the primary fluid inclusions are mostly two phase, liquid-rich inclusions. Although rare, the CO_2-bearing fluid inclusions are also detected in quartz and barite minerals at both deposits.

2) These inclusions show temperatures of formation from 180^{o}C to 310^{o}C with variability of fluid salinities up to 14 wt % NaCl equivalent. The homogenisation temperature range and similar or slightly higher salinity than that of seawater (3.2 wt % NaCl) suggests that modified

seawater was the main source in the formation of these deposits. In addition to seawater sources, the presence of CO_2 inclusions, high salinity fluid characteristics coupled with sulphur and lead isotopic compositions (Chapter 7 and 8) imply that magmatic contribution cannot be ruled out in the ore-forming fluids for the formation of both the Bukit Botol and Bukit Ketaya deposits.

3) The relationships between fluid salinity and homogenisation temperature from both the deposits also provide evidence that fluid mixing was an important process in the evolution of the ore-forming fluids. The fluid characteristics also suggest the formation of both the Bukit Botol and Bukit Ketaya deposits were controlled by ore-fluids of medium to low temperature, low density, low pressure and mineralisation occurring in deep marine environments (c.a. 1500m).

CHAPTER 10 SUMMARY AND CONCLUSIONS

10.1 Introduction

This Chapter summarises the geological, petrologic, geochemical, isotopic and fluid inclusion data of both the Bukit Botol and Bukit Ketaya VHMS deposits, and is followed by discussion of the implications of this study. The potential use of this knowledge in mineral exploration, along with future research is also discussed.

10.2 Summary and Conclusions

10.2.1 Regional geology and tectonic setting

The Peninsular Malaysia is characterised by three north-south parallel geological and tectonic belts: the Western, Central and Eastern Belts. The Western Belt is part of the Palaeozoic Sibumasu Terrane and is characterised by passive margin sequences. In this study, the Central and Eastern Belts are considered to have a similar origin to that of the East Malaya Terrane to the east based on similar Carboniferous to Permian ancient flora and fauna affinities, and on U-Pb detrital zircon and radiogenic isotopic data (Chapters 2 and 4).

The similarity in origin of the Central and Eastern Belts from the East Malaya Terrane are confirmed by the presence of similar age Proterozoic detrital zircons populations (Sevastjanova et al., 2011; Hall and Sevastjanova, 2012; this study). The initial Hf isotopic compositions of detrital zircons from both belts suggest a similar mixture of crustal and

mantle source basements (Sevastjanova et al., 2011), which is similar to those of Indochina and Tethyan Himalaya Terranes (e.g., Zhu et al., 2011; Usuki et al., 2013).

However, the Central Belt is considered here to represent a Permian volcanic arc developed on the margin of the East Malaya Terrane (Eastern Belt), and this is surmised by the marked contrast of the stratigraphic successions within the Central Belt that show Permian to Cretaceous ages in stratigraphic sequences with representing different tectonic environments (Chapter 3 and 4), whereas the confirmed oldest rocks in the Eastern Belt are predominantly submarine Carboniferous (Lee, 2004, 2009; Surjono, 2007). In addition, this interpretation is further supported by the Nd–Sr isotope signature of Permian–Triassic igneous rocks in the Central Belt of Peninsular Malaysia that demonstrate a mixture of oceanic island basalt (OIB) and enriched mantle I (EMI) of subduction-related magmatic reservoirs, suggesting that they formed in an island arc and back-arc setting above a crustal basement, whereas I- and S- type granitoids in the Eastern Belt plot more closely near the EMI field that have a lower crustal affinity (Chapter 4).

The Bukit Botol and Bukit Ketaya deposits in the Tasik Chini district formed in the Central Belt of Peninsular Malaysia, which is a part of the Permian volcanic arc superimposed the East Malaya Terrane. The Permo-Triassic magma occurrence in this arc is directly related to the magmatism that is compatible with the hypothesis of back-arc spreading that was followed by subduction-collision processes in the Peninsular Malaysia. Both deposits are hosted by the rhyolite to rhyodacite and volcaniclastic rocks of the earliest Permo-Triassic volcanism episode. In contrast, the associations of later volcanic rocks and related intrusions that are widespread in the Tasik Chini area most probably represent the products of subduction-collision related processes. In mainland Southeast Asia, the back-arc setting of the

Tasik Chini deposits is mostly similar to the formations of the Dapingzhang VHMS deposit, Lancangjiang zone or Lincang Terrane of Sone and Metcalfe (2008) in Yunnan. The Dapingzhang deposit is related to the early evolution of a rifting and back-arc event at the northeastern Gondwana of the Simao Block, part of Indochina Block (Lehmann et al., 2013). Other examples of VHMS deposits in similar settings include the Kuroko deposits, Japan (Ohmoto, 1996), Mount Windsor districts, Queensland (Duhig et al., 1992) and Kutcho Creek deposit, Canada (Barrett et al., 1996).

10.2.2 Local geological setting

The Bukit Botol and Bukit Ketaya deposits occur in a similar package of Permian age, with coherent felsic volcanic and volcaniclastic rocks. Lithogeochemical data indicate that the footwalls of both deposits contain rhyodacite rocks, but the ore horizon units at both deposits are significantly different. The ore horizon unit at Bukit Botol contains felsic volcanic and rhyodacitic volcaniclastic rocks, but the ore horizon succession to the Bukit Ketaya consists of volcanic breccia of rhyolitic composition. The hangingwall unit consists of similar sedimentary rocks of Permo-Triassic age that unconformable underlies Jurassic-Cretaceous sedimentary formations. The presence and deposition of this sedimentary succession and volcaniclastic rocks are interpreted to cause the termination of the mineralising process due to rapid sedimentation of the volcano-sedimentary sequence within the Tasik Chini area.

The ore zones and host rocks of the Bukit Botol deposit have been affected by several fault generations but are relatively unfolded and dip moderately to the east. However, the ore bodies and mine stratigraphic units at the Bukit Ketaya deposit are particularly involved in faults and folds. The syncline with the S-E axial plane is present in the Bukit Ketaya deposit and is later cut by N-S strike-slip fault. This structural deformation transects and offsets both the mine stratigraphic units and the ore types (Chapter 3).

In this study, the LA-ICPMS zircon U-Pb ages of 272.8 ± 7.6 Ma, 286.1±3.6 Ma and 292.2 ± 3.1 Ma were obtained from felsic volcanic rocks at the Bukit Botol deposit. These ages indicate an Early Permian age for mineralisation at Bukit Botol. Similarly, the age determined by U-Pb LA-ICPMS of zircons for felsic volcanic rocks in the Bukit Ketaya deposit mine successions are also an Early Permian age of 286.0 ± 2.0 Ma to 288.3 ± 4.0 Ma. The similarity suggests that these two deposits are comparable in host rock stratigraphy (Chapter 4).

The petrogenesis of felsic rocks of the Tasik Chini area reveals volcanism of transitional-calcalkaline rhyolite-rhyodacite suite and transitional-tholeiitic dacite-rhyolite suite magmatic affinities of mainly volcanic arc types. The host rock succession for both the Bukit Botol and Bukit Ketaya deposit consist of transitional-calc-alkaline rhyolite-rhyodacite and volcaniclastic rocks. These rocks from both deposits plot on the FII and FIII groups, with the exception of the FI group for the ore horizon unit of Bukit Ketaya showing strong characteristics of evolved environments, most likely island arc and back-arc environments. Examples for a group of VHMS formations at back-arc or intra arc rift setting of evolved tectonic environments that have the same petrogenesis as both deposits are the Kuroko deposit, the Que River deposit and the Mount Windsor districts (e.g., Hart et al., 2004). In addition, the Pb isotopic data of sulphides and volcanic host rocks from the Early Permian Bukit Botol and Bukit Ketaya deposits are also consistent with the mineralisation and igneous rocks at both deposits being derived from evolved sources and formed in a back-arc or island arc environment.

As discussed above, the geological, geochemical and isotopic signatures indicate a different source contributing to the source materials of the volcano-plutonic emplacements in the Tasik

Chini area. This is consistent with the Central Belt of the Peninsular Malaysia representing the volcanic arc and continental basement of the Sukhothai Arc that was developed on the margin of the East Malaya Terrane part of western Indochina Terrane (derived from Gondwana in the Devonian), separated from East Malaya in the Permian by back-arc spreading, and re-attached with East Malaya in the Triassic.

10.2.3 Mineralisation features

The Bukit Botol and Bukit Ketaya deposits share many similarities in style of mineralisation, but the alterations are very different. Four distinctive mineralisation features were identified in both deposits: 1) stringer sulphide/zone, 2) massive sulphide lens/layer, 3) barite layer, and 4) Fe-Mn and Fe-Si layers. In general, the stringer and massive sulphides form directly below the mineralised zone at the footwalls, whereas the barite, Fe-Mn and Fe-Si layers are observed at the top of the mineralised zone or upper stratigraphic levels.

The main sulphide phases at the Bukit Botol and Bukit Ketaya deposits are pyrite, chalcopyrite, sphalerite, rare galena and traces of Sn-bearing minerals. Gold and Ag-bearing minerals are also present in the massive sulphide or barite layers, and have been found locally at the Bukit Botol deposit, but are absent at the Bukit Ketaya deposit. Precipitation of late minerals are characterised by the formation of barite, Fe-Mn and Fe-Si layers. The field relationships, texture, mineralogy and chemical features of the Fe-Mn and Fe-Si layers at both deposits suggest that they were pure chemical sediments developed during formation of the massive sulphide deposit. The Fe-Mn and Fe-Si layers demonstrate a mixing of hydrothermal and possibly hydrogenous origin. They were formed as a result of changing oxidation-reduction conditions of fluid compositions with increasing distance from hydrothermal sources in a local submarine environment.

Different alteration assemblages were identified within the host volcanic rocks of the Bukit Botol and Bukit Ketaya deposits. These alteration zones form semi-conformable or stratabound-like alteration around the deposits. The Bukit Botol deposit is characterised by proximal quartz-sericite-pyrite and distal quartz-sericite alteration zones, whereas distal quartz-chlorite-sericite-pyrite-pyrophyllite±kaolinite and proximal quartz-chlorite-pyrite±carbonate±pyrophyllite form the alteration assemblages at the Bukit Ketaya deposit. These different alteration assemblages may represent the deposits in one large hydrothermal system. However, the distinct zonation of alteration minerals from quartz-sericite zones in the Bukit Botol deposit to quartz-chlorite-sericite-pyrophyllite in the Bukit Ketaya deposit suggest increasing temperature and pH of hydrothermal fluids with depth (e.g., Schardt et al., 2001).

10.2.4 Chemistry of ore-forming fluids

The sphalerite compositions from the Bukit Botol deposit are more FeS rich with a bimodal distribution, whereas the FeS compositions in sphalerite of the Bukit Ketaya deposit are narrow in range and contain <2.5 mole% FeS. The large FeS content differences in sphalerite between the both deposits in the Tasik Chini area may display compositional changes, temperature control and activity of sulphur during ore formation with the depositional process or environment. The bimodal distributions of FeS at the Bukit Botol deposit may be related to the changes in stratigraphic level and coexisting mineral assemblages, temperature and total sulphur concentration. The narrow range of FeS compositions in sphalerite at the Bukit Ketaya deposit may show the nature of ore formation, compatible with the mineral assemblages that controlled the decrease in temperature and sulphur activity.

The LA-ICPMS analysis of trace element concentrations in pyrite from the Bukit Botol deposit demonstrates significant variation of trace elements in different pyrite types, indicating different mechanisms of pyrite formation. Gold is present in pyrite in two forms: invisible gold in early pyrite and as an inclusion of native Au, Au-Ag and Au-Bi-Te minerals in pyrite structure. The trace element content of the pyrite is controlled by the evolution of ore forming fluids through time, which are largely seawater source fluids with minor inputs from magmatic fluids. The trend of Co/Ni, Au/Ag and Bi/Pb ratios in pyrites from Bukit Botol deposit are mostly plotted towards the VHMS sections (Chapter 6).

The lead isotope systematics of sulphides and volcanic host rocks from the Bukit Botol and Bukit Ketaya deposits were consistent with less radiogenic character, and most of the lead compositions show the characteristics of lead derived from juvenile arc and mantle sources (Chapter 8). The uniform Pb isotope compositions from both deposits suggest homogenisation of Pb in the hydrothermal system, and the metals in the deposits were supplied by the host volcanic rocks that were linked to the magmatic fluid. Both deposits display a range of lead compositions which are typical of back-arc hosted VHMS deposits. Possible modern tectonic and associated deposits include the VHMS deposits at Manus Basin and Lau Basin.

10.2.5 Source of sulphur

In general, the $\delta^{34}S$ values show increasing trends at both the Bukit Botol and Bukit Ketaya deposits from base (sulphide) to top (sulphate) (Chapter 7). The sulphur isotope values of the sulphides at both deposits are distributed in a narrow range that suggests a homogeneous source, and they are close to the average ratio in the magmatic sulphur, whereas the $\delta^{34}S$ composition of sulphate minerals has similar or slightly higher values than Permian seawater sulphate. The uniform range of $\delta^{34}S$ composition, isotopically homogeneous and mixing of

magmatic sulphur features in sulphides support the derivation of hydrothermal sulphide sulphur from seawater involving inorganic or chemically reduced seawater sulphate with a probably leaching of igneous sulphur from the volcanic host rocks at both deposits. The source of sulphur for the abundant sulphate minerals from both the Bukit Botol and Bukit Ketaya deposits fall within the range accepted for Permian seawater sulphate, at about 10 to 12 permil. Thus, it is indicated that the sulphate sulphur for barite precipitation in the Tasik Chini hydrothermal fluids were sourced directly from the seawater sulphate. The variation of sulphide and sulphate $\delta^{34}S$ compositions at both deposits is also comparable to the sulphur isotope variation in a few Permian VHMS deposits (e.g., Bully Hill—Eastoe and Gustin, 1996; Yanahara—Yamamoto et al., 1968, Kajiwara and Date, 1971; and Red Ledge—Fifarek, 1985).

10.2.6 Fluid chemistry

The characteristics of the fluid inclusions in quartz and barite are similar between the Bukit Botol and Bukit Ketaya deposits (Chapter 9). The primary fluid inclusions consist of two phase, liquid-rich inclusions and CO_2-bearing fluids. Based on petrographic relationships and microthermometric data, it is suggested that the primary inclusions show formation temperatures from 180^{o}C to 310^{o}C with variability of fluid salinities up to 14 wt % NaCl equivalent. The similar or slightly higher salinity than that of seawater (3.2 wt % NaCl) suggests that seawater was the main source in the formation of these deposits. In addition to seawater sources, the presence of CO_2 inclusions, high saline fluids characteristics combined with the sulphur and lead isotopic compositions, it can be interpreted that the magmatic influence was important in the ore forming fluids for the formation of both the Bukit Botol and Bukit Ketaya deposits. In addition, the relationships between fluid salinity and homogenisation temperature from both deposits provide evidence that fluid mixing was an

important process in the evolution of the ore-forming fluids. The fluid characteristics also suggest the formation of both the Bukit Botol and Bukit Ketaya deposits were controlled by ore forming fluids of medium to low temperature, low density, low pressure and mineralisation occurring in the deep marine environments (c.a. 1500m).

Table 10.1. Summary of geological characteristics of the Bukit Botol and Bukit Ketaya deposits in the Tasik Chini district.

	Bukit Botol deposit	Bukit Ketaya deposit
Tectonic setting	Island arc volcanic rock or back-arc basin	Island arc volcanic rock or back-arc basin
Age	Early Permian	Early Permian
Stratigraphy		
Enclosing unit	Permo-Triassic volcano-sedimentary successions	Permo-Triassic volcano-sedimentary successions
Hangingwall unit	Sedimentary rock	Sedimentary rock
Ore horizon unit	Altered rhyodacitic and volcaniclastic rocks	Altered rhyolitic and volcaniclastic rocks
Footwall unit	Altered rhyodacitic rocks	Altered rhyodacitic rocks
Petrogenesis of felsic volcanic rock	Transitional to calc-alkaline; FII - FIII	Transitional to calc-alkaline; FII – FIII, FI (ore horizon)
Intrusive	Microgranite	Microgranite
Structure	Mine stratigraphy strikes from 20° to 36° and dip moderately to the east. Several faults of N-S, NE-SW and E-W trends. Most of these faults transect and offset both mine stratigraphic units and sulphide lenses. The E-W trend major fault is dextral which separates the upper part massive sulphide from the lower part stringer sulphides zone.	The bedding in the mine area shifts inconsistently from south facing to nearly N-S trending strike, and suggest a large faulted syncline structure. The syncline with S-E axial plane present in the Bukit Ketaya deposit and was later cut by N-S strike-slip fault. Several faults of minor displacement are identified by offsets in the bedding of mine sequences.
Mineralisation	Two small massive sulphide lenses which is overlie by barite and Fe-Mn layers. Underlying orebodies are stringer zone. Mineralogy: Pyrite, sphalerite, galena, chalcopyrite, bornite±Sn-and Ag-bearing minerals ±gold	A few massive sulphide layers/ sheets but no lens.Barite and Fe-Si layers form at top of mineralised zone, whereas small stringer zone occurs below at the footwall. Mineralogy: Pyrite, sphalerite, galena±chalcopyrite±Sn-bearing mineral
Alteration	Proximal: quartz-sericite-pyrite±phengite Distal: quartz-sericite±paragonite	Proximal: quartz-chlorite-pyrite±carbonate ±pyrophyllite Distal: quartz-chlorite-sericite-pyrite ±pyrophyllite±kaolinite
Range of $\delta^{34}S$ (‰)	Sulphide: -0.8 to +8.3 Sulphate: +11 to +18	Sulphide: -2.9 to +3.6 Sulphate: +11 to +22
Fluid inclusions	Inclusion types : Two-phase and CO_2-bearing fluids Temperature : 180->300°C Salinity : 1.0 to 9.9 wt.% NaCl equivalent Depth (m) : ~ 1500 m	Inclusion types : Two-phase and CO_2-bearing fluids Temperature : 190->310°C Salinity : 1.4 to 14.3 wt.% NaCl equivalent Depth (m) : ~ 1500 m
Source of sulphur, metals	Reduced of Permian seawater sulphate with a leaching igneous sulphur from the volcanic host rocks	Reduced of Permian seawater sulphate with a leaching igneous sulphur from the volcanic host rocks
Source of Pb	Leached host rock and magmatic-hydrothermal sources?	Leached host rock and magmatic-hydrothermal sources?
Source of fluids	Seawater and magmatic sources	Seawater and magmatic sources

10.3 Comparison with Other VHMS Deposits

A comparison of the Tasik Chini deposits (both the Bukit Botol and Bukit Ketaya deposits) with other VHMS deposits shows that they are similar and that they also differ in several respects (Table 10.2).

Table 10.2. Comparison between the Tasik Chini deposits, the Mount Chalmers deposits in Queensland and the Kuroko deposits in Japan.

	Tasik Chini deposits, Malaysia	Mount Chalmers deposits, Queensland	Kuroko deposits, Japan
Tectonic setting	Island arc volcanic rock or back-arc basin	Host graben style extension across back-arc basin	Island arc volcanic rock or back-arc basin
Age	Early Permian	Early Permian	Middle Miocene
Regional metamorphism	Low grade metamorphism/Lower greenschist ?	Low grade metamorphism /subgreenschist	Low grade metamorphism
Host rock	Rhyolite-rhyodacite and volcaniclastic	Rhyolite, andesite and volcaniclastic	Andesite-dacite and rhyolite
Structure	Associated with lava dome. Controlled by faults and folds	Associated with lava dome. Controlled by faults and folds	Associated with lava domes/synvolcanic faults
Style of ore deposits			
Orebody	Lens- to sheet like-shaped and stringers	Mound-like morphology	Mound-like morphology
Ore type	Massive sulphide, banded/layered sulphide, disseminated and vein sulphides	Massive sulphide , layered sulphide, fragmented sulphide and vein sulphides	Massive sulphide, banded sulphide, disseminated and vein sulphides, brecciated sulphide
Ore mineralogy	Pyrite, chalcopyrite, sphalerite, galena ±bornite±Sn-and Ag-bearing minerals ±gold	Pyrite, copper, gold with traces of zinc, silver and lead	Sphalerite, galena, pyrite chalcopyrite±gold
Gangue	Barite, quartz	Barite, quartz	Barite, gypsum-anhydrite, quartz
Exhalites	Fe-Mn and Fe-Si layers	No	Hematite-rich cherty units
Alteration facies	Proximal: 1)quartz-sericite-pyrite±phengite 2)quartz-chlorite-pyrite±carbonate ±pyrophyllite Distal: 1)quartz-sericite±paragonite 2)quartz-chlorite-sericite-pyrite ±pyrophyllite±kaolinite	Footwall: 1)silica and chlorite Hangingwall: 1)dolomite, sericite and kaolinite	Proximal: 1)inner quartz-sericite zone 2)sericite-Mg chlorite-montmorillonite (chlorite zone) Distal: 1)sericite zone 2)zeolite-carbonate-clay minerals
Hydrothermal geochemistry			
Range of δ34S (‰)	Sulphide: -2.9 to +8.3 Sulphate: +11 to +22	Sulphide: -17.6 to +5.7 Sulphate: +7 to +14	Sulphide: 1.0 to +8.2 Sulphate: +10 to +15
Fluid inclusions	T = 180->310°C	T= 160 to 285 °C	T= 200-300 °C
Source of sulphur, metals	Reduced of Permian seawater sulphate with a leaching igneous sulphur from the volcanic host rocks	Reduced of Permian seawater sulphate with a leaching igneous sulphur from the volcanic host rocks	Major source of the ore-forming sulfur was Miocene seawater sulfate.
Source of Pb	Leached host rock and magmatic-hydrothermal sources?	Leached host rock and magmatic-hydrothermal sources?	Leached host rock and magmatic-hydrothermal sources?
Source of fluids	Seawater and magmatic sources	Seawater and magmatic sources	Seawater and magmatic sources
References	This study	Large and Both (1980), Gulson and Vaasjoki (1987); McPhie and Hunns (1995), Huston (1999), Hunns (2001), Khin Zaw et al. (2003)	Kajiwara and Date (1971), Franklin et al. (1981), Fehn et al. (1983), Kuroda (1983), Kalogeropoulos and Scott (1983), Pisutha-Arnond and Ohmoto (1983)

The tectonic history of the Early Permian Tasik Chini deposits has similar features to the setting of the Permian Mount Chalmers deposits in Queensland and the Miocene Kuroko deposits in Japan, which formed in an arc-related environment. Both the Tasik Chini deposits and the Kuroko deposits, Japan, were formed on continental margin island arc-back arc basins. However, VHMS deposits in the Mount Chalmers, Queensland occurred on host graben style extensional setting across a back-arc basin (e.g., Hunns, 2001).

The host rock controls on mineralisation at Tasik Chini, Mount Chalmers and Kuroko deposits appear to be similar, consisting mainly of felsic volcanic and volcaniclastic rocks. The occurrence of feldspar phyric lava flows and resedimented breccias in the Tasik Chini deposits, Mount Chalmers, Queensland (e.g., McPhie and Hunns, 1995) and Kuroko deposits, Japan (e.g., Kuroda, 1983) have characteristics of the volcanic units on the submarine volcanic breccia domes. However, an obvious syn-volcanic fault that could have controlled the hydrothermal up-flow, such as at the Kuroko deposits (e.g., Kuroda, 1983) has not been identified in the Tasik Chini and Mount Chalmers deposits.

The style of ore deposits is similar for these three deposits. However, unlike a typical mound-shaped morphology of the Mount Chalmers in Queensland and Kuroko deposits in Japan, the Tasik Chini deposits orebody forms lens, sheet and stringer morphologies similar to those of the Mount Read Volcanics (MRV) deposits, Tasmania. The Bukit Botol and Bukit Ketaya deposits (Tasik Chini deposits) most closely resemble the polymetallic lens and sheet-like deposits (e.g., Roseberry, Hellyer, Que River, Thalanga deposits—Large, 1992; Large et al., 2001b). The mineralogy of the Mount Chalmers deposits, Queensland and Kuroko deposits, Japan is identical to the massive sulphide mineralisations observed within the Tasik Chini deposits. In addition, a baritic layer occurs across the top of the Bukit Botol and Bukit Ketaya

deposits (Tasik Chini deposits), also similar to Mount Chalmers deposits, Queensland and Kuroko deposits, Japan. In addition, similarities with Kuroko deposits, Japan, include the presence of distinctive cap rocks of a hydrothermal Fe-Mn layer at Bukit Botol and a Fe-Si layer at Bukit Ketaya. However, the Tasik Chini deposits contain Sn- bearing minerals, a diagnostic feature of Bukit Botol and Bukit Ketaya. Furthermore, an anhydrite/gypsum-rich layer is also absent at Tasik Chini deposits, similar to Mount Chalmers deposits possibly because of low temperatures or the dissolution of anhydrite below 150°C at seafloor pressures (e.g., Haymon and Kastner, 1981).

The alteration characteristics at the Tasik Chini deposits are similar to those of the Mount Chalmers and Kuroko deposits. However, alteration associated with the Bukit Botol deposit resembles the stratabound or semi-conformable quartz-sericite±chlorite-pyrite altered zone in a few MRV deposits, Tasmania, such as the Roseberry deposit (Green et al., 1981; Large et al., 2001b). At Bukit Botol, the composition of the muscovite on the SWIR profiles is a distinctive marker of proximal versus distal alteration. In proximal alteration zones, the composition of muscovite shows a normal to phengitic muscovite, whereas the distal alteration zone is characterised by normal muscovite and paragonite. The occurrence of phengite in the proximity of ore bodies has also been described in MRV deposits, Tasmania, such as at Prince Lyell (Hendry, 1981).

In contrast, the Bukit Ketaya deposit has distal alteration characterised by quartz-chlorite-sericite-pyrite–pyrophyllite±kaolinite assemblages, whereas the weakly enveloped proximal alteration to the footwall is an intense quartz-chlorite-pyrite±carbonate±pyrophyllite assemblage. Both SWIR and XRD data from both alterations show distinctive muscovite with minor pyropyhllite and paragonite but no chlorite spectral profile was identified. However,

molar element ratios of Na_2O/Al_2O_3 versus K_2O/Al_2O_3 and MgO/Al_2O_3 versus K_2O/Al_2O_3 show that chlorite and muscovite are the main alteration minerals reflecting the intensity of alteration at the Bukit Ketaya deposit, and the chlorite is mainly Mg-rich chlorite. The Bukit Ketaya deposit also has a semi-conformable alteration type similar to that of the Bukit Botol deposit, but this probably demonstrates chlorite altered zones of Large (1992), or a chlorite alteration pattern with a proximal Mg-chlorite and an intermediate to Fe-chlorite distal zone (McLeod and Stanton, 1984). This pattern has been observed in several Kuroko deposits, Japan (Urabe et al., 1983). In addition, the presence of pyrophyllite and kaolinite has also been reported from MRV deposits in Tasmania, such as the Western Tharsis deposit, Mount Lyell, Tasmania (Huston and Kamprad, 2001).

Comparison between the chemistry of ore fluid and isotopic signatures from the Tasik Chini deposits with both the Mount Chalmers deposits, Queensland and Kuroko deposits, Japan, indicate a similar feature of the mineralising fluids. The sulphur isotopic compositions of sulphide and sulphate minerals for the three deposits indicate that the source of hydrothermal fluids are derived from seawater, but contribution of magmatic a source also played an important role during the mineralisation stage such as at the Tasik Chini deposits and the Mount Chalmers deposits, Queensland. As for lead isotopic data, the three deposits' lead compositions are consistent with the lead derivation from leached volcanic host rock and magmatic-hydrothermal sources. In addition, most of the lead isotopic signatures show the same characteristics of lead originated from primitive arc and mantle supplies, indicating an island arc and back-arc setting for the Tasik Chini deposits (this study), the Mount Chalmers deposits, Queensland (Gulson and Vaasjoki, 1987) and the Kuroko deposits, Japan (Fehn et al., 1983). Based on fluid inclusion data, the homogenisation temperature range during formation of Tasik Chini deposits (this study) is broadly comparable with temperatures

obtained from the Mount Chalmers deposits, Queensland (e.g., Khin Zaw et al., 2003) and the Kuroko deposits, Japan (e.g., Pisutha-Arnond and Ohmoto, 1983). The source of ore fluids from the three deposits is also consistent and suggests mixing of seawater with minor magmatic fluids.

Furthermore, a number of characteristics of the Tasik Chini deposits are consistent with the bimodal-felsic VHMS type in the classification scheme of Barrie and Hannington (1999), and later refined by Franklin et al. (2005) and Galley et al. (2007). In addition, the Zn-Pb-Cu rich composition related with evolved environments (e.g., back-arc basin) is also typical of bimodal-felsic VHMS deposits (Piercey, 2010; 2011) (Chapter 1).

10.4 Tectonic Model

Based on the geological and geochemical characteristics of the Bukit Botol and Bukit Ketaya deposits, the following tectonic model for the Tasik Chini area deposit is discussed below and diagrammatically shown in Figure 10.1.

In the Early Permian, volcanism took place in the Central Belt island arc due to the eastward subduction of the Palaeo-Tethys beneath the East Malaya Terrane which led to the opening of a back-arc basin. This Early Permian magmatism comprises volcanic rocks of transitional to calc-alkaline rhyolite-andesite volcanic and volcaniclastic rocks, and related I–type intrusions. The Tasik Chini deposits formed during this early stage of magmatism, within the back-arc basin near the Central Belt continental margin of the East Malaya Terrane.

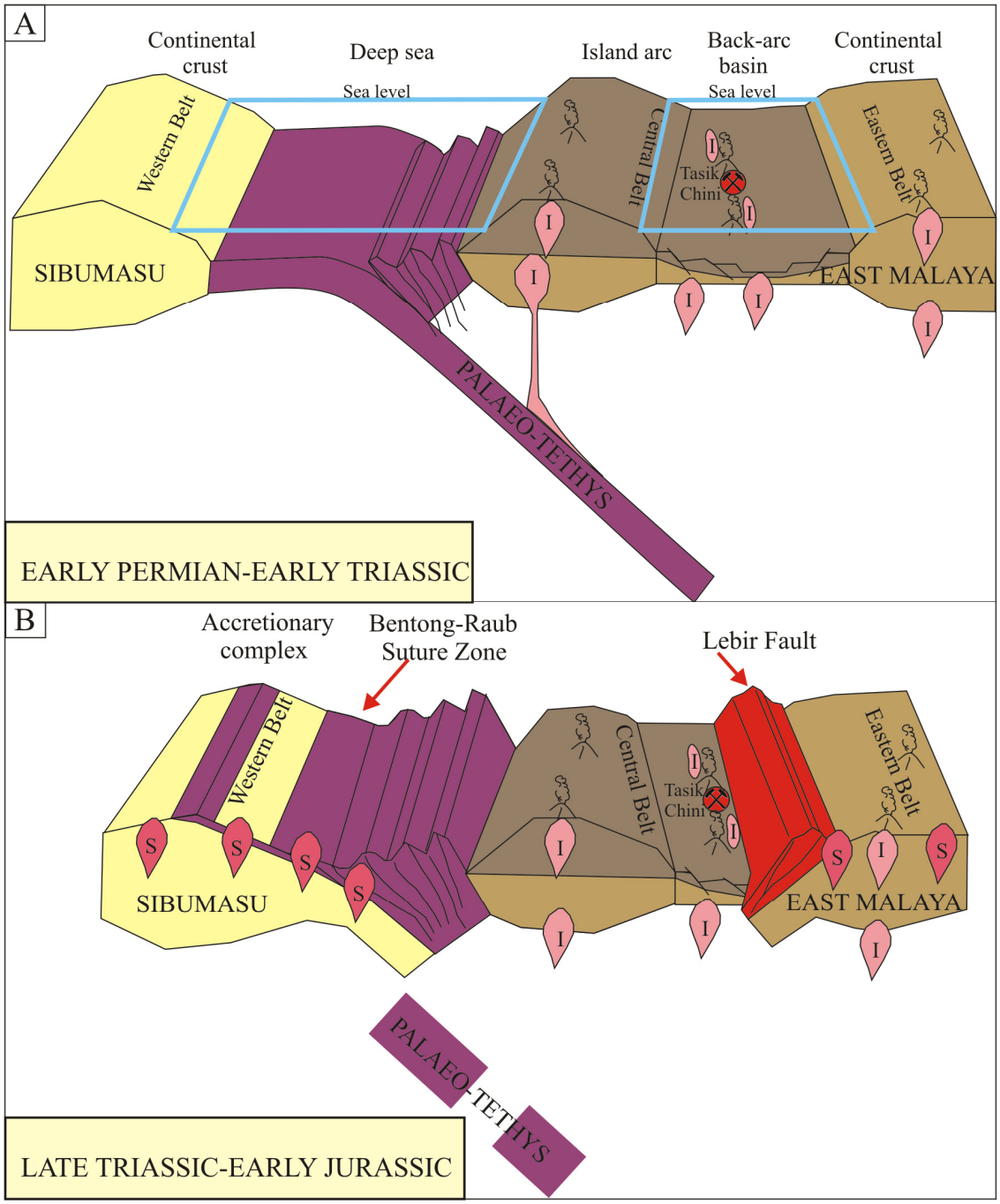

Fig. 10.1. Schematic diagrams that illustrate the proposed tectonic environment prior to the formation of the Tasik Chini deposits. **A**. Early Permian-Early Triassic tectonic environment. **B**.Late Triassic-Early Jurassic tectonic environment.

As time progressed, rapid opening caused the subduction process of the Palaeo-Tethys in the Middle Permian-early Late Triassic. As a result, the magmatism further generated I–type

subduction-related granitoids and associated transitional-tholeiitic felsic volcanic rocks in the East Malaya Terrane (Fig. 10.1A). However, during the Early Triassic the entire Eastern Belt may have been uplifted. This is evidenced by the absence of Triassic sedimentary rocks in the Eastern Belt (Hutchison, 2007), and the limited occurrences of Middle to Late Triassic volcanic and volcaniclastic rocks with associated I-type granitoids compared to those of the Central Belt (e.g., Metcalfe, 2013; Oliver et al., 2014).

In the Late Triassic, destruction of the Central Belt back-arc basin was initiated and it then collided with the Eastern Belt. The boundary between these two belts was represented by the Lebir Fault zone. The collisional boundary between the Sibumasu and the East Malaya Terranes was marked by the Bentong-Raub Suture comprises the ophiolitic zone and the accretionary complex of widespread chert sequences west of the Bentong-Raub Suture ophiolitic zone. The two collision events have generated S-type crustal-thickened granites that were responsible for forming the tin deposits found in the Western and Eastern Belts until the Early Jurassic (Fig. 10.1B).

The stages of ore-forming processes for the Tasik Chini deposits are shown in Figure 10.2. The Bukit Botol and Bukit Ketaya deposits formed and terminated during the period of active volcanism and sedimentation, and the areas were a small rhyolite dome field within a submarine felsic dominated volcanic centre. The unit associated within the felsic volcanic rocks comprise massive, flow banded and associated breccias that formed through submarine volcanism by effusive rhyolitic eruptions (e.g., McPhie and Allen, 1992; Large et al., 2001a). Prior to mineralisation at Tasik Chini, the volcanism was rhyodacitic (rhyolite type 1 of the Bukit Botol deposit; quartz-feldspar phyric rhyolite of the Bukit Ketaya deposit) and was coeval with mineralising hydrothermal fluids. Emplacement of effusive eruptions and

associated intrusions continued, but shifted from rhyodacitic to rhyolitic compositions. Due to rapid eruption through the seafloor, this event formed thick transported or resedimented breccia units (Resedimented 1) that overlie the massive sulphide and coherent rhyodacitic flows at both the Bukit Botol and Bukit Ketaya deposits. The occurrence of sedimentary units comprised mudstone, shale, siltstone and sandstone that directly overlay the volcanic facies at both deposits, possibly indicating proximity to a continental land. However, the presence of the volcanic breccia with minor sedimentary units (Resedimented 2) on the top of the Bukit Botol deposit suggest further downslope resedimentation around this deposit than those at the Bukit Ketaya deposit. Thus, these differences may indicate that the Bukit Botol deposit formed in a more distal setting than the mineralisation at Bukit Ketaya (Fig. 10.2).

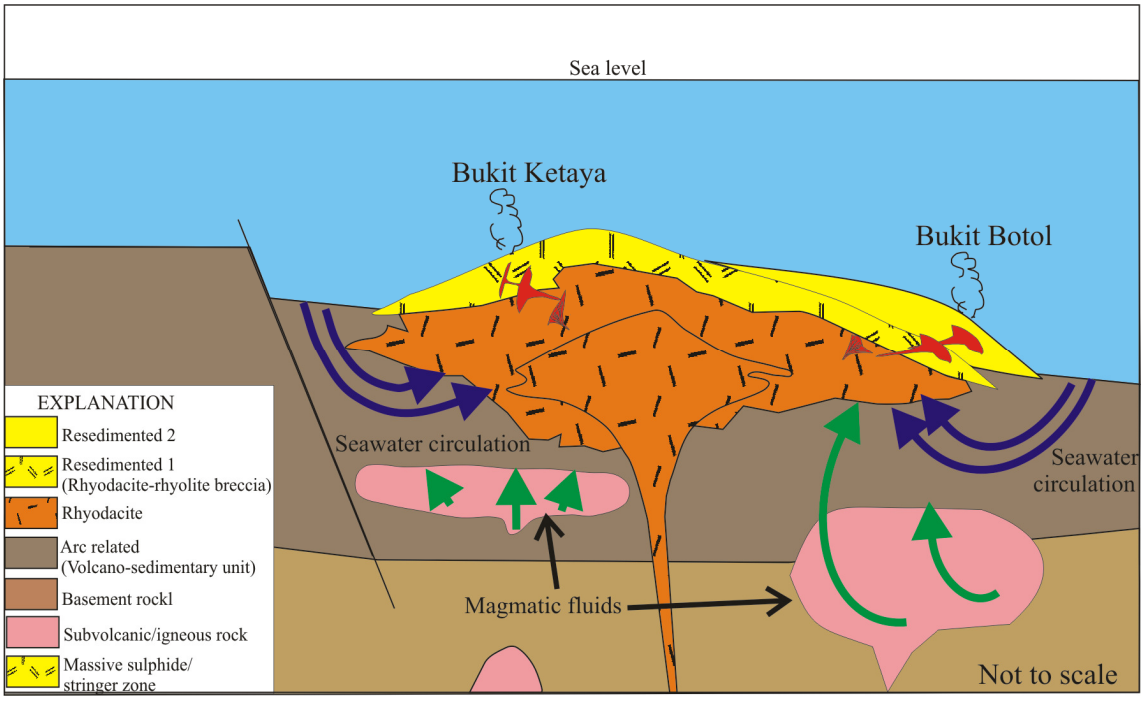

Fig. 10.2. Schematic diagrams that illustrate the formation of the Tasik Chini deposits (Bukit Botol and Bukit Ketaya), Central Peninsular Malaysia.

The proposed ore-forming model also shows that evolved seawater played a major role in the origin of the Tasik Chini deposits. However, a minor magmatic fluid contribution to the ore-

forming fluid is possible. This is supported by the stable and radiogenic isotopic and fluid inclusion systematic data obtained from Bukit Botol and Bukit Ketaya deposits in this work.

10.5 Exploration Implications

This research helps constrain the origin of the Tasik Chini deposits (Bukit Botol and Bukit Ketaya). It is recognised that both deposits are of VHMS type. Therefore, a number of general statements and geologic characteristics can be established, with implications for mineral exploration of similar mineralised systems in the Tasik Chini and surrounding areas.

1) This research provides comprehensive documentation of an economically significant mineralised system that has not been studied in any significant detail. The work here is first built on an understanding of the regional geology, deposit-scale setting, volcanic stratigraphy and deposit architecture.

2) At present, there is some evidence to suggest that the Central Belt of Peninsular Malaysia and Sukhothai Arc further north had a linked tectonic history, suggesting that the Tasik Chini deposits may be related to large scale plate motion organisation on the western margin of the Indochina-East Malaya Terrane. The occurrence of an island arc and back-arc basin likely played a role in providing hydrothermal fluid flow and abundant sulphide sources for massive sulphide deposits. Thus, better documentation of these relationships may provide insight for exploration area selection, and could provide a better understanding of VHMS formation.

3) The geological and geochemical features observed in Bukit Botol and Bukit Ketaya associated felsic volcanic rocks may indicate the prospective environments that could be applied in similar mineralised system exploration in Tasik Chini and surrounding areas. It is important to target stratigraphic successions containing transitional-calc-alkaline felsic

volcanic and volcaniclastic rocks. Therefore, much of the outcrop of this unit in the Central Belt would be good exploration ground.

4) Both the Bukit Botol and Bukit Ketaya deposits are relatively small in volume and area. However, the hydrothermal systems were active, as shown by alteration assemblages. Thus, recognition of similar alteration patterns may indicate proximity to similar mineralised systems in the Tasik Chini and surrounding area.

5) Understanding the sulphide chemistry may also be useful in mineral exploration in the Tasik Chini and surrounding area. For example, a preliminary study using the electron microprobe indicates that trace element compositions in sphalerites vary between the mineralised zones at the Bukit Botol and Bukit Ketaya deposits. Variations in the trace element distributions were interpreted to reflect the temperature and chemistry of the mineralising fluid. In addition, trace element data of pyrite from the Bukit Botol deposit obtained by LA-ICPMS analysis also provided a chemical evolution of ore fluids, trace element signatures for invisible gold or native gold forms and important data to distinguish different ore systems.

10.6 Future Research

Although this thesis has significantly contributed to the understanding and knowledge of the Bukit Botol and Bukit Ketaya deposits, a Permian VHMS system in the Tasik Chini district of Central Peninsular Malaysia, unanswered research questions would provide future research directions. These are listed below:

1) A more extensive lithogeochemical and isotopic study of the volcano-sedimentary successions may provide further insight into the palaeo-tectonic setting in which the Tasik Chini deposits was formed. Furthermore, a detailed study of the chemistry of fluid inclusions using modern technology (e.g., LA-ICPMS) would also help to clarify the depositional environment and the possible role of boiling and/or direct magmatic contributions to the ore fluids in the Tasik Chini hydrothermal system.

2) VHMS systems that occurred during the Permian are rare in the Earth's geologic record. The examples of Permian VHMS deposits include Afterthought-Bully Hill, California (Eastoe and Gustin, 1996), Yanahara, Japan (Yamamoto et al., 1968; Kajiwara and Date, 1971), Red Ledge, Idaho (Fifarek, 1985) and Mount Chalmers, Queensland (Huston, 1999; Hunns, 2001; Khin Zaw et al., 2003). Thus, the Permian Tasik Chini deposits in Peninsular Malaysia are also broadly related to these global VHMS formations. Therefore, further studies and better documentation of the relationships are required and may provide significant insight as to why they rarely host VHMS deposits.

3) The detailed studies of the facies architecture of submarine volcanic successions for old VHMS provinces (e.g., Mount Read Volcanics, Tasmania, McPhie and Allen, 1992, 2003; Noranda district, Quebec, Canada, Gibson and Galley, 2007; and Iberian Pyrite Belt, Portugal-Spain, Rosa et al., 2010) have proved to be important in providing the framework for characterisation of ore genesis and exploration. Hence, the volcanic facies characteristics and studies of the volcano-sedimentary sequences in Tasik Chini and the surrounding area may be helpful in reconstructing the VHMS ore forming environments and process.

4) Many of the other outstanding questions at the Tasik Chini deposit area will be answered by additional data collected by future drilling, geophysical surveys, and a general increase in exploration activities.

REFERENCES

Agapova, A.A., Bortnikov, N.S., Chernyshev, I.V., Vikent'ev, I.V., Lisitsyn, A.P., Troitski, A., and Shadlun, T.N., 1994, The lead isotope composition of sulfide ores in the rift zones of the Manus and Lau Basins-southwestern margin of the Pacific Ocean: Geology of Ore Deposits, v. 36, p. 165–170.

Ahmad Jantan, 1973, Stratigraphic of the Singa Formation (Upper Palaeozoic) in the southwestern part of the Langkawi Island Group, West Malaysia, Unpub. MSc. thesis: University of Malaya, Malaysia.

Ames, D.E., Franklin, J.M., and Hannington, M.D., 1993, Mineralogy and geochemistry of active and inactive chimneys and massive sulfide, Middle Valley, northern Juan de Fuca Ridge; an evolving hydrothermal system: Canadian Mineralogist, v. 31, p. 997-1024.

Archbold, N.W., Pigram, C.J., Ratman, N., and Hakim, S., 1982, Indosinian Permian braciopod fauna and Gondwana-South-East Asia relationships: Nature, v. 296, p. 556-558.

Arnold, M., and Sheppard, S.M.F., 1981, East Pacific Rise at latitude 21°N: isotopic composition and origin of the hydrothermal sulphur: Earth and Planetary Science Letters, v. 56, p. 148-156.

Asama, K., 1973, Lower Carboniferous Kuantan flora, Pahang, West Malaysia, in Kobayashi, T., and Toriyama, R., ed., Geology and Palaentology of Southeast Asia 17: University of Tokyo Press, p. 109-117.

Asama, K., 1984. Gigantopteris flora in China and Southeast Asia, in: Kobayashi, T., and Toriyama, R., ed., Geology and Palaeontology of Southeast Asia 25: University of Tokyo Press, p. 311-325.

Aw, P.C., 1978, Preliminary barite investigation in Sungai Mentiga, Pahang: Geological Reports Mg(N)21/1978, Geological Survey Malaysia Annual Report 1978.

Ayuso, R.A., Karl, S.M., Slack, J.F., Haeussler, P.J., Bittenbender, P.E., Wandless, G.A., and Colvin, A.S., 2005, Oceanic Pb-isotopic sources of Proterozoic and Paleozoic volcanogenic massive sulfide deposits on Prince of Wales Island and vicinity, Southeastern Alaska: U.S. Geological Survey Professional Paper 1732-E, p. E1-E20.

Bajwah, Z.U., Seccombe, P.H., and Offler, R., 1987, Trace element distribution, Co:Ni ratios and genesis of the Big Cadia iron–copper deposit, New South Wales, Australia: Mineralium Deposita, v. 22, p. 292-300.

Barber, A.J., and Crow, M.J., 2003, An evaluation of plate tectonic models for the development of Sumatra: Gondwana Research, v. 6, p. 1-28.

Barber, A.J., Crow, M.J., and De smet, M.E.M., 2005, Tectonic evolution, in Barber, A. J., Crow, M.J., and Milsom, J.S., ed., Sumatra: Geology, resources and tectonic evolution: Geological Society Memoir No. 31, p. 234-259.

Barber, A.J., and Crow, M.J., 2009, Structure of Sumatra and its implications for the tectonic assembly of Southeast Asia and the destruction of Paleotethys: Island Arc, v. 18, p. 3-20.

Barker, S.L.L., Hickey, K.A., Cline, J.S., Dipple, G.M., Kilburn, M.R., Vaughan, J.R. and Anthony, L.A.A., 2009,

Uncloaking invisible gold: use of NanoSIMS to evaluate gold, trace elements, and sulfur isotopes in pyrite from Carlin-type gold deposits: Economic Geology, v. 104, p. 897-904.

Barrett, T.J., 1981, Chemistry and mineralogy of Jurassic bedded chert overlying ophiolites in the north Appenines, Italy: Chemical Geology, v. 34, p. 289-317.

Barrett, T.J., and MacLean, W.H., 1994, Mass changes in hydrothermal alteration zones associated with VMS deposits of the Noranda area: Exploration and Mining Geology, v. 3, p. 131-160.

Barrett, T.J., and MacLean, W.H., 1999, Volcanic sequences, lithogeochemistry, and hydrothermal alteration in some bimodal volcanic-associated massive sulfide deposits, in Barrie, C.T., and Hannington, M.D., eds., Volcanic-associated massive sulfide deposits—Processes and examples in modern and ancient settings: Reviews in Economic Geology, v. 8, p. 101–131.

Barrett, T.J., Thompson, J.F.H., and Sherlock, R.L., 1996, Stratigraphic, lithogeochemical and tectonic setting of the Kutcho Creek massive sulphide deposit, northern British Columbia: Exploration and Mining Geology, v. 5, p. 309-338.

Barrie, C.T., Ludden, J.N., and Green, T.H., 1993, Geochemistry of volcanic rocks associated with Cu-Zn and Ni-Cu deposits in the Abitibi Subprovince: Economic Geology, v. 88, p. 1341–1358.

Barrie, C.T., and Hannington, M.D., 1999, Introduction: classification of VMS deposits based on host rock composition: Reviews in Economic Geology, v. 8, p. 2-10.

Barrie, C.T., Taylor, C., and Ames, D.E., 2005, Geology and metal contents of the Ruttan volcanogenic massive sulfide deposit, Northern Manitoba, Canada: Mineralium Deposita, v. 39, p. 795-812.

Barton, P.B.Jr., and Skinner, B.J., 1979, Sulfide mineral stabilities in Barnes, H.L., ed., Geochemistry of hydrothermal ore deposits: New York, Wiley Interscience, 278-403 p.

Barton, P.B.Jr., and Bethke, P.M., 1987, Chalcopyrite disease in sphalerite: Pathology and epidemiology: American Mineralogist, v. 72, p. 451-467.

Basir Jasin., Che Aziz Ali., and Kamal Roslan Mohamed., 1995, Late Triassic radiolaria from the Kodiang Limestone, northwest Peninsular Malaysia: Journal of Southeast Asian Earth Sciences, v. 12, p. 31-39.

Basir Jasin., and Che Aziz Ali., 1997a, Lower Permian Radiolaria from the Pos Blau area, Ulu Kelantan, Malaysia: Journal of Asian Earth Sciences, v. 15, p. 327-339.

Basir Jasin., and Che Aziz Ali., 1997b, Significance of Early Carboniferous radiolaria from Langkap, Negeri Sembilan, Malaysia: Geological Society Malaysia Bulletin, v. 41, p. 109-125.

Basir Jasin., and Zaiton Harun., 2011, Radiolarian biostratigraphy of Peninsular Malaysia—An update: Geological Society Malaysia Bulletin, v. 57, p. 27-38.

Belkabir, A., Gibson, H.L, Marcoux, E., Lentz, D., and Rziki, S., 2008, Geology and wall rock alteration at the Hercynian Draa Sfar Zn-Pb-Cu massive sulphide deposit, Morocco: Ore Geology Reviews, v. 33, p. 280-306.

Bennett, H., and Oliver, G., 1992, XRF analysis of ceramics, minerals and allied materials: Chichester, United Kingdom, Wiley, 298 p.

Bischoff, J.L., and Rosenbauer, R.J., 1985, An empirical equation of state for hydrothermal seawater (3.2 percent NaCl): American Journal of Science, v. 285, p. 725-763.

Bluth, G.J., and Ohmoto, H., 1988, Sulphide-sulphate chimneys on the East Pacific Rise, 11' and 13' N latitudes,

Part II: sulphur isotopes: Canadian Mineralogist, v. 26, p. 505-516.

Bodnar, R.J., 1992, The system H20-NaCl [abs.], Biennial PACROFI 4th, Program and Abstracts: Lake Arrowhead, California, May 22-24, p. 108-111.

Bodnar, R.J., 1993, Revised equation and table for determining the freezing point depression of H2O-NaCl solutions: Geochimica et Cosmochimica Acta, v. 57, p. 683-684.

Böhlke, J.K., and Shanks, W.C.III., 1994, Stable isotope study of hydrothermal vents at Escanaba Trough: observed and calculated effects of sediment-seawater interaction, in Morton, J.L., Zierenberg, R.A., and Reiss, C.A., eds., Geologic, hydrothermal and biologic studies at Escanaba Trough, Gorda Ridge, Offshore northern California: U.S. Geological Survey Bulletin, v. 2022, p. 223-239.

Bonatti, E., 1975, Metallogenesis at oceanic spreading centers: Ann. Rev. Earth Planet. Sci, v. 3, p. 401-433.

Böstrom, K., 1973, The origin and fate of ferromanganoan active ridge sediments: Stockholm Contributions to Geology, v. 27, p. 147-243.

Böstrom, K., and Peterson, M.N.A., 1969, The origin of aluminum-poor ferromanganoan sediments in areas of high heat flow on the East Pacific Rise: Marine Geology, v. 7, p. 427-447.

Bouse, R.M., Ruiz, J., Titley, S.R., and Tosdal, R.M., 1999, Lead isotopic compositions of late Cretaceous and early Tertiary igneous rocks and sulfide minerals in Arizona: implications for the sources of plutons and metals in porphyry copper deposits: Economic Geology, v. 94, p. 211-244.

Bozkaya, G., 2011, Sulphur-and lead-isotope geochemistry of the Arapucandere lead-zinc-copper deposit, Biga Peninsula, northwest Turkey: International Geology Review, v. 53, p. 116-129.

Bozzo, A.T., Chen, R., and Barduhn, A.J., 1973, The properties of hydrates of chlorine and carbon dioxide, in Delyannis, A., and Delyannis, E., eds., Fourth International Symposium on Fresh Water from the Sea, v. 3, p. 437--451.

Bradford, E. F., 1972, The geology and mineral resouces of the Gunung Jerai area, Kedah, Geological Survey of Malaysia District Memoir 13, p. 242.

Brezonik, P.L., 1994, Chemical kinetics and process dynamics in aquatic systems: Boca Raton, Florida, Lewis Publishers.

Brill, B.A., 1989, Trace element contents and partitioning of elements in ore minerals from the CSA Cu–Pb–Zn deposit, Australia: Canadian Mineralogist, v. 27, p. 263-274.

Broman, C., 1987, Fluid inclusions of the massive sulfide deposits in the Skellefte District, Sweden: Chemical Geology, v. 61, p. 161-168.

Brusnitsyn, A.I., and Zhukov, I.G., 2012, Manganese deposits of the Devonian Magnitogorsk palaeovolcanic belt (Southern Urals, Russia): Ore Geology Reviews, v. 47, p. 42-58.

Bunapos, S., 1982, Palaeogeographic history of Waestern Thailand and adjecent parts of Southeast Asia-a plate tectonic interpretation, Geological Survey Paper No.5, Department of Mineral Resources of Thailand, p. 810.

Burrett, C., and Stait, B., 1985, South-East Asia as part of an Ordovician Gondwanaland: Earth and Planetary Science Letters, v. 75, p. 184–190.

Burrett, C., Long, J., Stait, B., 1990, Early–Middle Palaeozoic biogeography of Asian terranes derived from Gondwana, in McKerrow, W.S., Scotese, C.R., eds., Palaeozoic Palaeogeography and Biogeography, Geological Society Memoir No. 12, p. 163–174.

Burton C.K., 1973, Mesozoic, in Geology of the Malay Peninsula, Gobbett D.J., and Hutchison, C.S., eds., Geological Society of Malaysia: Wiley-Interscience, p. 97-141.

Cabri, L.J., Campbell, J.L., Laflamme, J.H.G., Leigh, R.G., Maxwell, J.A., and Scott, J.D., 1985, Proton-microprobe analysis of trace elements in sulfides from some massive-sulfide deposits: Canadian Mineralogist, v. 23, p. 123-148.

Cagatay, M.N., and Eastoe, C.J., 1995, A sulfur isotope study of volcanogenic massive sulfide deposits of the Eastern Black Sea province, Turkey: Mineralium Deposita, v. 30, p. 55-66.

Campbell, F.A., and Ethier, V.G., 1984, Nickel and cobalt in pyrrhotite and pyrite from the Faro and Sullivan orebodies: Canadian Mineralogist, v. 22, p. 503-506.

Cazañas, X., Alfonso, P., Melgarejo, J. C., Proenza, J. A., and Fallick, A. E., 2003, Source of ore-forming fluids in El Cobre VHMS deposit (Cuba): evidence from fluid inclusions and sulphur isotopes: Journal of Geochemical Exploration, v. 78-79, p. 85-90.

Charvet, J., Cluzel, D., Faure, M., Caridroit, M., Shu, L., Lu, H., 1999, Some tectonic aspects of the pre-Jurassic accretionary evolution of East Asia., in Metcalfe, I., ed., Gondwana Dispersion and Asian Accretion. IGCP 321 Final Results Volume: A.A. Balkema, Rotterdam, p. 37-65.

Chiaradia, M., and Fontbote, L., 2001, Radiogenic lead signatures in Au-rich Volcanic-Hosted Massive Sulfide ores and associated volcanic rocks of the Early Tertiary Macuchi Island Arc (Western cordillera of Ecuador): Economic Geology, v. 96, p. 1361-1378.

Chiba, H., Uchiyama, N., and Teagle, D.A.H., 1998, Stable isotope study of anhydrite and sulfide minerals at the TAG hydrothermal mound, Mid-Atlantic Ridge 26°N, in Herzig, P.M., Humphris, S.E., and Miller, J., ed., Proc ODP 158, Scientific Results, College Station, TX., p. 85-90.

Chu, L.H., Chand, F., and Singh, D.S., 1988, Primary tin mineralization in Malaysia: aspects of geological setting and exploration strategy, in Hutshison, C.S., ed., Geology of tin deposits in Asia and the Pacific: Springer, Berlin, p. 593-613.

Clarke, A.H., and Sillitoe, R.H., 1970, Cuprian sphalerite and a probable copper-zinc sulfide, Cachiyuyo de Llampos, Copiapò, Chile: American Mineralogist, v. 55, p. 1021-1025.

Claypool, G. E., Holser, W.T., Kaplan, I.R., Sakai, H., and Zak, I., 1980, The age curves of sulfur and oxygen isotopes in marine sulfate and their mutual interpretation: Chemical Geology, v. 28, p. 199-260.

Cobbing, E.J., Pitfield, P.E.J., Derbyshire, D.P.F., and Mallick, D.I.J., 1992, The granites of the Southeast Asian Tin Belt: Overseas Memoirs of the British Geological Survey, v. 10.

Cobbing, E.J., Mallick, D.I.J., Pitfield, P.E.J., and Teoh, I.H., 1986, The granites of the Southeast Asian Tin Belt: Journal of the Geological Society of London, v. 143, p. 537-550.

Cook, N.J., Ciobanu, C.L., and Mao, J., 2009a, Textural control on gold distribution in As-free pyrite from the Dongping, Huangtuliang and Hougou gold deposits, North China Craton (Hebei Province, China): Chemical Geology, v. 264, p. 101-121.

Cook, N.J., Ciobanu, C.L., Pring, A., Skinner, W., Shimizu, M., Danyushevsky, L., Saini-Eidukat, B., and

Melcher, F., 2009b, Trace and minor elements in sphalerite: a LA-ICPMS study: Geochimica et Cosmochimica Acta, v. 73, p. 4761-4791.

Cook, N.J., and Chryssoulis, S.L., 1990, Concentration of "invisible" gold in the common sulfides: Canadian Mineralogist, v. 28, p. 1-16.

Cook, R.H., undated, Field record, Volume 4: Geological Survey, p. 577-582. (Unpublished).

Craig, J. R., Vokes, F.M., and Solberg, T.N., 1998, Pyrite: physical and chemical textures: Mineralium Deposita, v. 34, p. 82-101.

Craig, J.R., Vaughan, D.J., 1994 Ore Microscopy and Ore Petrography, 2nd edition: New York, Wiley, p. 434.

Crawford, M.L., 1981, Phase equilibria in aqueous fluid inclusions, in Hollister, L.S., and Crawford, M.L., eds., Short course in fluid inclusions: applications to petrology. , v. 6, p. 75-100.

Crawford, A.J., and Berry, R, F., 1992, Tectonic implications of Late Proterozoic-Early Palaeozoic igneous rock associations in Western Tasmania: Tectonophysics, v. 214, p. 37-56.

Crerar, D.A., Namson, J., Chyi, S., Williams, L., and Feigenson, M.D., 1982, Manganiferous cherts of the Franciscan assemblage: I. General geology, ancient and modern analogues and implications for hydrothermal convection at oceanic spreading centers: Economic Geology, v. 77, p. 519-540.

Cruzat Ossa, A., 1970, Genesis of manganese deposits in northern Chile: Economic Geology, v. 65, p. 681-689.

Danyushevsky, L., Robinson, P., Gilbert, S., Norman, M., Large, R., McGoldrick, P., and Shelley, M., 2011, Routine quantitative multi-element analysis of sulphide minerals by laser ablation ICP-MS: standard development and consideration of matrix effects: Geochem. Explor. Environ. Anal., v. 11, p. 51-60.

Danyushevsky, L., Robinson, P., McGoldrick, P., Large, R., and Gilbert, S., 2003, LA-ICPMS of sulphides: evaluation of an XRF glass disc standard for analysis of different sulphide matrixes: Geochimica et Cosmochimica Acta, v. 67, p. A73.

Darbyshire, D.P.F., 1988, Geochronology of Malaysian granites: Natural Environment Research Council, Isotope Geology Centre Open File Report 88/3.

Davidson, G. J., Stolz, A.J., and Eggins, S.M., 2001, Geochemical anatomy of silica iron exhalites: Evidence for hydrothermal oxyanion cycling in response to vent fluid redox and thermal evolution (Mt. Windsor Subprovince, Australia): Economic Geology, v. 96, p. 1201-1226.

Davies, J.F., and Whitehead, R.E., 2006, Alkali-alumina and MgO-alumina molar ratios of altered and unaltered rhyolites: Exploration and Mining Geology, v. 15, p. 75-88.

Diamond, L.W., 1992, Stability of CO_2-clathrate-hydrate+CO_2-liquid+CO_2-vapor + aqueous KCl-NaCl solutions: Experimental determination and application to salinity estimates of fluid inclusions: Geochimica et Cosmochimica Acta, v. 54, p. 545–552.

Deditius, A., Utsunomiya, S., Ewing, R.C., and Kesler, S.E., 2009a, Nanoscale "liquid" inclusions of As-Fe-S in arsenian pyrite: American Mineralogist, v. 94, p. 391-394.

Deditius A., Utsunomiya, S., Ewing R.C., Chryssoulis S.L., Venter D. and Kesler S.E., 2009b, Decoupled geochemical behavior of As and Cu in hydrothermal systems: Geology, v. 37, p. 707-710.

Deditius A., Utsunomiya, S., Reich M., Kesler S. E., Ewing R. C., Hough R. and Walshe J., 2011, Trace metal nanoparticles in pyrite: Ore Geology Reviews, v. 42, p. 32-46.

Delaney, J.R., Mogk, D.W., and Mottl, M.J., 1987, Quartz-cemented breccias from the Mid-Atlantic Ridge:

samples of a high-salinity hydrothermal up-flow zone: Journal of Geophysical Research, v. 92, p. 9175-9192.

de Ronde, C.E.J., 1995, Fluid chemistry and isotopic characteristics of seafloor hydrothermal systems and associated VMS deposits: potential for magmatic contributions: Mineralogical Association of Canada Short Course, v. 23, p. 479-510.

de Ronde, C.E.J., Hannington, M.D., Stoffers, P., Wright, I.C., Ditchburn, R.G., Reyes, A.G., Baker, E.T., Massoth, G.J., Lupton, J.E., Walker, S.L., Greene, R.R., Soong, C.W.R., Ishibashi, J., Lebon, G.T., Bray, C.J., and Resing, J.A. , 2005, Evolution of a submarine magmatic-hydrothermal system: Brothers Volcano, Southern Kermadec Arc, New Zealand: Economic Geology 100th Anniversary Volume.

Doe, B.R., and Zartman, R.E., 1979, Plumbotectonics, I.The Phanerozoic, in Barnes, H. L., ed., Geochemistry of hydrothermal ore deposits: New York, John Wiley and Sons, p. 22–70.

Downes, P.M., and Seccombe, P.K., 2004, Sulfur isotope distribution in Late Silurian volcanic-hosted massive sulfide deposits of the Hill End Trough, eastern Lachlan Fold Belt, New South Wales: Australian Journal of Earth Science, v. 51, p. 123-139.

Doyle, M.G., and Allen, R.L., 2003, Sub-sea floor replacement in volcanic-hosted massive sulfide deposits: Ore Geology Reviews, v. 23, p. 183-222.

Dube, B., Langevin-Mercier, P., Hannington, M., Lafrance, B., Gosselin, G., and Gosselin, P., 2007, The LaRonde Penna World-Class Au-Rich Volcanogenic Massive Sulfide Deposit, Abitibi, Québec: Mineralogy and Geochemistry of Alteration and Implications for Genesis and Exploration: Economic Geology, v. 102, p. 633-666.

Dube, R.K., 2006, Interrelation between gold and tin: a historical perspective: Gold Bulletin 2006, v. 39, p. 103-113.

Duckworth, R.C., Fallick, A.E., and Rickard, D., 1994, Mineralogy and sulfur isotopic composition of the Middle Valley massive sulfide deposit, northern Juan de Fuca Ridge, in Mottl, M.J., Davis, E.E., Fisher, A.T., and Slacks, J.F., ed., Proc ODP 139: Sci Res, College Station, TX., p. 373-385.

Duckworth, R.C., Knott, R., Fallick, A.E., Rickard, D., Murton, B.J., and van Dover C., 1995, Mineralogy and sulphur isotope geochemistry of the Broken Spur sulphides, 29°N, Mid-Atlantic Ridge, in Parson, L.M., Walker, C.L., and Dixon, D.R., ed., Hydrothermal vents and processes: Geological Society Special Publication, v. 87, p. 175-189.

Duhig, N.C., Stolz, J., Davidson, G.J., and Large, R.R., 1992, Cambrian microbial and silica gel textures preserved in silica iron exhalites from the Mount Windsor volcanic belt, Australia: Their petrography, chemistry, and origin: Economic Geology, v. 87, p. 764-784.

Eagle, M., Paytan, A., Arrigo, K.R., van Dijken, G., and Murray, R.W., 2003, A comparison between excess barium and barite as indicators of carbon export: Paleoceanography, v. 18, p. 1-13.

Eastoe, C.J., and Nelson, S.E., 1988, A Permian Kuroko-style hydrothermal system, Afterthought-Ingot area, Shasta County, California: lateral and vertical sections and geochemical evolution: Economic Geology, v. 83, p. 588-605.

Eastoe, C.J., and Gustin, M.M., 1996, Volcanogenic massive sulfide deposits and anoxia in the Phanerozoic oceans: Ore Geology Reviews, v. 10, p. 179-197.

Eastoe, C.J., Solomon, M., and Walshe, J.L., 1987, District-scale alteration associated with massive sulfide deposits in the Mount Read Volcanics, western Tasmania: Economic Geology, v. 82, p. 1239-1258.

Eremin, N.I., 1983, Differentiation of volcanogenic sulfide deposits (in Russian): Moscow, Moscow State University Press, 256 p.

Fehn, U., Doe, B.R., Delevaux, M.H., 1983. The distribution of lead isotopes and the origin of Kuroko ore deposits in the Hokuroku district, Japan: Economic Geology Monograph, v. 5, p. 488-506.

Fifarek, R.H., 1985, Alteration geochemistry, fluid Inclusion, and stable isotope study of the Red Ledge volcanogenic massive sulfide deposit, Idaho: Unpub. PhD. thesis: Oregon State University, Texas, 187 p.

Fifarek, R.H., Field, C.W., and Rye, R.O., 1984, Mineralization and isotopic geochemistry of the Red Ledge volcanogenic massive sulfide deposit, Idaho. Geological Society of America Abstracts with Programs, v. 16, p. 508.

Fleet, M.E., Chryssoulis, S.L., MacLean, P.J., Davidson, R., and Weisener, C.G., 1993, Arsenian pyrite from gold deposits: Au to As distribution investigated by SIMS and EMP and color staining and surface oxidation by XPS and LIMS: Canadian Mineralogist, v. 31, p. 1-17.

Foo, K.Y., 1983, The Palaeozoic sedimentary rocks of Peninsular Malaysia-stratigraphy and correlation, Proceedings of the workshop on stratigraphic correlation of Thailand and Malaysia 1: Technical papers. Geological Society of Thailand and Geological Society of Malaysia, p. 1-19.

Fouquet, Y., Wafic, A., Cambon, P., Mevel, C., Meyer, C., and Gente, P., 1993, Tectonic setting and mineralogical and geochemical zonation in the Snake Pit Sulfide Deposit (Mid Atlantic Ridge at 23 ºN): Economic Geology, v. 88, p. 2018-2036.

Franklin, J.M., 1993, Volcanic-associated massive sulphide deposits: Geological Association of Canada Special Paper, v. 40, p. 315-334.

Franklin, J.M., 1995, Volcanic-associated massive sulphide base metal: Geological Survey of Canada, v. 8, p. 158–183.

Franklin, J.M., Sangster, D.M., and Lydon, J. W., 1981, Volcanic-associated massive sulfide deposits: Economic Geology 75th Anniversary Volume, p. 485-627.

Franklin, J.M., Gibson, H.L., Jonasson, I.R. and Galley, A.G., 2005, Volcanogenic massive sulphide deposit: Economic Geology 100th Anniversary Volume, p. 523-560.

Galley, A.G., Bailes, A.H., and Kitzler, G., 1993, Geological setting and hydrothermal evolution of the Chisel Lake and North Chisel Zn-Pb-Ag-Au massive sulphide deposit, Snow Lake, Manitoba: Exploration and Mining Geology, v. 2, p. 271–295.

Galley, A.G., Watkinson, D.H., Jonasson, I.R., and Riverin, G., 1995, The subsea-floor formation of volcanic-hosted massive sulfude: Evidence from the Ansil deposit, Rouyn-Noranda, Canada: Economic Geology, v. 90, p. 2006-2017.

Galley, A.G., and Koski, R.A., 1999, Setting and characteristics of ophiolite-hosted volcanogenic massive sulfide deposits, in Barrie, C.T., and Hannington, M.D., eds., Volcanic-Associated Massive Sulfide Deposits: Processes and Examples in Modern and Ancient Settings: Reviews in Economic Geology, v. 8, p. 215-236.

Galley, A.R., van Breeman, O., and Franklin, J.M., 2000, The relationship between intrusion-hosted Cu-Mo

mineralization and the VMS deposits of the Archean Sturgeon Lake mining camp, northwestern Ontario: Economic Geology, v. 95, p. 1543–1550.

Galley, A.G., Hannington, M., and Jonasson, I., 2007, Volcanogenic massive sulphide deposits, in Goodfellow, W. D., ed., Mineral deposits of Canada: A synthesis of major deposit-types, district metallogeny, the evolution of geological provinces, and exploration methods, 5, Geological Association of Canada, Mineral Deposits Division, p. 141–161.

Gemmell, J.B., and Large, R.R., 1992, Stringer system and alteration zones underlying the Hellyer volcanogenic massive sulfide deposit, Tasmania, Australia: Economic Geology, v. 87, p. 620–649.

Gemmell, J.B., and Sharpe, R., 1998, Detailed sulfur-isotope investigation of the TAG hydrothermal mound and stockwork zone, 26 degrees north, Mid-Atlantic Ridge in Herzig, P.M., Humphris, and S.E., and Miller, J., ed., Proc ODP 158: Scientific Results, College Station, TX., p. 71-84.

Gemmell, J.B., Fulton, R.R., 2001, Geology, genesis, and exploration implications of the footwall and hanging-wall alteration associated with the Hellyer volcanic-hosted massive sulfide deposit, Tasmania, Australia: Economic Geology, v. 96, p. 1003-1035.

German, C.R., and Von Damm, K.L., 2003, Hydrothermal processes, in Elderfield, H., ed., The oceans and marine geochemistry: Treatise on Geochemistry, Amsterdam, Elsevier Ltd, 181-222 p.

Gifkins, C., Hermann, W., and Large, R.R., 2005, Altered volcanic rocks-a guide to description and interpretation Centre for Ore Deposit Research.

Ghani, A.A., 2000, The Western Belt granite of Peninsular Malaysia: some emergent problems on granite classification and its implication: Geosciences Journal, v. 4, p. 283-293.

Ghani, A.A., 2009a, Plutonism, in Hutchison, C. S., and Tan, D.N.K., ed., Geology of Peninsular Malaysia: University of Malaya and the Geological Society of Malaysia, p. 211-223.

Ghani, A.A., 2009b, Volcanism, in Hutchison, C. S., and Tan, D.N.K., ed., Geology of Peninsular Malaysia: University of Malaya and the Geological Society of Malaysia, p. 197-210.

Ghani, A.A., Lo, C.H., and Chung, S.L., 2013, Ar-Ar geochronology of volcanic rocks from Eastern Part of Peninsular Malaysia [abs.], National Geological Conference, Ipoh, Perak, Malaysia, 2013.

Gibson, H.L. and Watkinson, D.H. 1990. Volcanogenic massive sulphide deposits of the Noranda cauldron and shield volcano, Quebec, in Rive, M., Verpaelst, P., Gagnon, V., Lulin, J.M., Riverin, G., and Simard, A., ed., The northwestern Quebec polymetallic belt, Special Volume 4: Canadian Institute of Mining Metallurgy, p. 119-132.

Gibson, H.L., and Galley, A.G., 2007, Volcanogenic Massive Sulphide Deposits of the Archean, Noranda District, Quebec, in Goodfellow, W.D., ed., Mineral Deposits of Canada: A synthesis of major deposit, types district metallogeny, the evolution of geological provinces and exploration methods, Special Publication 5, Mineral Deposits Division: Geological Association of Canada, p. 533–552.

Gifkins, C., Hermann, W. and Large, R.R., 2005, Altered volcanic rocks-a guide to description and interpretation Centre for Ore Deposit Research.

Gobbett, D.J., 1965, The Lower Palaeozoic rocks of Kuala Lumpur Federation Museums Journal, v. 9, p. 67-79.

Gobbett, D.J., and Hutchison, C.S., 1973, Geology of the Malay Peninsula: New York, Wiley-Interscience., 438 p.

Goldfarb, R.J., Phillips, G.N., and Nokleberg, W.J., 1998, Tectonic setting of synorogenic gold deposits of Pacific Rim: Ore Geology Reviews, v. 13, p. 185-218.

Goldfarb, R.J., Taylor, R.D., Collins, G.S., Nikolay A. Goryachev, N.A., Omero Felipe and Orlandini, O.F., 2013, Phanerozoic continental growth and gold metallogeny of Asia: Gondwana Research. DOI: 10.1016/j.gr.2013.03.002.

Goldstein, R.H., and Reynolds, T.J., 1994, Systematics of fluid inclusions in diagenetic minerals: SEPM (Society for Sedimentary Geology) Short Course, v. 31, p. 214.

Goodfellow, W.D., and Peter, J.M., 1994, Geochemistry of hydrothermally altered sediment, Middle Valley, northern Juan de Fuca Ridge, in Mottl, M. J., Davis, E.E., Fisher, A.T., Slack, J.F., ed., Middle Valley, Juan de Fuca Ridge, sites 855–858, 139, Proceedings of the Ocean Drilling Program, Scientific Results, p. 207–289.

Goodfellow, W.D., and Blaise, B., 1988, Sulfide formation and hydrothermal alteration of hemipelagic sediment in Middle Valley, northern Juan de Fuca Ridge: Canadian Mineralogist, v. 26, p. 675-696.

Goodfellow, W.D., and Franklin,J., 1993, Geology, mineralogy and chemistry of sediment-hosted clastic massive sulfides in shallow cores, Middle Valley, N. Juan de Fuca Ridge: Economic Geology, v. 88, p. 2037–2068.

Goodfellow, W.D., Zierenberg, R.A., and ODP 196 Shipboards Science Party, 1999, Genesis of massive sulfide deposits at sediment-covered spreading centers, in Barrie, C.T., and Hannington, M.D., eds., Volcanic-Associated Massive Sulfide Deposits: Processes and Examples in Modern and Ancient Settings: Reviews in Economic Geology, v. 8, p. 297-324.

Goutier, J., McNicoll, V., Dion, C., Lafrance, B., Legault, M., Ross, P.-S., Mercier-Langevin, P., Cheng, L.-Z., de Kemp, E., and Ayer, J., 2009, L'impact du Plan Cuivre et de L'ICG -3 sur la géologie de l'Abitibi et du Groupe de Blake River, Proceedings Congrès Abitibi 2009 – Abitibi Cuivre, Rouyn-Noranda, September 28th, 2009, p. 9-13.

Green, G.R., Solomon, M., and Walshe, J.L., 1981, The formation of the volcanic-hosted massive sulphide ore deposit at Rosebery, Tasmania: Economic Geology, v. 76, p. 304-338.

Grenne, T., and Slack, J.F., 2005, Geochemistry of jasper beds from the Ordovician Løkken ophiolite, Norway-Origin of proximal and distal siliceous exhalites: Economic Geology, v. 100, p. 1511-1527.

Grenne, T., and Vokes F.M., 1990, Sea-floor sulfides at the Hoydal volcanogenic deposit, central Norwegian Caledonides: Economic Geology, v. 85, p. 344-359.

Griffith, M. E., and Paytan, A., 2012, Barite in the ccean-occurrence, geochemistry and paleoceanographic applicators: Sedimentology, v. 59, p. 1817-1835.

Groves, D.I., Condie, K.C., Goldfarb, R.J., Hronsky, J.M.A., and Vielreicher, R.M., 2005, Secular changes in global tectonic processes and their influence on the temporal distribution of gold-bearing mineral deposits: Economic Geology, v. 100, p. 203-224.

Grubb, P.L.C., Geology and bauxite deposits of the Pengerang area, southeast Johor:Geological Survey of Malaysia Memoir 14, Ipoh.

Gulson, B.L., 1986, Lead isotopes in mineral exploration: Amsterdam, Elsevier, 245 p.

Gulson, B.L., and Vaasjoki, M., 1987, Lead isotope data from the Thalanga, Dry River and Mt Chalmers base

metal deposits and their bearing on exploration and ore genesis in eastern Australia: Australian Journal of Earth Science, v. 34, p. 159-173.

Gustin, M.M., 1990, Geology and geochemistry of the Bully Hill area of the East Shasta District, Shasta County, California, Unpub. PhD. thesis: University of Arizona, Tucson, 261 p.

Gustin, M.M., and Eastoe, C.J., 2000, Geology and ore petrography of Permian Kuroko-type volcanogenic massive Sulfide deposits of the Bully Hill area, east Shasta district, California: Economic Geology, v. 95, p. 343-360

Haas, J.L.Jr., 1971, The effect of salinity on the maximum thermal gradient of a hydrothermal system at a hydrostatic pressure: Economic Geology, v. 66, p. 940-946.

Halbach, P., Nakamura, K., Wahsner, M., Lange, J., Sakai, H., Käselitz, L., Hansen, R.-D., Yamano, M., Post, J., Prause, B., Seifert, R., Michaelis, W., Teichmann, F., Kinoshita, M., Märten, A., Ishibashi, J., Czerwinski, S., and Blum, N., 1989, Probable modern analogue of Kuroko-type massive sulphide deposits in the Okinawa Trough back-arc basin: Nature, v. 338, p. 496-499.

Hall, R., 2011, Australia-SE Asia collision; plate tectonic and crustal flow, The SE Asian Gateway; History and tectonics of Australia-Asia collision: Geological Society Special Publication 355, p. 75-109.

Hall, R., and Sevastjanova, I., 2012, Australian crust in Indonesia: Australian Journal of Earth Sciences, v. 59, p. 827-844.

Hannington, M.D., de Ronde, C.E.J., and Petersen, S., 2005. Sea-floor tectonics and submarine hydrothermal systems, in Hedenquist, J.W., et al., ed., Economic Geology 100th Anniversary Volume, 111-141.

Hannington, M.D., Bleeker, W., and Kjarsgaard, I., 1999a, Sulphide mineralogy, geochemistry, and genesis of the Kidd Creek deposit: Part I. North, Central, and South orebodies: Economic Geology Monograph, v. 10, p. 163-224.

Hannington, M.D., Bleeker, W., and Kjarsgaard, I., 1999b, Sulphide mineralogy, geochemistry, and genesis of the Kidd Creek deposit: Part II. The Bornite Zone: Economic Geology Monograph, v. 10, p. 225-266.

Hannington, M.D., and Scott, S.D., 1988, Mineralogy and geochemistry of a hydrothermal silica-sulphide-suphate spire in the caldera of Axial Seamount, Juan de Fuca Ridge: Canadian Mineralogist, v. 26, p. 603-626.

Harbury, N.A., Jones, M.E., Audley-Charles, M.G., Metcalfe, I., and Mohamed, K.R., 1990, Structural evolution of Mesozoic Peninsular Malaysia: Journal of the Geological Society of London, v. 147, p. 11-26.

Harkins, S.A., Appold, M.S., Nelson, B.K., Brewer, A.M., and Groves, I.M., 2008, Lead isotope constraints on the origin of nonsulfide zinc and sulfide zinc-lead deposits in the Flinders Ranges, South Australia: Economic Geology, v. 103, p. 353-364.

Hart, T.R., Gibson, H.L., and Lesher, C.M., 2004, Trace element geochemistry and petrogenesis of felsic volcanic rocks associated with volcanogenic massive Cu–Zn–Pb sulfide deposits: Economic Geology, v. 99, p. 1003–1013.

Haymon, R.M., and Kastner, M., 1981, Hot Spring Deposits on the East Pacific Rise at 21°N: preliminary description of mineralogy and genesis: Earth and Planetary Letters, v. 53, p. 363-381.

Hegner, E., and Tatsumoto, M., 1987, Pb, Sr and Nd isotopes in basalts and sulfides from the Juan de Fuca Ridge: Journal of Geophysical Research, v. 92, p. 11380–11386.

Hein, J.R., Koschinsky, A., and McIntyre, B.R., 2005, Mercury- and silver-rich ferromanganese-oxides, southern California borderland: deposit model and environmental implications: Economic Geology, v. 100, p. 1151-1168.

Hekinian, R., Fevrier, M., Bischoff, J.L., Picot, P., and Shanks, W.C. III., 1980, Sulfide deposits from the East Pacific Rise near 21°N: Science, v. 207, p. 1433-1444.

Hendry, D.A.F., 1981, Chlorites, phengites and siderites from the Prince Lyell ore deposit, Tasmania, and the origin of the deposit: Economic Geology, v. 76, p. 285-303.

Herrmann, W., Blake, M., Doyle, M., Huston, D., Kamprad, J., Merry, N., and Pontual, S., 2001, Short wavelength infrared (SWIR) spectral analysis of hydrothermal alteration zones associated with base metal sulfide deposits at Rosebery and Western Tharsis, Tasmania, and Highway-Reward, Queensland: Economic Geology, v. 96, p. 939–955.

Herzig, P.M., Petersen S., and Hannington, M.D., 1998, Geochemistry and sulfur-isotopic composition of the TAG hydrothermal mound, mid-Atlantic Ridge, 26'N: Proc ODP, Sci Results, v. 158, p. 47-70.

Hill, A.P., 1996, Structure, volcanic setting, hydrothermal alteration and genesis of the Thalanga massive sulphide deposit. Unpub. PhD. thesis: University of Tasmania, Australia.

Hoefs, J., 2004, Stable Isotope Geochemistry: Berlin, Springer-Verlag, p. 201.

Hoefs, J., 1997, Stable Isotope Geochemistry: Berlin, Springer-Verlag, p. 201.

Hosking, K.F.G., 1979, Tin distribution patterns: Geological Society Malaysia Bulletin, v. 9, p. 141-157.

Hou, Z.-Q., and Zhang, Q.-L., 1998, CO2 and hydrocarbon-rich fluids in submarine active hydrothermal system in the Okinawa trough: evidence from fluid inclusions: Sciences in China, v. 18, p. 142-148.

Hou, Z., Khin Zaw, Li, Y.-H., Zhang, Q.-L., Zeng, Z.-G., and Urabe, T., 2005, Contribution of magmatic fluid to the active hydrothermal system in the JADE field, Okinawa trough: evidence from fluid inclusions, and oxygen and helium isotopes: International Geology Reviews, v. 47, p. 420-437.

Hou, Z., Khin Zaw, Qu, X.-M., Ye, Q.-T., Yu, J.-J., Xu, M.-J., Fu, D.-M., and Yin, X.-K.. 2001, Origin of the Gacun volcanic-hosted massive sulfide deposit in Sichuan, China: fluid inclusion and oxygen isotope evidence: Economic Geology, v. 96, p. 1491-1512.

Hou, Z., Khin Zaw, Rona, P., Li, Y., Qu, X., Song, S., Ligui, P., and Huang, J., 2008, Geology, fluid inclusions, and oxygen isotope geochemistry of the Baiyinchang Pipe-Style volcanic-hosted massive sulfide Cu Deposit in Gansu Province, Northwestern China: Economic Geology, v. 103, p. 269-292.

Hunns, S.R., 2001, Style and setting of volcanic-hosted massive sulphide mineralisation in the Early Permian Berserker beds, Mount Chalmers, Queensland, Unpub. PhD. thesis: University of Tasmania, Australia, 351 p.

Huston, D.L., 1993, The effect of alteration and metamorphism on wall rocks to the Balcooma and Dry River South volcanic-hosted sulfide deposits, Queensland, Australia: Journal of Geochemical Exploration, v. 48, p. 277–307.

Huston, D.L., 1999, Stable isotopes and their significance for understanding the genesis of volcanic-hosted massive sulfide deposits—A review, in Barrie, C. T., and Hannington, M.D., ed., Volcanic-associated massive sulfide deposits—Processes and examples in modern and ancient settings, Reviews in Economic Geology, v. 8, p. 157–179.

Huston, D.L., Power, M., Gemmell, J.B., and Large, R. R., 1995a, Design, calibration and geological application of the first operational Australian laser ablation sulfur isotope microprobe: Australian Journal of Earth Science v. 42, p. 549-555.

Huston, D.L., Sie, S.H., Suter, G.F., Cooke, D.R., and Both, R.A., 1995b, Trace elements in sulfide minerals from eastern Australian volcanic-hosted massive sulfide deposits: Part I. Proton microprobe analyses of pyrite, chalcopyrite, and sphalerite, and Part II. Selenium levels in pyrite: Comparison with δ34S values and implications for the source of sulfur in volcanogenic hydrothermal systems: Economic Geology, v. 90, p. 1167-1196.

Huston, D.L., and Kamprad, J., 2001, Zonation of alteration facies at Western Tharsis: implications for the genesis of Cu-Au deposits, Mount Lyell field, western Tasmania: Economic Geology, v. 96, p. 1123-1132.

Huston, D.L., Pehrson, S., Eglington, B.M., and Zaw, K., 2010, The geology and metallogeny of volcanic-hosted massive sulfide deposits: Variations through geologic time and with tectonic setting: Economic Geology, v. 105, p. 571-591.

Huston, D.L., Relvas, J.M.R.S., Gemmell, J.B., and Drieberg, S., 2011, The role of granites in volcanic-hosted massive sulphide ore-forming systems: an assessment of magmatic–hydrothermal contributions: Mineralium Deposita, v. 46, p. 473-507.

Hutchison, C.S., 1973, Plutonic activity, in Gobbett, D. J., and Hutchison, C.S., ed., Geology of the Malay Peninsula: New York, Wiley-Interscience., p. 215-252.

Hutchison, C.S., 1975, Ophiolite in Southeast Asia: Geological Society of America Bulletin, v. 86, p. 797-806.

Hutchison, C.S., 1977, Granite emplacement and tectonic subdivision of Peninsular Malaysia: Geological Society Malaysia Bulletin, v. 9, p. 187-207.

Hutchison, C.S., 1989, Geological evolution of South-east Asia: Oxford, UK, Clarendon Press.

Hutchison, C.S., 2007, Geological evolution of South-east Asia: Geological Society of Malaysia, Kuala Lumpur.

Hutchison, C. S., 2009a, Tectonic evolution, in Hutchison, C. S., and Tan, D. N.K., ed., Chapter 14, Geology of Peninsular Malaysia, University of Malaya and the Geological Society of Malaysia, p. 309-330.

Hutchison, C.S., and Sivam, S.P., 1992, Discussion on structural evolution of Mesozoic Peninsular Malaysia: Journal of the Geological Society of London, v. 149, p. 679-680.

Hutchison, C.S., and Tan, D.N.K., 2009, Geology of Peninsular Malaysia: University of Malaya and the Geological Society of Malaysia, 479 p.

Hutchison, M.N., and Scott, S.D., 1981, Sphalerite geobarometry in the Cu–Fe–Zn–S system: Economic Geology, v. 76, p. 143-153.

Hutchinson, R.W., 1973, Volcanogenic massive sulfide deposits and their metallogenic significance: Economic Geology, v. 68, p. 1223-1246.

Hutchinson, R.W., 1986, Massive sulphide deposits and their possible significant to other ores in Southeast Asia: Geological Society Malaysia Bulletin, v. 19, p. 1-22.

Ingham, F.T., and Bradford, E.F., 1960, The geology and mineral resouces of the Kinta Valley, Perak, Federation of Malaya Geological Survey District Memoir 9, 347 p.

Inverno, C.M.C., Solomon, M., Barton, M.D., and Foden, J., 2008, The Cu stockwork and massive sulfide ore of

the Feitais Volcanic-Hosted Massive Sulfide deposit, Aljustrel, Iberian Pyrite Belt, Portugal: a mineralogical, fluid inclusion, and isotopic investigation: Economic Geology, v. 103, p. 241-267.

Ishihara, S., Sawata, H., Arpornsuwan, S., Busaracome, P., and Bungbrakearti, N., 1979, The magnetite-series and ilmenite-series granitoids and their bearing on tin mineralization, particularly in the Malay Peninsula region: Geological Society Malaysia Bulletin, v. 11, p. 103-110.

Ishikawa, Y., Sawaguchi, T., Iwaya, S., and Horiuchi, M., 1976, Delineation of prospecting targets for Kuroko deposits based on modes of volcanism of underlying dacite and alteration halos: Mining Geology, v. 26, p. 105-117.

Janecky, D.R., and Shanks, W.C.III., 1988, Computational mopdeling of chemical and sulfur isotopic reaction processes in seafloor hydrothermal systems: chimneys, massive sulfides and subjacent alteration zones: Canadian Mineralogist, v. 26, p. 805-825.

Jennings, J.R., and Lee, C.P., 1985, Preliminary note on occurrence of Carboniferous age coals and in-situ plant fossils in eastern Peninsular Malaysia: Geological Society of Malaysia Warta Geologi, v. 11, p. 117-121.

Jones, S., Herrmann, W., and Gemmell, J.B., 2005, Short wavelength infrared spectral characteristics of the HW horizon: implications for exploration in the Myra Falls volcanic-hosted massive sulfide Camp, Vancouver island, British Columbia, Canada: Economic Geology, v. 100, p. 273-294.

Jones, C.R., 1961, A revision of the stratigraphical sequence of the Langkawi Islands, Federation of Malaya: Proceedings 9th Pacific Science Congress 12, 1961, p. 287-300.

Jones, C.R., 1973, Lower Palaeozoic, in Gobbett, D.J., and Hutchison, C.S., ed., Geology of the Malay Peninsula: New York, Wiley-Interscience, p. 25-60.

Kajiwara, Y., and Date, J., 1971, Sulfur isotope study of Kuroko type and Kieslager-type strata-bound massive sulfide deposits in Japan: Geochemical Journal, v. 5, p. 133-150.

Kalogeropoulus, S.I., and Scott, S.D., 1989, Mineralogy and geochemistry of an Archean tuffaceous exhalite: The Main Contact Tuff, Millenbach mine area, Noranda, Quebec: Canadian Journal of Earth Science, v. 26, p. 88-105.

Kalogeropoulus, S.I., and Scott, S.D., 1983, Mineralogy and geochemistry of tuffaceous exhalites (tetsusekiei) of the Fukazawa mine, Hokuroko district, Japan: Economic Geology Monograph, v. 5, p. 412-432.

Kamaludin Hassan, 1990, A summary of the Quaternary geology investigations in Seberang Prai, Pulau Pinang and Kuala Kurau: Geological Society Malaysia Bulletin, v. 26, p. 47-53.

Kamaludin Hassan., 2004, Part 3 Cenozoic, in Lee, C.P., Leman, M.S., Hassan, K., Nasib, B.M., and Karim, R., eds., Stratigraphic Lexicon of Malaysia: Geological Society of Malaysia, p. 124-125.

Kampschulte, A., and Strauss, H., 2004, The sulfur isotopic evolution of Phanerozoic seawater based on the analysis of structurally substituted sulfate in carbonates: Chemical Geology, v. 204, p. 255-286.

Kase, K., Yamamoto, M., and Shibata, T., 1990, Copper-rich sulfide deposits near 23°N, Mid-Atlantic Ridge: chemical composition, mineral chemistry, and sulfur isotopes, in Detrick, R., Honnorez, J., Bryan, W.B., and Juteau, T., ed., Proc ODP, vols 106/109: Scientific Results, College Station, TX., p. 163-172.

Kerridge, J.F., Haymon, R.M., and Kastner, M., 1983, Sulfur isotope systematics at the 21°N site, East Pacific Rise: Earth and Planetary Science Letters, v. 66, p. 91-100.

Kesler, S.E., Appold, M.S., Cumming, G.L., and Krstic, D., 1994a, Lead isotope geochemistry of Mississippi Valley-type mineralization in the Central Appalachians: Economic Geology, v. 89, p. 1492-1500.

Kesler S.E., Cumming, G.L., Krstic, D., and Appold, M.S., 1994b, Lead isotope geochemistry of Mississippi Valley-type deposits of the Southern Appalachians: Economic Geology, v. 89, p. 307-321.

Khin Zaw, 1991, The effect of Devonian metamorphism and metasomatism on the mineralogy and geochemistry of the Cambrian VMS deposits in the Rosebery–Hercules district, western Tasmania, Unpub. PhD. thesis: University of Tasmania, Australia, 302 p.

Khin Zaw and Large, R.R., 1996, Petrology and geochemistry of sphalerite from the Cambrian VHMS deposits in the Roseberry Hercules district, Western Tasmania: implications for gold mineralisation and Devonian metamorphic-metasomatic processes: Mineralogy and Petrology, v. 57, p. 97-118.

Khin Zaw, Gemmell., J.B., Large, R.R, Mernagh, T., and Ryan, C.G., 1996, Evolution and source of ore fluids in the stringer system, Hellyer VHMS deposit, Tasmania, Australia: evidence from fluid inclusion microthermometry and geochemistry: Ore Geology Reviews, v. 10, p. 251-278.

Khin Zaw, Hunns., S.R., Large, R.R., Gemmell, B.J., Ryan, C.G., and Mernagh, T.P., 2003, Microthermometry and chemical composition of fluid inclusions from the Mt Chalmers volcanic-hosted massive sulphide deposits, central Queensland, Australia: implications for ore genesis: Chemical Geology, v. 194, p. 225-244.

Khin Zaw, Meffre, S., and the team, 2010, Final report on “Ore Deposits of SE Asia” Project, Hobart, Tasmania.

Khin Zaw., Meffre, S., Lai, C.K., Santosh, M., Burrett, C., Graham, I., Manaka, T., Salam, A., Kamvong, T., Cromie, P., and Makoundi, C., 2014, Tectonics and metallogeny of mainland Southeast Asia – A review and contribution: Gondwana Research.

Khoo, H.P., 1983, Mesozoic stratigraphy in Peninsula Malaysia, Proceeding of the workshop on stratigraphic correlation of Thailand and Malaysia 1: Technical papers: Geological Society of Thailand and Geological Society of Malaysia, p. 370-383.

Knauth, L.P., 2005, Temperature and salinity history of the Precambrian ocean: implications for the course of microbial evolution: Palaeogeography, Palaeoclimatology, Palaeoecology, v. 219, p. 53-69.

Knott, R., Fallick, A.E., Rickard, D., Bäcker, H., 1995, Mineralogy and sulphur isotope characteristics of a massive sulphide boulder, Galapagos Rift, 85°55'W, in Parson, L.M., Walker, C.L., and Dixon, D.R., ed., Hydrothermal vents and processes: Geological Society Special Publication, v. 87, p. 207-222.

Koglin, N., Frimmel, H.E., Minter, W.E.L., and Brätz, H., 2010, Trace-element characteristics of different pyrite types in Mesoarchean to Paleoproterozoic placer deposits: Mineralium Deposita, v. 45, p. 259-280.

Kon’no, E., and Asama, K., 1970, Some Permian plants from the Jengka Pass, Pahang, West Malaysia, in Kobayashi, T., and Toriyama, R., ed., Geology and Palaeontology of Southeast Asia 8: University of Tokyo Press., p. 87-132.

Kon’no, E., Asama, K., and Rajah, S.S., 1971, The Late Permian Linggiu flora from the Gunung Blumut area, Johore, Malaysia in Kobayashi, T., and Toriyama, R., ed., Geology and Palaeontology of Southeast Asia 9: University of Tokyo Press., pp. 1–85.

Kontak, D.J., Cumming, G.L., Krstic, D., Clark, A.H., and Farrar, E., 1990, Isotopic composition of lead in ore deposits of the cordillera Oriental, Southeastern Peru: Economic Geology, v. 85, p. 1584-1603.

Koski, R.A., Shanks, W.C.III., Bohrson, W.A., and Oscarson, R.L., 1988, The composition of massive sulfide deposits from the sedimen-tcovered floor of Escanaba Trough, Gorda Ridge: implications for depositional processes: Canadian Mineralogist, v. 26, p. 655-673.

Kullerud, G., 1953, The FeS-ZnS system, a geological thermometer: Norsk Geol Tidsskr v. 32, p. 6l-147.

Kuroda, H., 1983 Geologic characteristics and formation environments of the Furutobe and Matsuki Kuroko deposits, Akita Prefecture, Northeast Japan: Economic Geology Monograph, v. 5, p. 149-166.

Kusakabe, M., Mayeda, S., and Nakamura, E., 1990, S, O and Sr isotope systematics of active vent materials from the Mariana backarc basin spreading axis at 18°N: Earth and Planetary Science Letter, v. 100, p. 275-282.

Lapidus, D.F., and Winstanley, I., 1990, Collins dictionary of geology: Harper Collins, p. 565.

Large, D.J., Sawlowicz, Z., and Spratt, J., 1999, A cobaltite–framboidal pyrite association from the Kupferschiefer; possible implications for trace element behaviour during the earliest stages of diagenesis: Mineral.Mag., v. 63, p. 353-361.

Large, R.R., 1977, Chemical evolution and zonation of massive sulfide deposits in volcanic terrains: Economic Geology, v. 72, p. 549-572

Large, R.R., 1992, Australian volcanic-hosted massive sulfide deposits: Features, styles, and genetic models: Economic Geology, v. 87, p. 471–510.

Large, R.R., Belousov, I., and Meffre, S., 2013, Western Australia pyrite and magnetite fingerprint database: assesment of phase 1 pyrite analyses: In Ore Deposit Geochemistry, Hydrology and Geochronology, Master of Economic Geology Cource Work, CODES, University of Tasmania.

Large, R.R., Danyushevsky, L.D., Hollit, C., Maslennikov, V.V., Meffre, S., Gilbert, S., Bull, S., Scott, R., Emsbo, P., Thomas, H., Singh, R., and Foster, J., 2009, Gold and trace element zonation in pyrite using a laser imaging technique; Implications for the timing of gold in orogenic and Carlin-style sediment-hosted deposits: Economic Geology, v. 104, p. 635-668.

Large, R.R., Gemmell, J.B., and Paulick, H., 2001a, The alteration box plot: A Simple approach to understanding the relationship between alteration mineralogy and lithogeochemistry associated with volcanic-hosted massive sulfide deposits: Economic Geology, v. 96, p. 957-971.

Large, R.R., Allen, R.L., Blake, M.D., and Herrmann, W., 2001b, Hydrothermal alteration and volatile element halos for the Rosebery K Lens volcanic-hosted massive sulfide deposit, Western Tasmania: Economic Geology, v. 96, p. 1055–1072.

Large, R.R., and Both R.A., 1980, The volcanogenic ores at Mount Chalmers, eastern Queensland: Economic Geology, v. 75, p. 992-1009.

Larocque, A. C. L., Hodgson, C.J., Cabri, L.J., and Jackman, J.A., 1995, Ion-microprobe analysis of pyrite, chalcopyrite, and pyrrhotite from the Mobrun VMS deposit in northwestern Quebec: Evidence for metamorphic remobilization of gold: Canadian Mineralogist, v. 33, p. 373-388.

Lecuyer, C., Dubois, M., Marignac, C., Gruau, G., Fouquet, Y., and Raboz, C., 1999, Phase separation and fluid mixing in subseafloor back arc hydrothermal systems: a microthermometric and oxygen isotope study of fluid inclusions in the barite-sulfide chimneys of the Lau basin: Journal of Geophysical Research, v. 104 (B8), p. 17911-17927.

Lee, C.P., 2004, Part I Palaeozoic, in Lee, C.P., Leman, M.S., Hassan, K., Nasib, B.M., and Karim, R., ed., Stratigraphic Lexicon of Malaysia: Geological Society of Malaysia, p. 3-35.

Lee, C.P., 2009, Palaeozoic Stratigraphy, in Hutchison, C.S., and Tan, D.N.K., eds., Geology of Peninsular Malaysia: University of Malaya and Geological Society of Malaysia, Kuala Lumpur, p. 55-86.

Lehmann, B., Zhao, X., Zhou, M., Du, A., Mao, J., Zeng, P., Henjes-Kunst, F., and Heppe, K., 2013, Mid-Silurian back-arc spreading at the northeastern margin of Gondwana: The Dapingzhang dacite-hosted massive sulfide deposit, Lancangjiang zone, southwestern Yunnan, China: Gondwana Research, v. 24, p. 648-663.

Lein, A.Y., Ulyanova, N.V., Grinenko, V.A., YeV, B., and Lisitsyn, A.P., 1993, Mineralogical and geochemical features of the Manus Basin hydrothermal sulfide ores, Bismarck Sea: Geochemical International, v. 30, p. 57-71.

Leistel, J.M., Marcoux, E., and Deschamps, Y., 1998, Chert in the Iberian pyrite belt: Mineralium Deposita, v. 33, p. 59-81.

Leitch, C.H.B., and Lentz, D.R., 1994, The Gresens approach to mass balance constraints of alteration systems—Methods, pitfalls, examples, in Lentz, D. R., ed., Alteration and alteration processes associated with ore-forming systems: Geological Association of Canada Short Course Notes, v. 11, p. 161–192.

Lentz, D.R., 1998, Petrogenetic evolution of felsic volcanic sequences associated with Phanerozoic volcanic-hosted massive sulfide systems: the role of extensional geodynamics: Ore Geology Reviews, v. 12, p. 289-327.

Lentz, D.R., and Goodfellow, W.D., 1994a, Petrology and geochemistry of altered volcanic and sedimentary rocks associated with stringer sulphide zone, Bathurst, New Brunswick: Geological Survey of Canada, v. 94-1D, p. 123-133.

Lentz, D.R., and Goodfellow, W.D., 1994b, Character,distribution and origin of zoned hydrothermal alteration features at the Brunswick 12 massive sulphide deposit, Bathurst Mining Camp, New Brunswick: New Brunswick Department of Natural Resources and Mineral Resources, v. 94-1, p. 94-119.

Lesher, C.M., Goodwin, A.M., Campbell, I.H., and Gorton, M. P., 1986, Trace element geochemistry of ore-associated and barren felsic metavolcanic rocks in the Superior province, Canada: Canadian Journal of Earth Science, v. 23, p. 222–237.

Liew, T.C., and McCulloch, M.T., 1985a, Genesis of granitoid batholiths of Peninsular Malaysia and implications for models of crustal evolution: evidence from Nd–Sr isotopic and U–Pb zircon study: Geochimica et Cosmochimica Acta, v. 49, p. 587-600.

Liew, T.C., and Page, R.W., 1985b, U–Pb zircon dating of granitoid plutons from the west coast province of Peninsular Malaysia: Journal of the Geological Society, London, v. 142, p. 515-526.

Loftus-Hills, G., and Solomon, M., 1967, Cobalt, nickel, and selenium in sulfides as indicators of ore genesis: Mineralium Deposita, v. 2, p. 228-242.

Longerich, H.P., Jackson, S.E., and Gunter, D., 1996, Laser ablation inductively coupled plasma mass spectrometric transient signal data acquisition and analyte concentration calculation: Journal of Analytical Atomic Spectrometry, v. 11 p. 899-904.

Lowenstern, J.B., 2001, Carbon dioxide in magmas and implications for hydrothermal systems: Mineralium

Deposita, v. 36, p. 490-502.

Lu¨ders, V., Pracejus, B., and Halbach, P., 2001, Fluid inclusion and sulfur isotope studies in probable modern analogue Kuroko-type ores from the JADE hydrothermal field (Central Okinawa Trough, Japan): Chemical Geology, v. 173, p. 45-58.

Lydon, J.W., 1984, Volcanogenic massive sulphide deposits, Part 1-A descriptive model: Geoscience Canada, v. 11, p. 195-202.

Lydon, J.W., 1988. Volcanogenic massive sulphide deposits, Part 2-Genetic models: Geoscience Canada, v. 15, p. 43-65.

Lydon, J.W., and Galley, A., 1986, Chemical and mineralogical zonation of the Mathioti alteration pipe, Cyprus, and genetic significance: London, Institution of Mining and Metalurgy.

Maas, R., Kamenetsky, M.B., Sobolev, A.V., Kamenetsky, V.S., and Sobolev, N.V., 2005, Sr, Nd, and Pb isotope evidence for a mantle origin of alkali chlorides and carbonates in the Udachnaya Kimberlite, Siberia: Geology, v. 33, p. 549-552.

MacDonald, S., 1970, Geology and mineral resources of the Lake Chini-Sungei Bera-Sungei Jeram area of south-central Pahang: Geological Survey Malaysia Map Bulletin 1.

MacLean, W.H., and Barrett T.J., 1993, Lithogeochemical techniques using immobile elements: Journal of Geochemical Exploration, v. 48, p. 109-133.

MacLean, W.H., and Kranidiotis, P., 1987, Immobile elements as monitors of mass transfer in hydrothermal alteration: Phelps Dodge massive sulfide deposit, Matagami, Quebec: Economic Geology, v. 82, p. 951–962.

Makoundi, C., 2012, Geology, geochemistry and metallogenesis of selected sediment-hosted gold deposits in the Central Gold Belt, Peninsular Malaysia: Unpub. MSc thesis: University of Tasmania, Australia, 212 p.

Manaka, T., 2014, A study of mineralogical, geochemical and geochronological characteristics and ore genesis in Phuoc Son gold deposit area, Central Vietnam: Unpub. PhD thesis: University of Tasmania, Australia, 206 p.

Marcoux, E., 1998, Lead isotope systematics of the giant massive sulfide deposits in the Iberian Pyrite Belt.: Mineralium Deposita, v. 33, p. 45-58.

Maslennikov, V.V., Maslennikova, S.P., Large, R.R., and Danyushevsky, L.V., 2009, Study of trace element zonation in vent chimneys from the Silurian Yaman-Kasy Volcanic-Hosted Massive Sulfide Deposit (Southern Urals, Russia) using Laser Ablation-Inductively Coupled Plasma Mass Spectrometry (LA-ICPMS: Economic Geology, v. 104, p. 1111-1141.

Maslennikov, V.V., Ayupova, N. R., Herrington, R.J., Danyushevsky, L.V., and Large, R.R., 2012, Ferruginous and manganiferous haloes around massive sulphide deposits of Urals: Ore Geology Reviews, v. 47, p. 5-41.

Maslennikov, V.V., Maslennikova, S.P., Large, R.R., Danyushevsky, L.V., Herrington, R.J., and Stanley C.J., 2013, Tellurium-bearing minerals in zoned sulfide chimneys from Cu-Zn massive sulfide deposits of the Urals, Russia: Mineralogy and Petrology, v. 107, p. 67-99.

Marchig, V., Puchelt, H., Rösch, H., and Blum, N., 1990, Massive sulfides from ultra-fast spreading ridge, East Pacific Rise at 18–21°S: a geochemical stock report: Mar Min, v. 9, p. 459-493.

Marcoux, E., Moelo, Y., and Leistel, J.M., 1996, Bismuth and cobalt minerals as indicators of stringer zones to massive sulphide deposits, Iberian pyrite belt: Mineralium Deposita, v. 31, p. 1-26.

McArthur, G.J., 1996, Textural evolution of the Hellyer massive sulphide deposit: Unpub. PhD. thesis: University of Tasmania, Australia, 272 p.

McClenaghan, S. H., Lentz, D.R., Martin, J., and Diegor W.G., 2009, Gold in the Brunswick No. 12 volcanogenic massive sulfide deposit, Bathurst Camp, Canada: Evidence from bulk ore analysis and laser ablation ICP-MS data on sulfide phases.: Mineralium Deposita, v. 44, p. 523-577.

McConachy, T.F., 1988, Hydrothermal plumes and related deposits over spreading ridges in the northeast Pacific Ocean: the East Pacific Rise near 11°N and 21°N, Explorer Ridge, and the J.Tuzo Wilson Seamounts., University of Toronto, 403 p.

McLeod, R.L., and Stanton, R.L., 1984, Phyllosilicates and associated minerals in some Paleozoic stratiform sulfide deposits of southeastern Australia: Economic Geology, v. 79, p. 1-21.

McNutt, R.H., Clark, A.H., and Zentili, M., 1979, Lead isotope compositions of Andean igneous rocks, latitude 26' to 29' S: petrologic and metallogenic implications: Economic Geology, v. 74, p. 827-837.

McPhie, J., and Allen, R. L., 1992, Facies architecture of mineralised submarine volcanic sequences: Cambrian Mount Read Volcanics, western Tasmania: Economic Geology, v. 87, p. 587-598.

McPhie, J., and Hunns, S.R., 1995, Secondary welding of submarine, pumice-lithic breccia at Mount Chalmers, Queensland, Australia: Bull. Volcanol. v. 57, p. 170– 178.

McPhie, J., and Allen, R.L., 2003. Submarine, silicic, syn-eruptive pyroclastic units in the Mount Read Volcanics, Western Tasmania: influences of vent setting and proximity on lithofacies characteristics, in White, J.D.L., Smellie, J.L., and Clague, D.A., ed., Explosive Subaqueous Volcanism: Geophysical Monograph Series, p. 245-258.

Meffre, S., Large, R.R., Scott, R., Woodhead, J., Chang, Z., Gilbert, S., Danyushevsky, L.V., Maslennikov, V., and Hergt, J.M., 2008, Age and pyrite Pb-isotopic composition of the giant Sukhoi Log sediment-hosted gold deposit, Russia: Geochimica et Cosmochimica Acta, v. 72, p. 2377–2391.

Meffre, S., Khin Zaw and team, 2011, Tectonic models and orogenesis. Report for the implementation meeting of Ore Deposits of SE Asia Project, 17th October, 2011, Hobart, Tasmania.

Mernagh, T.P., and Wygralak, A.S., 2007, Gold ore-forming fluids of the Tanami region, Northern Australia: Mineralium Deposita, v. 42, p. 145-173.

Metcalfe, I., 1980, Upper Carboniferous conodont faunas of the Panching limestone, Pahang, West Malaysia: Paleontology, v. 23, p. 297-314.

Metcalfe, I., 1988. Origin and assembly of Southeast Asian continental terrane, in Audley-Charles, M.G., and Hallam, A., ed., Gondwana and Tethys: Geological Society of London Special Publications 37, p. 101-118.

Metcalfe, I., 1996. Gondwanaland dispersion, Asian accretion and evolution of Eastern Tethys: Australian Journal of Earth Sciences, v. 43, p. 605-623.

Metcalfe, I., 2000, The Bentong–Raub Suture Zone: Journal of Asian Earth Sciences, v. 18, p. 691-712.

Metcalfe, I., 2006, Palaeozoic and Mesozoic tectonic evolution and palaeogeography of East Asian crustal fragments: The Korean Peninsula in context: Gondwana Research, v. 9, p. 24-46.

Metcalfe, I., 2009, Late Palaeozoic and Mesozoic tectonic and papaleogeographical evolution of SE Asia: Geological Society Malaysia of London Special Publication, v. 315, p. 7-23.

Metcalfe, I., 2011, Tectonic framework and Phanerozoic evolution of Sundaland: Gondwana Research, v. 19, p. 3-21.

Metcalfe, I., 2013, Tectonic evolution of the Malay Peninsula: Journal of Asian Earth Sciences, DOI: http://dx.doi.org/10.1016/j.jseaes.2012.12.020.

Metcalfe, I., Idris, M., Tan, J.T., 1980, Stratigraphy and palaentology of the Carboniferous sediments in Panching area, Pahang, West Malaysia: Geological Society of Malaysia Bulletin, v. 13, p. 1-26.

Metcalfe, I., Sivam, S.P., and Stauffer, P.H., 1982, Stratigraphy and sedimentology of Middle Triassic rocks exposed near Lanchang, Pahang, Peninsular Malaysia: Geological Society of Malaysia Bulletin, v. 15, p. 19–30.

Metcalfe, I., and Chakraborty, K.R., 1988, Diamictite along the eastern margin of the Central Basin of the Malay Peninsula: Geological Society of Malaysia Warta Geologi, v. 14, p. 191-198.

Metcalfe, I., and Chakraborty, K.R., 1996, A stratigraphic log of Semantan Formation along the Mentakab-Temerloh By-Pass, Pahang: Geological Society of Malaysia Bulletin v. 35, p. 37-46.

Miller, A.R., Densmore, C.D., Degens, E.T., Hatha, J.C., Manheim, F.T., McFarlin, P.F., Pocklington, R., and Jokela, A., 1966, Hot brines and recent iron deposits in deeps of the Red Sea: Geochimica et Cosmochimica Acta, v. 30, p. 341-359.

Minerals and Geoscience Department of Malaysia, 2004, Geological map of Peninsular Malaysia 8th Ed. (1:750000): Published by Directorate of Mineral and Geoscience Department of Malaysia, Kuala Lumpur.

Mitchell, A.H.G., 1989, The Shan Plateau and Western Burma: Mesozoic-Cenozoic plate boundaries and correlation with Tibet, in Sengor, A. M. C., ed., Tectonic Evolution of the Tethyan Region, Kluwer: Academic Publishers., p. 567– 583.

Moles, N.R., 1983, Sphalerite composition in relation to deposition and metamorphism of the Foss stratiform Ba-Zn-Pb deposit, Aberfeldy, Scotland: Mineral Mag, v. 47, p. 487-500.

Mohd Rozi Umor, and Syed Sheikh Almashoor., 2000, Jujukan usia batuan di dalam Kompleks Benta, Pahang berdasarkan cirian lapangan dan penentuan usia batuan secara K/Ar keseluruhan batuan: Prosiding Persidangan Tahunan Geologi Pulau Pinang, 2000, p. 111-120 (in Malay).

Mohd Rozi Umor, Ghani, A.A., Mohamad, H., Leman, M.S., Khin Zaw., and Hussin, A., 2011, Re-evaluation of geochemical classification of the Western Belt, Central Belt and Eastern Belt granitoids, Malaysia Peninsular and their tectonic implications, Proceedings GEOMYANMAR 2011.

Mohd Shafeea Leman., 2003, An early Permian (Early Sakmarian) brachiopod fauna from the Sungai Itau Quarry and its relationship to other Early Permian brachiopod horizons in Langkawi, Malaysia: Geological Society of Malaysia Bulletin, v. 46, p. 155-160.

Mohd Shafeea Leman., 2004, Part 2 Mesozoic, in Lee, C.P., Leman, M.S., Hassan, K., Nasib, B.M., and Karim, R., eds., Stratigraphic Lexicon of Malaysia: Geological Society of Malaysia, p. 37-64.

Moore, P.B., 1971, Mineralogy and chemistry of Langban-type deposits in Bergslagen, Sweden: Mining Rec., v. Winter 1971, p. 154-172.

Morley, C.K., 2012, Late Cretaceous-Early Palaeogene tectonic development of SE Asia: Earth-Science Reviews, v. 115, p. 37-75.

Mortensen, J.K., Hall, B.V., Bissic, T., Friedman, R.M., Danielson, T., Oliver, J., Rhys, D.A., Ross, K.V., and Gabites, J.E., 2008, Age and Paleotectonic Setting of Volcanogenic Massive Sulfide Deposits in the Guerrero Terrane of Central Mexico: Constraints from U-Pb Age and Pb Isotope Studies: Society of Economic Geologists, v. 103, p. 117-140.

Morton, R.L., and Franklin, J.M., 1987, Two-fold classification of Archean volcanic-associated massive sulfide deposits: Economic Geology, v. 82, p. 1057–1063.

Mottl, M.J., Holland, H.D., and Corr, R.F., 1979, Chemical exchange during hydrothermal alteration of basalt by seawater-II, Experimental results for Fe, Mn and sulfur species: Geochimica et Cosmochimica Acta, v. 43, p. 869-884.

Moura, A., 2005, Fluids from the Neves Corvo massive sulphide ores, Iberian Pyrite Belt, Portugal: Chemical Geology, v. 223, p. 153-169.

Moura, A., 2008a, Metamorphosed and metamorphogenic ores of the Neves Corvo volcanogenic massive silfide deposits, Iberian Pyrite Belt, Portugal: International Geology Review, v. 50, p. 89-96.

Moura, A., 2008b, Metallogenesis at the Neves Corvo VHMS deposit (Portugal): a contribution from the study of fluid inclusions: Ore Geology Reviews, v. 34, p. 354-368.

Moura, A., Noronha, F., Cathelineau, M., Boiron, M., and Ferreira, A., 1997, Evidence of metamorphic fluid migration within the Neves-Corvo ore deposits: the fluid inclusion data, in Barriga, F.J.A.S., ed., Society of Economic Geologists Neves Corvo Field Conference, May 11-14: Lisbon, Portugal. Abstract and Program, p. 92.

Mukasa, S.B., Vidal, C.E., and Injoque-Espinoza, J., 1990, Pb isotope bearing on the metallogenesis of sulfide ore deposits in central and southern Peru: Economic Geology, v. 85, p. 1438-1446.

Murakami, H., and Ishihara, S., 2013, Trace elements of Indium-bearing sphalerite from tin-polymetallic deposits in Bolivia, China and Japan: A femto-second LA-ICPMS study: Ore Geology Reviews.

Murphy, J.B., and Hynes, A.J., 1986. Contrasting secondary mobility of Ti, P, Zr, Nb and Y in two metabasaltic suites in the Appalachians: Canadian Journal of Earth Sciences, v. 23, p. 1138-1144.

Murthy, K.N., undated, Bukit Bottle barite locality. Geological Survey Malaysia Report (Unpublished).

Norman, M., Robinson, P., and Clark, D., 2003, Major- and trace-element analysis of sulfide ores by laser-ablation ICP-MS, solution ICP-MS, and XRF: New data on international reference materials: Canadian Mineralogist, v. 41, p. 293–305.

Norrish, K., and Chappell, B.W., 1977, X-ray fluorescence spectrometry, in Zussman, J., ed., Physical methods in determinative mineralogy: London, Academic Press, p. 201-272.

Ohana, T., Kimura, T., and Khoo, T.T., 1991, Further discovery of some Carboniferous plant fossils from Tanjung Mat Amin, Trengganu, Peninsular Malaysia: Journal of Southeast Asian Earth Sciences, v. 6, p. 93-101.

Ohmoto, H., 1972, Systematics of sulfur and carbon isotopes in hydrothermal ore deposits: Economic Geology, v. 67, p. 551-578.

Ohmoto, H., 1986, Stable isotope geochemistry of ore deposits: Reviews in Mineralogy v. 16, p. 491–559.

Ohmoto, H., 1996. Formation of volcanogenic massive sulfide deposits: the Kuroko perspective: Ore Geology Reviews, v. 10, p. 135-177.

Ohmoto, H., and Rye, O., 1979, Isotopes of sulfur and carbon, in Barnes, H. L., ed., Geochemistry of hydrothermal ore deposits, 2nd ed: New York, Wiley.

Ohmoto, H., and Skinner, B.J., 1983, The Kuroko and related volcanogenic massive sulfide deposits: Introduction and summary of new findings, in Ohmoto, H., and Skinner, B.J., ed., The Kuroko and related volcanogenic massive sulfide deposits: Economic Geology Monograph, v. 5, p. 1-8.

Ohmoto, H., and Goldhaber, M.B., 1997, Sulfur and carbon isotopes: New York, John Wiley and Sons.

Oliver, G., Khin Zaw., Hotson, M., Meffre, S., and Manaka, T., 2014, U–Pb zircon geochronology of Early Permian to Late Triassic rocks from Singapore and Johor: A plate tectonic reinterpretation: Gondwana Research. DOI: 1639 10.1016/j.gr.2013.03.019.

Oo, T., Hlaing, T., and Htay, N., 2002, Permian of Myanmar: Journal of Asian Earth Sciences, v. 20, p. 683-689.

Palenik, C.S., Utsunomiya, S., Reich, M., Kesler, S.E., Wang, L.M., and Ewing, R.C., 2004, "Invisible" gold revealed: direct imaging of gold nanoparticles in a Carlin-type deposit: American Mineralogist, v. 89, p. 1359-1366.

Panagos, A.G., and Varnavas, S.P., 1984, On the genesis of some manganese deposits from eastern Greece: Springer, Berlin, 553-561 p.

Paulick, H., Herrmann, W., Gemmel, J.B., 2001, Alteration of felsic volcanics hosting the Thalanga massive sulfide deposit (Northern Queensland, Australia) and geochemical proximity indicators to ore: Economic Geology, v. 96, p. 1175-1200.

Paytan, A., Mearon, S., Cobb, K., and Kastner, M., 2002 Origin of marine barite deposits: Sr and S isotope characterization: Geology, v. 30, p. 747-750.

Pearce, J.A., and Cann, J.R., 1973, Tectonic setting of basic volcanic rocks determined using trace element analysis: Earth and Planetary Science Letters, v. 19 p. 290-300.

Pearce, J.A., Harris, N.B.W., and Tindle, A.G., 1984 Trace element discrimination diagrams for the tectonic interpretation of granitic rocks: Journal of Petrology, v. 25 p. 956-983.

Pearce, J.A., and Peate, D.W., 1995, Tectonic implications of the composition of volcanic arc magmas: Annual Review of Earth and Planetary Sciences, v. 23, p. 251-285.

Peter, J.M., Goodfellow, W.D., and Doherty, W., 2003, Hydrothermal sedimentary rocks of the Heath Steele belt, Bathurst mining camp, New Brunswick—Part 2. Bulk and rare earth element geochemistry and implications for origin, in Goodfellow, W.D., McCutcheon, S.R., and Peter, J.M., eds., Massive sulfide deposits of the Bathurst mining camp, New Brunswick, and northern Maine: Economic Geology Monograph, v. 11, p. 391-415.

Peter, J.M., and Scott, S.D., 1999, Windy Craggy, northwestern British Colombia: The world's largest Besshi-type deposit: Reviews in Economic Geology, v. 8, p. 261-295.

Peter, J.M., and Goodfellow, W.D., 1996, Mineralogy, bulk and rare earth element geochemistry of massive sulphide-associated hydrothermal sediments of the Brunswick horizon, Bathurst mining camp, New Brunswick: Canadian Journal of Earth Science, v. 33, p. 252-283.

Peter, J.M., and Shanks, W.C.III., 1992, Sulfur, carbon, and oxygen isotope variations in submarine

hydrothermal deposits of Guaymas Basin, Gulf of California, USA: Geochimica et Cosmochimica Acta, v. 56, p. 2025-2040.

Peter, J.M., and Scott, S.D., 1988, Mineralogy, composition and fluid inclusion microthermometry of seafloor hydrothermal deposits in the southern trough of Guaymas Basin, Gulf of California: Canadian Mineralogist, v. 26, p. 567-587.

Peter, J.M., and Scott, S.D., 1993, Fluid inclusion and light stable isotope geochemistry of the Windy Craggy Besshi-type massive sulfide deposit, northwestern British Columbia: Resource Geology Special Issue, v. 17, p. 229-248.

Piercey, S.J., 2009, Lithogeochemistry of volcanic rocks associated with volcanogenic massive sulphide deposits and applications to exploration, in Cousens, B., and Piercey, S.J., ed., Submarine volcanism and mineralization—Modern through ancient: Geological Association of Canada, Short Course Notes, v. 19, p. 15–40.

Piercey, S.J., 2010, An overview of petrochemistry in the regional exploration for volcanogenic massive sulphide (VMS) deposits: Geochem Explor Environ Anal, v. 10, p. 119-136.

Piercey, S.J., 2011, The setting, style, and role of magmatism in the formation of volcanogenic massive sulfide deposits: Mineralium Deposita, v. 46, p. 449-471.

Pisutha-Arnold, V., and Ohmoto, H., 1983, Thermal history and chemical and isotopic compositions of the ore-forming fluids reponsible for the Kuroko massive sulfide deposits in the Hokuroko district of Japan, in Skinner, B.J., ed., Economic Geology Monograph, v. 5.

Pontual, S., Merry, N., and Gamson, P., 1997, G-Mex Vol. 7, Volcanic-hosted massive sulfide systems: Kew, Victoria 3101, Australia, Ausspec International Pty. Ltd.

Raj, J.K., Abdul Hadi Abd. Rahman, and Mustaffa Kamal Shuib, 1998, Tertiary basins of inland Peninsular Malaysia: review and tectonic evolution: Geological Society Malaysia Bulletin, v. 42, p. 197-210.

Raj, J.K., Tan, D. N. K., and Wan Hasiah Abdullah, 2009, Cenozoic Stratigraphy, in Hutchison, C.S., and Tan, D. N.K., eds., Geology of Peninsular Malaysia: University Malaya and Geological Society of Malaysia Publication, Kuala Lumpur, p. 133-173.

Rajah, S.S., 1968, Geology of the Gunung Blumut area: Geological Survey of Malaysia Annual Report 1968, p. 79-83.

Rajah, S.S., Chand, F., and Singh, S.D., 1977, The granitoids and the tin mineralization of the Eastern Belt of Peninsular Malaysia.: Geological Society Malaysia Bulletin, v. 9, p. 209-232.

Ramboz, C., Oudin, E., and Thisse, Y., 1988, Geyser-type discharge in Atlantis II Deep, Red Sea: evidence of boiling from fluid inclusions in epigenetic anhydrite: Canadian Mineralogist, v. 26, p. 765-786.

Raymond, O. L., 1996, Pyrite composition and ore genesis in the Prince Lyell copper deposit, Mt. Lyell mineral field, western Tasmania, Australia: Ore Geology Reviews, v. 10, p. 231-250.

Reed, M. H., 1997, Hydrothermal alteration and its relationship to ore fluid composition in Barnes, H. L., ed., Geochemistry of Hydrothermal Ore Deposits: New York, John Wiley and Sons, p. 303 - 365.

Rees, C.E., Jenkins, W.J., and Monster, J., 1978, The sulphur isotope geochemistry of ocean water sulphate: Geochimica et Cosmochimica Acta, v. 42, p. 377-382.

Reich, M., Kesler, S.E., Utsunomiya, S., Palenik, C. S., Chryssoulis, S. L., and Ewing R. C., 2005, Solubility of gold in arsenian pyrite: Geochimica et Cosmochimica Acta, v. 69, p. 2781–2796.

Reich, M., Utsunomiya, S., Kesler, S.E., Wang, L. M., Ewing, R. C., and Becker, U., 2006, Thermal behavior of metal nanoparticles in geologic materials: Geology, v. 34, p. 1033–1036.

Relvas, J.M.R.S., Tassinari, C.C.G, Munha, J., and Barriga, F.J.A.S., 2001, Multiple sources for the ore-forming fluids in the Neves Corvo VHMS deposit of the Iberian Pyrite Belt (Portugal): strontium, neodymium and lead isotope evidence: Mineralium Deposita, v. 36, p. 416-427.

Relvas, J.M.R.S., Barriga, F.J.A.S., Ferreira, A., Noiva, P.C., and Carvalho, P., 1997, Footwall alteration and stringer ores, Corvo orebody, Neves, Corvo, Portugal, in Barriga, F.J.A.S., ed., SEG Neves Corvo Field Conference, p. 93.

Ridd, M.F., 2013. A Middle Permian-Middle Triassic accretionary complex and a Late Triassic foredeep basin: forerunners of an Indosinian (Late Triassic) thrust complex in the Thailand-Malaysia border area: Journal of Asian Earth Sciences.

Ridler, R.H., 1971, Analysis of Archean volcanic basins in the Canadian Shield using the exhalite concept [abs.]: Bulletin of the Canadian Institute of Mining and Metallurgy, v. 64, p. 20.

Ripley, E.M., and Ohmoto, H., 1977, Mineralogic, sulfur isotope and fluid inclusion studies of the stratabound copper deposits of the Raul mine, Peru: Economic Geology, v. 72, p. 1017-1041.

Riverin, G., and Hodgson, C.J., 1980, Wall-rock alteration at the Millenbach Cu-Zn mine, Noranda, Quebec: Economic Geology, v. 75, p. 424-444.

Robinson B.W., and Kusakabe, M., 1975, Quantitative preparation of sulfur dioxide, for 34S/32S analyses, from sulfides by combustion with cuprous oxide: Analytical Chemistry, v. 47, p. 1179-1181.

Roedder, E., 1984, Fluid Inclusions, Reviews in Mineralogy: Blacksburg, VA, Virginia Polytechnic Institute and State University press, 646 p.

Rona, P. A., 1988, Hydrothermal mineralization at oceanic ridges: Canadian Mineralogist, v. 26, p. 431-465.

Rosa, C.J.P., McPhie, J., and Relvas, J.M.R.S., 2010, Type of volcanoes hosting the massive sulfide deposits of the Iberian Pyrite Belt: Journal of Volcanology and Geothermal Research, v. 194, p. 107-126.

Rouxel, O., Fouquet, Y., and Ludden, J.N., 2004, Subsurface processes at the Lucky Strike hydrothermal field, Mid-Atlantic Ridge—Evidence from sulfur, selenium, and iron isotopes: Geochimica et Cosmochimica Acta, v. 68, p. 2295–2311.

Ryall, P.J.C., 1982, Some thoughts on the crustal structure of Peninsular Malaysia-resultsof a gravity traverse: Geological Society of Malaysia Bulletin, v. 15, p. 9-18.

Sakai, H., Gamo, T., Kim, E.-S., Tsutsumi, M., Tanaka, T., Ishibashi, J., Wakita, H., Yamano, M., and Oomori, T., 1990, Venting of carbon dioxide-rich fluid and hydrate formation in mid-Okinawa Trough backarc basin: Science, v. 248, p. 1093-1096.

Salam, A., 2013, Geology and genesis of the Chatree Au-Ag deposits, Phetchabun Province, central Thailand: Unpub. PhD thesis: CODES University of Tasmania, Australia, 250 p.

Sanchez Espana, F.J., Velasco, F., and Yusta, I., 2000, Hydrothermal alteration of felsic volcanic rocks associated with massive sulphide deposition in the Northern Iberian Pyrite Belt (SW Spain): Applied Geochemistry, v. 15, p. 1265-1290.

Sanchez Espana, F.J., Velasco, F., Boyce, A.J., and Fallick, A.E., 2003, Source and evolution of ore-forming hydrothermal fluids in the northern Iberian Pyrite Belt massive sulphide deposits (SW Spain): evidence from fluid inclusions and stable isotopes: Mineralium Deposita, v. 38, p. 519-537.

Sangameshwar, S. R. R., 1972, Trace element and sulphur isotope geochemistry of sulphide deposits from the Flin Flon and Snow Lake areas of Saskatchewan and Manitoba, Unpub. PhD thesis: University of Saskatchewan, Canada.

Sangster, D.F., 1968, Relative sulphur isotope abundances of ancient seas and strata-bound sulfide deposits: Proceedings of the Geological Association of Canada, v. 19, p. 79-91.

Sangster, D.F., 1976, Sulfur and lead isotopes in strata-bound deposits, in Wolf, K. H., ed., Hand book of strata-bound and stratiform ore deposits: Amsterdam Elsevier.

Sangster, D.F., 1990, Mississippi Valley-type and sedex lead-zinc deposits: a comparative examination: Trans Inst Mining Metall (Sect B: Appl Earth Sci) v. 99, p. B21-B42.

Sangster, D.F., 2002, The role of dense brines in the formation of vent-distal sedimentary-exhalative (SEDEX) lead-zinc deposits: field and laboratory evidence: Mineralium Deposita, v. 37, p. 149-157.

Sangster, D.F., Outridge, P.M., Davis, W.J., 2000. Stable lead isotope characteristics of lead ore deposits of environmental significance: Environmental Reviews, v. 8, p. 115-147.

Sasaki, A., and Kajiwara, Y., 1971, Evidence of isotopic exchange between seawater sulfate and some syngenetic sulfide ores: Society of Mining Geologists Japan, v. 3, p. 289-294.

Sawkins, F.J., 1976, Massive sulphide deposits in relation to geo-tectonics: Geol. Assoc. Canada Special Paper, v. 14, p. 221-240.

Schardt, C., Cooke, D. R., Gemmell, J. B. and Large, R. R., 2001, Geochemical modeling of the zoned footwall alteration pipe, Hellyer volcanic-hosted massive sulfide deposit, Western Tasmania, Australia: Economic Geology, v. 96, p. 1037-1054.

Schmincke, H. U., 2004, Volcanism: Berlin, Springer, 324 p.

Schwartz, M.O., Rajah, S.S. Askury, A.K., Putthapiban, P., and Djaswadi, S., 1995, The Southeast Asian tin belt: Earth Science Reviews, v. 38, p. 95-293.

Scotney, P.M., Roberts, S., Herrington, R.J., Boyce, A.J., and Burgess, R., 2005, The development of volcanic hosted massive sulphide and barite-gold orebodies on Wetar Island, Indonesia: Mineralium Deposita, v. 40, p. 76-99.

Scott, S.D., and Barnes, H. L., 1971, Sphalerite geothermometry and geobarometry: Economic Geology, v. 66, p. 653-669.

Scrivenor, J.B., 1928, The geology of the Malayan ore deposits: London, MacMillan Press, 216 p.

Searle, M.P., Whitehouse, M.J., Robb, L.J., Ghani, A., Hutchison, C.S., Sone, M., Ng, W. P., Roselee, M.H., Chung, S. L., and Oliver, G. J. H., 2012, Tectonic evolution of the Sibumasu-Indochina terrane collision zone in Thailand and Malaysia constraints from new U -Pb zircon chronology of SE Asian tin granitoids: Journal of the Geological Society of London, v. 169, p. 489-500.

Seccombe, P.K., 1977, Sulphur isotope and trace element composition of stratiform sulphides as an ore guide in the Canadian Shield: Journal of Geochemical Exploration, v. 8, p. 117-137.

Sengor, A.M.C., 1984, The Cimmeride orogenic system and tectonics of Eurasia: Geological Society of America

Special Paper, v. 195, p. 1-82.

Sevastjanova, I., Clements, B., Hall, R., Belousova, E.A., Griffin, W.L., and Pearson, N., 2011, Granitic magmatism, basement ages, and provenance indicators in the Malay Peninsula: insights from detrital zircon U-Pb and Hf-isotope data: Gondwana Research, v. 19, p. 1024-1039.

Shanks, W.C.III., 2001, Stable isotopes in seafloor hydrothermal systems—Vent fluids, hydrothermal deposits, hydrothermal alteration, and microbial processes, in Valley, J. W., and Cole, D.R., eds., Stable isotope geochemistry 43: Reviews in Mineralogy and Geochemistry, p. 469–525.

Shanks, W.C.III., Böhlke, J.K., and Seal, R.R. II., 1995, Stable isotopes in midocean ridge hydrothermal systems: interactions between fluids, minerals, and organisms. In: Humphris, S.E., Zierenberg, R.A.,Mullineaux, L.S., Thomson, R.E., (eds) Seafloor Hydrothermal Systems: Physical, Chemical, Biological and Geological Interactions: Geophysical Monograph, v. 91, p. 194-221.

Shanks, W.C.III., and Seyfried, W.E.Jr., 1987, Stable isotope studies of vent fluids and chimney minerals, southern Juan de Fuca Ridge: sodium metasomatism and sea-water sulfate reduction: Geophysical. Research, v. 92, p. 11387-11399.

Shanks, W.C.III., Bischoff, J.L., and Rosenbaun, R.J., 1981, Seawater sulfate reduction and sulfur isotope fractionation in basaltic systems: interaction of seawater with fayalite and magnetite at 200-350'C: Geochimica et Cosmochimica Acta, v. 45, p. 1977-1996.

Shepherds, T.J., Rankin, A.N., and Alderton, D.H.M., 1985, A Practical Guide to Fluid Inclusion Studies. : London, Blackie & Son Press, 238 p.

Sherlock, R.L., Roth, T., Spooner, E.T.C., and Bray, C.J., 1999, Origin of the Eskay Creek precious metal-rich volcanogenic massive sulfide deposit: Fluid inclusion and stable isotope evidence: Economic Geology, v. 94, p. 803-824.

Shi, G.R., and Waterhouse, J.B., 1991, Early Permian braciopods from Perak, west Malaysia: Journal of Southeast Asian Earth Sciences, v. 6, p. 25-39.

Shimazaki, Y., 1974. Ore minerals of the Kuroko-type deposits: Society of Mining Geologists of Japan Special Issue, v. 6, p. 311-322.

Sillitoe, R.H., 1975, Lead-silver, manganese and native sulfur mineralization within a stratovolcano, El Queva, northwest Argentina: Economic Geology, v. 70, p. 1190-1201.

Silitoe, R.H., 1982, Extensional habitats of rhyolite-hosted massive sulfide deposits: Geology, v. 10, p. 403-407.

Sillitoe, R.H., and Hart, S.R., 1984, Lead isotope signature of porphyry copper deposits in oceanic and continental settings, Colombian Andes: Geochimica et Cosmochimica Acta, v. 48, p. 2135-2142.

Sillitoe, R.H., Hannigton, M.D., and Thompson, J.F.H., 1996, High sulfidation deposits in the volcanogenic massive sulfide environment: Economic Geology, v. 91, p. 204-212.

Simon, G., Kesler, S.E., and Chryssoulis, S., 1999a, Geochemistry and textures of gold-bearing arsenian pyrite, Twin Creeks, Nevada: implications for deposition of gold in Carlin-type deposits: Economic Geology, v. 94, p. 405-422.

Skirrow, R.G., and Franklin, J.M., 1994, Silicification and metal leaching in subconcordant alteration zones beneath the Chisel Lake massive sulphide deposit, Snow Lake, Manitoba: Economic Geology, v. 89, p. 31-50.

Skirrow, R., and Coleman, M.L., 1982, Origin of sulfur and geothermometry of hydrothermal sulfides from the Galapagos Rift, 86°N: Nature, v. 299, p. 142-144.

Solomon, M., 1976, 'Volcanic' massive sulphide deposits and their host rocks-a review and explanation, in Wolf, K.H., ed., Handbook of Strata-Bound and Stratiform Ore Deposits: Elsevier, Amsterdam, v. 6, p. 21-54.

Solomon, M., 1981, An introduction to the geology and metallic mineral resources of Tasmania: Economic Geology, v. 76, p. 194– 208.

Solomon, M., and Groves, D.I., 1994, The geology and origin of Australia's mineral deposits: Oxford Clarendon Press, p. 951.

Solomon, M., Eastoe, C.J., Walshe, J.L., and Green, G.R., 1988, Mineral deposits and sulfur isotope abundances in the Mount Read volcanics between Que River and Mount Darwin, Tasmania: Economic Geology, v. 83, p. 1307-1328.

Solomon, M., Gemmell, J.B., and Khin Zaw., 2004a, Nature and origin of the fluids responsible for forming the Hellyer Zn-Pb-Cu volcanichosted massive sulphide deposit, Tasmania, using fluid inclusions, and stable and radiogenic isotopes: Ore Geology Reviews, v. 25, p. 89-124.

Solomon, M., Tornos, F., Large, R.R., Badham, J.N.P., Both, R.A., and Khin Zaw., 2004b, Zn-Pb-Cu volcanic-hosted massive sulphide deposits: Criteria for distinguishing brine pool-type from black smoker-type sulphide deposition: Ore Geology Reviews v. 25, p. 259-283.

Sone, M., and Metcalfe, I., 2008, Parallel Tethyan sutures in mainland Southeast Asia: New insights for Palaeo-Tethys closure and implications for the Indosinian orogeny: Comptes Rendus Geosciences, v. 340, p. 166-179.

Sone, M., Metcalfe, I., and Chaodumrong, P., 2012, The Chanthaburi terrane of southeastern Thailand: Stratigraphic confirmation as a disrupted segment of the Sukhothai Arc: Journal of Asian Earth Sciences, v. 61, p. 16-32.

Spiller, F.C.P., 1996, Late Paleozoic radiolarians from the Bentong-Raub suture zone, Peninsular Malaysia: Island Arc, v. 5, p. 91-103.

Spiller, F.C.P., and Metcalfe, I., 1995, Late Palaeozoic radiolarians from the Bentong–Raub suture zone and Semanggol Formation, Peninsular Malaysia-initial findings: Journal of Southeast Asian Earth Sciences, v. 11, p. 217-224.

Spry, P.G., Peter, J.M., and Slack, J.F., 2000, Metaexhalites as exploration guides to ore: Reviews in Economic Geology v. 11, p. 163–201.

Stacey, J.S., and Kramers, J.D., 1975, Approximation of terrestrial lead isotope evolution by two-stage model: Earth and Planetary Science Letters, v. 26, p. 207-221.

Stanton, R.L., 1990, Magmatic evolution and the ore type-lava type affiliations of volcanic exhalative ores: Australas. Inst. Min. Metall. Monogr., v. 14, p. 101-107.

Steele-MacInnis, M., Han, L., Lowell, R.P., Rimstidt, J.D., and Bodnar, R.J., 2012a, Quartz precipitation and fluid inclusion characteristics in sub-seafloor hydrothermal systems associated with volcanogenic massive sulfide deposits: Central European Journal of Geosciences, v. 4, p. 275-286.

Steele-MacInnis, M., Lecumberri-Sanchez, P., and Bodnar, R.J., 2012b, HOKIEFLINCS_H2O-NACL: A

Microsoft Excel spreadsheet for interpreting microthermometric data from fluidinclusions based on the PVTX properties of H2O–NaCl: Computers &Geosciences.

Stauffer, P.H., and Lee, C.P., 1986, Late Palaeozoic glacial marine facies in Southeast Asia and its implications: Geological Society Malaysia Bulletin, v. 20, p. 363-397.

Stuart, F.M., Harrop, P.J., Knott, R., Fallick, A.E., Turner, G., Fouquet, Y., and Rickard, D., 1995, Noble gas isotopes in 25,000 years of hydrothermal fluids from 13°N on the East Pacific Rise, in Parson, L.M., Walker, C.L., and Dixon, D.R., ed., Hydrothermal vents and processes: Geological Society Special Publication, v. 87, p. 133-143.

Stuart, F.M., Duckworth, R., Turner, G., and Schofield, P.F., 1994, Helium and sulfur isotopes of sulfide minerals from Middle Valley, northern Juan de Fuca Ridge, in Mottl, M.J., Davis, E.E., and Fisher, A.T., eds., Proc ODP 139, Scientific Results: College Station, TX., p. 387-392.

Stuart, F. M., Ellam, R. M., and Duckworth, R. C., 1999, Metal sources in the Middle Valley massive sulphide deposit, northern Juan de Fuca Ridge: Pb isotope constraints: Chemical Geology, v. 153, p. 213-225.

Styrt, M.M., Brackmann, A.J., Holland, H.D., Clark, B.C., Pisutha-Arnond ,V., Eldridge, C.S., and Ohmoto, H., 1981, The mineralogy and the isotopic composition of sulfur in hydrothermal sulfide/sulfate deposits on the East Pacific Rise, 21°N latitude: Earth and Planetary Science Letter, v. 53, p. 382-390.

Su, W.C., Xia, B., Zhang, H.T., Zhang, X.C., and Hu, R.Z., 2008, Visible gold in arsenian pyrite at the Shuiyindong Carlin-type gold deposit, Guizhou, China: implications for the environment and processes of ore formation: Ore Geology Reviews, v. 33, p. 667-679.

Sundblad, K., 1994, A genetic reinterpretation of the Falun and Ammeberg ore types, Bergslagen, Sweden: Mineralium Deposita, v. 29, p. 170-179.

Sunblad, K., Zachrisson, E., Smeds, S.A., Berglund, S. and Ålinder, C., 1984, Sphalerite geobarometry and arsenopyrite geothermometry applied to metamorphosed sulfide ores in the Swedish Caledonides: Economic Geology, v. 79, p. 1660-1668.

Sun, S.S., and Mcdonough, W.F., 1989, Chemical and isotopic systematics of oceanic basalts: implications for mantle composition and processes, in Saunders, A.D., and Norry, M.J., eds., Magmatism in the Ocean Basins: Geological Society, London, Special Publications, v. 42, p. 313-345.

Sun, S.S., 1980, Lead isotope study of young volcanic rocks gfrom mid-ocean ridges, ocean islands and island arcs: Philosophical Transactions of the Royal Society of London, v. A297, p. 409-445.

Sung, Y.H., Brugger, J., Ciobanu, C.L., Pring, A., Skinner W., and Nugus, M., 2009, Invisible gold in arsenian pyrite and arsenopyrite from a multistage Archaean gold deposit: Sunrise Dam, Eastern Goldfields Province, Western Australia: Mineralium Deposita, v. 44, p. 765–791.

Surjono, S.S., 2007, Stratigraphy and sedimentology of the East Johor Palaeozoic basin, Peninsular Malaysia, Unpub. PhD thesis: Universiti Kebangsaan Malaysia, Malaysia, 335 p.

Tan, B.K., 1984, Tectonic framework and evolution of the central belt and its margins, Peninsular Malaysia: Geological Society Malaysia Bulletin, v. 17, p. 307-322.

Tan, B.K., and Khoo, T.T., 1981, Ultramalic rocks in peninsular Malaysia and their tectonic implications: Proceedings 4th Regional Conf. on Geology of Southeast Asia, Manila, Philippines, 1981, p. 259-264.

Tapponnier, P., Peltzer, G., and Armijo, R., 1986, On the mechanism of collison between India and Asia, in

Coward, M. P., and Ries, A.C., ed., Collision tectonics: Geological Society of London Special Publication, v. 19, p. 115-157.

Taube, A., 1986, The Mount Morgan gold-copper mine and environment, Queensland: a volcanogenic massive sulfide deposit associated with penecontemporaneous faulting: Economic Geology, v. 81, p. 1322-1340.

Taylor, D., 1971, An outline of the geology of the Bukit Ibam orebody, Rompin, Pahang: Geological Society Malaysia Bulletin, v. 4, p. 71-89.

Taylor, D., and Toh, S.C., 1981, Regional mineral exploration, Pahang Tenggara: a case history of base-metal project in the Malay Peninsula: Asia Mining, Proceedings of the 1981 meeting, 1981, p. 67-78.

Taylor, S.R., 1964, Abundance of chemical elements in the continental crust: A new table: Geochimica et Cosmochimica Acta, v. 28, p. 1273-1284.

Teh, G.H., Shahrul Amin Ahmad, Mohd Suhaimi and Abd Khalik Hj Wood, 1991, Gold and REE distribution patterns in Tasik Cini volcanogenic massive sulphide deposits: Geological Society of Malaysia Warta Geologi, v. 17 (3), p. 159.

Teh, G.H., Mohammad Hafizi Osman, Shahrul Amin Ahmad and Jasmi Hafiz Abd Aziz, 2004, Invisible gold in massive sulphides at Tasik Chini, Pahang: Geological Society of Malaysia Warta Geologi, v. 30 (2), p. 33-36.

Teh, G.H., Mohammad Hafizi Osman, Shahrul Amin Ahmad and Jasmi Hafiz Abd Aziz, 2006, Interesting tin mineralization associated with the massive sulphide deposit at Tasik Chini, Pahang, Persidangan Bersama Geosains UKM-ITB 2006, p. 151-153.

Teh, G.H., Khin Zaw, Goh Swee Heng, Mohammad Hafizi Osman, Shahrul Amin Ahmad and Jasmi Hafiz Abd. Aziz, 2008, Tasik Chini volcanic-hosted massive sulphide deposit, Pahang, Malaysia-Geology, geochemistry and implications of ore genesis, Proceedings of the International Symposia on Geoscience Resources and Environments of Asian Terranes (GREAT 2008), 4th IGCP 516, and 5th APSEG.

Thompson, A.J.B., Hauff, P.L., and Robitaille, A.J., 1999, Alteration mapping in exploration: Application of short-wave infrared (SWIR) spectroscopy: Society of Economic Geologists Newsletter 39, v. 1, p. 16–27.

Thompson, J.F.H., Sillitoe, R.H., Baker, T., Lang, J.R., and Mortensen, J.K., 1999, Intrusion related gold deposits associated with tungsten-tin provinces: Mineralium Deposita, v. 34, p. 323-334.

Tilton, G.R., Pollak, R.J., Clark, A.H., and Robertson, R.C.R., 1981, Isotopic composition of Pb in Central Andean ore deposits: Geological Society of America Memoir 154, p. 791-816.

Tjia H.D., 1972, Strike slip faults in West Malaysia: 24th Int. Geol. Cong. Montreal, Canada. Sect. 3, p. 255-262.

Tjia H.D., 1989, The Bentong Suture, Proceedings of The 6th Regional Conference on Geology, Mineral and Hydrological Resources SE Asia, 1989, p. 73-85.

Tjia, H.D., 1996, Tectonics of deformed and undeformed Jurassic-Cretaceous strata of Peninsular Malaysia: Geological Society Malaysia Bulletin, v. 39, p. 131-156.

Tornos, F., 2006, Environment of formation and styles of volcanogenic massive sulfides: The Iberian Pyrite Belt: Ore Geology Reviews, v. 28, p. 259-307.

Tosdal, R.M., and Munizaga, F., 2003, Lead sources in Mesozoic and Cenozoic Andean ore deposits, north-

central Chile (30-34' S): Mineralium Deposita, v. 38, p. 234-250.

Townsend, A.T., Yu, Z., McGoldrick, P., and Hutton, J. A., 1998, Precise lead isotope ratios in Australian galena samples by high resolution inductively coupled plasma mass spectrometry: Journal of Analytical Atomic Spectrometry, v. 13, p. 809-813.

Turekian, I.K., and Wedepohl, K.H., 1961, Distribution of the elements in some major units of the earth‘s crust.: Geological Society of America Bulletin v. 72, p. 175-192.

Turner, F.J., and Campbell, I.H., 1987, Temperature, density and buoyancy fluxes in "black smoker" plumes, and the criterion for buoyancy reversal: Earth and Planetary Science Letters, v. 86, p. 85-92.

Ulrich, T., Golding, S.D., Kamber, B.S., Khin Zaw, and Taube, A., 2002, Different mineralization styles in a volcanic-hosted ore deposit: The fluid and isotopic signatures of the Mt. Morgan Au-Cu deposit, Australia: Ore Geology Reviews, v. 22, p. 61-90.

Ulrich, T., Long, D.G., Kamber, B.S., and Whitehouse, M.J., 2011, In situ trace element and sulfur isotope analysis of pyrite in a Paleoproterozoic Gold Placer Deposit, Pardo and Clement Townships, Ontario, Canada: Economic Geology, v. 106, p. 667-686.

UNESCO, 2012, “The Man and the Biosphere (MAB) Programme”. http://www.unesco.org/new/en/natural-sciences/environment/ecologicalsciences/man-and- biosphere-programme/

Urabe, T., 1974, Iron content of sphalerite coexisting with pyrite from some Kuroko deposits: Soc. Mining Geologists Japan Spec, p. 377-384

Urabe, T., Scott, S.D., and Hattori, K., 1983, A comparison of footwall-rock alteration and geothermal systems beneath some Japanese and Canadian volcanogenic massive sulfide deposits: Economic Geology Monograph, v. 5, p. 345–364.

Urabe, T., Baker, E.T., Ishibash, J., Feely, R.A., and Marumo, K., 1995, The effect of magmatic activity on hydrothermal venting along the superfast-spreading East Pacific Rise: Science, v. 269, p. 1092-1095.

Usuki, T., Lan, C-Y., Wang, K-L., and Chiu, H-Y., 2013, Linking the Indochina block and Gondwana during Early Paleozoic: evidence from U-Pb ages and Hf isotopes of detrital zircons: Tectonophysics, v. 586, p. 145-159.

Vanko, D.A., Bach, W., Roberts, S., Yeats, C.J., and Scott, S.D., 2004, Fluid inclusion evidence for subsurface phase separation and variable fluid mixing regimes beneath the deep-sea PACMANUS hydrothermal field, Manus basin back arc rift, Papua New Guinea: Journal of Geophysical Research, v. 109, p. B03201.

Vaughan, J. P., and Kyin, A., 2004, Refractory gold ores in Archaean greenstones, Western Australia: mineralogy, gold paragenesis, metallurgical characterization and classification: Mineral.Mag., v. 68, p. 255-277.

Velasco, F., Sanchez-Espana, J., Boyce, A.J., Fallick, A.E., Saez, R., and Almodovar, G.R., 1998, A new sulphur isotpic study of some Iberian pyrite belt deposits: evidence of a textural control on sulphur isotope composition: Mineralium Deposita, v. 34, p. 4-18.

Vidal, P., and Clauer, N., 1981, Pb and Sr isotopic systematics of some basalts and sulfides from the East Pacific Rise at 21°8N-project RITA: Earth Planetary Science Letter, v. 55, p. 237–246.

Von Damm, K. L., Lilley, M.D., Shanks, W.C., III, Brockington, M., Bray, A.M., O’Grady, K.M., Olson, E., Graham, A., Proskurowski, G., and the SouEPR Science Party., 2003 Extraordinary phase separation

and segregation in vent fluids from the southern East Pacific Rise: Earth and Planetary Science Letters, v. 206, p. 365–378.

Wagner, T., Klemd, R., Wenzel, T., and Mattsson, B., 2007, Gold upgrading in metamorphosed massive sulfide ore deposits: Direct evidence from laser ablation inductively coupled plasma–mass spectrometry analysis of invisible gold: Geology, v. 35, p. 775-778.

Wakita, K., and Metcalfe I., 2005, Ocean Plate Stratigraphy in East and Southeast Asia: Journal of Asian Earth Sciences, v. 24, p. 679-702.

Walshe, J.L., and Solomon, M., 1981, An investigation into the environment of formation of the volcanic-hosted Mount Lyell copper deposits using geology, mineralogy, stable isotopes, and a six-component chlorite solid solution model.: Economic Geology, v. 76, p. 246-284.

Watson, J.S., 1996, Fast, simple method of powder pellet preparation for X-Ray fluorescence analysis: X-Ray Spectrometry, v. 25, p. 173-174.

Wan Fuad Wan Hassan and Purwanto, H. S., 2002, Type deposits of primary gold mineralisation in the Central Belt of Pennsular Malaysia: Geological Society of Malaysia Bulletin, v. 45, p. 111-115.

Wan Fuad Wan Hassan and Purwanto, H. S., 2004, Radiometric age of Kampung Awah andesite: Geological Society Malaysia Bulletin, v. 48, p. 51-54.

Willbourn, E. S., 1917, The Pahang volcanic series: Geological Magazine, v. 54, p. 447-462.

Wilkinson, J. J., 2001, Fluid inclusions in hydrothermal ore deposits: Lithos, v. 55, p. 229-272.

Winchester, J.A., and Floyd, P.A., 1977, Geochemical discrimination of different magma series and their differentiation products using immobile elements: Chemical Geology, v. 20 p. 325-343.

Wonder, J.D., Spry, P.G., and Windom, K.E. , 1988 Geochemistry and origin of manganese-rich rocks related to iron-formation and sulfide deposits, western Georgia: Economic Geology, v. 83 p. 1070-1081.

Woodruff, L.G., and Shanks, W.C.III., 1988, Sulfur-isotope study of chimney minerals and hydrothermal fluids from 21' n East Pacific Rise: Hydrothermal sulfur sources and sisequilibrium sulfate reduction: Geophysical Research, v. 93, p. 4562-4572.

Wopenka, B., and Pasteris, J. D., 1987, Raman intensities and detection limits of geochemically relevant gas mixtures for a laser Raman microprobe: Analytical Chemistry, v. 59, p. 2165-2170.

Xuexin, S., 1984, Minor elements and ore genesis of the Fankou lead-zinc deposit, China: Mineralium Deposita, v. 19, p. 95-104.

Yamaguchi, K. E., and Ohmoto, H., 2006, Evidence from sulfur isotope and trace elements in pyrite for their multiple postdepositional processes in uranium ores at the Stanleigh mine, Elliot Lake, Ontario, Canada: Geological Society of America Memoir, v. 198, p. 143-156.

Yamamoto, M., Ogushi, N., and Sakai, H., 1968, Distribution of sulfur isotopes, selenium and cobalt in the Yanahara ore deposits, Okayama-Ken, Japan: Geochemical Journal, v. 2, p. 137-156.

Yang, K., and Scott, S.D., 1996, Possible contribution of a metal-rich magmatic fluid to a sea-floor hydrothermal system: Nature, v. 383, p. 420-423.

Yang, K., and Scott, S.D., 2002, Magmatic degassing of volatiles and ore metals into a hydrothermal system on the modern sea floor of the eastern Manus back-arc basin, western Pacific: Economic Geology, v. 97, p. 1079-1100.

Yang, K., Scott, S.D., and Goodfellow, W.D., 2003, Footwall alteration associated with some massive sulfide deposits in the Bathust Mining Camp, New Brunswick: Implication for seafloor hydrothermal mixing processes in Goodfellow, W.D., McCutcheon, S.R., and Peter, J.M., eds., Massive sulfide deposits of the Bathurst mining camp, New Brunswick, and northern Maine: Economic Geology Monograph, v. 11, p. 435-456.

Yeap, E.B., 1993, Tin and gold mineralisation in Peninular Malaysia and their relationships to the tectonic development: Journal of Southeast Asian Earth Sciences, v. 8, p. 329-348.

Yu, Z., Robinson, P., Townsend, A.T, Munker, C., and Crawford, A. J. , 2000, Determination of HFSE, Rb, Sr, Mo, Sb, Cs, Tl and Bi at ng g-1 levels in geological reference materials by magnetic sector ICP-MS after HF/HCLO4 high pressure digestion: Geostandards Newsletter, v. 24, p. 39-50.

Zantop, H., 1981, Trace elements in volcanogenic manganese oxides and iron oxides: the San Francisco mangenese deposit, Jalisco, Mexico: Economic Geology, v. 76, p. 545-555.

Zartman, R. E., and Doe, B.R., 1981, Plumbotectonics-the model: Tectonophysics v. 75, p. 135-162.

Zartman, R.E., and Smith, J.V., 2009, Mineralogy and U-Th-Pb age of a uranium-bearing jasperoid vein, Sunshine Mine, Coeur d'Alene district, Idaho, USA: Chemical Geology, v. 261, p. 185-195.

Zhou, M.F., Yan, D.P., Kennedy, A.K., Li, Y., and Ding, J., 2002, SHRIMP U-Pb zircon geochronological and geochemical evidence for Neoproterozoic arc-magmatism along the western margin of the Yangtze Block, South China: Earth and Planetary Science Letters, v. 196, p. 51-67.

Zhu, D.C., Zhao, Z.D., Niu, Y., Dilek, Y., Mo, X.X., 2011, Lhasa terrane in southern Tibet came from Australia: Geology, v. 39, p. 727-730.

Zierenberg, R.A., 1994, Data report: sulfur content of sediments and sulfur isotope concentrations of sulfide and sulfate minerals from Middle Valley, in Mottl, M.J., Davis, E.E., Fisher, A.T., and Slacks, J.F., eds., Proc ODP 139: Scientific Results, College Station, TX.

Zierenberg, R.A., Koski, R.A., Morton, J.L., Bouse, R.M., and Shanks, W.C.III., 1993, Genesis of massive sulfide deposits on a sediment-covered spreading center, EscanabaTrough, southern Gorda Ridge: Economic Geology, v. 88, p. 2069-2098.

Zierenberg, R. A., Shanks, W.C.III., and Bischoff, J.L., 1984, Massive sulfide deposits at 21°N, East Pacific Rise: chemical composition, stable isotopes, and phase equilibria: Geological Society America Bulletin, v. 95, p. 922-929.

Zindler, A., and Hart, S.R., 1986, Chemical geodynamics: Annual Review of Earth and Planetary Sciences, v. 14, p. 493-571.

APPENDICES

Appendix I: Rock Catalogue

Appendix II: Sample localities/Sampling details

Appendix III: LA-ICPMS zircon U-Pb age results

Appendix IV: XRF whole-rock geochemical results

Appendix V: SWIR results

Appendix VI: XRD results

Appendix VII: Microprobe results of sphalerite geochemistry

Appendix VIII: LA-ICPMS pyrite trace element geochemical results

Appendix IX: Fluid inclusion microthermometric results

Appendix X: Laser Raman Spectroscopic results

Appendix XI: Calculated density and pressure of fluids

Appendix I: Rock Catalogue

Deposit/ sample ID	Rock unit	Analyses												Remarks
		XRF geochemistry	REE	LA-ICPMS Zr U-Pb dating	Sm-Nd and Rb-Sr isotopes	Sphalerite geochemistry	Pyrite trae element chemistry	S isotope	Pb isotope	FI microthermometry	LRS (gas composition)	SWIR	XRD	
Tasik Chini														
BR1	Sandstone			x										
BR2	Sandstone			x										
BR3	Dacite	x		x	x									2 analyses
BR4	Sandstone			x										
BR305	Sandstone			x										
BR307	Sandstone			x										
BR315	Rhyolite	x		x										
BR317	Granite	x		x										
BR318	Diorite	x		x	x									
BR321	Granite	x		x	x									
BR323	Rhyolite	x		x	x									
BR325	Rhyolite	x		x										
BR326	Granite	x		x	x									
402	Phyllite			x										
402(2)	Phyllite			x										
Bukit Botol														
BB1	Massive sulphide ore						x	x						pyrite LA-ICPMS spot analyses
BB1a	Massive sulphide ore							x						
BB1b	Massive sulphide ore							x	x					
BB1d	Massive sulphide ore					x								54 spot analyses from 7 sph. grains
BB2	Massive sulphide ore						x	x						pyrite LA-ICPMS spot analyses

Deposit/ sample ID	Rock unit	Analyses												Remarks
		XRF geochemistry	REE	LA-ICPMS Zr U-Pb dating	Sm-Nd and Rb-Sr isotopes	Sphalerite geochemistry	Pyrite trae element chemistry	S isotope	Pb isotope	FI microthermometry	LRS (gas composition)	SWIR	XRD	
BB2a	Massive sulphide ore							x						
BB2b	Massive sulphide ore					x		x						19 spot analyses from 6 sph. grains
BB2c	Massive sulphide ore							x						
BB2d	Massive sulphide ore							x	x					
BB2e	Rhyolite											x		
BB2f	Massive sulphide ore							x						
BB3	Rhyolite	x										x		
BB3b	Rhyolite	x	x											
BB5a	Rhyolite											x		
BB6	Rhyolite	x	x	x	x							x		
BB9	Rhyolite								x					2 analyses for Pb
BB10	Massive sulphide ore							x						
BB10a	Massive sulphide ore	x							x			x		
BB10c	Massive sulphide ore							x	x					2 analyses for S,
BB11	Rhyolite			x	x							x		
BB24	Rhyolite											x		
BB25	Rhyolite	x			x									
BB25(a)	Rhyolite	x												
BB26	Rhyolite											x		
BB27	Rhyolite											x		
BB28	Rhyolite											x		
BB30	Rhyolite	x	x									x		
BB30a	Rhyolite	x												
BB40	Rhyolite	x										x		

Deposit/ sample ID	Rock unit	Analyses												Remarks
		XRF geochemistry	REE	LA-ICPMS Zr U-Pb dating	Sm-Nd and Rb-Sr isotopes	Sphalerite geochemistry	Pyrite trae element chemistry	S isotope	Pb isotope	FI microthermometry	LRS (gas composition)	SWIR	XRD	
MBTCS1	Rhyolite						x							pyrite LA-ICPMS spot analyses
MBTCS2	Rhyolite	x	x						x			x		
MBTCS4(1)	Rhyolite	x	x						x					
TasikChini-2	Rhyolite	x										x		
BBotolDump-1	Massive sulphide ore					x				x	x			5 spot analyses from 1 sph. grain
T5	Massive sulphide ore							x						2 analyses for S,
T6	Massive sulphide ore							x						2 analyses for S,
T7	Massive sulphide ore							x		x				2 analyses for S,
T8	Massive sulphide ore							x						3 analyses for S,
T10	Massive sulphide ore							x						4 analyses for S,
Tasik	Barite							x						3 analyses for S,
Barite	Barite							x		x	x			
MBTCS3	Barite							x						
BB1 (barite)	Barite							x						
BB2 (barite)	Barite							x						
B1	Barite							x						
B2	Barite							x						
BB2-X	Barite							x						
S3	Rhyolite											x		
S4	Rhyolite											x		
SQ2	Rhyolite											x		
SQS1	Rhyolite											x		
SQS2	Rhyolite											x		
SQS3	Rhyolite											x		

Deposit/ sample ID	Rock unit	Analyses												Remarks
		XRF geochemistry	REE	LA-ICPMS Zr U-Pb dating	Sm-Nd and Rb-Sr isotopes	Sphalerite geochemistry	Pyrite trae element chemistry	S isotope	Pb isotope	FI microthermometry	LRS (gas composition)	SWIR	XRD	
SQS4	Rhyolite											x		
301	Ironstone	x												
302	Ironstone	x												
405	Ironstone	x												
Bukit Ketaya														
BK01	Rhyolite	x			x			x				x	x	
BK01(a)	Rhyolite	x												
BK02	Rhyolite	x						x				x	x	
BK03	Rhyolite	x										x		
BK04	Rhyolite	x										x		
BK05	Ironstone	x												
BK05a	Ironstone	x												
BK06	Barite							x						
BK07	Rhyolite	x										x		
BK08	Barite							x						
BK08a	Barite							x						
BK09	Barite							x						
BK10	Rhyolite			x								x		
BK10a	Rhyolite					x								
BK11	Rhyolite	x			x				x			x		4 analyses Pb, 39 spot analyses from 7 sph. grains
BK11a	Rhyolite	x							x	x			x	
BK12	Rhyolite	x										x		
BK12a	Massive sulphide ore								x					2 analyses Pb, 3 spot analyses from 1 sph. Grain, 3 analyses forS

Deposit/ sample ID	Rock unit	Analyses												Remarks
		XRF geochemistry	REE	LA-ICPMS Zr U-Pb dating	Sm-Nd and Rb-Sr isotopes	Sphalerite geochemistry	Pyrite trae element chemistry	S isotope	Pb isotope	FI microthermometry	LRS (gas composition)	SWIR	XRD	
BK13	Ironstone	x												
BK13a	Ironstone	x												
BK13b	Ironstone	x												
KIRI2/3	Rhyolite	x												
KIRI3	Rhyolite	x	x											
KNN2	Rhyolite	x	x											
HR1	Rhyolite	x	x		x									
MBTCBK	Rhyolite	x	x											
MBTCS5	Rhyolite	x										x	x	
S6/a3	Rhyolite			x										
BMSE1	Massive sulphide ore					x		x	x					3 analyses for S, 6 spot analyses from 2 sph. grains, 3 analyses for S
BKCL	Massive sulphide ore							x						2 analyses for S,
KZMA	Massive sulphide ore							x						3 analyses for S,
14AR	Barite							x						
S6/7a12	Rhyolite							x		x	x			
S6/7a13	Rhyolite							x						
BK1	Barite							x						
BK2	Barite							x						
BK-X	Barite							x						
S5/6a4	Barite							x						
TasikChini-1	Rhyolite	x												
BKCL	Rhyolite											x		
CL1	Rhyolite											x		
CL2	Rhyolite											x		

Deposit/ sample ID	Rock unit	Analyses												Remarks
		XRF geochemistry	REE	LA-ICPMS Zr U-Pb dating	Sm-Nd and Rb-Sr isotopes	Sphalerite geochemistry	Pyrite trae element chemistry	S isotope	Pb isotope	FI microthermometry	LRS (gas composition)	SWIR	XRD	
SQTBK	Rhyolite											x		
SQTB2BK	Rhyolite											x		
BKHOST	Rhyolite											x		
BKHOST2	Rhyolite	x												
FeMn1-KNN	Ironstone	x												
FeMn2	Ironstone	x												
FeMn3	Ironstone	x												
Mn1	Ironstone	x												

Appendix II: Sample localities/ Sampling details

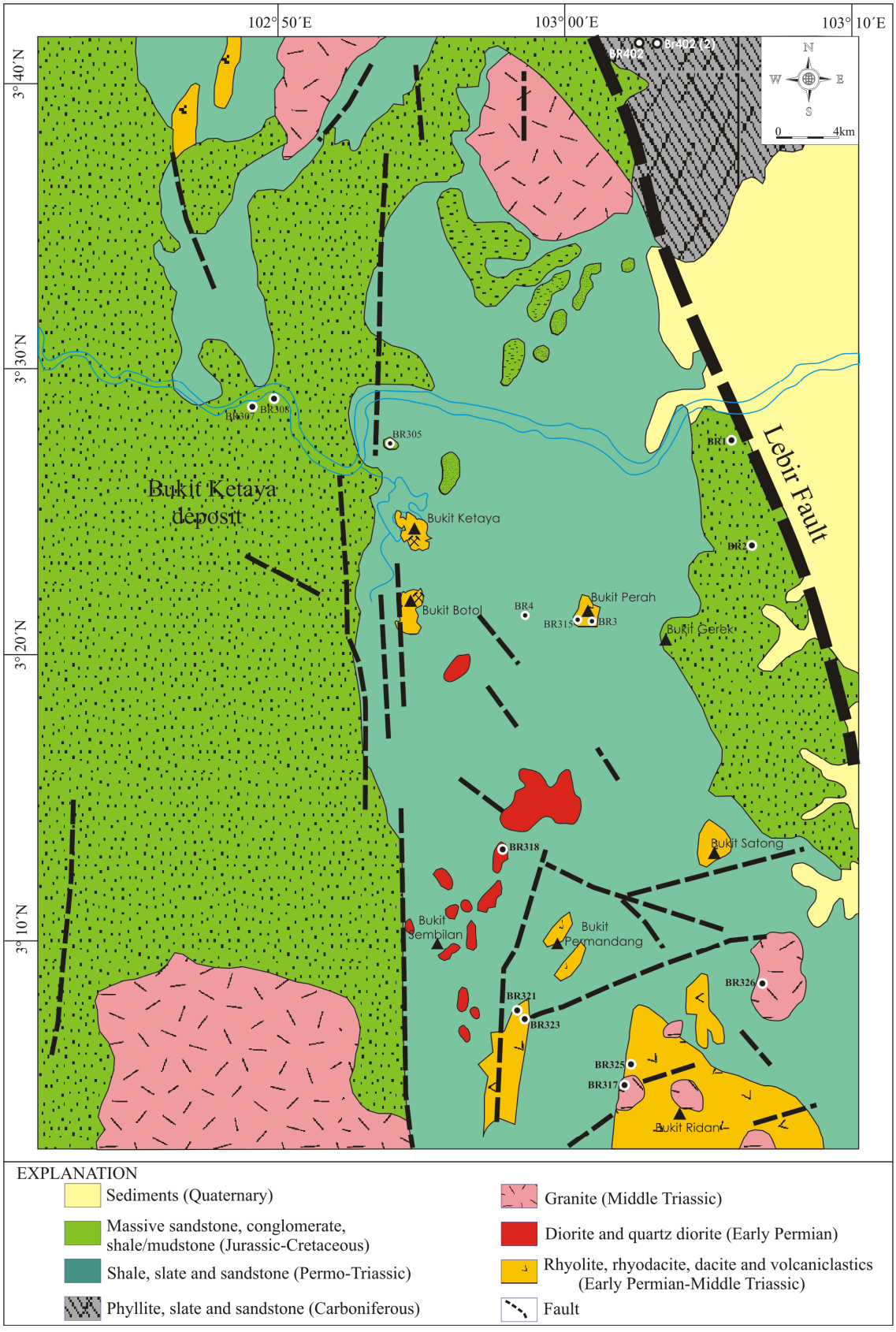

District-scale of the Tasik Chini and surrounding area, Central Peninsular Malaysia

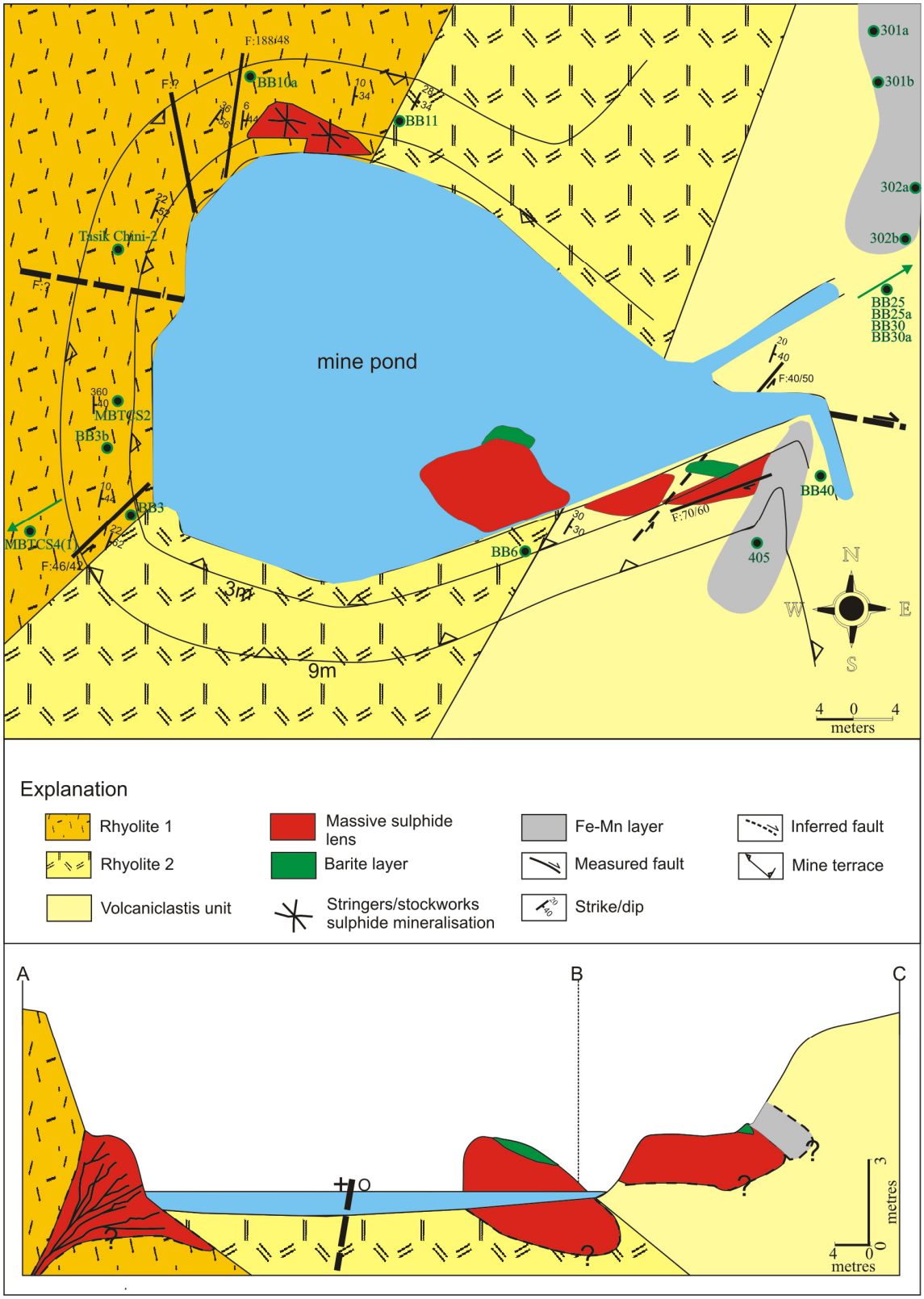

Deposit-scale of the Bukit Botol deposit, Central Peninsular Malaysia

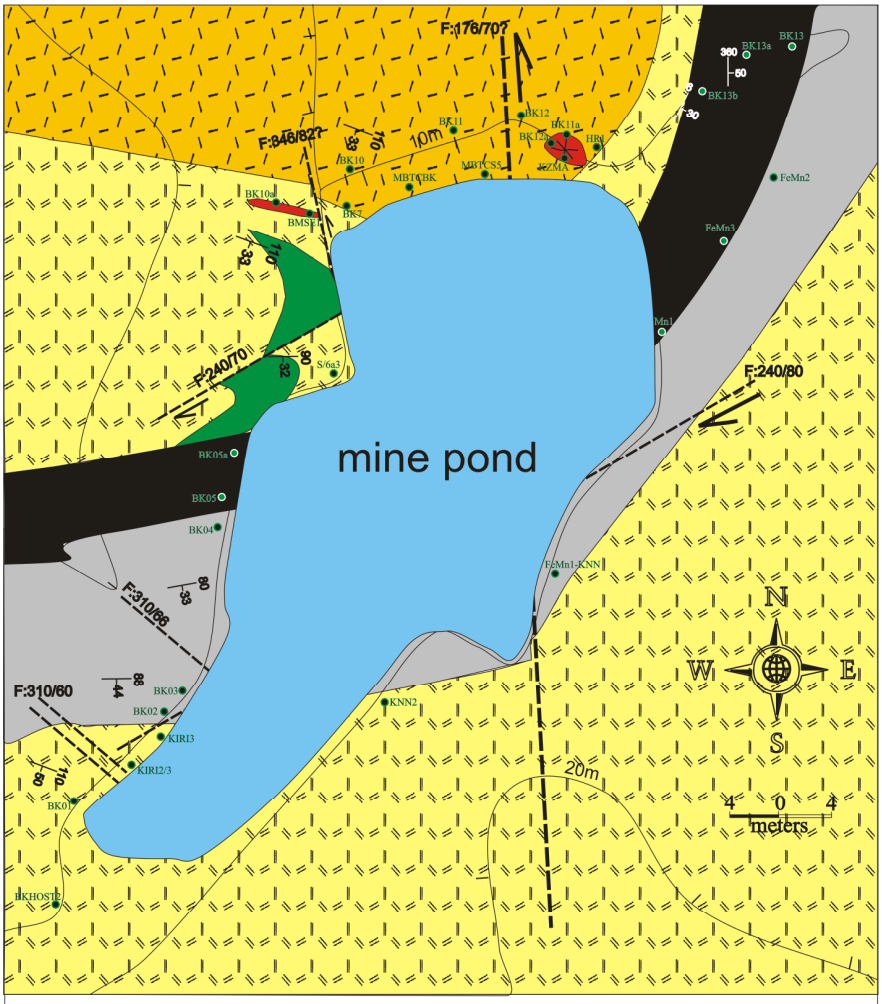

Explanation

- Quartz feldspar phyric rhyolite
- Rhyolite breccias
- Massive sulphide
- Hematite-silica
- Fe-oxyhydroxide
- Fe-Si layer
- Barite layer
- Stringers/stockworks sulphide mineralisation
- Thin sheets
- Mine terrace
- Inferred fault

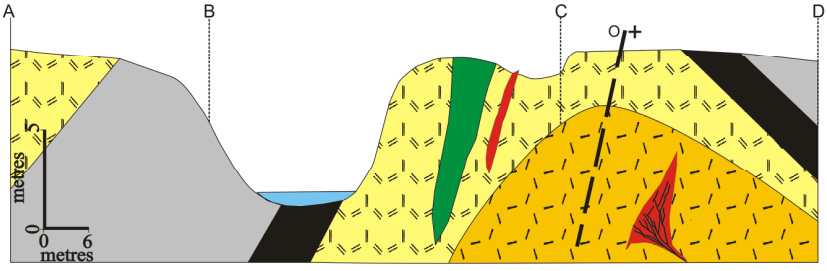

District-scale of the Bukit Ketaya deposit, Central Peninsular Malaysia

Appendix III: LA-ICPMS zircon U-Pb age results

Sample No.(& analysis number)	Lab ID	Comments	Spot size micron	207 cor $^{206}Pb/^{238}U$ age	0 +/-1 ster	U ppm	Th ppm	Pb ppm	Hf ppm	Ti ppm	Common Pb at age of zirc	$^{206}Pb/^{238}U$ ratio	+/-1 RSE	$^{208}Pb/^{232}Th$ ratio	+/-1 RSE	$^{207}Pb/^{206}Pb$ ratio	+/-1 RSE	Comments
402																		
402	oc12b008	ok	32	**330**	**4**	461	299	26	10823	3	0.858	0.0525	1.2%	0.0166	1.9%	0.0530	2.1%	Mean = 336.4±6.6 [1.9%] 95% conf. Wtd by data-pt errs only, 0 of 5 rej. MSWD = 1.7, probability = 0.16
402	oc12b010	Older domain in middle	32	**332**	**7**	309	179	16	10320	6	0.858	0.0536	2.1%	0.0181	2.9%	0.0627	3.7%	
402	oc12b015	ok	32	**335**	**4**	388	280	23	10466	7	0.858	0.0535	1.3%	0.0170	1.9%	0.0564	2.1%	
402	oc12b011	ok	32	**339**	**3**	785	535	45	9773	13	0.858	0.0540	0.9%	0.0161	1.8%	0.0542	1.5%	
402	oc12b012	ok	32	**343**	**4**	370	291	22	10586	28	0.859	0.0548	1.2%	0.0174	2.0%	0.0548	2.3%	
402	oc12b021	Mixing Rad. Pb in middle	32	**351**	**5**	682	309	36	11082	10	0.859	0.0561	1.5%	0.0172	2.3%	0.0556	2.7%	
402	oc12b020	Common Pb @ begin	32	**352**	**5**	343	140	20	10989	16	0.859	0.0561	1.5%	0.0172	2.7%	0.0539	3.0%	Mean = 356±17 [4.8%] 95% conf. Wtd by data-pt errs only, 0 of 3 rej. MSWD = 2.0, probability = 0.13
402	oc12b019	Common Pb at begin	32	**362**	**4**	718	264	43	11387	2	0.860	0.0579	1.1%	0.0188	2.3%	0.0544	2.0%	
402	oc12b007	Pb loss, may be metamict - use w/ caution	32	1049	12	737	313	146	11226	19	0.915	0.1807	1.1%	0.0483	2.0%	0.0926	1.4%	
402	oc12b014	Metmaict - Pb loss - use only 7/6age and w/ caution	32	1087	18	870	232	164	10265	7	0.917	0.1869	1.7%	0.0968	1.7%	0.0905	0.7%	
402	oc12b018	Minor Pb loss - use 7/6 age	32	1462	13	356	148	92	10633	9	0.950	0.2561	0.9%	0.0686	1.8%	0.0968	0.8%	
402	oc12b009	Metmaict, but concordant	32	1492	12	604	245	161	12126	16	0.952	0.2613	0.8%	0.0664	1.7%	0.0961	0.7%	
402	oc12b016	Metamict, but concordant - common Pb at end	32	1625	18	407	427	135	10793	8	0.965	0.2878	1.2%	0.0791	1.7%	0.1035	1.0%	
402	oc12b013	ok	32	2535	26	224	180	128	9171	19	1.059	0.4812	0.9%	0.1325	1.7%	0.1664	0.7%	
402	oc12b017	Metamict - DO NOT USE	32	962	14	1154	1941	271	11315	338	0.922	0.1964	1.4%	0.0250	2.5%	0.2244	0.9%	
402(2)																		
2012-038	JA18A050	ok	32	329	4	352	371	18	371	5	0.858	0.0524	1.2%	0.0160	1.5%	0.0542	2.2%	Mean = 330.4±3.0 [0.92%] 95% conf. Wtd by data-pt errs only, 0 of 7 rej. MSWD = 0.20, probability = 0.98
2012-038	JA18A045	ok	32	329	4	522	535	27	535	8	0.858	0.0523	1.1%	0.0166	1.6%	0.0532	2.0%	
2012-038	JA18A052	ok	32	329	4	368	300	19	300	6	0.858	0.0525	1.2%	0.0165	1.5%	0.0547	1.9%	
2012-038	JA18A055	Common Pb @ beginning	32	332	4	540	517	29	517	10	0.858	0.0528	1.2%	0.0167	1.6%	0.0537	2.4%	
2012-038	JA18A058	Slightly Variable U/Pb	32	332	5	969	599	49	599	4	0.858	0.0530	1.4%	0.0170	1.8%	0.0557	1.7%	
2012-038	JA18A042	Older domain? @ end	32	332	5	731	324	36	324	6	0.858	0.0531	1.5%	0.0160	1.9%	0.0566	2.3%	
2012-038	JA18A051	ok	32	333	5	329	450	17	450	5	0.858	0.0529	1.4%	0.0168	1.6%	0.0518	2.8%	
2012-038	JA18A040	ok	32	345	4	406	313	22	313	10	0.859	0.0550	1.2%	0.0162	1.6%	0.0540	2.1%	
2012-038	JA18A054	Slighlty variable U/Pb	32	345	4	1203	567	65	567	10	0.859	0.0552	1.2%	0.0188	1.4%	0.0564	1.6%	
2012-038	JA18A048	ok	32	346	5	254	182	14	182	5	0.859	0.0550	1.3%	0.0187	1.6%	0.0511	2.5%	
2012-038	JA18A061	Older domain (375Ma @ beginning)	32	347	4	570	269	33	269	6	0.859	0.0554	1.3%	0.0147	2.6%	0.0549	2.6%	
2012-038	JA18A053	Mixing w/ a younger domain @ end?	32	393	4	435	498	27	498	12	0.862	0.0630	1.1%	0.0204	1.5%	0.0559	2.2%	
2012-038	JA18A044	ok	32	399	4	459	551	30	551	7	0.863	0.0639	1.0%	0.0202	1.4%	0.0550	2.0%	
2012-038	JA18A060	Pb loss @ beginning, Minor Common Pb	32	581	5	1513	158	148	158	47	0.876	0.0950	0.9%	0.0327	2.1%	0.0644	1.1%	
2012-038	JA18A041	Pb mobility	32	1392	14	785	142	179	142	20	0.943	0.2412	1.0%	0.0571	1.8%	0.0893	0.8%	
2012-038	JA18A047	Pb loss @ end	32	1480	21	734	382	178	382	13	0.951	0.2584	1.4%	0.0766	1.6%	0.0939	0.8%	
2012-038	JA18A043	ok	32	1561	13	892	184	243	184	7	0.958	0.2733	0.9%	0.0745	1.3%	0.0943	0.6%	
2012-038	JA18A039	Slight Pb loss - use 7/6 age	32	1436	12	872	566	216	566	6	0.948	0.2509	0.9%	0.0666	1.6%	0.0949	0.6%	
2012-038	JA18A057	Not Zircon, U rich phase, Datable, but U in analog, use 7/6 age	32								0.943	0.2403	0.8%	0.0648	1.1%	0.0960	0.3%	
2012-038	JA18A038	Slight Pb loss- use 7/6 age	32	1501	12	702	226	180	226	19	0.953	0.2632	0.8%	0.0730	1.3%	0.0967	0.7%	
2012-038	JA18A049	Pb loss- use 7/6 Age	32	1322	11	563	405	131	405	3	0.938	0.2311	0.9%	0.0640	1.3%	0.0979	0.7%	
2012-038	JA18A059	Metamict- use 7/6 age - w/ caution	32	1721	20	508	205	150	205	10	0.975	0.3084	1.2%	0.0770	1.4%	0.1122	1.0%	
2012-038	JA18A056	Pb mobility, Look @ 208/232 Age	32	1938	18	267	121	93	121	9	0.995	0.3486	0.9%	0.1015	1.4%	0.1135	0.8%	
2012-038	JA18A046	Pb loss- use 7/6 age	32	1455	20	294	317	80	317	37	0.952	0.2609	1.4%	0.0551	1.8%	0.1169	1.2%	
BR4																		
2012-352	JL11A389	ok	32	**310**	**3**	383	402	18	10701	6	0.856	0.0493	1.1%	0.0151	1.4%	0.0536	1.9%	younger than 310±3Ma
2012-352	JL11A394	Older @ end	32	325	6	172	191	8	8041	22	0.857	0.0519	1.8%	0.0158	2.5%	0.0555	5.0%	
2012-352	JL11A392	ok	32	565	7	206	166	19	10353	4	0.875	0.0917	1.2%	0.0273	1.5%	0.0599	1.8%	
2012-352	JL11A391	ok	32	602	6	458	194	44	11648	6	0.877	0.0980	0.9%	0.0295	1.4%	0.0606	1.2%	
2012-352	JL11A402	ok	32	842	7	948	451	129	11461	5	0.896	0.1397	0.8%	0.0424	1.2%	0.0682	0.7%	
2012-352	JL11A398	ok	32	1100	10	314	346	57	12417	20	0.917	0.1861	0.9%	0.0542	1.2%	0.0764	0.9%	
2012-352	JL11A390	Pb mobility, use 7/6 age	32	1123	9	1736	527	316	17391	4	0.919	0.1903	0.9%	0.0570	1.2%	0.0774	0.5%	
2012-352	JL11A400	ok	32	1125	11	115	94	22	13106	8	0.919	0.1912	1.1%	0.0570	1.4%	0.0798	1.5%	
2012-352	JL11A396	ok	32	1186	11	178	201	35	12931	13	0.924	0.2019	1.0%	0.0589	1.2%	0.0791	1.1%	
2012-352	JL11A388	Pb loss @ beginning	32	1256	12	166	113	36	9906	4	0.931	0.2152	1.0%	0.0663	1.4%	0.0830	1.2%	
2012-352	JL11A399	ok	32	1611	15	144	90	40	10822	9	0.964	0.2844	0.9%	0.0813	1.3%	0.1006	1.0%	
2012-352	JL11A395	ok	32	1738	16	191	86	58	11395	8	0.976	0.3098	0.9%	0.0871	1.3%	0.1072	0.7%	
2012-352	JL11A393	slight Pb loss	32	1825	17	269	158	86	11170	17	0.985	0.3282	0.9%	0.0908	1.2%	0.1138	0.7%	
2012-352	JL11A397	ok	32	1853	18	302	155	99	9658	4	0.987	0.3332	1.0%	0.0939	1.3%	0.1137	0.7%	
2012-352	JL11A401	ok	32	1883	17	246	192	80	9707	333	0.990	0.3386	0.9%	0.0982	1.2%	0.1136	0.6%	
2012-352	JL11A387	Pb loss	32	2485	24	193	87	91	11233	12	1.060	0.4837	0.9%	0.1413	1.3%	0.1879	0.6%	
BR305																		
2012-039	JA18A085	Slightly Variable U/Pb , younger @ end	32	148	2	536	446	12	11561	4	0.845	0.0232	1.3%	0.0072	1.8%	0.0509	2.4%	younger than 148±2Ma
2012-039	JA18A077	ok	32	194	3	259	127	8	9910	5	0.848	0.0305	1.5%	0.0096	2.4%	0.0473	3.5%	
2012-039	JA18A076	Variable U/Pb- older domain @ beginning	32	226	2	1183	784	43	11315	5	0.851	0.0357	1.0%	0.0108	1.8%	0.0526	1.8%	
2012-039	JA18A086	ok	32	228	3	517	176	18	10040	33	0.851	0.0362	1.2%	0.0121	2.2%	0.0561	2.1%	
2012-039	JA18A073	Common Pb throughout	32	233	2	1430	713	55	11309	13	0.852	0.0386	0.9%	0.0168	1.5%	0.0902	1.6%	
2012-039	JA18A074	ok	32	254	3	773	389	31	9623	9	0.852	0.0403	1.1%	0.0137	1.6%	0.0542	1.9%	
2012-039	JA18A067	ok	32	257	4	222	95	9	10894	5	0.853	0.0408	1.4%	0.0131	2.5%	0.0521	3.5%	
2012-039	JA18A082	ok	32	274	4	210	97	9	8869	11	0.854	0.0436	1.5%	0.0144	2.3%	0.0537	2.9%	
2012-039	JA18A079	Variable U/Pb- younger domain @ beginning	32	304	4	602	114	30	13721	7	0.856	0.0486	1.3%	0.0137	3.9%	0.0577	2.6%	
2012-039	JA18A083	Older (397Ma) low U beginning, younger(372Ma) high U end	32	372	5	936	1126	58	11887	3	0.861	0.0600	1.3%	0.0179	1.6%	0.0612	2.4%	
2012-039	JA18A066	ok	32	426	4	861	148	59	12907	15	0.864	0.0685	0.9%	0.0234	1.8%	0.0573	1.1%	
2012-039	JA18A080	ok	32	431	5	409	209	28	11648	16	0.865	0.0694	1.1%	0.0227	1.6%	0.0590	2.0%	
2012-039	JA18A087	Common Pb @ end	32	459	5	444	268	32	11291	6	0.867	0.0737	1.1%	0.0218	1.6%	0.0562	1.9%	
2012-039	JA18A075	ok	32	536	5	604	332	53	9808	21	0.873	0.0877	0.9%	0.0261	1.7%	0.0672	1.4%	
2012-039	JA18A072	Pb loss & common Pb in middle - use only 7/6 age & w/ caution	32	1411	35	174	214	45	9766	10	0.948	0.2525	1.6%	0.0580	2.0%	0.1158	2.0%	
2012-039	JA18A081	Pb loss @ beginning	32	1413	22	209	117	51	9482	9	0.945	0.2456	1.1%	0.0738	1.5%	0.0911	1.1%	
2012-039	JA18A068	Pb loss - use 7/6 age	32	1596	18	148	94	42	11620	14	0.964	0.2858	1.0%	0.0585	1.7%	0.1134	1.0%	
2012-039	JA18A070	Pb loss- use 7/6 age	32	1652	22	264	182	74	10986	9	0.969	0.2953	1.7%	0.0711	1.8%	0.1108	1.2%	
2012-039	JA18A084	Younger Domain (~2000Ma +/-14) @ beginning, Pb loss throughout- use 7/6 age	32	2183	13	409	465	174	11368	9	1.023	0.4067	1.2%	0.1305	1.3%	0.1443	0.8%	
2012-039	JA18A071	Pb loss - use 7/6 age	32	2322	9	209	129	93	9192	4	1.043	0.4485	0.9%	0.1046	1.4%	0.1775	0.6%	
2012-039	JA18A069	DO NOT USE- metamict	32	555		1898	1590	177	10552	140	0.876	0.0938	1.3%	0.0287	1.2%	0.0927	0.8%	
2012-039	JA18A078	Mixing age domains & common Pb , DO NOT USE	32	564		210	23	18	11820	8	0.875	0.0922	2.7%	0.0466	3.0%	0.0650	2.2%	

Sample No.(& analysis number)	Lab ID	Comments	Spot size micron	207 cor $^{206}Pb/^{238}U$ age	0 +/-1 ster	U ppm	Th ppm	Pb ppm	Hf ppm	Ti ppm	Common Pb at age of zirc	$^{206}Pb/^{238}U$ ratio	+/-1 RSE	$^{208}Pb/^{232}Th$ ratio	+/-1 RSE	$^{207}Pb/^{206}Pb$ ratio	+/-1 RSE	Comments
BR307																		
BR307	jn29a016	ok	32	139	3	338	281	8	10215	16	0.845	0.0219	1.8%	0.0070	0.022063602	0.0558	4.5%	younger than 139±6 Ma
BR308	jn29a019	ok	32	149	3	519	664	14	9669	8	0.845	0.0236	1.8%	0.0080	0.017612018	0.0533	3.7%	
BR309	jn29a018	ok	32	150	3	480	567	13	9576	10	0.845	0.0236	1.8%	0.0078	0.018205126	0.0545	3.6%	
BR310	jn29a017	ok	32	237	6	85	62	3	9124	18	0.851	0.0377	2.5%	0.0129	0.031254009	0.0571	6.1%	
BR311	jn29a015	ok	32	243	3	890	552	33	11680	6	0.852	0.0383	1.2%	0.0114	0.015914519	0.0504	2.1%	
BR312	jn29a021	ok	32	247	3	1097	436	40	12197	2	0.852	0.0390	1.3%	0.0129	0.015147505	0.0503	1.7%	
BR313	jn29a007	older core at end (>300 Ma)	32	266	6	201	69	7	11628	33	0.853	0.0423	2.2%	0.0137	0.042356588	0.0545	4.8%	
BR314	jn29a011	ok	32	266	3	1495	482	57	11842	7	0.853	0.0423	1.2%	0.0144	0.015250044	0.0546	1.3%	
BR315	jn29a026	ok	32	349	4	731	127	38	12669	13	0.859	0.0565	1.2%	0.0359	0.022746706	0.0654	1.6%	
BR316	jn29a025	ok	32	389	5	907	629	57	10586	149	0.862	0.0628	1.4%	0.0200	0.014673953	0.0623	1.4%	
BR317	jn29a022	through crystal at end	32	402	10	178	161	12	10339	60	0.863	0.0653	2.6%	0.0208	0.029380567	0.0669	5.5%	
BR318	jn29a024	ok	32	406	5	739	195	42	13115	12	0.863	0.0651	1.2%	0.0206	0.016757362	0.0567	1.5%	
BR319	jn29a013	ok	32	428	5	2082	577	126	12722	9	0.865	0.0687	1.2%	0.0222	0.013487829	0.0551	1.0%	
BR320	jn29a008	ok	32	436	6	296	142	20	10322	9	0.865	0.0700	1.4%	0.0237	0.018744944	0.0562	2.2%	
BR321	jn29a006	ok	32	439	5	408	75	25	12370	11	0.865	0.0704	1.3%	0.0232	0.022407298	0.0550	1.8%	
BR322	jn29a023	ok	32	443	6	263	50	16	12872	11	0.866	0.0710	1.4%	0.0226	0.026002419	0.0542	2.4%	
BR323	jn29a014	ok	32	454	6	289	79	19	13021	11	0.866	0.0728	1.4%	0.0261	0.024400732	0.0534	2.5%	
BR324	jn29a009	ok	32	456	5	605	568	47	11712	9	0.866	0.0731	1.2%	0.0221	0.013219426	0.0540	1.6%	
BR325	jn29a010	ok	32	631	9	229	141	23	8634	29	0.880	0.1032	1.4%	0.0343	0.017801426	0.0633	2.1%	
BR326	jn29a012	Pb loss at end	32	773	14	431	159	46	11079	22	0.890	0.1276	1.9%	0.0340	0.023660836	0.0666	2.2%	
BR327	jn29a020	ok	32	876	12	826	161	107	10310	7	0.899	0.1464	1.5%	0.0550	0.019181028	0.0734	0.9%	
BR1A																		
BR1A	jn29b044	ok	32	207	4	251	139	8	10305	17	0.849	0.0328	1.7%	0.0117	0.02451581	0.0523	3.8%	younger than 207±8 Ma
BR1A	jn29b043	ok	32	239	3	679	400	24	10844	15	0.851	0.0377	1.4%	0.0115	0.01992248	0.0501	2.3%	
BR1A	jn29b048	young rim with older core	32	243	4	2343	206	82	14676	11	0.852	0.0389	1.6%	0.0179	0.033223663	0.0612	2.2%	
BR1A	jn29b049	young rim with >500 Ma core	32	258	9	984	604	43	10168	41	0.853	0.0411	3.6%	0.0152	0.053028198	0.0582	7.9%	
BR1A	jn29b050	ok	32	259	3	366	150	14	11498	18	0.853	0.0412	1.3%	0.0130	0.021024909	0.0540	2.6%	
BR1A	jn29b053	Pb-rcih inclusion in mddle	32	271	7	294	75	13	11863	16	0.854	0.0451	2.6%	0.0270	0.08115856	0.0900	6.7%	
BR1A	jn29b051	ok	32	318	4	585	506	30	10100	14	0.857	0.0507	1.3%	0.0151	0.014899082	0.0537	1.9%	
BR1A	jn29b046	though crystal	32	340	21	1190	570	53	11900	23	0.859	0.0553	6.3%	0.0074	0.101511595	0.0710	7.9%	
BR1A	jn29b047	ok	32	396	6	502	24	27	13008	6	0.863	0.0642	1.5%	0.0482	0.063036162	0.0658	2.1%	
BR1A	jn29b042	ok	32	641	7	236	415	32	9164	21	0.880	0.1047	1.1%	0.0316	0.013073542	0.0624	1.9%	
BR1A	jn29b041	through crystal at end	32	675	14	904	198	81	13687	31	0.883	0.1115	2.1%	0.0212	0.027506738	0.0699	1.3%	
BR1A	jn29b052	ok	32	727	9	943	473	127	12987	38	0.892	0.1315	1.3%	0.0495	0.015477627	0.1402	0.7%	
BR1A	jn29b054	ok	32	727	7	549	632	72	9001	12	0.887	0.1199	1.0%	0.0319	0.013385037	0.0671	1.1%	
BR1A	jn29b045	old core with younger rim	32	750	19	212	194	26	11581	19	0.891	0.1294	2.6%	0.0295	0.024282546	0.1025	2.5%	
BR2																		
BR2	JA18A014	ok	32	149	3	254	386	6	8498	15	0.845	0.0237	1.8%	0.0079	1.9%	0.0566	3.6%	Mean = 150.5±3.0 [2.0%] 95% conf. Wtd by data-pt errs only, 0 of 4 rej. MSWD = 0.30, probability = 0.82
BR2	JA18A019	Variable U/Pb throughout	32	149	3	276	176	6	8090	12	0.845	0.0233	1.9%	0.0077	2.7%	0.0457	5.3%	
BR2	JA18A030	Slightly Variable U/Pb from beginning to End	32	152	3	957	286	22	11082	2	0.846	0.0240	1.7%	0.0083	2.3%	0.0507	2.9%	
BR2	JA18A029	Variable U/Pb	32	151	6	101	106	3	9051	8	0.845	0.0237	4.0%	0.0073	4.6%	0.0487	14.7%	
BR2	JA18A008	ok	32	168	2	838	553	22	11242	3	0.847	0.0264	1.1%	0.0080	1.6%	0.0495	1.9%	
BR2	JA18A015	ok	32	176	2	976	267	27	11529	1	0.847	0.0277	1.3%	0.0090	1.8%	0.0496	2.0%	
BR2	JA18A022	Common Pb throughout	32	227	4	124	130	5	9117	19	0.851	0.0370	1.8%	0.0141	2.4%	0.0763	4.0%	
BR2	JA18A024	~250Ma domain @ beginning	32	228	3	989	1529	37	7621	16	0.851	0.0367	1.5%	0.0099	1.8%	0.0654	3.2%	
BR2	JA18A028	Monazite - Datable	32	230	2						0.851	0.0368	0.9%	0.0100	1.1%	0.0632	1.3%	
BR2	JA18A023	Common Pb in middle	32	233	6	288	344	11	8335	11	0.851	0.0375	2.6%	0.0125	3.2%	0.0652	6.4%	
BR2	JA18A031	Minor Common Pb	32	234	2	2377	425	88	12679	13	0.851	0.0371	0.9%	0.0120	1.5%	0.0533	1.0%	
BR2	JA18A032	Common Pb in Middle- small integration - use w/ caution	32	239	8	272	112	10	8870	20	0.852	0.0387	3.3%	0.0148	6.0%	0.0714	6.3%	
BR2	JA18A009	ok	32	289	4	209	135	10	11665	8	0.855	0.0459	1.4%	0.0153	2.0%	0.0530	3.1%	
BR2	JA18A010	ok	32	362	4	397	237	23	9246	5	0.860	0.0578	1.1%	0.0176	1.5%	0.0552	1.9%	
BR2	JA18A020	ok	32	447	8	123	216	9	10043	9	0.866	0.0717	1.7%	0.0230	1.8%	0.0539	3.8%	
BR2	JA18A027	Pb loss @ beginning	32	718	10	91	115	11	10214	8	0.886	0.1179	1.5%	0.0351	1.8%	0.0642	2.9%	
BR2	JA18A011	ok	32	747	9	144	173	18	10717	6	0.889	0.1236	1.2%	0.0500	1.5%	0.0692	2.0%	
BR2	JA18A007	Pb loss a\@ beginning	32	846	10	356	300	51	12729	9	0.896	0.1406	1.2%	0.0396	1.4%	0.0693	1.4%	
BR2	JA18A016	ok	32	961	12	134	234	22	10962	7	0.905	0.1606	1.3%	0.0503	1.5%	0.0704	1.9%	
BR2	JA18A025	Common Pb @ beginning	32	991	10	481	312	82	11582	7	0.908	0.1663	1.1%	0.0526	1.4%	0.0728	1.1%	
BR2	JA18A017	ok	32	1352	21	233	161	54	10062	8	0.939	0.2334	1.0%	0.0708	1.3%	0.0867	1.1%	
BR2	JA18A012	ok	32	1840	13	307	167	101	11094	9	0.986	0.3312	1.0%	0.0962	1.3%	0.1145	0.7%	
BR2	JA18A021	ok	32	1853	11	561	104	184	12865	8	0.987	0.3332	1.0%	0.0641	1.8%	0.1140	0.6%	
BR2	JA18A013	ok	32	1870	40	26	21	8	8320	14	0.987	0.3335	1.7%	0.0959	1.9%	0.1063	2.2%	
BR2	JA18A026	Pb mobility	32	2507	8	625	426	287	10968	337	1.056	0.4751	1.6%	0.1330	1.4%	0.1646	0.5%	
BR325																		
2012-030	JA18A166	Minor common Pb	32	226	3	790	658	29	8547	7	0.851	0.0364	1.2%	0.0124	1.5%	0.0667	1.6%	Mean = 225.6±3.4 [1.5%] 95% conf. Wtd by data-pt errs only, 0 of 2 rej. MSWD = 0.0021, probability = 0.96
2012-030	JA18A172	Common Pb Throughout - use w/ caution	32	226	2	745	568	28	10065	7	0.852	0.0383	1.0%	0.0163	1.4%	0.1075	1.3%	
2012-030	JA18A178	Common Pb @ beginning	32	233	3	650	398	26	9823	6	0.852	0.0387	1.1%	0.0181	1.9%	0.0888	2.2%	
2012-030	JA18A177	Common Pb @ end	32	234	5	1308	832	47	9665	11	0.851	0.0378	2.0%	0.0143	1.7%	0.0691	2.0%	
2012-030	JA18A167	Common Pb @ beginning & middle	32	235	4	490	288	19	10041	5	0.851	0.0380	1.8%	0.0145	2.5%	0.0703	3.7%	
2012-030	JA18A173	ok	32	237	3	698	428	26	9692	4	0.851	0.0375	1.1%	0.0119	1.4%	0.0518	2.0%	Mean = 237.4±1.7 [0.71%] 95% conf. Wtd by data-pt errs only, 0 of 12 rej. MSWD = 0.47, probability = 0.92
2012-030	JA18A181	ok	32	237	2	695	426	26	9453	5	0.851	0.0375	1.0%	0.0117	1.5%	0.0515	1.5%	
2012-030	JA18A171	Common Pb in middle	32	238	6	676	367	27	11565	4	0.852	0.0387	2.4%	0.0152	3.2%	0.0757	3.2%	
2012-030	JA18A169	Common Pb @ end	32	238	3	1099	775	39	9610	5	0.851	0.0376	1.4%	0.0116	1.9%	0.0505	2.6%	
2012-030	JA18A175	High common Pb	32	238	3	1511	1626	64	8649	25	0.854	0.0429	1.1%	0.0211	1.8%	0.1500	1.9%	
2012-030	JA18A180	common Pb @ end	32	238	3	355	172	13	8643	7	0.851	0.0380	1.4%	0.0134	2.3%	0.0579	2.8%	
2012-030	JA18A168	ok	32	239	3	638	372	24	9715	5	0.851	0.0377	1.1%	0.0121	1.6%	0.0509	1.8%	
2012-030	JA18A176	ok	32	239	3	466	255	18	9741	6	0.851	0.0380	1.1%	0.0119	1.8%	0.0539	2.1%	
2012-030	JA18A174	ok	32	239	2	594	329	22	9760	5	0.851	0.0378	1.0%	0.0121	1.6%	0.0503	1.8%	
2012-030	JA18A179	ok	32	245	3	460	254	18	9518	4	0.852	0.0386	1.1%	0.0124	1.6%	0.0497	2.4%	
2012-030	JA18A170	High common Pb - Use w/ caution	32	249	7	795	534	35	9484	1318	0.854	0.0431	2.7%	0.0246	6.4%	0.1208	8.1%	

Sample No.(& analysis number)	Lab ID	Comments	Spot size micron	207 cor $^{206}Pb/^{238}U$ age	0 +/-1 ster	U ppm	Th ppm	Pb ppm	Hf ppm	Ti ppm	Common Pb at age of zirc	$^{206}Pb/^{238}U$ ratio	+/-1 RSE	$^{208}Pb/^{232}Th$ ratio	+/-1 RSE	$^{207}Pb/^{206}Pb$ ratio	+/-1 RSE	Comments
BR3																		
BR3	jn29a042	ok	32	221	4	219	178	10	10579	14	0.852	0.0382	1.9%	0.0169	0.023909276	0.1186	3.1%	Mean = 232.7±3.8 [1.6%] 95% conf. Wtd by data-pt errs only, 0 of 11 rej. MSWD = 2.2, probability = 0.015
BR3	jn29a039	ok	32	224	4	161	78	6	9647	13	0.851	0.0361	1.9%	0.0129	0.027297606	0.0660	4.6%	
BR3	jn29a044	ok	32	228	4	177	98	7	9732	17	0.852	0.0384	1.8%	0.0177	0.022012363	0.1007	3.3%	
BR3	jn29a043	ok	32	229	5	190	105	7	9860	20	0.851	0.0373	2.0%	0.0159	0.027440041	0.0755	4.2%	
BR3	jn29a041	ok	32	230	4	304	157	11	11143	9	0.851	0.0373	1.5%	0.0145	0.021961323	0.0697	2.8%	
BR3	jn29a033	ok	32	232	4	216	110	8	10307	14	0.851	0.0367	1.7%	0.0121	0.02369698	0.0520	4.0%	
BR3	jn29a037	ok	32	236	4	397	320	17	10116	19	0.852	0.0389	1.6%	0.0151	0.018484155	0.0851	2.5%	
BR3	jn29a040	ok	32	236	2	1525	854	54	10697	4	0.851	0.0373	1.0%	0.0116	0.014757051	0.0517	1.4%	
BR3	jn29a045	ok	32	239	5	131	60	5	9491	16	0.851	0.0377	2.0%	0.0122	0.029890774	0.0504	5.2%	
BR3	jn29a035	ok	32	239	4	215	119	8	10297	17	0.851	0.0378	1.7%	0.0123	0.026522694	0.0534	3.9%	
BR3	jn29a038	ok	32	239	4	255	108	9	9986	12	0.852	0.0382	1.8%	0.0134	0.024744942	0.0590	3.5%	
BR3	jn29a032	ok	32	263	5	281	157	12	10376	11	0.853	0.0418	1.9%	0.0156	0.021800007	0.0533	2.9%	
BR3	jn29a046	ok	32	349	5	241	182	14	9499	9	0.859	0.0558	1.4%	0.0175	0.017726442	0.0577	3.0%	
BR3	jn29a034	ok	32	365	5	458	324	27	11134	7	0.860	0.0583	1.3%	0.0188	0.016687643	0.0541	1.8%	
BR3	jn29a036	ok	32	388	5	467	293	29	10976	12	0.862	0.0620	1.4%	0.0207	0.015217751	0.0555	1.9%	
BR317																		
2012-019	JA18A119	metamict, DO NOT USE	32	201	4	3071	5192	105	8767	14	0.849	0.0329	2.0%	0.0100	1.4%	0.0788	1.7%	Mean = 234.9±1.5 [0.65%] 95% conf. Wtd by data-pt errs only, 0 of 13 rej. MSWD = 0.66, probability = 0.79
2012-019	JA18A120	Common Pb in middle	32	230	3	739	580	25	8546	10	0.851	0.0369	1.5%	0.0120	1.8%	0.0616	3.1%	
2012-019	JA18A118	ok	32	230	3	658	321	24	10793	4	0.851	0.0366	1.1%	0.0122	1.8%	0.0554	2.0%	
2012-019	JA18A117	Pb loss? @ beginning	32	233	3	609	390	24	11284	9	0.851	0.0378	1.3%	0.0135	2.2%	0.0710	2.9%	
2012-019	JA18A123	Common Pb beginning & middle, small integration	32	234	5	598	362	24	9159	4	0.851	0.0379	2.1%	0.0143	2.8%	0.0700	4.7%	
2012-019	JA18A122	ok	32	235	3	703	291	26	10937	2	0.851	0.0370	1.1%	0.0123	1.7%	0.0502	1.9%	
2012-019	JA18A125	ok	32	235	2	734	589	27	8382	9	0.851	0.0371	1.0%	0.0122	1.5%	0.0510	1.8%	
2012-019	JA18A114	ok	32	235	2	1413	707	52	12412	6	0.851	0.0375	1.1%	0.0118	1.6%	0.0598	1.5%	
2012-019	JA18A112	ok	32	236	2	805	404	30	10656	4	0.851	0.0374	1.0%	0.0119	1.6%	0.0543	2.0%	
2012-019	JA18A113	ok	32	236	3	363	239	13	8228	17	0.851	0.0373	1.4%	0.0124	1.9%	0.0520	2.6%	
2012-019	JA18A115	ok	32	236	3	569	265	21	10881	3	0.851	0.0374	1.3%	0.0118	1.8%	0.0536	2.0%	
2012-019	JA18A124	ok	32	237	2	799	525	29	9331	5	0.851	0.0374	1.0%	0.0122	1.5%	0.0514	1.8%	
2012-019	JA18A126	Common Pb @ end	32	238	3	558	215	20	10794	4	0.851	0.0376	1.3%	0.0133	2.1%	0.0520	2.7%	
2012-019	JA18A111	ok	32	238	3	748	538	28	8621	4	0.851	0.0378	1.2%	0.0119	1.5%	0.0533	1.8%	
2012-019	JA18A121	ok	32	241	2	863	488	33	10429	3	0.852	0.0381	1.0%	0.0126	1.5%	0.0524	1.6%	
2012-019	JA18A116	Variable U/Pb - older domain @ end	32	242	4	555	351	20	8141	7	0.852	0.0383	1.8%	0.0127	2.2%	0.0517	2.9%	
BR326																		
326	oc12b050	Common Pb @ end	32	**231**	**3**	759	475	29	9208	16	0.851	0.0369	1.5%	0.0129	2.2%	0.0604	2.4%	Mean = 234.4±2.2 [0.95%] 95% conf. Wtd by data-pt errs only, 0 of 6 rej. MSWD = 0.58, probability = 0.71
326	oc12b051	ok	32	**232**	**3**	769	471	29	10201	4	0.851	0.0368	1.2%	0.0110	2.1%	0.0525	2.4%	
326	oc12b046	Through grain @ end	32	**234**	**3**	965	486	35	11161	4	0.851	0.0370	1.2%	0.0106	2.3%	0.0515	2.4%	
326	oc12b059	ok	32	**235**	**3**	587	374	23	8764	12	0.851	0.0371	1.2%	0.0120	2.0%	0.0517	2.5%	
326	oc12b055	ok	32	**236**	**3**	737	461	29	9659	7	0.851	0.0375	1.1%	0.0114	1.9%	0.0539	2.0%	
326	oc12b053	ok	32	**236**	**2**	1001	346	36	11681	3	0.851	0.0373	1.0%	0.0119	2.0%	0.0508	1.8%	Mean = 242.0±2.2 [0.90%] 95% conf. Wtd by data-pt errs only, 0 of 7 rej. MSWD = 0.76, probability = 0.61
326	oc12b052	ok	32	**239**	**3**	737	339	28	10587	5	0.851	0.0378	1.1%	0.0116	2.0%	0.0514	1.9%	
326	oc12b060	Common Pb @ begin	32	**241**	**3**	565	277	23	10618	13	0.852	0.0382	1.4%	0.0124	2.4%	0.0538	2.7%	
326	oc12b054	ok	32	**241**	**3**	682	363	27	9494	6	0.851	0.0381	1.3%	0.0124	2.1%	0.0502	2.2%	
326	oc12b056	Minor common Pb	32	**242**	**3**	1302	886	54	12162	8	0.852	0.0391	1.1%	0.0100	1.8%	0.0689	1.3%	
326	oc12b057	ok	32	**242**	**3**	634	188	23	11205	3	0.852	0.0382	1.2%	0.0123	2.2%	0.0505	2.0%	
326	oc12b048	ok	32	**245**	**3**	643	230	24	10785	3	0.852	0.0387	1.1%	0.0124	2.2%	0.0528	2.1%	
326	oc12b058	reverse discordant @ end	32	**247**	**4**	731	348	28	9540	3	0.852	0.0390	1.4%	0.0124	2.3%	0.0501	2.4%	
326	oc12b049	Common Pb and Pb loss - Use w/ caution	32	676	13	418	587	52	10323	18	0.887	0.1188	1.9%	0.0150	2.6%	0.1191	1.0%	
326	oc12b047	Metmaict - DO NOT USE	32	175	2	7032	4302	208	15000	26	0.847	0.0284	1.3%	0.0076	1.8%	0.0755	1.1%	
BB6																		
2012-040	JA18A094	Common Pb beginning & end, small integration use w/ caution	32	237	4	650	836	25	10282	88	0.851	0.0376	1.8%	0.0106	3.1%	0.0558	5.9%	Mean = 273.8±7.6 [2.8%] 95% conf. Wtd by data-pt errs only, 0 of 4 rej. MSWD = 1.2, probability = 0.29
2012-040	JA18A105	Older (272 +/-3Ma) beginning & middle	32	242	3	1662	2867	68	10173	405	0.852	0.0392	1.4%	0.0121	2.2%	0.0703	3.0%	
2012-040	JA18A100	Common Pb @ beginniing, small integration	32	266	5	935	962	41	10407	5	0.853	0.0424	1.8%	0.0133	2.2%	0.0569	2.8%	
2012-040	JA18A099	Minor Common Pb, Variable U/Pb	32	274	4	508	519	24	10542	8	0.855	0.0453	1.5%	0.0165	1.7%	0.0832	2.4%	
2012-040	JA18A098	Variable U/ Pb	32	276	4	297	177	13	11789	7	0.854	0.0441	1.4%	0.0144	2.1%	0.0575	2.8%	Mean = 292.2±3.1 [1.1%] 95% conf. Wtd by data-pt errs only, 0 of 8 rej. MSWD = 0.87, probability = 0.53
2012-040	JA18A092	Common Pb throughout	32	277	5	187	110	9	10338	6	0.855	0.0454	1.7%	0.0193	2.7%	0.0787	3.8%	
2012-040	JA18A104	Common Pb in middle, small integration	32	287	7	1637	1630	70	9409	13	0.855	0.0467	2.4%	0.0164	1.7%	0.0740	2.6%	
2012-040	JA18A097	Common Pb @ beginning	32	289	4	474	432	23	10567	8	0.855	0.0464	1.3%	0.0150	1.8%	0.0627	2.5%	
2012-040	JA18A103	ok	32	290	3	404	357	19	10023	41	0.855	0.0464	1.2%	0.0157	1.6%	0.0609	2.1%	
2012-040	JA18A106	Common Pb @ middle	32	291	5	376	310	16	10032	12	0.855	0.0465	1.9%	0.0145	3.6%	0.0589	4.2%	
2012-040	JA18A101	Variable U/ Pb	32	291	4	581	545	27	10590	16	0.855	0.0466	1.4%	0.0141	1.8%	0.0591	2.3%	
2012-040	JA18A096	Variable U/Pb	32	296	4	341	303	16	10503	106	0.856	0.0482	1.3%	0.0171	2.0%	0.0713	2.1%	
2012-040	JA18A095	Common Pb @ end	32	297	8	208	162	10	10222	10	0.856	0.0497	2.8%	0.0180	4.3%	0.0936	5.5%	
2012-040	JA18A102	ok	32	299	4	248	178	12	10760	5	0.855	0.0475	1.5%	0.0162	2.0%	0.0537	3.5%	
2012-040	JA18A093	Common Pb inclusion in middle, smal integration, use w/ caution	32	311	11	638	445	28	9877	5	0.857	0.0500	3.5%	0.0163	4.4%	0.0626	7.3%	
BB11																		
BB11	jn29b012	ok	32	278	3	1569	1457	74	9578	10	0.854	0.0442	1.1%	0.0136	1.3%	0.0542	1.1%	Mean = 286.1±3.6 [1.3%] 95% conf. Wtd by data-pt errs only, 0 of 11 rej. MSWD = 1.8, probability = 0.058
BB11	jn29b010	Pb loss at end	32	278	5	734	731	41	9335	19	0.855	0.0468	1.7%	0.0186	3.51%	0.0982	4.8%	
BB11	jn29b017	ok	32	285	4	421	280	19	9697	9	0.855	0.0453	1.3%	0.0135	1.78%	0.0541	2.1%	
BB11	jn29b005	slight Pb loss at beginning	32	285	4	396	359	20	8784	9	0.855	0.0455	1.5%	0.0135	1.65%	0.0561	2.7%	
BB11	jn29b021	Pb loss at end	32	286	3	2102	2677	109	8783	22	0.855	0.0457	1.2%	0.0146	1.36%	0.0598	1.6%	
BB11	jn29b008	through crysal at end	32	287	4	1438	1428	68	9061	12	0.855	0.0458	1.4%	0.0137	1.40%	0.0548	1.9%	
BB11	jn29b006	ok	32	289	3	829	612	39	8944	7	0.855	0.0460	1.1%	0.0143	1.40%	0.0528	1.4%	
BB11	jn29b007	ok	32	291	5	171	78	7	9457	7	0.855	0.0465	1.7%	0.0153	2.86%	0.0582	3.7%	
BB11	jn29b009	Pb inclusion in middle, Pb loss at end	32	292	12	704	476	36	8393	7	0.856	0.0479	3.9%	0.0184	11.45%	0.0787	14.6%	
BB11	jn29b013	ok	32	293	3	1390	1422	71	9443	20	0.855	0.0469	1.1%	0.0148	1.34%	0.0593	1.3%	
BB11	jn29b016	complex at beginning	32	294	10	140	73	7	10449	10	0.856	0.0481	3.4%	0.0200	3.68%	0.0748	4.4%	
BB11	jn29b018	ok	32	297	5	122	52	5	10191	17	0.856	0.0477	1.6%	0.0162	2.87%	0.0619	4.0%	
BB11	jn29b011	ok	32	297	4	196	125	9	9554	12	0.855	0.0473	1.5%	0.0149	2.05%	0.0532	3.1%	
BB11	jn29b019	older core in middle	32	299	17	434	279	18	9781	6	0.856	0.0477	5.7%	0.0148	4.08%	0.0576	6.2%	

Sample No.(& analysis number)	Lab ID	Comments	Spot size micron	207 cor $^{206}Pb/^{238}U$ age	0 +/-1 ster	U ppm	Th ppm	Pb ppm	Hf ppm	Ti ppm	Common Pb at age of zirc	$^{206}Pb/^{238}U$ ratio	+/-1 RSE	$^{208}Pb/^{232}Th$ ratio	+/-1 RSE	$^{207}Pb/^{206}Pb$ ratio	+/-1 RSE	Comments
BB11	jn29b015	ok	32	299	3	1209	1048	60	9171	8	0.855	0.0475	1.1%	0.0146	1.29%	0.0518	1.2%	
BB11	jn29b014	ok	32	299	3	661	457	31	9716	13	0.856	0.0475	1.2%	0.0148	1.41%	0.0530	1.7%	
BB11	jn29b020	ok	32	304	3	1222	1055	61	9387	6	0.856	0.0482	1.1%	0.0146	1.28%	0.0513	1.1%	
S/6a3																		
2012-353	JL11A406	Pb loss @ high U part, Common Pb inclusion @ end	32	271	5	805	567	31	11404	10	0.854	0.0436	1.8%	0.0135	1.8%	0.0627	2.7%	Mean = 286.0±2.0 [0.71%] 95% conf. Wtd by data-pt errs only, 0 of 10 rej. MSWD = 1.12, probability = 0.34
2012-353	JL11A408	ok	32	272	3	338	277	15	9023	12	0.854	0.0435	1.2%	0.0139	1.6%	0.0594	2.2%	
2012-353	JL11A417	ok	32	**283**	**3**	505	345	22	10573	6	0.854	0.0448	1.1%	0.0138	1.4%	0.0521	1.7%	
2012-353	JL11A409	ok	32	**283**	**3**	893	685	40	11209	8	0.854	0.0451	0.9%	0.0144	1.3%	0.0571	1.2%	
2012-353	JL11A413	ok	32	**283**	**3**	234	115	10	10599	68	0.854	0.0448	1.2%	0.0140	1.8%	0.0518	2.4%	
2012-353	JL11A405	Pb loss @ common Pb in middle	32	**283**	**4**	388	200	16	11356	4	0.854	0.0451	1.3%	0.0135	2.1%	0.0554	3.2%	
2012-353	JL11A416	ok	32	**287**	**3**	633	325	29	11675	6	0.855	0.0457	1.0%	0.0143	1.6%	0.0545	1.9%	
2012-353	JL11A419	ok	32	**288**	**3**	274	138	12	10878	5	0.855	0.0457	1.1%	0.0144	1.9%	0.0539	2.5%	
2012-353	JL11A418	Fe- Common Pb @ end	32	**288**	**3**	409	197	18	10545	7	0.855	0.0461	1.2%	0.0159	1.7%	0.0594	2.3%	
2012-353	JL11A410	ok	32	**288**	**3**	366	185	17	11158	3	0.855	0.0459	1.1%	0.0146	1.7%	0.0551	1.8%	
2012-353	JL11A407	ok	32	**291**	**4**	303	161	13	11043	6	0.855	0.0462	1.3%	0.0145	1.8%	0.0530	2.6%	
2012-353	JL11A412	Older @ end	32	**294**	**5**	162	88	7	8763	8	0.855	0.0465	1.6%	0.0148	2.1%	0.0500	3.4%	
2012-353	JL11A414	ok	32	295	4	151	81	7	10849	6	0.855	0.0467	1.5%	0.0152	2.1%	0.0503	3.3%	
2012-353	JL11A411	ok	32	295	3	375	217	17	11527	6	0.855	0.0469	1.1%	0.0148	1.7%	0.0534	2.0%	
2012-353	JL11A415	Older @ end	32	296	5	351	193	15	11265	4	0.855	0.0470	1.5%	0.0142	2.3%	0.0522	4.0%	
BK10																		
2012-354	JL11A421	Common Pb @ beginning	32	**250**	**4**	426	435	18	9005	11	0.853	0.0411	1.4%	0.0147	1.8%	0.0826	2.2%	Mean = 256.3±8.7 [3.4%] 95% conf. Wtd by data-pt errs only, 0 of 5 rej. MSWD = 1.7, probability = 0.14
2012-354	JL11A423	Fe-Ti inclusion throughout	32	**260**	**5**	101	52	5	9683	945	0.854	0.0452	2.0%	0.0270	2.7%	0.1238	3.4%	
2012-354	JL11A432	through grain @ end	32	**262**	**8**	151	100	6	8950	8	0.855	0.0461	2.9%	0.0261	4.1%	0.1329	5.9%	
2012-354	JL11A429	common Pb middle to end. Small interval	32	**265**	**6**	292	209	12	9383	11	0.854	0.0452	2.2%	0.0214	3.4%	0.1083	3.6%	
2012-354	JL11A422	older @ beginning	32	**261**	**8**	137	76	6	8781	7	0.854	0.0438	3.0%	0.0217	3.8%	0.0981	5.2%	Mean = 288.3±4.0 [1.4%] 95% conf. Wtd by data-pt errs only, 0 of 8 rej. MSWD = 1.6, probability = 0.14
2012-354	JL11A433	Common Pb in middle	32	**275**	**5**	218	172	10	9101	10	0.855	0.0462	1.9%	0.0191	2.9%	0.0966	3.9%	
2012-354	JL11A430	Common Pb middle to end	32	**281**	**8**	150	81	7	9109	10	0.856	0.0489	2.6%	0.0318	7.3%	0.1231	5.4%	
2012-354	JL11A431	older @ end	32	**287**	**4**	246	158	10	9249	7	0.855	0.0458	1.5%	0.0148	2.2%	0.0567	4.0%	
2012-354	JL11A434	common Pb @ end	32	**287**	**4**	315	185	14	10089	5	0.855	0.0466	1.5%	0.0173	1.9%	0.0684	3.1%	
2012-354	JL11A424	ok	32	**288**	**2**	3300	4402	148	9770	11	0.855	0.0459	0.8%	0.0143	1.1%	0.0560	0.7%	
2012-354	JL11A425	ok	32	**288**	**4**	135	87	6	8277	11	0.855	0.0460	1.5%	0.0145	2.2%	0.0567	3.5%	
2012-354	JL11A427	ok	32	**292**	**3**	449	299	20	10359	8	0.855	0.0466	1.0%	0.0154	1.6%	0.0564	1.9%	
2012-354	JL11A426	Older @ beginning	32	**295**	**5**	159	105	8	9668	7	0.855	0.0471	1.7%	0.0145	2.7%	0.0556	4.3%	
2012-354	JL11A428	DO NOT USE - Common Pb, older @ end, Fe-Ti inclusions.	32	225	7	188	245	8	9088	1049	0.855	0.0457	2.9%	0.0229	2.3%	0.2289	3.4%	
318																		
318	oc12b069	ok	32	240	3	942	736	38	9642	6	0.851	0.0380	1.1%	0.0110	1.9%	0.0523	1.8%	Mean = 294.0±4.0 [1.4%] 95% conf. Wtd by data-pt errs only, 0 of 12 rej. MSWD = 4.1, probability = 0.000
318	oc12b075	Through grain @ end	32	**283**	**3**	1124	896	52	11539	12	0.855	0.0452	1.1%	0.0116	2.0%	0.0575	1.8%	
318	oc12b070	ok	32	**287**	**3**	573	414	28	9865	3	0.855	0.0458	1.1%	0.0137	1.9%	0.0555	2.0%	
318	oc12b067	ok	32	**289**	**3**	546	242	25	10618	3	0.855	0.0458	1.0%	0.0140	2.1%	0.0519	2.0%	
318	oc12b080	ok	32	**290**	**3**	520	333	24	11249	6	0.855	0.0463	1.2%	0.0124	2.2%	0.0553	2.6%	
318	oc12b071	ok	32	**292**	**3**	439	211	20	10937	4	0.855	0.0463	1.1%	0.0139	2.2%	0.0531	2.3%	
318	oc12b079	Through grain @ end	32	**294**	**4**	685	604	34	8560	9	0.855	0.0467	1.2%	0.0142	1.9%	0.0519	2.9%	
318	oc12b077	ok	32	**294**	**2**	1318	1049	66	9961	10	0.855	0.0468	0.9%	0.0131	1.7%	0.0533	1.4%	
318	oc12b072	ok	32	**296**	**3**	359	172	17	10413	4	0.855	0.0471	1.1%	0.0145	2.1%	0.0536	2.7%	
318	oc12b068	ok	32	**297**	**3**	703	431	35	11603	5	0.855	0.0472	1.0%	0.0144	1.8%	0.0546	1.7%	
318	oc12b076	ok	32	**300**	**3**	1425	1299	76	9497	26	0.856	0.0482	0.9%	0.0137	1.7%	0.0625	1.4%	
318	oc12b066	ok	32	**303**	**4**	479	217	23	10892	5	0.856	0.0482	1.2%	0.0154	2.1%	0.0522	2.1%	
318	oc12b074	ok	32	**305**	**3**	564	295	28	10705	6	0.856	0.0484	1.1%	0.0148	1.9%	0.0521	2.1%	
318	oc12b073	Mixing age domains 335±29 & 1678±64 Ma	32			715	213	74	11641	6	0.879	0.1021	4.3%	0.0199	2.3%	0.0778	1.8%	
318	oc12b078	Metamict - Use w/ caution	32	270	3	2895	3611	138	10267	54	0.854	0.0433	1.1%	0.0104	1.7%	0.0604	1.4%	

Appendix IV: XRF whole-rock geochemical results

Sample	**BK01**	**BK01(a)**	**BK02***	**BK03***	**BK4**	**KIRI3**	**KNN2**	**KIRI2/3**	**BKHOST-2**	**BK7**	**BK11**	**BK11a**	**MB-TC-S5**	**MB-TC-BK**	**BK12**	**Tasik Chini-1**	**HR1**
Rock Type	Rhyolite	Rhyolite	Rhyolite	Rhyolite	Rhyolite	Rhyolite	Rhyolite	Rhyolite	Rhyolite	Rhyolite	Rhyolite	Rhyolite	Rhyolite	Rhyolite	Rhyolite	Rhyolite	Rhyolite
Location	Bukit Ketaya	Bukit Ketaya	Bukit Ketaya	Bukit Ketaya	Bukit Ketaya	Bukit Ketaya	Bukit Ketaya	Bukit Ketaya	Bukit Ketaya	Bukit Ketaya	Bukit Ketaya	Bukit Ketaya	Bukit Ketaya	Bukit Ketaya	Bukit Ketaya	Bukit Ketaya	Bukit Ketaya
(wt%)																	
SiO_2	70.95	70.93	90.12	90.18	96.10	88.75	83.8	88.94	87.61	77.09	63.84	63.99	93.34	88.69	73.06	62.81	83.47
TiO_2	0.48	0.47	0.30	0.23	0.42	0.258	0.351	0.266	0.156	0.32	0.61	0.60	0.24	0.26	0.33	0.39	0.313
Al_2O_3	20.80	20.80	3.67	6.78	1.43	7.97	9.93	7.93	3.86	0.29	15.87	15.88	0.20	0.18	0.31	0.26	7.72
Fe_2O_3	2.70	2.70	4.22	0.43	0.93	0.21	2.13	0.21	5.81	1.15	8.88	8.88	3.60	6.65	10.36	31.45	3.36
MnO	<0.01	<0.01	0.00	0.00	<0.01	0	0	0	0.011	0.01	0.01	0.01	<0.01	<0.01	0.01	0.01	0.01
MgO	0.09	0.11	0.03	0.04	0.01	0.03	0.05	0.03	0.07	0.01	0.10	0.09	0.02	0.03	0.01	0.01	0.32
CaO	0.01	0.01	0.01	0.01	0.01	0	0	0	0.01	0.01	0.01	0.01	0.01	0.01	0.01	0.03	0
Na_2O	0.24	0.24	0.15	0.26	0.08	0.25	0.31	0.25	0.19	0.10	0.43	0.43	0.03	0.03	0.09	0.03	0.09
K_2O	0.57	0.57	0.52	0.59	0.16	0.39	0.85	0.39	0.58	0.03	0.51	0.52	0.04	0.04	0.05	0.02	2.18
P_2O_5	0.03	0.03	0.02	0.02	0.03	0.025	0.017	0.025	0.033	0.01	0.03	0.04	0.01	0.01	0.01	0.02	0.026
BaO	0.145	0.144	0.041	0.062	0.013				0.641	12.93	0.748	0.751	0.17	0.07	10.16	2.91	
CuO													0.130	0.115			
ZnO	0.000	0.000	0.000	0.000	0.000					0.000	0.007	0.007	0.002	0.001	0.005		
PbO	0.002	0.002	0.002	0.001	0.002					0.011	0.590	0.587	0.008	0.005	0.002		
Loss inc.S-	3.84	3.84	1.00	1.52	0.51	1.63	2.08	1.64	1.01	1.07	8.08	8.01	2.2	3.74	0.70	0.46	1.96
Total	99.86	99.84	100.07	100.12	99.68	99.51	99.52	99.68	99.98	93.02	99.70	99.78	99.96	99.79	95.10	98.37	99.45
S	0.01	0.01	0.01	0.01	0.02	<0.01	<0.01	<0.01	0.07	2.81	7.52	7.53	2.78	5.33	2.18	0.67	0.39
(ppm)																	
Sc	10.0	11.0	7.8	6.2	6.3	7.5	7.2	6	3.2	2.9	9.7	9.2	<1.5	2	3.0	3	15.8
Ba	1300	1291	364	553	121	515	504	515	5200	116000	6700	6730	1498	612	91000	26060	1581
V	26	26	<3	4	8	9	14.1	8.7	9.8	15	23	23	<3	<3	19	12	<3
Cr	2.6	2.5	1.5	1.7	3.3	1.2	<1	1.3	5.6	<2	16.8	15.9	2	1	<2	53	1.3
Ni	2	2	2	4	3	2.1	2.3	1.7	4.1	11	9	10	15	14	8	3	3.5
Cu	10	10	15	15	35	4.9	4.2	4.1	43.8	79	293	291	1073	920	14	94	20.9
Zn	1	2	2	1	1	<1	1.4	<1	412	4	59	58	18	9	8	9	5.8
As	<3	2	4	3	4	4.8	<3	3.8	25.9	10	33	30	34	55	<3	23	51.8
Rb	20	20	25	25	6.9	18.1	39.8	18	17.5	1.9	14	14	2	2	1.7	1.3	70.1
Sr	99	99	67	52	58	87.4	51.6	88.0	53.4	1108	126	125	19	6	751	236	45.8
Y	29.2	30.0	14.1	13.7	12.8	18.3	25.5	18.6	12.3	6.4	28.4	28.3	18	23	11.2	13	25.3
Zr	471	471	280	234	278	267	337	267	169	82	282	278	122	161	205	233	151
Nb	16.9	17.0	10.5	9.5	9.6	11.0	15.4	10.9	5.0	2.0	10.2	10.3	5	6	2.5	8.5	6.3
Sn	12	12	7	2	19	6.8	19.7	5.5	5.6	237	25	26	4	13	52	52	3
Pb	23	23	21	11	18	20.2	9.3	19.9	384	102	5480	5450	77	42	16	46	106
Bi	9	7	4	<2	3	<2	5.8	<2	<2	19	3	3	3	7	<2	4	<2
U	5.3	4.3	4.0	2.9	5.6	3.6	3.4	3.2	<2	<4	7.3	7.2	3	3	<4	3	<2
Th	18.2	18.8	11.3	7.7	9.8	10.9	12.9	10.5	2.9	<4	9.7	9.5	5	7	BDL	5	5.0
La	47	49	18	22	29	21.4	30.1	21.6	9.0	BDL	4	7	7	8	BDL	30	16.3
Ce	103	103	34	46	63	49.6	72.5	51.2	12.7	BDL	BDL	BDL	19	20	BDL	30	35.6
Nd	47	46	12	16	28	15.3	28.7	15.7	<4	BDL	BDL	BDL	8	9	BDL	29	13.8
FeO (wt%)	2.42	2.43	3.80	0.39	0.84	0.19	1.92	0.19	5.23	1.03	7.99	7.99	3.24	5.98	9.32	28.30	3.02
AI(Ishikawa)	72.53	73.19	77.17	69.45	66.31	62.69	74.38	62.69	76.47	25.72	58.08	58.09	60.12	63.64	38.42	33.10	96.53
CCPI(Large)	75.61	75.97	85.14	33.36	78.31	25.49	62.90	25.49	87.31	88.64	89.67	89.56	97.89	98.85	98.58	99.82	59.56
GI (Ghandi)	3.43	3.50	6.37	0.55	4.01	0.38	1.88	0.38	7.64	8.67	9.63	9.52	51.54	95.43	76.95	631.72	1.62
Molar ratios																	
Na_2O/Al_2O	0.01	0.01	0.04	0.04	0.05	0.03	0.03	0.03	0.05	0.36	0.03	0.03	0.15	0.17	0.28	0.12	0.01
K_2O/Al_2O	0.03	0.03	0.14	0.09	0.11	0.05	0.09	0.05	0.15	0.10	0.03	0.03	0.20	0.22	0.16	0.08	0.28
Fe_2O_3/Al_20_3	0.13	0.13	1.15	0.06	0.65	0.03	0.21	0.03	1.51	4.03	0.56	0.56	17.90	36.94	33.94	120.96	0.44
MgO/Al_2O_3	0.00	0.01	0.01	0.01	0.01	0.00	0.01	0.00	0.02	0.03	0.01	0.01	0.10	0.17	0.03	0.04	0.04

Appendix V: SWIR results

Sample	Lithology	SWIR identified Min1 sTSAS	SWIR identified Min2 sTSAS	TSG interpreted mineral
Bukit Botol				
BB2enew.000	orehorizon unit	Muscovitic Illite	NULL	muscovite
BB2enew.001	orehorizon unit	Muscovitic Illite	NULL	muscovite
BB2enew.002	orehorizon unit	NULL	NULL	
BB6.001	orehorizon unit	Paragonite	NULL	paragonite
BB6.002	orehorizon unit	Paragonite	NULL	paragonite
BB11.000	orehorizon unit	Paragonitic Illite	Montmorillonite	paragonite
BB11.001	orehorizon unit	Paragonitic Illite	Montmorillonite	paragonite
BB11.002	orehorizon unit	Paragonitic Illite	NULL	muscovite
BB11.003	orehorizon unit	Paragonitic Illite	Montmorillonite	muscovite
BB11.004	orehorizon unit	Paragonitic Illite	Montmorillonite	muscovite
BB11.005	orehorizon unit	Paragonitic Illite	Montmorillonite	muscovite
BB24.001	orehorizon unit	Paragonite	Kaolinite PX	paragonite
BB24.002	orehorizon unit	Paragonite	Kaolinite PX	paragonite
BB26.001	orehorizon unit	muscovite	NULL	muscovite
BB26.002	orehorizon unit	Muscovite	NULL	muscovite
BB27new.001	orehorizon unit	Muscovite	NULL	muscovite
BB27new.002	orehorizon unit	Muscovite	NULL	muscovite
BB27new.003	orehorizon unit	NULL	NULL	
BB28anew.001	orehorizon unit	Paragonite	NULL	paragonite
BB28anew.002	orehorizon unit	Paragonite	NULL	paragonite
BB30.000	orehorizon unit	Paragonite	NULL	paragonite
BB30.001	orehorizon unit	Paragonite	NULL	paragonite
BB40.000	orehorizon unit	Paragonitic Illite	Kaolinite PX	
BB40.001	orehorizon unit	Paragonitic Illite	Montmorillonite	
BB40.002	orehorizon unit	Paragonitic Illite	Montmorillonite	
BB3.001	footwall unit	Muscovitic Illite	NULL	phengite
BB3.002	footwall unit	Muscovitic Illite	NULL	phengite

Sample	Lithology	SWIR identified Min1 sTSAS	SWIR identified Min2 sTSAS	TSG interpreted mineral
BB3anew.000	footwall unit	NULL	NULL	
BB3anew.001	footwall unit	Muscovite	NULL	muscovite
BB3anew.002	footwall unit	NULL	NULL	muscovite
BB3b.001	footwall unit	Muscovite	NULL	phengite
BB3b.002	footwall unit	Muscovite	NULL	phengite
BB5anew.001	footwall unit	Muscovite	NULL	
BB5anew.002	footwall unit	Muscovitic Illite	NULL	
BB9anew.001	footwall unit	Muscovite	NULL	muscovite
BB9anew.002	footwall unit	Muscovite	NULL	muscovite
BB9new.001	footwall unit	Muscovite	NULL	muscovite
BB10a.001	footwall unit	Muscovite	NULL	muscovite
BB10a.002	footwall unit	Muscovite	NULL	muscovite
MBTCS2.001	footwall unit	Muscovite	NULL	
MBTCS2new.001	footwall unit	Muscovite	NULL	muscovite
MBTCS2new.002	footwall unit	Muscovite	NULL	
S3.000	footwall unit	Muscovite	NULL	
S3.001	footwall unit	Muscovite	NULL	muscovite
S3.002	footwall unit	Muscovite	NULL	muscovite
S4.000	footwall unit	Muscovitic Illite	NULL	phengite
S4.001	footwall unit	Muscovitic Illite	NULL	phengite
S4new.000	footwall unit	NULL	NULL	
S4new.001	footwall unit	Muscovitic Illite	NULL	muscovite
S4new.002	footwall unit	Muscovitic Illite	NULL	
S4new.003	footwall unit	Muscovitic Illite	NULL	
SQ2.000	footwall unit	NULL	NULL	
SQ2.001	footwall unit	Muscovite	NULL	muscovite
SQ2.002	footwall unit	Muscovite	NULL	muscovite
SQS1.000	footwall unit	NULL	NULL	
SQS1.001	footwall unit	Muscovite	NULL	muscovite

Sample	Lithology	SWIR identified Min1 sTSAS	SWIR identified Min2 sTSAS	TSG interpreted mineral
SQS1.002	footwall unit	Muscovite	NULL	muscovite
SQS1.003	footwall unit	Muscovite	NULL	muscovite
SQS2.000	footwall unit	NULL	NULL	
SQS2.001	footwall unit	Muscovite	NULL	
SQS2.002	footwall unit	Muscovite	NULL	muscovite
SQS2.003	footwall unit	Muscovite	NULL	muscovite
SQS2.004	footwall unit	Muscovite	NULL	muscovite
SQS3.000	footwall unit	Muscovite	NULL	muscovite
SQS3.001	footwall unit	Muscovite	NULL	muscovite
SQS3.002	footwall unit	Muscovite	NULL	muscovite
SQS3.003	footwall unit	Muscovite	NULL	muscovite
SQS3new.000	footwall unit	NULL	NULL	
SQS3new.001	footwall unit	Muscovitic Illite	NULL	phengite
SQS3new.002	footwall unit	Muscovite	NULL	muscovite
SQS4.000	footwall unit	Muscovitic Illite	NULL	muscovite
SQS4.001	footwall unit	Muscovite	NULL	muscovite
SQS4.002	footwall unit	Muscovite	NULL	muscovite
SQS4.003	footwall unit	Muscovitic Illite	NULL	phengite
TChini-2.000	footwall unit	NULL	NULL	
TChini-2.001	footwall unit	Muscovite	NULL	muscovite
TChini-2.002	footwall unit	Muscovite	NULL	muscovite
TChini-2new.000	footwall unit	NULL	NULL	
TChini-2new.001	footwall unit	Muscovite	NULL	muscovite
TChini-2new.002	footwall unit	Muscovite	NULL	muscovite
TChini-2new.003	footwall unit	Muscovite	NULL	muscovite
TChini-2new.004	footwall unit	Muscovite	NULL	muscovite
Bukit Ketaya				
BK01.001	orehorizon unit	Pyrophyllite	Muscovite	pyrophyllite

Sample	Lithology	SWIR identified Min1 sTSAS	SWIR identified Min2 sTSAS	TSG interpreted mineral
BK01.002	orehorizon unit	Aspectral	NULL	
BK01_01.000	orehorizon unit	Pyrophyllite	NULL	pyrophyllite
BK01_01.001	orehorizon unit	NULL	NULL	
BK02.000	orehorizon unit	NULL	NULL	
BK02.001	orehorizon unit	Aspectral	NULL	
BK02-1.000	orehorizon unit	Muscovite	NULL	muscovite
BK02-1.001	orehorizon unit	Paragonite	NULL	muscovite
BK02-1.002	orehorizon unit	Aspectral	NULL	
BK02new.000	orehorizon unit	Muscovite	NULL	muscovite
BK02new.001	orehorizon unit	NULL	NULL	
BK03.000	orehorizon unit	NULL	NULL	
BK03.001	orehorizon unit	Muscovitic Illite	Pyrophyllite	pyrophyllite
BK03.002	orehorizon unit	Muscovitic Illite	Pyrophyllite	pyrophyllite
BK03.003	orehorizon unit	Muscovite	Pyrophyllite	pyrophyllite
BK03.004	orehorizon unit	Paragonitic Illite	Pyrophyllite	pyrophyllite
BK03.005	orehorizon unit	Paragonite	Pyrophyllite	pyrophyllite
BK03_03.000	orehorizon unit	Pyrophyllite	Muscovitic Illite	pyrophyllite
BK03_03.001	orehorizon unit	Pyrophyllite	Muscovitic Illite	pyrophyllite
BK03new.000	orehorizon unit	Paragonite	Pyrophyllite	pyrophyllite
BK03new.001	orehorizon unit	Paragonite	Pyrophyllite	pyrophyllite
BK03new.002	orehorizon unit	Muscovite	Pyrophyllite	pyrophyllite
BK03new.003	orehorizon unit	Paragonitic Illite	Pyrophyllite	pyrophyllite
BK03new.004	orehorizon unit	Paragonite	Pyrophyllite	pyrophyllite
BK04.000	orehorizon unit	NULL	NULL	
BK04.001	orehorizon unit	Kaolinite PX	NULL	muscovite
BK04.002	orehorizon unit	Kaolinite WX	NULL	muscovite
BK04.003	orehorizon unit	Aspectral	NULL	
BK04.004	orehorizon unit	NULL	NULL	
BK04.005	orehorizon unit	Aspectral	NULL	

Sample	Lithology	SWIR identified Min1 sTSAS	SWIR identified Min2 sTSAS	TSG interpreted mineral
BK04_04.000	orehorizon unit	Aspectral	NULL	
BK04_04.001	orehorizon unit	Paragonitic Illite	Kaolinite WX	paragonite
BK04_04.002	orehorizon unit	Paragonite	NULL	paragonite
BK07.000	orehorizon unit	NULL	NULL	
BK07.001	orehorizon unit	NULL	NULL	
BK07.002	orehorizon unit	Aspectral	NULL	
BK07.003	orehorizon unit	NULL	NULL	
BK07.004	orehorizon unit	Aspectral	NULL	
BK07.005	orehorizon unit	Aspectral	NULL	
BK07new.000	orehorizon unit	NULL	NULL	
BK07new.001	orehorizon unit	Aspectral	NULL	
BK07new.002	orehorizon unit	Muscovite	NULL	muscovite
BK07new.003	orehorizon unit	Aspectral	NULL	
BK07new.004	orehorizon unit	Aspectral	NULL	
BK07new.005	orehorizon unit	Aspectral	NULL	
MBTCS5.000	footwall unit	Aspectral	NULL	
MBTCS5.001	footwall unit	Aspectral	NULL	muscovite
KIRI2.000	orehorizon unit	Pyrophyllite	NULL	muscovite
KIRI2.001	orehorizon unit	Pyrophyllite	Muscovite	
KIRI2.002	orehorizon unit	Pyrophyllite	Muscovite	
KIRI2_a.000	orehorizon unit	NULL	NULL	
KIRI2_a.001	orehorizon unit	Pyrophyllite	Muscovite	
KIRI2_a.002	orehorizon unit	Pyrophyllite	NULL	
KIRI2_a.003	orehorizon unit	Kaolinite WX	Paragonite	
KIRI2new.000	orehorizon unit	NULL	NULL	
KIRI2new.001	orehorizon unit	Pyrophyllite	Muscovite	
KIRI2new.002	orehorizon unit	Pyrophyllite	Muscovite	
KIRI3.000	orehorizon unit	NULL	NULL	
KIRI3.001	orehorizon unit	Montmorillonite	Paragonite	

Sample	Lithology	SWIR identified Min1 sTSAS	SWIR identified Min2 sTSAS	TSG interpreted mineral
KIRI3.002	orehorizon unit	Paragonitic Illite	Kaolinite WX	
KIRI3.003	orehorizon unit	Kaolinite WX	Paragonitic Illite	
KIRI3new.000	orehorizon unit	NULL	NULL	
KIRI3new.001	orehorizon unit	NULL	NULL	
KIRI3new.002	orehorizon unit	Kaolinite WX	Paragonitic Illite	
KIRI3new.003	orehorizon unit	Kaolinite WX	Paragonitic Illite	
KNN.000	orehorizon unit	NULL	NULL	
KNN.001	orehorizon unit	Muscovitic Illite	Pyrophyllite	
KNN.002	orehorizon unit	NULL	NULL	
KNNnew.000	orehorizon unit	NULL	NULL	
KNNnew.001	orehorizon unit	Paragonitic Illite	Pyrophyllite	
KNNnew.002	orehorizon unit	Paragonitic Illite	NULL	
KNNnew.003	orehorizon unit	Aspectral	NULL	
KNN2.000	orehorizon unit	NULL	NULL	
KNN2.001	orehorizon unit	Aspectral	NULL	
KNN2.002	orehorizon unit	Kaolinite WX	NULL	
KNN2.003	orehorizon unit	Kaolinite WX	NULL	
KNN2.004	orehorizon unit	Paragonitic Illite	Kaolinite WX	
S4/5_a8.000	orehorizon unit	NULL	NULL	
S4/5_a8.001	orehorizon unit	Aspectral	NULL	
S4/5_a8.002	orehorizon unit	Aspectral	NULL	
S5/6_a10.000	orehorizon unit	NULL	NULL	
S5/6_a10.001	orehorizon unit	Aspectral	NULL	
S5/6_a10.002	orehorizon unit	Aspectral	NULL	
S5/6_a10.003	orehorizon unit	Aspectral	NULL	
hrbknew.000	orehorizon unit	Pyrophyllite	NULL	pyrophyllite
hrbknew.001	orehorizon unit	Pyrophyllite	NULL	pyrophyllite
hrbknew.002	orehorizon unit	Pyrophyllite	NULL	pyrophyllite
hrbknew.003	orehorizon unit	Pyrophyllite	NULL	pyrophyllite

Sample	Lithology	SWIR identified Min1 sTSAS	SWIR identified Min2 sTSAS	TSG interpreted mineral
hrbknew.004	orehorizon unit	Pyrophyllite	NULL	pyrophyllite
BK10new.000	footwall unit	NULL	NULL	
BK10new.001	footwall unit	Aspectral	NULL	
BK10new.002	footwall unit	Aspectral	NULL	
BK10new.003	footwall unit	NULL	NULL	
BK11.000	footwall unit	Pyrophyllite	NULL	pyrophyllite
BK11.001	footwall unit	Pyrophyllite	NULL	pyrophyllite
BK11.002	footwall unit	Pyrophyllite	NULL	pyrophyllite
BK11new.000	footwall unit	NULL	NULL	
BK11new.001	footwall unit	Pyrophyllite	NULL	pyrophyllite
BK11new.002	footwall unit	Pyrophyllite	NULL	pyrophyllite
BK12.000	footwall unit	NULL	NULL	
BK12.001	footwall unit	NULL	NULL	
BK12.002	footwall unit	Aspectral	NULL	
BKCL-1.000	footwall unit	Aspectral	NULL	
BKCL-1.001	footwall unit	Muscovite	NULL	muscovite
BKCL-1.002	footwall unit	Aspectral	NULL	
BKCL-2.000	footwall unit	Pyrophyllite	NULL	pyrophyllite
BKCL-2.001	footwall unit	Pyrophyllite	NULL	
CL1-BB.000	footwall unit	Muscovite	NULL	muscovite
CL1-BB.001	footwall unit	Muscovite	NULL	
CL1-BB.002	footwall unit	Muscovite	NULL	
CL1-BB.003	footwall unit	Muscovite	NULL	
CL1-BB.004	footwall unit	Aspectral	NULL	
CL1-BBa.000	footwall unit	NULL	NULL	
CL1-BBa.001	footwall unit	Muscovite	NULL	muscovite
CL1-BBa.002	footwall unit	NULL	NULL	
CL2-BK.000	footwall unit	NULL	NULL	
CL2-BK.001	footwall unit	Muscovite	NULL	

Sample	Lithology	SWIR identified Min1 sTSAS	SWIR identified Min2 sTSAS	TSG interpreted mineral
CL2-BK.002	footwall unit	Muscovite	NULL	
CL2-BK.003	footwall unit	Muscovite	NULL	muscovite
CL3-BB.000	footwall unit	NULL	NULL	
CL3-BB.001	footwall unit	NULL	NULL	
SQTBK.000	footwall unit	Paragonite	Pyrophyllite	muscovite
SQTBK.001	footwall unit	Paragonitic Illite	Pyrophyllite	muscovite
SQTBK.002	footwall unit	Muscovitic Illite	Pyrophyllite	muscovite
SQTBK.003	footwall unit	Muscovite	Pyrophyllite	muscovite
SQT2BK.000	footwall unit	NULL	NULL	
SQT2BK.001	footwall unit	Paragonite	Pyrophyllite	
SQT2BK.002	footwall unit	NULL	NULL	
SQT2BK.003	footwall unit	Aspectral	NULL	
hostrock.000	footwall unit	NULL	NULL	
hostrock.001	footwall unit	Pyrophyllite	NULL	pyrophyllite
hostrock.002	footwall unit	Pyrophyllite	NULL	pyrophyllite
hostrock.003	footwall unit	Pyrophyllite	NULL	pyrophyllite

Notes: NULL=Not detected

Appendix VI: XRD results

Mineral Resources Tasmania

Mineralogy/Petrology Report

LJN2013/040

XRD ANALYSES: BUKIT KETAYA, MALAYSIA

An unpublished Mineral Resources Tasmania report for

Basril Basori, CODES, University of Tasmania

by R S Bottrill and R N Woolley

23 April 2013

INTRODUCTION

The objective of this particular study is to determine the mineralogy of four altered host rock samples from the Bukit Ketaya mine, Malaysia, collected by Basril Basori, CODES. The sample details are shown in Table 1.

Table 1: Sample details

Field No.	Location	Sample Description
BK01	Bukit Ketaya, Malaysia	Altered Rock
BK02	Bukit Ketaya, Malaysia	Altered Rock
BK11a	Bukit Ketaya, Malaysia	Altered Rock
MBTCS5	Bukit Ketaya, Malaysia	Altered Rock

TREATMENT

The samples were prepared, examined and analysed in the MRT laboratories, Rosny Park, Tasmania. They were run on an automated Philips X-Ray diffractometer (XRD) system: PW 1729 generator, PW 1050 goniometer and PW 1710 microprocessor with nickel-filtered copper radiation at 40kV/30mA, a graphite monochromator (PW1752), sample spinner and a proportional detector (sealed gas filled PW1711). The PW1710 system is presently driven by the CSIRO XRD software: "PW1710 for Windows" and "XPLOT for Windows". Interpretation and quantification is largely manual, using a series of prepared standards of the more common minerals to enable some semi-quantitative analysis.

The XRD results are shown in appendix 1.

RESULTS AND INTERPRETATION

The samples are all quartz rich with trace to moderate amounts of pyrite or hematite and phyllosilicates. The phyllosilicates include minor to trace amounts of pyrophyllite, kaolinite, paragonite and an unidentified mica (sericite?). There are also minor amounts of barite and barian celestine ($[Ba,Sr]SO_4$) in one sample. Most of these minerals could be of hydrothermal origin, but some could be pre-alteration.

R. S. Bottrill
Mineralogist-petrologist

R. N. Woolley
Technical Officer

Appendix 1: XRD Analysis

Client: Basril Basori, CODES
Sample Source: Bukit Ketaya, Malaysia
MRT Job Number: LJN2013/040
Analysis: Approximate Mineralogy
Method: X-Ray Diffraction

Results (approx wt %)

Sample	*>80%*	*65%-80%*	*10%-15%*	*5%-10%*	*2%-5%*	*<2%*
BK01	Quartz				Pyrophyllite, Mica*, Hematite Kaolinite	
BK02	Quartz			Hematite	Mica*, Kaolinite	
BK11a		Quartz	Pyrite	Pyrophyllite	Paragonite, Mica*	Ba-Celestine, Barite
MB-TC-S5	Quartz				Pyrite	

Peak overlap may interfere with identifications and quantitative calculations
Amorphous material and minerals present in trace amounts may not be detected

* insufficiently abundant to enable identification of type

Analyst: R.N. Woolley
Date: 23 April 2013

Appendix VII: Microprobe results of sphalerite geochemistry

Sample No.	S	Pb	Ag	Cu	Zn	Sn	Sb	As	Mn	Fe	Cd	Total	FeS mole %	CdS mole %	MnS mole %	Zn/Fe	Zn/Cd	Zn/Mn	Cd/Zn
Bukit Botol																			
BB1d	33.17	<0.11	<0.07	0.25	65.85	<0.03	<0.03	<0.02	0.00	0.39	0.54	100.21	0.66	0.55	0.00	167.81	121.05	0.00	0.00
BB1d	32.87	<0.10	<0.06	0.28	65.90	<0.03	<0.03	<0.02	0.01	0.41	0.50	99.96	0.68	0.50	0.02	162.44	132.96	5435.10	0.00
BB1d	32.98	<0.11	<0.06	0.29	66.04	<0.03	<0.03	<0.02	0.00	0.46	0.54	100.31	0.77	0.55	0.00	142.18	122.36	0.00	0.00
BB1d	33.00	<0.11	0.08	0.14	66.22	<0.03	<0.03	<0.02	0.00	0.33	0.54	100.31	0.55	0.54	0.00	202.22	123.63	0.00	0.00
BB1d	32.76	<0.11	<0.06	0.16	65.73	<0.03	<0.03	<0.02	0.00	0.27	0.57	99.49	0.45	0.58	0.00	243.38	116.21	0.00	0.00
BB1d	33.10	<0.10	0.06	0.16	66.06	<0.03	<0.03	0.03	0.01	0.38	0.56	100.36	0.63	0.57	0.02	174.95	117.80	5490.66	0.00
BB1d	33.00	<0.11	<0.06	0.17	66.18	<0.03	<0.03	<0.02	0.00	0.39	0.53	100.26	0.64	0.53	0.00	171.76	125.46	0.00	0.00
BB1d	33.04	<0.1	<0.07	0.25	66.04	<0.03	<0.03	<0.02	0.00	0.44	0.54	100.31	0.74	0.55	0.00	149.40	121.92	0.00	0.00
BB1d	33.04	<0.10	<0.07	0.15	66.16	<0.03	<0.03	<0.02	0.00	0.37	0.50	100.22	0.62	0.51	0.00	177.81	131.22	0.00	0.00
BB1d	32.89	<0.11	<0.07	0.23	65.96	<0.03	<0.03	<0.02	0.00	0.40	0.52	100.00	0.66	0.53	0.00	166.03	126.13	0.00	0.00
Average1	**32.98**	**<0.11**	**0.07**	**0.21**	**66.01**	**<0.03**	**<0.03**	**0.03**	**0.00**	**0.38**	**0.53**	**100.14**	**0.64**	**0.54**	**0.00**	**175.80**	**123.87**	**1092.58**	**0.00**
BB1d-A	33.15	<0.12	<0.07	0.27	65.88	<0.03	<0.03	<0.02	0.00	0.48	0.51	100.29	0.81	0.52	0.00	136.10	127.92	0.00	0.00
BB1d-A	33.17	<0.11	<0.06	0.27	65.77	<0.03	<0.03	<0.02	0.00	0.46	0.52	100.20	0.78	0.54	0.00	141.63	125.28	0.00	0.00
BB1d-A	32.92	<0.09	0.10	1.03	64.30	<0.03	<0.03	<0.02	0.00	1.07	0.53	99.94	1.81	0.55	0.00	60.21	121.68	0.00	0.00
BB1d-A	33.03	<0.10	0.10	0.13	66.12	<0.03	<0.03	<0.02	0.00	0.36	0.57	100.31	0.60	0.58	0.00	182.31	115.21	0.00	0.00
BB1d-A	33.15	<0.09	<0.06	0.21	66.12	<0.03	<0.03	<0.02	0.00	0.34	0.51	100.33	0.57	0.52	0.00	193.57	129.95	0.00	0.00
BB1d-A	33.04	<0.11	<0.06	0.16	66.13	<0.03	<0.03	<0.02	0.00	0.35	0.55	100.23	0.58	0.55	0.00	190.81	121.23	0.00	0.00
Average2	**33.08**	**<0.10**	**0.10**	**0.34**	**65.72**	**<0.03**	**<0.03**	**<0.02**	**0.00**	**0.51**	**0.53**	**100.22**	**0.86**	**0.54**	**0.00**	**150.77**	**123.54**	**0.00**	**0.00**
BB1d-B	33.18	<0.10	<0.06	0.09	66.44	<0.03	<0.03	<0.02	0.16	0.48	0.51	100.87	0.80	0.52	0.27	138.13	129.31	406.75	0.00
BB1d-B	32.86	<0.12	0.07	0.07	66.31	<0.03	<0.03	<0.02	0.16	0.43	0.50	100.39	0.71	0.50	0.27	155.05	132.99	417.92	0.00
BB1d-B	33.05	<0.10	<0.06	0.04	66.00	<0.03	<0.03	<0.02	0.14	0.42	0.52	100.16	0.70	0.52	0.24	157.10	127.90	471.77	0.00
BB1d-B	32.95	<0.10	<0.06	0.05	66.04	<0.03	0.04	<0.02	0.16	0.43	0.50	100.17	0.71	0.51	0.26	154.38	132.56	422.05	0.00
BB1d-B	33.05	<0.12	<0.06	0.05	66.09	<0.03	<0.03	<0.02	0.11	0.40	0.50	100.21	0.67	0.51	0.19	163.82	132.23	591.96	0.00
BB1d-B	33.28	<0.12	<0.07	0.10	66.35	<0.02	<0.03	<0.02	0.17	0.48	0.50	100.87	0.79	0.51	0.28	139.35	132.08	395.72	0.00
BB1d-B	33.07	<0.11	<0.07	0.32	65.77	<0.03	<0.03	<0.02	0.02	0.51	0.55	100.23	0.85	0.56	0.04	129.67	119.77	2983.26	0.00
BB1d-B	33.21	<0.12	<0.06	0.20	65.98	<0.03	<0.03	<0.02	0.00	0.32	0.57	100.28	0.54	0.58	0.00	205.78	115.29	0.00	0.00
BB1d-B	33.45	<0.11	<0.06	0.16	66.14	<0.03	<0.03	<0.02	0.02	0.40	0.57	100.75	0.67	0.58	0.03	165.27	115.09	3786.16	0.00
BB1d-B	33.30	<0.12	<0.07	0.18	65.93	<0.03	<0.03	<0.02	0.00	0.39	0.53	100.33	0.65	0.54	0.00	170.64	123.45	0.00	0.00
Average3	**33.14**	**<0.11**	**0.07**	**0.13**	**66.11**	**<0.03**	**0.04**	**<0.02**	**0.09**	**0.43**	**0.53**	**100.43**	**0.71**	**0.53**	**0.16**	**157.92**	**126.07**	**947.56**	**0.00**
BB1d-C	33.49	<0.11	<0.07	0.61	65.28	<0.03	<0.03	<0.02	0.02	0.83	0.55	100.78	1.39	0.57	0.03	78.84	118.32	4053.27	0.00
BB1d-C	33.13	<0.11	<0.07	0.11	66.15	<0.03	<0.03	<0.02	0.00	0.36	0.54	100.29	0.59	0.54	0.00	185.56	123.60	0.00	0.00
BB1d-C	33.25	0.10	<0.06	0.21	66.04	<0.03	<0.03	<0.02	0.01	0.49	0.59	100.69	0.81	0.59	0.02	136.02	112.71	4755.92	0.00
BB1d-C	33.21	<0.12	<0.06	0.28	65.80	<0.03	<0.03	<0.02	0.02	0.53	0.57	100.40	0.88	0.58	0.03	124.50	115.80	3725.15	0.00
BB1d-C	33.07	<0.11	<0.06	0.08	66.27	<0.03	<0.03	<0.02	0.01	0.31	0.57	100.32	0.52	0.58	0.03	210.52	116.13	4442.42	0.00
Average4	**33.23**	**0.10**	**<0.06**	**0.26**	**65.91**	**<0.03**	**<0.03**	**<0.02**	**0.01**	**0.50**	**0.56**	**100.50**	**0.84**	**0.57**	**0.02**	**147.09**	**117.31**	**3395.35**	**0.00**
BB1d-D	33.14	<0.10	<0.06	0.11	66.04	<0.03	<0.03	<0.02	0.00	0.35	0.59	100.23	0.58	0.60	0.00	190.98	111.32	0.00	0.00
BB1d-D	33.17	<0.10	<0.06	0.22	66.10	<0.03	0.05	<0.02	0.00	0.43	0.53	100.50	0.71	0.54	0.00	155.41	123.63	0.00	0.00
BB1d-D	32.81	<0.11	<0.07	0.07	66.00	<0.03	<0.03	<0.02	0.00	0.32	0.56	99.76	0.54	0.57	0.00	204.95	118.72	0.00	0.00
BB1d-D	33.25	<0.10	<0.07	0.21	65.89	<0.03	<0.03	<0.02	0.00	0.44	0.55	100.33	0.73	0.56	0.00	150.57	119.26	0.00	0.00
BB1d-D	33.16	<0.13	<0.06	0.23	65.89	<0.03	<0.03	<0.02	0.00	0.48	0.61	100.37	0.80	0.62	0.00	137.55	107.78	0.00	0.00
BB1d-D	32.89	<0.12	<0.06	0.08	66.16	<0.03	<0.03	<0.02	0.00	0.37	0.58	100.08	0.62	0.59	0.00	177.68	113.61	0.00	0.00
BB1d-D	33.06	<0.10	<0.06	0.30	64.45	<0.03	<0.03	<0.02	0.00	0.48	0.56	98.85	0.82	0.58	0.00	134.18	115.30	0.00	0.00
BB1d-D	33.19	<0.10	<0.07	0.09	65.99	<0.03	<0.03	<0.02	0.00	0.34	0.60	100.21	0.57	0.61	0.00	194.36	109.50	0.00	0.00
Average5	**33.08**	**<0.10**	**<0.06**	**0.17**	**65.81**	**<0.03**	**0.05**	**<0.02**	**0.00**	**0.40**	**0.57**	**100.04**	**0.67**	**0.58**	**0.00**	**168.21**	**114.89**	**0.00**	**0.00**
BB1d-E	33.38	<0.11	0.11	0.10	66.39	<0.03	<0.03	<0.02	0.00	0.19	0.51	100.69	0.32	0.52	0.00	346.06	129.68	0.00	0.00

Sample No.	S	Pb	Ag	Cu	Zn	Sn	Sb	As	Mn	Fe	Cd	Total	FeS mole %	CdS mole %	MnS mole %	Zn/Fe	Zn/Cd	Zn/Mn	Cd/Zn
BB1d-E	32.95	<0.09	<0.06	0.09	66.33	<0.03	<0.03	<0.02	0.00	0.24	0.53	100.14	0.40	0.54	0.00	278.00	124.32	0.00	0.00
BB1d-E	32.84	<0.12	<0.06	0.09	66.25	<0.03	<0.03	<0.02	0.00	0.26	0.57	100.00	0.43	0.57	0.00	258.15	116.95	0.00	0.00
BB1d-E	32.78	<0.11	0.10	0.11	66.06	<0.03	<0.03	<0.02	0.00	0.22	0.57	99.83	0.37	0.58	0.00	301.20	116.43	0.00	0.00
BB1d-E	32.58	<0.12	<0.06	0.15	65.64	<0.03	<0.03	<0.02	0.00	0.25	0.55	99.16	0.43	0.56	0.00	258.55	120.42	0.00	0.00
Average6	**32.91**	**<0.11**	**0.11**	**0.11**	**66.13**	**<0.03**	**<0.03**	**<0.02**	**0.00**	**0.23**	**0.54**	**99.96**	**0.39**	**0.55**	**0.00**	**288.39**	**121.56**	**0.00**	**0.00**
BB1d-F	33.09	0.13	<0.07	0.10	66.21	<0.03	<0.03	<0.02	0.01	0.33	0.60	100.47	0.55	0.61	0.02	202.11	110.68	5267.14	0.00
BB1d-F	32.54	<0.12	<0.06	0.22	66.03	<0.03	<0.03	<0.02	0.01	0.27	0.50	99.56	0.45	0.51	0.02	246.25	132.23	5089.66	0.00
BB1d-F	32.82	<0.12	<0.06	0.09	66.24	<0.03	<0.03	<0.02	0.01	0.19	0.47	99.82	0.31	0.48	0.02	355.66	140.21	5176.58	0.00
BB1d-F	32.96	<0.11	<0.07	0.10	66.16	<0.03	0.04	<0.02	0.01	0.22	0.53	100.01	0.37	0.53	0.02	301.26	125.90	5854.11	0.00
BB1d-F	32.80	<0.11	0.09	0.15	65.93	<0.03	<0.03	<0.02	0.00	0.21	0.52	99.69	0.35	0.53	0.00	315.20	127.62	0.00	0.00
BB1d-F	32.90	<0.10	0.07	0.06	66.41	<0.03	<0.03	<0.02	0.00	0.16	0.43	100.03	0.26	0.44	0.00	421.72	154.16	0.00	0.00
BB1d-F	32.96	<0.12	<0.06	0.07	66.04	<0.03	<0.03	<0.02	0.01	0.25	0.55	99.89	0.41	0.56	0.02	268.29	120.58	4697.19	0.00
BB1d-F	33.54	<0.10	<0.06	0.07	66.32	<0.03	<0.03	<0.02	0.00	0.25	0.44	100.62	0.41	0.45	0.00	267.40	149.06	0.00	0.00
BB1d-F	32.90	<0.10	<0.07	0.13	65.78	<0.03	<0.03	<0.02	0.00	0.15	0.59	99.55	0.26	0.60	0.00	432.26	110.97	0.00	0.00
BB1d-F	32.49	<0.10	0.08	0.08	65.81	<0.03	<0.03	<0.02	0.00	0.22	0.50	99.18	0.38	0.51	0.00	292.88	131.29	0.00	0.00
Average7	**32.90**	**0.13**	**0.08**	**0.11**	**66.09**	**<0.03**	**0.04**	**<0.02**	**0.01**	**0.22**	**0.51**	**99.88**	**0.37**	**0.52**	**0.01**	**310.30**	**130.27**	**2608.47**	**0.00**
BB02b	32.98	0.16	<0.06	1.73	62.39	<0.03	<0.03	<0.02	0.00	2.62	0.24	100.12	4.45	0.26	0.00	23.79	263.40	0.00	0.00
BB02b	32.82	<0.10	<0.06	4.70	55.44	<0.03	<0.03	<0.02	0.00	5.61	0.25	98.81	10.09	0.30	0.00	9.88	226.11	0.00	0.00
BB02b	36.84	<0.11	0.09	5.82	43.55	<0.03	<0.03	<0.02	0.00	13.46	0.19	99.96	25.53	0.30	0.00	3.23	226.04	0.00	0.00
Average8	**34.21**	**0.16**	**0.09**	**4.09**	**53.79**	**<0.03**	**<0.03**	**<0.02**	**0.00**	**7.23**	**0.22**	**99.63**	**13.36**	**0.28**	**0.00**	**12.30**	**238.52**	**0.00**	**0.00**
BB02b-A	36.07	<0.11	0.09	1.26	54.94	<0.03	0.04	<0.02	0.01	8.01	0.24	100.66	13.92	0.29	0.03	6.86	228.58	3950.52	0.00
Average9	**36.07**	**#####**	**0.09**	**1.26**	**54.94**	**<0.03**	**0.04**	**<0.02**	**0.01**	**8.01**	**0.24**	**100.66**	**13.92**	**0.29**	**0.03**	**6.86**	**228.58**	**3950.52**	**0.00**
BB02b-B	32.62	<0.12	0.07	0.80	64.77	<0.03	<0.03	<0.02	0.00	1.53	0.27	100.07	2.55	0.28	0.00	42.31	238.33	0.00	0.00
BB02b-B	32.85	<0.10	<0.07	6.61	52.89	<0.03	<0.03	<0.02	0.00	6.27	0.19	98.81	11.61	0.25	0.00	8.44	273.14	0.00	0.00
BB02b-B	33.21	<0.10	0.09	4.14	58.30	<0.03	<0.03	<0.02	0.00	4.35	0.24	100.32	7.65	0.28	0.00	13.39	241.77	0.00	0.00
Average10	**32.89**	**#####**	**0.08**	**3.85**	**58.65**	**<0.03**	**<0.03**	**<0.02**	**0.00**	**4.05**	**0.24**	**99.73**	**7.27**	**0.27**	**0.00**	**21.38**	**251.08**	**0.00**	**0.00**
BB02b-C	32.75	<0.11	<0.06	1.88	62.53	<0.03	<0.03	<0.02	0.00	2.69	0.26	100.11	4.55	0.28	0.00	23.23	236.13	0.00	0.00
BB02b-C	32.84	0.12	0.07	2.08	62.06	<0.03	<0.03	<0.02	0.00	2.72	0.23	100.12	4.63	0.25	0.00	22.83	268.35	0.00	0.01
BB02b-C	32.55	<0.12	<0.06	1.71	62.45	<0.03	<0.03	<0.02	0.00	2.59	0.27	99.57	4.40	0.29	0.00	24.10	230.04	0.00	0.00
Average11	**32.71**	**0.12**	**0.07**	**1.89**	**62.35**	**<0.03**	**<0.03**	**<0.02**	**0.00**	**2.67**	**0.26**	**99.93**	**4.53**	**0.28**	**0.00**	**23.39**	**244.84**	**0.00**	**0.00**
BB02b-2A	32.35	0.11	<0.07	1.28	62.87	<0.03	<0.03	<0.02	0.00	2.24	0.28	99.13	3.80	0.30	0.00	28.07	223.49	0.00	0.00
BB02b-2A	33.04	0.24	0.20	4.33	58.02	<0.03	<0.03	<0.02	0.00	4.70	0.28	100.82	8.25	0.32	0.00	12.33	209.42	0.00	0.00
Average12	**32.70**	**0.18**	**0.20**	**2.81**	**60.44**	**<0.03**	**<0.03**	**<0.02**	**0.00**	**3.47**	**0.28**	**99.98**	**6.02**	**0.31**	**0.00**	**20.20**	**216.46**	**0.00**	**0.00**
BB02b-2B	32.89	<0.11	<0.06	2.21	61.93	<0.03	<0.03	<0.02	0.00	2.82	0.25	100.10	4.81	0.27	0.00	21.93	244.65	0.00	0.00
BB02b-2B	33.12	<0.12	<0.06	7.40	50.77	<0.03	<0.03	<0.02	0.00	7.31	0.25	98.85	13.77	0.33	0.00	6.94	205.48	0.00	0.00
BB02b-2B	33.30	<0.12	<0.06	9.93	45.99	<0.03	<0.03	<0.02	0.00	9.40	0.20	98.82	18.47	0.29	0.00	4.89	229.82	0.00	0.00
BB02b-2B	32.82	<0.10	<0.06	1.75	62.85	<0.03	<0.03	<0.02	0.00	2.48	0.28	100.18	4.20	0.30	0.00	25.30	224.67	0.00	0.00
BB02b-2B	33.47	<0.10	0.12	10.78	45.65	<0.03	<0.03	<0.02	0.00	10.37	0.20	100.59	20.12	0.29	0.00	4.40	231.27	0.00	0.00
BB02b-2B	33.43	<0.12	0.08	10.57	45.82	<0.03	<0.03	<0.02	0.00	10.12	0.18	100.19	19.66	0.27	0.00	4.53	250.62	0.00	0.00
BB02b-2B	32.20	0.20	0.12	2.05	61.39	0.03	<0.03	<0.02	0.00	2.97	0.28	99.24	5.09	0.30	0.00	20.69	222.30	0.00	0.00
Average13	**33.03**	**0.20**	**0.11**	**6.39**	**53.48**	**0.03**	**<0.03**	**<0.02**	**0.00**	**6.50**	**0.23**	**99.71**	**12.30**	**0.29**	**0.00**	**12.67**	**229.83**	**0.00**	**0.00**
BBotol_Dump_1	32.81	<0.11	0.07	5.17	55.75	<0.03	<0.03	<0.02	0.00	5.43	0.19	99.42	9.74	0.23	0.00	10.27	296.37	0.00	0.00
BBotol_Dump_1	32.70	<0.11	<0.06	2.17	61.73	<0.03	<0.03	<0.02	0.00	2.85	0.24	99.69	4.87	0.27	0.00	21.65	253.13	0.00	0.00
BBotol_Dump_1	32.65	<0.10	<0.06	2.64	60.95	<0.03	<0.04	<0.02	0.00	3.15	0.22	99.60	5.42	0.25	0.00	19.37	274.04	0.00	0.00
BBotol_Dump_1	32.69	<0.10	<0.07	2.06	61.82	<0.02	<0.03	<0.02	0.00	2.86	0.25	99.67	4.87	0.27	0.00	21.64	248.49	0.00	0.00
BBotol_Dump_1	33.22	<0.12	<0.06	9.83	45.98	<0.03	0.04	0.03	0.00	9.38	0.18	98.66	18.45	0.26	0.00	4.90	261.34	0.00	0.00

Sample No.	S	Pb	Ag	Cu	Zn	Sn	Sb	As	Mn	Fe	Cd	Total	FeS mole %	CdS mole %	MnS mole %	Zn/Fe	Zn/Cd	Zn/Mn	Cd/Zn
Average14	**32.81**	**<0.11**	**0.07**	**4.37**	**57.25**	**<0.03**	**0.04**	**0.03**	**0.00**	**4.73**	**0.22**	**99.41**	**8.67**	**0.25**	**0.00**	**15.57**	**266.67**	**0.00**	**0.00**
Bukit Ketaya																			
BMSE-1 Sphalerite	32.83	<0.11	<0.06	0.19	66.30	<0.02	<0.03	<0.02	0.00	0.43	0.22	99.99	0.72	0.23	0.00	152.74	296.67	0.00	0.00
BMSE-1 Sphalerite	33.08	<0.11	<0.06	0.04	66.77	<0.03	<0.03	<0.02	0.00	0.40	0.24	100.53	0.67	0.24	0.00	165.22	280.71	0.00	0.00
BMSE-1 Sphalerite	32.89	<0.10	<0.06	0.04	66.82	<0.03	<0.03	<0.02	0.00	0.34	0.24	100.33	0.56	0.24	0.00	197.40	278.15	0.00	0.00
Average1	**32.93**	**<0.11**	**<0.06**	**0.09**	**66.63**	**<0.03**	**<0.03**	**<0.02**	**0.00**	**0.39**	**0.23**	**100.28**	**0.65**	**0.24**	**0.00**	**171.79**	**285.18**	**0.00**	**0.00**
BMSE-1-A Sphalerite	32.71	<0.12	0.06	0.05	66.68	<0.03	<0.03	<0.02	0.00	0.41	0.27	100.17	0.67	0.27	0.00	164.45	248.00	0.00	0.00
BMSE-1-A Sphalerite	32.64	<0.10	<0.06	0.10	66.69	<0.03	<0.03	<0.02	0.00	0.41	0.23	100.08	0.68	0.24	0.00	161.36	285.39	0.00	0.00
BMSE-1-A Sphalerite	32.93	<0.09	<0.06	0.42	65.99	<0.03	<0.03	<0.02	0.00	0.70	0.25	100.29	1.15	0.26	0.00	94.93	262.48	0.00	0.00
Average2	**32.76**	**<0.10**	**0.06**	**0.19**	**66.45**	**<0.03**	**<0.03**	**<0.02**	**0.00**	**0.50**	**0.25**	**100.18**	**0.84**	**0.25**	**0.00**	**140.25**	**265.29**	**0.00**	**0.00**
BK11-A Sphalerite	33.05	<0.12	0.11	0.09	66.82	<0.03	<0.03	<0.02	0.02	0.28	0.18	100.54	0.46	0.18	0.03	240.03	372.38	4269.73	0.00
BK11-A Sphalerite	33.04	<0.11	0.08	0.04	66.37	<0.02	<0.03	<0.02	0.00	0.34	0.18	100.05	0.57	0.19	0.00	192.75	359.20	0.00	0.00
BK11-A Sphalerite	33.12	<0.10	<0.07	0.12	66.59	<0.03	0.05	<0.02	0.01	0.44	0.17	100.51	0.73	0.18	0.02	150.99	381.31	5798.73	0.00
Average3	**33.07**	**<0.11**	**0.09**	**0.08**	**66.59**	**<0.03**	**0.05**	**<0.02**	**0.01**	**0.35**	**0.18**	**100.37**	**0.59**	**0.18**	**0.02**	**194.59**	**370.97**	**3356.15**	**0.00**
BK11-B Sphalerite	33.32	<0.11	<0.06	0.04	66.43	<0.03	<0.03	<0.02	0.00	0.19	0.20	100.18	0.31	0.20	0.00	358.36	333.96	0.00	0.00
BK11-B Sphalerite	32.91	<0.11	<0.06	<0.02	66.76	<0.03	<0.03	<0.02	0.00	0.19	0.22	100.09	0.32	0.22	0.00	342.48	302.08	0.00	0.00
BK11-B Sphalerite	33.02	<0.11	<0.06	0.05	66.74	<0.02	<0.03	<0.02	0.01	0.20	0.18	100.20	0.32	0.18	0.02	340.17	372.09	4828.69	0.00
Average4	**33.08**	**<0.11**	**<0.06**	**0.05**	**66.64**	**<0.03**	**<0.03**	**<0.02**	**0.00**	**0.19**	**0.20**	**100.16**	**0.32**	**0.20**	**0.01**	**347.00**	**336.04**	**1609.56**	**0.00**
BK11	32.12	0.14	0.08	0.02	64.87	<0.03	<0.03	<0.02	0.00	0.20	0.20	97.63	0.33	0.21	0.00	330.22	325.64	0.00	0.00
BK11	33.02	<0.12	0.10	0.05	64.79	<0.02	<0.03	<0.02	0.00	0.20	0.20	98.35	0.34	0.20	0.00	323.05	330.50	0.00	0.00
BK11	31.12	<0.09	<0.06	0.03	64.81	<0.02	<0.03	<0.02	0.00	0.21	0.20	96.37	0.35	0.21	0.00	315.52	322.87	0.00	0.00
BK11	32.80	<0.10	<0.06	0.08	64.35	<0.02	0.07	0.03	0.00	0.18	0.24	97.74	0.31	0.25	0.00	358.62	271.00	0.00	0.00
Average5	**32.26**	**0.14**	**0.09**	**0.05**	**64.70**	**<0.02**	**0.07**	**0.03**	**0.00**	**0.20**	**0.21**	**97.52**	**0.33**	**0.22**	**0.00**	**331.85**	**312.50**	**0.00**	**0.00**
BK11_A	32.39	<0.11	0.07	0.11	65.65	<0.02	<0.03	<0.02	0.00	0.15	0.20	98.58	0.26	0.20	0.00	427.10	331.43	0.00	0.00
BK11_A	32.50	<0.11	<0.06	0.06	66.03	<0.03	<0.03	<0.02	0.00	0.20	0.22	99.02	0.34	0.22	0.00	327.99	299.71	0.00	0.00
BK11_A	32.74	<0.09	0.07	0.06	66.05	<0.02	<0.03	<0.02	0.00	0.17	0.21	99.30	0.28	0.21	0.00	389.29	320.43	0.00	0.00
BK11_A	32.21	<0.11	<0.06	0.04	66.12	<0.02	<0.03	<0.02	0.00	0.20	0.22	98.78	0.33	0.22	0.00	334.70	306.72	0.00	0.00
BK11_A	32.65	<0.11	<0.05	0.05	65.96	<0.02	<0.03	<0.02	0.00	0.17	0.18	99.01	0.29	0.19	0.00	382.00	361.60	0.00	0.00
BK11_A	32.33	<0.10	0.07	0.05	66.25	<0.03	<0.03	<0.02	0.00	0.17	0.22	99.09	0.28	0.23	0.00	399.08	297.23	0.00	0.00
BK11_A	32.51	<0.10	<0.06	0.07	66.20	<0.02	<0.03	<0.02	0.00	0.18	0.19	99.13	0.29	0.19	0.00	377.37	353.15	0.00	0.00
BK11_A	32.35	<0.09	<0.06	0.03	66.07	<0.03	<0.03	<0.02	0.00	0.32	0.22	98.99	0.53	0.23	0.00	209.41	293.72	0.00	0.00
Average6	**32.46**	**<0.10**	**0.07**	**0.06**	**66.04**	**<0.03**	**<0.03**	**<0.02**	**0.00**	**0.19**	**0.21**	**98.99**	**0.32**	**0.21**	**0.00**	**355.87**	**320.50**	**0.00**	**0.00**
BK11_B	32.36	<0.11	<0.06	0.04	65.97	<0.03	<0.03	<0.02	0.00	0.20	0.20	98.77	0.33	0.20	0.00	334.33	333.87	0.00	0.00
BK11_B	32.24	<0.11	<0.06	0.04	66.25	<0.02	<0.03	<0.02	0.00	0.19	0.18	98.91	0.31	0.18	0.00	351.68	364.02	0.00	0.00
BK11_B	32.33	<0.11	<0.06	<0.02	65.95	<0.03	<0.03	<0.02	0.00	0.19	0.20	98.67	0.31	0.21	0.00	355.99	324.90	0.00	0.00
BK11_B	32.28	<0.11	<0.06	0.04	65.76	<0.02	<0.03	<0.02	0.00	0.18	0.21	98.48	0.31	0.21	0.00	360.14	316.04	0.00	0.00
BK11_B	32.52	<0.12	<0.07	0.06	65.32	<0.02	<0.03	<0.02	0.00	0.17	0.22	98.30	0.29	0.23	0.00	375.24	295.88	0.00	0.00
BK11_B	32.37	<0.11	<0.06	0.05	66.11	<0.02	<0.03	<0.02	0.00	0.20	0.21	98.94	0.34	0.22	0.00	324.99	312.95	0.00	0.00
Average7	**32.35**	**<0.12**	**<0.06**	**0.05**	**65.89**	**<0.02**	**<0.03**	**<0.02**	**0.00**	**0.19**	**0.20**	**98.68**	**0.32**	**0.21**	**0.00**	**350.39**	**324.61**	**0.00**	**0.00**
BK11_C	32.19	<0.11	<0.07	<0.02	66.26	<0.03	<0.03	<0.02	0.00	0.23	0.22	98.91	0.39	0.23	0.00	282.19	295.87	0.00	0.00
BK11_C	32.66	<0.11	<0.06	0.05	66.11	<0.02	<0.03	<0.02	0.01	0.40	0.22	99.45	0.66	0.22	0.02	166.48	299.95	4668.75	0.00
BK11_C	32.51	<0.11	<0.06	<0.02	66.42	<0.02	<0.03	<0.02	0.00	0.32	0.20	99.46	0.53	0.21	0.00	206.18	324.64	0.00	0.00
BK11_C	32.63	<0.13	<0.06	0.03	66.23	<0.03	<0.03	<0.02	0.00	0.25	0.18	99.32	0.42	0.19	0.00	264.86	362.57	0.00	0.00
BK11_C	32.49	<0.10	0.07	0.04	66.41	<0.03	<0.03	<0.02	0.01	0.25	0.20	99.47	0.41	0.20	0.02	269.92	330.36	5882.83	0.00
BK11_C	32.52	<0.12	<0.07	0.04	66.50	<0.02	<0.03	<0.02	0.02	0.25	0.20	99.52	0.41	0.20	0.03	269.52	330.83	4298.66	0.00

Sample No.	S	Pb	Ag	Cu	Zn	Sn	Sb	As	Mn	Fe	Cd	Total	FeS mole %	CdS mole %	MnS mole %	Zn/Fe	Zn/Cd	Zn/Mn	Cd/Zn
BK11_C	32.38	<0.10	<0.06	0.03	66.14	<0.03	<0.03	<0.02	0.01	0.27	0.20	99.04	0.45	0.20	0.02	247.65	331.23	5425.63	0.00
BK11_C	31.92	<0.10	<0.06	0.04	65.79	<0.02	<0.03	<0.02	0.00	0.23	0.19	98.17	0.38	0.20	0.00	290.40	343.35	0.00	0.00
BK11_C	32.19	<0.12	<0.06	0.03	65.92	<0.03	<0.03	<0.02	0.00	0.48	0.18	98.80	0.79	0.18	0.00	138.71	369.44	0.00	0.00
BK11_C	32.22	<0.11	<0.06	0.03	66.27	<0.03	<0.03	<0.02	0.00	0.28	0.21	99.02	0.47	0.21	0.00	235.32	313.14	0.00	0.00
Average8	**32.37**	**<0.11**	**0.07**	**0.04**	**66.21**	**<0.03**	**<0.03**	**<0.02**	**0.01**	**0.29**	**0.20**	**99.11**	**0.49**	**0.20**	**0.01**	**237.12**	**330.14**	**2027.59**	**0.00**
BK11_D	32.43	<0.12	<0.07	0.06	65.75	<0.02	<0.03	<0.02	0.02	0.19	0.22	98.67	0.32	0.22	0.03	346.73	304.51	3462.13	0.00
BK11_D	33.06	<0.12	<0.06	0.04	65.32	<0.02	<0.03	<0.02	0.00	0.20	0.16	98.78	0.33	0.17	0.00	334.09	397.15	0.00	0.00
BK11_D	32.21	0.13	<0.06	0.07	64.79	<0.02	<0.03	<0.02	0.00	0.20	0.22	97.62	0.34	0.23	0.00	320.46	298.82	0.00	0.00
BK11_D	32.39	<0.10	<0.07	0.05	64.60	<0.02	<0.03	<0.02	0.00	0.15	0.17	97.37	0.25	0.18	0.00	434.54	377.64	0.00	0.00
BK11_D	32.75	<0.11	0.08	0.05	64.08	<0.02	<0.03	<0.02	0.00	0.15	0.21	97.33	0.27	0.22	0.00	416.44	306.36	0.00	0.00
Average9	**32.57**	**0.13**	**0.08**	**0.06**	**64.91**	**<0.02**	**<0.03**	**<0.02**	**0.00**	**0.18**	**0.20**	**97.95**	**0.30**	**0.20**	**0.01**	**370.45**	**336.90**	**692.43**	**0.00**
BKCL-1	33.42	<0.11	<0.06	0.16	65.99	<0.03	<0.03	<0.02	0.05	0.64	0.28	100.55	1.07	0.28	0.08	102.83	238.88	1336.65	0.00
BKCL-1	33.06	<0.11	<0.07	0.06	66.05	<0.03	<0.03	<0.02	0.05	0.48	0.30	99.99	0.80	0.30	0.08	137.25	223.37	1457.70	0.00
BKCL-1	32.95	<0.09	<0.06	0.72	65.08	<0.03	<0.03	<0.02	0.05	1.16	0.29	100.25	1.94	0.30	0.09	56.19	223.85	1184.48	0.00
BKCL-1	32.73	<0.10	<0.07	0.10	65.57	<0.02	<0.03	<0.02	0.05	0.54	0.33	99.32	0.91	0.33	0.09	120.83	200.95	1207.76	0.00
BKCL-1	32.90	<0.11	<0.06	0.07	66.31	<0.03	<0.03	<0.02	0.05	0.53	0.31	100.17	0.88	0.31	0.09	125.60	216.15	1212.89	0.00
BKCL-1	33.38	<0.11	<0.06	0.09	66.11	<0.03	<0.03	<0.02	0.02	0.50	0.31	100.41	0.83	0.31	0.03	132.15	216.60	3279.61	0.00
Average10	**33.07**	**<0.10**	**<0.06**	**0.20**	**65.85**	**<0.03**	**<0.03**	**<0.02**	**0.05**	**0.64**	**0.30**	**100.12**	**1.07**	**0.31**	**0.08**	**112.47**	**219.97**	**1613.18**	**0.00**
BKCL-1_A	33.16	<0.12	<0.07	0.33	65.75	<0.03	<0.03	<0.02	0.03	0.67	0.31	100.25	1.11	0.31	0.06	98.44	214.36	1923.32	0.00
BKCL-1_A	33.30	<0.10	<0.07	0.12	66.12	<0.03	<0.03	<0.02	0.05	0.48	0.28	100.35	0.81	0.28	0.09	136.40	238.82	1206.20	0.00
BKCL-1_A	33.22	<0.11	<0.07	0.11	66.16	<0.03	<0.03	<0.02	0.06	0.51	0.30	100.36	0.85	0.31	0.10	129.81	217.05	1125.82	0.00
BKCL-1_A	32.93	<0.11	<0.06	0.17	65.78	<0.03	<0.03	<0.02	0.05	0.59	0.26	99.79	0.98	0.26	0.08	111.72	254.92	1435.99	0.00
BKCL-1_A	33.01	<0.09	<0.07	0.11	66.10	<0.03	<0.03	<0.02	0.05	0.50	0.30	100.07	0.83	0.30	0.08	133.15	221.01	1333.35	0.00
Average11	**33.13**	**<0.10**	**<0.07**	**0.17**	**65.98**	**<0.03**	**<0.03**	**<0.02**	**0.05**	**0.55**	**0.29**	**100.17**	**0.92**	**0.29**	**0.08**	**121.90**	**229.23**	**1404.94**	**0.00**
BKCL-1_B	33.01	<0.11	<0.06	0.57	65.36	<0.03	<0.03	<0.02	0.02	0.90	0.28	100.14	1.50	0.29	0.04	73.01	231.02	2718.21	0.00
BKCL-1_B	33.15	<0.11	<0.06	0.92	64.40	<0.03	<0.03	<0.02	0.00	1.14	0.30	99.91	1.93	0.31	0.00	56.35	217.76	0.00	0.00
BKCL-1_B	33.13	<0.12	<0.06	0.34	65.66	<0.03	<0.03	<0.02	0.01	0.65	0.28	100.07	1.09	0.29	0.02	100.36	231.94	5466.80	0.00
BKCL-1_B	32.87	<0.12	<0.06	0.44	65.63	<0.03	<0.03	<0.02	0.02	0.76	0.33	100.05	1.26	0.34	0.03	86.54	198.97	3223.03	0.01
BKCL-1_B	32.69	<0.11	<0.06	0.76	64.32	<0.03	<0.03	<0.02	0.00	0.98	0.30	99.04	1.66	0.31	0.00	65.69	215.29	0.00	0.00
BKCL-1_B	33.05	<0.12	<0.06	0.18	65.61	<0.03	<0.03	<0.02	0.01	0.56	0.29	99.69	0.93	0.29	0.02	118.06	229.22	4872.84	0.00
Average12	**32.98**	**<0.12**	**<0.06**	**0.53**	**65.16**	**<0.03**	**<0.03**	**<0.02**	**0.01**	**0.83**	**0.30**	**99.82**	**1.40**	**0.31**	**0.02**	**83.33**	**220.70**	**2713.48**	**0.00**
BKCL-1_C	32.80	<0.12	0.07	0.08	66.06	<0.02	<0.03	<0.02	0.13	0.50	0.23	99.87	0.84	0.24	0.22	131.11	282.78	517.27	0.00
BKCL-1_C	33.01	<0.11	<0.06	0.04	66.03	<0.03	<0.03	<0.02	0.15	0.53	0.28	100.04	0.89	0.28	0.26	123.42	238.36	435.23	0.00
BKCL-1_C	33.18	<0.10	0.06	0.06	66.15	<0.03	<0.03	<0.02	0.14	0.53	0.29	100.42	0.87	0.30	0.24	125.69	226.36	468.16	0.00
BKCL-1_C	33.16	<0.10	<0.06	0.09	65.88	<0.03	<0.03	<0.02	0.13	0.57	0.23	100.07	0.96	0.23	0.23	114.59	291.05	494.92	0.00
BKCL-1_C	33.16	<0.11	<0.06	0.05	66.17	<0.02	<0.03	<0.02	0.17	0.55	0.28	100.37	0.91	0.28	0.28	120.10	237.64	399.18	0.00
BKCL-1_C	33.04	<0.11	<0.07	0.09	66.04	<0.03	<0.03	<0.02	0.11	0.50	0.29	100.08	0.83	0.30	0.18	132.36	223.98	621.87	0.00
BKCL-1_C	33.04	<0.12	<0.06	0.06	66.22	<0.03	<0.03	<0.02	0.09	0.50	0.30	100.20	0.82	0.30	0.15	133.62	221.99	769.22	0.00
Average13	**33.06**	**<0.11**	**0.07**	**0.07**	**66.08**	**<0.03**	**<0.03**	**<0.02**	**0.13**	**0.53**	**0.27**	**100.15**	**0.88**	**0.28**	**0.22**	**125.84**	**246.02**	**529.41**	**0.00**
BKCL-1_D	33.04	<0.11	0.10	0.05	65.72	<0.03	<0.03	0.03	0.06	0.54	0.26	99.79	0.90	0.27	0.10	121.74	248.40	1154.29	0.00
BKCL-1_D	33.12	<0.12	<0.06	0.20	65.78	0.03	<0.03	<0.02	0.06	0.69	0.26	100.15	1.15	0.26	0.10	95.43	255.89	1075.41	0.00
BKCL-1_D	33.10	0.15	<0.06	0.14	65.94	<0.03	0.04	<0.02	0.06	0.58	0.29	100.29	0.97	0.29	0.10	113.64	229.39	1104.54	0.00
BKCL-1_D	33.06	<0.10	<0.06	0.04	66.50	<0.03	<0.03	<0.02	0.04	0.46	0.26	100.35	0.76	0.26	0.07	145.42	260.12	1574.75	0.00
BKCL-1_D	32.61	<0.10	<0.06	0.06	65.65	<0.03	<0.03	<0.02	0.08	0.60	0.29	99.27	1.00	0.29	0.13	110.24	228.21	863.36	0.00
BKCL-1_D	33.07	<0.10	<0.06	0.03	66.20	<0.02	<0.03	<0.02	0.06	0.71	0.29	100.34	1.17	0.29	0.09	93.80	231.92	1201.86	0.00
BKCL-1_D	33.15	<0.10	0.06	0.05	66.13	<0.03	<0.03	<0.02	0.06	0.47	0.28	100.21	0.79	0.29	0.10	139.99	233.54	1124.77	0.00

Sample No.	S	Pb	Ag	Cu	Zn	Sn	Sb	As	Mn	Fe	Cd	Total	FeS mole %	CdS mole %	MnS mole %	Zn/Fe	Zn/Cd	Zn/Mn	Cd/Zn
Average14	**33.02**	**0.15**	**0.08**	**0.08**	**65.99**	**0.03**	**0.04**	**0.03**	**0.06**	**0.58**	**0.27**	**100.06**	**0.96**	**0.28**	**0.10**	**117.18**	**241.07**	**1157.00**	**0.00**
BKCL-1_E	32.91	<0.11	<0.06	0.07	66.27	<0.03	<0.03	<0.02	0.03	0.49	0.26	100.03	0.81	0.27	0.04	135.95	251.99	2627.13	0.00
BKCL-1_E	32.99	<0.11	<0.07	0.52	64.43	<0.03	<0.04	<0.02	0.00	0.78	0.31	99.04	1.33	0.32	0.00	82.17	210.57	0.00	0.00
BKCL-1_E	32.98	0.11	<0.06	0.06	65.99	<0.03	<0.03	<0.02	0.04	0.45	0.33	99.96	0.75	0.33	0.07	146.43	202.18	1504.69	0.00
BKCL-1_E	32.90	<0.11	0.08	0.03	65.86	<0.03	<0.03	<0.02	0.05	0.44	0.25	99.60	0.73	0.26	0.08	151.16	263.22	1319.30	0.00
BKCL-1_E	33.11	<0.11	<0.06	0.06	66.07	<0.03	<0.03	<0.02	0.04	0.49	0.31	100.09	0.82	0.31	0.07	133.50	214.08	1532.58	0.00
BKCL-1_E	33.25	0.13	<0.07	0.07	66.15	<0.03	<0.03	<0.02	0.04	0.53	0.29	100.44	0.87	0.29	0.07	125.82	228.42	1707.53	0.00
BKCL-1_E	33.10	<0.10	<0.06	0.08	66.27	<0.03	<0.03	<0.02	0.05	0.52	0.30	100.32	0.86	0.30	0.08	127.97	223.26	1456.53	0.00
BKCL-1_E	33.11	<0.11	<0.06	0.05	65.52	<0.03	<0.03	<0.02	0.00	0.44	0.34	99.46	0.74	0.34	0.00	149.71	194.89	0.00	0.01
BKCL-1_E	33.30	<0.10	0.09	0.05	65.96	<0.03	<0.03	<0.02	0.03	0.58	0.29	100.29	0.96	0.29	0.04	114.08	228.82	2514.44	0.00
BKCL-1_E	33.20	<0.12	<0.06	0.05	66.07	<0.03	<0.03	<0.02	0.04	0.48	0.29	100.13	0.81	0.29	0.07	136.50	230.75	1581.09	0.00
Average15	**33.09**	**0.12**	**0.09**	**0.10**	**65.86**	**<0.03**	**<0.03**	**<0.02**	**0.03**	**0.52**	**0.30**	**99.94**	**0.87**	**0.30**	**0.05**	**130.33**	**224.82**	**1424.33**	**0.00**
BKCL-1_F	33.37	<0.11	<0.06	1.28	63.34	<0.03	<0.03	<0.02	0.01	1.48	0.29	99.78	2.52	0.31	0.02	42.93	214.88	4770.28	0.00
BKCL-1_F	33.60	<0.12	0.06	0.13	64.41	<0.03	<0.03	<0.02	0.00	0.48	0.27	98.95	0.81	0.28	0.00	135.57	241.50	0.00	0.00
BKCL-1_F	33.05	<0.10	<0.06	0.04	65.07	<0.03	<0.03	<0.02	0.00	0.44	0.27	98.87	0.75	0.28	0.00	146.44	241.41	0.00	0.00
BKCL-1_F	33.19	<0.11	<0.06	0.04	65.44	<0.03	<0.03	<0.02	0.00	0.43	0.33	99.43	0.73	0.33	0.00	151.28	200.87	0.00	0.00
Average16	**33.30**	**<0.11**	**0.06**	**0.37**	**64.57**	**<0.03**	**<0.03**	**<0.02**	**0.00**	**0.71**	**0.29**	**99.26**	**1.20**	**0.30**	**0.01**	**119.06**	**224.66**	**1192.57**	**0.00**
BK12a Sphalerite	33.13	<0.12	<0.07	0.79	64.99	<0.03	<0.03	<0.02	0.02	0.86	0.56	100.33	1.44	0.57	0.03	75.86	116.71	3618.85	0.01
BK12a Sphalerite	32.95	<0.12	<0.07	0.58	65.30	<0.03	<0.03	<0.02	0.02	0.72	0.51	100.06	1.21	0.52	0.03	90.78	129.01	3900.85	0.01
BK12a Sphalerite	33.14	<0.10	<0.06	0.90	64.63	<0.03	<0.03	<0.02	0.03	1.02	0.50	100.23	1.72	0.52	0.05	63.19	129.18	2237.90	0.01
Average17	**33.07**	**<0.11**	**<0.07**	**0.75**	**64.97**	**<0.03**	**<0.03**	**<0.02**	**0.02**	**0.87**	**0.52**	**100.21**	**1.46**	**0.54**	**0.04**	**76.61**	**124.97**	**3252.53**	**0.01**

Appendix VIII: LA-ICPMS pyrite trace element geochemical results

Analysis ID	Sample No.	Pyrite type	Ti49	Cr 53	Mn 55	Fe57	Co59	Ni60	Cu65	Zn66	As75	Se77	Zr90	Mo95	Ag107	Cd111	Sn118	Sb121	Te125	Ba137	La139	W182	Au197	Tl205	Pb208	Bi209	Th232
JL13A03	BB02/bluepy1	py1	<4.2349	3.817	503.544	465000.000	4.075	21.440	1179.811	47.427	885.092	88.460		1.714	432.644			18.694	1.051				0.280	4.581	517.994	50.055	
JL13A04	BB02/bluepy2	py1	21.544	<3.7573	356.466	465000.000	6.377	26.871	1151.953	34.346	1163.743	61.369		5.766	287.866			24.393	0.940				0.203	8.860	490.280	38.141	
JL13A05	BB02/bluepy3	py1	<7.7137	<7.7515	93.727	465000.000	7.868	22.504	717.921	17.181	1059.127	42.435		2.916	102.628			19.571	0.000				0.170	7.066	284.785	55.685	
JL13A06	BB02/bluepy4	py1	<3.8943	4.375	184.747	465000.000	8.726	27.773	1218.416	22.689	1302.407	56.694		5.713	344.749			24.205	1.182				0.239	9.161	415.774	46.232	
JL13A07	BB02/bluepy5	py2	<3.4729	<4.5341	140.890	465000.000	2.946	29.602	644.600	8.005	1214.409	91.241		1.290	43.953			25.004	0.425				0.000	20.435	1266.061	42.324	
JL13A08	BB02/bluepy6	py2	73.091	<4.3657	137.492	465000.000	6.492	139.182	372.194	5.432	932.699	81.484		2.383	18.454			9.784	0.000				0.079	30.245	323.487	8.825	
JL13A09	BB02/bluepy7	py2	4.168	5.081	121.401	465000.000	5.330	30.906	1108.063	13.170	1408.592	91.107		3.300	185.826			25.052	0.772				0.142	21.246	721.342	36.534	
JL13A10	BB02/bluepy8	py1	31.709	2.477	296.736	465000.000	0.225	14.134	46234.023	20.128	689.914	21.033		0.253	56.299			30.211	0.939				0.471	201.156	1094.874	63.519	
JL13A11	BB02/bluepy9	py2	6.331	7.391	315.022	465000.000	6.752	67.963	291.023	17.775	998.940	90.075		28.988	29.168			16.788	0.541				0.060	51.475	672.042	33.806	
JL13A12	BB02/bluepy10	py2	3.788	11.353	148.156	465000.000	12.052	97.918	2639.458	23.804	1934.691	65.530		4.241	95.470			65.786	1.103				0.244	23.405	1566.164	97.031	
JL13A13	BB02/bluepy11	py2	20.607	12.508	250.502	465000.000	4.254	45.349	781.500	17.209	1241.840	89.656		2.800	91.324			32.228	0.000				0.293	13.703	596.923	50.892	
JL13A18	BB01/top	py1	35.340	<4.7787	126.532	465000.000	98.274	11.848	2875.037	131.679	2592.976	647.928		62.315	787.308			44.286	50.803				1.448	0.913	366.305	735.073	
JL13A19	BB01/top	py1	71.665	<3.5496	162.012	465000.000	143.928	22.196	3616.838	84.058	1735.791	353.668		191.032	1213.905			39.041	61.449				1.687	2.399	528.231	836.844	
JL13A20	BB01/top	py1	112.625	5.148	53.798	465000.000	55.878	19.500	1017.120	22.496	2012.639	407.545		31.201	1362.564			59.369	72.179				1.375	1.237	1517.033	1379.058	
JL13A21	BB01/top	py3	16.736	<3.7416	26.565	465000.000	33.757	1.785	76.709	10.722	630.489	36.542		18.523	88.406			5.621	13.890				0.144	0.075	265.884	243.082	
JL13A22	BB01/top	py2	445.328	13.062	347.966	465000.000	188.482	40.625	3440.230	267.816	3746.526	567.506		449.044	1841.922			78.148	91.291				3.056	9.382	1089.479	1108.075	
JL13A23	BB01/top	py1	282.173	4.842	136.209	465000.000	164.010	35.390	5979.012	301.403	2001.448	362.278		383.920	1400.691			24.018	77.609				1.812	3.243	482.038	747.451	
JL13A24	BB01/top	py2	97.081	<3.2732	120.380	465000.000	59.666	87.056	765.747	172.812	1469.461	58.597		74.257	322.282			363.356	28.370				0.724	2.928	3002.556	553.933	
JL13A027	MBTCS1/TOP	py1	4.352	6.468	2383.946	465000.000	145.183	34.273	1526.850	184.642	8511.429	130.796		135.479	595.640			310.319	49.374				2.651	94.856	2536.907	1002.379	
JL13A028	MBTCS1/TOP	py3	<4.2578	<2.6347	<0.83002	465000.000	83.092	4.283	383.970	<1.6031	203.140	121.044		<0.21214	3.442			0.279	12.365				0.183	<0.030818	8.892	34.653	
JL13A029	MBTCS1/TOP	py1	19.111	<3.0198	10.424	465000.000	304.207	14.886	2554.257	31.677	1241.664	318.520		230.985	224.488			23.421	25.183				1.288	1.135	1851.998	433.061	
JL13A030	MBTCS1/TOP	py1	10.188	3.719	16.866	465000.000	279.607	8.231	1238.512	99.248	882.443	102.743		12.080	76.074			10.125	16.530				0.995	9.829	2884.120	346.196	
JL13A031	MBTCS1/TOP	py2	20.693	9.620	876.860	465000.000	63.653	46.916	1765.353	162.635	4768.866	72.764		14.291	194.349			30.665	46.005				2.636	530.243	1410.857	391.905	
JL13A032	MBTCS1/TOP	py3	<4.0077	3.730	56.908	465000.000	59.365	10.267	292.070	12.737	5001.660	6.557		3.264	11.985			9.283	2.387				0.116	320.589	172.899	26.156	
JL13A033	MBTCS1/Others	py3	<3.5738	<2.8187	2.446	465000.000	483.829	61.487	1465.965	<1.8725	1730.660	146.737		5.210	1.714			<0.25604	0.764				0.000	<0.031673	9.435	6.463	
JL13A034	MBTCS1/Others	py3	<3.9561	<2.7311	<0.87656	465000.000	400.500	88.292	<1.621	<1.1128	4384.591	203.419		<0.080648	0.000			<0.17855	0.404				0.000	<0.024036	<0.061544	0.049	
JL13A035	MBTCS1/Others	py1	4.708	<3.2855	5.564	465000.000	1078.221	35.160	1727.806	140.472	2695.040	56.731		10.094	107.480			384.833	28.512				3.092	23.560	1724.534	201.164	
JL13A036	MBTCS1/Others	py2	<3.4126	3.034	20.233	465000.000	1192.153	28.061	2818.163	176.830	2231.776	131.240		42.067	221.042			493.160	33.298				2.453	15.726	5168.259	717.037	
JL13A037	MBTCS1/Others	py3	9.971	<2.3952	23.194	465000.000	25.970	4.209	1614.205	53.427	89.893	37.555		3.619	38.961			5.163	57.640				0.306	0.502	13.259	99.882	
JL13A038	MBTCS1/Others	py3	4.465	<3.0073	<0.85346	465000.000	711.149	23.977	2066.617	76.883	195.616	125.292		0.915	15.198			0.978	47.538				0.201	<0.038026	2.490	29.273	
JL13A039	MBTCS1/TOP	py1	7448.697	24.086	582.272	465000.000	558.972	22.107	7755.594	27.611	3555.831	262.770		649.904	242.660			21.391	36.460				3.443	10.175	2177.436	684.809	
JL13A040	MBTCS1/TOP	py1	35.447	25.880	285.271	465000.000	280.392	45.956	7234.017	280.125	2910.337	778.720		98.176	613.402			36.958	91.304				3.242	70.241	9477.365	1876.995	

Appendix IX: Fluid inclusion microthermometric results

Sample No./ Section	Mineral studied	1st-ice Tm	Tm-ice	Th (L-V)-L	NaCl eq wt %	Inclusion type	Inclusion size (µm)	Tr	Remarks
Bukit Botol									
Barite-A	barite	-38.2	-5.0	219.1	7.86	I	10	120.0	**barite ore**
	barite	nd	nd	223.2	nd	I	<5	nd	
	barite	nd	nd	212.1	nd	I	<5	nd	
	barite	nd	nd	215.7	nd	I	<5	nd	
	barite	-34.6	-3.4	239.6	5.56	I	<10	nd	
	barite	-39.1	-2.1	200.3	3.55	I	<10	150.0	
	barite	nd	nd	290.1	nd	I	<5	nd	
	barite	nd	nd	210.1	nd	I	<5	nd	
	barite	nd	nd	211.2	nd	I	<5	nd	
	barite	nd	nd	210.2	nd	I	<7	175.0	
	barite	nd	nd	209.2	nd	I	<5	172.2	
	barite	nd	nd	208.9	nd	I	<5	160.1	
Barite-B	barite	-38.4	-3.0	198.6	4.96	I	<10	147.1	**barite ore**
	barite	-39.7	-5.6	206.5	8.68	I	<10	nd	
	barite	nd	nd	196.4	nd	I	<5	145.7	
	barite	nd	nd	196.4	nd	I	<5	153.6	
	barite	nd	nd	215.4	nd	I	<5	174.8	
	barite	-21.5	-2.7	206.7	4.49	I	<10	170.0	
	barite	nd	nd	206.7	nd	I	<5	160.4	
	barite	nd	nd	222.0	nd	I	<5	167.3	
	barite	nd	nd	220.0	nd	I	<5	170.0	
	barite	nd	nd	222.0	nd	I	<5	nd	
	barite	nd	nd	206.3	nd	I	<5	nd	
	barite	nd	nd	210.9	nd	I	<5	176.2	
	barite	nd	nd	208.4	nd	I	<5	174.2	
	barite	nd	nd	193.0	nd	I	<5	175.9	
Barite-C	barite	nd	nd	210.3	nd	I	<7	177.0	**barite ore**
	barite	nd	-5.6	210.0	8.68	I	<5	177.9	
	barite	-19.4	-5.4	206.0	8.41	I	<5	nd	
	barite	nd	-2.1	210.8	3.55	I	<10	164.6	
	barite	-20.7	-6.3	214.4	9.60	I	<7	181.4	
	barite	-23.2	-5.3	211.1	8.28	I	<5	176.2	
	barite	nd	-5.5	217.4	8.55	I	<10	183.9	
	barite	-21.8	-6.4	223.3	9.73	I	<5	193.3	
	barite	-23.9	-6.1	210.4	9.34	I	<7	181.8	
	barite	nd	nd	204.5	nd	I	<5	181.0	
T7	quartz	-25.0	-2.3	195.0	3.87	I	10	154.0	**quartz vein**
	quartz	nd	nd	197.0	nd	I	<5	156.0	
	quartz	nd	nd	200.0	nd	I	<5	152.4	
	quartz	-17.0	-2.7	195.4	4.49	I	10	155.8	
	quartz	nd	nd	196.5	nd	I	<10	155.4	
	quartz	nd	-3.1	230.0	5.11	I	10	180.4	

Sample No./ Section	Mineral studied	1st-ice Tm	Tm-ice	Th (L-V)-L	NaCl eq wt %	Inclusion type	Inclusion size (µm)	Tr	Remarks
	quartz	nd	nd	230.0	nd	I	>10	206.0	
	quartz	-21.0	-3.1	197.7	5.11	I	10	154.4	
	quartz	nd	nd	203.4	nd	I	<5	160.1	
	quartz	nd	nd	196.0	nd	I	<5	154.0	
	quartz	nd	nd	196.0	nd	I	<5	152.0	
	quartz	nd	nd	197.4	nd	I	<5	155.0	
	quartz	nd	nd	203.1	nd	I	<5	167.0	
	quartz	nd	nd	203.4	nd	I	<5	169.0	
	quartz	nd	nd	nd	nd	I	<5	nd	
	quartz	nd	nd	196.2	nd	I	<5	152.0	
	quartz	nd	nd	196.5	nd	I	<5	151.0	
BBDump1-A	quartz	-22.7	-1.5	197.1	2.57	I	10	157.9	**stockwork zone**
	quartz	-22.3	-5.4	197.3	8.41	I	<10	160.3	
	quartz	-22.0	-4.0	235.2	6.45	I	<10	203.2	
	quartz	nd	nd	203.9	nd	I	<5	160.1	
	quartz	-19.7	-5.0	198.5	7.86	I	<10	163.5	
	quartz	-19.3	-5.7	199.0	8.81	I	10	186.7	
	quartz	-19.0	-1.0	200.4	1.74	I	<10	156.2	
	quartz	nd	-2.1	195.9	3.55	I	<7	163.8	
BBDump1-B	quartz	nd	-6.5	294.3	9.86	I	<7	266.4	**stockwork zone**
	quartz	-22.7	-6.3	214.4	9.60	I	<7	171.9	
	quartz	-22.9	nd	nd	nd	I	<5	nd	
	quartz	nd	-5.2	200.0	8.14	I	<5	162.1	
	quartz	-21.0	-5.5	215.8	8.55	I	<5	184.3	
	quartz	-20.6	-6.5	nd	9.86	I	<5	188.3	
	quartz	nd	nd	210.7	nd	I	<5	188.7	
	quartz	nd	-5.2	203.0	8.14	I	<10	nd	
	quartz	-21.9	-5.7	196.8	8.81	I	<10	174.4	
	quartz	-21.6	-5.1	212.9	8.00	I	<5	185.4	
	quartz	nd	nd	200.8	nd	I	<5	183.0	
	quartz	-22.9	-5.5	240.6	8.55	I	<10	200.3	
	quartz	nd	nd	218.3	nd	I	<5	nd	
BBDump1-C	quartz	nd	nd	205.2	nd	I	<5	178.6	**stockwork zone**
	quartz	-18.4	-3.4	209.6	5.56	I	<10	191.0	
	quartz	-19.0	-1.7	211.7	2.90	I	<7	191.3	
	quartz	-17.0	-2.8	208.9	4.65	I	<7	184.1	
	quartz	-19.0	-2.6	201.6	4.34	I	<10	177.2	
	quartz	nd	-0.8	193.5	1.40	I	<10	152.0	
	quartz	-17.1	-2.1	202.9	3.55	I	<7	187.4	
	quartz	nd	-2.0	203.2	3.39	I	<5	174.6	
	quartz	nd	nd	306.2	nd	I	<3	293.5	
	quartz	-17.4	-0.7	193.0	1.23	I	<3	nd	

Sample No./ Section	Mineral studied	1st-ice Tm	Tm-ice	Th (L-V)-L	NaCl eq wt %	Inclusion type	Inclusion size (µm)	Tr	Remarks
BBDump1-D	quartz	nd	nd	198.9	nd	I	<5	159.8	**stockwork zone**
	quartz	nd	nd	191.2	nd	I	<3	160.3	
	quartz	-17.1	-5.3	241.7	8.28	I	<7	170.2	
	quartz	-20.6	-3.8	240.3	6.16	I	<5	213.0	
	quartz	nd	-2.9	236.8	4.80	I	<3	218.7	
	quartz	nd	nd	192.8	nd	I	<3	160.5	
BBDump1-E	quartz	nd	-4.5	197.0	7.17	I	<7	nd	**stockwork zone**
	quartz	nd	-3.4	182.9	5.56	I	<5	149.5	
	quartz	nd	nd	252.8	nd	I	<5	228.5	
	quartz	nd	nd	203.7	nd	I	<3	185.1	
	quartz	-22.7	nd	196.9	nd	I	<5	nd	
	quartz	-23.0	-0.8	303.7	1.40	I	<7	290.7	
	quartz	nd	-5.0	212.1	7.86	I	<5	191.2	
	quartz	-21.9	-4.0	212.0	6.45	I	<5	198.1	
	quartz	nd	-3.7	267.8	6.01	I	<10	168.5	
	quartz	-21.8	-4.1	208.3	6.59	I	<5	180.8	
	quartz	-18.5	-1.9	215.0	3.23	I	<5	159.2	
Bukit Ketaya									
TC09	barite	-17.0	-3.7	307.0	6.01	I	10	292.0	**barite ore**
	barite	-21.0	-2.7	219.0	4.49	I	10	176.2	
	barite	nd	nd	192.0	nd	I	<5	151.2	
	barite	nd	nd	195.0	nd	I	<5	156.3	
	barite	nd	nd	242.0	nd	I	<5	215.0	
TC10-A	barite	-23.1	-8.0	230.0	11.70	I	<7	173.2	**barite ore**
	barite	nd	-4.0	222.8	6.45	I	<5	194.9	
	barite	-22.2	-9.4	229.8	13.29	I	<5	195.5	
	barite	-20.2	-3.9	244.2	6.30	I	<10	208.1	
	barite	-19.0	-4.0	260.2	6.45	I	<10	227.1	
	barite	-21.1	-8.2	218.8	11.81	I	<5	208.7	
	barite	nd	-5.0	260.2	7.86	I	<10	208.1	
	barite	-19.8	-2.9	230.9	4.80	I	<5	172.0	
	barite	-20.1	-3.0	253.3	4.96	I	<10	220.6	
	barite	nd	nd	231.7	nd	I	<10	201.5	
TC10-B	barite	-20.1	-8.6	219.3	12.39	I	10	173.6	**barite ore**
	barite	nd	-8.3	209.8	12.05	I	<7	170.3	
	barite	nd	-4.0	216.8	6.45	I	<7	191.9	
	barite	-19.8	-8.2	225.1	11.93	I	<7	191.3	
	barite	nd	-5.3	244.2	8.28	I	<7	159.8	
	barite	nd	nd	232.4	nd	I	<5	205.2	

Sample No./ Section	Mineral studied	1st-ice Tm	Tm-ice	Th (L-V)-L	NaCl eq wt %	Inclusion type	Inclusion size (μm)	Tr	Remarks
	barite	-22.9	-3.7	250.3	6.01	I	<10	224.0	
	barite	nd	nd	294.3	nd	I	<10	270.6	
	barite	nd	-3.8	245.6	6.16	I	<5	215.7	
S6/7 a12-A	barite	-22.4	-5.4	220.3	8.41	I	<7	184.0	**barite ore**
	barite	nd	-3.3	249.8	5.41	I	<7	215.2	
	barite	nd	nd	240.2	nd	I	<5	205.2	
	barite	-22.3	-4.2	217.1	6.74	I	<7	185.4	
	barite	-21.0	-3.1	216.9	5.11	I	<5	186.0	
	barite	nd	-3.5	229.2	5.56	I	<7	192.7	
	barite	nd	nd	202.7	nd	I	<7	172.0	
	barite	-20.3	nd	216.0	nd	I	<5	175.9	
	barite	nd	-4.5	254.5	7.17	I	<5	218.9	
	barite	nd	nd	227.8	nd	I	<5	206.7	
	barite	nd	-3.0	226.4	4.96	I	<5	192.2	
	barite	-21.5	-1.0	230.6	1.74	I	<7	185.7	
	barite	-20.1	-4.7	192.1	7.45	I	<7	152.7	
	barite	nd	-3.1	202.5	5.11	I	<5	nd	
S6/7 a12-B	barite	-19.5	-4.4	204.1	7.02	I	<7	171.8	**barite ore**
	barite	-20.1	-3.8	228.3	6.16	I	<7	215.2	
S6/7 a12-C	barite	-23.4	-11.4	248.4	15.37	I	<5	220.9	**barite ore**
	barite	-21.1	nd	256.6	nd	I	<5	230.8	
	barite	-20.0	nd	270.4	nd	I	<5	258.9	
S6/7 a12-D	barite	-28.4	-4.7	232.2	7.45	I	<5	198.9	**barite ore**
	barite	-19.2	-4.5	261.8	7.17	I	<5	236.5	
	barite	nd	nd	264.5	nd	I	<5	231.0	
	barite	nd	-3.3	290.8	5.41	I	<3	268.5	
	barite	nd	-1.5	296.9	2.57	I	<3	279.4	
	barite	nd	-4.4	297.3	7.02	I	<3	275.8	
TC10-C	barite	-22.7	-3.6	223.4	5.86	I	<5	197.1	**barite ore**
	barite	nd	-4.1	210.8	6.59	I	<3	nd	
	barite	-21.6	-4.0	217.1	6.45	I	<3	nd	
	barite	-21.0	-3.8	216.5	6.16	I	<5	190.2	
	barite	-22.5	-3.7	225.7	6.01	I	<5	189.4	
	barite	-21.7	-3.9	207.6	6.30	I	<5	184.1	
	barite	nd	-3.5	229.2	5.71	I	<3	190.9	
	barite	-17.7	-4.2	208.7	6.74	I	<3	188.2	

Sample No./ Section	Mineral studied	1st-ice Tm	Tm-ice	Th (L-V)-L	NaCl eq wt %	Inclusion type	Inclusion size (μm)	Tr	Remarks
TC10-D	barite	-21.9	-6.4	217.5	9.73	I	<3	183.2	**barite ore**
	barite	-22.0	-6.2	210.4	9.47	I	<3	172.1	
	barite	nd	-6.1	218.8	9.34	I	<3	192.1	
BK11a-A	quartz	-23.3	-9.8	201.2	13.72	I	<10	171.3	**stockwork zone**
	quartz	-19.7	-4.1	240.4	6.59	I	<10	207.0	
	quartz	-23.2	-7.3	233.4	10.86	I	<7	198.7	
	quartz	-23.4	-4.3	263.9	6.88	I	<5	217.2	
	quartz	-19.3	-8.8	210.7	12.62	I	<7	182.0	
	quartz	-19.0	-4.5	290.6	7.17	I	<5	270.3	
	quartz	nd	nd	292.7	nd	I	<5	270.5	
	quartz	-21.6	-3.8	243.0	6.16	I	<5	182.1	
	quartz	-23.2	-3.7	269.9	6.01	I	<5	245.3	
	quartz	-23.3	-5.4	251.7	8.41	I	<5	223.6	
	quartz	nd	nd	239.7	nd	I	<5	181.4	
	quartz	-22.5	nd	230.5	nd	I	<10	203.4	
	quartz	-22.1	-8.1	238.8	11.81	I	<10	203.0	
	quartz	-21.9	nd	200.3	nd	I	<10	165.4	
	quartz	-21.7	nd	203.4	nd	I	<5	169.4	
BK11a-B	quartz	-21.7	-5.7	282.6	8.81	I	<10	240.9	**stockwork zone**
	quartz	-21.6	-4.6	229.9	7.31	I	<5	200.3	
	quartz	-21.3	nd	nd	nd	I	<5	nd	
	quartz	nd	-7.0	310.7	10.49	I	<5	294.8	
	quartz	nd	-3.4	211.9	5.56	I	<5	178.6	
	quartz	nd	nd	nd	nd	I	<5	nd	
	quartz	nd	nd	225.4	nd	I	<5	192.0	
	quartz	nd	nd	260.2	nd	I	<5	230.1	
	quartz	nd	nd	236.1	nd	I	<5	207.3	
	quartz	nd	nd	218.1	nd	I	<5	188.7	
BK11a-C	quartz	-21.7	-6.6	239.6	9.80	I	<5	218.9	**stockwork zone**
	quartz	nd	nd	240.0	nd	I	<5	219.9	
	quartz	nd	-4.4	245.1	7.02	I	<5	217.2	
	quartz	nd	nd	259.8	nd	I	<5	235.3	
	quartz	-25.8	nd	284.2	nd	I	<7	261.5	
	quartz	-20.0	-4.1	206.9	6.59	I	<3	171.5	
	quartz	nd	-7.1	302.7	10.49	I	<5	284.7	
	quartz	-19.8	-2.4	243.6	4.03	I	<3	213.4	
	quartz	-20.3	-7.1	230.3	10.49	I	<5	200.0	
BK11a-D	quartz	-27.4	-8.2	202.1	11.93	I	<3	143.6	**stockwork zone**
	quartz	-22.8	-10.3	210.6	14.25	I	<5	157.4	
	quartz	-19.4	-8.2	210.9	11.93	I	<7	174.6	
	quartz	-19.7	nd	215.6	nd	I	<3	191.6	

Sample No./ Section	Mineral studied	1st-ice Tm	Tm-ice	Th (L-V)-L	NaCl eq wt %	Inclusion type	Inclusion size (µm)	Tr	Remarks
	quartz	nd	nd	203.4	nd	I	<3	158.5	
BK11a-E	quartz	-23.8	-7.4	221.3	10.86	I	<7	183.7	**stockwork zone**
	quartz	-21.6	-7.2	228.1	10.73	I	<5	200.0	
	quartz	-19.7	-0.8	237.3	1.40	I	<3	201.9	
BK11a-F	quartz	nd	-3.0	231.0	4.96	I	<7	194.9	**stockwork zone**
	quartz	nd	-2.9	230.8	4.80	I	<7	194.8	
	quartz	-21.8	-2.2	226.3	3.71	I	<7	195.0	
	quartz	nd	-7.4	241.2	10.98	I	<5	210.4	
	quartz	nd	-8.4	229.3	12.16	I	<10	198.6	

Th (L-V)-L = temperature of homogenisation into liquid phase
Tm-ice = temperature of last ice melting
1st-ice Tm = temperature of first ice melting
Salinity were calculated using equations of Potter et al. (1978)
Tr = temperature of buble pop in

Appendix X: Laser Raman Spectroscopic results

SAMPLE NUMBER	No. of analysis	CO_2 1285 cm-1	CO_2 1388 cm-1	CO_2 mol %	N_2 mol %	H_2S mol %	C_3H_8 mol %	CH_4 mol %	C_2H_6 mol %	NH_3 mol %	H_2 mol %
Barite	1		2475	100	0	0	0	0	0	0	0
BBotolDump1	1	900	3265.5	100	0	0	0	0	0	0	0
	2	318	2022.5	100	0	0	0	0	0	0	0
	3		1979.5	100	0	0	0	0	0	0	0
	4		450.5	100	0	0	0	0	0	0	0
BBotolDump2	1	1313	2291	100	0	0	0	0	0	0	0
	2	3403.5	7523	100	0	0	0	0	0	0	0
	3	3030	5488	100	0	0	0	0	0	0	0
	4	5336	9390	100	0	0	0	0	0	0	0
S6/7_a12	1		1520.5	100	0	0	0	0	0	0	0
	2	6370	11742.5	100	0	0	0	0	0	0	0
	3		1630	100	0	0	0	0	0	0	0

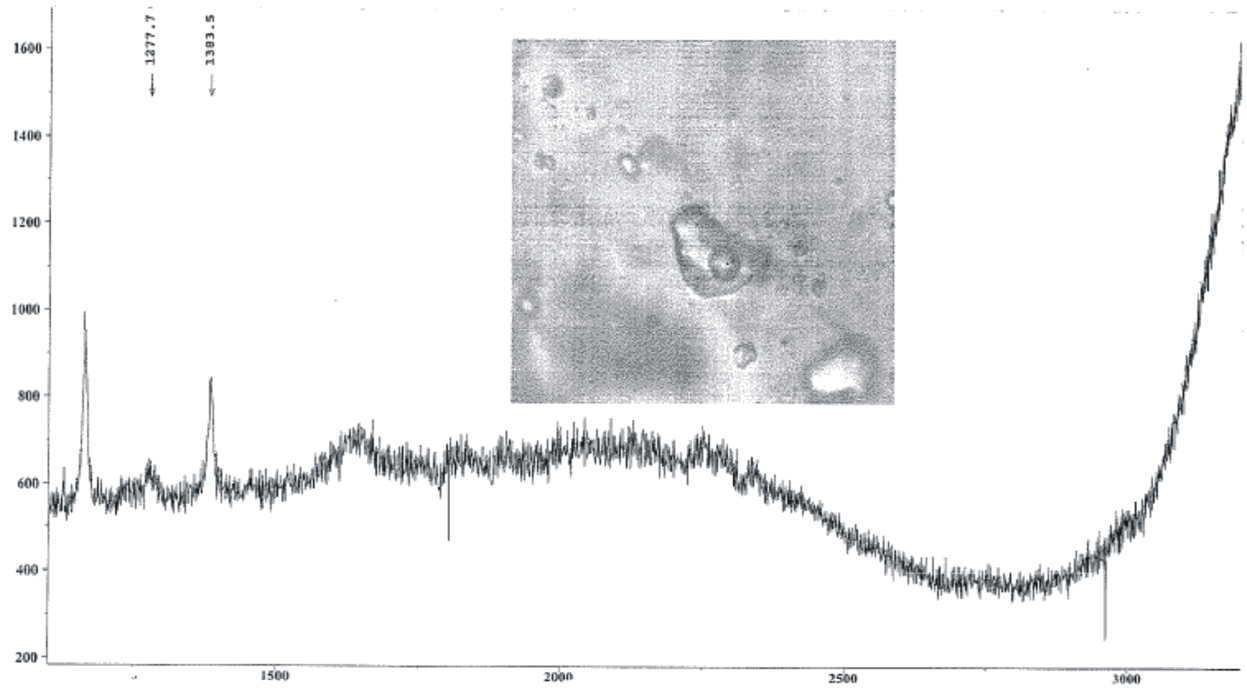

Sample : Barite -1
Operator : Mernagh
Date : 15-06-112
Power : 50
Time : 30

Excit_line : 514.532
Spectro : 1893.21
Grating : 1800
Slit : 100
Hole : 400

Filtr : ----
Accum : 1
Objectiv : x100
File : BBOT1_1
Remark : Vapour phase

Australian Government
Geoscience Australia

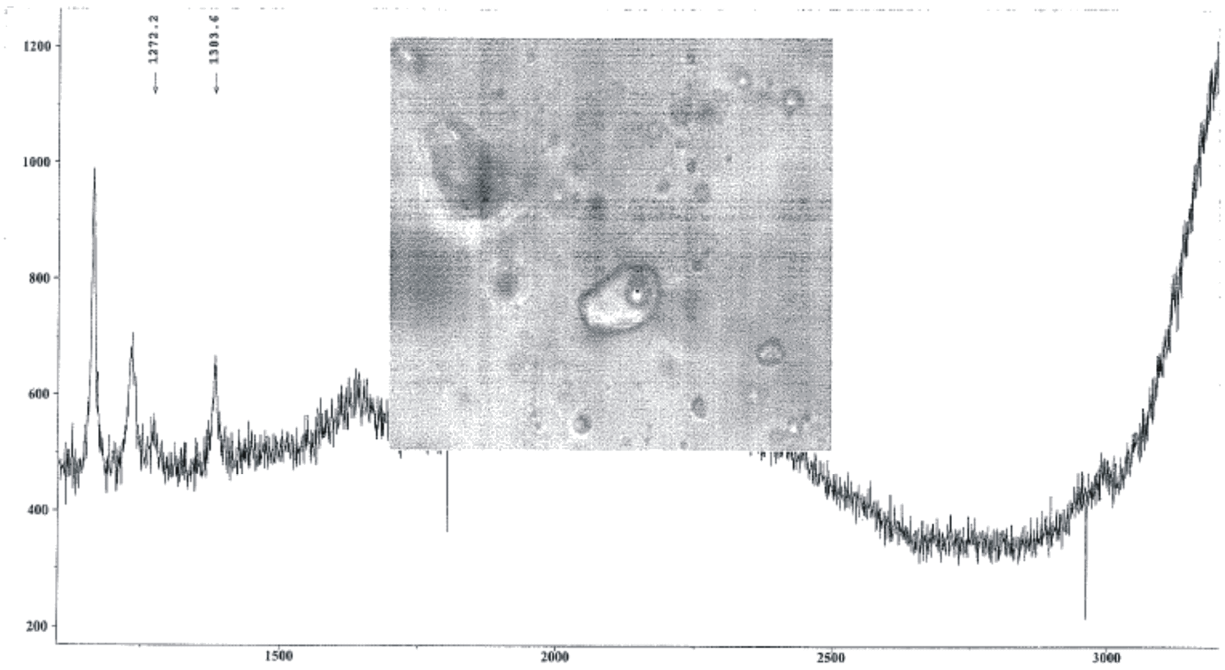

Sample	: Barite -1	Excit_line	: 514.532	Filtr	: ----		
Operator	: Mernagh	Spectro	: 1893.21	Accum	: 1		
Date	: 15-06-112	Grating	: 1800	Objectiv	: x100		
Power	: 50	Slit	: 100	File	: BBOT1_2		
Time	: 30	Hole	: 400	Remark	: Vapour phase		

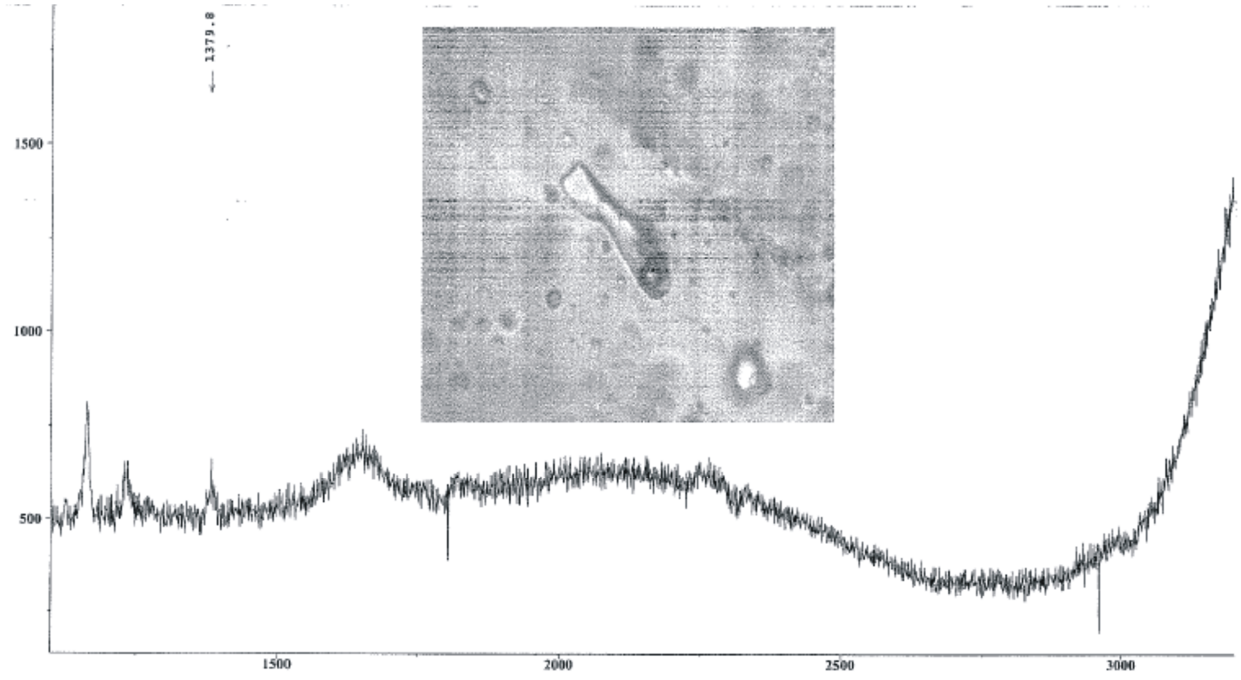

Sample	: Barite -1	Excit_line	: 514.532	Filtr	: ----		
Operator	: Mernagh	Spectro	: 1893.21	Accum	: 1		
Date	: 15-06-112	Grating	: 1800	Objectiv	: x100		
Power	: 50	Slit	: 100	File	: BBOT1_3		
Time	: 30	Hole	: 400	Remark	: Vapour phase		

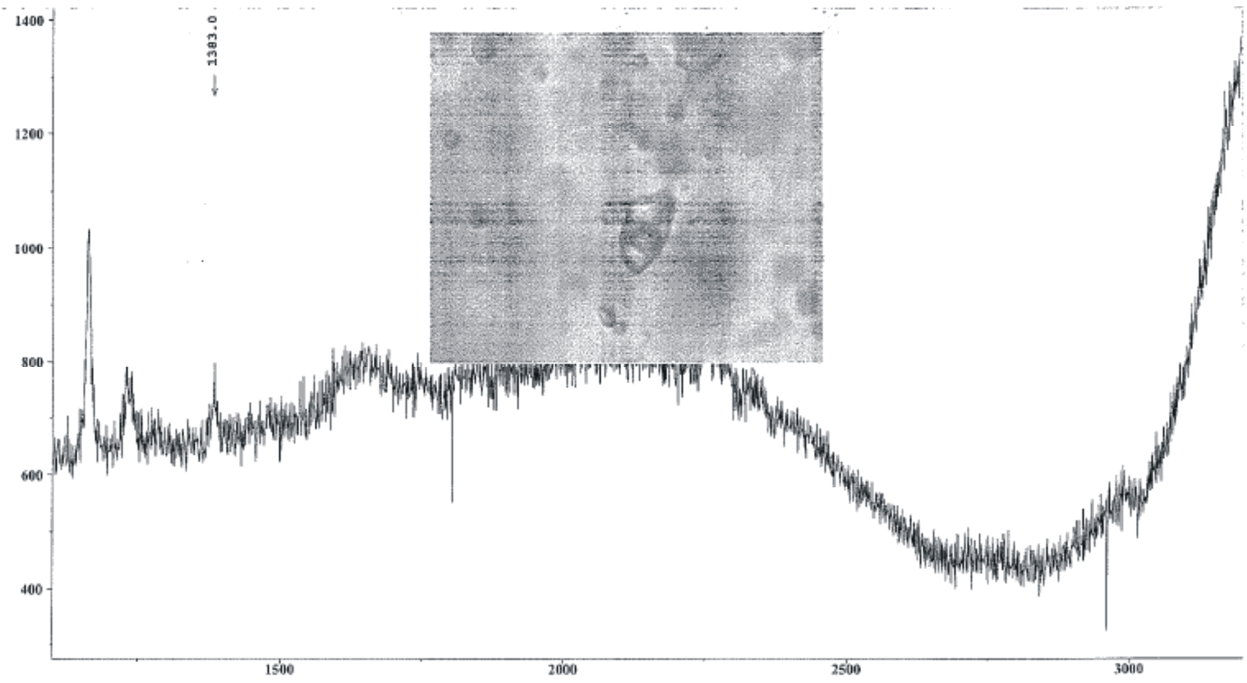

Sample	: Barite -1	Excit_line	: 514.532	Filtr	: ----		
Operator	: Mernagh	Spectro	: 1893.21	Accum	: 1		
Date	: 15-06-112	Grating	: 1800	Objectiv	: x100		
Power	: 50	Slit	: 100	File	: BBOT1_4		
Time	: 30	Hole	: 400	Remark	: Vapour phase		

Australian Government
Geoscience Australia

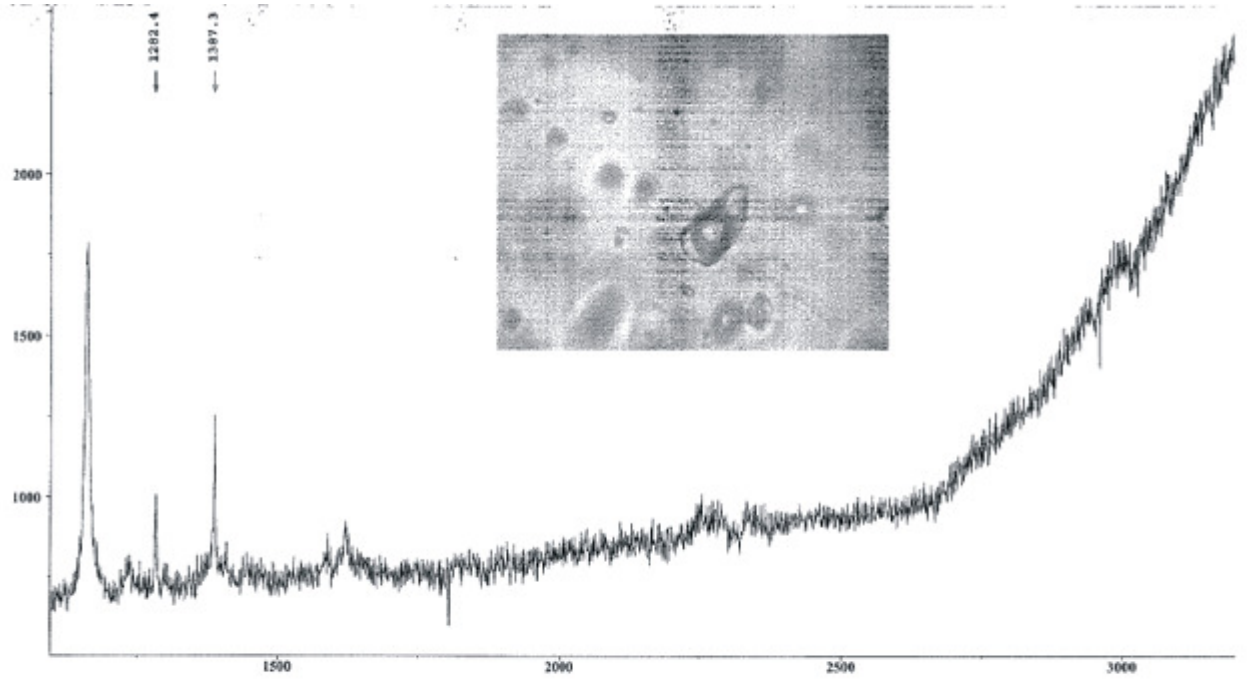

Sample	: Barite -1	Excit_line	: 514.532	Filtr	: ----		
Operator	: Mernagh	Spectro	: 1893.21	Accum	: 1		
Date	: 15-06-112	Grating	: 1800	Objectiv	: x100		
Power	: 50	Slit	: 100	File	: BBOT2_1		
Time	: 30	Hole	: 400	Remark	: Vapour phase		

Australian Government
Geoscience Australia

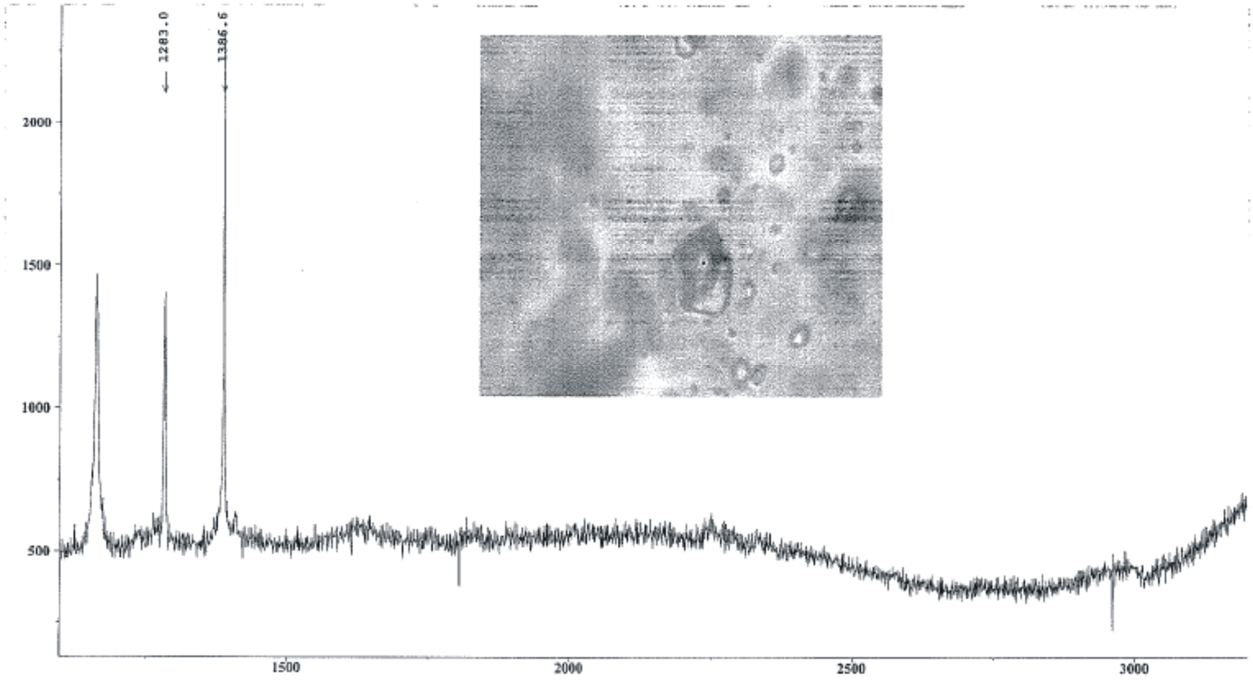

Sample	: Barite -1	Excit_line	: 514.532	Filtr	: ----		
Operator	: Mernagh	Spectro	: 1893.21	Accum	: 1		
Date	: 15-06-112	Grating	: 1800	Objectiv	: x100		
Power	: 50	Slit	: 100	File	: BBOT2_2		
Time	: 30	Hole	: 400	Remark	: Vapour phase		

Australian Government
Geoscience Australia

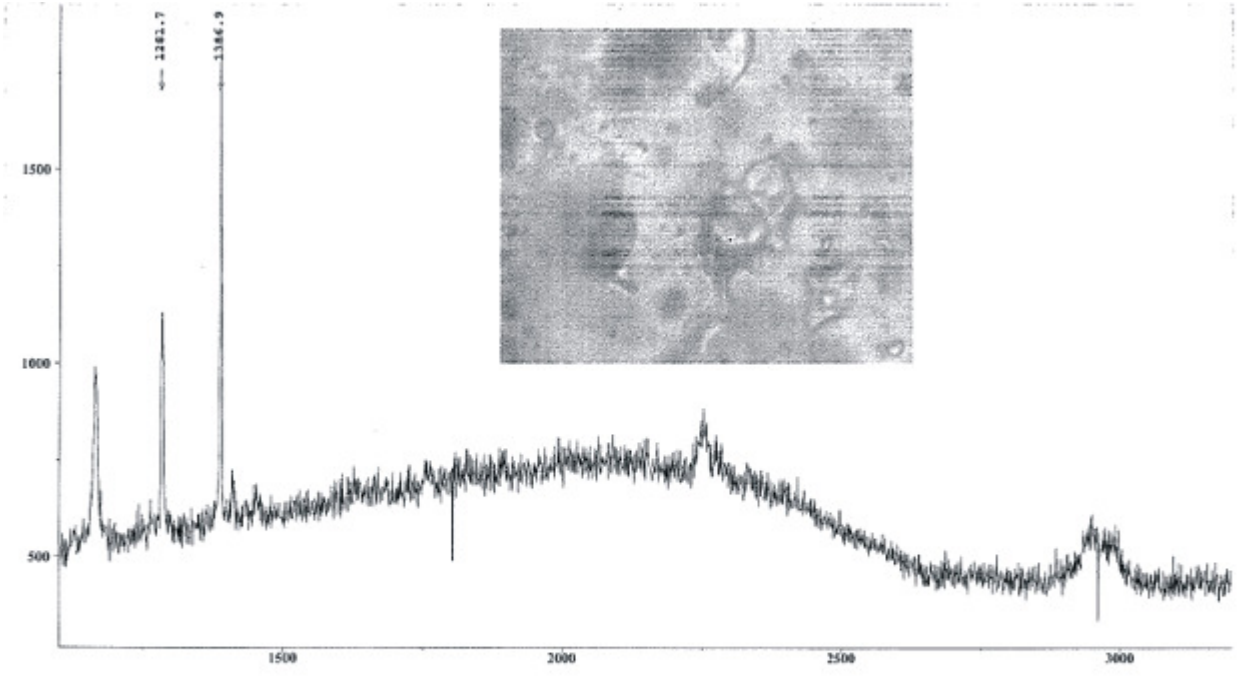

Sample	: Barite -1	Excit_line	: 514.532	Filtr	: ----		
Operator	: Mernagh	Spectro	: 1893.21	Accum	: 1		
Date	: 15-06-112	Grating	: 1800	Objectiv	: x100		
Power	: 50	Slit	: 100	File	: BBOT2_3		
Time	: 30	Hole	: 400	Remark	: Vapour phase		

Australian Government
Geoscience Australia

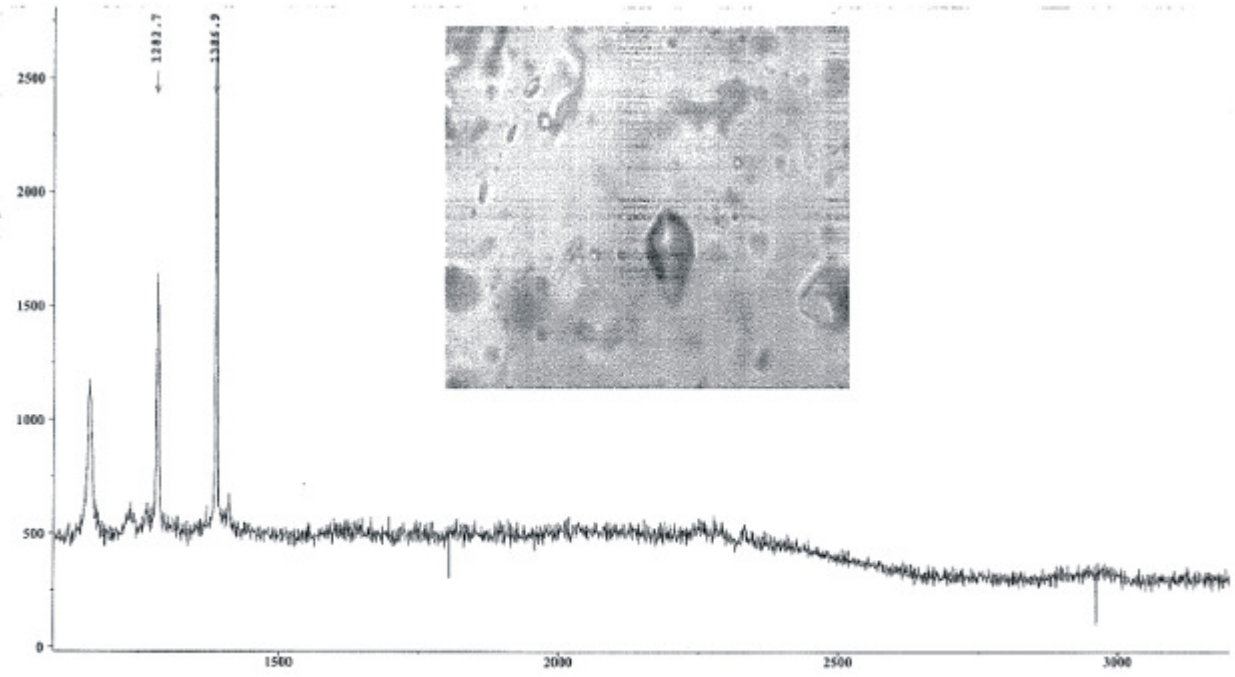

Sample	: Barite -1	Excit_line	: 514.532	Filtr	: ----		
Operator	: Mernagh	Spectro	: 1893.21	Accum	: 1		
Date	: 15-06-112	Grating	: 1800	Objectiv	: x100		
Power	: 50	Slit	: 100	File	: BBOT2_4		
Time	: 30	Hole	: 400	Remark	: Vapour phase		

Australian Government
Geoscience Australia

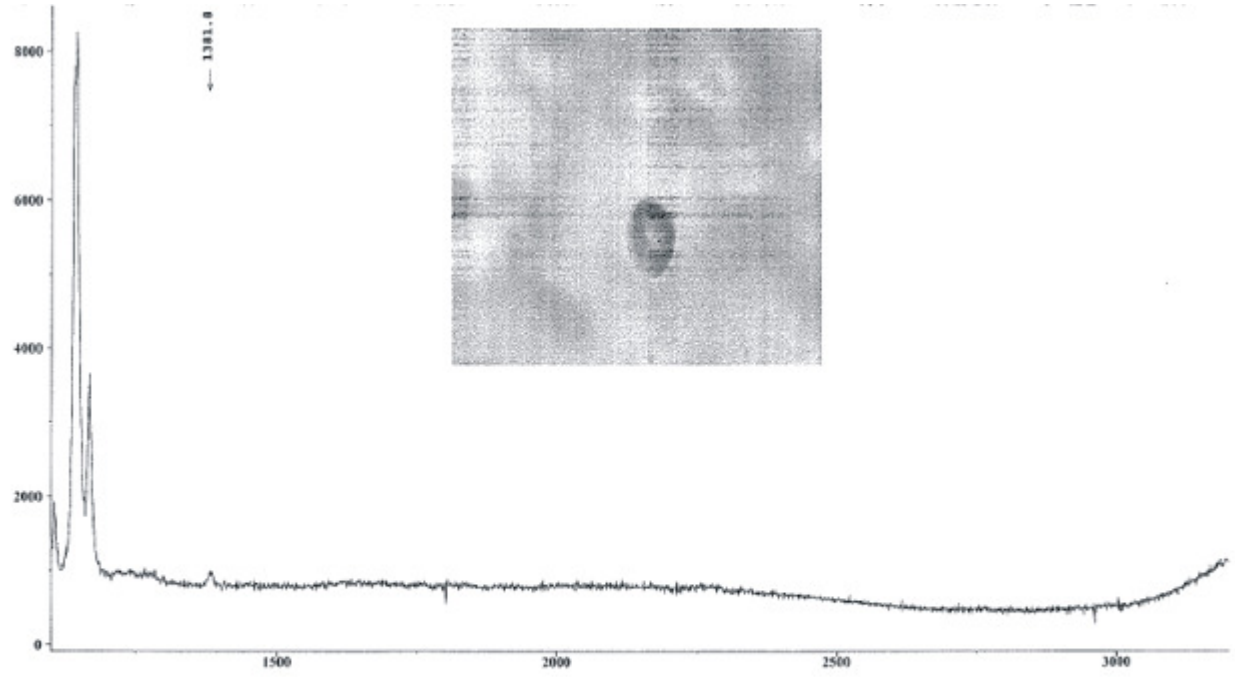

Sample	: Barite -1	Excit_line	: 514.532	Filtr	: ----		
Operator	: Mernagh	Spectro	: 1893.21	Accum	: 1		
Date	: 15-06-112	Grating	: 1800	Objectiv	: x100		
Power	: 50	Slit	: 100	File	: 7_A12_1		
Time	: 30	Hole	: 400	Remark	: Vapour phase		

Australian Government
Geoscience Australia

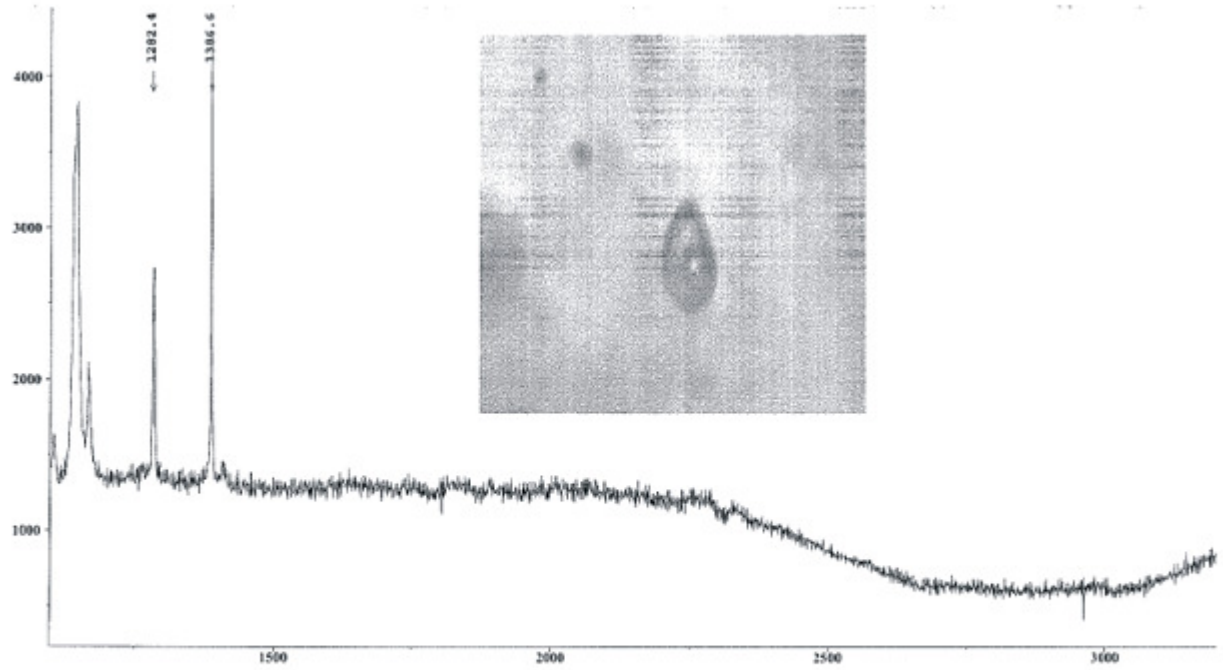

Sample	: Barite -1	Excit_line	: 514.532	Filtr	: ----		
Operator	: Mernagh	Spectro	: 1893.21	Accum	: 1		
Date	: 15-06-112	Grating	: 1800	Objectiv	: x100		
Power	: 50	Slit	: 100	File	: 7_A12_2		
Time	: 30	Hole	: 400	Remark	: Vapour phase		

Australian Government
Geoscience Australia

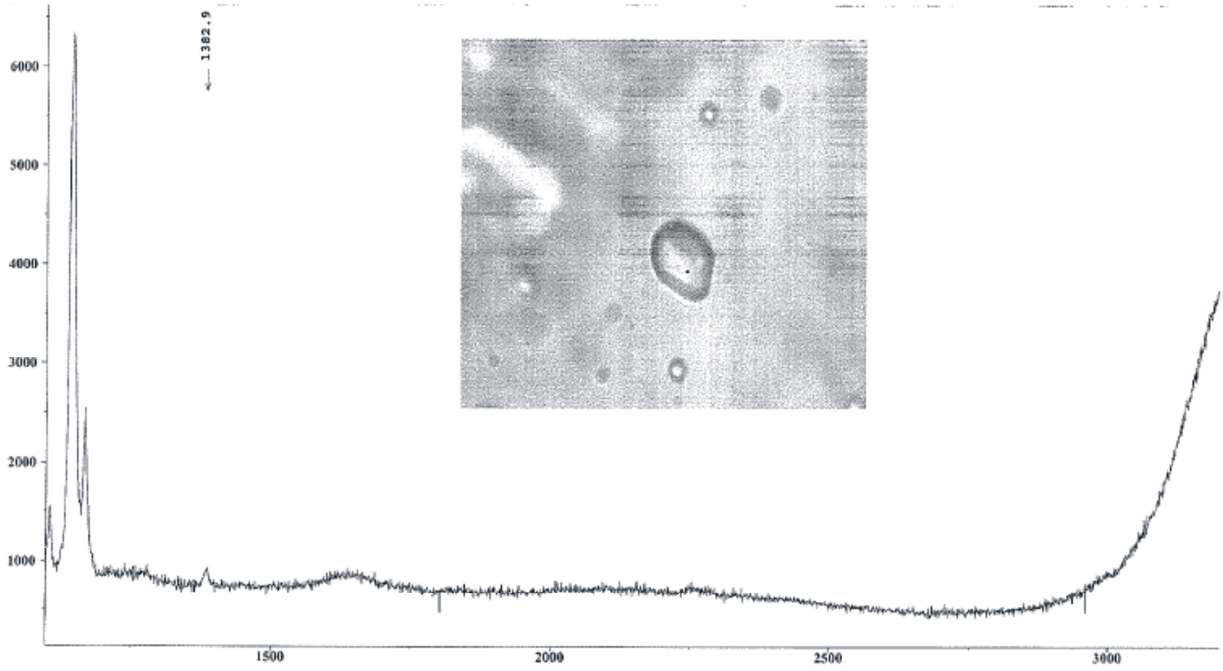

Sample	: Barite -1	Excit_line	: 514.532	Filtr	: ----		
Operator	: Mernagh	Spectro	: 1893.21	Accum	: 1		
Date	: 15-06-112	Grating	: 1800	Objectiv	: x100		
Power	: 50	Slit	: 100	File	: 7_A12_3		
Time	: 30	Hole	: 400	Remark	: Vapour phase		

Australian Government
Geoscience Australia

Appendix XI: Calculated density
and
pressure of fluids

HOKIEFLINCS_H2O-NACL

A numerical tool to calculate PVTX properties and trapping conditions of H_2O-NaCl fluid inclusions. .

To use the program, enter T_m data in column C in the "Main" worksheet. Column D contains a drop-down list to select the phase that melts last (at T_m). Enter Th data in colum E. Each row of data represents a single fluid inclusion. For example, if one inclusion has $T_m$ice of -10 °C and T_h of 300 °C, then the values "-10", "ice" and "300" are entered in cells (C28), (D28) and (E28), respectively.

The output data for each inclusion (each row) are the fluid inclusion salinity, density, pressure at homogenization, and dP/dT isochore slope. These are listed in columns H, J, K and L, respectively. To calculate a pressure correction (or to draw an isochore), select to input an estimate of either pressure or temperature in column N, and input the estimate in column O. Pressure-temperature conditions on the isochore are listed in columns Q and R. To **copy/paste** output data into another spreadsheet, use "Edit - Paste Special" and select "Values," because the contents of the output cells are formulae linked to the calculations.

Column T contains a variety of output messages, that will alert the user to possible errors in the input data or inputs that are out of the range of validity of the models. Please be careful to check column S for warning messages, especially in cases where the output data appear to be anomolous.

Column U contains the citation information for numerical models used in the calculations for each inclusion (which models are used depends on the input data). These citations should be included in descriptions of fluid inclusion analysis using HOKIEFLINCS_H2O-NACL.

The numerical models used by the tool are contained in a series of hidden worksheets that can be accessed by selecting Format - Sheet... - Unhide.
Any number of fluid inclusions can be interpreted in a single session, but the sheet is initially setup to compute properties up to **row 300**. If additional lines are needed, simply copy and paste the formulas in each of the worksheets. To do so, select "Format - Sheet... - Unhide" and unhide each of the hidden sheets (one by one). In each of the sheets, copy the formulae from the lowermost row and paste into as many additional rows as required (note that the file size increases with each additional row, so using only as many as needed will save space).

In addition to the citations included in column T, please cite:
Steele-MacInnis, M., Lecumberri-Sanchez, P., Bodnar, R.J., 2012. HOKIEFLINCS_H2O-NACL: A Microsoft Excel spreadsheet for interpreting microthermometric data from fluid inclusions based on the PVTX properties of H_2O-NaCl. *Computers & Geosciences* , XX, XXXX-XXXX.

Please direct and questions and/or comments to mjmaci@vt.edu, pilar@vt.edu or rjb@vt.edu

Inputs:			Outputs:					Inputs:		Outputs:		
			Salinity	T @ homog.	P @ homog.	r_{BULK}	dP/dT	Calculate a P correction?		Trapping Conditions		
Tm	phase	Th_{L-V} S (wt%)	wt% NaCl	(°C)	(bar)	/$cm_{3(g/cr}$	(bar/°C)	Based on:	T or P	T (°C)	P (bar)	References
0	ice	300	0.00	300.0	86	0.700	9.6	pressure estimate	1000 bar	395	1000	Bodnar, R.J. (1993) Revised equation and table for determining th
-2.3	ice	195.0	3.87	195.0	14	0.901	15.9					Bodnar, R.J. (1993) Revised equation and table for determining th
-2.7	ice	195.4	4.49	195.4	14	0.905	16.0					Bodnar, R.J. (1993) Revised equation and table for determining th
-3.1	ice	230.0	5.11	230.0	27	0.868	14.3					Bodnar, R.J. (1993) Revised equation and table for determining th
-3.1	ice	197.7	5.11	197.7	14	0.907	16.0					Bodnar, R.J. (1993) Revised equation and table for determining th
-1.5	ice	197.1	2.57	197.1	14	0.889	15.7					Bodnar, R.J. (1993) Revised equation and table for determining th
-5.4	ice	197.3	8.41	197.3	14	0.933	16.7					Bodnar, R.J. (1993) Revised equation and table for determining th
-4.0	ice	235.2	6.45	235.2	29	0.873	14.2					Bodnar, R.J. (1993) Revised equation and table for determining th
-5.0	ice	198.5	7.86	198.5	14	0.927	16.5					Bodnar, R.J. (1993) Revised equation and table for determining th
-5.7	ice	199.0	8.81	199.0	14	0.934	16.7					Bodnar, R.J. (1993) Revised equation and table for determining th
-1.0	ice	200.4	1.74	200.4	15	0.879	15.5					Bodnar, R.J. (1993) Revised equation and table for determining th
-2.1	ice	195.9	3.55	195.9	14	0.898	15.8					Bodnar, R.J. (1993) Revised equation and table for determining th
-6.5	ice	294.3	9.86	294.3	74	0.826	11.7					Bodnar, R.J. (1993) Revised equation and table for determining th
-6.3	ice	214.4	9.60	214.4	19	0.923	16.0					Bodnar, R.J. (1993) Revised equation and table for determining th
-5.2	ice	200.0	8.14	200.0	15	0.928	16.5					Bodnar, R.J. (1993) Revised equation and table for determining th
-5.5	ice	215.8	8.55	215.8	20	0.914	15.6					Bodnar, R.J. (1993) Revised equation and table for determining th
-5.2	ice	203.0	8.14	203.0	16	0.925	16.3					Bodnar, R.J. (1993) Revised equation and table for determining th
-5.7	ice	196.8	8.81	196.8	14	0.936	16.8					Bodnar, R.J. (1993) Revised equation and table for determining th
-5.1	ice	212.9	8.00	212.9	19	0.912	15.7					Bodnar, R.J. (1993) Revised equation and table for determining th
-5.5	ice	240.6	8.55	240.6	32	0.884	14.3					Bodnar, R.J. (1993) Revised equation and table for determining th
-3.4	ice	209.6	5.56	209.6	18	0.897	15.4					Bodnar, R.J. (1993) Revised equation and table for determining th
-1.7	ice	211.7	2.90	211.7	19	0.874	15.0					Bodnar, R.J. (1993) Revised equation and table for determining th
-2.8	ice	208.9	4.65	208.9	18	0.891	15.3					Bodnar, R.J. (1993) Revised equation and table for determining th
-2.6	ice	201.6	4.34	201.6	16	0.897	15.6					Bodnar, R.J. (1993) Revised equation and table for determining th
-0.8	ice	193.5	1.40	193.5	13	0.885	15.9					Bodnar, R.J. (1993) Revised equation and table for determining th
-2.1	ice	202.9	3.55	202.9	16	0.890	15.5					Bodnar, R.J. (1993) Revised equation and table for determining th
-2.0	ice	203.2	3.39	203.2	16	0.888	15.5					Bodnar, R.J. (1993) Revised equation and table for determining th
-0.7	ice	193.0	1.22	193.0	13	0.884	15.9					Bodnar, R.J. (1993) Revised equation and table for determining th
-5.3	ice	241.7	8.28	241.7	32	0.880	14.1					Bodnar, R.J. (1993) Revised equation and table for determining th
-3.8	ice	240.3	6.16	240.3	32	0.864	13.9					Bodnar, R.J. (1993) Revised equation and table for determining th
-2.9	ice	236.8	4.80	236.8	30	0.857	13.9					Bodnar, R.J. (1993) Revised equation and table for determining th
-4.5	ice	197.0	7.17	197.0	14	0.924	16.4					Bodnar, R.J. (1993) Revised equation and table for determining th
-3.4	ice	182.9	5.56	182.9	10	0.927	16.8					Bodnar, R.J. (1993) Revised equation and table for determining th
-0.8	ice	303.7	1.40	303.7	90	0.711	9.6					Bodnar, R.J. (1993) Revised equation and table for determining th
-5.0	ice	212.1	7.86	212.1	19	0.912	15.7					Bodnar, R.J. (1993) Revised equation and table for determining th
-4.0	ice	212.0	6.45	212.0	19	0.901	15.4					Bodnar, R.J. (1993) Revised equation and table for determining th
-3.7	ice	267.8	6.01	267.8	51	0.824	12.4					Bodnar, R.J. (1993) Revised equation and table for determining th
-4.1	ice	208.3	6.59	208.3	18	0.907	15.7					Bodnar, R.J. (1993) Revised equation and table for determining th
-1.9	ice	215.0	3.23	215.0	20	0.872	14.9					Bodnar, R.J. (1993) Revised equation and table for determining th
												#VALUE!
-5.0	ice	219.1	7.86	219.1	22	0.904	15.3					Bodnar, R.J. (1993) Revised equation and table for determining th
-3.4	ice	239.6	5.56	239.6	32	0.860	13.8					Bodnar, R.J. (1993) Revised equation and table for determining th
-2.1	ice	200.3	3.55	200.3	15	0.893	15.6					Bodnar, R.J. (1993) Revised equation and table for determining th
-3.0	ice	198.6	4.96	198.6	15	0.905	15.9					Bodnar, R.J. (1993) Revised equation and table for determining th
-5.6	ice	206.5	8.68	206.5	17	0.925	16.2					Bodnar, R.J. (1993) Revised equation and table for determining th
-2.7	ice	206.7	4.49	206.7	17	0.892	15.4					Bodnar, R.J. (1993) Revised equation and table for determining th
-5.6	ice	210.0	8.68	210.0	18	0.921	16.0					Bodnar, R.J. (1993) Revised equation and table for determining th
-5.4	ice	206.0	8.41	206.0	17	0.923	16.2					Bodnar, R.J. (1993) Revised equation and table for determining th
-2.1	ice	210.8	3.55	210.8	19	0.880	15.1					Bodnar, R.J. (1993) Revised equation and table for determining th
-6.3	ice	214.4	9.60	214.4	19	0.923	16.0					Bodnar, R.J. (1993) Revised equation and table for determining th
-5.3	ice	211.1	8.28	211.1	18	0.917	15.9					Bodnar, R.J. (1993) Revised equation and table for determining th
-5.5	ice	217.4	8.55	217.4	21	0.912	15.6					Bodnar, R.J. (1993) Revised equation and table for determining th
-6.4	ice	223.3	9.73	223.3	23	0.915	15.5					Bodnar, R.J. (1993) Revised equation and table for determining th
-6.1	ice	210.4	9.34	210.4	18	0.926	16.1					Bodnar, R.J. (1993) Revised equation and table for determining th
-10.6	ice	243.9	14.57	243.9	32	0.932	15.3					Bodnar, R.J. (1993) Revised equation and table for determining th
-2.5	ice	251.4	4.18	251.4	39	0.831	13.0					Bodnar, R.J. (1993) Revised equation and table for determining th
-5.8	ice	205.1	8.95	205.1	16	0.928	16.4					Bodnar, R.J. (1993) Revised equation and table for determining th
-6.1	ice	228.1	9.34	228.1	25	0.906	15.1					Bodnar, R.J. (1993) Revised equation and table for determining th
-3.8	ice	228.9	6.16	228.9	26	0.878	14.5					Bodnar, R.J. (1993) Revised equation and table for determining th
-0.5	ice	298.9	0.88	298.9	84	0.714	9.8					Bodnar, R.J. (1993) Revised equation and table for determining th
-1.6	ice	187.2	2.74	187.2	12	0.902	16.2					Bodnar, R.J. (1993) Revised equation and table for determining th
												#VALUE!
-9.8	ice	201.2	13.72	201.2	14	0.970	17.8					Bodnar, R.J. (1993) Revised equation and table for determining th
-4.1	ice	240.4	6.59	240.4	32	0.867	13.9					Bodnar, R.J. (1993) Revised equation and table for determining th
-7.3	ice	233.4	10.86	233.4	27	0.912	15.1					Bodnar, R.J. (1993) Revised equation and table for determining th
-4.3	ice	263.9	6.88	263.9	48	0.838	12.7					Bodnar, R.J. (1993) Revised equation and table for determining th
-8.8	ice	210.7	12.62	210.7	18	0.952	16.9					Bodnar, R.J. (1993) Revised equation and table for determining th

Inputs:			Outputs:					Inputs:		Outputs:		
			Salinity	T @ homog.	P @ homog.	r_{BULK}	dP/dT	Calculate a P correction?		Trapping Conditions		
Tm	phase	Th_{L-V} S (wt%)	wt% NaCl	(°C)	(bar)	/$cm_{3(g/cr}$	(bar/°C)	Based on:	T or P	T (°C)	P (bar)	References
-4.5	ice	290.6	7.17	290.6	72	0.802	11.4					Bodnar, R.J. (1993) Revised equation and table for determining th
-3.8	ice	243.0	6.16	243.0	34	0.860	13.7					Bodnar, R.J. (1993) Revised equation and table for determining th
-3.7	ice	269.9	6.01	269.9	53	0.821	12.3					Bodnar, R.J. (1993) Revised equation and table for determining th
-5.4	ice	251.7	8.41	251.7	39	0.869	13.6					Bodnar, R.J. (1993) Revised equation and table for determining th
-8.1	ice	238.8	11.81	238.8	30	0.914	15.0					Bodnar, R.J. (1993) Revised equation and table for determining th
-5.7	ice	282.6	8.81	282.6	63	0.831	12.1					Bodnar, R.J. (1993) Revised equation and table for determining th
-4.6	ice	229.9	7.31	229.9	26	0.887	14.6					Bodnar, R.J. (1993) Revised equation and table for determining th
-7.0	ice	310.7	10.49	310.7	93	0.809	11.0					Bodnar, R.J. (1993) Revised equation and table for determining th
-3.4	ice	211.9	5.56	211.9	19	0.894	15.3					Bodnar, R.J. (1993) Revised equation and table for determining th
-6.6	ice	239.6	9.98	239.6	31	0.898	14.6					Bodnar, R.J. (1993) Revised equation and table for determining th
-4.4	ice	245.1	7.02	245.1	35	0.865	13.7					Bodnar, R.J. (1993) Revised equation and table for determining th
-4.1	ice	206.9	6.59	206.9	17	0.908	15.7					Bodnar, R.J. (1993) Revised equation and table for determining th
-7.1	ice	302.7	10.61	302.7	83	0.822	11.4					Bodnar, R.J. (1993) Revised equation and table for determining th
-2.4	ice	243.6	4.03	243.6	35	0.840	13.5					Bodnar, R.J. (1993) Revised equation and table for determining th
-7.1	ice	230.3	10.61	230.3	26	0.914	15.3					Bodnar, R.J. (1993) Revised equation and table for determining th
-8.2	ice	202.1	11.93	202.1	15	0.955	17.3					Bodnar, R.J. (1993) Revised equation and table for determining th
-10.3	ice	210.6	14.25	210.6	17	0.965	17.3					Bodnar, R.J. (1993) Revised equation and table for determining th
-8.2	ice	210.9	11.93	210.9	18	0.946	16.7					Bodnar, R.J. (1993) Revised equation and table for determining th
-7.4	ice	221.3	10.98	221.3	22	0.927	15.9					Bodnar, R.J. (1993) Revised equation and table for determining th
-7.2	ice	228.1	10.73	228.1	25	0.917	15.4					Bodnar, R.J. (1993) Revised equation and table for determining th
-0.8	ice	237.3	1.40	237.3	31	0.826	13.7					Bodnar, R.J. (1993) Revised equation and table for determining th
-3.0	ice	231.0	4.96	231.0	27	0.866	14.2					Bodnar, R.J. (1993) Revised equation and table for determining th
-2.9	ice	230.8	4.80	230.8	27	0.865	14.2					Bodnar, R.J. (1993) Revised equation and table for determining th
-2.2	ice	226.3	3.71	226.3	25	0.861	14.3					Bodnar, R.J. (1993) Revised equation and table for determining th
-7.4	ice	241.2	10.98	241.2	31	0.904	14.7					Bodnar, R.J. (1993) Revised equation and table for determining th
-8.4	ice	229.3	12.16	229.3	25	0.928	15.7					Bodnar, R.J. (1993) Revised equation and table for determining th
												#VALUE!
-3.7	ice	307.0	6.01	307.0	91	0.763	10.3					Bodnar, R.J. (1993) Revised equation and table for determining th
-2.7	ice	219.0	4.49	219.0	22	0.877	14.8					Bodnar, R.J. (1993) Revised equation and table for determining th
-8.0	ice	230.0	11.70	230.0	26	0.923	15.5					Bodnar, R.J. (1993) Revised equation and table for determining th
-4.0	ice	222.8	6.45	222.8	23	0.888	14.9					Bodnar, R.J. (1993) Revised equation and table for determining th
-9.4	ice	229.8	13.29	229.8	25	0.937	15.9					Bodnar, R.J. (1993) Revised equation and table for determining th
-3.9	ice	244.2	6.30	244.2	34	0.860	13.7					Bodnar, R.J. (1993) Revised equation and table for determining th
-4.0	ice	260.2	6.45	260.2	45	0.839	12.9					Bodnar, R.J. (1993) Revised equation and table for determining th
-8.2	ice	218.8	11.93	218.8	21	0.937	16.3					Bodnar, R.J. (1993) Revised equation and table for determining th
-5.0	ice	260.2	7.86	260.2	45	0.853	13.1					Bodnar, R.J. (1993) Revised equation and table for determining th
-2.9	ice	230.9	4.80	230.9	27	0.864	14.2					Bodnar, R.J. (1993) Revised equation and table for determining th
-3.0	ice	253.3	4.96	253.3	41	0.835	13.0					Bodnar, R.J. (1993) Revised equation and table for determining th
-8.6	ice	219.3	12.39	219.3	21	0.941	16.3					Bodnar, R.J. (1993) Revised equation and table for determining th
-8.3	ice	209.8	12.05	209.8	17	0.948	16.8					Bodnar, R.J. (1993) Revised equation and table for determining th
-4.0	ice	216.8	6.45	216.8	21	0.896	15.2					Bodnar, R.J. (1993) Revised equation and table for determining th
-8.2	ice	225.1	11.93	225.1	23	0.931	15.9					Bodnar, R.J. (1993) Revised equation and table for determining th
-5.3	ice	244.2	8.28	244.2	34	0.877	14.0					Bodnar, R.J. (1993) Revised equation and table for determining th
-3.7	ice	250.3	6.01	250.3	38	0.849	13.3					Bodnar, R.J. (1993) Revised equation and table for determining th
-3.8	ice	245.6	6.16	245.6	35	0.857	13.6					Bodnar, R.J. (1993) Revised equation and table for determining th
-5.4	ice	220.3	8.41	220.3	22	0.907	15.4					Bodnar, R.J. (1993) Revised equation and table for determining th
-3.3	ice	249.8	5.41	249.8	38	0.844	13.3					Bodnar, R.J. (1993) Revised equation and table for determining th
-4.2	ice	217.1	6.74	217.1	21	0.898	15.2					Bodnar, R.J. (1993) Revised equation and table for determining th
-3.1	ice	216.9	5.11	216.9	21	0.885	15.0					Bodnar, R.J. (1993) Revised equation and table for determining th
-3.5	ice	229.2	5.71	229.2	26	0.874	14.4					Bodnar, R.J. (1993) Revised equation and table for determining th
-4.5	ice	254.5	7.17	254.5	41	0.854	13.3					Bodnar, R.J. (1993) Revised equation and table for determining th
-3.0	ice	226.4	4.96	226.4	25	0.872	14.4					Bodnar, R.J. (1993) Revised equation and table for determining th
-1.0	ice	230.6	1.74	230.6	28	0.839	14.1					Bodnar, R.J. (1993) Revised equation and table for determining th
-4.7	ice	192.1	7.45	192.1	12	0.931	16.7					Bodnar, R.J. (1993) Revised equation and table for determining th
-3.1	ice	202.5	5.11	202.5	16	0.902	15.7					Bodnar, R.J. (1993) Revised equation and table for determining th
-4.4	ice	204.1	7.02	204.1	16	0.915	16.0					Bodnar, R.J. (1993) Revised equation and table for determining th
-3.8	ice	228.3	6.16	228.3	26	0.879	14.5					Bodnar, R.J. (1993) Revised equation and table for determining th
-11.4	ice	248.4	15.37	248.4	34	0.934	15.2					Bodnar, R.J. (1993) Revised equation and table for determining th
-4.7	ice	232.2	7.45	232.2	28	0.885	14.5					Bodnar, R.J. (1993) Revised equation and table for determining th
-4.5	ice	261.8	7.17	261.8	46	0.844	12.9					Bodnar, R.J. (1993) Revised equation and table for determining th
-3.3	ice	290.8	5.41	290.8	73	0.783	11.1					Bodnar, R.J. (1993) Revised equation and table for determining th
-1.5	ice	296.9	2.57	296.9	81	0.739	10.3					Bodnar, R.J. (1993) Revised equation and table for determining th
-4.4	ice	297.3	7.02	297.3	79	0.791	11.0					Bodnar, R.J. (1993) Revised equation and table for determining th
-3.6	ice	223.4	5.86	223.4	24	0.883	14.7					Bodnar, R.J. (1993) Revised equation and table for determining th
-4.1	ice	210.8	6.59	210.8	18	0.904	15.5					Bodnar, R.J. (1993) Revised equation and table for determining th
-4.0	ice	217.1	6.45	217.1	21	0.895	15.2					Bodnar, R.J. (1993) Revised equation and table for determining th
-3.8	ice	216.5	6.16	216.5	21	0.894	15.1					Bodnar, R.J. (1993) Revised equation and table for determining th
-3.7	ice	225.7	6.01	225.7	25	0.881	14.6					Bodnar, R.J. (1993) Revised equation and table for determining th

Inputs:			Outputs:					Inputs:		Outputs:		
			Salinity	T @ homog.	P @ homog.	r_{BULK}	dP/dT	Calculate a P correction?		Trapping Conditions		
Tm	phase	Th_{L-V} S (wt%)	wt% NaCl	(°C)	(bar)	/$cm_{3(g/cr}$	(bar/°C)	Based on:	T or P	T (°C)	P (bar)	References
-3.9	ice	207.6	6.30	207.6	17	0.905	15.6					Bodnar, R.J. (1993) Revised equation and table for determining th
-3.5	ice	229.2	5.71	229.2	26	0.874	14.4					Bodnar, R.J. (1993) Revised equation and table for determining th
-4.2	ice	208.7	6.74	208.7	18	0.907	15.7					Bodnar, R.J. (1993) Revised equation and table for determining th
-6.4	ice	217.5	9.73	217.5	21	0.921	15.8					Bodnar, R.J. (1993) Revised equation and table for determining th
-6.2	ice	210.4	9.47	210.4	18	0.927	16.2					Bodnar, R.J. (1993) Revised equation and table for determining th
-6.1	ice	218.8	9.34	218.8	21	0.917	15.6					Bodnar, R.J. (1993) Revised equation and table for determining th